

---

**OSA Proceedings on**

**SHORT WAVELENGTH COHERENT RADIATION:**  
**GENERATION AND APPLICATIONS**

---

**Volume 2**

---

## Technical Program Committee

---

- Roger W. Falcone**, *Cochair*  
University of California, Berkeley
- Janos Kirz**, *Cochair*  
SUNY-Stony Brook
- D. T. Attwood**  
Lawrence Berkeley Laboratory
- J. Bokor**  
AT&T Bell Laboratories
- Philip H. Bucksbaum**  
AT&T Bell Laboratories
- E. M. Campbell**  
Lawrence Livermore National Laboratory
- W. Eberhardt**  
Exxon Research and Engineering Company
- R. R. Freeman**  
AT&T Bell Laboratories
- S. E. Harris**  
Stanford University
- J. B. Hastings**  
Brookhaven National Laboratory
- Yoshiaki Kato**  
Osaka University, Japan
- J. M. J. Madey**  
Stanford University
- Thomas J. McIlrath**  
University of Maryland
- Y. Petroff**  
LURE, France
- E. D. Poliakoff**  
Boston University
- Charles K. Rhodes**  
University of Illinois
- G. Schmahl**  
University of Gottingen,  
Federal Republic of Germany

**OSA Proceedings on**  
**Short Wavelength Coherent Radiation:**  
**Generation and Applications**  
**Volume 2**

---

**Editors**  
**Roger W. Falcone and Janos Kirz**

**Proceedings of the Fourth Topical Meeting**  
**September 26-29, 1988**  
**North Falmouth, MA**

Sponsored by the Optical Society of America, the Air Force Office  
of Scientific Research, the U.S. Department of Energy, the  
National Science Foundation, and the Office of Naval Research.

Optical Society of America  
1816 Jefferson Place, N.W.  
Washington, DC 20036  
(202) 223-8130

tion For	
CRA&I	<input checked="" type="checkbox"/>
TAB	<input type="checkbox"/>
referred	<input type="checkbox"/>
action	
\$ 75.00	
per call	
A-1 21	



Articles in this publication may be cited in other publications. To facilitate access to the original publication source, the following form for the citation is suggested:

Name of Author(s), Title of Paper, OSA Proceedings on Short Wavelength Coherent Radiation: Generation and Applications, R. W. Falcone and J. Kirz, eds. (Optical Society of America, Washington, DC, 1988), Vol. 2, pp. xx-xx.

ISBN 1-55752-053-4

Library of Congress Catalog Card Number 88-63559

Copyright © 1988, Optical Society of America

Individual readers of this proceedings and libraries acting for them are permitted to make fair use of the material in it, such as to copy an article for use in teaching or research, without payment of fee, provided that such copies are not sold.

Permission is granted to quote excerpts from articles in this proceedings in scientific works with the customary acknowledgment of the source, including the author's name, name of the proceedings and the publisher, year, volume, and page. Reproduction of figures and tables is likewise permitted in other articles and books provided that the same information is printed with them, permission of one of the original authors is obtained, and notification is given to the Optical Society of America. Republication or systematic or multiple reproduction of any material in this proceedings is permitted only under license from the Optical Society of America; in addition, the Optical Society may require that permission also be obtained from one of the authors. In the case of articles whose authors are employees of the United States Government or its contractors or grantees, the Optical Society of America recognizes the right of the United States Government to retain a nonexclusive, royalty-free license to use the author's copyrighted article for United States Government purposes. Address inquiries and notices to Director of Publications, Optical Society of America, 1816 Jefferson Place, N.W., Washington, DC 20036.

The views and conclusions contained in this proceedings are those of the author(s) and should not be interpreted as necessarily representing endorsements, either expressed or implied, of the editors or the Optical Society of America.

Printed in the United States of America





---

## Preface

---

The Fourth Topical Meeting on Short Wavelength Coherent Radiation: Generation and Applications was held in North Falmouth, Massachusetts, September 26-29, 1988. This volume is a record of the exciting research presented at the conference. The most recent previous conferences in this series were held in Monterey, California (1986) and Boulder, Colorado (1984 and 1982).

The meeting brought together 164 participants, including scientists from Australia, Austria, Canada, China, England, France, Germany, Japan, the Soviet Union, Sweden, and the United States. It is a reflection of the continuing growth in the areas covered by the conference that the attendance at the meetings continues to grow and that the number of contributed papers grows even faster. This made it necessary to schedule many of the contributions for a particularly lively poster session that lasted far past its scheduled end at 10:00 pm.

Much of the conference was devoted to new results on short wavelength lasers. Progress in short wavelength synchrotron sources and nonlinear-optics techniques was also reported. Theoretical and experimental research was presented to describe the coupling of intense lasers with matter and the study of multiphoton and above-threshold ionization. A session was devoted to the remarkable coherence properties of nuclear Bragg-scattered radiation. In the applications area, new results were presented on x-ray optics, microscopy, holography, and spectroscopy.

We wish to express our appreciation to the Technical Program Committee for their help and valuable advice. The Optical Society of America made our task easy with excellent management, organization, and editorial support. We are particularly grateful to Mary Ellen Malzone, Barbara Hicks, Cindy Martin, and Donna Leggett for their tireless efforts. Janice Fleming has expertly guided the publication of the proceedings book with great efficiency. We gratefully acknowledge the generous financial support that was provided for the conference by the Air Force Office of Scientific Research, the Office of Naval Research, the U.S. Department of Energy, the National Science Foundation, and the Optical Society of America. We are also grateful to our industrial sponsor, Acton Research Corporation.

Roger W. Falcone  
Berkeley, CA

Janos Kirz  
Stony Brook, NY

December 1988



## Contents

---

### Part 1    Short Wavelength Lasers and Other Sources

---

Progress Toward a 44-Å X-Ray Laser by B. J. MacGowan, J. L. Bourgade, P. Combis, C. J. Keane, R. A. London, M. Louis-Jacquet, D. L. Matthews, S. Maxon, D. Naccache, M. D. Rosen, G. Thiell, and D. A. Whelan . . . . .	2
Observation of Extreme Ultraviolet Amplification in 3-2 (42 ~ 46Å), 4-3 (130.5Å) and 5-4 (305Å) Transitions in Laser Produced He-like Al Plasma by H. Kuroda, K. Muroo, K. Naito, and Y. Tanaka . . . . .	11
12.8 eV Laser in Neutral Cesium by C. P. J. Barty, D. A. King, G. Y. Yin, K. H. Hahn, J. E. Field, J. F. Young, and S. E. Harris . . . . .	13
X-Ray Laser Experiment with Double Pass Device and Long-Recombining-Plasma Column by P. Jaegle, A. Carillon, P. Dhez, B. Gauthe, F. Gadi, G. Jamelon, and A. Klisnick . . . . .	21
Short Wavelength Lasers: Something New, Something Old by P. L. Hagelstein . . . . .	28
X-Ray Laser Related Experiments and Theory at Princeton by S. Suckewer . . . . .	36
Amplification in Na XI H $\alpha$ , Mg XII H $\alpha$ and Al XIII H $\alpha$ Transitions by Y. Kato, M. Yamanaka, H. Daido, T. Tachi, H. Nishimura, H. Shiraga, E. Miura, P. R. Herman, H. Takabe, T. Jitsuno, M. Takagi, S. Nakai, C. Yamanaka, M. H. Key, G. J. Tallents, and S. J. Rose . . . . .	47
Population Inversion through Charge Exchange Process in Plasmas by T. Kato, K. Masai, and T. Fujimoto . . . . .	52
Prepulsing to Increase the Efficiency of Laser-Produced-Plasma Pumped Lasers by M. H. Sher and S. J. Benerofe . . . . .	60

Amplification and Gain Measurement of Extreme Ultraviolet Radiation (42.4Å, 45Å and 46Å) in He-like Al Laser Plasma by K. Muroo, Y. Tanaka, and H. Kuroda . . . . .	65
Population Inversions between $n = 5, 4, 3$ and 2 Levels of He-Like Al Plasma Observed by Spatially Resolved X-Ray Spectroscopy by H. Kuroda, M. Katsuragawa, K. Muroo, and Y. Tanaka . . . . .	67
Probability of Soft X-Ray Radiation for 3p-3s Transition in Neon-Like Iron by Huimin Peng, Guoping Zhang, Jiatian Sheng, and Yunfeng Shao . . . . .	69
Harmonic Generation in Laser-Free Electron Scattering Reconsidered by Anna K. Puntajer and C. Leubner . . . . .	76
Gain Guided X-Ray Beams by Ernst E. Fill . . . . .	78
CO <sub>2</sub> Laser-Heated Plasmas for Electron-Collisionally Pumped XUV Laser Studies by G. D. Enright and N. H. Burnett . . . . .	84
Ne-Like Ion X-Ray Laser Experiments in Plasmas Produced by 0.53- $\mu$ m and 0.35- $\mu$ m Laser Light by C. J. Keane, J. L. Bourgade, P. Combis, R. A. London, M. Louis-Jacquet, B. J. MacGowan, D. L. Matthews, D. Naccache, O. Peyrusse, M. D. Rosen, G. Thiell, and B. Whitten . . . . .	93
Capillary Discharge Plasmas as Extreme Ultraviolet Laser Sources by J. J. Rocca, M. C. Marconi, M. Villagran Muniz, and D. C. Beethe . . . . .	99
High Power, Short Pulse Ultra-Violet Laser for the Development of a New X-Ray Laser by L. D. Meixler, C. H. Nam, J. Robinson, W. Tighe, K. Krushelnick, S. Suckewer, J. Goldhar, J. Seely, and U. Feldman . . . . .	106
Soft X-Ray Amplification in a Magnetically Confined Recombining H-like and Li-like Plasma by D. Kim, C. H. Skinner, A. Wouters, E. Valeo, D. Voorhees, and S. Suckewer . . . . .	116
Calculation and Design of Ni-Like W Soft X-Ray Lasers by S. Maxon, S. Dalhed, P. Hagelstein, B. MacGowan, R. London, and M. Rosen . . . . .	123
Quantum-Mechanical Interference in Four-Wave Mixing by P. B. Chapple, K. G. H. Baldwin, and H.-A. Bachor . . . . .	125
Transversely Optically Pumped Ultraviolet Laser in the Range of 330-390 nm by Junhua Yu, Shangwen Sun, Yongkang Cheng, Chen Tang, and Zuguang Ma . . . . .	129

Spectra of Lead, Bismuth, Thorium and Uranium Relevant to a Neodymium-Like Soft X-Ray Lasing Scheme by W. L. Hodge, P. C. Filbert, D. A. Kohler, C. L. Navoda, J. D. Perez, P. L. Hagelstein, S. Maxon, J. H. Scofield, and J. M. Peek . . . . .	133
Soft X-Ray Lasing of Li-like Ions in Laser-Produced Plasmas by Yim T. Lee and W. M. Howard . . . . .	135
Time Development of Amplification in Na XI $H\alpha$ -Line at 54.19 Å by H. Nishimura, H. Shiraga, H. Daido, T. Tachi, P. R. Herman, E. Miura, H. Takabe, M. Yamanaka, Y. Kato, G. J. Tallents, and M. H. Key . . . . .	137
Gain Measurement on a 18.2-nm Carbon Recombination Laser Produced by an Intense CO <sub>2</sub> Laser by H. Daido, E. Miura, Y. Kitagawa, K. Nishihara, Y. Kato, C. Yamanaka, and S. Nakai . . . . .	141
Narrow Line X-Ray Transition Radiation by Electron Beam Traversing a Solid-State Superlattice by A. E. Kaplan and C. T. Law . . . . .	145
VUV Amplification of Neon-Like Titanium Ion by Hidehiko Yashiro, Tamio Hara, Kozo Ando, Yoshinobu Aoyagi, Toshihiko Dote, and Susumu Namba . . . . .	154
X-Ray Laser Research at Physics International by C. Deeney, J. Levine, T. Nash, P. D. LePell, and M. Krishnan . . . . .	157
Continuous Anti-Stokes Raman Laser Operation by A. Feitisch and B. Welleghausen . . . . .	163
Ultrahigh Peak Power Pulses Produced by Chirped Pulse Amplification by P. Maine, D. Strickland, B. Bado, and G. Mourou . . . . .	165
Multiterawatt Excimer Laser System by S. Watanabe, A. Endoh, M. Watanabe, and N. Sarukura . . . . .	167
Narrowband Tunable VUV/XUV Radiation Generated by Frequency Mixing of Pulsed and CW Laser Radiation by G. Hilber, A. Lago, and R. Wallenstein . . . . .	175
High Efficiency, Scalable, 130 nm Coherent Source by Four-Wave Mixing in Hg Vapor by C. H. Muller, III, C. E. Hamilton, D. D. Lowenthal, and A. V. Smith . . . . .	177
Intense Coherent Radiation in the VUV and XUV Region with Electron Beam Pumped Rare Gas Excimer Lasers by Wataru Sasaki, Kou Kurosawa, Peter R. Herman, Kunio Yoshida, and Yoshiaki Kato . . . . .	184

X-Ray Emission Studies of Sub-Picosecond Laser Produced Plasmas by M. M. Murnane, H. C. Kapteyn, and R. W. Falcone . . . . .	189
Observations of High Density Plasmas Produced with a Picosecond High Power KrF Laser by O. Willi, G. Kiehn, J. Edwards, V. Barrow, and R. Smith . . . . .	194
Current Prospects for Free-Electron Lasers in the Extreme Ultraviolet by Brian E. Newnam . . . . .	200
Compact X-Ray Free-Electron Laser by W. Barletta, M. Atac, A. Bhowmik, B. Bobbs, D. B. Cline, R. A. Cover, F. P. Dixon, J. Gallardo, J. Kolonko, C. Pellegrini, G. Rakowsky, X. Wang, and G. Westenskow . . . . .	202
Targets for Efficient Femtosecond-Time-Scale X-Ray Generation by J. D. Kmetec and S. E. Harris . . . . .	209

---

## Part 2    High Intensity Laser Interaction with Matter

---

The Stark Effect in Atoms at Extremely High Intensities: Ponderomotive Potentials and All That by Richard R. Freeman . . . . .	214
Strong-Field Processes in the Ultraviolet Region by K. Boyer, G. Gibson, H. Jara, T. S. Luk, I. A. McIntyre, A. McPherson, R. Rosman, J. C. Solem, and C. K. Rhodes . . . . .	220
Multiphoton Ionization for the Production of X-Ray Laser Plasmas by P. B. Corkum and N. H. Burnett . . . . .	225
Charge-Displacement Self-Channeling as a Method for Energy Concentration by K. Boyer, T. S. Luk, J. C. Solem, and C. K. Rhodes . . . . .	233
Stimulated Compton Backscattering and the High Intensity Kapitza-Dirac Effect by D. W. Schumacher, P. H. Bucksbaum, and M. Bashkansky . . . . .	236
Search for X-Rays Generated by Collisionless Multiphoton Processes by Peter H. Y. Lee, Donald E. Casperson, and Gottfried T. Schappert . . . . .	242
Characteristics of a Non-Equilibrium Picosecond Laser Plasma by G. Gibson, R. Rosman, T. S. Luk, I. A. McIntyre, A. McPherson, G. Wendin, K. Boyer, and C. K. Rhodes . . . . .	246
Investigations of Multiphoton Excitation and Ionization in a Short Range Potential by S. M. Susskind, S. C. Cowley, and E. J. Valeo . . . . .	251

Multiphoton Spectroscopy of Multielectron Atoms and the Quest for Direct Two-Electron Ejection by P. Lambropoulos . . . . .	256
Symmetries and Asymmetries in Above-Threshold Ionization by P. H. Bucksbaum, M. Bashkansky, and D. W. Schumacher . . . . .	258
Multiphoton Ionization with Femtosecond Laser Pulses by H. G. Muller . . . . .	265
High-Order Harmonics in Light Scattering by Atomic Electrons Above Threshold by J. H. Eberly, Q. Su, and J. Javanainen . . . . .	266

---

### Part 3    Microscopy and Holography

---

X-Ray Microscopy for the Life and Physical Sciences by D. Attwood, Y. Vladimirovsky, D. Kern, W. Meyer-Ilse, J. Kirz, S. Rothman, H. Rarback, N. Iskander, K. McQuaid, H. Ade, and T. H. P. Chang . . . . .	274
Contact Microscopy with a Soft X-Ray Laser by D. S. DiCicco, D. Kim, R. J. Rosser, C. H. Skinner, S. Suckewer, A. P. Gupta, and J. G. Hirschberg . . . . .	277
X-Ray Fourier-Transform Holographic Microscope by W. S. Haddad, D. Cullen, J. C. Solem, K. Boyer, and C. K. Rhodes . . . . .	284
First Images from the Stanford Tabletop Scanning Soft X-Ray Microscope by J. A. Trail and R. L. Byer . . . . .	290
Progress in Optical Reconstruction of Submicron X-Ray Holograms by D. Joyeux and F. Polack . . . . .	295
X-Ray Holographic Microscopy: Improved Images of Zymogen Granules by Chris Jacobsen, Malcolm Howells, Janos Kirz, Kenneth McQuaid, and Stephen Rothman . . . . .	303
Amplitude- and Phase-Contrast Microscopy by G. Schmahl . . . . .	309
X-Ray Holography: X-Ray Interactions and Their Effects by Richard A. London, James E. Trebes, and Mordecai D. Rosen . . . . .	310

---

**Part 4 Optics and Detectors**

---

Recent Advances and Prospects of Bragg-Fresnel Optics by V. V. Aristov . . . . .	318
Reflectance of Aluminum Reflectors in the Extreme Ultraviolet by Marion L. Scott . . . . .	322
Soft X-Ray Lenses with 400 Å Outer Zone Width by Y. Vladimirovsky, D. Kern, T. H. P. Chang, W. Meyer-Ilse, P. Guttman, B. Greinke, and D. Attwood . . . . .	325
Soft X-Ray Spectroscopy of Laser-Produced Plasma by Shi-sheng Chen, Zhi-zhan Xu, and Zheng-quan Zhang . . . . .	326
Large Holographic Diffraction Gratings Made by a Multiple Exposure Technique by L. Wosinski and M. Breidne . . . . .	327
Effectiveness of Metal-Coated Diffraction Gratings at Grazing and Near Normal Incidence as Harmonic Scrubbers by P. J. Wantuck, Q. D. Appert, K. Tong, and D. J. Pistoressi . . . . .	329
Saddle Toroid Arrays: Novel Grazing Incidence Optics for Synchrotron X-Ray Lithography by R. J. Rosser and P. M. J. H. Wormell . . . . .	339
Diffraction Contrast of a Bragg-Fresnel Lens in White and Monochromatic Radiation by V. V. Aristov, Yu. A. Basov, R. Frahm, W. Graeff, G. Materlik, and A. A. Snigirev . . . . .	347
Proposed Method for the Measurement of the Spatial Coherence of Laboratory X-Ray Lasers by James Trebes, Troy Barbee, Howard Nathel, and Abraham Szoke . . . . .	350
Coplanar Vacuum Photodiode for Measurement of Short-Wavelength Picosecond Pulses by J. Bokor, A. M. Johnson, W. M. Simpson, and R. H. Storz . . . . .	355
X-Ray Optics for X-Ray Laser Research Applications by N. M. Ceglio . . . . .	357
Sub-Nanosecond, Photon Counting, Imaging, X-Ray Camera by D. A. Whelan, M. R. Carter, D. F. Price, and R. E. Stewart . . . . .	371
Parabolic Mirror Electron Energy Analyzer for Multiphoton Photoemission Spectroscopy by L. D. Van Woerkom, D. J. Trevor, and R. R. Freeman . . . . .	378



---

**Part 5    Spectroscopy and Other Applications**

---

Vacuum Ultraviolet Laser Spectroscopy of Molecular Autoionizing States by D. Milburn, D. J. Hart, and J. W. Hepburn . . . . .	384
Time-Resolved Study of Surface Recombination at Si(111) Surfaces by N. J. Halas and J. Bokor . . . . .	392
Coherent Excitations of Nuclei in Crystals by Synchrotron Radiation Pulses by G. T. Trammell and J. P. Hannon . . . . .	394
Nuclear Bragg Diffraction Using Synchrotron Radiation by Rudolf Ruffer . . . . .	400
The Production of Long Coherence-Length Hard X-Rays Using Nuclear Bragg Scattering of Synchrotron Radiation by D. P. Siddons . . . . .	401
Measurement of the Quenching of Spontaneous Emission Coefficients in Laser-Produced Plasmas by Y. Chung, H. Hirose, and S. Suckewer . . . . .	402
Ultra-High Resolution VUV-XUV Laser: Application to the Hyperfine Study of Krypton by A. H. Kung, T. Trickl, E. Cromwell, M. J. J. Vrakking, and Y. T. Lee . . . . .	411
Non-Reciprocity of Autoionizing Interferences: Lasers Without Inversion by S. E. Harris . . . . .	414
Studies of Hot, Solid Materials Produced by an Ultrashort Pulse Laser by H. M. Milchberg and R. R. Freeman . . . . .	418
All Short Pulse Multiphoton Ionization is Resonant Ionization by W. Cooke, R. R. Freeman, and T. J. McIlrath . . . . .	422
Index of Authors . . . . .	425



---

**Part 1**  
**Short Wavelength Lasers and Other Sources**

---

## Progress Towards a 44-Å X-Ray Laser

B. J. MacGowan,<sup>\*</sup> J. L. Bourgade,<sup>†</sup> P. Combis,<sup>†</sup> C. J. Keane,<sup>‡</sup> R. A. London,<sup>‡</sup>  
M. Louis-Jacquet,<sup>†</sup> D. L. Matthews,<sup>‡</sup> S. Maxon,<sup>‡</sup> D. Naccache,<sup>†</sup>  
M. D. Rosen,<sup>‡</sup> G. Thiell,<sup>†</sup> and D. A. Whelan<sup>‡</sup>

<sup>\*</sup>*Center for X-Ray Optics, Lawrence Berkeley Laboratory, 1 Cyclotron Road  
University of California, Berkeley, California 94720*

<sup>†</sup>*Centre d'Etudes de Limeil-Valenton, B.P. 27, 94190 Villeneuve St. Georges, France*

<sup>‡</sup>*Lawrence Livermore National Laboratory, University of California  
P.O. Box 808, Livermore, California 94550*

### Abstract

Since 1984 when soft x-ray amplification was convincingly demonstrated at XUV wavelengths near 200 Å, much effort has gone into obtaining soft x-ray gain at shorter wavelengths. One motivation is the possibility of using a high brightness source of amplified spontaneous emission to perform holography of live biological specimens over short time scales.

### Introduction

A strong motivation for the development of a soft x-ray laser is the possibility of imaging biological specimens holographically. This application would require a bright source of coherent radiation with a wavelength close to the 43.76-Å K absorption edge of carbon.<sup>1</sup>

This article will summarize progress to date in the field of soft x-ray laser development. The main emphasis will be on experiments carried out at Lawrence Livermore National Laboratory although the large amount of progress at other laboratories will be mentioned.

Collisionally pumped schemes for producing population inversion and hence gain in both neon-like and nickel-like high-Z ions will be described. The results of experiments with recombination schemes in lower Z ions will also be briefly discussed.

### Neon-like Schemes

The possibility of producing a 3p - 3s population inversion, within a hot plasma of ions isoelectronic to Ne I, was first published in the literature by Zherikhin et al.,<sup>2</sup> in 1976. Subsequent work<sup>3,4</sup> indicated that the population

inversion should be maintained, steady state, within a plasma produced by short-pulse optical laser irradiation of matter. The population inversion was predicted to be produced by the plasma thermal electrons collisionally exciting electrons from the Ne-like 2p<sup>6</sup> ground state to the 2p<sup>5</sup><sub>1/2</sub>3p<sub>1/2</sub>)<sub>0</sub> (J = 0) level. The population of the J = 0 level was then expected to produce large gains (10-20 cm<sup>-1</sup>) on the 2p<sup>5</sup><sub>1/2</sub>3p<sub>1/2</sub>)<sub>0</sub> - 2p<sup>5</sup><sub>1/2</sub>3s)<sub>1</sub> (J = 0 - 1) transition (at 182 Å in Se<sup>24+</sup>). The population inversion is maintained by the very rapid 3s - 2p radiative decay rate.

Experiments at LLNL in 1984 succeeded in demonstrating gain in Ne-like selenium at 206 and 209 Å in an exploding foil amplifier.<sup>5,6</sup> The amplifier consisted of a thin foil of Se on a Fornvar (C<sub>11</sub>H<sub>18</sub>O<sub>5</sub>) substrate that was irradiated by two opposed high-intensity beams of short-pulse optical laser light focused into a 1.1-cm-long line. The plasma formed by the heating and subsequent explosion of the foil served as the amplifying medium. The large density scale lengths (of order 100 μm) within the plasma allowed 200-Å radiation to propagate down the length of the amplifier without being refracted out of the gain region. The ability to propagate radiation over large lengths is essential in order to achieve a large gain length product and hence significant amplification. The electron density and temperature in the gain region were 3-5 x 10<sup>20</sup> cm<sup>-3</sup> and 1 keV, respectively. Various other mechanisms contribute to the population of the J = 0 and other levels in the 3p manifold, (dielectronic recombination from F-like, cascading from higher n states and the 3d levels), leading to the possibility of gain on other 3p - 3s transitions such as the 206 and 209 Å, J = 2 - 1 lines.<sup>7</sup> A surprising result of the experiments of Ref. 5 was

that, although large amplification was observed for the  $J = 2 - 1$  lines, the  $J = 0 - 1$  line was not even unambiguously identified.

Figure 1 shows sample time integrated spectra from Se exploding foil plasmas of different lengths. The spectra were taken "on-axis", that is looking down the long axis of the cylindrical plasma produced by the line focus. The brightest lines are the  $J = 2 - 1$  transitions at 206.38 and 209.78 Å (Ref. 8) which are observed to increase dramatically in intensity as the length of the target is increased. The spectra were taken from exploding foils of Se of areal density  $45 \mu\text{g cm}^{-2}$  irradiated with a total of  $7 \times 10^{13} \text{ W cm}^{-2}$  in a 450 psec pulse of  $2\omega$  ( $\lambda = 0.53 \mu\text{m}$ ) light. The data are from the original Novette experiments of Ref. 5 when the maximum length line focus achievable with the cylindrical optics, then available, was 1.1 cm.

In the 0.5- and 1-cm experiments shown in Fig. 1, the irradiance was obtained by superposing the two 1.1-cm beams on either side of the target. For the last spectrum, from the 2.2-cm plasma, the target was irradiated by offsetting the two 1.1-cm-long line foci on either side of the foil, end to end, making a total length of 2.2 cm. The irradiation geometry in the latter case was not optimum. In experiments limited to foils irradiated with the superposed beams, a gain of  $5.5 \text{ cm}^{-1}$  was measured by fitting the increase in line intensity with plasma length to the formula:

$$I = I_0 e^{\alpha l} (\alpha l)^{-1/2} \quad (1)$$

for the scaling of the output of a spatially and temporally uniform source of amplified

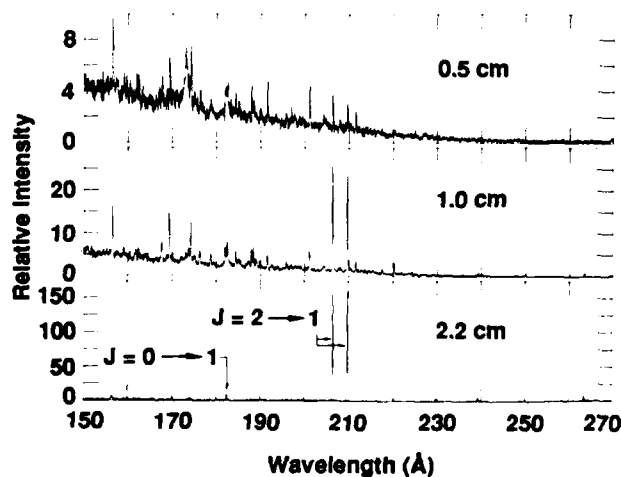


Figure 1. On axis spectra from Se exploding foil plasmas of various lengths showing the non-linear increase in intensity of the Ne-like lines as a function of plasma length.

spontaneous emission of length  $l$  and line center gain  $\alpha$ . Due to the irradiation geometry, the observed line intensity for the 2.2-cm data is not consistent with such a gain; however, it was the brightest signal obtained in the experiments of Ref. 5 and serves to illustrate how intense the neon-like lines are when amplified. The equivalent Planckian radiation temperature of the line emission at 206 and 209 Å was estimated in Ref. 5 to be 30 keV, far in excess of the temperature of any component of the plasma and, hence, further evidence that the line emission was being amplified. Additional, time-resolved data, demonstrated that the amplified spontaneous emission had a time duration of order 200 ps, much shorter than that of the heating pulse and indicative that it was being produced by a strongly time varying phenomenon such as a transient gain.

In later experiments performed at the Nova laser,<sup>9,10</sup> the length of the line focus available for each of two superposed beams was increased to 5 cm. The subsequent observations of the scaling of the brightness of the neon-like lines over lengths up to 5 cm resulted in gain measurements for three other lines besides the 206 and 209 Å,  $J = 2 - 1$  transitions observed in the first experiments. In particular, the  $J = 0 - 1$  line was identified at 182.43 Å (Ref. 8) but with significantly less gain than expected.

The scaling of line-intensity data was fit to the equation:

$$I = I_0 (e^{\alpha l} - 1)^{3/2} (\alpha l e^{\alpha l})^{-1/2} \quad (2)$$

for the output power of a source of unsaturated amplified spontaneous emission of length  $l$ .<sup>11</sup> This formula is an approximation for the frequency integrated power, assuming constant gain  $\alpha$  in space and time, for the usual case of a Doppler broadened line. It is exact in the large and small positive  $\alpha l$  limits, with a maximum error of 10% for intermediate  $\alpha l$ . Equation (2) is more accurate than Eq. (1) which is not valid for  $\alpha l$  less than 2. Figure 2 shows the intensity of the 206.38 Å,  $J = 2 - 1$  line of selenium for target lengths up to 4 cm. The fit to Eq. (2) results in a gain of  $4.0 \text{ cm}^{-1}$ . The gains of the other four Ne-like 3p - 3s lines were measured in the same way and are summarized in Table 1.

The Ne-like Se result has been isoelectronically scaled to higher Z ions. Y<sup>29+</sup> has shown gain at 155.0 and 157.1 Å, whilst Mo<sup>32+</sup> has produced a gain of  $4 \text{ cm}^{-1}$  at 131.0 and 132.7 Å (Ref. 12). Cu<sup>19+</sup> and Ge<sup>22+</sup> have shown gain near 280 and 230 Å in experiments carried out at the Naval Research Laboratory.<sup>13</sup> Also experiments performed at the Centre d'Etudes de Limeil-Valenton<sup>14</sup> have

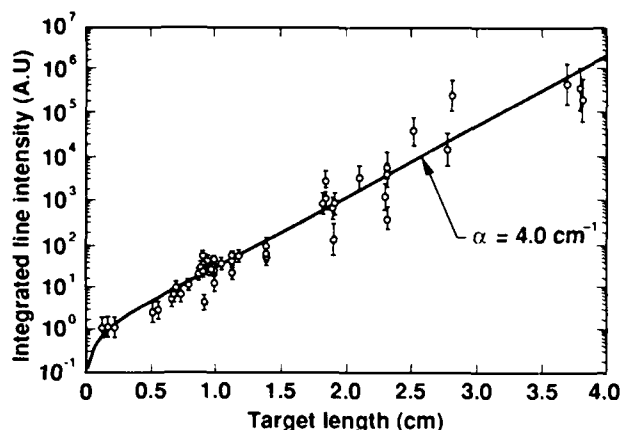


Figure 2. The scaling of intensity of the 206.38-Å Ne-like Se  $J = 2 - 1$  transition with target length. The data can be fit to a small signal gain of  $4.0 \text{ cm}^{-1}$ .

demonstrated gain at 164.1 and 166.5 Å in a plasma of  $\text{Sr}^{28+}$ . The observed gains and gain lengths for all of the experiments mentioned are summarized in Table 1 along with the experimental conditions.

One observation to be made from Table 1 is that the required pump laser intensity is increasing very rapidly as the wavelength of the lasing transition is reduced.<sup>15</sup> The increase in irradiance between  $\text{Se}^{24+}$  and  $\text{Mo}^{32+}$  was from  $7 \times 10^{13}$  to  $4 \times 10^{14} \text{ W cm}^{-2}$ . So far attempts to produce gain in the 80 to 100 Å region, with  $\text{Ag}^{37+}$  at irradiances of up to  $10^{16} \text{ W cm}^{-2}$ , have been unsuccessful.<sup>16</sup> To obtain gain near 43.76 Å, with a  $3p - 3s$  transition in a Ne-like ion, would require  $\text{Gd}^{54+}$  with an estimated irradiance in excess of  $10^{16} \text{ W cm}^{-2}$ . Such an irradiance would be difficult to produce over a long line focus with currently available laser drivers.

A further observation to be made from Table 1 is that the  $J = 0 - 1$  line ( $E(0-1)$ ) has not been observed to have a significantly higher gain than other transitions, in contradiction to predictions<sup>2-4,6</sup>. The explanation for the low gain on the  $J = 0 - 1$  line is still not understood.

### Nickel-like Schemes

The concept of a Ni-like  $4d - 4p$  analog to the Ne-like  $3p - 3s$  scheme has been described in the literature<sup>16-18</sup> and has recently been demonstrated experimentally<sup>19-21</sup>. The population inversion necessary for amplification is produced between the  $3d^9 4d$  and  $3d^9 4p$  levels, the latter level then decays radiatively to a  $3d^{10}$  Ni-like closed-shell ground state. Because of the larger

splitting between the  $4d$  and  $4p$  levels (compared to that between the  $3p$  and  $3s$  levels of a Ne-like ion with the same ionization potential), the wavelengths of lasing transitions are significantly shorter than those of Ne-like ions produced with the same heating laser intensity.

A Ni-like laser was first demonstrated<sup>19,20</sup> with  $\text{Eu}^{35+}$  produced by the irradiation of a thin ( $60 \mu\text{g cm}^{-2}$ ) foil of  $\text{EuF}_2$  by two superposed beams of  $2\omega$  light with a total irradiance of  $7 \times 10^{13} \text{ W cm}^{-2}$ . This irradiance was similar to that used to produce lasing transitions near 200 Å in  $\text{Se}^{24+}$  during the first Ne-like experiments; however, the  $4d - 4p$  lasing transitions observed from the  $\text{Eu}^{35+}$  were at 71.00 and 65.83 Å.

Figure 3 shows details from the spectra of different length  $\text{EuF}_2$  targets, in the region near the lasing lines. The two  $J = 0 - 1$  lines are observed to increase at a rate faster than linear as the target length is increased whilst other (non-lasing) lines increase linearly or at a rate less than linear. Fitting the scaling of line intensity to Eq. (2) resulted in gains of 1.1 and  $0.6 \text{ cm}^{-1}$  for the 71.00 and 65.83 Å lines, respectively. These measured gains were in good agreement with the predicted gains from detailed calculations<sup>19</sup>.

Two other Ni-like  $4d-4p$  lines were identified at 100.39 and 104.56 Å. These are the  $3d^9_{5/2} 4d_{5/2} \rightarrow 3d^9_{5/2} 4p_{3/2}$ ,  $J = 2-1$ , and the  $3d^9_{5/2} 4d_{5/2} \rightarrow 3d^9_{5/2} 4p_{3/2}$ ,  $J = 1-1$ , transitions,

respectively. Although these lines were observed to be bright, in an axis spectra, their length

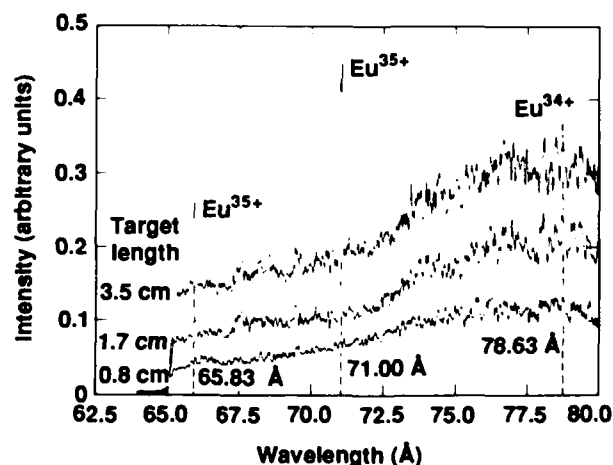


Figure 3. Details from on-axis spectra of  $\text{EuF}_2$  targets of various lengths, showing the exponential increase in intensity of the  $J = 0 - 1$  line at 65.83 and 71.00 Å with target length. Reproduced with permission from Ref. 20. Copyright 1987, The American Physical Society.

Table 1. Summary of achievements to date with neon-like schemes.

Ion	Transition	$\lambda(\text{\AA})$	Target Areal Density ( $\mu\text{gcm}^{-2}$ )	Irradiance ( $\text{Wcm}^{-2}$ ) (Pulselength)	$\lambda_{\text{pump}}$ ( $\mu\text{m}$ )	Gain ( $\text{cm}^{-1}$ )	Gain Length	Ref
Cu <sup>19+</sup>	A(2-1)	279.31	1200	6x10 <sup>12</sup> (2ns)	1.05	1.7	2.7	13
	B(2-1)	284.67				1.7	2.7	
	E(0-1)	221.11				2.0	3.2	
Ge <sup>22+</sup>	A(2-1)	232.24	Solid	6x10 <sup>12</sup> (2ns)	1.05	4.1	6.2	13
	B(2-1)	236.26				Blend	Blend	
	E(0-1)	196.06				3.1	4.6	
Se <sup>24+</sup>	A(2-1)	206.38	45	7x10 <sup>13</sup> (0.5ns)	0.53	4.0	16.0	9,10
	B(2-1)	209.78				3.8	15.2	
	C(2-1)	262.94				3.5	11.8	
	D(1-1)	220.28				2.2	9.2	
	E(0-1)	182.43				2.4	9.6	
Sr <sup>28+</sup>	A(2-1)	164.1	90(SrF <sub>2</sub> )	1.4x10 <sup>14</sup> (0.5ns)	0.53	4.4	9.7	14
	B(2-1)	166.5				4.0	8.8	
	E(0-1)	159.8				Blend	Blend	
Y <sup>29+</sup>	A(2-1) + E(0-1)	155.0	47	1.4x10 <sup>14</sup> (0.5ns)	0.53	~ 4	~ 11	-
	B(2-1)	157.1				~ 4	~ 11	
Mo <sup>32+</sup>	A(2-1)	131.0	88(Mo <sub>2</sub> N)	4x10 <sup>14</sup> (0.5ns)	0.53	4.1	7.1	12
	B(2-1)	132.7				4.2	7.3	
	D(1-1)	139.4				2.9	5.0	
	E(0-1)	141.6				0	0	
	F(0-1)	106.4				2.2	3.8	
Ag <sup>37+</sup>	A(2-1)	99.3		> 10 <sup>15</sup>	Prediction only			
	B(2-1)	100.3				Prediction only		
	E(0-1)	122.7				Prediction only		
	F(0-1)	81.5				Prediction only		
Transitions:	A(2-1)	2p <sup>5</sup> <sub>3/2</sub> 3p <sub>3/2</sub> ) <sub>2</sub> - 2p <sup>5</sup> <sub>3/2</sub> 3s) <sub>1</sub>						
	B(2-1)	2p <sup>5</sup> <sub>1/2</sub> 3p <sub>3/2</sub> ) <sub>2</sub> - 2p <sup>5</sup> <sub>1/2</sub> 3s) <sub>1</sub>						
	C(2-1)	2p <sup>5</sup> <sub>3/2</sub> 3p <sub>1/2</sub> ) <sub>2</sub> - 2p <sup>5</sup> <sub>3/2</sub> 3s) <sub>1</sub>						
	D(1-1)	2p <sup>5</sup> <sub>3/2</sub> 3p <sub>3/2</sub> ) <sub>1</sub> - 2p <sup>5</sup> <sub>3/2</sub> 3s) <sub>1</sub>						
	E(0-1)	2p <sup>5</sup> <sub>1/2</sub> 3p <sub>1/2</sub> ) <sub>0</sub> - 2p <sup>5</sup> <sub>1/2</sub> 3s) <sub>1</sub>						
	F(0-1)	2p <sup>5</sup> <sub>3/2</sub> 3p <sub>3/2</sub> ) <sub>0</sub> - 2p <sup>5</sup> <sub>3/2</sub> 3s) <sub>1</sub>						

scaling was close to linear ( $\alpha \sim 0$ ). This observation was in contradiction to calculations<sup>19</sup> which predicted gains of order  $1 \text{ cm}^{-1}$  on both lines. A possible reason for the lack of gain on these lines could be that the plasma electron temperature is lower than in the calculation.<sup>22</sup> Just like the  $J = 2$  and  $J = 1$  levels in Ne-like ions, these lines should be fed by many processes, but a significant contribution should come from

dielectronic recombination from the cobalt-like ion stage which would be reduced by a lower electron temperature. Another possibility is that trapping by self-absorption of photons from the  $4p - 3d$  dump lines are elevating the population in the  $4p$  state. This process would discriminate against the  $J = 2 - 1$  and  $J = 1 - 1$  compared to the  $J = 0 - 1$  lines due to the ratio of the statistical weights of the upper and lower levels being

larger for the former transitions. The population inversions, and hence gains, of the  $J = 2 - 1$  and  $J = 1 - 1$  are affected more by a change in the lower level population than are the  $J = 0 - 1$  transitions.

The Ni-like scheme is particularly attractive because it should allow extrapolation to wavelengths close to 44 Å without a prohibitive increase in pump power. Figure 4 shows the scaling of the wavelengths of the four most prominent Ni-like 4d - 4p lines with nuclear charge. The shorter wavelength  $J = 0 - 1$  line (65.83 Å in Eu) is the most promising candidate for a 44-Å laser. Both the 65.83 and 71.00 Å,  $J = 0 - 1$  transitions originate from the same level. The main reason for their different gains is that, in  $\text{Eu}^{35+}$ , the 65.83-Å line has a smaller oscillator strength. Although this line has less gain than the 71.00-Å line in Eu, its oscillator strength becomes larger than that of the longer wavelength  $J = 0 - 1$  at a nuclear charge of 70 (Ref. 23). At a nuclear charge near 74 (tungsten), the oscillator strength of the shorter wavelength line (at 43.16 Å) is a factor of two larger than that of the longer wavelength line.

The extrapolation of the Ni-like scheme to higher  $Z$  has been investigated in experiments<sup>21</sup> with  $\text{Yb}^{42+}$ . Targets of 100  $\mu\text{g cm}^{-2}$  of Yb on 10  $\mu\text{g cm}^{-2}$  of CH were irradiated with  $1.4 \times 10^{14} \text{ W cm}^{-2}$

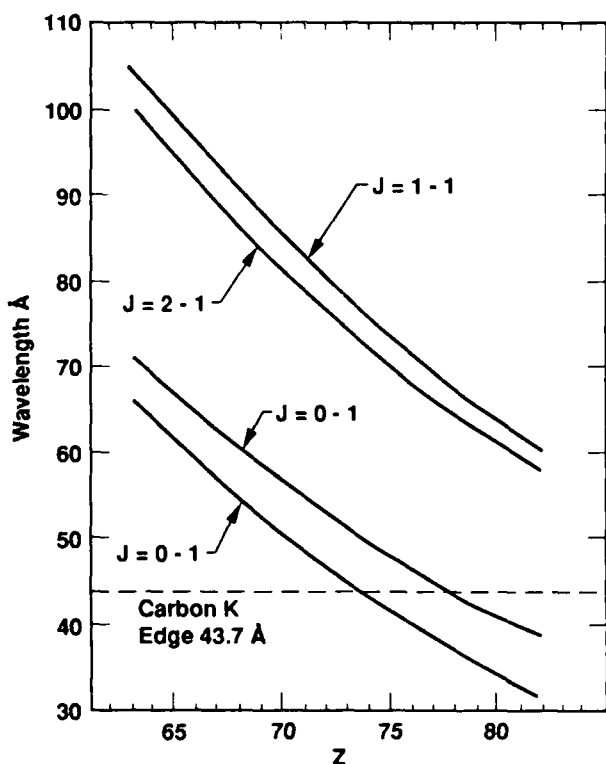


Figure 4. The scaling of the wavelength of the four most prominent Ni-like 4d - 4p lines with nuclear charge.

in a 1-ns pulse. The  $J = 0 - 1$  lines analogous to those in  $\text{Eu}^{35+}$  were observed at 50.26 and 56.09 Å. The 50.26 Å,  $J = 0 - 1$  was observed to increase with target length, consistent with a gain of  $1.2 \pm 0.4 \text{ cm}^{-1}$ . The measurement of gain on the second  $J = 0 - 1$  (at 56.09 Å) was complicated by the presence of nearby lines making its identification difficult for short length targets. Detailed calculations predicted gains up to  $9 \text{ cm}^{-1}$  on both of the  $J = 0 - 1$  lines for the target and irradiance conditions used in the experiment. However, using a new version of the LASNEX hydrodynamics code, which produces lower electron temperatures, leads to gain predictions of order  $3 \text{ cm}^{-1}$  for both lines. The predicted gains on the  $J = 2 - 1$  and  $1 - 1$  lines are reduced in the new calculations and in good agreement with the near zero gains observed on these lines.<sup>22</sup> The experiment and calculation are not in serious disagreement. Due to the uncertainties in the electron temperatures produced by the calculations, it is possible that the temperature in the experiment is lower than we think. Hence, it is possible that the  $J = 0 - 1$  gain can be increased by increasing the pump laser irradiance, as will be attempted in future experiments.

Table 2 lists the Ni-like 4d-4p laser lines observed to date. Also shown in Table 2 are the predicted wavelengths of the analogous short wavelength  $J = 0 - 1$  transition in tantalum, tungsten and rhenium. These elements should produce lasing transitions near 44 Å with predicted pumping irradiances in excess of  $4 \times 10^{14} \text{ W cm}^{-2}$ . Preliminary experiments at lower irradiance<sup>16</sup> have produced under-ionized plasmas not suitable for observation of amplification near 44 Å. Future experiments will be able to irradiate targets up to 2 cm in length with in excess of  $4 \times 10^{14} \text{ W cm}^{-2}$  and, hence, make a measurement of gain possible.

A Ni-like Ta x-ray laser would saturate at an output power of approximately  $3 \times 10^{11} \text{ W cm}^{-2}$ , where saturation is defined as the rate of stimulated emission producing a two-fold reduction in the small signal gain. If a 100  $\mu\text{m}$  by 100  $\mu\text{m}$  output aperture and emission time of 200 psec are assumed, the laser would produce at least 6 mJ. If the divergence of the x-ray laser were 1 mrad by 1 mrad, then 17 gain lengths would be required to reach saturation and the laser would have about 500 transverse modes. Recent calculations<sup>22</sup> indicate that gains of order  $5 \text{ cm}^{-1}$  should be achievable with Ni-like W. Hence, a Ni-like Ta or W x-ray laser of 4 cm length could be capable of providing of order 10  $\mu\text{J}$  per transverse mode. This energy would be sufficient to expose high-resolution photo resists such a polymethyl methacrylate which requires of



Table 2. Summary of achievements to date with nickel-like schemes.

Ion	Transition	$\lambda(\text{\AA})$	Target Areal Density ( $\mu\text{gcm}^{-2}$ )	Irradiance ( $\text{Wcm}^{-2}$ ) (Pulselength)	$\lambda_{\text{pump}}$ ( $\mu\text{m}$ )	Gain ( $\text{cm}^{-1}$ )	Gain Length	Ref
Eu <sup>35+</sup>	A(2-1)	100.39	60	7x10 <sup>13</sup> (1ns)	0.53	0.1	-	20
	B(1-1)	104.56				-0.1	-	
	C(0-1)	71.00				1.1	3.8	
	D(0-1)	65.83				0.6	2.1	
Yb <sup>42+</sup>	B(1-1)	84.40	110	1.4x10 <sup>14</sup> (1ns)	0.53	-1.0	-	21
	D(0-1)	50.26				1.2	2.0	
Ta <sup>45+</sup>	D(0-1)	44.83		> 4x10 <sup>14</sup>	Prediction only			
W <sup>46+</sup>	D(0-1)	43.16		> 4x10 <sup>14</sup>	Prediction only			
Re <sup>47+</sup>	D(0-1)	41.54		> 4x10 <sup>14</sup>	Prediction only			
Transitions:								
	A(2-1)	3d <sup>9</sup> <sub>5/2</sub> 4d <sub>5/2</sub> 2 - 3d <sup>9</sup> <sub>5/2</sub> 4p <sub>3/2</sub> 1						
	B(1-1)	3d <sup>9</sup> <sub>5/2</sub> 4d <sub>5/2</sub> 1- 3d <sup>9</sup> <sub>5/2</sub> 4p <sub>3/2</sub> 1						
	C(0-1)	3d <sup>9</sup> <sub>3/2</sub> 4d <sub>3/2</sub> 0- 3d <sup>9</sup> <sub>5/2</sub> 4p <sub>3/2</sub> 1						
	D(0-1)	3d <sup>9</sup> <sub>3/2</sub> 4d <sub>3/2</sub> 0 - 3d <sup>9</sup> <sub>3/2</sub> 4p <sub>1/2</sub> 1						

order  $0.1 \text{ J cm}^{-2}$  (Ref. 24). Therefore, it should be possible to perform Gabor holography on small ( $\sim$  a few  $\mu\text{m}$ ) samples using such a source of x-rays.<sup>24,25</sup> Such an x-ray laser would probably be pumped by 8 beams of the Nova laser (32 TW of power); however, experiments to demonstrate gain in Ni-like Ta and W will be attempted in early 1989 using the Nova Two Beam Chamber Facility with up to 8 TW of pump power.

A natural analog to the Ni-like 4d - 4p laser is the Nd-like 5f - 5d laser.<sup>23</sup> The Nd-like ground state is a closed 4f shell with a total of 60 atomic electrons. The electron collisional excitation rate between the 4f and the 5f levels for ions such as  $\text{U}^{32+}$  has been calculated to be large enough to pump a 5f - 5d population inversion. The candidate lasing transition in  $\text{U}^{32+}$  is at approximately 70  $\text{\AA}$ . Unfortunately there are not enough elements in the periodic table to scale Nd-like systems to significantly shorter wavelength. Their chief advantage is that a Nd-like system might produce a very efficient x-ray laser near 70  $\text{\AA}$  with pump laser irradiances as low as  $10^{13} \text{ W cm}^{-2}$ . Some experimental work has been performed at Lockheed Palo Alto, on laser irradiation of high Z elements such as U, but to date no clear evidence of the production of the Nd-like ion state has been observed.<sup>26</sup>

## Recombination Schemes

Table 3 summarizes demonstrations of amplification in recombination pumped schemes published to date. The schemes are separated into lithium- and hydrogen-like schemes. In both schemes, the dominant pump mechanism is three body recombination from the next ionization state. The higher principal quantum number states are favored by three body recombination (which scales as  $n^4$ ) and hence, if the recombination rate is fast enough, high n states can become inverted relative to low n states that are strongly coupled radiatively to the ground state. In Li-like Al, amplification has been demonstrated on the 4f - 3d and 5f - 3d transitions<sup>27-29</sup> and recently extrapolated to the 4f - 3d in silicon.<sup>29</sup> In H-like C, the 3 - 2 transition at 182  $\text{\AA}$  has been amplified up to 8 gain lengths in experiments performed at Princeton University.<sup>30,31</sup> The same scheme has produced 3.7 gain lengths at Rutherford Appleton Laboratory and been extrapolated to 81  $\text{\AA}$  in  $\text{F}^{8+}$  with 2.8 gain lengths being reported.<sup>28</sup>

In order to obtain a fast recombination rate, two methods have been used. In both, the objective is to heat the lasant material so that it is stripped beyond the ion state required, then cool it rapidly whilst keeping the density high so that rapid

Table 3. Summary of achievements to date with recombination schemes.

Ion	Transition	$\lambda(\text{\AA})$	Target	Irradiance ( $\text{Wcm}^{-2}$ ) (Pulse length)	$\lambda_{\text{pump}}$ ( $\mu\text{m}$ )	Gain ( $\text{cm}^{-1}$ )	Gain Length	Ref
<u>Li-Like</u>								
A1 <sup>10+</sup>	5f-3d	105.7	Solid	$4 \times 10^{12}$ (2.5ns)	1.06	1.0	2.0	27
A1 <sup>10+</sup>	4f-3d	154.7	7 $\mu\text{m}$ fibre	$1.7 \times 10^{14}$ (120ps)	0.53	3.0	2.0	28
	5f-3d	105.7				3.0	2.0	
A1 <sup>10+</sup>	4f-3d	154.7	Magnetically confined laser- produced plasma	$2 \times 10^{13}$ (50ns)	10.6	3.5	3.5	29
Si <sup>11+</sup>	4f-3d	129		$2 \times 10^{13}$ (50ns)	10.6	1.5	1.5	29
<u>H-Like</u>								
C <sup>5+</sup>	3-2	182	Magnetically confined laser- produced plasma	$5 \times 10^{12}$ (75ns)	10.6	8.0	8.0	30,31
C <sup>5+</sup>	3-2	182	7 $\mu\text{m}$ fibre	$1.5 \times 10^{14}$ (70ps)	0.53	4.1	3.7	28,32
F <sup>8+</sup>	3-2	81	7 $\mu\text{m}$ fibre	$5.7 \times 10^{14}$ (70ps)	0.53	5.5	2.8	28

recombination occurs. The technique used at Princeton<sup>29-31</sup> heats the plasma using a long-pulse (75-ns) CO<sub>2</sub> laser, the plasma then flows into a region where it is confined by a strong magnetic field (90 kG) which keeps the electron density high ( $10^{18}$ - $10^{19} \text{ cm}^{-3}$ ). The plasma then cools through radiation, either from the lasant ions or from added high-Z impurities such as Fe. This technique was used to produce a H-like C amplifier of 8 gain lengths.<sup>30,31</sup> The pulse of amplified spontaneous emission at 182  $\text{\AA}$  was observed to have a time duration of 10-30 ns and a total energy of 1-3 mJ (Ref. 31).

In the experiments at Ecole Polytechnique<sup>27</sup> and Rutherford Appleton Laboratory,<sup>28,32</sup> the mechanism employed was a combination of short-pulse laser irradiation of a solid target followed by cooling through adiabatic expansion of the almost cylindrical plasma. In the Ecole Polytechnique experiments, the targets were slabs of Al and a 2.5-ns irradiating pulse was used. For the Rutherford Appleton Laboratory experiments, the targets were, typically, 7- $\mu\text{m}$ -thick carbon fibres, either bare or coated with the lasant material, irradiated with 70-ps pulses. The fibres were irradiated symmetrically so that the plasma formed a cylindrically expanding amplifier medium.<sup>28,32</sup> At Nova, targets consisting of 50  $\mu\text{g}$

$\text{cm}^{-2}$  thick, 100  $\mu\text{m}$  wide strips of the lasant material, sandwiched between two 5  $\mu\text{g cm}^{-2}$  thick CH foils have been used in similar experiments. Al strips have been irradiated with up to  $2.5 \times 10^{14} \text{ W cm}^{-2}$  in 120-ps pulses, but the resultant plasma was only ionized to H-like Al (Ref. 33). Hence the possibility of pumping an inversion in H-like Al by recombination from the fully stripped state would require more irradiance. Similar targets of CaF<sub>2</sub> and Cr led to the identification of the 4f - 3d transitions (at 57.7  $\text{\AA}$ ) in Li-like Ca and Cr (at 38.6  $\text{\AA}$ ), but no observation of amplification was made.

Since the cooling mechanism is adiabatic expansion, it is necessary to use short pulse irradiation so that the plasma is heated and ionized beyond the required ion state whilst it still has a small volume. The use of shorter pulse irradiation will therefore result in higher electron density at the time of peak recombination, and thus higher gain. Achieving high density during recombination is particularly important for short wavelength recombination x-ray laser schemes since the recombination rate has to compete with the spontaneous emission rate from the upper laser level. In the near future, short wavelength experiments with H-like and Li-like recombination systems will be performed with irradiating pulses

as short as 20 ps. Candidates for operation near 44 Å are H-like Mg at 45.5 Å and Li-like Ti, 4f - 3d at 46.7 Å.

### Acknowledgements

This work was sponsored in part by the U.S. Department of Energy, Lawrence Livermore National Laboratory under contract No. W-7405-Eng-48, and by the Air Force Office of Scientific Research under contract F49620-87-K-0001, through the U.S. Department of Energy, Lawrence Berkeley Laboratory, under contract DE-AC03-76SF00098. We also gratefully acknowledge the support of the Centre d'Etudes de Limeil-Valenton, France.

### References

1. R.A. London, J.E. Trebes and M.D. Rosen, "X-ray holography: x-ray interactions and their effects," Paper WB3, These Proceedings (1988).
2. A.N. Zherikhin, K.N. Koshelev and V.S. Letokhov, "Gain in the far vacuum ultraviolet region due to transitions in multiply charged ions," *Kvantovaya Elektron. (Moscow)* **3**, 152 (1976) [*Sov. J. Quantum Electron.* **6**, 82 (1976)].
3. A.V. Vinogradov, I.I. Sobel'man and E.A. Yukov, "Population inversion of transitions in neon-like ions," *Kvantovaya Elektron. (Moscow)* **4**, 63 (1977) [*Sov. J. Quantum Electron.* **7**, 32 (1977)].
4. A.V. Vinogradov and V.N. Shlaptsev, "Amplification of ultraviolet radiation in a laser plasma," *Kvantovaya Elektron. (Moscow)* **10**, 2325 (1983) [*Sov. J. Quantum Electron.* **13**, 1511 (1983) and references therein].
5. D.L. Matthews, et al. "Demonstration of a soft x-ray amplifier," *Phys. Rev. Lett.* **54**, 110 (1985).
6. M.D. Rosen, et al. "The exploding foil technique for achieving a soft x-ray laser," *Phys. Rev. Lett.* **54**, 106 (1985).
7. B. L. Whitten, R.A. London and R.S. Walling, "Scaling of neon-like lasers using exploding foil targets," available as a Lawrence Livermore National Laboratory report (Report No. UCRL-99001, June, 1988).
8. M.J. Eckart, J.H. Scofield, and A.U. Hazi, "XUV emission feature from the Livermore soft x-ray laser experiments," *Proceedings of the International Colloquium on UV and X-Ray Spectroscopy*, Beaulieu-sur-Mer, France, September 1987, *J. Phys (Paris)* **49**, C1-361 (1988).
9. B.J. MacGowan et al. "Lawrence Livermore National Laboratory soft x-ray laser research: recent results," in Multilayer Structures and Laboratory X-Ray Laser Research, N.M. Ceglio and P. Dhez, Eds., Soc. Photo-Opt. Instrum. Eng. **688**, 36 (1986).
10. B.J. MacGowan, et al. "Gain measurements for long neon-like selenium soft x-ray amplifiers," Lawrence Berkeley Laboratory, Berkeley, CA (unpublished).
11. G.J. Linford, E.R. Peressini, W.R. Sooy, and M.L. Spaeth, "Very long lasers," *Appl. Opt.* **13**, 379 (1974).
12. B.J. MacGowan, et al., "Observation of soft x-ray amplification in neon-like molybdenum," *J. Appl. Phys.* **61**, 5243 (1987).
13. T.N. Lee, E.A. McLean, and R.C. Elton, "Soft x-ray lasing in neon-like germanium and copper plasmas," *Phys. Rev. Lett.* **59**, 1185 (1987).
14. C.J. Keane, et al., "Study of soft x-ray amplification in a laser produced Sr plasma," Lawrence Livermore National Laboratory, Livermore, CA (unpublished).
15. R.A. London and M.D. Rosen, "Hydrodynamics of exploding foil x-ray lasers," *Phys. Fluids* **29**, 3813 (1986); M.D. Rosen, R.A. London, and P.L. Hagelstein, "The scaling of Ne-like x-ray laser schemes to short wavelength," *Phys. Fluids* **31**, 666 (1988).
16. Experiments carried out at Centre d'Etudes de Limeil-Valenton, unpublished.
17. S. Maxon, P. Hagelstein, J. Scofield, and Y. Lee, "Estimated gains for a Ni-like exploding foil target," *J. Appl. Phys.* **59**, 239 (1986).
18. P.L. Hagelstein, "Relativistic distorted wave results for nickel like gadolinium," *Phys. Rev. A* **34**, 874 (1986).
19. S. Maxon, P.L. Hagelstein, B.J. MacGowan, R.A. London, M.D. Rosen, J.H. Scofield, S. Dalhed, and M.H. Chen, "Calculation and design of a Ni-like Eu soft x-ray laser," *Phys. Rev. A* **37**, 2227 (1988).
20. B.J. MacGowan, S. Maxon, P.L. Hagelstein, C.J. Keane, R.A. London, D.L. Matthews, M.D. Rosen, J.H. Scofield and D.A. Whelan, "Demonstration of soft x-ray amplification in nickel like ions," *Phys. Rev. Lett.* **59**, 2157 (1987).
21. B.J. MacGowan, S. Maxon, C.J. Keane, R.A. London, D.L. Matthews, and D.A. Whelan, "Soft x-ray amplification at 50.3 Å in nickel like ytterbium," *J. Opt. Soc. Am. B* **5**, 1858 (1988).
22. S. Maxon, S. Dalhed, P.L. Hagelstein, B.J. MacGowan, M.D. Rosen and R.A. London, "New calculations for Ni-like soft x-ray lasers: Optimization for W(43.1 Å)", available as a

- Lawrence Livermore National Laboratory report (Report No. UCRL-99841, October, 1988).
23. P.L. Hagelstein and S. Dalhed, "On strong monopole electron collisional excitation in highly stripped ions," *Phys. Rev. A* **37**, 1537 (1988).
  24. M. Howells, et al., "X-ray holograms at improved resolution: A study of zymogen granules," *Science* **238**, 514 (1987).
  25. J.E. Trebes, et al., "Demonstration of x-ray holography with an x-ray laser," *Science* **238**, 517 (1987).
  26. W.L. Hodge, et al., "Spectra of lead, bismuth, thorium, and uranium relevant to a neodymium like soft x-ray lasing scheme," Paper TuC25, these Proceedings (1988).
  27. P. Jaegle, et al., "Soft x-ray amplification by lithium-like ions in recombining hot plasmas," *J. Opt. Soc. Am. B* **4**, 563 (1987).
  28. C.L.S. Lewis, et al., "Status of soft x-ray laser research at the Rutherford Appleton Laboratory," *Pl. Phys. Con. Fus.* **30**, 35 (1988).
  29. D. Kim, et al., "Soft x-ray amplification in lithium-like A XI (154 Å) Si XII (129 Å)," *J. Opt. Soc. Am. B* **6**(1)(1989). (In press)
  30. S. Suckewer, C.H. Skinner, H. Milchberg, C. Keane, and D. Voorhees, "Amplification of stimulated emission in a confined plasma column," *Phys. Rev. Lett.* **55**, 1753 (1985).
  31. S. Suckewer, C.H. Skinner, D. Kim, E. Valeo, D. Voorhees, and A. Wouters, "Divergence measurements of a soft x-ray laser beam," *Phys. Rev. Lett.* **57**, 1004 (1986).
  32. C. Chenais-Popovics, et al., "Laser amplification at 18.2 nm in recombining plasma from a laser irradiated carbon fiber," *Phys. Rev. Lett.* **59**, 2161 (1987).
  33. C. Keane, B. MacGowan, D. Matthews, and D. Whelan, "Progress towards demonstration of soft x-ray amplification at shorter x-ray wavelengths," in High Intensity Laser Matter Interactions, E.M. Campbell and H. Baldis Eds. Soc. Photo-Opt. Instrum. Eng. **913**, 105 (1988).

Observation of Extreme Ultraviolet Amplification in 3-2  
(42~46Å), 4-3(130.5Å) and 5-4(305Å) Transitions  
in Laser Produced He-like Al Plasma

H. Kuroda, K. Muroo, K. Naito and Y. Tanaka

The Institute for Solid State Physics

The University of Tokyo

Roppongi 7-22-1, Minato-ku, Tokyo 106 Japan

Phone: 03-478-6811

To demonstrate the XUV stimulated emission process in plasma produced by 100ps glass-laser pulse, close to the water window region, XUV and X-ray spectroscopic measurements are done by adopting He-like Al 3-2, 4-3 or 5-4 transition scheme. This scheme is simple and predictable by the spectroscopic analysis, and suitable to demonstrate the induced emission of the shorter wavelength than any other transition ever attained.

First, intensities of 2p-1s, 3p-1s, 4p-1s and 5p-1s transitions of He-like Al in X-ray region, and those of 3-2, 4-3 and 5-4 transitions in XUV region were measured, at various laser energy. Enhancements of XUV intensities of 3-2(42.4 ~ 46Å), 4-3(130.5Å) and 5-4(305Å) transitions were seen compared to intensities of 3-1, 4-1 and 5-1 transitions as the laser energy was increased. These enhancements were probably

due to the induced emission process.

Next, intensities of 3-2 transition were measured at various line-focus length, keeping the laser energy density as constant. Intensities of He-like 3d-2p, 3p-2s and 3s-2p transitions grew exponentially compared to the linear growth of transitions of lower ionized Al. These exponential growth are found to be due to the induced emission process. Gain coefficients are estimated as  $4\sim 10\text{cm}^{-1}$

## 12.8 eV Laser in Neutral Cesium

C. P. J. Barty, D. A. King, G. Y. Yin, K. H. Hahn, J. E. Field  
J. F. Young, and S. E. Harris

*Edward L. Ginzton Laboratory, Stanford University  
Stanford, California 94305*

### Abstract

We report the operation of a saturated 12.8 eV (96.9 nm) laser in Cs vapor that has an extrapolated small signal gain of  $\exp(83)$  in a total length of 17 cm. We believe that lasing occurs from a core-excited level embedded in the continuum of the valence electron. The laser is pumped by soft x-rays from a synchronous, traveling-wave, laser-produced (2.5 J, 15 ps, 1064 nm) plasma.

### Introduction

Recently, it has been the aim of several research efforts to achieve lasing action at wavelengths below 100 nm. In general, successful efforts such as the 20.6 nm Se laser[1] have involved transitions in highly ionized atoms created within a dense laser-produced plasma and have required kilojoule class laser systems as pumping sources. In this work, we report the first operation of a new class of short wavelength lasers in which the upper level of the lasing transition is embedded in the continuum of the valence electron[2]. Consequently, it requires less than a joule of pumping energy to saturate the lasing transition.

We believe that the upper level of the laser is a core-excited level in neutral Cs and is pumped by photoelectrons generated by soft x-rays emitted from a laser produced plasma. Core-excited

levels that are embedded within a continuum usually autoionize on a picosecond timescale, making the accumulation of population difficult. But this need not be the case; recent work by Spong *et al.*[3,4] has shown, for example, that there are many levels in neutral Rb that have autoionization lifetimes exceeding 10 ps and several that exceed 100 ps. Such long lifetimes can result either from angular momentum and spin selection rules that to first order prohibit autoionization, or from fortuitous radial matrix element cancellations. The possibility of using such levels to make extreme ultraviolet and soft x-ray lasers has been noted by several workers[5,6,7]. The existence of an inversion from an upper level embedded within a continuum has been inferred from fluorescence intensity measurements by Silfvast *et al.*[8].

### Spectroscopy

An energy level diagram of the Cs 96.9 nm laser system is shown in fig. 1. The  $117,702 \text{ cm}^{-1}$  energy of the upper level has been measured by vacuum ultraviolet absorption spectroscopy [9,10], and the energy of the  $5p^6 5d^2 D_{3/2}$  lower level is well known[10]. The difference, 96.897 nm, agrees with our measured emission wavelength of  $96.86 \pm 0.05 \text{ nm}$ . The upper level designation is

based upon a comparison of a computer generated ground state absorption spectra, using the RCN/RCG atomic physics code developed by Robert Cowan[11], the known absorption spectra of Connerade[9], and the ejected electron spectra of Pejcev *et al.*[12].

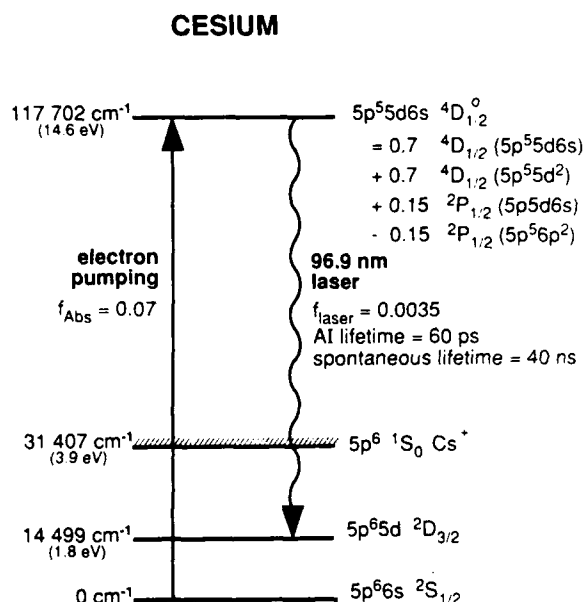


Figure 1. Energy level diagram of neutral Cs

The four largest components of the code generated eigenvector of the upper level are shown in fig. 1. The two large quartet terms, arising from the  $5d6s$  and the  $5d^2$  configurations, allow the level to have a relatively long autoionization lifetime, while the doublet terms allow for large pumping and laser oscillator strengths. It should also be noted that of all the core excited levels in the 90 nm to 120 nm region of the neutral Cs spectra, this level has the most favorable combination of code calculated lifetime, pumping cross section, and gain cross section with respect to achieving laser action.

The relatively long spontaneous decay time of 40 ns yields a branching

ratio to radiation of 0.0014. Therefore, it should be very difficult to observe spontaneous emission from this transition. Significant outputs will occur only if the upper level is excited very rapidly and the stimulated emission rate exceeds the autoionization rate.

## Experimental Arrangement

In our experiments, rapid excitation is provided via an intense 15 ps laser pumping pulse. The pulse is focused by a cylindrical lens onto a target which resides within a Cs heatpipe cell. At the surface of the target, a hot plasma is created which radiates incoherent soft x-rays and, in the process, photoionizes the surrounding Cs vapor. The resulting photoelectrons may then collisionally excite the 96.9 nm laser transition. In order to achieve large single pass gains with this excitation, it is necessary that the length of the line focus be extended to several cm. However, the short autoionization lifetime of the upper level and the finite transit time of the 96.9 nm radiation through the gain region limit the useful length of the line focus, unless a traveling-wave excitation is used.

The synchronous traveling-wave excitation used in this experiment is shown schematically in fig. 2.

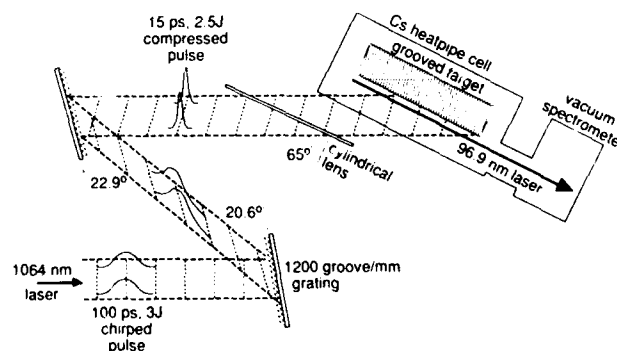


Figure 2. Grating-assisted, traveling-wave geometry



The geometry is a modification of that used by Sher *et al.*[13] for the Xe 108.9 nm Auger laser. A 2.5 J, 15 ps, 1064 nm pulse is incident upon a cylindrical lens at 65 deg from normal and is focussed onto a target which is parallel to the lens. The large angle of incidence expands the length of the line focus by  $1/\cos(65) = 2.4$ , producing a 17 cm long plasma. By itself, this geometry would produce a plasma sweeping along the target at a speed of  $c/\sin(65) = 1.1 \times c$ , resulting in a synchronism mismatch of 3.1 ps per cm of target length. In this experiment, however, the 15 ps long pulse is formed by chirping a mode-locked 1064 nm pulse in a fiber, amplifying it in Nd:YAG and Nd:glass stages, and compressing the resulting 120 ps pulse with a parallel grating pair[14]. The second grating of this pair is tilted off true parallelism by 2.3 deg so as to produce a tilted wave front[15] that exactly compensates for the group velocity lead of the oblique geometry. The result is a plasma, and its associated pulse of soft x-rays, which travels along the target at the speed of light.

The Cs heatpipe target chamber was operated at a Cs density of  $6.3 \times 10^{16} \text{ cm}^{-3}$ . The surface of the stainless steel target rod is grooved at a pitch of 43 per cm and during the experiments is wet with liquid Cs. Radiation from a ~1cm region in front of the target was collected by a 1m normal incidence spectrometer and detected by a microchannel plate having a 600 ps time resolution. Thin films of In and Al, and LiF windows were used to check for possible grating second order and ghost signals. For wavelength measurements, the 96.9 nm laser beam was scattered from two ground glass plates before entering the spectrometer.

## Results

Small signal gain was determined by measuring the relative 96.9 nm energy as a function of plasma length for short sections of the target and fitting the data to the functional form for frequency-integrated superfluorescence

output[16]. The length was varied by masking the input plasma producing beam. The gain was measured at several sections along the 17 cm target and was uniform, averaging  $4.9 \text{ cm}^{-1}$ . This yields a total extrapolated small signal gain of  $\exp(83)$ . A typical gain measurement is shown in fig. 3.

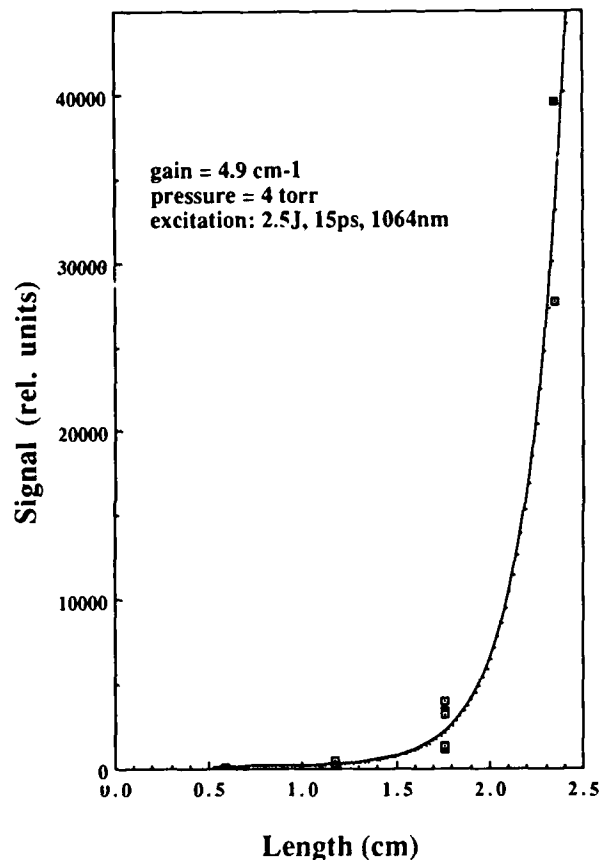


Figure 3. Small signal gain measurement

The solid line represents a computer generated fit to the superfluorescence function. Fig. 4 shows the dependence of the 96.9 nm output energy on total plasma length. The linear increase after 4 cm clearly indicates saturation of the transition. In this case, a 4 cm plasma length corresponds to only 400 mJ of pump energy on target.

The absolute output energy was measured with an Al vacuum photodiode and a calibrated In filter to be  $1.5 \mu\text{J}$ .

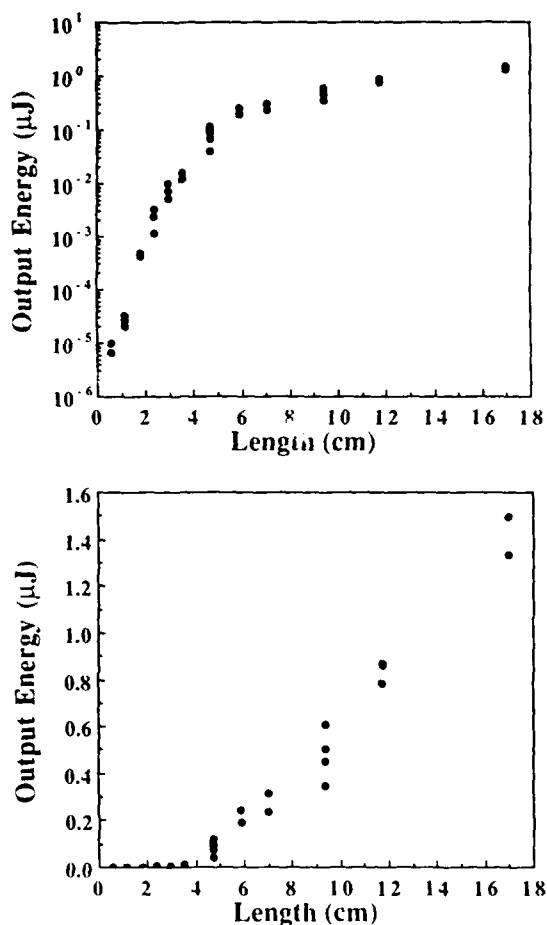


Figure 4. Output energy at 96.9 nm as a function of plasma length. Semi-log and linear plots

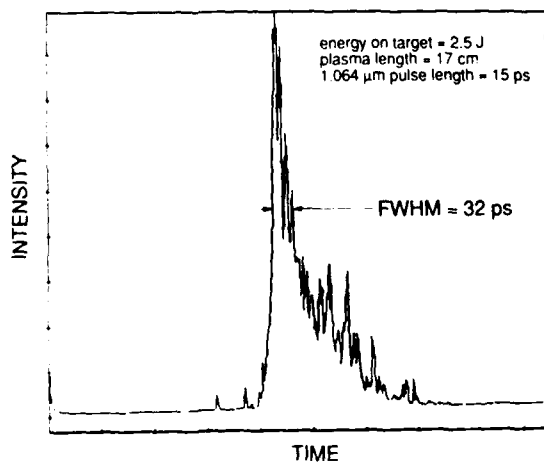


Figure 5. Streak camera output of 96.9 nm radiation

The temporal profile of the full length output is shown in fig. 5. The measurement was made with a Kentec x-ray streak camera equipped with a KBr coated In photocathode. The resolution of the camera is  $\sim 20$  ps.

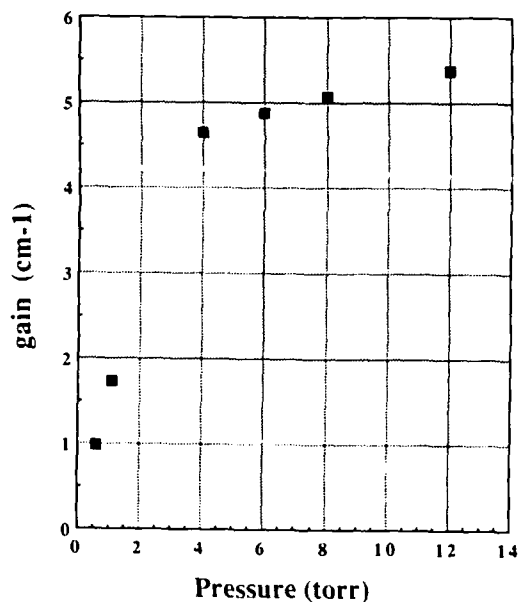


Figure 6. Gain vs. Cs pressure

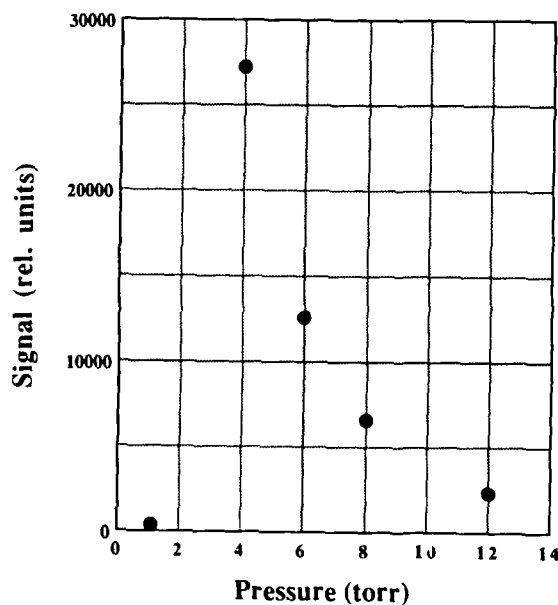


Figure 7. Small signal output vs. Cs pressure. 2 cm plasma length

Using a two dimensional vidicon detector placed ~1 m from the end of the plasma, the beam divergence was estimated to be < 2 mrad.

Variation of small signal gain with ambient Cs pressure and of small signal output with Cs pressure is shown in figs. 6 and 7. Taken together, these curves imply that the ambient Cs absorption cross section at 96.9 nm is  $0.3 \times 10^{-18} \text{ cm}^2$ .

Several experiments were performed to test the importance of synchronous traveling-wave pumping. The grating angle and target angle of incidence were changed to produce a group velocity lead for the traveling excitation of 10 ps per cm of target length. For this condition, the output signal for a 2.4 cm plasma length was reduced by a factor of 525, and the gain was reduced to  $1.8 \text{ cm}^{-1}$ .

Using synchronous pumping, we also compared the 96.9 nm gain using the normal 15 ps pumping pulse and an unchirped 190 ps pulse of the same energy. The result is shown in fig. 8. The

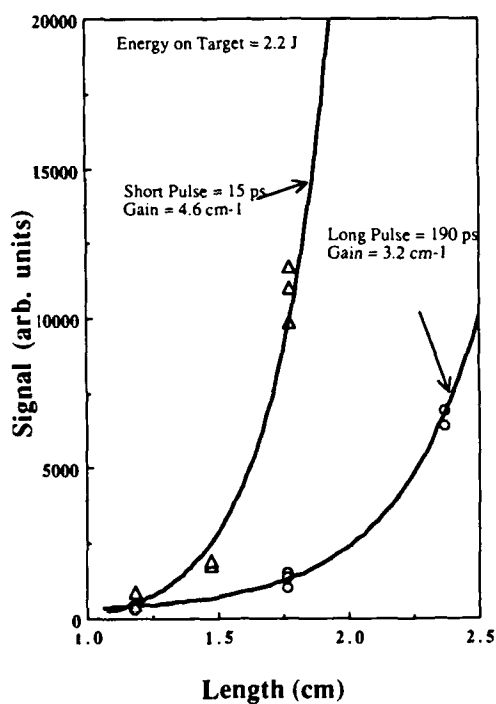


Figure 8. Small signal gain for long and short pulse excitation

signal levels of the 90.1 nm Cs II resonance line and the 63.8 nm Cs III resonance line were unchanged for short and long pulse excitation, indicating that the laser signal reduction with longer pulse pumping should not be attributed to reduced x-ray conversion.

## Discussion

The measured gains are in good agreement with simple estimates of photoelectron pumped gain. For our 1064 nm power density on target of  $1.5 \times 10^{12} \text{ W cm}^{-2}$ , assuming that only 3% of the 1064 nm laser energy is converted to soft x-rays, the resulting laser produced plasma will have an effective blackbody temperature of 25 eV. At a distance of 1mm from target, the flux from this blackbody will create, in Cs, a photoelectron density of about  $10^{16} \text{ cm}^{-3}$  with a Maxwell-Boltzmann temperature of ~30 eV. At this temperature, the RCN/RCG code calculates a temperature-averaged electron excitation times velocity product for the upper laser level of  $3.5 \times 10^{-9} \text{ cm}^3 \text{ sec}^{-1}$ . Using the calculated upper level autoionizing lifetime of 62 ps as the effective pumping time, yields an upper level population density of  $1.4 \times 10^{14} \text{ cm}^{-3}$ . This is consistent with experiments demonstrating that laser-produced plasmas can produce populations in excess of  $10^{14} \text{ cm}^{-3}$  in metastable levels embedded within a continuum[17]. This upper level population times the calculated gain cross section of  $1.7 \times 10^{-14} \text{ cm}^2$  gives a gain coefficient of  $2.4 \text{ cm}^{-1}$ , assuming the lower level is empty, as compared to our measured value of  $4.9 \text{ cm}^{-1}$ . The autoionization lifetime and oscillator strength calculated by the RCN/RCG code can vary by about a factor of two depending on the relative energy spacing used between the  $5d6s$ ,  $5d^2$ , and  $6p^2$  configurations. Direct excitation by the plasma soft x-rays may also play a role in the production of upper level population.

The above calculation assumes that the lower level of the laser transition is empty. However, current calculations indicate that electron rates into the lower level are larger than those into the upper level, and that electron collisional rates out of the lower level alone cannot empty the level and produce an inversion. The mechanism by which the population of the lower laser level is reduced below that of the upper level has not been determined and is critical to the understanding of this system. A 1064 nm two-photon transition to the continuum, with the  $4f$  valence level as an intermediary, may play a role in this process. We also note that, in principal, for levels embedded in a continuum, Fano type interferences between autoionizing lines[18] that cause a cancellation of absorption and allow stimulated emission without inversion[19,20]. However, no such lines appear to exist in the correct proximity of the  $117,702\text{ cm}^{-1} 4D_{1/2}$  upper level.

The predicted poor radiative yield of the upper laser level implies that it should be difficult to observe 96.9 nm spontaneous emission. Using a very short, 0.6 cm long, plasma in the same cell, we were unable to observe 96.9 nm radiation, and estimate that its intensity was at least a factor of 40 smaller than the 90.1 nm Cs II resonance line, a factor of 60 smaller than the 63.8 nm Cs III resonance line, and a factor of 40 smaller than the 87.5 nm Cs IV resonance line, all of which we observed. Emission at 96.9 nm may have been observed from a discharge in earlier work at a signal level  $\sim 200$  below the 90.1 nm Cs II resonance line[21].

Although difficult to detect unless large gains are present, lasers of this type have some intrinsic advantages over short wavelength lasers created in highly stripped laser plasmas[1]. The most striking is the 100 fold or more reduction in pump energy required to produce large single pass gains. Because the upper level is at a much lower energy than it would be in a typical ionic species, it can be pumped by much

cooler electrons. The lower electron temperature and excitation energy can yield a much larger cross section for excitation. This, in addition to the lack of energy lost to ionization, results in much lower pumping requirements. Furthermore, since the lasing media is an atomic vapor, plasma diffraction effects that can limit the gain interaction region and beam quality, are no longer present. This is evident in our long interaction length of 17 cm and our estimated beam divergence of  $< 2$  mrad.

Finally, in order to take advantage of the possibility of long gain regions, it is necessary to use a traveling-wave excitation. We found that the highest gains were obtained with an excitation that traveled across the surface of the target with a velocity  $v = c$ . However, in all our tests of gain vs. traveling-wave, the speed at which the excitation swept across the surface of the target was greater than or equal to  $c$ . In general, the group velocity in an inverted media for a pulse on line center is slower than the speed of light in vacuum. It is therefore believed that excitations traveling at less than the speed of light may further improve gain.

## Summary

We believe this is the first observation of laser action on a transition having an upper level embedded within the continuum of an outer electron. Extremely large gains were produced using only 2.5 J of pumping energy, and this fact bodes well for the extension of this concept to even shorter wavelengths.

The authors would like to thank M. H. Sher for his participation in the Kentec streak camera measurement and acknowledge many helpful discussions with A. Imamoglu, J. J. Macklin, M. H. Sher, and P. J. K. Wisoff. This work was jointly supported by the U. S. Office of Naval Research, U. S. Air Force Office of Scientific Research, the U. S. Army Research Office, and the Strategic Defense Initiative Organization. K. H.

Hahn acknowledges the support of a National Science Foundation Fellowship.

## References

1. D. L. Matthews, P. L. Hagelstien, M. D. Rosen, N. M. Ceglio, A. U. Hazi, H. Medeck, B. J. MacGowan, J. E. Trebes, B. L. Whitten, E. M. Campbell, C. W. Hatcher, A. M. Hawryluk, R. L. Kauffman, L. D. Pleasance, G. T. A. Weaver, "Demonstration of a Soft X-Ray Amplifier," *Phys. Rev. Lett.* **54**, 110-113 (January 1985).
2. S. E. Harris and J. F. Young, "Core-Excited Metastable Levels: Application to Spectroscopy, to the Generation of Picosecond Extreme-Ultraviolet Pulses, and to Lasers," *J. Opt. Soc. Am. B* **4**, 547-562 (April 1987).
3. J. K. Spong, J. D. Kmetec, S. C. Wallace, J. F. Young, and S. E. Harris, "Laser Spectroscopy of Core-Excited Levels of Neutral Rubidium," *Phys. Rev. Lett.* **58**, 2631-2634 (June 1987).
4. J. K. Spong, A. Imamoglu, R. Buffa, and S. E. Harris, "Laser Depletion Spectroscopy of Core-Excited Levels of Neutral Rubidium," *Phys. Rev. A* (to be published).
5. E. J. McGuire and M. A. Duguay, "Soft X-Ray Gain in the Alkali Earths," *Appl. Opt.* **16**, 83 (January 1977).
6. S. E. Harris, "Proposal for a 207 Å Laser in Lithium," *Opt. Lett.* **5**, 1-3 (January 1980).
7. H. Egger, T. S. Luk, W. Muller, H. Pummer, and C. K. Rhodes, "Collision-Free Multiple Ionization of Atoms and XUV Stimulated Emission in Krypton at 193nm," in Laser Techniques for Extreme Ultraviolet Spectroscopy, S. E. Harris and T. B. Lucatorto, eds. (Boulder, Colorado: AIP, 1984), pp. 64-78.
8. W. T. Silfvast and O. R. Wood II, "Photoionization Lasers Pumped by Broadband Soft-X-Ray Flux from Laser-Produced Plasmas," *Opt. Soc. Am. B* **4**, 609-618 (April 1987).
9. J. P. Connerade, "Absorption Spectrum of Cs I in the Vacuum Ultraviolet," *Astrophys. J.* **159**, 685-694, (February 1970).
10. C. E. Moore, Atomic Energy Levels, Natl. Stand. Ref. Data Ser. (U. S. GPO, Washington, D. C., 1971), Vol. III, p. 124.
11. R. D. Cowan, The Theory of Atomic Structure and Spectra (University of California, Berkeley, 1981) Sects. 8-1, 16-1, and 18-7.
12. V. Pejcev and K. J. Ross, "High-Resolution Ejected-Electron Spectrum of Caesium Vapour Autoionising Levels Excited by 30 to 400 eV Electrons," *J. Phys. B: Atom. Molec. Phys.* **10**, 2935-2941 (1977).
13. M. H. Sher, J. J. Macklin, J. F. Young, S. E. Harris, "Saturation of the Xe III 109nm Laser Using Traveling-Wave Laser-Produced-Plasma Excitation," *Opt. Lett.* **12**, 891-893 (November 1987).
14. D. Strickland and G. Mourou, "Compression of Amplified Chirped Optical Pulses," *Opt. Com.* **56**, 219-221 (December 1985).
15. Zs. Bor, S. Szatmari, and Alexander Muller, "Picosecond Pulse Shortening by Travelling Wave Amplified Spontaneous Emission," *Appl. Phys. B* **32**, 101-104 (August 1983).
16. G. J. Linford, E. R. Peressini, W. R. Sooy, and M. L. Spaeth, "Very Long Lasers," *App. Optics* **13**, 379-390 (February 1974).
17. J. C. Wang, R. G. Caro, and S. E. Harris, "Novel Short-Pulse Photoionization Electron Source:  $\text{Li}(1s2s2p)^4\text{P}^0$  Deexcitation Measurements in a Plasma," *Phys. Rev. Lett.* **51**, 767-770 (August 1983).
18. S. E. Harris, "Non-reciprocity of Autoionizing Interferences: Lasers Without Inversion," Conference on Short Wavelength Coherent Radiation: Generation and Applications, North Falmouth, MA (September 1988).
19. S. E. Harris (to be published).
20. V. G. Arkhipkin, and Yu. I. Heller, "Radiation Amplification Without Population Inversion at Transitions

- to Autoionizing States," Phys. Lett. 98A, 12-14 (October 1983).
21. A. J. Mendelsohn, C. P. J. Barty, M. H. Sher, J. F. Young, and S. E. Harris, "Emission Spectra of Quasimetastable Levels of Alkali-metal Atoms," Phys. Rev. A 35, 2095-2101 (March 1987).

## X-Ray Laser Experiment with Double Pass Device and Long-Recombining-Plasma Column

P. Jaegle,<sup>+</sup> A. Carillon,<sup>+</sup> P. Dhez,<sup>\*</sup> B. Gauthe,<sup>+</sup> F. Gadi,<sup>+</sup> G. Jamelon,<sup>+</sup> and A. Klisnick<sup>+</sup>

*Laboratoire de Spectroscopie Atomique et Ionique, Bat. 350  
Université Paris-Sud, F-91405 Orsay, France*

### Summary

The results reported here, are time integrated measurements of soft X-ray amplification obtained with our new experimental set-up involving a single normal incidence multilayered mirror, put at the rear of a 60mm laser-plasma column. After a brief description of the experimental system, we report the first results obtained at 10.57nm by comparing intensities of single-pass ASE and of double-pass with the mirror. The target is a thin aluminum layer with a thickness optimizing the population inversion on lithium-like  $Al^{+10}$  ions. The pumping is produced by recombination mechanisms during the plasma cooling.

From the single to the double pass X-ray beam, the lines exhibit significant differences, both in peak intensities and widths. First, double-passing enhances the 10.57nm line intensity much more than mirror reflection would do without any amplification by the plasma. Secondly, and concomitantly, one observes a line width decreasing of about 30%.

This is supposed due to a core size decreasing of the zone emitting the line. To explain how the cross-section of the double pass beam can be reduced

during propagation through the plasma column we suggest to consider the focussing effects due to the gain coefficient profile.

### 1. Introduction

On the way to get a usable soft x-ray laser, significant advances have been achieved since the first observations, ten years ago, of Amplified Spontaneous Emission (ASE) at 10.57nm in lithium-like ions obtained with laser-produced plasma and massive aluminum targets (1,2) as well as at 18.2 nm in hydrogenic carbon (3). Considering that a usable soft X-ray laser would need a gain-length product (GL) about 15 to 20, subsequent efforts were done on both factors. Higher G for different wavelengths, from some tens to few nanometers, are continuously searched through several kinds of transitions using three basic population inversion schemes: recombination during plasma cooling, collisional excitation (4) and the more hypothetical direct pumping by X-ray. Large L were first obtained through a direct increase of the length of the plasma column to reach now several centimeters in some experiments. First suggestions to increase the effective path length by a double pass using normal incidence X-UV multilayers mirror came in 1984 (5) on the basis of reflectivity

achieved by such mirror (6,7) and gain measurements obtained by comparing ASE from plasma of different lengths. Even few percent of reflectivity at the rear of a plasma column produce a noticeable effect so long as the mirror orientation is correct and as well as the variation of gain lifetime matches the extra pass length introduced by reflection. In fact, investigation of line shape and intensity change with and without rear mirror is a very efficient test of GL increase with only shot to shot comparisons for identical plasma column characteristics. With time component resolved measurement, a single shot gives a direct access to the time dependent gain-length product by comparing relative intensities of the time components: the direct and time delayed reflected beam. Until now only two experiments have successfully observed path length increase with such half cavity mirrors (8,9). More recently (10), an additional semi-transparent multilayer has been introduced as a beam splitter in front of the plasma to get three pass amplification and test the feasibility of real X-ray laser cavities.

Beside the intensity increase itself, line shape and divergency variation of amplified beam are interesting features to observe as signs of coherence modification.

The results presented here are time-integrated measurements obtained with our new experimental set-up and a single normal incidence multilayered mirror put at the rear of a 60mm laser-plasma column (11). After a brief description of the experimental system, we will report the first results obtained at 10.57nm by comparing single-pass ASE and double-pass using the mirror. The target was a thin aluminum layer, able to optimize the population inversion on lithium-like  $Al^{+10}$  ions which are pumped by recombination during the plasma cooling.

## 2. Experimental set-up

### 2.1. Plasma production.

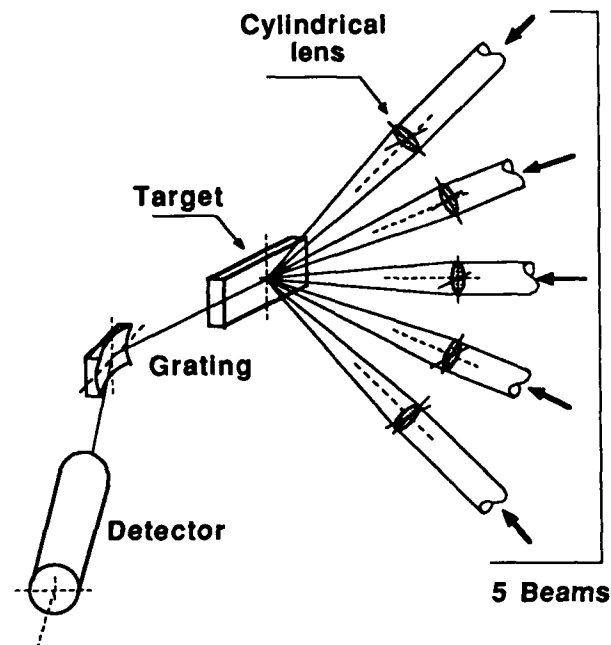


**Figure 1.** The geometry of the five beam experiment is indicated on this scheme. The central beam is horizontal, all the laser beam axes are contained in a vertical plane and have a  $22^\circ 5'$  angular separation. The Nd laser pulse ( $1.06\mu\text{m}$ ,  $5 \times 100 \text{ J}$ ,  $2.5 \text{ ns}$ ) is focused on a 60mm horizontal line by five cylindrical lens. The spectrometer plane is horizontal.

The figure 1 shows the geometry and the main characteristics of the new five beam Nd-laser experiment recently installed at the laboratory facility LULI. In our case the wavelength is  $1.06 \mu\text{m}$  and the pulse duration  $2.5 \text{ ns}$ . Focussing on a single side of the target was achieved by using cylindrical lenses plus square diaphragms to insure illumination homogeneity along the focal spot line. The focal spot was a rectangular surface  $64$



mm x 200  $\mu\text{m}$ ; the estimated power was  $2 \times 10^{12} \text{ W/cm}^2$  which is sufficient to ionize the plasma up to He-like ions which will recombine to Li-like ions.

Although massive aluminum slab target have been used for preliminary studies of the aluminum spectrum and monochromator tests, the results reported here were obtained with a 100 nm aluminum layer evaporated on a thick standard commercial polymer. The aluminum layer thickness has been chosen with the help of calculation performed with an hydrodynamical simulation. This corresponds to a thickness slightly smaller than the ablation length. That minimizes the density of the aluminum plasma between active plasma and the target surface, in view to help to a radial escape of photons better than in the case of massive target. This is necessary to avoid radiation trapping effect which destroys the population inversion by pumping from the ground level to the lower level of lasing transition.

## 2.2. Soft X-ray spectrometer.

The figure 2 presents a scheme of the optical system showing the spectrometer, the plasma column and the multi-layered mirror.

It is known that, among the X-UV light emitted when looking axially at a long

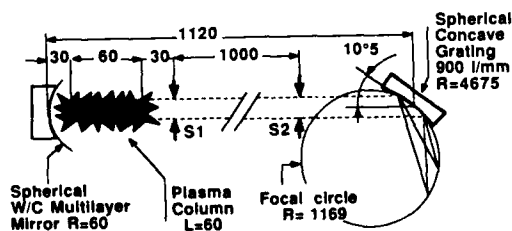


**Figure 2.** Scheme of the spectrometer, plasma column and mirror arrangement. The distance between each element is indicated. All indicated lengths are in millimeter. Typical slit widths are: 450  $\mu\text{m}$  for the exit slit S2 and 300  $\mu\text{m}$  for the entrance slit S1.

plasma column, the lines for which the plasma does amplify radiation have a noticeable directivity. So an improvement of sensitivity to amplification phenomena will be obtained if the spectrometer is designed in order to

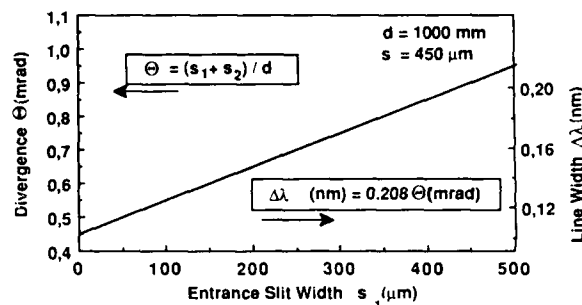


**Figure 3.** Divergence variations, and corresponding line widths, of the 10.57nm line for the spectrometer arrangement shown on Fig.2. The divergences and line widths, versus the entrance slit S1, correspond to a S1-S2 distance 1000mm and a fixed exit slit width 400  $\mu\text{m}$ .

focus more efficiently the parallel rather than the divergent light.

To increase the sensitivity to parallel light our grazing incidence grating spectrometer works on a focalisation circle which is the half of the classical Rowland circle as indicated on Fig. 2. With such an optical scheme, only the parallel light falling on the grating is perfectly focussed on the focalisation circle where the detector is located.

In the present experiment the detector was a flat scintillator of 12mm length coupled to an Optical Multichannel Analyzer (OMA), which gives time-integrated flux measurements. The OMA, has a 25  $\mu$  linear resolution matching the dispersion of the grating ( 900 grooves/mm, curvature radius  $R = 4675 \text{ mm}$ , grazing angle of  $10^\circ 50'$ ).

Optical calculations show that, for a beam falling on the grating with a divergence  $\Theta$ , the instrumental line width is:

$$\Delta\lambda \text{ (nm)} = 0.208 \times \Theta \text{ (mrad)} \quad (1)$$

Therefore, with a divergent source, the resolution of such a spectrometer is dependent on the distance  $d$  between the S1 and S2 slits, represented on figure 2, and to their aperture widths  $s_1$  and  $s_2$ . In our experiment a typical setting is to vary only  $s_2$ , keeping fixed the slit distance  $d = 1000\text{mm}$ . The fixed  $s_1 = 300 \mu\text{m}$  value is the supposed plasma column diameter. The full divergence for this simple slit system is:

$$\Theta \text{ (mrad)} = 10^3 (s_1 + s_2) / d \quad (2)$$

For a range of typical slit width  $s_2$ , the theoretical line width and the divergence are plotted on the graph Fig. 3, as deduced from Eqs. 1 and 2. These values will be used later to discuss the results.

### 2.3. Multilayered mirror.

The mirror was a spherical blank, radius of curvature 60mm, coated with tungsten/carbon multilayer (12). A shutter near the mirror surface can be opened or shut from shot to shot in order to compare the spectra corresponding respectively to single- and double-pass. In addition a screen with a 1mm hole diameter is set on the plasma column axis to avoid large surface mirror damage. Slight movements of the blank between two successive shots permit to use the same mirror for several shots. The distance from the mirror to the plasma end was of 30 mm, so the mirror sphere center is just in the middle of the plasma column length. The role of the mirror curvature will be considered later. This short distance makes easier the alignment and relax the tolerances for angular precision and stability. In our case, assuming a 300  $\mu\text{m}$  diameter for the active plasma, the angular precision needed is no more than 2mrad. The proper setting of the mirror is performed at atmospheric pressure by the help of a small He-Ne laser beam sent from the rear of the spectrometer to the mirror and coinciding with the plasma column axis. Then the mirror is oriented until

coincidence between the incoming and the reflected laser beam is obtained

The mirror has 15 tungsten/carbon bilayers with a period adjusted to get the theoretical 0.2nm halfwidth centered on the 10.57nm line. On this spherical multilayer none absolute reflectivity measurement have been done for this wavelength but, according to reflectivity tests achieved at 0.154 nm, with K line from copper X-ray tube on flat similar mirrors, the real reflectivity at 10.57 nm has been evaluated to 5% .

### 3. Experimental results.

Figures 4 a and 4 b, show spectra corresponding respectively to single- and double-pass in the region of the 3d-5f ( $\lambda = 10.57 \text{ nm}$ ) and 3p-5d ( $\lambda = 10.38 \text{ nm}$ ) transitions. From the single- to the double-pass, these lines exhibit significant differences, both in peak intensities and line widths. As observed previously at other wavelengths by two groups (8,9), one sees that double-passing enhances the 10.57 nm line much more than a simple mirror reflection would do without any amplification by the plasma. From the experimentally observed enhancement the gain coefficient can be deduced if the mirror reflectivity is known. We find  $G = 0.5 \text{ cm}^{-1}$ . It is clear that a weaker intensity enhancement affects the 10.38 nm line for which population inversion is also predicted.

Besides this main result one observes an half width decreasing of the 10.57 nm line, about 30%, from 0.17 to 0.12 nm as indicated on Fig. 4. We comment this point as follows

One can evaluate the geometrical divergence of the beam emitted by a plasma column diameter  $D$  and length  $L$  by the usual  $2D/L$  value. In our case that would correspond to 6 mrad. But, according to Eqs. 1 and 2 summarized on the Fig. 3, the slit setting ( $s_1 = 300 \mu\text{m}$   $s_2 = 450 \mu\text{m}$  and  $d = 1000 \text{ mm}$ ) leads to a

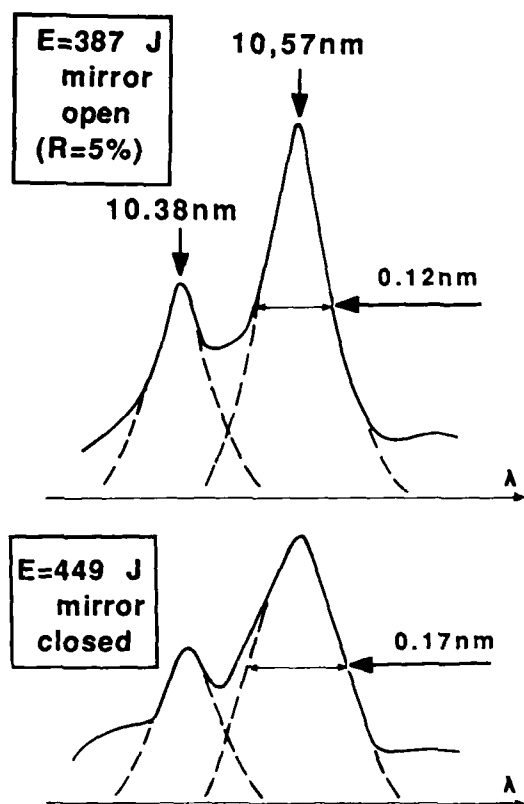


**Figure 4.** Comparison of intensities and widths obtained with a single- and double-pass for the two aluminum lines 3d-5f ( $\lambda = 10.57 \text{ nm}$ ) and 3p-5d ( $\lambda = 10.38 \text{ nm}$ ). The target is a 100 nm aluminum layer evaporated on a thick polymer. The reflectivity of the multilayer, for double pass spectra, is about 5%.

0.75 mrad maximum divergence and a theoretical half width  $\Delta\lambda = 0.16 \text{ nm}$ . So with sources having divergence larger than 0.75 mrad the observed widths is due to slit collimation and is quite similar for all lines. With an experimental uncertainty less than 10% this corresponds to the 0.17 nm experimental width obtained on the single-pass spectrum without mirror. From the 0.12 nm half width observed on the double-pass spectrum, through the same Eqs. 1 and 2, we can now infer a 0.5 mrad divergence. This 30% in reduction

compared to the single-pass spectrum needs to be explained.

At the present stage of our analysis it should be more than hazardous to ascribe the 0.50 mrad divergence to a corresponding parallel beam produced by the double-passing. Another hypothesis to explain such divergence-reduction, is the possibility to get a decrease from the 300  $\mu\text{m}$  in single-pass to about 100  $\mu\text{m}$  in double pass for the diameter of the emitting zone at the end of the plasma. In such case the  $s_1 = 300 \mu\text{m}$  would not be the effective entrance collimator, at the contrary to the single-pass plasma which has a diameter comparable to  $s_1$ .

To explain a decreasing of the active beam diameter in the double-pass case, we can identify two possible reasons: mirror focus-sing effect and beam steering induced by a radial gradient of index or gain. Although the radial gradient index has not a perfectly cylindrical symmetry and cannot be modelled precisely, this effect has been tentatively tested with the help of a 1-D model and plane or spherical waves coming out from different plasma points. At the present stage of the analysis (11) that leads to disregard a coarse geometrical effect due to the mirror shape. On another side, the refraction index contribution is also certainly negligible in our case, because the electronic density is at least two orders of magnitude below that which is known for inducing noticeable effects. However one can have focussing effects due to the gain coefficient profile. The so-called lenslike medium effect (13) should explain the reduction of the cross-section of the reflected beam during the propagation through the plasma column. Its magnitude has been calculated for plasma column characteristics close to the experimental ones. Considering the gain lifetime of the recombination system and the short distance from plasma end to mirror we supposed we don't need to use time dependent gain model or to take into account time degradation for the mirror.

In such calculation our plasma was considered in a steady state and the radiation path was modelled through a formal constant complex optical index, the imaginary part of which being set in such way to represent an amplification of the medium. We conclude that the most realistic explanation for the importance of the observed 30% width decreasing on the 10.57 nm line in the double pass spectrum is to suppose that the emissive zone is reduced by comparison to the single pass.

### **Conclusions**

A new experimental set-up has been organized to study the 10.75 nm line which is now well known to present ASE. Our first experiment had shown a large amplification effect and also a noticeable narrowing of the line-shape. Such new observations are due partially to two main differences of the geometry of our plasma experiment compared to the other ones. The first is the long length of our plasma column; because beam steering effect is a function of the plasma length column. The second is the peculiarity of the optical scheme of the spectrometer. At the contrary to the Rowland circle and flat field optical designs, which work well for point source and divergent beam, our system is more adapted to parallel light beam and so to source with large depth like long plasma columns. By comparison to the other spectrometers used in similar experiments, that means a better collection efficiency for the part of the light emitted with low divergence than for iso-tropic emission. So even if the same phenomena were present in other experiments, we were more able to detect it with our new spectrometer.

The high sensitivity of this spectrometer to discriminate the divergence of different components in a plasma spectrum encourages us to pursue on this way and to look more about coherence

effects in different plasma conditions. The side illuminated thin foil target permit to set mirrors cavity close to the plasma ends without blocking laser illumination. Combined with the long gain life time, we can explore a maximum number of path lengths with different kind of double side cavity models. The long 60mm length column increases also the possibility of studying beam guiding effects.

The recombination scheme we are using is less demanding in laser energy than the collisional excitation does and have longer gain time life. This is specially important to study shorter wavelength lasing transitions without need of exceptional powerful laser facilities.

### **Acknowledgements**

The authors thank heartily J.C. Lagron, C. Vinsot, M. Cousy and G. Tevanian for their crucial technical preparation. They acknowledge the financial support of the D.R.E.T under contract 85/186.

+ National Facility for Use of Intense Lasers from CNRS and Ecole Polytechnique, 91128 Palaiseau Cedex (France)

\* LURE Batiment 209D Université Paris Sud 91405 Orsay (France)

### **References and Notes**

1. P. Jaeglé, G. Jamelot, A. Carillon and C. Wehenkel, "X-Ray studies in laser-produced plasma," Abstract of paper presented at the International Conference on X-Ray and X-UV Spectroscopy, Sendai, Japan (1987) and published in Japanese Journal of Appl. Phys. **17**, p.483 (1978).
2. G. Jamelot, P. Jaeglé, A. Carillon, A. Bideau, C. Möller, H. Guennou and A. Sureau, "Evidence of population Inversion in Li-like aluminum ions in a laser-produced-plasma," in Proceedings

- of the International Conference on Lasers' 81, C.B. Collins, eds. (STS Press Mc Lean, Va. 1981), p.181.
3. D. Jacoby, G.J. Pert, S.A. Ramsden, L.D. Shorrock and G.J. Tallents, Opt. Comm. 37, p.193 (1981).
  4. D. Matthews et al., "X-ray laser research at the Lawrence Livermore National Laboratory Nova laser facility," J. Opt. Soc. Am. B, 4, p.p.575-587 (1987).
  5. P. Dhez, G. Jamelot, A. Carillon and P. Jaeglé, "X-UV gain amplification studies in laser plasma using normal incidence multilayer mirrors," in Proceedings of the Second Topical Meeting on Laser Techniques in the Extreme Ultraviolet, AIP Conf. Proceedings N° 119, D.E. Harris and T.B. Lucatorto, eds., p.199.1(1984)
  6. E. Spiller, "Evaporated multilayer dispersion elements for soft X-rays", in AIP Proceedings: Low Energy XRay Diagnostics, N°75, D.T. Atwood and B.L. Henke, eds. (1981) p.p. 124-
  7. T.W. Barbee, "Sputtered layered synthetic microstructure (LSM) dispersion elements" in AIP Proceedings: Low Energy XRay Diagnostics, N°75, D.T. Atwood and B.L. Henke, eds. (1981)
  8. S. Suckewer et al., "Amplification of stimulated soft X-ray emission in a confined plasma column," Phys. Rev. Lett., 35, (1985), p.p-1753-1756
  9. N. M. Ceglio, D.P. Gaines, D.G. Stearns and A.M. Hawryluk, "Double pass amplification of laser radiation at 131Å", submitted to Optics Communications. and N. M. Ceglio, D.P. Gaines, R.A. London, J.E.. Trebes and D.G. Stearns, "Time resolved measurement of double pass amplification of soft X-rays", submitted to Applied Optics.
  10. N. M. Ceglio et al., "Multipass amplification of soft X-rays in a laser cavity", Optics Letters 13, 108 (1988).
  11. P. Jaeglé, A. Carillon, P. Dhez, B. Gauthé, F. Gadi, G. Jamelot and A. Kisnick, "X-ray experiment with a long recombining-plasma column," Euro-physics letters Z, pp.337-342 (1988) .
  12. We are are grateful to the Institut d'Optique d'Orsay who prepared the blank and to R. Rivoira and Y. Lepetre from University of Aix Marseille (Dept. de Physique des Interactions Photon-Matière) for the multilayer coating.
  13. H. Kogelnick, Applied Optics, 4, p.1562. (1985)

# Short Wavelength Lasers: Something New, Something Old

P. L. Hagelstein

*Massachusetts Institute of Technology, Research Laboratory of Electronics  
Cambridge, Massachusetts 02139*

## Abstract

Significant amplification in the EUV and soft x-ray spectral regimes have been demonstrated recently at a number of laboratories using very high power ICF class lasers as pump sources. We discuss in this paper the possibility of developing short wavelength lasers on a smaller scale by scaling the electron collisional scheme in nickel-like ions to lower  $Z$ . Additionally, we examine population inversions in neodymium-like ions as an alternate route towards a small scale soft x-ray laser.

We consider specifically the design of a transient nickel-like molybdenum collisional laser based on a  $4d - 4p$  transition near 194 Å. Such a laser could be driven by a 10 Joule Nd:glass pump laser system. In addition we consider the extension of the electron collisional scheme to neodymium-like U, in which the monopole-excited  $5f - 5d$  transition occurs near 71 Å.

## Introduction

During the past several years, progress in the area of laboratory x-ray laser research has been made principally at laboratories specializing in inertial confinement or magnetic confinement fusion research. Currently, successful x-ray laser experiments generally involve teams of experimentalists, theorists, major pump facilities and sophisticated diagnostics.

No one has yet developed an x-ray laser at home in their garage.

Laboratory x-ray laser systems are not commercially available at this time from any company. If such systems were easily available, one might imagine that they would be used for tasks similar to those for which UV lasers are currently employed, except at shorter wavelength.

The major point of this paper is to show that, at least in principle, it should be possible to extend the electron collisional scheme to lower  $Z$  to a regime accessible to small scale laser pump sources. Specifically, that laboratory x-ray laser experimental research may one day (soon) be considered within the realm of "small science" (although perhaps still not accessible to a hobbyist in his/her garage) through the use of the schemes described here or through other methods.

Substantial effort has recently been focussed on the physics of plasmas produced by very high intensity sub-picosecond optical pulses. The argument has been made that the requisite energy density for x-ray laser studies can easily be produced and that the pump sources are benchtop few joule systems. Precise details of how such lasers might work in practice seems largely (except for inner-shell photo-pumped schemes) to be determined. In spite of an impressive array of talent and resources currently involved in this work, there are no reports to date of significant amplification in the EUV or soft x-ray regime using short pulse techniques.

The present proposal concerns primarily the development of a short wavelength (194 Å) laser at the university level. The method which we plan to use is a version of the nickel-like excitation scheme, which at shorter wavelengths (50-70 Å) has been very successful at LLNL,<sup>1-6</sup> scaled down to work with a "tabletop" pump laser.

This work is motivated by a number of observations:

1. X-ray lasers which require very large drivers (pump lasers) will be expensive and impractical for applications.
2. The nickel-like scheme is by now a "proven" scheme, and is amenable to design using established computational tools.
3. Recent advances in slab laser technology have led to the development of high-power slab laser systems which can produce tens of joules of energy per pulse at ten hertz.<sup>7</sup> The EUV laser which we are proposing could in principle be used as a short wavelength convertor for a high power slab laser to produce a milliwatt average EUV output.

The extension of the electron collisional scheme to neodymium-like ions<sup>8</sup> is also considered in this work. In principle, one might expect that since the nickel-like system works "better" (in the sense that amplification at shorter wavelength is possible for a given laser intensity), that working with neodymium-like ions (which are analogs one shell further filled) would be better still.

We have begun an investigation of this suggestion, and have found that due to the presence of metastable states (which do not similarly degrade the operation of either the neon-like<sup>8-11</sup> or nickel-like systems) the neodymium-like ions are not as attractive as might otherwise be expected. Nevertheless, the collisional scheme in the Nd-like sequence is sufficiently interesting to warrant further investigation.

### Applications

We have argued that exploration of short wavelength (EUV) laser schemes which require relatively modest pump sources is motivated by applications. In our field, the question of precisely what applications are available for x-ray lasers is often asked, and the answers are not always obvious. For example, it is often said that x-ray lasers will have a large impact in biology through holographic imaging of living cells, and that this task will require a sub-44 Å x-ray laser. This argument, whether correct or incorrect, has for years and is currently driving research efforts in the field.

Our view is that ultimately a small-scale "benchtop" x-ray laser system which is relatively cheap and easy to use will have many uses for research in academia and in industry.

Examples of potential applications include nonlinear spectroscopy and mixing of EUV radiation with both optical and EUV light. Such studies might be of interest in a number of scenarios:

- Actively driving resonant or ionizing transitions in neutral or ionized atomic systems in order to study population kinetics of interest for atomic physics, astrophysics and short wavelength laser research.
- Mixing EUV light with EUV light to produce very bright sources at shorter wavelengths. Such mixing would involve multi-photon transitions in moderately stripped complex ions.
- Mixing EUV with optical radiation to provide bright tunable sources in the EUV.

Phase sensitive diagnostics and holographic probing of thin (0.1 μ) samples or surfaces may prove useful. We envision solid state and biological samples. Although it would not be possible to resolve atoms or molecules, ultimately resolution on the order of a wavelength (200-300 Å) should be attainable. These techniques should be very sensitive in determining transverse profiles of absorbing monolayers on thin films. Time resolved imaging of the surfaces of cells *in vivo* may be useful for the biology community.

High intensity EUV radiation can in principle be generated by focusing the output of a short wavelength laser to a spot. Under such conditions one might expect to create small very dense hot plasmas. It is possible that multiphoton absorption of EUV radiation could be demonstrated.

It is possible that the x-ray laser will find applications in the area of photolithography, specifically in the areas of reduction or holographic lithography. An x-ray laser source for this application would have to have a very high average power (tens to hundreds of milliwatts)

and a wavelength comensurate with the schemes under discussion in this proposal.

### Electron collisional excitation in nickel-like ions

The proposed system is based on the collisional excitation scheme in low  $Z$  nickel-like ions in a dense laser-produced plasma (although amplification in nickel-like ions has been demonstrated at high  $Z$ ,<sup>4</sup> there are no reports of amplification at low  $Z$  due in part to difficulties to be discussed shortly - the method which we are proposing is in this sense novel). Nickel-like molybdenum (see Figure 1), for example, has a monopole-excited  $4d - 4p$  line which we estimate to be near 194 Å. Although the focus of our discussion will be on molybdenum, we are interested in the isoelectronic ions of neighboring  $Z$ .

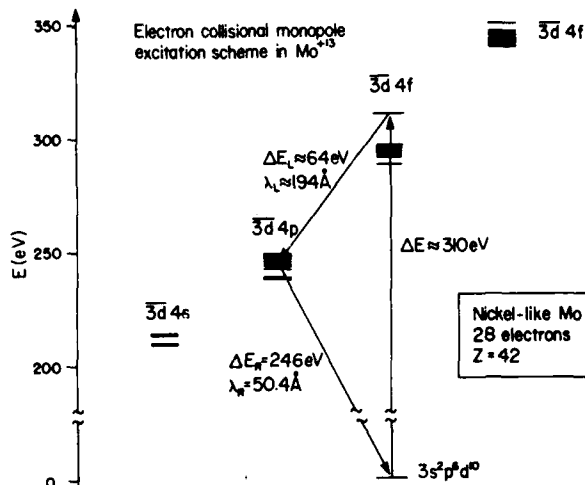


Figure 1: Electron monopole collisional excitation scheme in nickel-like molybdenum.

The nickel-like ions are attractive due to the relatively large ratio between laser transition energy and  $3 - 4$  excitation energy. This means that the ions are relatively easy to produce and excite at a given laser wavelength, relative to other schemes at the same laser wavelength. Nd-like ions have a ratio which is even more favorable.

In nickel-like ions, electron collisional excitation of the  $3s^2 3p^6 3d^{10}$  ground state can lead to substantial production of population in the  $3s^2 3p^6 3d^9 4d^1 S_0$  state. This requires that molybdenum be ionized thirteen times in a moderately dense ( $2 - 4 \times 10^{18}$  electrons/cm<sup>3</sup>) and transient plasma, and that an electron temperature in excess of 150 eV be present.

The monopole excited  $1S_0$  state serves as the upper laser state for a  $4d - 4p$  laser transition to the  $3s^2 3p^6 3d^9 4p^1 P_1$  lower state. Fast radiative decay of the  $1P_1$  state in the absence of radiation trapping ensures the production of a population inversion. The nickel-like system is more efficient than the neon-like system since the laser transition energy is a larger fraction of the excitation energy in the nickel-like system by a factor of about 2.5.

The nickel-like system has proven to be attractive both theoretically and experimentally at higher  $Z$  at

LLNL during the last few years.<sup>1-6</sup> Gain has been observed in europium ( $Z=63$ ) and ytterbium ( $Z=70$ ) at 66 Å and at 50.2 Å, respectively.<sup>4</sup>

### Population kinetics and gain

We have constructed a detailed atomic physics model of nickel-like molybdenum and surrounding sequences using a relativistic Hartree Fock model (the relativistic atomic physics code YODA,<sup>3</sup> which has been used with success in previous design work<sup>1,2,5,6,8,10</sup>), and we have examined the ionization balance and small signal gain.

Although a number of lines in the vicinity of 250 Å are calculated to have a small gain ( $0.1 \text{ cm}^{-1}$ ) (see Figures 2-4), the monopole-excited line at 194 Å does not show gain under steady state conditions. The reason for this is that the plasma is over-ionized in steady state at electron temperatures where significant excitation occurs. Substantial gain is computed on the 194 Å line under transient (non-steady state) conditions, and as a result we must arrange for such conditions in our target design, which is considered in the next section.

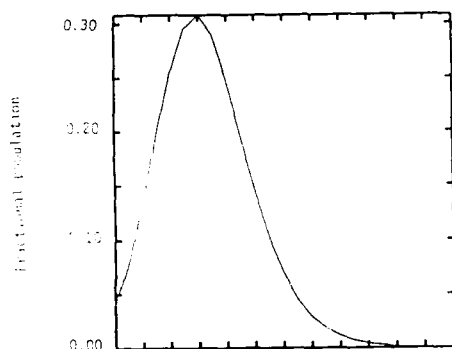


Figure 2: Fractional population of nickel-like ions vs. electron temperature at the optimum density ( $N_e = 2.8 \times 10^{18}/\text{cm}^3$ ) in steady state. Since the 3d-4d excitation energy is 300 eV, very little direct excitation occurs since the significant nickel-like population occurs under 100 eV.

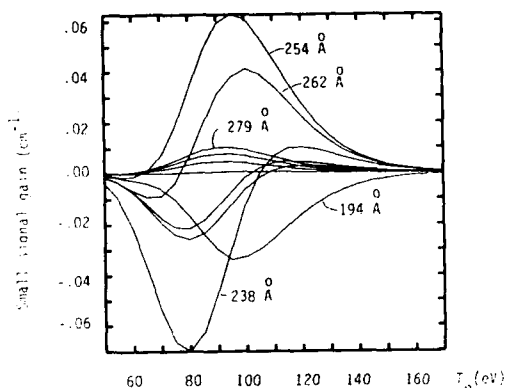


Figure 3: Gain on the 4d - 4p transitions as a function of electron temperature at the optimum density ( $N_e = 2.8 \times 10^{18}/\text{cm}^3$ ) in steady state. High gain can be achieved only under non-steady state conditions.

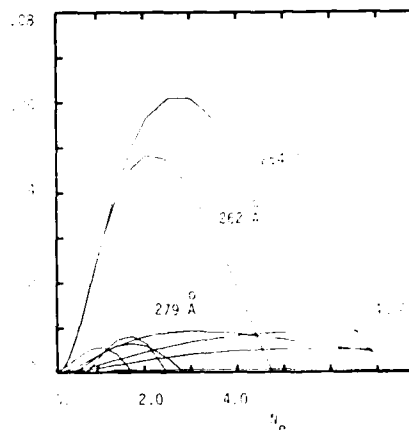


Figure 4: Gain on the 4d - 4p transitions as a function of electron density 100 eV in steady state.

If the electron temperature rises rapidly (within 100 psec) to 200-300 eV at low density, then the plasma ionizes through the nickel-like sequence relatively slowly. During this transient stage, both high electron temperature and nickel-like ions are present, and as a result very substantial ( $3-5 \text{ cm}^{-1}$ ) gain can be produced on the 194 Å line.

The low- $Z$  nickel-like ions tend to be sensitive to radiation trapping on the 3d - 4p transition at 50.4 Å (see Figure 1). As a result, the optical depth of the molybdenum must be restricted in at least one transverse dimension. A characteristic length under the conditions of interest is roughly  $40 \mu$ . This requirement leads us to consider "tamped" plasmas, where the laser medium ions are restricted in space in at least one dimension.

### Target design and plasma modeling

Our current target design for a molybdenum collisional excitation laser is essentially a thick-film design in which the molybdenum is laterally tamped (see Figure 5).

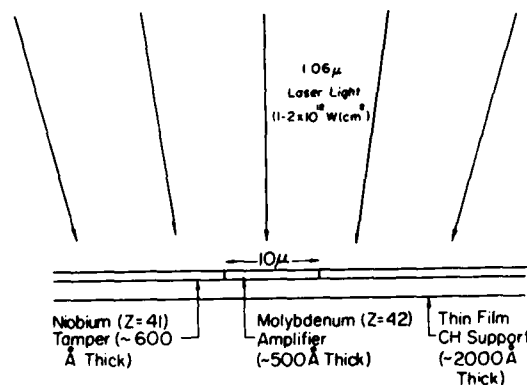


Figure 5: Schematic of a simple tamped thick film laser target.

A sequence of approximately 5 short (100 picosecond) pulses of  $1 \mu$  radiation is incident on the metal surface. The molybdenum coating initially has dimension of  $10 \mu$  by 1 cm, and is approximately 500 Å thick.



The incident laser pulse is larger, imaging on the surface at  $50 \mu$  by  $1 \text{ cm}$  and centered on the molybdenum strip.

If the incident intensity peaks at  $2 \times 10^{12} \text{ W/cm}^2$ , then coronal plasma temperatures in the neighborhood of  $400 \text{ eV}$  may be expected over part of the duration of the laser pulse. This expectation is realized in 2-D numerical simulations using the LASNEX laser fusion code at LLNL.

For example, we consider some results from a 2-D LASNEX simulation of a Mo/CH thin film target. This calculation was done by Steve Maxon at LLNL. The plasma expands dramatically away from the initial surface of the foil, and a thin strip which is initially  $10 \mu$  at the surface expands to  $40 \mu$  at  $150 \mu$  above the surface (the Lagrangian mesh is shown in Figure 6). (This result is for an initial laser illumination width of  $90 \mu$  instead of  $50 \mu$ , but we expect similar behavior for narrower illumination).

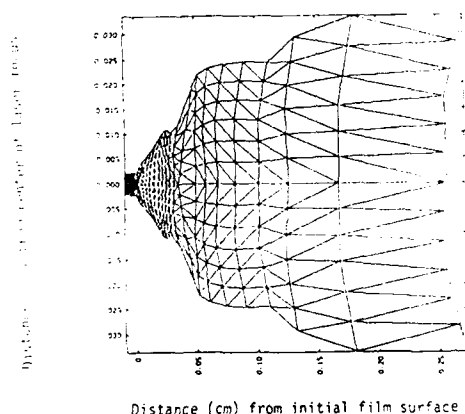


Figure 6: Part of the Lagrangian mesh (initial  $40 \mu$  spot) from 2-D (LASNEX) simulation of a laser target. Snapshot is from the first "strong" pulse of a Gaussian train.

We show the temperature and density profiles in Figure 7 and 8. The electron density is roughly  $1 - 2 \times 10^{19} \text{ cm}^{-3}$  and the temperature is  $200-300 \text{ eV}$  in the region of interest to us. (Temperatures exceeding  $500 \text{ eV}$  are observed later in this calculation).

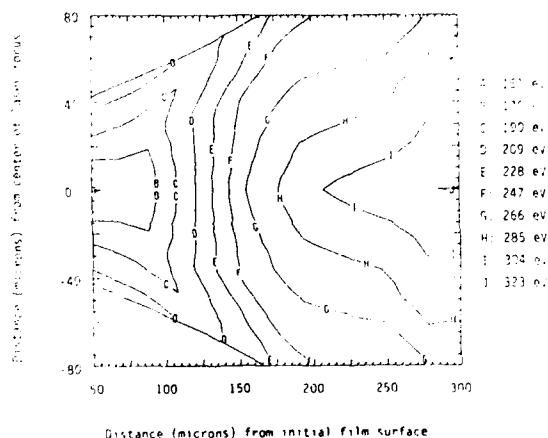


Figure 7: Temperature profile computed during the first strong pulse for the problem of Figure 7.

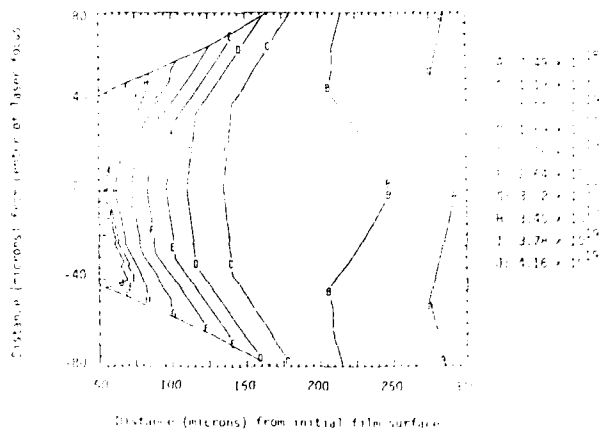


Figure 8: Electron density isocontours for the conditions during the first strong pulse for the problem of Figure 7.

Gain contours from XRASER for the  $194 \text{ \AA}$  line are shown in Figure 9 under the assumption of no radiation trapping. Small signal gains of  $5-10 \text{ cm}^{-1}$  are computed for this simulation. The trapped gains are lower and dependent on the width of the initial molybdenum strip. For the case of  $10 \mu$  initial width, the trapped gain is roughly half of the values shown.

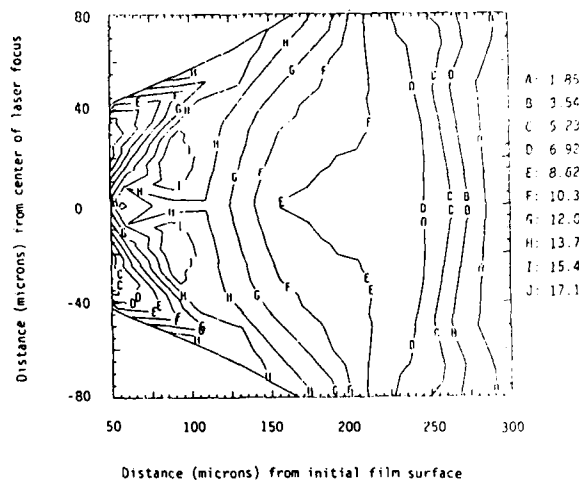


Figure 9: Small signal gain contours for the  $194 \text{ \AA}$  line assuming no trapping. (If the initial molybdenum width were  $3-5 \mu$  instead of  $10 \mu$ , then gains of this magnitude should be observed over  $12-20 \mu$  transverse distances).

The plasma expansion between pulses is significant. Our calculations so far suggest that for pulses which lie within a Gaussian envelope, the first 2-3 (weak) pulses prepare the plasma. The first 2-3 strong pulses produce plasma conditions for  $100 \text{ psec}$  around the peak of the pulse which appear to be attractive for our requirements (where  $7 \text{ nsec}$  between pulses is used). During the following pulses, serious plasma expansion occurs.

Although useful temperatures and densities are produced, the operation of the amplifier will degrade.

A reduction in plasma degradation may be available through using either a smaller spot size or by arranging to have a thin high  $Z$  substrate to cool the plasma between pulses and to slow down plasma expansion.

The laser energy required to illuminate two amplifiers over 1 cm by  $50\mu$  (each) is estimated to be

$$E = 2NIA\Delta t$$

$$= 2 \times 5 \times (2 \times 10^{13} \text{ W/cm}^2) \times (5 \times 10^{-3} \text{ cm}^2) \times (10^{-10} \text{ sec})$$

$$= 10 \text{ J}$$

The plasma is pumped by a pulse train, and gain is realized in the modeling for a short time while a pulse is incident. Since several nanoseconds elapse between subsequent pulses, there is time for an amplified EUV pulse to travel to a reflector<sup>12,13</sup> and back to provide feedback.

#### Collisional excitation in Nd-like ions

The electron collisional excitation scheme in neon-like and in nickel-like ions is based on the existence of very strong monopole excitation cross sections from the ground state. The neon-like ground state contains 10 electrons in completely filled  $K$  and  $L$  shells. The nickel-like ground state contains 28 electrons in completely filled  $K$ ,  $L$  and  $M$  shells. The occurrence of a completely filled low-lying ground state (with low degeneracy) enables a substantial fraction of population to be concentrated in that state, which aids in developing gain.

The neodymium-like ion is the analog of the nickel-like ion for highly stripped systems. The ground state contains 60 electrons which completely fills orbitals of the  $K$ ,  $L$ ,  $M$ , and  $N$  shells. From a consideration of the scaling of distorted wave collisional cross sections in different sequences, it was noted that the neodymium-like ions should possess a very large monopole excitation cross section for the  $4f - 5f$   $^1S$  to  $^1S$  transition.<sup>6</sup> Because of these points, there seemed to be significant motivation to consider the design of short wavelength lasers based on the collisional scheme in neodymium-like ions.

Further motivation for considering neodymium-like ions comes from the favorable scaling of the ratio of laser transition energy to excitation energy. For example, in neon-like selenium, one must excite a 1550 eV transition to obtain gain at 68 eV (the strongest  $J = 2$  transitions are pumped primarily through other mechanisms in selenium), giving a ratio of about 1/23. In nickel-like gadolinium, the  $3d - 4d$  excitation occurs near 1340 eV, and the strongest  $4d - 4p$  monopole-excited line is near 181 eV, resulting in a ratio of 1/7.4. This favorable scaling for the nickel-like ions has enabled gain to be observed at rather short wavelengths (50.2 Å in ytterbium) at LLNL. The same ratio is yet more favorable in Nd-like ions. In Nd-like uranium, the excitation energy for the  $4f - 5f$  strong monopole transition is near 600 eV, and the expected  $5f - 5d$  laser transition energy is near 175 eV, giving a ratio of 1/3.4.

We have focussed our attention so far on Nd-like uranium, primarily because the atomic physics seems to fa-

vor gain in higher  $Z$  systems in the Nd-like sequence. Due to the relative radiative decay rates of the  $5f - 5d$  laser transition and  $5d - 4f$  transition which empties the lower laser state, the monopole excitation scheme in lower  $Z$  ions may not work particularly well. The laser scheme is illustrated in Figure 10.

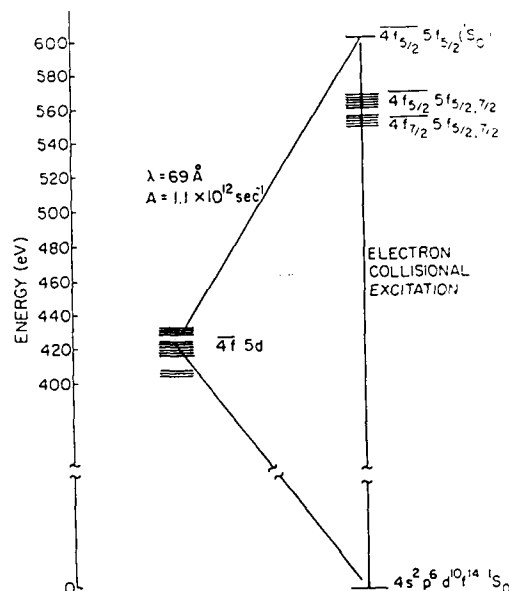


Figure 10: Electron monopole collisional excitation scheme in neodymium-like uranium.

We have modified YODA to handle the neodymium-like sequence, and we have created an atomic physics data set to describe the laser kinetics in Nd-like uranium. The monopole collisional excitation collision strength, which was estimated to be 0.22 in reference 6, is found to be closer to 0.20 near threshold. We have plotted the distorted wave excitation cross section near threshold in Figure 11.

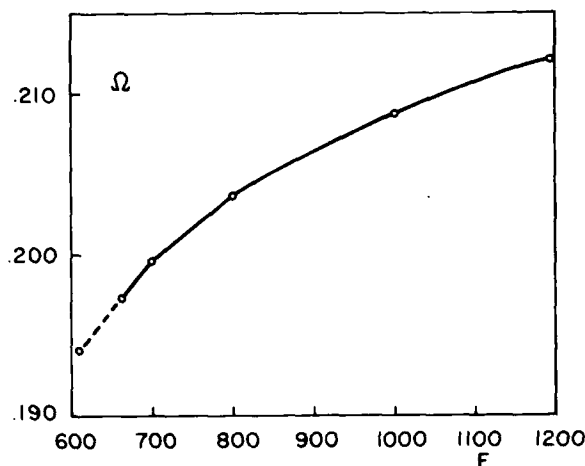


Figure 11: Collision strength for the  $4f - 5f$   $^1S_0 - ^1S_0$  transition in neodymium-like uranium.

We noted earlier that nickel-like molybdenum develops only small gain under steady-state conditions, since the nickel-like ions are present only when the temperature is relatively low in comparison to the monopole excitation energy. We have found a similar result from a calculation of the laser kinetics of neodymium-like uranium – specifically, that there is essentially no gain on any 5 – 5 transition under steady state conditions. Because of this we must consider a *transient* plasma and time-dependent ionization effects in order to discuss gain in Nd-like uranium.

#### Nd-like U gain in a transient plasma

We consider a target design and associated pumping by a Nd:glass laser at  $1\ \mu$  similar to the nickel-like molybdenum laser described earlier. The excitation energy in Ni-like molybdenum is 300 eV, the excitation energy in Nd-like uranium is 600 eV, hence the required temperature is twice as high in uranium. Additionally, due to the larger energy differences between states in the  $n = 5$  manifold, and due to the higher residual nuclear charge, the optimum electron density (close to  $10^{30}$  electrons/cm<sup>3</sup>) for transient gain in neodymium-like uranium is higher by a factor of 5-10 than the corresponding electron density in Ni-like molybdenum.

In order to model the kinetics of the transient laser plasma, we shall adopt a temperature history similar to that observed in the LASNEX calculation described earlier (see Figure 12), and consider a range of densities centered around  $10^{30}$  electrons/cm<sup>3</sup>. The temperature is high for about 200 picoseconds in this model.

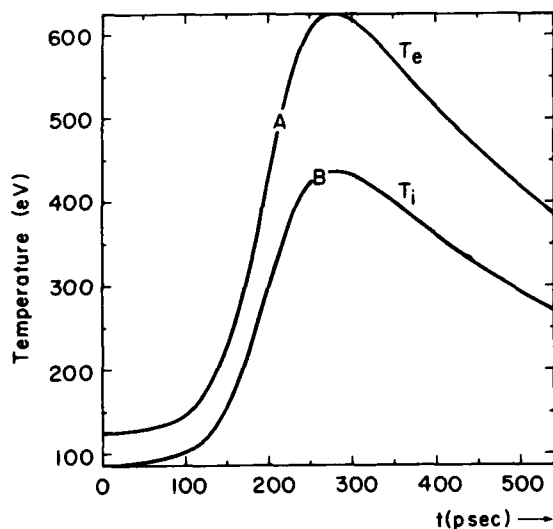


Figure 12: Electron and ion temperature histories assumed for the Nd-like uranium transient plasma simulation.

We find that under these conditions, the plasma ionizes through the neodymium-like sequence while the temperature is high, as shown in Figure 13. The ionization balance was assumed initially to be centered five sequences back.

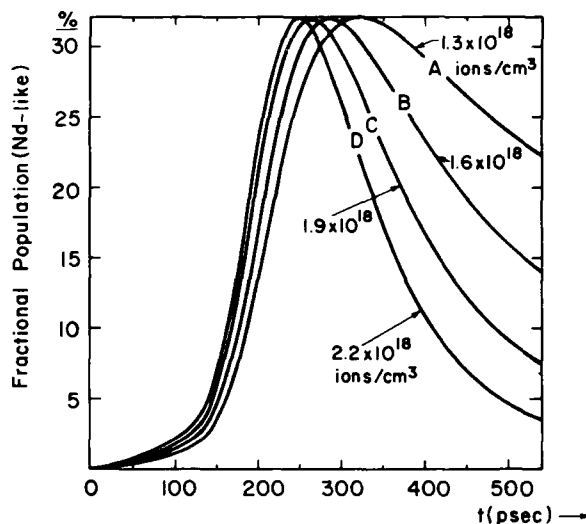


Figure 13: Total neodymium-like sequence fractional population for four different initial total ion densities.

The computation of ionization balance for such complicated ions is nontrivial. As a first cut at the problem, we have connected a detailed model for the neodymium-like sequence with hydrogenic models for neighboring sequences, adjusting the degeneracies of the hydrogenic states to account for the nonhydrogenic splittings which occur. Such a model underestimates multistep collisional processes which lead to ionization through highly split  $n$ -manifolds. Additionally, the dielectronic recombination rates for these ions are completely unknown. They are expected to be large (several times  $10^{-10}$  cm<sup>3</sup>/sec) based on what is known for nickel-like ions, yet there are differences due to large numbers of the doubly-excited states being below the ionization threshold.

As a result of these issues, we recognize that an accurate computation of the ionization balance in the vicinity of Nd-like uranium is well beyond the current state of the art. For the purposes of our estimates, no matter what the precise forward and backward rates are, a plasma transiently heated under the conditions considered here will definitely strip well past the Nd-like sequence, and do so in a time not so different from what we have modeled (since for the 60- and 61-electron ions our models do take into account most of the forward collisional processes). Hence, our model, even though it is relatively crude, should suffice to begin a study of transient gain in Nd-like uranium.

One feature of the collisional scheme in closed-shell ions is the ground state  $^1S$  which tends to be well-populated in neon-like and in nickel-like ions. In the neodymium-like sequence, the total sequence population is very highly fractionated due to the presence of low-lying metastable  $5s$  and  $5p$  states. For example, in both mid- $Z$  neon-like and nickel-like ions, the large majority of the total sequence population up to  $n = 10$  resides in the  $^1S_0$  ground state. In Nd-like uranium, less than 10 per cent of the total sequence population is in the ground state as shown in Figure 14. The remaining population is largely in the  $5s$  and  $5p$  metastables. Because of this,

Nd-like uranium is not as sensitive to radiation trapping as the nickel-like molybdenum scheme is, and the associated characteristic length is somewhat larger than  $100 \mu$ .

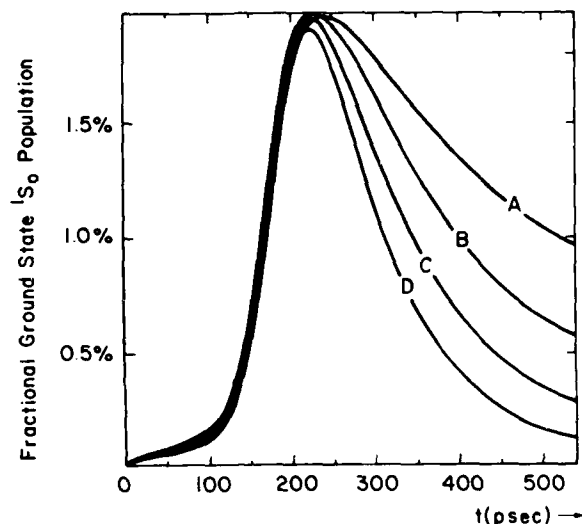


Figure 14: Neodymium-like ground state  $1S_0$  fractional population for four different initial total ion densities.

As a result of this, the monopole-excited small-signal gain is relatively low, as is shown in Figure 15. Peak gains in the vicinity of  $0.7 - 0.8 \text{ cm}^{-1}$  are calculated. Such gains are sufficiently low that our initial excitement and optimism are in retrospect unjustified. Nevertheless, the gain is high enough such that a practical soft x-ray laser could be developed based on the scheme, assuming that resonant absorption or some other effect does not prevent it from being realized experimentally.

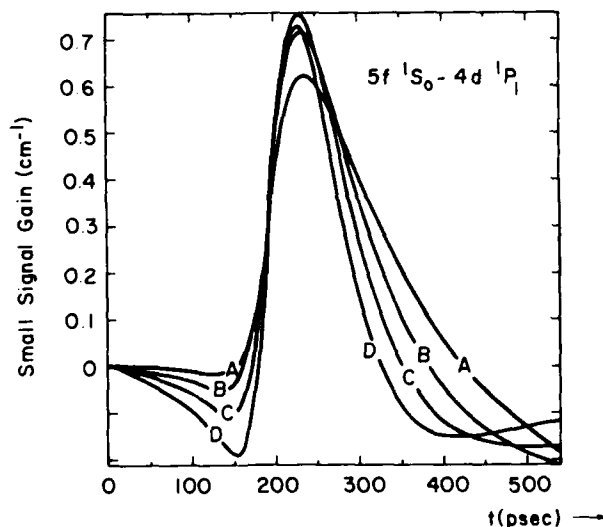


Figure 15: Small signal gain on the monopole-excited  $5f - 5d$  laser transition at  $71 \text{ Å}$  in neodymium-like uranium.

## Summary and conclusions

We have explored the design of an electron collisional laser in nickel-like molybdenum ( $\lambda = 194 \text{ Å}$ ), in order to scale the nickel-like laser scheme down to a more accessible level. We have found that low- $Z$  nickel-like systems do not develop high gain under steady-state conditions (the neon-like and nickel-like lasers developed at LLNL do achieve their observed gain under steady-state conditions), and that the target design and pumping scheme must develop gain under transient conditions.

A transient target design has been proposed and modeled, and the resulting small signal gain at  $194 \text{ Å}$  is found to be very high. The system is sensitive to radiation trapping with a  $40 \mu$  scale length, which requires a laterally tapered target design. (Neither the neon-like nor the nickel-like systems developed at LLNL suffered sufficiently from trapping to require a tapered target design.) The total energy requirement to pump the laser (assuming a cavity made with lossy multilayer mirrors) is about 10 Joules.

We have also examined transient gain in Nd-like uranium at  $71 \text{ Å}$ . The near threshold excitation collision strength is found to be 0.20, which is ten percent less than estimated in Reference 6. No gain is predicted under steady state conditions, and under transient conditions a peak gain of  $0.75 \text{ cm}^{-1}$  is predicted at  $71 \text{ Å}$  on the monopole-excited line at an electron density near  $10^{20} \text{ electrons/cm}^3$ . The fractionation of the sequence population between the ground state and low-lying metastable levels is responsible for the relatively low gain. We have concluded that the system deserves further attention in spite of the fractionation problem.

## References

1. S. Maxon, P. Hagelstein, K. Reed and J. Scofield, "A Gas Puff Soft X-ray Laser Design," *Appl. Phys. Lett.*, **57**, 971 (1985).
2. S. Maxon, P. Hagelstein, J. Scofield and Y. Lee, "Estimated Gains for a Ni-like Exploding Foil Target," *J. Appl. Phys.*, **59**, 293 (1986).
3. P. L. Hagelstein, "Relativistic Distorted Wave Results for Nickel-like Gadolinium," *Phys. Rev. A*, **34**, 874 (1986).
4. B. J. MacGowan, S. Maxon, P. Hagelstein, C. J. Keane, R. A. London, D. L. Matthews, M. D. Rosen, J. H. Scofield and D. A. Whelan, "Demonstration of Soft X-ray Amplification in Nickel-like Ions," *Phys. Rev. Lett.*, **59** 2157 (1987).
5. S. Maxon, P. L. Hagelstein, B. MacGowan, R. London, M. D. Rosen, J. Scofield, S. Dalhed and M. H. Chen, "Calculation and design of a Ni-like soft x-ray laser," *Phys. Rev. A*, **37** 2227 (1988).
6. P. L. Hagelstein and S. Dalhed, "Strong Monopole Collisional Excitation in Highly Stripped Ions," *Phys. Rev. A*, **37** 1375 (1988).
7. Murray Reed at Stanford is developing a high power slab system which runs at a few hertz and at ten

joules/shot (private communication). The high average-power laser group at LLNL is developing a slab system which will produce 30 joules/pulse at 10 hertz (J. Trenholme, private communication).

8. P. L. Hagelstein, "Review of Radiation-Pumped Soft X-ray Lasers," *Plasma Physics*, **25**, 1345 (1984).
9. D. L. Matthews, P. L. Hagelstein, M. D. Rosen, M. J. Eckart, N. M. Ceglio, A. U. Hazi, H. Medeck, B. MacGowan, J. Trebes, B. L. Whitten, E. M. Campbell, C. W. Hatcher, A. M. Hawryluk, R. L. Kauffman, L. D. Pleasance, G. Rambach, J. H. Scofield, G. Stone and T. A. Weaver, "Demonstration of a Soft X-ray Amplifier," *Phys. Rev. Lett.*, **54**, 110 (1985).
10. M. D. Rosen, P. L. Hagelstein, D. L. Matthews, E. M. Campbell, A. U. Hazi, B. L. Whitten, B. MacGowan, R. E. Turner, R. W. Lee, G. Charatis, G. E. Busch, C. L. Shepard and P. D. Rockett, "Exploding-Foil Technique for Achieving a Soft X-ray Laser," *Phys. Rev. Lett.*, **54**, 106 (1985).
11. B. J. MacGowan, M. D. Rosen, M. J. Eckart, P. L. Hagelstein, D. L. Matthews, D. G. Nilson, T. W. Phillips, J. H. Scofield, G. Shimkaveg, J. E. Trebes, R. S. Walling, B. L. Whitten and J. G. Woodworth, "Observation of soft x-ray amplification in neonlike molybdenum," *J. Appl. Phys.*, **61** (1987).
12. N. M. Ceglio, D. G. Stearns, D. P. Gaines, A. M. Hawryluk, and J. E. Trebes, "Multipass amplification of soft x-rays in a laser cavity," *Optics Letters*, **13** 108 (1987).
13. A. B. C. Walker, Jr., T. W. Barbee, Jr., R. B. Hoover and J. F. Lindblom, "Soft X-ray Images of the Solar Corona with a Normal-Incidence Cassegrain Multilayer Telescopy," *Science*, **241**, 1781, (1988).

# X-Ray Laser Related Experiments and Theory at Princeton

S. Suckewer<sup>+</sup>

*Princeton University, Plasma Physics Laboratory, Princeton, New Jersey 08543*

## Abstract

This paper describes a new system for the development of an X-ray laser in the wavelength region from 5 nm to 1 nm utilizing a Powerful Sub-Picosecond Laser (PP-Laser) of expected peak power up to 0.5 TW in a 300 fs pulse. Soft X-ray spectra generated by the interaction of the PP-Laser beam with different targets are presented and compared to the spectra generated by a much less intense laser beam (20-30 GW). A theoretical model for the interaction of atoms with such a strong laser EM field is also briefly discussed. The development of additional amplifiers for the recombining soft X-ray laser and the design of a cavity are presented from the point of view of applications for X-ray microscopy and microlithography. The overview ends with the presentation of recent results on the quenching of spontaneous emission radiation and its possible effect on the absolute intensity calibration of soft X-ray spectrometers.

## 1. Introduction

There is rapid progress in a number of laboratories in the direction of the development of X-ray lasers in much shorter wavelength regions than the ones presently operating near 20 nm as well as progress in the development of lasers in VUV region near 100 nm and below. However in this paper we will not discuss those works, some of which represent very important achievements such as reaching very high gain (much above saturation) in Cesium near 90 nm by the Stanford Group [1]

using relatively low pumping power, generation of very high power density radiation (above  $10^{18}$  W/cm<sup>2</sup>) by the Chicago Group [2] for application for X-ray lasers and the proposal to construct a "table top" VUV laser at 30-40 nm using Ni-like or Nd-like ions by the MIT Group [3].

The intention of this paper is to give a short overview and provide an introduction to the experimental and theoretical work at Princeton presented in series of five papers [4-8] on (i) the development of a powerful sub-picosecond laser system and generated soft X-ray spectra with such a laser related to a new approach to X-ray laser development; (ii) a theoretical model for atoms in very strong EM fields; (iii,iv), improvement of present 18.2 nm laser and its applications for X-ray microscopy; as well as (v) some difficulties with the calibration of the soft X-ray spectrometers due to quenching of Einstein A-coefficients.

## 2. Approach Toward a 1 nm X-ray Laser

The main difficulty in approaching shorter and shorter wavelengths is the requirement for very large pumping power. For example, for X-ray lasers pumped primarily by recombination or electron-excitation processes, the pumping power  $P$  is proportional approximately to  $\lambda^{-4}$  for constant gain  $g$ . This follows from a simple relation between gain, wavelength  $\lambda$ , and population inversion  $\Delta N_{inv}$ . (see e.g. [9])

$$g \sim \lambda^4 \Delta N_{inv}$$

while

$$\Delta N_{inv} \sim P$$

Therefore, in order to decrease the lasing wavelength from 10 nm down to 1 nm, the pumping power would have to be increased approximately by a factor of  $10^4$ . The presently operating laser at 18.2 nm requires a pumping laser of energy  $\sim 300$  J. Without changing a pulse length its energy would have to be in the order of tens of MJ for lasing at 1 nm. Because the size and cost of the laser increases rapidly with energy (but not with power), such a system would be very large and very expensive. Therefore a lot of attention is devoted to the schemes for X-ray lasers in which the metastable and autoionizing levels can be used for storage of pumping energy as was proposed by S. Harris [10] or schemes based on very short (picosecond and sub-picosecond) pumping pulses [11]. This last approach is particularly attractive because with decreasing wavelength of the lasing transition the lifetime of the ion in the upper state  $\tau = 1/\Lambda$ , decreases as  $\lambda^2$  ( $\Lambda$  is the spontaneous transition probability) and is of the order of  $10^{-12}$  -  $10^{-13}$  sec for a transition wavelength of  $\sim 1$  nm.

Therefore pumping is required only for a picosecond or sub-picosecond time duration. After this time energy would just be wasted in heating the target material. Lasers with beam energy of order of only 1 joule and pulse duration of 1 psec can provide a very large power  $P \sim 10^{12}$  Watts. Even more important, such a laser operating in the UV (e.g. KrF excimer laser with wavelength 0.25  $\mu$ ) can be focussed to a 2-3 micron size providing tremendous power density on the target. The power density can be in excess of  $10^{18}$  W/cm<sup>2</sup> (with corresponding electric field  $\sim 10^{11}$  V/cm = 1 kV/A). With this power density it is possible to provide multiphoton excitation and multiphoton ionization of highly ionized ions and use such processes for the creation of population inversion and gain at wavelengths down to 1 nm. However, it seems to be a very difficult problem to both create highly ionized ions and provide selective multiphoton excitation of such ions with a single laser. Therefore our approach is based on using two lasers [12]. The role of one laser with relatively low power and high energy (e.g. 0.5 kJ, 50 ns CO<sub>2</sub> or 100 J, 3 ns, Nd/YLF laser) is to create a plasma column of highly ionized ions which may be confined in a strong magnetic

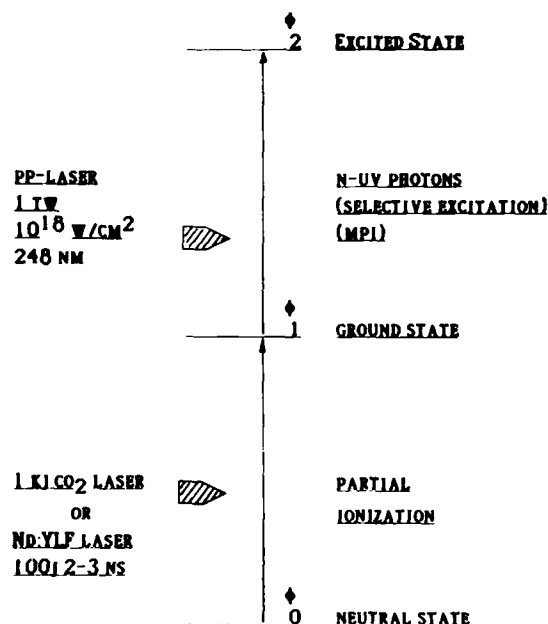


Figure 1. Basic idea of "Two-Laser Approach" to X-ray lasers: a relatively low power and high energy laser "is preparing" ions and an extremely high power sub-picosecond laser creates a population inversion.

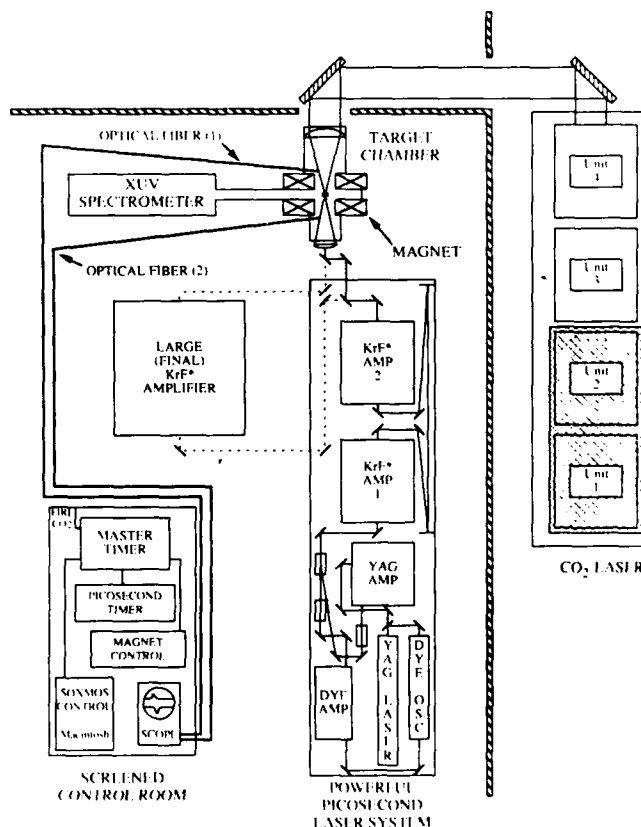


Figure 2. Scheme of the experimental arrangement for the "Two Laser Approach".

field. The role of the second, extremely high power laser (1 J, 1 psec KrF laser) is to generate gain by multiphoton ionization (MPI) or by a very fast ionization (e.g. inner shell ionization) or by selective multiphoton excitation. This approach is illustrated in Fig. 1 and more details about our Powerful Picosecond (Sub-Picosecond) Laser (PP-Laser) system are presented in L. Meixler et.al. [4] paper in this proceeding. In Fig. 2 is shown the scheme of experimental arrangement. The same 0.5 kJ CO<sub>2</sub> laser (or 100 J Nd/YLF laser) which is used for pumping the 18.2 nm laser [13] is re-directed by a system of mirrors and focussed onto a thin foil or fiber target by cylindrical lenses producing an up to  $\sim 1$ -1.5 cm long and 100-150  $\mu$  wide line focus. The target is placed in a vacuum chamber inside a 20 cm long solenoidal magnet, designed for a magnetic fields of up to 150 kG. Axial radiation from the plasma column in the range 0.5 nm-30 nm can be measured by the grazing incidence Schwob-Fraenkel spectrometer "SOXMOS" [14]. The core of the experiment is the PP-Laser which is focussed on the plasma column from the opposite side to the CO<sub>2</sub> or Nd/YLF laser. The PP-Laser can be focussed on the plasma in such a way that travelling wave gain will be provided. Synchronization of the lasers which constitute the PP-Laser system (a simplified block diagram of PP-Laser is shown in Fig. 3), time control of the PP-Laser system in relation to the triggering of the CO<sub>2</sub> or Nd/YLF lasers, magnet and diagnostics is provided by several "Fast" and "Master" (slow) electronic timers. (These timers were specially developed in our laboratory for the experiment). The control system, timers and data acquisition (computers) are located inside a double shielded Faraday Cage in order to isolate them from strong EM noise coming mainly from the CO<sub>2</sub> laser, the large aperture KrF amplifier and magnet. Most of the signals to and from the Faraday Cage are transmitted by optical fibers.

In Fig. 4 is shown a picture of the PP-Laser system without the final KrF amplifier. Located on the right hand side of the picture are the mode-locked YAG laser, dye laser, and three-stage of dye amplifier pumped by a 3J Quantel Nd/Glass laser. On the left hand side are shown two Lambda-Physics KrF amplifiers. A large aperture (5 x 10 cm) KrF amplifier (3rd KrF amplifier) was added to the system and is shown

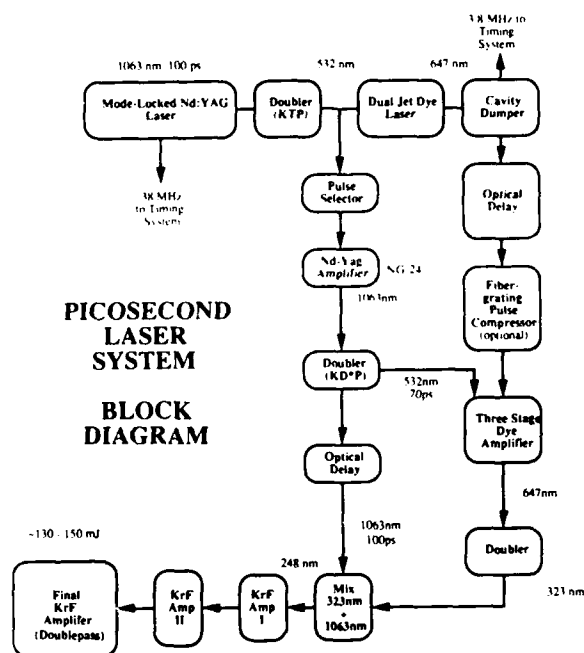


Figure 3. Simplified block diagram of the PP-Laser System.

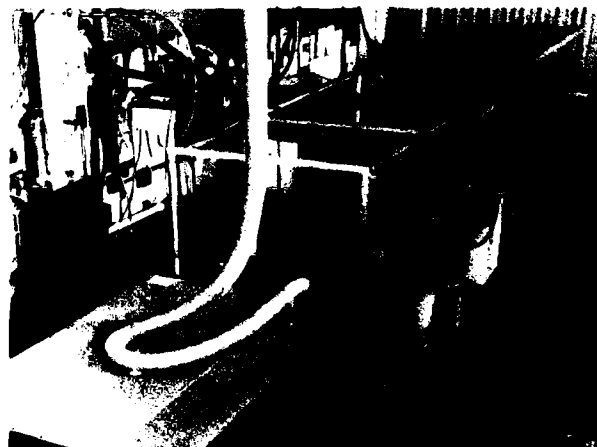


Figure 4. Photo of the PP-Laser System without the final KrF amplifier.





Figure 5. Photo of the large aperture KrF amplifier (final amplifier KrF III, in center of laboratory), magnet (far left), and vacuum system.

in Fig. 5. This amplifier was developed at Princeton University in cooperation with J. Goldhar (Univ. of Maryland) during the last  $\sim 2.5$  years and presently is operating routinely as part of the PP-Laser system. It is a 100 cm long, fast discharge amplifier, which is operated in a double pass mode. The energy of seed pulse from the second KrF amplifier is 10-15 mJ and pulse duration (without compression) is  $\sim 1$  psec. Using a fiber-gratings system for pulse compression (work done in cooperation with J. Fujimoto, MIT) the pulse duration is 250-300 fsec and output energy from final amplifier  $\sim 150$  mJ. In Fig. 6 is shown the result of measurement of the pulse duration using a two-photon excitation technique in Xe [15]. More details about the large aperture KrF amplifier and measurements of the pulse duration for non-compressed and compressed pulses are presented in [4]. During the writing of this paper, measurements of pulse duration of the beam after final amplifier were not yet available however, indirect measurements indicate that final amplifier does not increase the pulse duration implying a PP-laser beam power of  $P \sim 0.5$  TW. The focal spot of such a beam using a less than optimal f/10 lens is expected to be  $\sim 7-8 \mu$  in diameter providing a power density close to  $10^{18}$  W/cm<sup>2</sup> (with a new f/2 or f/3 focussing system the power density should be several times higher).

One of the first experiments with such a high power density laser beam

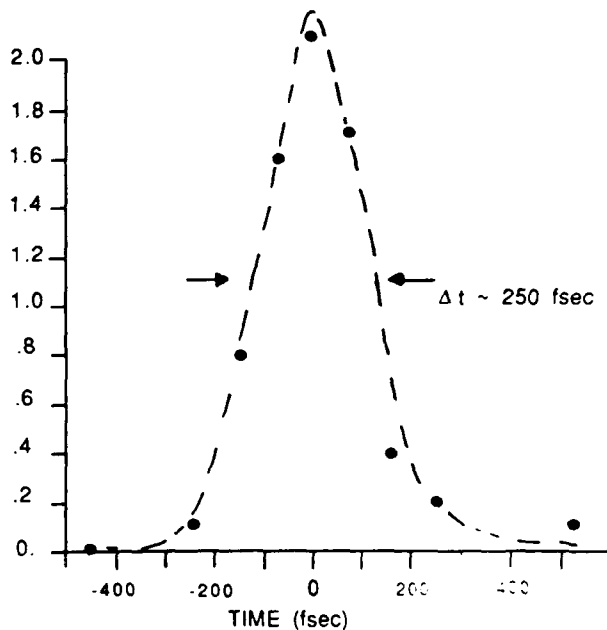


Figure 6. Autocorrelation trace of a compressed pulse after the second KrF\* amplifier.

was the measurement of the soft X-ray spectra of carbon and fluorine. The laser beam was focussed on a rotating cylindrical teflon target and a soft X-ray grazing incidence Schwob-Fraenkel spectrometer "SOXMOS" with multichannel detector monitored the plasma radiation from the target surface. In the lower part of Fig. 7 is shown the spectrum in vicinity of the CVI 33.74 Å and CV 40.27 Å lines (both from  $2 \rightarrow 1$  transitions). Beside the enormous line broadening one may see strongly pronounced unusual structure in the lines. Both broadening and structure are larger than in the spectra obtained with the 20-30 GW, 1 psec PP-Laser beam (without final KrF amplifier) shown in the upper part of Fig. 7. It should also be noticed that the number of shots needed for this short wavelength spectra is not proportional to the laser beam energy but rather to its power (the energy of the laser beam increased by factor of 5-7 while the number of shots decreased by a factor of 20). In earlier spectra obtained with the 20-30 GW PP-Laser ( $10^{16}$  W/cm<sup>2</sup>), part of the large broadening and asymmetry of FVII lines in the 120-140 Å region was attributed to the Stark effect and radiation of forbidden components of the lines [16]. Very recently K. Koshelov [17] interpreted

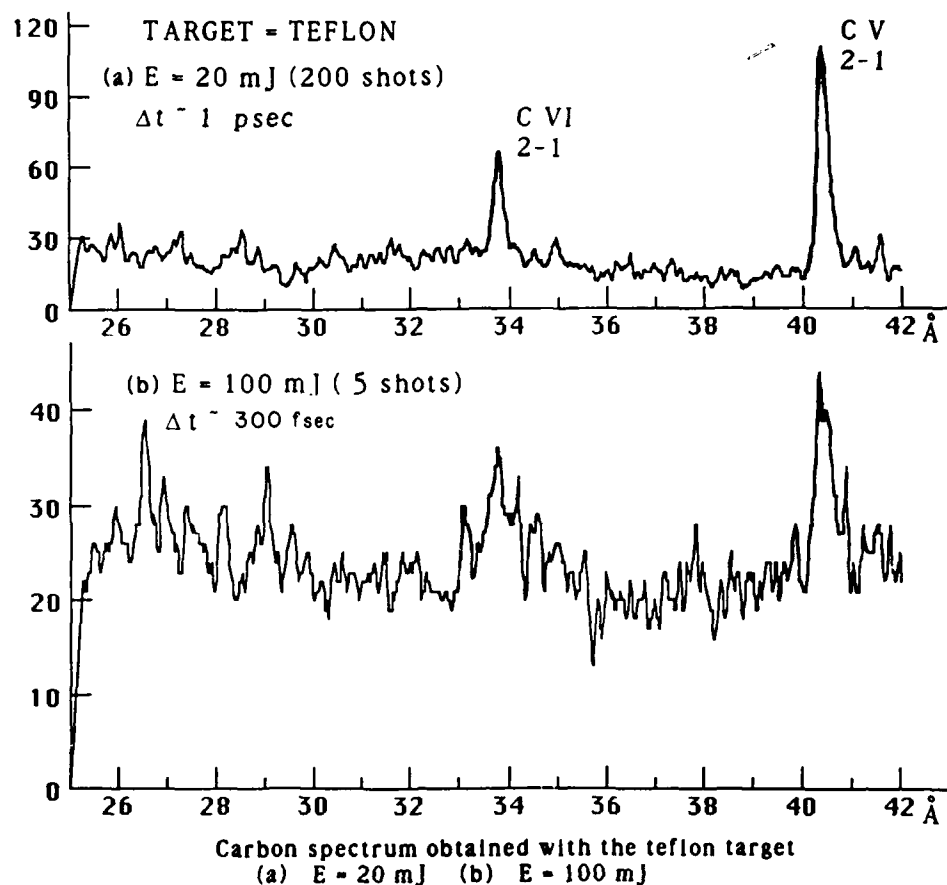


Figure 7. Spectra obtained (a) without compression and (b) with compressed pulse and final KrF\* amplifier.

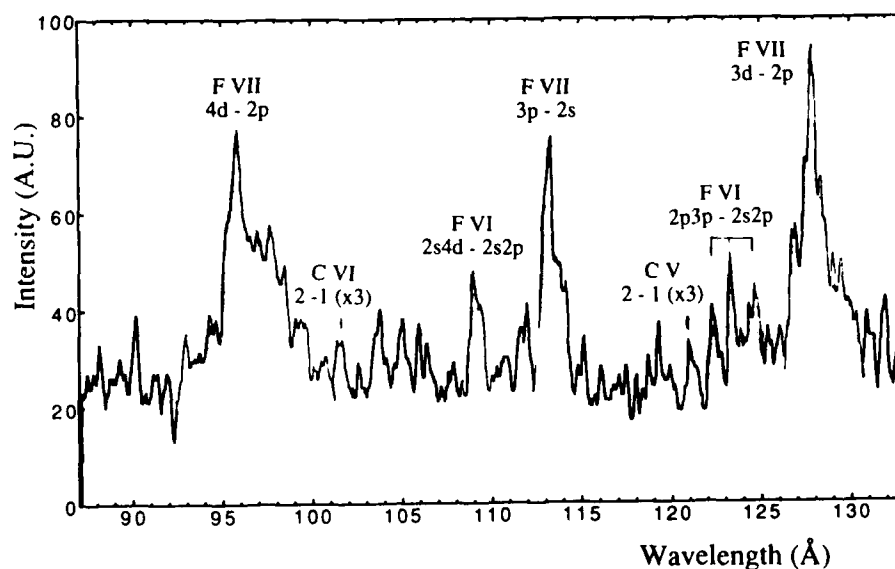


Figure 8. Spectra of FVII obtained with compressed pulse and with final KrF\* amplifier.

asymmetric broadening of the FVII lines as a result of satellite line radiation. Spectral lines of CVI, CV and FVII (Figs. 7,8) excited by the very high power beam seems to indicate a complicated satellite type structure. Of course, the very strong electric field created by such a laser beam may be responsible for these effects. Spectroscopic data for different targets as well as experiments in which a highly ionized plasma will be initially generated by CO<sub>2</sub> or Nd/YLF lasers and after that excited by PP-Laser should enable us to develop a clearer picture of the behavior of highly ionized ions in strong laser fields.

In the meantime, theoretical work is in progress with the aim of answering basic questions related to the use of the PP-Laser for the creation of population inversion for X-ray lasing in the region 5-4 nm down to 1 nm. One such question is: how the ratio between the rate of excitation of the chosen level and the rate of ionization from this level is dependent on the laser intensity (multiphoton processes) and Z of ions? Another question for consideration is: does the presence of other bound states influence the ionization from a given bound state?

The theoretical model is based on a sequence of  $\delta$ -function confining potentials as an approximation to a continuous potential. Such a model allows for relatively simple analytical and numerical calculations of the multiphoton ionization rate under strong field conditions and some of the results are presented in the paper by S. Susskind et.al. [8] in this proceeding.

### 3. Progress in Recombining Soft X-Ray Laser

#### (a) Development of an Additional Amplifier at 18.2 nm

Presently the highest beam energy of our X-ray laser [18] at 18.2 nm (CVI 3-2 transition) pumped by a  $W_L \approx 300$  J CO<sub>2</sub> laser in a 90 kG solenoidal magnetic field is  $W_X \approx 3$  mJ with a 3 min repetition rate. A higher repetition rate is predicted for a recently designed commercial prototype soft X-ray laser (SXL) with a superconducting coil. This system would also be more compact than our laboratory SXL at PPL. The beam energy  $W_X$  is one of the most important parameters at present for applications of the SXL. In order to increase  $W_X$  we have developed an

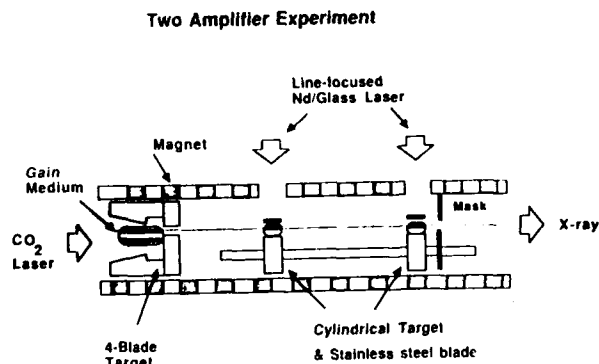


Figure 9. Scheme of arrangement of CO<sub>2</sub> laser pumped X-ray laser (SXL) with two additional SXL amplifiers.

additional SXL amplifier (3 mm long), at 18.2 nm pumped by a line focussed Nd/YLF laser beam on a carbon target. In Fig. 9 the arrangement of CO<sub>2</sub> laser pumped SXL with two additional SXL amplifiers inside the solenoidal magnet is shown schematically. (The magnetic field is crucial for the CO<sub>2</sub> laser pumped SXL but it is much less important for SXL amplifiers pumped by the Nd/YLF laser). Located on the left hand side of the system is the CO<sub>2</sub> laser beam which is focussed on the center of carbon disc target with four carbon blades. Along the path of the soft X-ray laser beam are located two cylindrical carbon targets whose length can be changed from 1 mm to 3 mm by rotation. Thin iron blades in the front of the targets provide additional radiation cooling of the plasma column. We have demonstrated gain up to  $g \approx 8$  cm<sup>-1</sup> in one SXL amplifier with 25 J Nd/YLF laser beam energy (see D. Kim et.al. paper [6] in this proceedings). In Fig. 10 are shown axial spectra in the vicinity of the lasing line CVI 18.2 nm (3-2 transition) and in the vicinity of CVI 13.5 nm (4-2 transition) for 1, 2 and 3 mm long targets. One may see a strong non-linear increase of intensity of the 18.2 nm line (Fig. 11) in comparison to near-linear increase of the intensity of 13.5 nm line. (Note that this line should be optically thin due to the expected population inversion between levels 4 and 2, also in axial spectrometer there is no contribution of the 4th order of the CVI 3.37 nm line to the intensity of the 13.5 nm line). A significant problem here is to match the transverse size ("aperture") of SXL amplifier to the original SXL. We were able to create significant gain with only 6 J pumping energy of Nd/YLF laser,

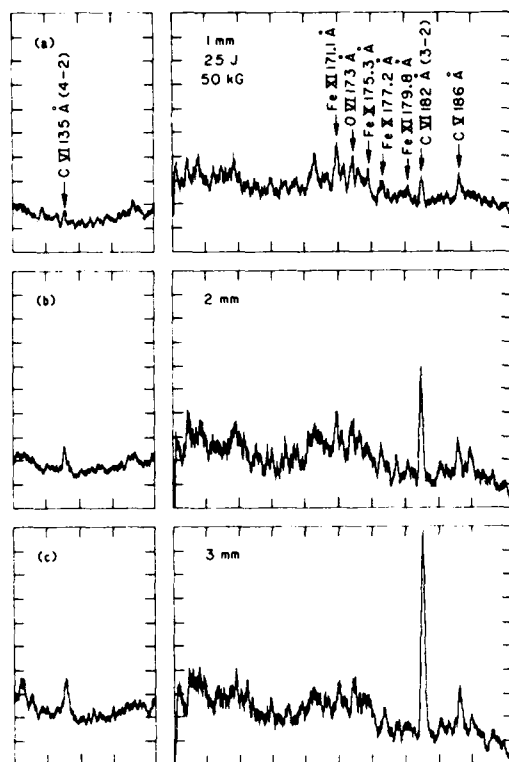


Figure 10. Axial spectra in vicinity of CVI 18.2 nm lasing line and CVI 13.5 nm line for 1, 2, and 3 mm long targets.

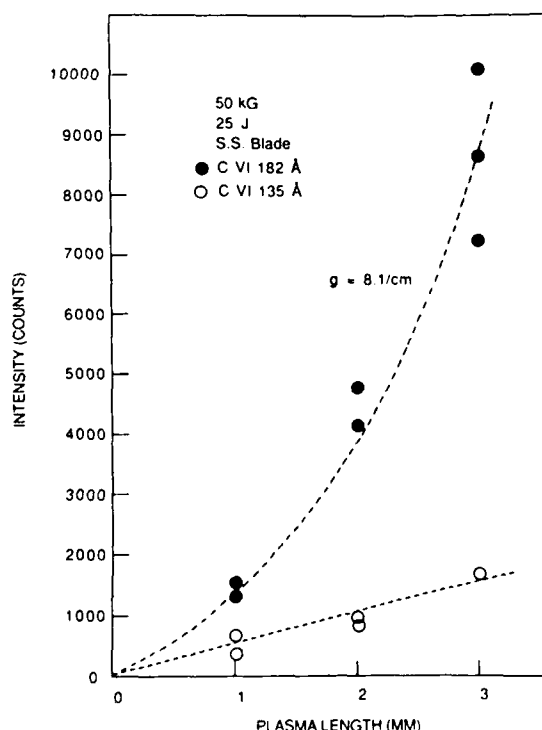


Figure 11. Gain measurements for CVI.

however in this case the SXL amplifier had too small an "aperture". We have not yet been able to match temporally and spatially the SXL laser with SXL amplifier. This may be due to jitter of the CO<sub>2</sub> laser and difficulty in alignment of SXL amplifier along SXL beam path in vacuum.

### (b) Cavity

A laser cavity can increase the brightness of the SXL beam by several orders of magnitude by decreasing the divergence to close to the diffraction limit. In order to establish the proper cavity modes, a number of passes through the gain medium are needed and a relatively long duration gain is necessary. The Princeton SXL at 18.2 nm with a gain duration of 10-30 nsec seems to be well suited to cavity development.

In our early work using a newly developed multilayer mirror [19], we demonstrated, for the first time, an 120% increase in 18.2 nm radiation due to amplification of stimulated emission by a mirror of reflectivity only 12% [14]. However, the mirror alignment posed tremendous difficulties and made it practically impossible to use a cavity in the original SXL setup. We have therefore designed an unstable resonator type cavity [20] with a transversely pumped carbon fiber as the lasing medium (Fig. 12). A specially designed fiber transport mechanism will enable the use of 15 fibers without opening the vacuum chamber. For the spherical multilayer

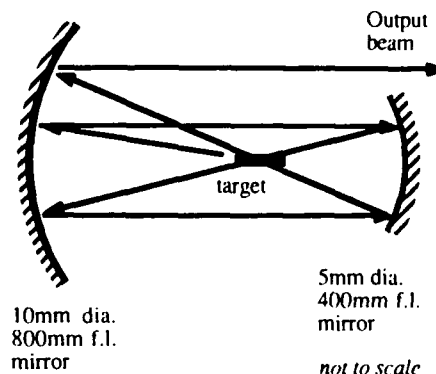


Figure 12. Unstable resonator type cavity for the SXL.

cavity mirrors a small vacuum chamber was built in which the position of the mirror can be remotely adjusted with high precision. The same cavity will also be used for a 1 cm long SXL created by a line focussed Nd/YLF laser beam incident on the cylindrical carbon target described in section (a).

In the cavity design, particularly in choosing distances between lasing medium and mirrors, we were concerned with the possibilities of damaging the multilayer mirrors by X-ray radiation. Recently, however, Ceglio et.al. [21] have demonstrated, in a very elegant cavity experiment, that such mirrors are quite stable against soft X-ray beam damage even at a distance of a few centimeters from lasing medium.

#### (c) Gain in Li-Like Ions at 15.4 nm and 12.9 nm

Pioneering work for Li-like AlXI ions particularly for the 5f-3d transition at 10.5 nm was done by P. Jaegle and his group (see e.g. [22]) using a Nd/Glass laser (initial plasma electron density  $N_e = 10^{21} \text{ cm}^{-3}$ ) for the pumping lasing medium. In our system with a CO<sub>2</sub> pump laser the critical electron density is  $N_e = 10^{19} \text{ cm}^{-3}$ . For such an electron density, the largest gain in AlXI and SiXII is expected for the 4f-3d transition at 15.4 nm and 12.9 nm respectively.

The aluminum or silicon targets used in the experiment were very similar to the SXL carbon target with the exception that the blades were a combination of lasing element (Al or Si) and fast radiator (Fe). The measured one-pass gain was  $g_l \approx 3-4$  for 15.4 nm and  $g_l \approx 1-2$  for 12.9 nm radiation. Details about the experiment and theoretical modeling are presented [5].

It is worthwhile noticing here that Li-like ions provide a more efficient lasing medium than H-like ions. In Fig. 13 is shown the lasing wavelength of H-like (3-2 transition) and Li-like (4f-3d transition) ions versus the ionization energy of these ions. Because the required pumping energy increases with ionization energy, lasing action in Li-like ions can be generated at shorter wavelength than in H-like ions, with the same pumping energy particularly if one considers 5f-3d transitions.

#### 4. Applications of Soft X-Ray Laser

The 18.2 nm laser (SXL) has been used for X-ray contact microscopy of biological specimens. This work is also closely

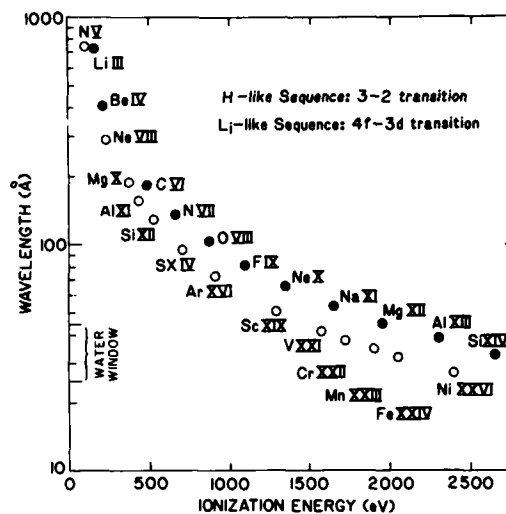


Figure 13. Lasing wavelengths of H-like and Li-like ions versus the ionization energy.

related to X-ray microlithography, which we are very much interested in. The ultimate goal of our X-ray laser microscopy program is to obtain images of living cells, preferably holographical images with three dimensional reconstruction. As a first step in this direction we have built a simple contact microscope with help from J. Kirz (Univ. of Stony Brook) and D. Sayre (IBM). The details of this work as well as our other X-ray laser microscopy works are described in the following paper by D. DiCicco et.al. [6]. In such a microscope, a thin ( $\sim 0.1 \mu$ ) silicon nitride window  $0.2 \text{ mm} \times 0.2 \text{ mm}$  square separates the vacuum tube, in which X-rays travel, from the biological cells located on photoresist at atmospheric pressure (see e.g. [6, 23]). An aluminum filter less than  $0.1 \mu$  thick with a highest transmissivity near 18.2 nm prevents visible and UV radiation from interacting with the photoresist. The X-ray laser beam was directed towards the microscope and focussed to a  $1 \text{ mm} \times 0.8 \text{ mm}$  spot by an ellipsoidal grazing incidence mirror. We have demonstrated in this experiment that the SXL beam has sufficient energy to expose photoresist in a single shot. After the initial experiments in which an image of 100 mesh was obtained on PMMA photoresist, images of Diatom fragments (silicified skeleton of planktonic algae) were also recorded on photoresists. In Fig. 14 is presented such an image on photoresist viewed with a scanning electron microscope (SEM). The picture indicates the resolution on the photoresist is better than  $0.1 \mu$ .

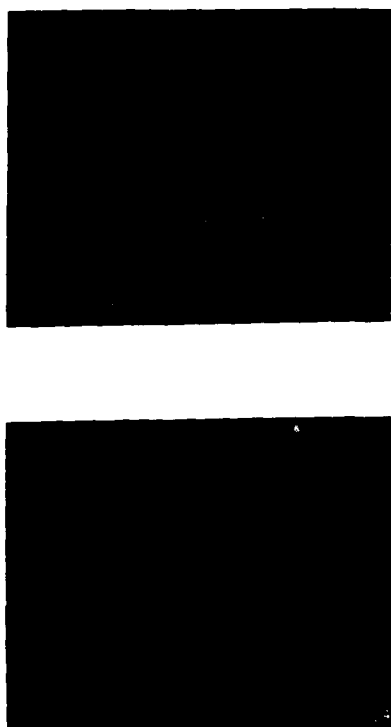


Figure 14. Image of Diatom fragments (silicified skeleton of planktonic algae) on PMMA photoresist viewed with scanning electron microscope (SEM).

One may also regard Diatom fragments as a kind of lithographic mask and Fig. 14 as an illustration of potential application of the SXL to microlithography.

In the next step, we built a Composite Optical/X-Ray Laser Microscope (COXRALM) shown schematically in Fig. 15 and described in [6]. COXRALM allows a biologist to select and observe biological cells using an optical phase contrast microscope [24]. The cells are located directly on a optically transparent photoresist. After selection and initial observations, the images of the cell is created on photoresist with the SXL beam in order to obtain higher resolution than with an optical microscope. In this procedure the X-ray laser tube with the  $0.1 \mu$  silicon nitride window on its tip is lowered until contact with the cell is made. The photoresist is exposed by triggering the SXL. In Fig. 16, is shown a photograph of COXRALM oriented horizontally (COXRALM can also

COMPOSITE X-RAY LASER MICROSCOPE (COXRALM)

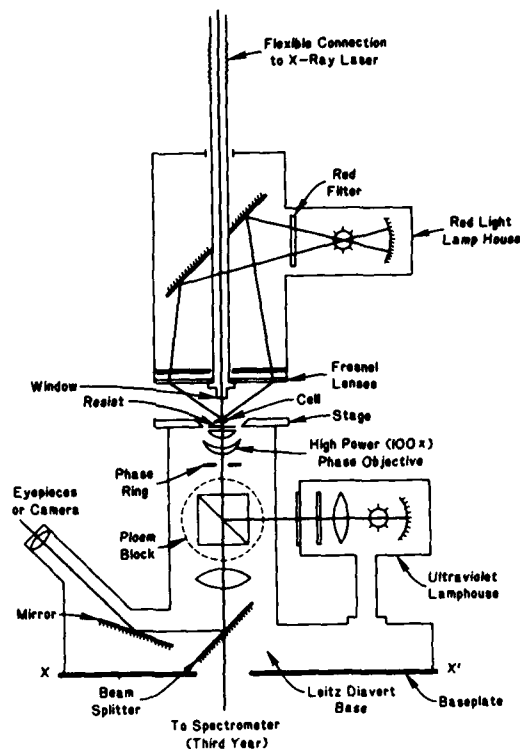


Figure 15. Scheme of Composite Optical X-Ray Laser Microscope (COXRALM).

be in the vertical position) on the SXL system (the lasing medium of SXL is  $\sim 300$  cm away, on the left).

In Fig. 17, as an example, is shown SEM image of the replica of dehydrated hela cells (Helen Lane cervical cancer cell) obtained from the Biology Dept. of Princeton University.

Presently our work is concentrated on the preparation of experiments with live cells in a wet environment and on the design of an Imaging X-Ray Laser Microscope (IXRALM).

##### 5. Effect of Quenching of Spontaneous Emission on XUV Spectrometer Calibration Using Branching Ratio Technique

The intensity ratio of two spectral lines from the same upper level in an optically thin plasma is equal to the ratio of the respective spontaneous emission,  $A$ , coefficients (Einstein coefficients). If the wavelength of one line is in the visible spectral region and the wavelength of the second line is in VUV or XUV region, by measuring the ratio of signals of these lines and knowing the absolute intensity of the first line the absolute intensity of the XUV line can be obtained from the ratio of the  $A$ -coefficients.

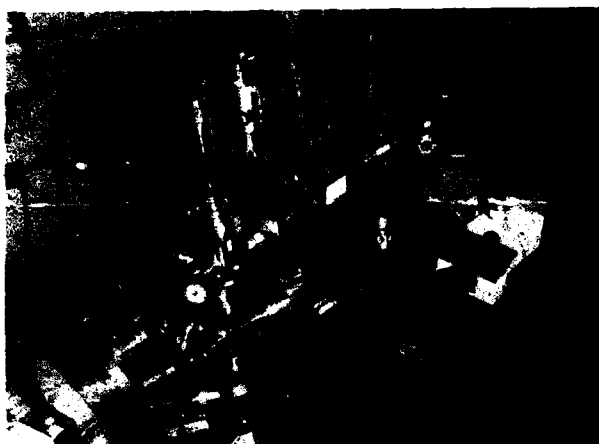


Figure 16. Photo of horizontally oriented COXRALM attached to the SXL.

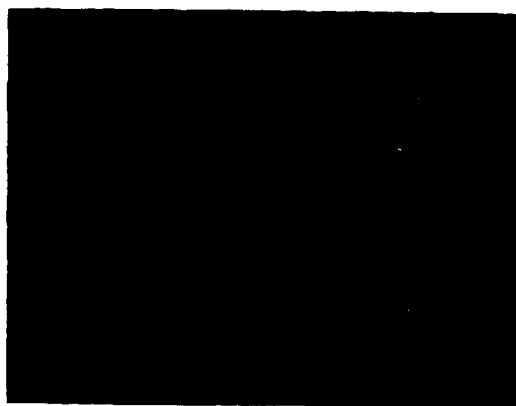


Figure 17. SEM image of a replica of hela cells (Helen Lane cervical cancer cells).

This technique is known as the branching ratio technique for the calibration of VUV and XUV spectrometers [25] and is based on assumption that the A-coefficients are independent of plasma conditions. Using this technique for the calibration of XUV spectrometers for the X-ray laser experiment we discovered that the ratio of some of A-coefficients, in sufficiently dense plasmas, differed significantly from the ratio in lower density plasmas. Many series of very precise measurements of the ratio of A-coefficients for CIV 5801-12 Å (3p-3s)/312 Å (3p-2s) lines confirmed that first observation [26]. Recently, similar measurements of NV 4603-20 Å (3p-3s)/209 Å (3p-2s) and

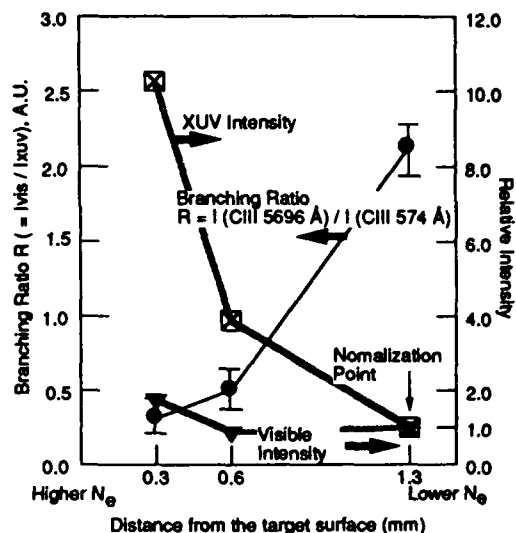


Figure 18. Relative intensities and branching ratio for two CIII lines.

CIII 5696 Å (3d-3p)/574 Å (3d-2p) lines showed the same phenomena. In Fig. 18 are shown the intensities and intensity ratios for CIII. More extensive and detailed information about these measurements are presented by Y. Chung, et.al. [17] in this proceedings. In [17] there is also a discussion of theoretical approaches to the problem. However up to now we do not have a model which provides a convincing explanation of the experimentally observed quenching of spontaneous radiation.

#### Acknowledgements

The presented data were results of very dedicated work by members of the scientific and technical staff and graduate students of the X-Ray Laser Project whose names, as authors, appear in the accompany papers; by visiting scientists, particularly P. Lemaire, J.L. Schwob, and G. Umesh; and a number of scientists associated with us, among them, C. Clark, P.C. Cheng, J. Fujimoto, E. Kohen, R. Kulsrud, M. Littman, T. McIlrath, R. Miles, and C. Oberman. I would like to thank H. Furth for helpful discussions and stimulation of the work on applications of the SXL.

The work was possible due to financial support by U.S. DOE Advanced Energy Projects of Basic Energy Sciences and U.S. Air Force Office of Scientific Research.

\* Invited talk presented at the conference on Short Wavelength Coherent Radiation, Cape Cod, Mass., Sept. 26-29, 1988.

+ Also Mechanical and Aerospace Engineering Dept.

#### References

1. C.P. Barty et.al., Phys. Rev. Lett. 61, 2201 (1988).
2. K. Boyer, et.al. "Strong Field Processes in the Ultraviolet Region," in Proc. of Conf. on Short Wavelength Coherent Radiation: Generation and Applications, Cape Cod, Mass., Sept. 1988.
3. P.L. Hagelstein, "Short Wavelength Lasers: Something Old, Something New," Ibid.
4. L. Meixler, C.H. Nam, J. Robinson, W. Tighe, K. Krushelnick, S. Suckewer, and J. Goldhar, "High Power Short Pulse Ultraviolet Laser for the Development of a New X-Ray Laser," Ibid.
5. D. Kim, C.H. Skinner, A. Wouters, E. Valeo, D. Voorhees, S. Suckewer, "Soft X-Ray Amplification in a Magnetically Confined Recombined H-like and Li-like Plasma," Ibid.
6. D.S. DiCicco, D. Kim, R.J. Rosser, C.H. Skinner, S. Suckewer, A.P. Gupta, and J. Hirschberg, "Constant Microscopy with a Soft X-Ray Laser," Ibid.
7. Y. Chung, H. Hirose, and S. Suckewer, "Measurement of the Quenching of Einstein A-Coefficients in Laser produced Plasmas," Ibid.
8. S.M. Susskind, S.C. Cowley, and E.J. Valeo, "Investigations of Multiphoton Excitation and Ionization in a Short Range Potential," Ibid.
9. R.W. Waynant and R.C. Elton, Proc. IEEE 64, 1059 (1976).
10. S.E. Harris, Optics Lett. 5, 1 (1980).
11. T.S. Luk et.al., Phys. Rev. Lett. 51, 110 (1983).
12. C.W. Clark et.al., J. Opt. Soc. Am. B 3, 371 (1986).
13. S. Suckewer, C.H. Skinner, H. Milchberg, C. Keane, and D. Voorhees, Phys. Rev. Lett. 55, 1753 (1985).
14. J.L. Schwob, A. Wouters, S. Suckewer, and M. Finkenthal, Rev. Sci. Instrum. 58, 1601 (1987).
15. M.H.R. Hutchinson, I.A. McIntyre, G.W. Gibson, and C.K. Rhodes, Opt. Lett. 12, 102 (1987).
16. C.H. Nam et.al., Phys. Rev. Lett. 59, 2427 (1987).
17. K.N. Koshelev, J. Phys. B 21, L593 (1988).
18. S. Suckewer et.al., Phys. Rev. Lett. 57, 1004 (1986).
19. T.W. Barbee, Jr., S. Mrowka, and M.C. Hettrick, Appl. Opt. 24, 883 (1985).
20. C.H. Skinner, private communication.
21. N. Ceglio et.al., Optics Lett. 13, 108 (1988).
22. P. Jaegle et.al., J. Opt. Soc. Am. B 4, 563 (1987).
23. C.H. Skinner et.al., IEEE Transactions on Plasma Science, 16, 512 (1988).
24. J. Hirschberg et.al., "A High Resolution Grating Microspectrofluoremeter with Topographic Option for Studies in Living Cells," ACS Symposium Series, No. 102 Ed: Y. Talmi, American Chemical Society (1979).
25. E. Hinnov and F. Hofmann, J. Opt. Soc. Amer. 53, 1259 (1963).
26. Y. Chung, P. Lemaire, and S. Suckewer, Phys. Rev. Lett. 60, 1122 (1988).



## Amplification in Na XI $H_\alpha$ , Mg XII $H_\alpha$ and Al XIII $H_\alpha$ Transitions

Y. Kato, M. Yamanaka, H. Daido, T. Tachi, H. Nishimura, H. Shiraga, E. Miura  
P. R. Herman, H. Takabe, T. Jitsuno, M. Takagi, S. Nakai, and C. Yamanaka

*Institute of Laser Engineering, Osaka University  
2-6 Yamada-oka, Suita, Osaka 565, Japan*

M. H. Key, G. J. Tallents, and S. J. Rose

*SERC Rutherford Appleton Laboratory  
Chilton, Didcot, Oxfordshire OX11 0QX, United Kingdom*

### Abstract

Observation of gain in Balmer- $\alpha$  ( $H_\alpha$ ) transitions in Na XI, Mg XII and Al XIII is reported. Planer stripe targets were irradiated with intense, line-focused 351 nm laser light. Time evolution of the gain in Na XI  $H_\alpha$  is also presented.

### Introduction

Early in 1988, a joint experiment was done using the Gekko XII facility at ILE between the Institute of Laser Engineering (ILE), Osaka University and the Rutherford Appleton Laboratory, U.K. on short wavelength scaling of recombining plasma soft x-ray laser. This experiment resulted in observation of gain in Balmer ( $H_\alpha$ ) transitions in Na XI and Mg XII and also an indication of gain in  $H_\alpha$  of Al XIII.

Extention of XUV lasers to shorter wavelengths due to isoelectronic scaling of recombination pumping of H-like ions has been pursued using fiber targets at the Rutherford Laboratory [1,2] and using planer targets at ILE [3,4]. Amplification in C  $H_\alpha$  at 182 Å and F  $H_\alpha$  at 81 Å has been observed in both cases. Promising extension of these works will be to test amplification in  $H_\alpha$  transitions in higher-Z ions such as Na XI, Mg XII and Al XIII.

The wavelength of the  $H_\alpha$  transition scales as  $\lambda \sim Z^{-2}$ . In order to obtain sufficient ionization balance in the initial production of the plasma, the electron temperature has to be increased at least as  $T_e \sim Z^2$ . This leads to increase in laser intensity as  $I_L \sim Z^4 \lambda_L^{-1}$  where  $\lambda_L$  is the laser wavelength. The initial

density of the plasma scales as  $n_e \sim Z \lambda_L^{-1}$ , favouring target irradiation with short wavelength lasers. Still the gain will scale as  $g \sim Z^{-5.7} \lambda_L^{-1.7}$ , suggesting less gain at shorter wavelengths [5,6]. This reduced gain at higher Z is mainly because that the initial electron density does not scale as  $Z^7$  as is required from isoelectronic scaling for the recombining  $H_\alpha$  laser. Careful diagnostic procedure is required in order to observe amplification in higher Z ions.

High intensity, short wavelength laser irradiation on target became possible with the use of the frequency-tripled two beams of the Gekko XII glass laser facility [7]. Determination of gain (or loss) was made by comparing the intensity ratios along and transverse to the x-ray laser axis as will be described later. Major emphasis of the experiment was placed on demonstration of gain in the  $H_\alpha$  transition of Na XI. After obtaining major results on the Na  $H_\alpha$ , the experiment was extended to the Mg  $H_\alpha$  and Al  $H_\alpha$  to test amplification at shorter wavelengths.

### Experiment

Experimental arrangement is shown in Fig. 1. A laser pulse of 130 ps duration and 351 nm wavelength was focused to a line of 7 mm length and 30  $\mu$ m width. The maximum laser energy was 150 J corresponding to the intensity of  $5 \times 10^{14}$  W/cm<sup>2</sup> with one-beam irradiation.

Most of the data were taken with stripe targets where a laser material of 1  $\mu$ m thickness was coated on a 0.13  $\mu$ m-thick planer plastic substrate of 6 mm width. The laser materials were NaF,

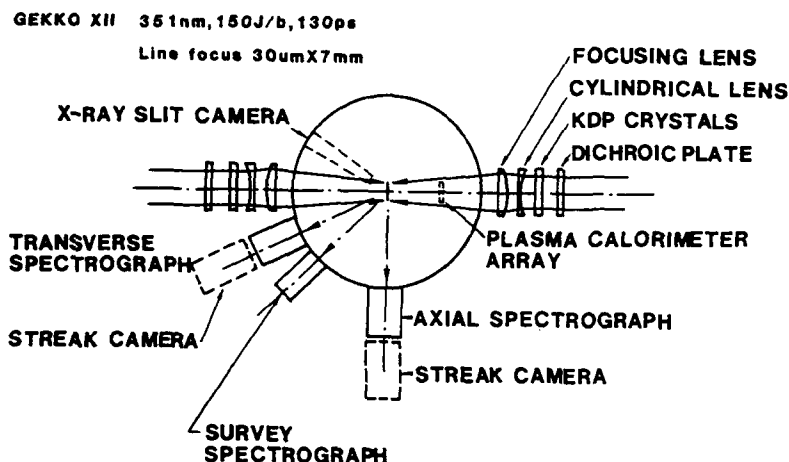


Figure 1. A schematic drawing of the experimental arrangement.

MgF<sub>2</sub> and Al for observing amplification in Na, Mg and Al, respectively. A split-field imaging microscope system [8] was used to accurately align the target on a horizontal reference position.

In the axial and transverse spectrographs shown in Fig. 1, a grazing-incidence spherical mirror formed a 10:1 reduced astigmatic image of the source onto the horizontally-positioned entrance slit of each spectrograph. Both slits were opened wide in order to ensure that the source images were completely contained within the widths of the slits.

Both spectrographs were equipped with varied-space gratings for flat-field imaging of the spectra. Spectral recordings were made either with photographic films for time-integrated measurements or with streak cameras for time-resolved measurements.

Relative sensitivity of these spectrographs was carefully determined by recording spectra from a plasma of a small size which produced identical emissions to both spectrographs. Once the cross-calibration is made carefully, the gain length product  $g\ell$  is obtained from each data shot by  $I_a/I_t = [\exp(g\ell) - 1]/(g\ell)$  where  $I_a/I_t$  is the axial-to-transverse intensity ratio normalized by the cross calibration data.

The spectral resolution of the axial (1200 line/mm grating) and the transverse (2400 line/mm grating) spectrographs with the film recording were 0.2 Å and 0.1 Å at around 50 Å, respectively. Figures 2-4 show time-integrated spectra observed in the axial direction for NaF, MgF<sub>2</sub> and Al target, respectively. The spectra were assigned using the Kelly's Table [9]. In Fig. 2, for example, the Na H<sub>α</sub> line marked by an

asterisk is blended with the 4p-2s line of Li-like Na and the 5d-2p line of H-like F. Also the H<sub>α</sub> line itself is composed of 3 fine structure components without including splittings due to Lamb shift. These blended lines were deconvolved by using a least-squared curve fitting program in order to determine the intensity of each component. The gain was determined for the strongest component of the H<sub>α</sub> line, i.e. 3d <sup>2</sup>D<sub>5/2</sub>-2p <sup>2</sup>P<sub>3/2</sub> transition. The characteristic response curve of the Kodak 101-07 film used for time-integrated measurement was determined in an independent experiment.

### Experimental Results

Figure 5 shows the axial and the transverse spectra, and the axial-to-transverse intensity ratios for NaF, MgF<sub>2</sub> and Al, respectively. In all cases, only the H<sub>α</sub> lines have the intensity ratios greater than 1 showing that they have positive gains. On the other hand, the resonance lines such as CV 2p-1s as well as non-resonant lines of lower ionic species including blended lines show absorption.

The gain coefficients for the H<sub>α</sub> transitions in Na XI, Mg XII and Al XIII thus determined are  $1.7 \pm 0.6 \text{ cm}^{-1}$ ,  $1.5 \pm 0.6 \text{ cm}^{-1}$  and  $0.3 \pm 0.6 \text{ cm}^{-1}$ , respectively. These gain values were obtained with the laser energies of 73 J, 143 J and 152 J, respectively. As is evident from the small intensity ratio of the 2p-1s transitions of H-like and He-like ions for Al, the laser intensity was insufficient to achieve good ionization balance in the case of Al, thus resulting in the low gain value.

Also time-resolved measurements on

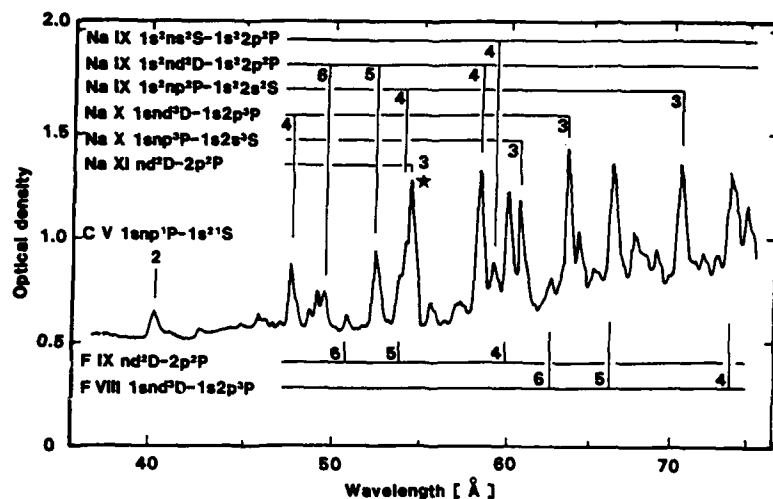


Figure2. Time-integrated spectrum for a NaF target observed in an axial direction.

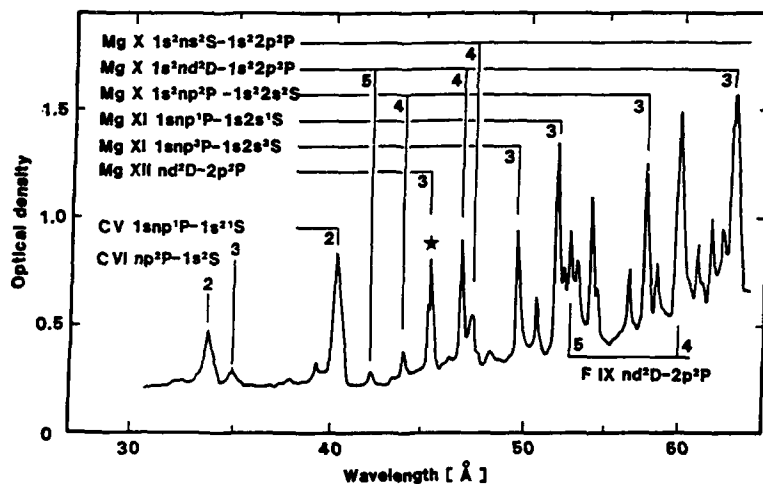


Figure3. Time-integrated spectrum for a MgF<sub>2</sub> target observed in an axial direction.

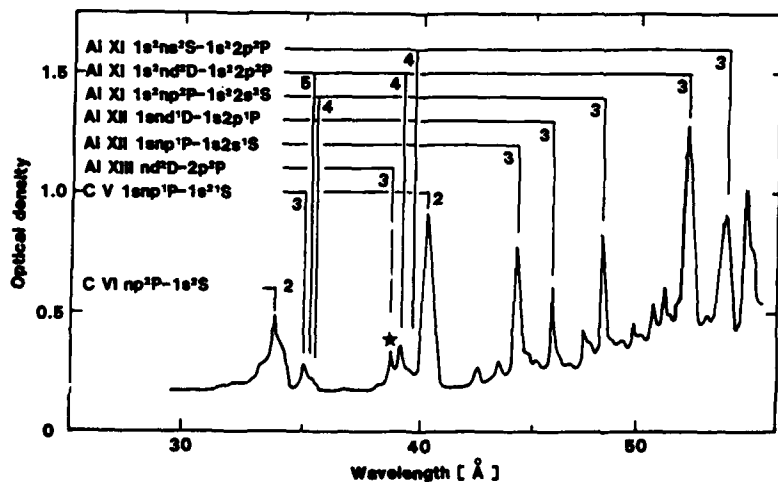


Figure4. Time-integrated spectrum for an Al target observed in an axial direction.

amplification of Na XI  $H_\alpha$  line were made using the streak cameras attached to the axial and the transverse spectrographs. Details are presented in another paper [10]. The gain of the Na  $H_\alpha$  line starts at 80-100 psec after the peak of the laser pulse, becomes maximum at 150-200 psec reaching to  $2-4 \text{ cm}^{-1}$ , and decays gradually to zero at  $\sim 600 \text{ psec}$  when the  $H_\alpha$  emission ceases.

### Analyses

Population inversion between  $n=3$  and  $n=2$  states are created during collisional-recombination cascade to lower levels when an initially fully-stripped ions is cooled. When the electron temperature  $T_e$  and the electron density  $n_e$  are expressed in reduced units of  $T_e/Z^2$  and  $n_e/Z^7$  respectively, the gain coefficient  $g$  scales as  $g \sim Z^{7.5}$  [11]. High amplification is obtained in higher density, lower temperature plasmas. However initial temperature has to be increased to obtain sufficient ionization balance leading to lower density due to plasma expansion during and after plasma formation. Comparison of the theoretical analyses with the experimental results are given in an accompanying paper [10].

### Summary

Extention of recombining-plasma  $H_\alpha$  laser to shorter wavelengths were

studied using Na, Mg and Al. By irradiating stripe targets with short wavelength laser at higher intensity, gain was observed for Na  $H_\alpha$  at 54.1 Å and Mg  $H_\alpha$  at 45.5 Å. Also an indication of gain was obtained for Al  $H_\alpha$  at 38.8 Å. These results will be useful in designing soft x-ray lasers near and within the "water window" wavelength region.

Based on the hydrodynamic analyses on Al, it is expected that a higher gain will be obtained by irradiating a target at higher intensity with a laser pulse of shorter duration.

### References

1. C. Chenais- Popovics, R. Corbett, C. J. Hooker, M. H. Key, G. P. Kiehn, C. L. S. Lewis, G. J. Pert, C. Regan, S. J. Rose, S. Sadaat, R. Smith, T. Tomie and O. Willi, "Laser amplification at 18.2 nm in recombining plasma from a laser-irradiated carbon fiber," Phys. Rev. Lett, **59**, 2161-2164 (1987).
2. G. P. Kiehn, I. Edwards, R. A. Smith, O. Willi, G. Pert, S. Ramsden, M. Grande, M. H. Key, S. J. Rose, A. Carillon, M. Guennou, P. Jaegle, G. Jamelot, A. Klisnick, and A. Sureau, "X-ray laser research at the Rutherford Laboratory," SPIE **831**, 270-274 (1987).
3. Y. Kato, P. R. Herman, T. Tachi, K. Shihoyama, K. Kamei, and H.

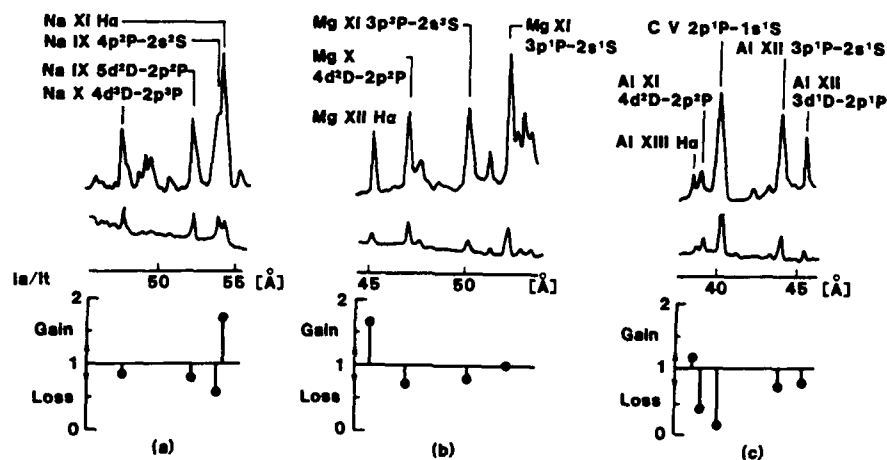


Figure 5. The axial (upper traces) and transverse (lower traces) spectra and the normalized intensity ratios  $I_a/I_t$  produced by (a) NaF, (b) MgF<sub>2</sub> and (c) Al targets. The wavelength scale is in Å unit.

- Shiraga, "Amplification of XUV emission in H-like and Li-like ions with thin foil targets," SPIE 831, 299-304 (1987).
4. P. R. Herman, T. Tachi, K. Shihoyama, H. Shiraga, and Y. Kato, "Soft x-ray recombination laser research at the Institute of Laser Engineering," IEEE Trans. Plasma Science 16, [5] (1988).
  5. M. H. Key, "Isoelectronic scaling of plasma XUV lasers," Annual Report to the Laser Facility Committee 1987, Rutherford Appleton Laboratory, RAL-87-041, 100-103 (1987).
  6. M. H. Key, "Some theoretical consideration for the scaling to short wavelength of XUV lasers operating by recombination to hydrogenic ions," unpublished.
  7. T. Jitsuno, "L-Project: third harmonic conversion of GEKKO XII," ILE Quarterly Progress Report, Institute of Laser Engineering, ILE-QPR-87-21, 3-5 (1987).
  8. I. N. Ross, J. Boon, R. Corbett, A. Damerell, P. Gottfeldt, C. Hooker, M. H. Key, G. Kiehn, C. Lewis and O. Willi, "Design and performance of a new line focus geometry for x-ray laser experiments," Appl. Opt. 26, 1584-1588 (1987).
  9. R. L. Kelly, "Atomic and ionic spectrum lines below 2000 Å," J. Phys. Chem. Ref. Data, 16, Suppl. No. 1-3 (1987).
  10. H. Nishimura, H. Shiraga, H. Daido, T. Tachi, P. R. Herman, E. Miura, H. Takabe, M. Yamanaka, Y. Kato, G. J. Tallents, and M. H. Key, "Time development of amplification in Na XI H<sub>α</sub>-line at 54. 19 Å," in this Proceedings.
  11. Y. Kato, P. R. Herman, T. Tachi, K. Shihoyama, K. Kamei, and H. Shiraga, "Amplification of extreme-ultraviolet radiation in recombining plasmas with thin foil targets," International Symposium on Short Wavelength Lasers and their Applications, Nov. 11-13 (1987), Proceedings to be published from Springer-Verlag.

# Population Inversion through Charge Exchange Process in Plasmas

T. Kato and K. Masai

*Institute of Plasma Physics, Nagoya University, Nagoya 464-01, Japan*

T. Fujimoto

*Department of Engineering Science, Kyoto University, Kyoto 606, Japan*

## Abstract

Population inversion due to charge exchange processes is investigated for helium-like ions in tokamaks by using a collisional radiative model. Dependence of charge exchange cross sections on the quantum numbers  $n$ ,  $l$  is estimated from the observed spectra.

## 1. Introduction

X-ray spectral lines associated with He-like ions have been observed for many tokamak plasmas and their emission intensities have been discussed in terms of the population mechanism of excited states. In quantitative analysis of the spectra, ionization, excitation and recombination processes have been taken into consideration, but the charge exchange process has generally been ignored. Although the influence of the charge exchange process to the spectra is mentioned in the discussion of some experiments, only a qualitative account is presented. Charge exchange process is important for He-like spectral lines in relation with population inversion following the electron capture into higher

energy levels. We investigate this process using a collisional radiative model which includes all the sublevels up to  $n = 40$ . We apply this model to the spectra obtained from Alcator tokamak plasmas [1, 2] and derive  $n - l$  distribution of charge exchange cross sections.

## 2. X-ray spectra from Alcator tokamak

This section summarizes the results of the experiments on Alcator tokamak [1, 2]. Our investigation described in the subsequent sections is based on these observations.

Space-resolved X-ray spectra of  $\text{Ar}^{16+}$  (He-like) were observed from Alcator tokamak plasmas with Ar gas puffing. In Fig.1, reproduced from ref.1, spectral lines from  $n = 2$  to  $n = 1$  transitions, w ( $1s^2 \ ^1S - 1s2p \ ^1P$ ), x ( $1s^2 \ ^1S - 1s2p \ ^3P_2$ ), y ( $1s^2 \ ^1S - 1s2p \ ^3P_1$ ) and z ( $1s^2 \ ^1S - 1s2s \ ^3S$ ), are shown for three different lines of sight through the plasma; these are at the center (a), and through the points of  $d = 8.3$  (b) and  $11.3$  cm (c) off from the center, where  $d$  is the shortest distance to the chord of observation from the plasma axis. One can see a drastic change in the spectra from the central chord to the outer

ones. The relative intensities of the forbidden line  $I_z$ , and the intercombination lines,  $I_x$  and  $I_y$ , to the resonance line intensity  $I_w$ , increase remarkably towards the outer chord. This relative enhancement could be accounted for by an increasing contribution from radiative recombination to the excited-level populations[3] towards the outer region. The spectrum in Fig.1(c), however, cannot be accounted for only by the radiative recombination process. Specifically, the observed intensity ratios of  $I_z/(I_x + I_y) = 0.9 \pm 0.2$ , is considerably smaller than the value 1.5 expected from radiative recombination. A possible interpretation would be that a charge exchange process between  $\text{Ar}^{17+}$  (H-like) and deuteron atoms dominates the population of highly excited states, and that the relative enhancement of the intercombination lines results through cascade[1].

X-ray spectra of the transitions  $1s^2 - 1snp$  with  $3 \leq n \leq \infty$  were also obtained[2]. Fig.2 shows the observed spectra with  $7 \leq n \leq 13$  through the three chords  $d = 3.9$  cm (a), 8.0 cm (b) and 13.5 cm (c). As seen in Fig.2, the transitions from  $n = 9$  and  $n = 10$  are enhanced relatively to those from  $n = 7$  and 8 towards the outer chord. This is regarded as clear evidence of charge exchange recombination between  $\text{Ar}^{17+}$  and neutral hydrogen in the ground state into the levels of  $n = 9$  and 10 [2, 5]. Other observed spectra corresponding to highly excited states  $n \geq 10$  are shown in Fig.3 which was obtained for  $d = 8.3 - 13.2$  cm. The spectrum in Fig.3 shows a broad feature from 3.01 to 3.02 Å. A peak at around 3.013 Å corresponds to the transitions from  $n \approx 27$  and the shoulder near 3.018 Å to the transition from  $n \approx 18$ . These

enhancements are attributed to electron capture from hydrogen atoms in the excited states with  $n_1 = 3$  and 2, respectively [2,6].

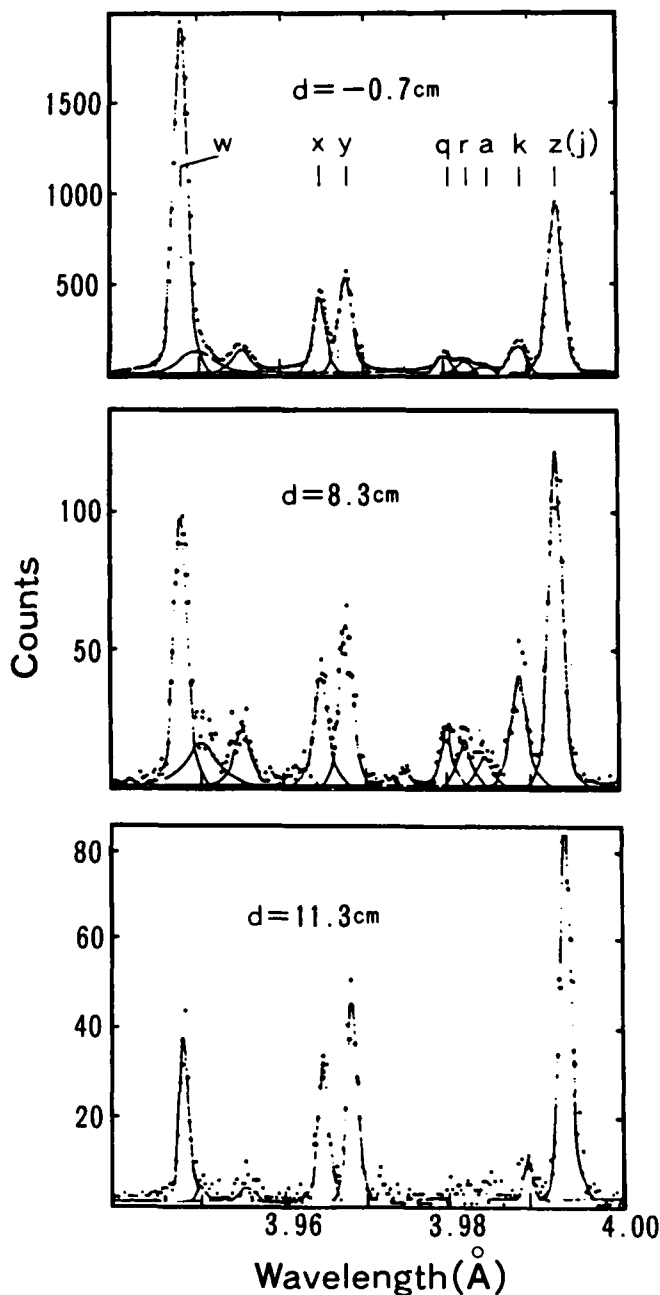


Fig.1 Observed spectra of  $1s^2 - 1s2l$  transitions in  $\text{Ar}^{16+}$  from Alcator tokamak for three different chords[1]. w:  $1s^2 1S - 1s2p 1P$ , x:  $1s^2 - 1s2p 3P_2$ , y:  $1s^2 1S - 1s2p 3P_1$ , z:  $1s^2 - 1s2s 3S$ .

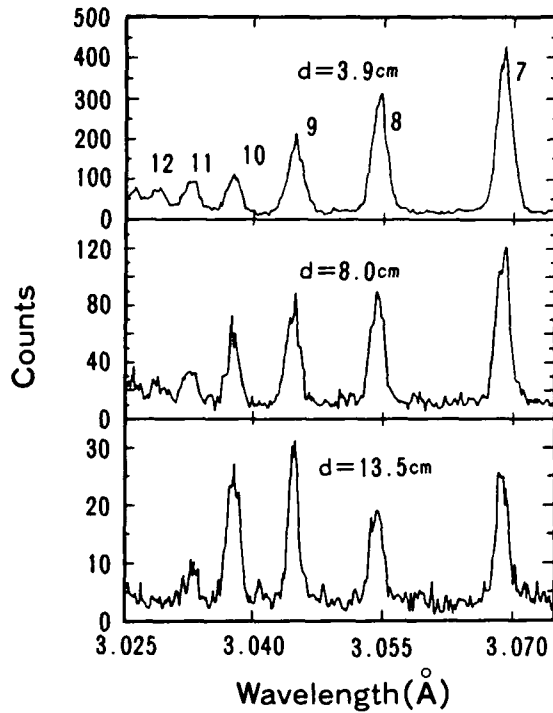


Fig.2 Observed spectra of  $1s^2 - 1snl$  transition with  $7 \leq n \leq 13$  in  $Ar^{16+}$  from Alcator tokamak for three different chords[2].

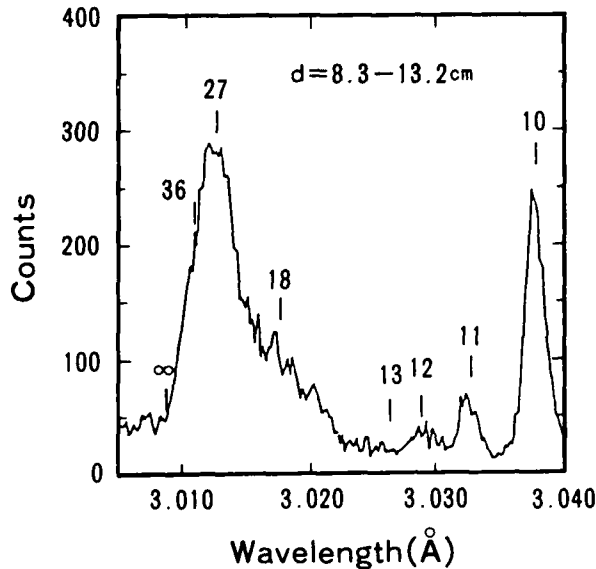


Fig.3 Observed spectra of  $1s^2 - 1snl$  transitions with  $n \geq 10$  in  $Ar^{16+}$  from Alcator tokamak[2].

### 3. Analysis and Discussion

We have constructed a collisional radiative model for He-like ions where the levels of  $n \leq 40$  are resolved with different angular momentum  $l$ . The total number of levels considered is 1641. In the present study, we include the charge exchange process,



as an additional population mechanism of excited levels. By adjusting the magnitude of the charge exchange cross sections, we try to fit our calculation to the experiment described in the preceding section.

#### i) Spectra for the transitions with $7 \leq n \leq 12$

The intensity  $I_{10}$  in Fig.3 is much stronger than those of  $I_{13}$  and  $I_{14}$ , where  $I_n$  means the line intensity of the  $1s^2 - 1snp$  transition. Emission lines of highly ionized ions (e.g.,  $Ar^{17+}$ ) are observed from the outer region as well as the inner hot region of the tokamak plasma. This indicates a considerable fraction of those highly ionized ions is present even in the outer region with temperatures as low as  $\sim 300$  eV, likely due to convective transport in the plasma[3].  $Ar^{16+}$  spectra under such a plasma condition exhibit a typical example of recombining plasma[4]. In fact as seen in Fig.3 the recombination continuum is detected at wavelengths shorter than 3.0088 Å which is the ionization limit of the  $1s^2$  state.

Assuming that  $I_{13}$  is produced by radiative recombination only, we derive the electron temperature  $T_e$  to be about 500 eV from the intensity ratio of  $I_{13}/I_{cont} \approx 2.8 \times 10^{-4}$ , where  $I_{cont}$  represents the intensity of continuum in units of photons / Å. The



value 500 eV is reasonable as a temperature around  $d = 8.5$  cm. From the intensity  $I_{13}$ , the contribution from radiative recombination is estimated to the line intensities,  $I_{10} - I_{12}$ , and  $I_n \geq 15$ . The resulting intensities are much lower than the observation.

Thus, the intensity  $I_{10}$  is understood to be dominated by direct charge exchange recombination with neutral hydrogen. From the intensity ratio of  $I_{10}/I_{\text{cont}}$ , the following relation is derived.

$$\begin{aligned} \sigma_{\text{cx}}(10p \ ^1P) v n_H(1)/n_e \\ = 5.0 \times 10^{-14} \text{ cm}^{-3} \text{ s}, \end{aligned} \quad (2)$$

where  $\sigma_{\text{cx}}(10p \ ^1P)$  is the charge exchange cross section to  $10p \ ^1P$  state,  $v$  the velocity of  $\text{Ar}^{17+}$  relative to hydrogen atom, and  $n_e$  and  $n_H(1)$  the densities of the electron and the neutral hydrogen in the ground state, respectively. For the values of  $n_e = 5 \times 10^{13} \text{ cm}^{-3}$ ,  $n_H(1) = 10^9 \text{ cm}^{-3}$  and  $v = 2.5 \times 10^7 \text{ cm/s}$  ( $T_i = T_e = 350 \text{ eV}$ ) given in Ref.[1, 2], the cross section  $\sigma(10p \ ^1P)$  is estimated to be  $1.0 \times 10^{-16} \text{ cm}^2$ . Assuming the statistical distribution for singlet and triplet states, we obtain  $\sigma(10p) = 4.0 \times 10^{-16} \text{ cm}^2$ .

We now turn to the lines from  $n = 7 - 9$  in Fig.2(c). These are also enhanced, and we assume that this enhancement is also attributed to charge exchange recombination. However in this case, it is unlikely that all the population of these upper levels are produced directly by this mechanism. Rather, the fact that the intensity  $I_7$  is higher than  $I_8$  strongly suggests some contribution from cascade from  $n = 10$  and 9. We consider two extreme cases; (a)  $I_7$  and  $I_8$  are produced only by cascades from  $n = 9$  and 10 levels, and (b)

$I_7$  and  $I_8$  are produced mainly by direct capture to the p state.

Case (a); Most of the electrons captured to  $9l$  or  $10l$  state flow to lower states ( $n = 1, 2, 3$  etc) through direct radiative transitions and a few percent of electrons flows to the  $7p$  state to produce  $I_7$ . The electron capture to s states enhances  $I_7$  and  $I_8$  through cascade most effectively. However, this results in too strong  $I_2$  to account for the observed ratios to  $I_x$ ,  $I_y$  and  $I_w$ . The electron capture to the levels of larger  $l$  values such as  $9f$  and  $9g$  is not efficient to produce the resonance series lines  $I_7$  and  $I_8$ . The best candidate is the charge exchange to  $9d$  and  $10d$  states, and we fit the line intensities of  $I_7$  and  $I_8$  to the experiment. The resulting cross section for  $10d$  state is larger by one order of magnitude than that for  $10p$  state. A part of  $I_9$  is ascribed to the direct capture to  $9p$  state through charge exchange. The cross sections thus derived are summarized as case (a) in Table I, (the cross sections for the g states are discussed later.) and the calculated spectra for  $I_7$  through  $I_{13}$  are compared with the measurement in Fig.4, where the density ratio of  $n(\text{Ar}^{17+})/n(\text{Ar}^{16+}) = 0.01$  is assumed. The hatched region in Fig.4 indicates the contribution from radiative recombination.

Case (b); The intensities  $I_7 - I_{11}$  are dominated by direct capture to np states. The intensity difference between  $I_7$  and  $I_8$ , however, is to be explained by cascade from  $n = 9$  and 10. The cross sections deduced under this assumption are listed in Table I as case (b). The values estimated in Ref.[2] are also given in bracket in Table I for comparison. Calculated spectrum for (b) is not shown in Fig.4 since it is nearly the same as for (a).

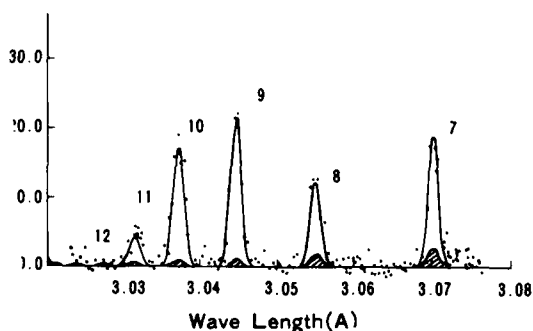


Fig.4 Calculated spectra (solid curve) and observed one (points) of  $1s^2 - 1snl$  transitions with  $7 \leq n \leq 13$ . The hatched regions show the contribution by radiative recombination.  $T_e = 350$  eV,  $n_e = 5 \times 10^{13} \text{ cm}^{-3}$ ,  $n_H = 10^9 \text{ cm}^{-3}$  and  $n(\text{Ar}^{17+})/n(\text{Ar}^{16+}) = 0.01$  are taken for calculations.

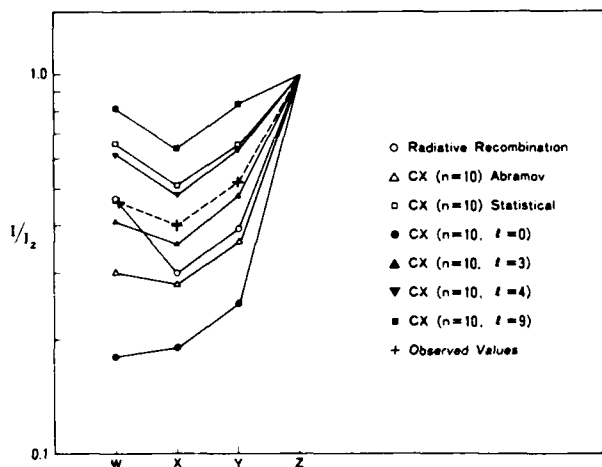


Fig.5 Intensity ratios of  $I_W/I_Z$ ,  $I_X/I_Z$  and  $I_Y/I_Z$  calculated by (○) radiative recombination only, (△) charge exchange recombination to  $n = 10$  levels with distribution by eq. (3) [7], (□) charge exchange recombination to  $n = 10$  levels with statistical distribution, (●) charge exchange recombination to 10s ( $l = 0$ ), (▲) to 10f ( $l = 3$ ), (▼) to 10g ( $l = 4$ ) and (■) to  $n = 10$  and  $l = 9$  state only. (+) observed values.

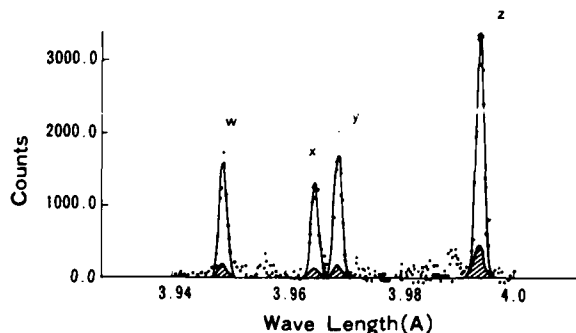


Fig.6 Calculated spectra (solid curve) and observed one (points) of  $1s^2 - 1s2l$  transitions. The hatched regions show the contribution by radiative recombination.

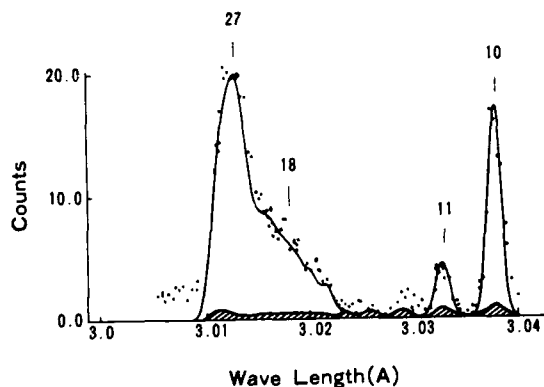


Fig.7 Calculated spectra (solid curve) and observed one (points) of  $1s^2 - 1snl$  transition with  $n \geq 10$ . The hatched regions show the contribution by radiative recombination.

Abramov et al.[7] obtained  $l$  distribution  $W_{nl}$  for the charge exchange process at low energies as [5],

$$W_{nl} = (2l+1)[(n-1)!]^2 / [(n+l)!(n-1-l)!]. \quad (3)$$

Our derived  $l$  distribution is quite different from eq.(3). The observed intensities  $I_7$  and  $I_8$  cannot be reproduced

Table I  
Charge exchange cross sections for  $\text{Ar}^{17+} + \text{H}(1) \rightarrow \text{Ar}^{16+} (n\ l) + \text{H}^+$

n =	7	8	9	10	11
p [Ref.2]			[1.5(-15)]	[7.5(-16)]	
p (a)	-	-	4.0(-16)	4.0(-16)	1.3(-16)
(b)	1.2(-16)	1.4(-16)	4.6(-16)	4.0(-16)	9.4(-17)
d (a)	-	-	8.4(-15)	8.4(-15)	-
(b)	1.1(-15)	1.3(-15)	4.6(-15)	4.0(-15)	9.4(-16)
g (a)	-	-	1.6(-14)	1.6(-14)	-
(b)	2.4(-15)	2.8(-15)	9.2(-15)	8.0(-15)	1.9(-15)
<hr style="border-top: 1px dashed;"/>					
Total (a)	5.0(-14) $\text{cm}^2$				
(b)	3.7(-14) $\text{cm}^2$				

Table II  
Charge exchange cross sections for  $\text{Ar}^{17+} + \text{H}(i) \rightarrow \text{Ar}^{16+} (n\ l) + \text{H}^+$   
( $i \geq 2$  and  $n \geq 15$ )

	i = 2		i = 3		i = 4
15p	1.4(-14)	24p	9.2(-14)	32p	9.2(-14)
16p	1.9(-14)	25p	1.0(-13)	33p	1.0(-13)
17p	2.2(-14)	26p	1.1(-13)	34p	1.1(-13)
18p	2.3(-14)	27p	1.2(-13)	35p	1.2(-13)
19p	2.3(-14)	28p	1.1(-13)	36p	1.2(-13)
20p	2.3(-14)	29p	1.0(-13)	37p	1.2(-13)
21p	2.2(-14)	30p	9.2(-14)	38p	1.1(-13)
22p	1.9(-14)	31p	7.6(-14)	39p	1.0(-13)
23p	1.4(-14)			40p	9.2(-14)
<hr style="border-top: 1px dashed;"/>					
Total	1.8(-13) $\text{cm}^2$		8.0(-13) $\text{cm}^2$		9.7(-13) $\text{cm}^2$
[Ref.2]	[1.0(-13)]		[2.5(-13)]		

by the distribution given by eq.(3) because the cascade contribution to  $I_7$  is too small.

#### ii) Spectra for the transitions of

$n = 2$  to  $n = 1$

The cascade contribution from large values of  $l$  such as d, f, g states enhances the intensity ratio  $(I_x + I_y)/I_z$ , whereas the cascade from small  $l$  values such as s state reduces this ratio. With increasing  $l$  values, the intensity ratio  $(I_x + I_y)/I_w$  becomes smaller. In Fig.5 calculated intensities of  $I_w$ ,  $I_x$  and  $I_y$  normalized to  $I_z$  are shown for the following cases; (i) only by radiative recombination, and by charge exchange to  $n = 10$  state (ii) with distribution according to eq.(3), (iii) with statistical distribution, and (iv), (v), (vi), (vii) with only one of the levels of  $l = 0, 3, 4$ , and 9. The observed values are also shown by the dashed line. When we note that the observed intensities consist of the two components due to radiative recombination and charge exchange recombination, we conclude that the capture to the levels  $l \geq 4$  are necessary to explain the observed intensity ratios of  $(I_x + I_y)/I_z$ . But the intensity ratio  $I_w/I_z$  would be too large for the values  $l > 4$ . Thus charge exchange to g states ( $l = 4$ ) of  $n = 9$  and 10 is the best selection to explain the observed relative intensities of  $I_w$ ,  $I_x$ ,  $I_y$  and  $I_z$ . The calculated spectrum for the transitions of  $n = 2$  to  $n = 1$  is compared with the measurement in Fig.6 and the deduced cross sections for the g states are listed in Table I.

#### iii) Spectra for the transitions with

$n \geq 15$

We consider that the broad feature for  $n \geq 15$  in Fig.3 is due to charge exchange

between hydrogen atoms in excited states and  $\text{Ar}^{17+}$ . The electrons are captured to the levels near  $n = 18, 27$  and 36 by charge exchange with hydrogen in the  $n_i = 2, 3$  and 4, respectively [2, 6]. The ratios of the hydrogen density in these excited states to that in the ground state are calculated to be  $n_H(n_i)/n_H(1) = 0.004, 0.001$  and  $0.0004$  for  $n_i = 2, 3$  and 4 [8]. Since the observed intensities  $I_{13}$  and  $I_{14}$  are considered to be produced by radiative recombination as discussed in Sec.3(i), the contribution of the cascade from higher levels are small for these lines. Then for the levels with  $n \geq 15$  we assume that almost of electrons are captured to  $l = 1$  state. Comparison of the calculated spectrum with the observed one is shown in Fig.7. The cross sections derived for  $n \geq 15$  are listed in Table II. These cross sections are roughly expressed in a form of Gaussian distribution as  $\sigma(np) = \sigma_0 \exp(-((n-n_0)/\Delta n)^2)$ , where the values of  $\sigma_0$  are  $2.3 \times 10^{-14}$ ,  $1.2 \times 10^{-13}$  and  $1.2 \times 10^{-13}$  and values of  $\Delta n$  are 5, 6 and 8 for  $n_0 = 19, 27$  and 36, respectively. The populations for the levels of  $n > 27$  are re-distributed due to  $l$  mixing. This effect is taken into account in our calculations. The spectral lines in Fig.7 are assumed to be emitted mainly at the plasma periphery near  $d = 13$  cm where  $T_e \approx 350$  eV, while continuum emission comes from inner region around at  $d = 8.5$  cm where  $T_e \approx 500$  eV.

#### 4. Summary

We have derived charge exchange cross sections to  $n - l$  states for the process (1) from the observed spectra obtained from the peripheral region of tokamak plasmas. We considered the two extreme cases (a) and (b), and both fitted well to the experiment. We may assume that the actual

distribution of the cross sections would be somewhere between case (a) and (b). The total cross section for  $n_1 = 1$  is  $5 \times 10^{-14} \text{ cm}^2$  in case (a) and  $3.7 \times 10^{-14} \text{ cm}^2$  in case (b). These values are about two times the theoretical ones given in ref[5]. The total cross sections for  $n_1 = 2, 3$  and  $4$  are  $1.8 \times 10^{-13}$ ,  $8.0 \times 10^{-13}$  and  $9.7 \times 10^{-13} \text{ cm}^2$ , respectively. This result indicates a weaker  $n_1$  dependence than that proportional to  $n_1^4$  [2, 6]. The absolute values obtained in the present paper may be uncertain with an error of factor of two or three depending on the uncertainties in  $v_{H(1)}/n_e$  in eq.(2).

There are few theoretical and experimental studies on  $n - l$  distribution for highly ionized ions, particularly at low energies. The distribution according to eq.(3) cannot reproduce the observed intensities from  $I_7$  to  $I_{10}$  as mentioned in Sec.3(i). The statistical distribution also has a difficulty that  $I_W/I_Z$  is too large as discussed in Sec.3(ii). The  $l$  distribution derived from the observed spectra appears to take a maximum around the  $g$  state for  $n = 9$  and  $10$ . The cross sections for the  $g$  state is larger than those for  $p$  state by more than one order of magnitude. The observed spectrum for  $n \geq 15$  is consistent with the  $l$  distribution having a maximum at the  $p$  state.

Population inversion for  $n = 9, 10$  and  $\geq 15$  states found from tokamak plasmas has been analysed in terms of the charge exchange processes. Our present investigation could be useful in exploration of the possibilities of the VUV coherent radiation through charge exchange recombination.

## Acknowledgement

We would like to thank Dr.J.E. Rice and his colleagues for giving us a permission of using figures in their articles.

## References

1. E. Kallne et al., Phys. Rev. Lett. **52**, 2245 (1984)
2. J.E. Rice et al., Phys. Rev. Lett. **56**, 50 (1986)
3. J.E. Rice, E.S. Marmor, E. Kallne and J. Kallne, Phys. Rev. A **35**, 3033 (1987)
4. T. Fujimoto and T. Kato, Astrophysical J. **246**, 994 (1981)
5. R.K. Janev, D.S. Belic and B.H. Bransden, Phys. Rev. A, **28**, 1293
6. R.E. Olson, J. Phys. B, **13**, 483 (1980)
7. A. Abramov, F.F. Baryshnikov and V.S. Lisitsa, JETP Lett. **27**, 464 (1978)
8. T. Fujimoto, I. Sugiyama and K. Fukuda, Memories of Faculty of Engineering, Kyoto University, Vol. XXXIV, Part 2, 249 (1972)

## Prepulsing to Increase the Efficiency of Laser-Produced-Plasma Pumped Lasers

M. H. Sher and S. J. Benerofe

*Edward L. Ginzton Laboratory, Stanford University  
Stanford, California 94305*

### Abstract

We have demonstrated the use of a low energy prepulse to enhance the soft-x-ray emission of laser produced plasmas in a parameter range which has been used to pump photoionization lasers. We present data on conversion efficiency and output pulse duration as a function of input intensity, pulselength, and prepulse conditions. Our goal in these studies is to allow the design of more efficient short-wavelength photoionization lasers, and to achieve high repetition rate operation of these lasers in the near future.

Several recently reported short wavelength lasers [1, 2] have utilized a laser-produced plasma "soft-x-ray flashlamp" as the pump source. We have characterized the soft-x-ray conversion efficiency in the parameter range of importance to these lasers and have demonstrated that the yield can be improved dramatically by the presence of a low energy prepulse [3 - 5]. For plasmas formed by 1064 nm radiation incident onto gold targets at intensities from  $4 \times 10^{10}$  to  $3 \times 10^{12}$  W cm<sup>-2</sup> and pulselengths of 170, 70, and 20 psec, we have measured the conversion efficiency and duration of the plasma emission into the photon energy range from 120 to 285 eV.

The experimental arrangement is shown in Fig. 1. 1064 nm pulses from a Nd:YAG laser system are focused into an evacuated chamber and onto a gold target at normal incidence. Soft-x-rays emitted by the plasma formed on the gold surface are detected at 30 deg off the target normal by a soft-x-ray streak camera and by a vacuum photodiode. The 70 and 170 psec pulses are generated directly by a q-switched, mode-locked Nd:YAG oscillator and are amplified in four succeeding Nd:YAG

heads. The 20 psec pulses are generated by passing a 150 psec pulse from the same oscillator through a single mode silica fiber (to produce a self phase modulation induced frequency chirp) and then using the gain narrowed spectral band pass of the Nd:YAG amplifiers to shorten the pulse [6]. The focal spots on target are 100 and 140  $\mu$ m in diameter for the main and prepulse beams respectively. The target surface is an approximately 1  $\mu$ m thick layer of gold electroplated with a matte finish onto an unpolished stainless steel disk. The disk is rotated to expose a fresh gold surface on each shot. The spectral sensitivity of the detectors

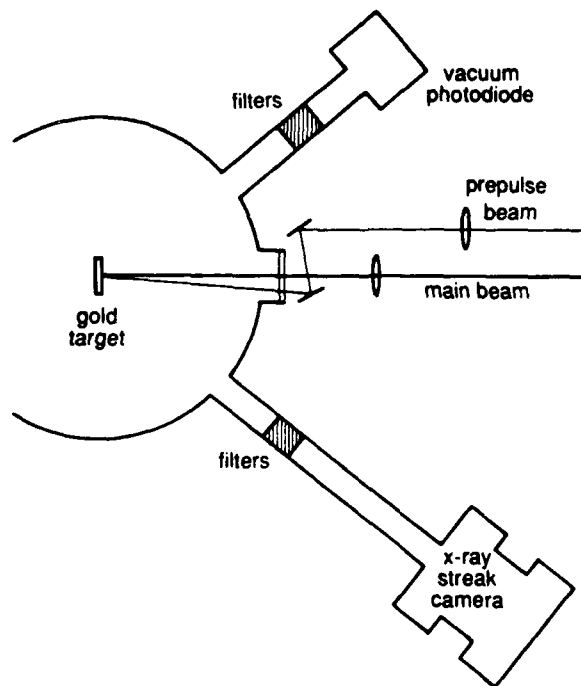


Figure 1. Experimental arrangement

(shown in Fig. 2) was defined by a filter set of  $1.0\ \mu\text{m}$  Paralene-N and  $0.15\ \mu\text{m}$  Ag [7] positioned in front of both the vacuum photodiode ( $\text{Al}_2\text{O}_3$  photocathode [8]) and the streak camera ( $0.01\ \mu\text{m}$  CsI on  $0.1\ \mu\text{m}$  Formvar photocathode [9]).

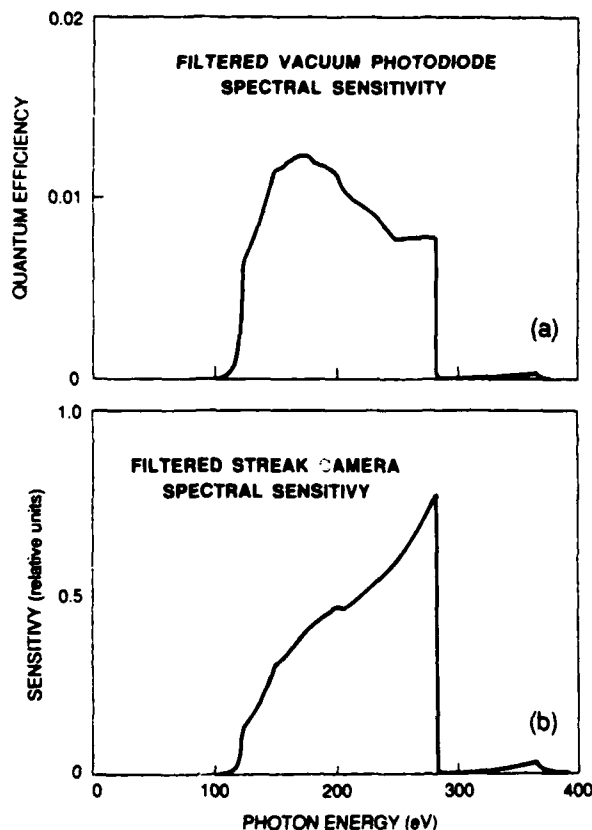


Figure 2. Calculated spectral sensitivity of a) vacuum photodiode and b) streak camera.

All of the measurements were made on a single shot basis, and readings for both the photodiode and the streak camera were recorded on each shot. Each of the points displayed in the following graphs represents the average of several shots, where shot to shot fluctuations were usually within 25 %.

Initial measurements determined the effect of the prepulse as a function of its intensity and temporal spacing from the main pulse. In Fig. 3 we show how the soft-x-ray yield of the main pulse varies as the temporal spacing between the pre- and main pulses is increased. The pulse length was 26 psec, the intensity in the main beam was  $1.8 \times 10^{12}\ \text{W cm}^{-2}$ , and separate data sets were taken for prepulse intensities of  $1.6 \times 10^{11}\ \text{W cm}^{-2}$  and  $3.3 \times 10^{10}\ \text{W cm}^{-2}$ . The higher intensity prepulse curve indicates that the yield increases as the time delay is increased up to approximately 1 nsec, after which it remains roughly constant out to our 2.3 nsec measurement limit. Although the lower intensity

prepulse produces less enhancement of the main pulse output, it too seems to be leveling off at approximately 1.5 nsec. In Fig. 4, we set the pulselength at 20 psec, the pulse spacing at 1.5 nsec,

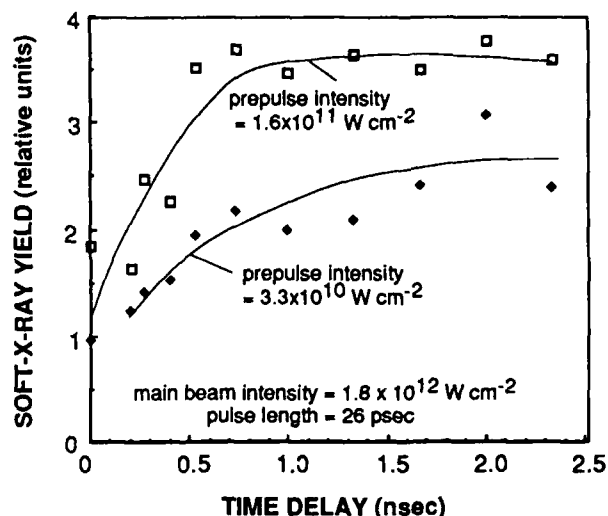


Figure 3. Soft-x-ray yield enhancement vs. time delay between prepulse and main pulse.

the main pulse intensity at  $1.3 \times 10^{12}\ \text{W cm}^{-2}$ , and we vary the prepulse intensity. The effect of the prepulse seems to asymptote at an intensity of about  $8 \times 10^{10}\ \text{W cm}^{-2}$ .

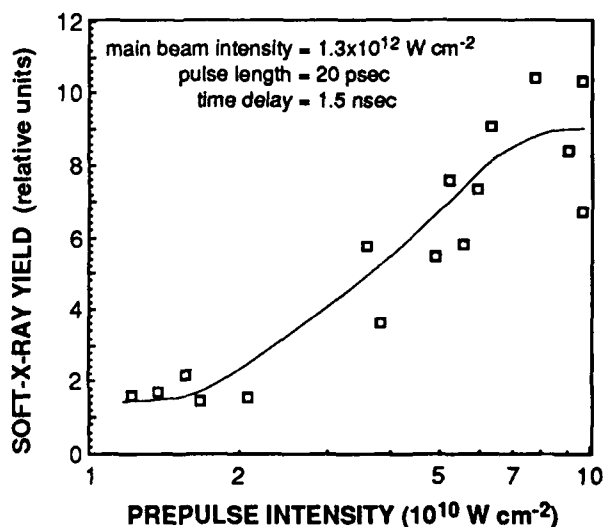


Figure 4. Soft-x-ray yield enhancement vs. prepulse intensity.

In Fig. 5 we show the conversion efficiency into the 120 to 285 eV bandwidth as a function of main beam intensity, with and without a prepulse, for 1064 nm pulselengths of 20 psec. In this case the pulse spacing was 1.5 nsec and the prepulse intensity was maintained at a value high enough to insure the

maximum enhancement. The data shows that the conversion efficiency is improved significantly and falls off more slowly with decreasing intensity in the presence of a prepulse. The slopes of the curves indicate an  $I^{(2.10)}$  dependence of conversion efficiency on main beam intensity for the main beam only and an  $I^{(1.25)}$  dependence for the prepulsed plasma. Figures 6 and 7 are analogous to Fig. 5 but are done at pulselengths of 70 and 170 psec. At  $10^{12} \text{ W cm}^{-2}$  the conversion efficiency (into the 120 - 285 eV bandwidth) of the un-prepulsed plasma is 0.9 %, 0.2 %, and 0.06 % for the 170, 70, and 20 psec pulses respectively. The prepulse increases these figures to 1.5 %, 0.6 %, and 0.3 %.

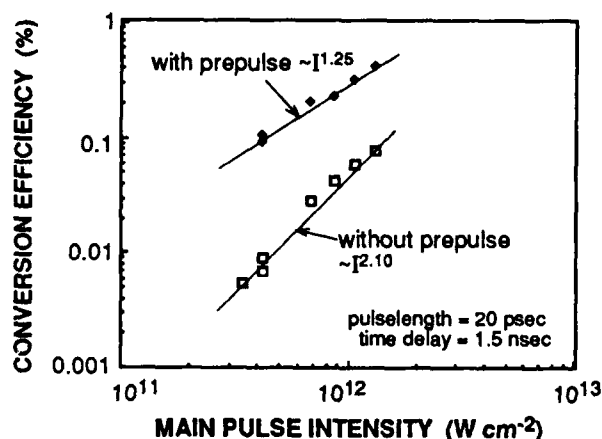


Figure 5. With pulselength = 20 psec, conversion efficiency (into 120 - 285 eV bandwidth) vs. main pulse intensity.

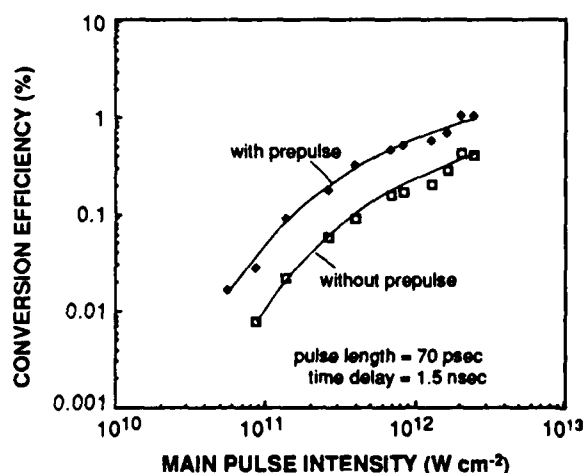


Figure 6. With pulselength = 70 psec, conversion efficiency (into 120 - 285 eV bandwidth) vs. main pulse intensity.

Calibration of the conversion efficiency in Figs. 5-7 is based on several assumptions: an isotropic angular distribution of the x-rays, the calculated spectral

sensitivity curve shown in Fig. 2a, and a 22 eV black body spectral distribution of the emission in the detector bandwidth. This black body temperature was chosen to match the vacuum photodiode signal for a single reference condition (pulse length = 70 psec and  $I_{\text{main}} = 1 \times 10^{12} \text{ W cm}^{-2}$ ), and all other conversion efficiencies were scaled linearly with no change in the assumed spectral shape. We estimate that these conversion efficiencies are accurate to within a factor of three.

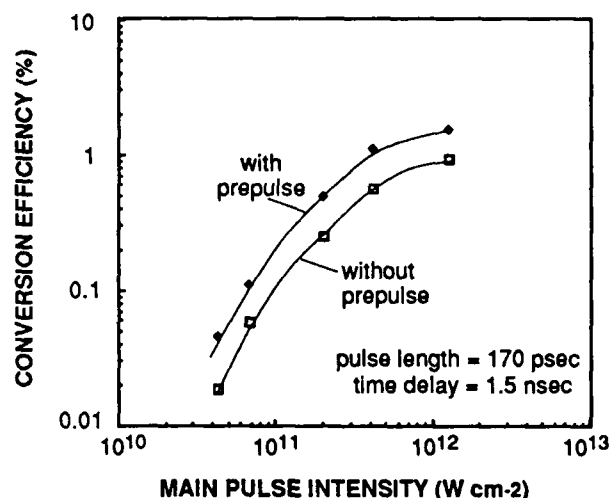


Figure 7. With pulselength = 170 psec, conversion efficiency (into 120 - 285 eV bandwidth) vs. main pulse intensity.

Unfortunately, the increases in time-integrated yield due to the prepulse are not obtained without some increase in the soft-x-ray pulselength. For the 20 psec, 1064 nm pulses the soft-x-ray emission lasted about 45

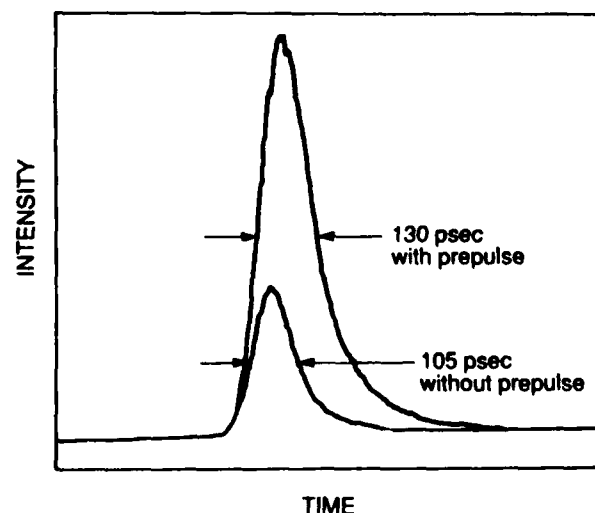


Figure 8. Streak camera traces of soft-x-ray emission from 70 psec pulse.

psec (FWHM) for the main pulse only and 70 psec for the prepulsed plasma. (Here we have deconvolved an



assumed streak camera resolution of 20 psec.) We note that the increase in FWHM caused by the prepulse comes predominantly from the falling edge of the pulse, while the rise time does not change significantly. Figure 8 shows streak camera traces for a 70 psec pulse at  $I_{\text{main}} = 4.4 \times 10^{11} \text{ W cm}^{-2}$  and  $I_{\text{pre}} = 1.7 \times 10^{10} \text{ W cm}^{-2}$ . Under these conditions the main pulse only emission has a FWHM of 105 psec which is increased to 130 psec by the prepulse. The emission time of the 170 psec pulse was approximately 250 psec and was not increased significantly by the prepulse.

In a situation where the total energy available for plasma production is limited, it may be necessary to divide a single beam into two parts in order to produce the largest x-ray yield. Figure 9 shows the x-ray enhancement available for a 22.5 psec, 1064 nm pulse with an intensity of  $1.6 \times 10^{12} \text{ W cm}^{-2}$  as a function of the fraction of that total energy which is diverted to the prepulse beam.

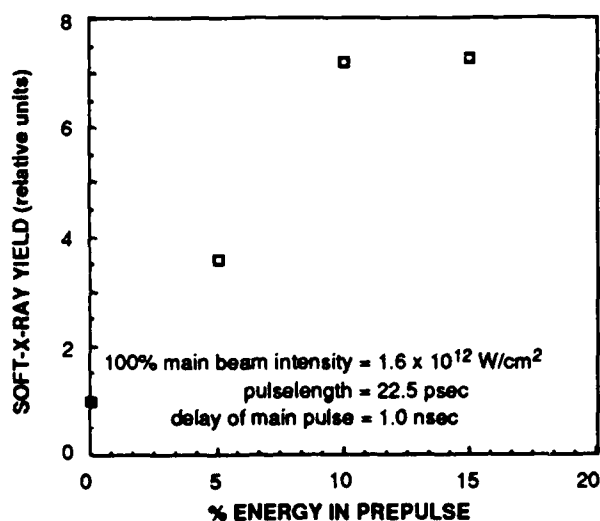


Figure 9. Soft-x-ray yield enhancement vs. fraction of main pulse energy diverted to prepulse.

While the presence of the prepulse alters the behavior of the main pulse plasma in many ways, we believe the mechanism which is primarily responsible for the enhanced soft-x-ray yield is an increase in the collisional absorption of the incident laser light. The pre-formed plasma (with its larger density scale length) is able to absorb a larger fraction of incident light than is the initially cold metal surface [10, 11]. Figure 10 is a graph similar to that in Fig. 3 where, in addition to the increase in soft-x-ray yield, we have plotted the decrease in 1064 nm light scattered from a 70 psec main pulse as the time delay between the pre- and main pulses is increased. Two photodiodes were positioned to detect light scattered to 30 and 90 deg off the target normal, and a third was placed above and behind the target to collect light bouncing off the front wall of the

chamber. All three photodiodes behaved in a similar manner as the time delay was changed, and the data shown is the average of the three diode signals. Our target chamber was not suitable to calibrate the photodiodes to measure absolute reflected fractions, but the correlation between the reflected 1064 nm light and the soft-x-ray output is clear.

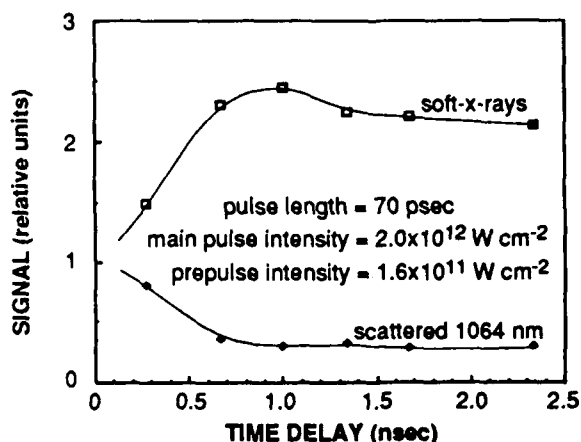


Figure 10. Scattered 1064 nm light and soft-x-ray yield vs. time delay between prepulse and main pulse.

While increasing the soft-x-ray yield is important to making photoionization lasers, there are other effects which must be considered when using a prepulsed plasma to pump these lasers. Soft-x-rays or blowoff material produced by the prepulse itself may degrade the ambient gain medium and, hence, reduce the effectiveness of the main pulse pumping. One way to reduce the x-ray yield of the prepulse is to form the prepulse plasma with shorter wavelength light. Because the shorter wavelength should have better mass ablation efficiency [12] while producing a colder plasma [10, 13], it should (in this sense) make a better prepulse. In preliminary experiments with 70 psec pulses at a main beam intensity of  $5 \times 10^{11} \text{ W cm}^{-2}$ , we measured the same 3 times enhancement of the main beam emission, with a  $7.5 \times 10^{10} \text{ W cm}^{-2}$ , 1064 nm prepulse and a  $4.3 \times 10^{10} \text{ W cm}^{-2}$ , 532 nm prepulse. The 532 nm prepulse, however, emitted 8 times less broadband (as detected by an unfiltered vacuum photodiode) soft-x-rays.

In this work, we have studied the soft-x-ray conversion efficiency of laser-produced plasmas in a parameter range which has been used to pump photoionization lasers. We find that the conversion efficiency decreases rapidly with pulse length, but the decrease can be slowed by the presence of a low energy prepulse. We have characterized the effects of the prepulse and addressed some of the practical considerations which will be important in pumping photoionization lasers. This information will aid in the design of more efficient photoionization lasers and in

the production of new short-wavelength lasers.

The authors acknowledge the assistance of J. J. Macklin, C. P. J. Barty, and G.-Y. Yin and the support of J. F. Young and S. E. Harris. M. H. Sher gratefully acknowledges an AT&T Bell Labs Ph.D. Scholarship. This work was supported by the Office of Naval Research and the Strategic Defense Initiative Organization.

#### References

1. M. H. Sher, J. J. Macklin, J. F. Young, and S. E. Harris, "Saturation of the Xe III 109-nm laser using traveling-wave laser-produced-plasma excitation," *Opt. Lett.* **12**, 891 (1987), and references therein.
2. C. P. J. Barty, D. A. King, G.-Y. Yin, K. H. Hahn, J. E. Field, J. F. Young, and S. E. Harris, "A 12.8 eV laser in neutral Cesium," submitted to *Phys. Rev. Lett.* and this Proceedings, and references therein.
3. R. Kodama, T. Mochizuki, K. A. Tanaka, and C. Yamanaka, "Enhancement of keV x-ray emission in laser-produced plasmas by a weak prepulse laser," *Appl. Phys. Lett.* **50**, 720 (1987).
4. D. Kuhlke, U. Herpers, and D. von der Linde, "Soft x-ray emission from subpicosecond laser-produced plasmas," *Appl. Phys. Lett.* **50**, 1785 (1987).
5. D. G. Stearns, O. L. Landen, E. M. Campbell, and J. Scofield, "The Generation of Ultrashort X-ray Pulses," *Phys. Rev. A* **37** 1684 (1988).
6. D. F. Voss and L. S. Goldberg, "Simultaneous amplification and compression of continuous-wave mode-locked Nd:YAG laser pulses," *Opt. Lett.* **11**, 210 (1986).
7. B. L. Henke, P. Lee, T. J. Tanaka, R. L. Shimabukuro, and B. K. Fujikawa, "Low-Energy X-Ray Interaction Coefficients: Photoabsorption, Scattering, and Reflection," *At. Data Nucl. Data Tables* **27**, 1 (1982).
8. L. R. Canfield and N. Swanson, "Far Ultraviolet Detector Standards," *Journal of Research of the National Bureau of Standards*, **92**, 97 (1987).
9. J. A. R. Samson, *Techniques of Vacuum Ultraviolet Spectroscopy* (Pied Publications, Lincoln, Nebraska, 1967).
10. T. P. Hughes, *Plasmas and Laser Light* (Wiley, New York, 1975), p. 285.
11. W. L. Kruer, *The Physics of Laser Plasma Interactions* (Addison-Wesley, New York, 1988).
12. R. Fabbro, E. Fabre, F. Amiranoff, C. Garban-Labaune, J. Virmont, M. Weinfeld, and C. E. Max, "Laser-wavelength dependence of mass-ablation rate and heat-flux inhibition in laser-produced plasmas," *Phys. Rev. A* **26**, 2289 (1982).
13. C. E. Max, "Physics of the Coronal Plasma in Laser Fusion Targets," in *Laser Plasma Interactions*, R. Balian and J. C. Adams, eds. (North Holland, Amsterdam, 1982).

Amplification and Gain Measurement of Extreme Ultraviolet  
Radiation (42.4Å, 45Å and 46Å) in He-like Al Laser Plasma

K. Muroo, Y. Tanaka and H. Kuroda

The Institute for Solid State Physics

The University of Tokyo

Roppongi 7-22-1, Minato-ku, Tokyo 106 Japan

Phone: 03-478-6811

Concerning the extreme ultraviolet lasing in the laser-produced plasma, He-like Al scheme is attractive because the wavelength of He-like 3-2 transitions are shorter than any other transition ever done, and very close to the water window. This scheme is expected to give a large population inversion caused by the rapid decaying of the  $n=2$  level, and the great feed to the  $n=3$  levels by the cascade radiative transitions and two electron transitions through the autoionized states.

A 100ps glass-laser pulse was line-focused on the solid Al target, and intensities of He-like 3-2 transitions were measured at various plasma length, keeping the laser input energy density as constant. Intensities of  $3d-2p(45\text{\AA})$ ,  $3s-2p(46\text{\AA})$  and  $3p^1P_0-2s^1S(42.4\text{\AA})$  grew exponentially and saturated, as the plasma length was increased. This exponential growth is due to the stimulated emission process,

and saturation is due to the escape of the XUV light from the line-shape-plasma axis caused by bending of XUV light in a density-graded plasma. Gain coefficients are estimated as  $9.8\text{cm}^{-1}$ ,  $7\text{cm}^{-1}$  and  $4.4\text{cm}^{-1}$  for He-like Al  $3d-2p$ ,  $3s-2p$  and  $3p1P0-2s1S$  transitions respectively.

Population Inversions between  $n=5$ , 4, 3 and 2 levels  
of He-like Al Plasma Observed by Spatially  
Resolved X-ray Spectroscopy

H. Kuroda, M. Katsuragawa, K. Murco and Y. Tanaka

The Institute for Solid State Physics

The University of Tokyo

Roppongi 7-22-1, Minato-ku, Tokyo 106 Japan

Phone: 03-478-6811

Population inversions between  $N=5$ , 4 and 3 levels are observed in a 100ps Laser-produced plasma. As a results, XUV of  $42\text{\AA}\sim 46\text{\AA}$ ,  $130\text{\AA}$  and  $305\text{\AA}$  corresponding to 3-2, 4-3 and 5-4 transitions are observed experimentally. Relative population densities are determined by measuring the intensities of spatially resolved X-ray line spectra of  $6.635\text{\AA}$ ,  $6.314\text{\AA}$  and  $6.18\text{\AA}$  corresponding to the 3-1, 4-1 and 5-1 transitions, which are normalized by their oscillation strengths. Careful absorption was paid to rule out the effect of reabsorption. Populations were inverted at the region located  $50\sim 100\mu\text{m}$  from the target surface. Laser light was focused into  $50\mu\text{m}$  diameter and amount of inversion was clearly increased when laser intensities was increased. As to the 5-4 and 4-3 inversion, similar result was observed in silicon target, however inversion between  $n=3$  and 2 was not confirmed at these

laser intensities. XUV gains are very promising especially as to 5-4 and 4-3 transitions in both target.

## Probability of Soft X-Ray Radiation for 3p-3s Transition in Neon-Like Iron

Huimin Peng, Guoping Zhang, Jiatian Sheng, and Yunfeng Shao

*Institute of Applied Physics and Computational Mathematics  
P.O. Box 8009, Beijing, China*

### ABSTRACT

Using 1-D non-LTE radiative hydrodynamic code JB-19 we simulated the interactions of basic and double frequency neodymium-glass laser beam which is focussed into a line onto target, with thin Formvar-iron foils. The values of population inversions and gains are calculated using steady rate equations. The profiles of laser-produced plasma conditions and the probabilities for 3p-3s transition in neon-like iron at peak intensities 5TW per square centimeter to 20TW per square centimeter and FWHM 800-1000ps are shown.

### INTRODUCTION

In recent years considerable interest has centered on the 3p-3s transitions in neon-like ions in the development of soft x-ray lasers, and incontrovertible success has been achieved in LLNL[1-2]. Other laboratories have got great progress too[3-4]. The computational simulation of soft x-ray lasers has been done for several years at Institute of Applied Physics and Computational Mathematics in order to get some interest results, construct, examine and improve computing codes and design useful experiments. Taking account of the capability of Nd-glass laser Shongguang which sets up at Shanghai High Power Laser Physics Laboratory, we chose thin iron foil which deposits on thin plastic substrate(Formvar-C11H18O5) as the laser medium in the calculation.

Laser-produced plasma condition is calculated using one dimensional non-local thermodynamic equilibrium radiative hydrodynamic code JB-19. In this code, the bremsstrahlung effect, radiative ionizations and recombinations, collisional ionizations by electrons

and threebody recombinations, collisional excitations and de-excitations by electrons, radiative line transitions and Compton scattering are considered. The multigroup flux-limited diffusion approximation is used in the radiative transport equations. Laser light via inverse bremsstrahlung absorption is considered to be the most important in our computational simulations. We used steady rate equations to calculate the populations in the some levels of the iron ions at different electron temperatures, densities and certain abundance of neon-like iron.

We simulated the interactions of basic and double frequency Nd-glass laser light which is focussed into a line onto target, with thin Formvar-iron foils. At first, we made the computational results of neon-like ion of selenium to be in agreement with the experimental results of LLNL, then we calculated the plasma conditions of thin plastic-iron targets.

In this paper we show the computational results of laser-produced plasma conditions and the probabilities of 3p-3s transitions in neon-like ion of iron. The thin foil targets consist of 300-750 angstrom coating of iron on 750-1000 angstrom Formvar(C11H18O5). A segment of the foil is illuminated with one gaussian laser beam on the surface of the iron or two opposing laser beams. The peak intensity of the incident laser pulse varies from 5TW per square centimeter to 10 TW per square centimeter for each of two opposing laser beams, and varies from 10TW-20 TW per square centimeter for one incident laser beam. The FWHM of incident pulse varies from 800ps to 1000ps, and the wavelengths of the incident laser light are 1.06  $\mu\text{m}$  and 0.53 $\mu\text{m}$ .

### BASIC EQUATIONS

1. The 1-D equations of radiative hydrodynamics

$$\frac{\partial R}{\partial t} = u, \quad (1)$$

$$\frac{\partial R}{\partial r} = \frac{\rho_0}{\rho} \frac{r}{R} \alpha, \quad (2)$$

$$\frac{\partial u}{\partial t} = -\frac{1}{\rho} \frac{\partial P}{\partial R}, \quad (3)$$

$$P = P_{ion} + P_e + P_r + q, \quad (4)$$

where  $\alpha=0,1,2$  means planar, cylindrical and spherical geometry respectively,  $P_{ion}$ ,  $P_e$  and  $P_r$  denote the pressure of the ions, electrons and radiation,  $q$  is the viscosity pressure.

There are two kinds of equations of electron energy for real and ideal gas respectively

$$\begin{aligned} \frac{\partial E_e}{\partial t} = & -\frac{1}{\rho R} \frac{\partial}{\partial R} (R Fe) - P_e \frac{\partial}{\partial t} \left( \frac{1}{\rho} \right) \\ & - W_r + W_{ie} + W_L, \end{aligned} \quad (5)$$

$$\begin{aligned} \frac{\partial}{\partial t} (C_v T_e + V) = & -\frac{1}{\rho R} \frac{\partial}{\partial R} (R Fe) - P_e \frac{\partial}{\partial t} \left( \frac{1}{\rho} \right) \\ & - W_r + W_{ie} + W_L, \end{aligned} \quad (6)$$

where  $E_e$  is the electron energy,  $W_r$  is the transfer rate of the energy from electrons into radiation,  $W_L$  is the rate of laser light energy deposition,  $W_{ie}$  is the exchange rate of the energies between electrons and ions,  $C_v$  is the specific heat capacity at constant volume for electron,  $T_e$  is the electron temperature,  $V$  is the electron potential energy and  $Fe$  is the limited flux of electron conduction.

The equation for ion energy is

$$\begin{aligned} \frac{\partial}{\partial t} (C_v T_i) = & -(P_i + q) \frac{\partial}{\partial t} \left( \frac{1}{\rho} \right) - \frac{1}{\rho R} \frac{\partial}{\partial R} (R F_i) \\ & - W_{ie}, \end{aligned} \quad (7)$$

2. Average atom population rate equations

$$\frac{dP_i}{dt} = A_i - B_i P_i, \quad (8)$$

where

$$A_i = A_{ir} + A_{ie} + A_{ile} + A_{ilr}$$

$$\begin{aligned} &= N_e \beta_{ir} + N_e^2 \beta_{ie} \\ &+ N_e \left[ \sum_{j>i} (g_j/g_i) \beta_{ji} P_j + \sum_{j<i} (g_j/g_i) \alpha_{ji} P_j \right] \\ &+ \sum_{j<i} (g_j/g_i) W_{ji} P_j \int_0^\infty b_{ji}(\nu) f_\nu d\nu, \end{aligned} \quad (9)$$

$$\begin{aligned} B_i &= A_i + B_{ir} + B_{ie} + B_{ile} + B_{ilr} \\ &= A_i + N_{ir} + N_e N_{ie} \end{aligned}$$

$$\begin{aligned} &+ N_e \left[ \sum_{j>i} (1-P_j) \alpha_{ij} + \sum_{j<i} (1-P_j) \beta_{ij} \right] \\ &+ \sum_{j<i} (g_j/g_i) W_{ji} (1-P_j) \int_0^\infty b_{ji}(\nu) (1+f_\nu) d\nu \end{aligned} \quad (10)$$

where  $i_r$ ,  $i_e$ ,  $i_{ie}$  and  $i_{lr}$  denote the radiation ionization and recombination, collisional ionization by electrons and three-body recombination, collisional excitation and de-excitation by electrons and radiative line transition for  $i$  level respectively,  $P_i$  is the population probability for  $i$  level,  $f_\nu$  is the number per mode (quantum state) for  $\nu$  photon and  $b_{ji}(\nu)$  is the profile of the radiative line transition from  $j$  to  $i$ ,  $g_i$  and  $g_j$  are the statistical weights of  $i$  and  $j$  levels, and  $W_{ji} = (g_i/g_j) A_{ij}$ , in which  $A_{ij}$  is spontaneous radiative decay rate from level  $i$  to  $j$ .

3. Multigroup fluxlimited diffusion equations for radiative transport

$$\begin{aligned} \frac{1}{\rho} \frac{\partial f_\nu}{\partial t} = & -\frac{1}{\rho R} \frac{\partial}{\partial R} (R F_r) + \frac{\nu}{3} \frac{\partial f_\nu}{\partial \nu} \frac{\partial}{\partial t} \left( \frac{1}{\rho} \right) \\ & + \frac{1}{\rho} (D_\nu - C_\nu f_\nu) \\ & + \frac{1}{\rho \nu^2} \frac{\partial}{\partial \nu} \left\{ \alpha_\nu \left[ (1+f_\nu) f_\nu + T_e \frac{\partial f_\nu}{\partial \nu} \right] \right\}, \end{aligned} \quad (11)$$

where  $F_r$  is the limited flux of radiation,  $\alpha_\nu$  is the radiative parameter for Compton scattering [5],  $C_\nu$  and  $D_\nu$  are parameters for photoelectric effect, bremsstrahlung effect and radiative line transition.

For simplicity, we assumed that laser light irradiates target with normal incidence. The absorption of laser light in plasma is considered via inverse bremsstrahlung. When incident laser light reaches critical surface, it is reflected, the reflected laser light is absorbed by plasma, in which the density approaches or is less than critical density, till it passes out through the system.



## LASERPRODUCED PLASMA CONDITIONS

In order to get population inversions and gains of 3p-3s transition in neon-like ions of iron, the laser-produced plasma condition must be suitable for lasing. We expect to design exploding foil to ensure that during incident laser pulse the target can be burned through and a roughly cylindrical plasma that contain neon-like ions can be produced. If such plasma condition can last enough time in enough wide region, the application of soft x-ray radiation can be obtained.

According to the theoretical and experimental results of LLNL for selenium and using scaling law[6], we estimated that the parameters of laser-produced plasma condition for thin iron foil ought to be  $T_e 4 \times 10^6$

$K$  and  $N_e 2 \times 10^{20} / \text{cm}^3$ . We suggest that thin Formvar-iron foil to be illuminated with one laser light beam on iron side or two opposing laser light beams. The incident gaussian laser light beams can be in wavelengths  $1.06 \mu\text{m}$  and  $0.53 \mu\text{m}$ , FWHM 800ps-1000ps, peak intensities 5TW-20TW per square centimeters.

In the calculation we let the time at  $I/I_0=0.01$  as the starting and ending time of gaussian laser pulse, where  $I_0$  is the peak intensity of incident laser pulse. So the intensity of incident pulse at  $t=T=1.289\tau$  reaches maximum  $I_0$ , where  $\tau$  is the FWHM of incident laser pulse. The calculated results are given as following.

In Fig.1 we showed the profiles of electron temperature of laser-produced plasma for thin Formvar-iron foil in which 300 angstrom thickness of iron deposits on a thickness 750 angstrom Formvar substrate. Two opposing incident gaussian laser beams with wavelength  $1.06 \mu\text{m}$ , FWHM 800ps and peak intensity 50TW per square centimeter were supposed to be focussed into lines onto target. From it we can see that at  $t=1066\text{ps}$ , that is nearly at the peak intensity of incident laser pulse (peak time  $t=T=1031\text{ps}$ ), the foil was burned through by the thermal-conduction wave, and after 100-200ps, the smooth electron density and temperature profiles occurred, in which the smooth region widens about  $100 \mu\text{m}$  and electron temperature

is about  $4 \times 10^6 K$  and electron density reaches  $2-3 \times 10^{20} / \text{cm}^3$ .

In Fig.2 we showed the profiles of electron density and temperature for the same thickness foil. The wavelength  $1.06 \mu\text{m}$ , FWHM 800ps and  $I_0$  equals 10TW per square centimeter one gaussian laser light pulse was focussed into a line onto the surface of iron. After the peak of incident laser pulse, the

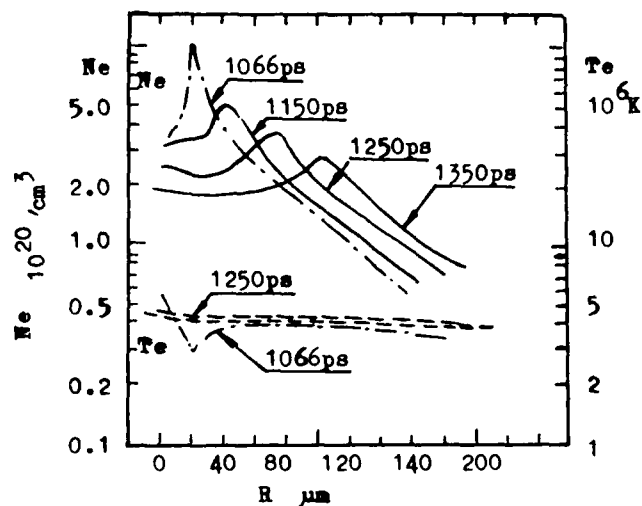


Fig.1 The electron density  $N_e$  and temperature  $T_e$  of laser-produced plasma of iron vs space  $R$  at different time for 750ÅFormvar + 300ÅFe foil. The dot-and-dash lines denote the profiles at burned time of iron foil. The peak of incident pulse is  $t=T=1031\text{ps}$ .

foil was burned through, then uniform profiles of electron density and temperature

produced, in which  $T_e$  is about  $4 \times 10^6 K$  and  $N_e \sim 2 \times 10^{20} / \text{cm}^3$ .

In Fig.3 the electron temperature in the middle of iron region varies with time  $t$  for above two geometries was shown.

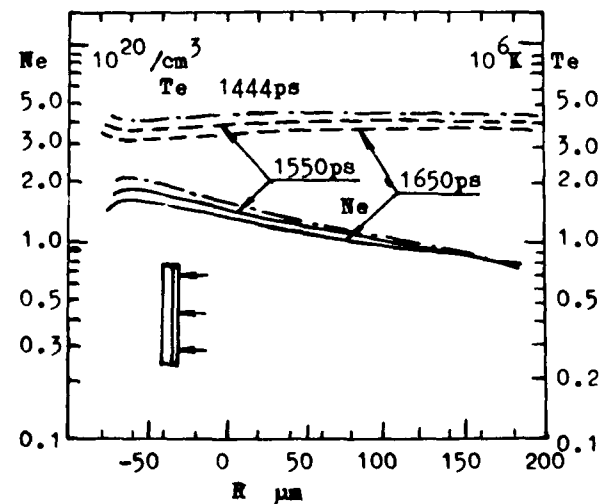


Fig.2 The electron density  $N_e$  and temperature  $T_e$  vs space  $R$  at different time in the plasma of iron. The dot-and-dash lines denote the profiles at burned through time of the foil. The peak of incident pulse occurs at  $t=T=1031\text{ps}$  and the burned through time is  $t=1444\text{ps}$ .

From Figs.1-3 we can see that using wavelength  $1.06\mu\text{m}$ , FWHM 800ps,  $I_0$  equals 50TW per square centimeter two opposing gaussian laser beams or  $I_0$  equals 10TW per square centimeter one beam laser light to irradiate thickness 300 angstroms iron which deposits on 750 angstroms Formvar substrate, the smooth profiles of electron density and temperature can be obtained after the foil was burned through by the thermal-conduction wave. If the thickness of iron medium and the FWHM of incident laser light to be increased suitably, good electron density and temperature profile can be obtained too. In Fig.4 we showed the computational results for thickness 500 angstroms iron which deposits on one side of thickness 750 angstroms Formvar. The foil was irradiated with wavelength  $1.06\mu\text{m}$ , FWHM 1000ps and  $I_0$  equals 5TW per square centimeter two opposing gaussian laser beams. The foil was burned through by thermal-conduction wave at  $t=1497\text{ps}$  (the peak of incident pulse is at  $t=1289\text{ps}$ ), after 100-200ps a uniform plasma of iron can be produced, in which  $T_e$  is about  $3-4 \times 10^6 \text{ K}$  and  $N_e$  is

about  $2-3 \times 10^{20} / \text{cm}^3$ . The more thickness of iron foil is increased the later of burned through time is reached, at last the foil of iron can't be burned through.

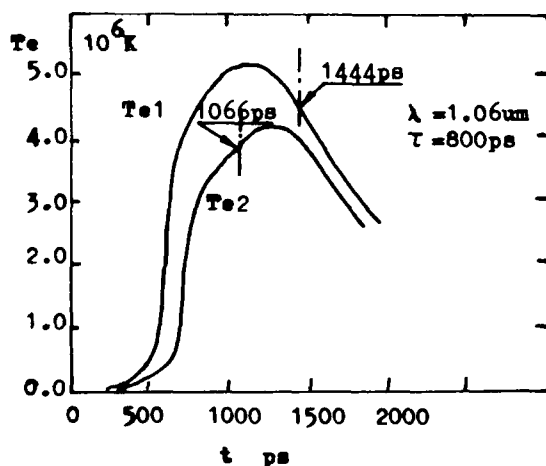


Fig.3 The electron temperature  $T_e$  in the middle of iron region vs time  $t$  for 750ÅFormvar+300ÅFe foil.  $T_{e1}$  denotes the foil was irradiated with a incident laser beam,  $I_0$  equals 10TW per square centimeter on the side of iron, and  $T_{e2}$  denotes two oppsing laser beams illuminated foil, each of them  $I_0$  equals 5TW per square centimeter.

In figs.5-8, we showed the laser-produced plasma conditions for 1000ÅFormvar+750ÅFe foil target which was irradiated with wavelength  $0.53\mu\text{m}$ , FWHM 800ps and peak intensity equals 10TW per square centimeter two oppo-

sing gaussian laser beams or peak intensity 20TW per square centimeter one laser beam on iron side. Because all laser light absorption and reflection processes occur at electron density less than critical density  $N_{ec}$ , and  $N_{ec}$  is inversely as the square of wavelength of laser light, so double frequency Nd-glass laser light can penetrate iron medium deeply.

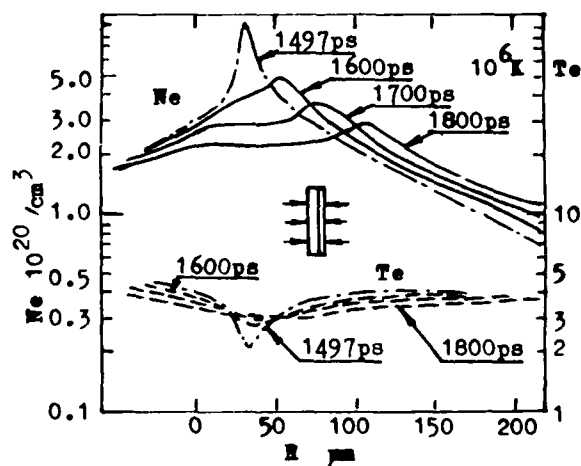


Fig.4 The profiles of electron density  $N_e$  and temperature  $T_e$  for 750ÅFormvar+500ÅFe foil, which was irradiated with  $\lambda=1.06\mu\text{m}$ ,  $\tau=$

1000ps and  $I_0=5 \times 10^9 \text{ W/cm}^2$  two opposing gaussian laser pulse. The peak of incident pulse is  $t=1289\text{ps}$  and the burned through time of the foil is  $t=1497\text{ps}$ .

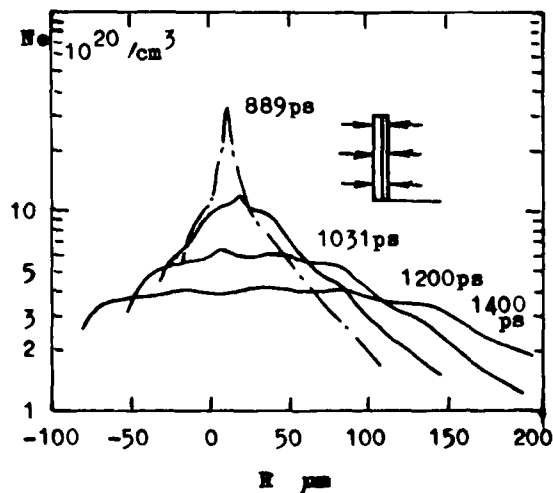


Fig.5 The profile of electron density for 1000ÅFormvar+750ÅFe foil which was irradi-

ated with  $\lambda=0.53\mu\text{m}$ ,  $\tau=800\text{ps}$  and  $I_0=1 \times 10^9 \text{ W/cm}^2$  two opposing gaussian laser beams. The burned through time of the foil  $t=889\text{ps}$  is before the peak time of the incident pulse.

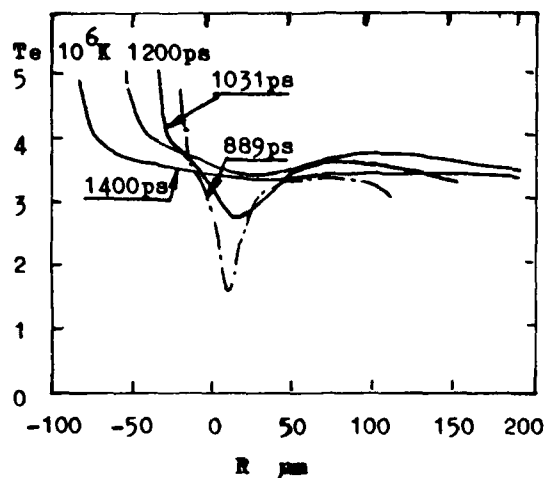


Fig.6 The profile of electron temperature  $T_e$  for 1000ÅFormvar+750ÅFe foil. The parameters of incident laser light are as same as mentioned in Fig.5.

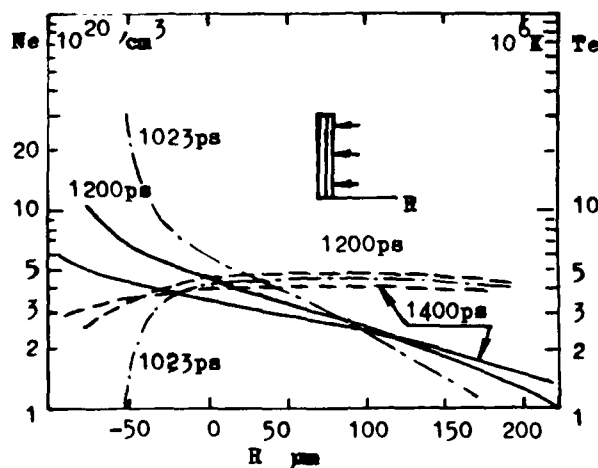


Fig.7 The profiles of electron density  $N_e$  and temperature  $T_e$  for 1000ÅFormvar+750ÅFe foil which was illuminated with  $\lambda=0.53\mu\text{m}$ ,  $\tau=800\text{ps}$  and  $I_0=2 \times 10^{13} \text{ W/cm}^2$  incident gaussian laser beam. The burned through time is  $t=1023\text{ps}$  and the peak of incident pulse is  $t=T=1031\text{ps}$ .

From calculated results we can see that for two opposing laser beams the foil can be burned through before the peak of incident laser pulse, and for one incident laser beam on the side of iron, the foil can be burned through nearly at the peak of laser pulse. Later is better for getting a uniform profile of plasma.

#### CALCULATION OF GAINS

##### 1. Steady rate equations

According to works[7-8], we use steady rate equations to calculate populations of diffe-

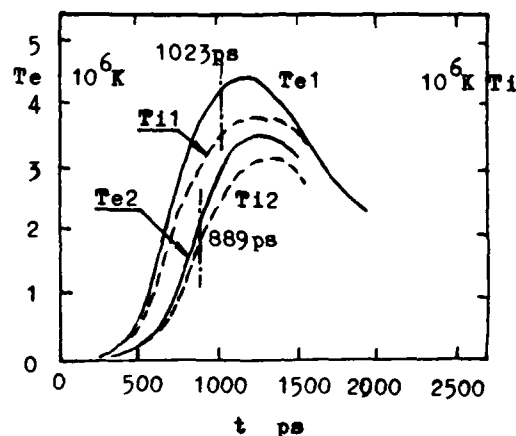


Fig.8 The electron temperature  $T_e$  and ion temperature  $T_i$  in the middle of iron vs time  $t$  for 1000ÅFormvar+750ÅFe foil. Number 1 means the foil was illuminated with one beam laser pulse  $I_0=2 \times 10^{13} \text{ W/cm}^2$  and number 2 means the foil was illuminated with two opposing laser beams each of them  $I_0=1 \times 10^{13} \text{ W/cm}^2$ ,  $\lambda=0.53\mu\text{m}$  and  $\tau=800\text{ps}$ .

rent levels of neon-like ions

$$N_j' \left[ \sum_{i < j} A_{ji} + N_e \left( \sum_{i < j} C_{ji}^d + \sum_{i > j} C_{ji}^e \right) \right] \\ = N_e \left[ \sum_{i < j} N_i' C_{ij}^e + \sum_{i > j} N_i' C_{ij}^d \right] + \sum_{i > j} N_i' A_{ij} \quad (12)$$

where  $N_j'=N_j/N_1$  is the ratio of the ion number density in the  $j$  level to the total number for all of the levels of the neon-like ion,  $C_{ij}$  and  $C_{ji}$  are the electron excitation and de-excitation rate coefficients. Atomic data are taken from [8], and only 27 configurations for 3s, 3p and 3d levels are considered in our calculation. The cascading from more highly excited configurations is neglected.

The gain coefficient from  $i$  to  $j$  level is

$$\alpha = \frac{\lambda^j}{8\pi} A_{ij} \left( \frac{M}{2\pi k T_i} \right)^{\frac{1}{2}} g_i (N_i/g_i - N_j/g_j) \quad (13)$$

where  $\lambda$  is the wavelength of the transition between  $i$  and  $j$  levels,  $T_i$  is the ion temperature.

perature,  $M$  is the atomic mass of the ion,  $k$  is Boltzmann constant. In the calculation only Doppler broadening was considered.

## 2. Calculated results

Supposing the abundance of neon-like ion of iron is  $\eta = 1/4$  in the plasma, we calculated the gain coefficients for 3p-3s transitions at different densities and temperatures. The calculated results are shown in Table 1-3.

In fig.9 we showed the gain coefficient vs electron density on conditions that  $\eta = 1/4$  and  $T_e = 4 \times 10^6$  K.

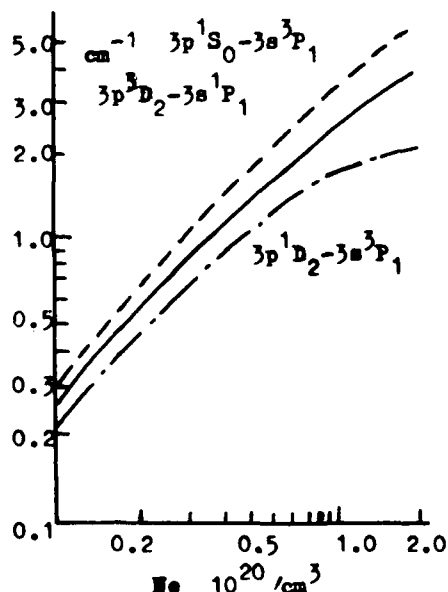


Fig.9 The gain coefficient of 3p-3s transition vs electron density  $N_e$  on conditions that  $\eta = 1/4$  and  $T_e = 4 \times 10^6$  K.

Table 1. The gain coefficient vs  $T_e$  and  $N_e$  for  $2s^2 2p^3 3p^1 S_0 - 2s^2 2p^3 3s^1 P_1$  transition on condition that  $\eta = 1/4$ .

$\alpha \backslash N_e$	0.1	0.2	0.3	0.5	0.7	1.0	2.0
$T_e$							
3.0	.177	.383	.584	.963	1.32	1.80	3.11
3.5	.246	.535	.818	1.35	1.85	2.54	4.11
4.0	.309	.678	1.04	1.72	2.35	3.23	5.63
5.0	.417	.919	1.41	2.34	3.20	4.40	7.68
6.0	.494	1.10	1.68	2.80	3.84	5.27	9.19

Table 2. The gain coefficient vs  $T_e$  and  $N_e$  for  $2s^2 2p^3 3p^1 D_2 - 2s^2 2p^3 3s^1 P_1$  transition on

condition that  $\eta = 1/4$ .

$\alpha \backslash N_e$	0.1	0.2	0.3	0.5	0.7	1.0	2.0
$T_e$							
3.0	.116	.239	.348	.525	.651	.751	.482
3.5	.165	.344	.507	.784	.999	1.22	1.22
4.0	.212	.445	.662	1.04	1.35	1.69	2.03
5.0	.292	.622	.933	1.49	1.97	2.55	3.58
6.0	.353	.756	1.14	1.85	2.46	3.24	4.97

Table 3. The gain coefficients vs  $T_e$  and  $N_e$  for  $2s^2 2p^3 3p^1 D_2 - 2s^2 2p^3 3s^1 P_1$  on  $\eta = 1/4$ .

$\alpha \backslash N_e$	0.1	0.2	0.3	0.5	0.7	1.0	2.0
$T_e$							
3.0	.152	.312	.464	.742	.983	1.28	1.87
3.5	.213	.438	.656	1.06	1.41	1.87	2.88
4.0	.271	.559	.837	1.36	1.82	2.44	3.87
5.0	.369	.763	1.15	1.87	2.53	3.41	5.62
6.0	.443	.918	1.38	2.26	3.07	4.15	6.96

In Table 1-3  $T_e$  in  $10^6$  K,  $N_e$  in  $10^{20}/\text{cm}^3$ , and  $\alpha$  in  $1/\text{cm}$ .

## DISCUSSION AND CONCLUSION

Our computational simulations showed that under following conditions: using 1. wavelength  $0.53 \mu\text{m}$ , FWHM 800ps and peak intensity 20TW per square centimeter one gaussian laser beam to irradiate  $1000\text{\AA}$  Formvar+750\AA Fe foil; or 2. wavelength  $1.06 \mu\text{m}$ , FWHM 800-1000ps, peak intensity 5TW per square centimeter two opposing gaussian laser beams to irradiate  $300-500\text{\AA}$  Fe+750\AA Formvar foil; or 3. wavelength  $1.06 \mu\text{m}$ , FWHM 800ps peak intensity 10TW per square centimeter one gaussian laser beam to irradiate  $300\text{\AA}$  Fe+750\AA Formvar foil; an electron density  $N_e = 2-3 \times 10^{20}/\text{cm}^3$  and electron temperature  $T_e = 4 \times 10^6$  K nearly uniform plasma can be obtained.

On conditions that the abundance of neon-like ion of iron  $\eta = 1/4$ ,  $T_e = 4 \times 10^6$  K and  $N_e = 2 \times 10^{20}/\text{cm}^3$ , the gain coefficient of 3p-3s transition can reach more than  $2/\text{cm}$ .

There are some problems in our calculation that have to resolve. The first is how many abundance of neon-like ion of iron actually occurs in the laser-produced plasma? It depends on atomic data and plasma conditions. Besides this, the trapping effect hasn't been considered in our calculation. It will reduce gain coefficient.

We hope that the experiments will provide

enough informations such as the profiles of electron density and temperature, the abundance of neon-like ion in laser-produced plasma, using them we can test, examine and improve our codes and design useful experiments for getting soft x-ray amplification.

#### ACKNOWLEDGMENTS

The authors express their thanks to S.F.Li and Y.C.Zhang for their useful computational calculations.

#### REFERENCES

1. M.D.Rosen, P.L.Hagelstein, D.L.Mattews, E.M.Campbell, A.U.Hazi, B.L.Whitten, B.MacGowan, R.E.Turner, R.W.Lee, G.Charatis, Gar.E.Busch C.L.Shepard, and P.D.Rockett, "Exploding-foil technique for achieving a soft x-ray laser", *Phys.Rev.Lett.* 54(2), 106(1985).
2. D.L.Mattews, P.L.Hagelstein, M.D.Rosen, M.J.Eckart, N.M.Geglio, A.U.Hazi, H.Meddecki, B.J.MacGowan, J.E.Trebes, B.L.Whitten, E.M.Campbell, C.W.Hatcher, A.M.Hawryluk, R.L.Kaffman, L.D.Pleasance, G.Rambach, J.H.Scofield, G.Stone and T.A.Weaver, "Demonstration of a soft x-ray amplifier", *Phys.Rev.Lett.* 54(2), 110(1985).
3. T.N.Lee, E.A.McLean, and R.C.Elton, "Soft x-ray laser in neon-like germanium and copper plasmas", *Phys.Rev.Lett.* 59(11), 1185 (1987).
4. M.Louis-Jacquet, Jean-Luk Bourgade, P.Combis, S.Jacquemot, Jean-Pierre.Le.Briton, D.Naccache, Jean-Perrine et O.Peyrusse, "Evidence of X-UV amplification in a germanium plasma generated by laser", *C.R.Acad.Sci. Paris* 306 Serie II 867870(1988)
5. G.Cooper, "Compton Fokker-Planck equation for hot plasma", *Phys.Rev. D* 3(10), 2312 (1971).
6. A.V.Vinogradov and V.N.Shlyaptsev, "Amplification of ultraviolet radiation in a laser plasma", *Sov.J.Quant.Electron.* 13 (11), 1511(1983).
7. U.Feldman, A.K.Bhatia and S.Suckewer, "Short wavelength laser calculations for electron pumping in neon-like krypton (KrXXVII)", *J.Appl.Phys.* 54(5), 2188(1983).
8. A.K.Bhatia, U.Feldman, and J.F.Seely, "Atomic data and spectral line intensities for the neon isoelectronic sequence (SiV through KrXXVII)", *Atom.Data and Nucl. Data Tab.* 32, 435(1985).

# HARMONIC GENERATION IN LASER-FREE ELECTRON SCATTERING RECONSIDERED

Anna K. Puntajer and C. Leubner

Inst. Theoret. Phys., University of Innsbruck, A-6020 Innsbruck, Austria

For zero electron drift velocity, the corrected version<sup>1</sup> of Vachaspati's classical cross sections<sup>1-2</sup> deviates strongly from a semi-classical one by Ehlötzky<sup>3</sup> and from an unpublished quantum electrodynamical cross section by Jafarpour.<sup>4</sup> Therefore, the cross section is recalculated within classical electrodynamics, which suffices for the experimental configurations in question.<sup>5</sup> This classical cross section, derivable more simply and with fewer approximations than the semi-classical one, nevertheless agrees perfectly with Ehlötzky's result<sup>3</sup> for all harmonics, but only to some extent with Vachaspati's earlier version<sup>2</sup> of the classical second harmonic cross section, and not at all with his corrected one,<sup>1</sup> nor with Jafarpour's quantum electrodynamical one.<sup>4</sup> Moreover, it also incorporates relativistic Thomson scattering as envisaged by McDonald.<sup>6</sup>

For second harmonic scattering, Fig. 1 shows perfect agreement between the semi-classical<sup>3</sup> cross section and the present classical one. Vachaspati's earlier version<sup>2</sup> agrees to some extent, whereas his corrected one<sup>1</sup> and Jafarpour's unpublished QED cross section<sup>4</sup> deviate strongly.

Even for zero electron drift velocity as in Fig. 1, the cross section exhibits a marked forward-backward asymmetry, briefly mentioned by Sarachik and Schappert.<sup>7</sup> It can be explained as an interference between the fields produced by the linear and nonlinear components of the electron motion, and it renders Englert and Rinehart's<sup>4</sup> direction of observation most unfavorable for observing second harmonic photons.

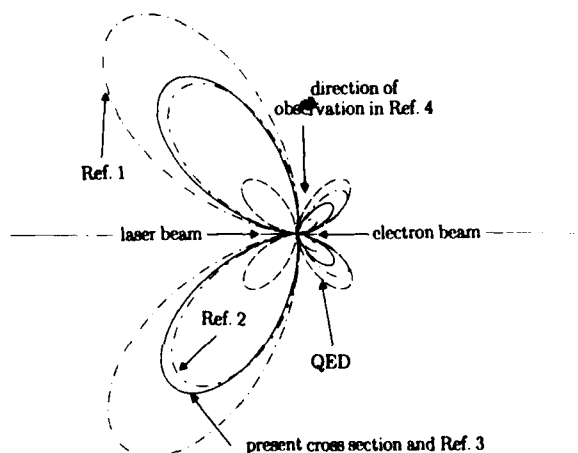


Figure 1

## REFERENCES

- <sup>1</sup> Vachaspati, 1963, Phys. Rev. **130**, Erratum, 2598.
- <sup>2</sup> Vachaspati, 1962, Phys. Rev. **128**, 662.
- <sup>3</sup> Ehlotzky, F., 1987, J. Phys. B: At. Mol. Phys. **20**, 2619.
- <sup>4</sup> Englert, T. J., Rinehart, E. A., 1983, Phys. Rev. **A28**, 1539.
- <sup>5</sup> Dobiasch, P., Fedorov, M. V., and Stenholm, S., 1987, J. Opt. Soc. Am. **B4**, 1109.
- <sup>6</sup> McDonald, K.T., 1986, *Proposal for experimental studies of nonlinear quantum electrodynamics*, preprint, Princeton University.
- <sup>7</sup> Sarachik, E. S., and Schappert, G. T., 1969, Lettere al Nuovo Cimento **2**, 7.

# Gain Guided X-Ray Beams

Ernst E. Fill

*Max-Planck-Institut für Quantenoptik  
D-8046 Garching, Federal Republic of Germany*

## Abstract

It is shown that with gain and index profiles of typical x-ray laser experiments the x-ray beam is guided by the gain profile rather than defocussed by the refractive index distribution. An arbitrary beam generated within the medium or injected into the medium is quickly transformed into a 'matching' beam, propagating without change. The effective gain of the matching beam is somewhat lower than the gain at the maximum of the gain distribution.

If the gain distribution exhibits a small curvature in direction of beam propagation the effective gain is dramatically reduced.

## Introduction

In laser plasma x-ray laser media strong electron density gradients transverse to the direction of x-ray beam propagation exist. These index gradients result from the free-electron contribution to the refractive index of a plasma, which - for frequencies far above the plasma frequency - can be approximated by

$$n = 1 - N_e/2N_c. \quad (1)$$

In Eq.(1)  $N_e$  is the electron density and  $N_c$  is the critical electron density for the x-ray beam given by

$$N_c = 1.1 \times 10^{13} \lambda^{-2}, \quad (2)$$

with  $N_c$  in  $\text{cm}^{-3}$  and  $\lambda$  in  $\text{cm}$ .

There is concern [1, 2] that the refractive index gradient may deflect the x-ray laser beam out of the high gain region, thus limiting the maximum achievable effective gain length.

In x-ray laser media, however, there is not only a refractive index gradient but also a strong gain distribution transverse to the beam propagation direction. Ray tracing studies [3] indicated that the gain gradient should have an influence on the beam propagation.

In this paper we show that under typical conditions of x-ray laser experiments beam spreading due to the refractive index gradient does not occur [4]. Approximating gain and index distributions with quadratic functions, formulae for Gaussian beams propagating in such media are derived. The analysis is done for the general case of non-coincident symmetry axes of the gain and index profiles and is extended to media with a slight curvature in direction of beam propagation.

## Beam Propagation in Square Law Media

We give a short review of the theory for the propagation of a Gaussian beam in a medium the complex propagation constant of which varies quadratically transverse to the propagation direction [5, 6].

The propagation constant  $k$  is decomposed into its real and imaginary parts according to

$$k = \beta + j\alpha, \quad (3)$$

where  $\beta$  is related to the refractive index  $n$  by

$$n = \frac{\lambda}{2\pi} \beta \quad (4)$$

and  $\alpha$  is the electric field gain coefficient related to the intensity gain coefficient by

$$g = 2\alpha. \quad (5)$$



Allowing for displaced gain and index distributions we may write for  $\alpha$  and  $\beta$

$$\alpha = \alpha_0 - 1/2 \alpha_1 x - 1/2 \alpha_2 x^2 - 1/2 \alpha_2 y^2 \quad (6a)$$

$$\beta = \beta_0 - 1/2 \beta_2 x^2 - 1/2 \beta_2 y^2, \quad (6b)$$

where  $x$  and  $y$  are coordinates perpendicular to the direction of beam propagation.

The particular form of Eqs. (6) puts the origin at the center of the index distribution whereas the gain parabola is displaced in  $x$ -direction by

$$x_0 = -\alpha_1/(2\alpha_2) \quad (7)$$

and the value of  $\alpha$  at  $x_0$  is given by

$$\alpha_{max} = \alpha_0 + \frac{1}{2} \alpha_2 x_0^2. \quad (8)$$

The gain- and index distributions given by Eqs. (6) are cylindrically symmetric. It may be noted that the analysis can be performed as well for a bi-axial distribution (in which the contours of equal gain or refractive index are ellipses). For simplicity, however, in this paper only the cylindrically symmetric case is treated.

It is convenient to decompose  $k$  according to

$$k = k_0 - \frac{1}{2}(k_{1x}x + k_{1y}y + k_{2x}x^2 + k_{2y}y^2). \quad (9)$$

From Eqs. (6) one has

$$k_0 = \beta_0 + j\alpha_0 \quad (10a)$$

$$k_{1x} = j\alpha_1; \quad k_{1y} = 0 \quad (10b)$$

$$k_2 = \beta_2 + j\alpha_2, \quad (10c)$$

where the second index of  $k_2$  was dropped since  $k_{2x} = k_{2y}$ .

Consider a Gaussian beam propagating in  $z$ -direction. The medium is assumed homogeneous along  $z$ . To obtain a solution of Maxwell's equations a transverse field component is written as

$$E = \psi(x, y, z) \exp[j(\omega t - k_0 z)]. \quad (11)$$

Neglecting the second derivative of  $\psi$  with respect to  $z$  the wave equation becomes

$$\frac{\partial^2 \psi}{\partial x^2} + \frac{\partial^2 \psi}{\partial y^2} - 2jk_0 \frac{\partial \psi}{\partial z} - k_0(k_{1x}x + k_{2x}x^2 + k_{2y}y^2)\psi = 0 \quad (12)$$

the solution of which can be written as [6]

$$\psi(x, y, z) = \exp\{-j[\frac{1}{2}Q(x^2 + y^2) + Sx + P]\}, \quad (13)$$

where  $Q(z)$ ,  $S(z)$  and  $P(z)$  are complex parameters.

This equation represents a cylindrically symmetric Gaussian beam displaced in  $x$ -direction from the  $(x = 0, y = 0)$ -axis. The parameter  $Q$  is related to the well known complex beam parameter  $q$  by

$$Q = 2\pi/(\lambda q). \quad (14)$$

The radius of curvature  $R$  of the wavefront and the beam width  $w$  are given by

$$R = 2\pi/(\lambda Q_R); \quad w = (-2/Q_I)^{1/2}, \quad (15)$$

where the subscripts  $R$  and  $I$  symbolize the real and imaginary parts of a quantity. The beam may be displaced from the axis with different displacements for amplitude and phase. The amplitude maximum and the center of curvature of the wavefront are displaced by

$$x_a = -S_I/Q_I; \quad x_p = -S_R/Q_R. \quad (16)$$

By inserting (13) into the wave equation and comparing equal powers of  $x$  and  $y$  one obtains the following differential equations for the parameters  $Q$ ,  $S$  and  $P$

$$k_0 \frac{dQ}{dz} + Q^2 + k_0 k_2 = 0 \quad (17)$$

$$k_0 \frac{dS}{dz} + QS + \frac{1}{2} k_0 k_{1x} = 0 \quad (18)$$

$$k_0 \frac{dP}{dz} + jQ + \frac{1}{2} S^2 = 0, \quad (19)$$

which have the solutions

$$Q(z) = Q_m \frac{Q(0) + Q_m + (Q(0) - Q_m) \exp(2j\gamma z)}{Q(0) + Q_m - (Q(0) - Q_m) \exp(2j\gamma z)}, \quad (20)$$

where  $Q_m$  is the 'matching' beam parameter, given by

$$Q_m = -j\sqrt{k_0 k_2} \quad (21)$$

and

$$\gamma = \sqrt{k_2/k_0}. \quad (22)$$

$$S(z) = \bar{S}(z) + Q(z)k_{1x}/(2k_2), \quad (23)$$

where

$$\bar{S}(z) = \frac{2\bar{S}(0)Q_m \exp(j\gamma z)}{Q(0) + Q_m - (Q(0) - Q_m) \exp(2j\gamma z)} \quad (24)$$

and

$$\bar{S}(0) = S(0) - Q(0)k_{1z}/(2k_2). \quad (25)$$

$$P(z) = \bar{P}(z) - Q(z)k_{1z}^2/(8k_2^2) + S(z)k_{1z}/(2k_2) + k_{1z}^2 z/(8k_2) \quad (26)$$

where

$$\begin{aligned} \bar{P} &= \bar{P}(0) \\ &- j \ln \frac{Q(0) + Q_m + (Q(0) - Q_m) \exp(2j\gamma z)}{2Q_m \exp(j\gamma z)} \\ &- \frac{\bar{S}(0)^2}{2} \frac{1 - \exp(2j\gamma z)}{Q(0) + Q_m - (Q(0) - Q_m) \exp(2j\gamma z)} \end{aligned} \quad (27)$$

and

$$\bar{P}(0) = Q(0)k_{1z}^2/(8k_2^2) - S(0)k_{1z}/(2k_2), \quad (28)$$

with  $P(0) = 0$ , to normalize the input field.

The field amplitude on the  $x = 0, y = 0$ -axis is given by  $\exp(\alpha_0 z + P(z)_I)$ . The local amplitude gain coefficient on axis is  $\alpha_0 + \frac{dP_I}{dz}$ . More interesting, however, are amplitude and gain at the center of the field distribution. Transforming into the 'beam center' at  $x = x_a$  one obtains

$$\hat{P}_I = P_I - \frac{1}{2}Q_I x_a^2 \quad (29)$$

and, after differentiation, using Eqs. (16)-(19) and  $k_0 \approx \beta_0$

$$\frac{d\hat{P}_I}{dz} = -Q_R/\beta_0 - \frac{1}{2}(\alpha_1 x_a + \alpha_2 x_a^2). \quad (30)$$

The effective amplitude gain coefficient at beam center is given by

$$\alpha_{eff} = \alpha_0 + \frac{d\hat{P}_I}{dz}. \quad (31)$$

The intensity gain coefficient at beam center is given by  $2\alpha_{eff}$ . One may define a power gain coefficient

$$g_p = \frac{1}{W_p} \frac{dW_p}{dz}, \quad (32)$$

where  $W_p = \pi w^2 I_c$  is the beam power and  $I_c$  is the intensity at beam center. The power gain coefficient is given by

$$g_p = \frac{1}{I_c} \frac{dI_c}{dz} + \frac{2}{w} \frac{dw}{dz}. \quad (33)$$

Using Eqs. (15) and (17) one derives

$$g_p = 2\alpha_{eff} + \frac{1}{Q_I} \left[ \frac{(Q^2)_I}{\beta_0} + \alpha_2 \right]. \quad (34)$$

### Stationary Solution

The parameters  $Q(z)$ ,  $S(z)$  and  $P(z)$  completely specify a beam as it propagates through a medium. If  $\gamma_I > 0$  the beam parameters become independent of the initial conditions in the limit of  $z \rightarrow \infty$  and settle to those of the stationary 'matching' beam. The propagation distance, at which this happens, is approximately given by  $1/\gamma_I$ . From Eqs. (19) and (10c) it is seen that  $\gamma_I > 0$  requires

$$\alpha_2 > 0 \quad (35)$$

implying a downward bent gain parabola. If  $\alpha_2 = 0$  (no gain profile) and  $\beta_2 > 0$ , the beam parameters oscillate without limit about those of the matching beam. (With no gain profile and  $\beta_2 < 0$  a matching beam doesn't exist).

From Eqs. (17), (20), (21), (23) and (24) one derives for the parameters of the stationary beam

$$Q = Q_m \quad (36)$$

$$S_m = Q_m k_{1z}/(2k_2) \quad (37)$$

$$P_m = \left(-\gamma + \frac{k_{1z}^2}{8k_2}\right) z + P_c, \quad (38)$$

where  $P_c$  is a constant given by

$$\begin{aligned} P_c &= -j \ln \frac{Q(0) + Q_m}{2Q_m} + (Q(0) - Q_m) \frac{k_{1z}^2}{8k_2^2} \\ &- (S(0) - S_m) \frac{k_{1z}}{2k_2} \end{aligned} \quad (39)$$

As a condition for a real beam width one obtains from Eqs. (15) and (18)

$$Re(\sqrt{k_0 k_2}) > 0 \quad (40)$$

which leads to

$$\alpha_2 \beta_0 + \alpha_0 \beta_2 > 0. \quad (41)$$

Under the condition of Eq. (41) the parameters of the matching beam can be expressed by  $\alpha_0, \beta_0, \alpha_1, \alpha_2$  and  $\beta_2$ . One obtains

$$\begin{aligned} R_m &= \beta_0 \sqrt{2} [\sqrt{(\beta_0 \beta_2 - \alpha_0 \alpha_2)^2 + (\alpha_2 \beta_0 + \alpha_0 \beta_2)^2} \\ &- \beta_0 \beta_2 + \alpha_0 \alpha_2]^{-1/2} \end{aligned} \quad (42)$$

$$w_m = 2^{3/4} [\sqrt{(\beta_0\beta_2 - \alpha_0\alpha_2)^2 + (\alpha_2\beta_0 + \alpha_0\beta_2)^2} + \beta_0\beta_2 - \alpha_0\alpha_2]^{-1/4}, \quad (43)$$

$$x_{am} = x_0 [1 - \beta_2/(\beta_2^2 + \alpha_2^2)^{1/2}], \quad (44)$$

$$x_{pm} = x_0 [1 + \beta_2/(\beta_2^2 + \alpha_2^2)^{1/2}]. \quad (45)$$

The effective gain coefficient of the matching beam becomes

$$\alpha_{effm} = \alpha_0 - 1/R_m + \frac{1}{2}\alpha_2^3 x_0^2 \beta_2^2 / (\beta_2^2 + \alpha_2^2), \quad (46)$$

which can be written as

$$\alpha_{effm} = \alpha_{maz} - 1/R_m - \frac{1}{2}\alpha_2 x_0^2 \beta_2^2 / (\beta_2^2 + \alpha_2^2). \quad (47)$$

Since the beam diameter is constant, both, the intensity- and power gain coefficients are given by  $2\alpha_{effm}$ .

The distance, at which an arbitrary beam injected into the medium approaches the stationary beam, is given approximately by ( $k_0 \approx \beta_0$ )

$$z_m \approx 1/\gamma_I = \sqrt{2\beta_0} [\sqrt{\beta_2^2 + \alpha_2^2} - \beta_2]^{-1/2}. \quad (48)$$

### Application to X-Ray Laser Experiments

The previous formalism can be easily applied to the conditions of laser plasma x-ray lasers. Assume an exploding foil target with a Gaussian electron density distribution, approximated, near the maximum, by a parabola. Since the electron density decreases away from the axis, the refractive index increases (see Eq. (1)) and the parameter  $\beta_2$  becomes negative.

We note, that the condition for a real stationary beam width (Eq. (41)) is easily satisfied in x-ray laser experiments. Furthermore, one usually has  $|\beta_0\beta_2| \gg \alpha_0\alpha_2$ ,  $|\beta_0\beta_2| \gg \alpha_2\beta_0 + \alpha_0\beta_2$ ,  $\beta_0\alpha_2 \gg |\alpha_0\beta_2|$  and  $|\beta_2| \gg \alpha_2$ . In this case the above equations can be considerably simplified. One obtains ( $\beta_2 < 0$ )

$$R_m \approx \sqrt{\beta_0/|\beta_2|}; \quad w_m \approx 2[|\beta_2|/(\beta_0\alpha_2^2)]^{1/4}, \quad (49)$$

$$x_{am} \approx 0; \quad x_{pm} \approx 2x_0 \quad (50)$$

$$\alpha_{eff} \approx \alpha_{maz} - 1/R_m - \alpha_2 x_0^2/2. \quad (51)$$

and

$$z_m \approx \sqrt{\beta_0/|\beta_2|}. \quad (52)$$

We evaluate an example with the following parameters, typical for laser plasmas with gain in the soft x-ray region:  $\lambda = 10 \text{ nm}$ ;  $N_e = 5 \times 10^{20} \text{ cm}^{-3}$ ;  $g_{maz} = 3 \text{ cm}^{-1}$ . Assume that the index of refraction reaches its free space value of 1 at a distance of  $100 \mu\text{m}$  from the axis of symmetry and that the gain becomes zero at  $50 \mu\text{m}$  from its maximum.

If the symmetry axes of the gain and index distributions coincide, one has from Eqs. (1)-(8)  $\beta_0 = 6.28 \times 10^6 \text{ cm}^{-1}$ ;  $\alpha_0 = 1.5 \text{ cm}^{-1}$ ;  $\alpha_1 = 0$ ;  $\beta_2 = -2.86 \times 10^6 \text{ cm}^{-3}$ ;  $\alpha_2 = 1.2 \times 10^5 \text{ cm}^{-3}$ . Inserting these values into Eqs. (42)-(47) one obtains for the parameters of the matching beam  $R_m = 1.48 \text{ cm}$ ;  $w_m = 4.74 \times 10^{-3} \text{ cm}$  and for the effective gain coefficient  $g_{eff} = 1.66 \text{ cm}^{-1}$ . The beam therefore propagates with a gain coefficient which is about half the gain coefficient at the center of the gain distribution. The parameters of the matching beam are approached at a propagation distance  $z_m = 1.48 \text{ cm}$ .

The situation changes if the gain maximum is displaced by, say,  $x_0 = 20 \mu\text{m}$  from the refractive index minimum. Now  $\alpha_0 = 1.26 \text{ cm}^{-1}$  and  $\alpha_1 = -4.8 \times 10^2 \text{ cm}^{-2}$ , while all the other parameters remain the same. Evaluation of the beam parameters reveals that the beam amplitude distribution and its phase front travel along parallel axes with  $x_{am} \approx 0$  and  $x_{pm} \approx 40 \mu\text{m}$ , while the values of  $R_m$ ,  $w_m$  and  $z_m$  are virtually unaltered. The effective gain coefficient  $g_{eff}$  of the beam, however, is smaller than previously, assuming a value of  $1.17 \text{ cm}^{-1}$ .

The evolution of a beam towards the matching beam is illustrated in Figs. 1-3. The medium is assumed to have the previous parameters with coincident symmetry axes for the gain and index distributions ( $x_0 = 0$ ;  $\alpha_1 = 0$ ). Beam propagation is demonstrated by plotting the  $1/e$ -boundary of the field amplitude distribution and the local power gain coefficient, normalized to the gain coefficient on axis.

The figures relate to different input beams: In Fig. 1 the diameter of the input beam is assumed a factor of 3 larger than the diameter of the matching beam with the beam entering on axis. Note that the power gain coefficient is initially negative, since the beam extends into the region of negative  $\alpha$ . After about  $1.5 \text{ cm}$ , however, the beam diameter and the gain coefficient acquire the values of the

matching beam.

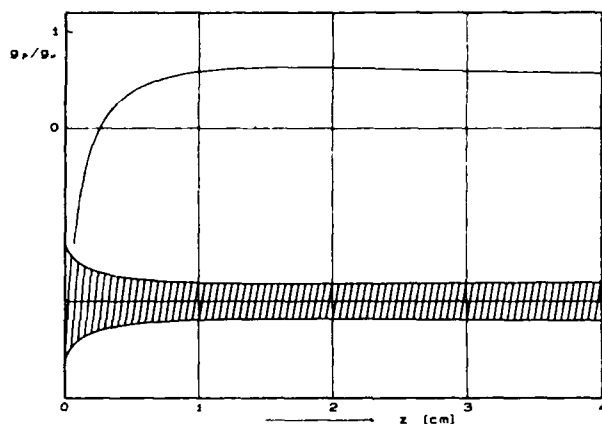


Fig. 1. Gaussian beam in a square law medium showing beam width  $w$  and normalized local power gain coefficient  $g_p/g_0$  versus propagation distance  $z$ . For medium parameters see text. Input beam width  $w_0 = 3w_m$ . Input radius of curvature of the wavefront  $R_0 = 100$  cm.

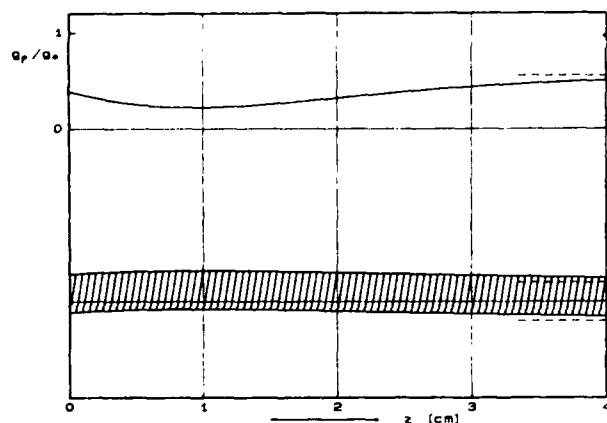


Fig. 2. Off-axis and oblique input beams. The parameters  $w_0$  and  $R_0$  are those of the matching beam. The dashed lines show position and gain coefficient of the matching beam.

In Fig. 2 the input beam has the parameters of the matching beam, but it starts displaced by  $20\mu\text{m}$  from the axis and at an angle of  $5\text{ mRad}$  away from the axis. It is seen, how the gain decreases as the beam is shifting away from the axis.

Only after about 3 cm approach the gain and the beam position the values of the stationary beam.

A situation as in Figs. 1 and 2 might occur if an x-ray laser beam is injected into a second laser medium acting as an amplifier.

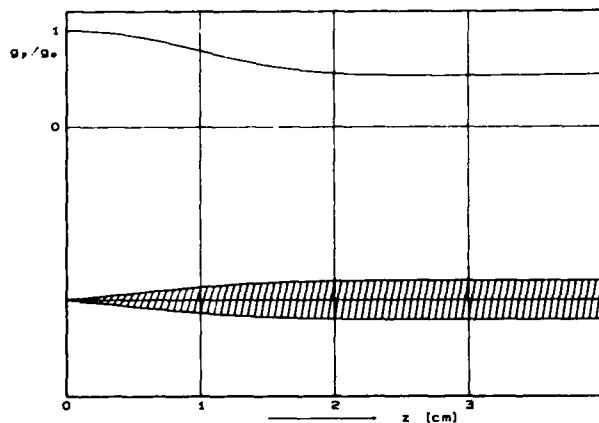


Fig. 3. Propagation of beam with input diameter  $1/50$  of the matching beam diameter.  $R_0 = 100$  cm. Input beam on axis.

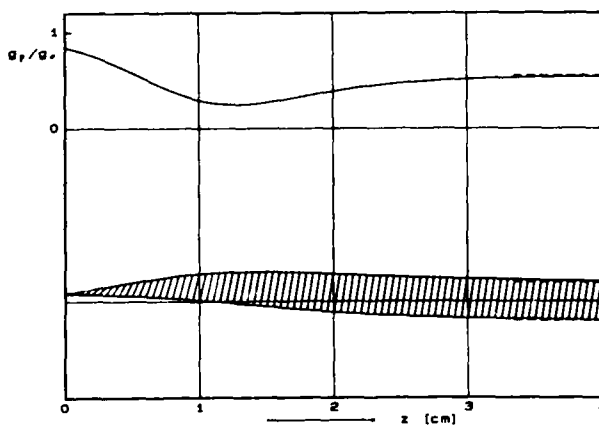


Fig. 4. Same as Fig. 3 but input beam  $20\mu\text{m}$  off axis and at an angle of  $2\text{ mRad}$  away from the axis. Dashed lines show position and gain of the matching beam.

In the examples of Figs. 3 and 4 the input

beams have a diameter which is 50 times smaller than the matching beam diameter. In Fig. 3 the beam starts on axis. It is seen how, at first, the beam spreads by diffraction, but after propagating about 1 cm, gain guiding takes over and the beam parameters approach the ones of the matching beam. In Fig. 4 the input beam has an offset of  $20\mu\text{m}$  and an angle of 2 mRad away from the axis and, correspondingly, the matching beam is attained only after a longer distance of propagation. Figures 3 and 4 may be relevant to the generation of an x-ray laser beam by amplified spontaneous emission (ASE) with many modes generated within the gain medium. As the various beamlets are pulled towards the matching beam, coherence of the total emission is approached.

### Curved Beams

The theory of beam propagation in square law media was extended to a situation in which the gain and index distributions lead the beam along a curved path. The original motivation for considering this case was the hope that an x-ray laser resonator could be realized by guiding the beam around a full circle, thus eliminating the need for high reflectivity x-ray mirrors. Unfortunately, however, the losses in this geometry were found high, except for rather large radii of curvature. A feasible x-ray ring resonator would therefore have rather exotic dimensions. The theory might, however, be useful to assess the losses in a medium in which the gain and index distributions exhibit a small curvature in the direction of beam propagation.

Details of the theory will be given elsewhere [7]. Here we only note, that a stationary curved beam exists, with an effective amplitude gain coefficient given by

$$\alpha_{effc} = \alpha_0 - 1/R_m - \frac{\beta_0^3}{2R_b^2} \frac{(k_0 k_2)_I}{|k_0 k_2|^2}, \quad (54)$$

where  $R_b$  is the bending radius of the gain and index distributions. Equation (54) is valid provided that  $R_b^2 \gg |k_0/k_2|$ . Coincident maxima of the gain and index distributions are assumed.

With the medium parameters of the previous section it turns out that the beam has gain only if  $R_b$  is larger than a 'threshold' bending radius of 5.9 m. If the bending radius is 10 m, an effective intensity gain coefficient of  $1.1 \text{ cm}^{-1}$  is obtained.

### Conclusions

The application of the well known theory of beam propagation in media with parabolic gain and index profiles shows that concern about beam defocussing or beam deflection due to the refractive index gradient in x-ray laser media is unfounded. Furthermore the useful length of a gain medium is not limited. Due to the gain distribution the beam is kept together and transformed into a 'matching' stationary beam which propagates without changing its parameters. The gain of the matching beam is somewhat lower than the gain at the maximum of the gain distribution.

Extending the theory to media with a bend in direction of beam propagation it turns out that a stationary beam still exists, but propagates with severe losses, unless the bending radius is very large.

### Acknowledgement

This work was supported, in part, by the Commission of the European Communities in the framework of the Association Euratom/IPP.

### References

1. P. L. Hagelstein, "Review of radiation pumped soft x-ray lasers," *Plasma Physics* **25**, 1345-1367 (1983).
2. J. G. Lunney, "Waveguiding in soft x-ray laser experiments," *Appl. Phys. Lett.* **48**, 891-893 (1986).
3. R. A. London, "Beam optics of exploding foil plasma x-ray lasers," *Phys. Fluids* **31**, 184-192 (1988).
4. E. E. Fill, "Gain guiding of x-ray laser beams," *Opt. Commun.* **67** 441-445 (1988).
5. H. Kogelnik, "On the propagation of Gaussian beams of light through lenslike media including those with a loss or gain variation," *Appl. Opt.* **4**, 1562-1569 (1965).
6. L. W. Casperson, "Gaussian light beams in inhomogeneous media," *Appl. Opt.* **12**, 2434-2441 (1973).
7. E. E. Fill, prepared for Applied Optics.

## CO<sub>2</sub> Laser-Heated Plasmas for Electron-Collisionally Pumped XUV Laser Studies

G. D. Enright and N. H. Burnett

*National Research Council of Canada, Division of Physics  
Ottawa, Ontario K1A 0R6, Canada*

### **Abstract**

We describe a series of experiments to characterize plasmas produced by moderate intensity ( $\approx 2 \times 10^{13}$  W/cm<sup>2</sup>), nanosecond pulse, CO<sub>2</sub> laser irradiation of planar targets using both line (150  $\mu$ m x 7 mm) and spherical (1 mm diam.) focussing optics. X-ray line and continuum diagnostics have been used to infer a heat front penetration of about 20  $\mu$ g/cm<sup>2</sup> at temperatures of approximately 300 eV. We observe only minor differences between targets whose mass is small compared to the hot electron range and much more massive ones, indicating a poor efficiency for hot electron reflexing in thin targets. In the case of Cu targets, observations of L shell x-ray transitions from neon and fluorine-like ions show a similar ionization distribution to 1  $\mu$ m laser produced plasmas in which gain has recently been demonstrated. The Ne-like Cu XX 3p-3s emission lines have been observed. A comparison of on-axis to off-axis spectra provides evidence for gain on these lines.

### **Introduction**

In the past few years, several laboratories [1]-[4] have reported gain in the soft x-ray region from electron collisionally pumped 3p-3s transitions in neon-like ions with Z in the range from 29-42. Initial successes in this field [1],[2] were achieved with plasmas produced by exploding thin ( $\approx 50$   $\mu$ g/cm<sup>2</sup>) Se targets

using a visible laser delivering about 2 kJ in a subnanosecond pulse. More recently, significant amplification has been reported from Cu and Ge plasmas heated with a 300 J, 1  $\mu$ m laser pulse of a few nanoseconds duration [4]. Although the possibility of exciting a neon-like copper plasma by means of CO<sub>2</sub> laser generated hot electrons has been discussed in a proposal predating the experimental successes with shorter wavelength drivers [5], we are unaware of any published data on plasmas produced by CO<sub>2</sub> laser heating of foil targets in line focus geometry at intensities of relevance to the 3p-3s laser problem. Several factors differentiate the plasmas which may be produced by a 10  $\mu$ m laser in this regard. Firstly since it is highly desirable to produce a plasma at an electron density near the maximum determined by collisional de-excitation of the upper laser level [6] ( $n_e > 10^{20}$  cm<sup>-3</sup>), the CO<sub>2</sub> laser heated medium must be overdense at the time of soft x-ray gain. Secondly, at driver intensities of relevance to the XUV laser problem ( $10^{13}$ - $10^{14}$  W/cm<sup>2</sup>) the absorption of 10  $\mu$ m laser radiation at a solid target surface will be dominated by collective processes which generate long mean free path (hot) electrons [7],[8]. These hot electrons will dominate energy transport in the case of an exploding foil and may introduce significantly enhanced lateral energy loss from a line focus [9]. It is not clear however that either of the above factors rules out the use of a 10  $\mu$ m driver in producing an exploding foil 3p-3s XUV laser medium. The fact that the

target plasma will remain overdense through the soft x-ray lasing process possibly allows the foil to be heated with longer driver pulses and at lower average density. This will result in a laser medium with considerably lower ion temperature which may lead to enhanced gain by reducing the doppler width of the laser line. The fact that target heating will be moderated by a hot electron population may introduce the possibility of alternative collisional excitation processes in which hot electron collisions lead directly to 3p-3s inversions [5],[10],[11]. Although this possibility opens some intriguing paths for scaling collisionally excited lasers to shorter wavelengths, it must be remembered that the hot electron population produced by long wavelength absorption can probably never exceed a few tenths of the critical electron density which probably limits the gain which can be achieved by CO<sub>2</sub> laser generated hot electron pumping.

In what follows, we will present some preliminary experimental studies of CO<sub>2</sub> laser heated targets in the  $10^{13}$  W/cm<sup>2</sup> intensity range using both line and spherical focussing geometry and employing targets whose areal mass density ranged from small compared to the hot electron range (thin targets) to much greater than the hot electron range (thick targets). We observe a hot electron heated zone which extends about 20  $\mu\text{m}/\text{cm}^2$  into these targets at an electron temperature of several hundred electron volts. In the case of Cu targets, we observe a similar ionization distribution (as evidenced by  $n = 3-2$  line emission) to that observed in 1  $\mu\text{m}$  laser heated targets in which gain has been observed [12].

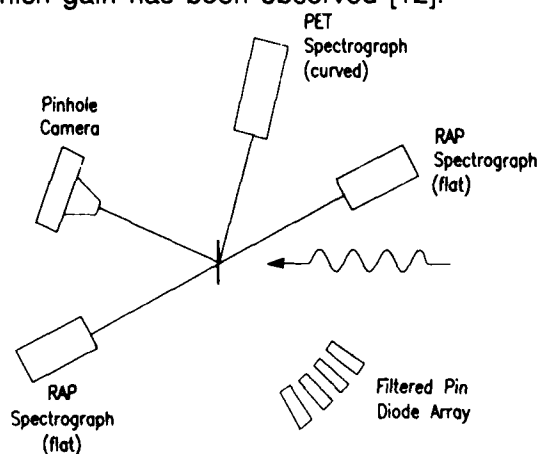


Figure 1. Experimental setup for layered target x-ray line diagnostics.

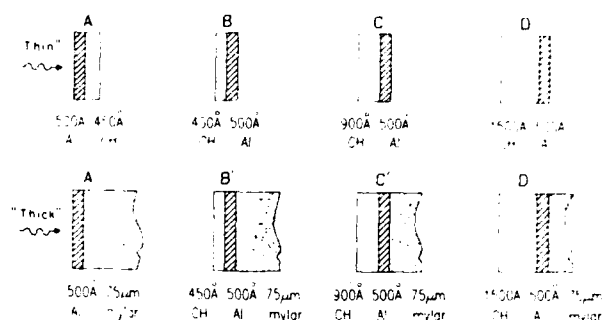


Figure 2. Target configurations employed in Aluminum line emission studies. Targets were 1 cm diameter, planar composites mounted on glass support stalks.

#### Layered Target X-Ray Line Diagnostics of 10 $\mu\text{m}$ Laser Heated Foils

In order to characterize the heating of low mass foils with moderate intensity CO<sub>2</sub> laser radiation, we have used the experimental setup shown in Fig. 1. A 300-400 J, 1-1.5 nsec 10  $\mu\text{m}$  laser pulse was focussed with a 3 m focal length, f/12 NaCl lens onto compound, CH (polystyrene), Al, mylar targets of the forms shown in Fig. 2. For most experiments a plano convex lens was used with the target situated in the near field of the laser beam at a beam diameter of 1 mm. In this position, the beam exhibited several diffraction rings introducing about a 2:1 intensity modulation across a radial profile. Data was also obtained with a 7 mm long x 150  $\mu\text{m}$  wide line focus produced by grinding a 30 m radius cylindrical surface on one side of the NaCl lens. The approximate spatially and temporally averaged laser intensity on target was about  $2.5 \times 10^{13}$  W/cm<sup>2</sup> for the spherical focus and  $2 \times 10^{13}$  W/cm<sup>2</sup> for the line focus. Al line emission in the 7-8.5Å region was recorded by three crystal spectrographs located as shown in Fig. 1. Spectrographs 1 and 2 used flat RAP crystals recording on KODAK DEF x-ray film and viewed the target rear and front surfaces at approximately 45° to the incident laser beam. Spectrograph 3 used

a 5 cm radius bent PET crystal in Von Hamos geometry and viewed the front surface of the target from above at an angle of about  $10^\circ$  to the plane of the target. An array of five filtered PIN diodes was used to characterize high energy x-ray continuum (Bremsstrahlung) emission in the energy range from 6 to 14 keV. The  $500\text{\AA}$  ( $13\text{ }\mu\text{g}/\text{cm}^2$ ) layer of Al imbedded in the  $(\text{CH})_n$  - mylar targets shown in Fig. 2 served as a marker to give crudely spatially resolved estimates of time averaged electron temperature and density in the overdense target material. Electron temperature was obtained from the ratio of He-like to H-like Al resonance lines, while electron density could be estimated from the He-like intercombination to resonance line ratio [13]. Previous studies at NRC and elsewhere indicate that the  $\text{CO}_2$  laser burn depth for planar targets at an intensity of  $2 \times 10^{13}\text{ W}/\text{cm}^2$  and a 1.5 nsec pulse is equivalent to less than  $300\text{\AA}$  of  $(\text{CH})_n$  ensuring that the Al in targets B,C,D and B',C',D' remained in the overdense zone during the  $10\text{ }\mu\text{m}$  heating pulse.

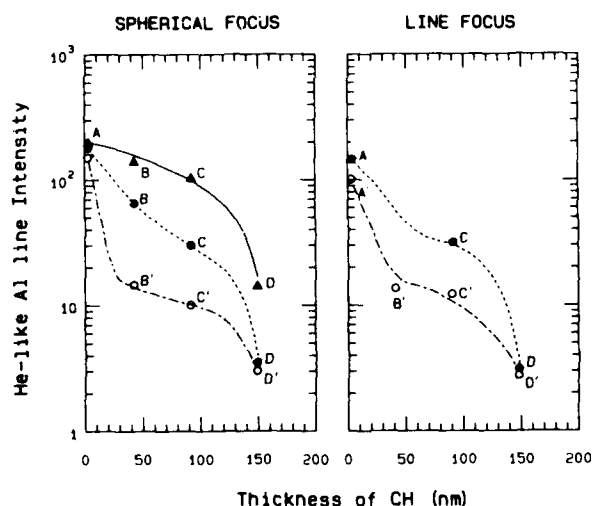


Figure 3. Yield of He-like Al resonance line for various thicknesses of  $(\text{CH})_n$  overlay. Solid triangles represent data from thin targets with spectrograph viewing target rear, open circles represent data from thick targets with spectrograph viewing target front surface, and solid circles represent data from front spectrograph with thin targets.

The He-like Al line intensities recorded by spectrographs 1 and 2 are plotted in Fig. 3 as a function of plastic overlay thickness. These spectrographs

lacked sufficient resolution to resolve the He like resonance and intercombination lines so that the plotted values represent the sum of these two lines. Although this data represents measurements made with a spherical focus, no significant difference was noted in Al line emission when switching from spherical to line focus. Lineouts of spectra obtained from

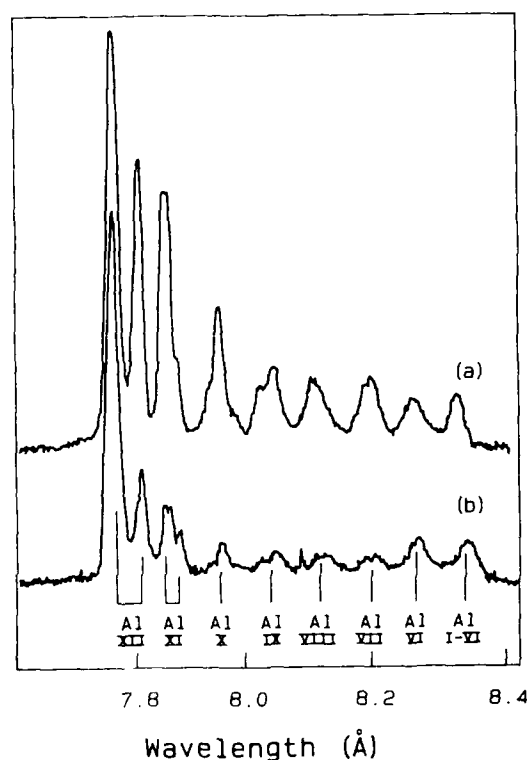


Figure 4. Al K-shell spectra for thin (a) and thick (b) targets coated with  $900\text{\AA}$   $\text{CH}_n$  (targets C and C' of Fig. 2).

spectrograph 3 for the same targets and focal geometry are shown in Fig. 4. From the data of Fig. 3, it is apparent that self absorption plays an important role in attenuating the He-like Al line emission detected by the spectrograph viewing the front surface of the target. In the case of thin targets where the Al tracer could be viewed directly from behind, He-like Al emission decreases only gradually for  $\text{CH}$  overlay thickness up to about  $15\text{ }\mu\text{g}/\text{cm}^2$  and quite rapidly thereafter. The spectrograph viewing the front surface of the target shows a much steeper decrease of He like line intensity indicating that He like emission is attenuated by about a factor of three for example by absorption in escaping through  $100\text{ nm}$  of  $\text{CH}$ . In the



case of thick targets only the front viewing spectrograph was useful. In this case a much more rapid falloff in He-like line emission is observed. Reference to the lineouts from spectrograph three (Fig. 4) indicates that this can be partially attributed to a more rapid falloff in the intercombination line in this case, due to higher electron densities being maintained for the thick targets. In summary when allowance is made for absorption, the He like resonance line decreases by about a factor of three for overlays up to about 150 nm of CH for thin targets and after allowing for intercombination line quenching it decreases by about a factor of five for the thick targets. The relatively minor difference between the thick and thin targets indicates that hot electron reflexing does not play a major role in the heating of the thin targets. A similar conclusion can be drawn from the spectra reproduced in Fig. 4.

TABLE I

TARGET  $T_e$  (eV)  $n_e(10^{19}\text{cm}^{-3})$

A	500	1.0
B	350	3.0
C	300	8.0
D	---	10.0
A'	500	1.0
B'	300	20.0
C'	300	60.0
D'	---	100.0

Temperatures inferred from the ratio of hydrogen to helium-like resonance lines and electron densities inferred from the ratio of helium-like intercombination to resonance lines are indicated in Table 1. As might be expected, the most striking difference between the thick and thin target spectra is the inference of higher densities for the thick targets. Because of the nonlinear density dependence of the ratio of resonance to intercombination line intensities and the time integration in these spectra, it is unreasonable to read too much into this difference, other than to observe that a double sided expansion (explosion) of the thin foils will lead to

lower time averaged densities than would be expected for the thick target case where expansion is inertially restricted on one side. It is apparent that hot electrons are playing a major role in the target heating in both cases with the presence of a complete inner shell transition sequence extending from cold K $\alpha$  (Al II) to Li-like states (Al XI). The form of this sequence suggests a need for caution in using the ratio of hydrogen-like to helium-like Al resonance lines to infer a cold electron temperature as has been done above. The relatively weak hydrogen-like resonance line may be produced by hot electron induced ionization from a thermal reservoir of He-like ions.

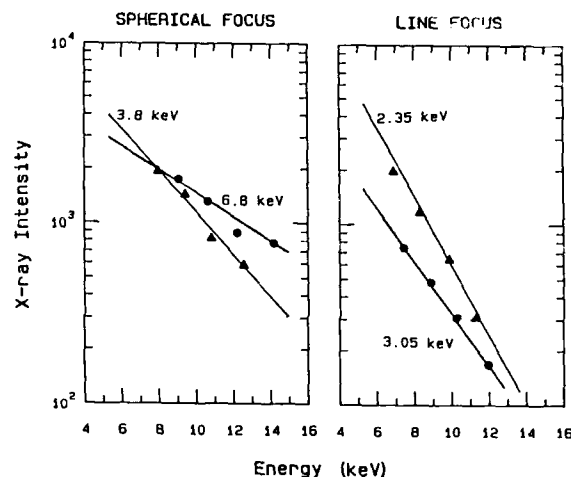


Figure 5. High energy x-ray continuum spectra from spherical focus (on left) with circles representing thick targets and triangles, thin targets and similar observations from line focus (on right).

Typical high energy x-ray continuum spectra from "thin" (400Å CH over 500Å Al) and "thick" (400Å CH over 75  $\mu\text{m}$  mylar) targets are shown in Fig. 5 for both line and spherical foci. It can be seen that the temperature inferred from the slopes of these spectra decreases by about a factor of two in going from spherical to line focus and also decrease sharply in going from "thick" to "thin" targets. Although the peak laser intensity was somewhat larger in the spherical focus due to more severe hot spots in the intensity distribution of the beam for this case, it is likely that the large temperature

variations inferred from the data are largely due to hot electron transport phenomena rather than absorption. The mass thickness of thin targets corresponds approximately to the range of a 2 keV electron, that is to say electrons with higher energy than this emerge from a single pass through the target with a significant fraction of their original energy. The large difference in slopes for the "thick" and "thin" target cases with spherical focus seems to imply that these high energy electrons suffer significant energy loss on reflection from the plasma sheath at the rear of the foil. For the line focus geometry it is likely that lateral energy transport on both the front and rear surfaces of the target plays an important role in determining the slope of the continuum. Lateral energy transport is likely to be more important in this geometry due to the narrow (150  $\mu\text{m}$ ) transverse width of the focal spot for the line focus. It is likely that energy losses associated with lateral transport ( $E \times B$  drift) are more severe for higher energy electrons. This effect may partially account for the "colder" bremsstrahlung spectra observed in line focus geometry.

The thermal temperatures and densities inferred from the aluminum line spectra discussed above are roughly consistent with previous interferometric observations of 10  $\mu\text{m}$  target irradiation in this intensity regime [14]. These studies using small spherical focal spots ( $\approx 100 \mu\text{m}$  diam.) have indicated that for thick (200  $\mu\text{g}/\text{cm}^2$ ) glass targets, a supercritical density plateau is formed which expands away from the target surface with a velocity of about  $7 \times 10^6 \text{ cm/sec}$  and maintains an approximately constant electron density of  $1-2 \times 10^{20} \text{ cm}^{-3}$ . The approximately constant density maintained by the plateau is strongly suggestive of a sonic expansion for this feature. An ion acoustic velocity of  $7 \times 10^6 \text{ cm/sec}$  corresponds to a temperature of approximately 200 eV. The mass thickness of the plateau observed interferometrically reaches about 20  $\mu\text{g}/\text{cm}^2$  near the end of a 1.5 nsec FWHM  $\text{CO}_2$  laser pulse. It is thus evident that the densities, heat front penetration and temperatures inferred in the present studies with the thick targets are consistent with the earlier optical diagnostics. The plasma conditions obtained are near those required to produce significant gain in neon-like Cu. In the remainder of this

paper we will present the results of x-ray spectroscopic diagnostics of copper plasmas produced under similar conditions to those used above.

### $\text{CO}_2$ Laser Heated Cu Plasmas

The experimental setup used to study  $\text{CO}_2$  laser heated Cu plasmas is shown in Fig. 6. The  $\text{CO}_2$  laser was focussed in line and spherical focal geometries onto the surface of either solid Cu targets or foils consisting of 45  $\mu\text{g}/\text{cm}^2$  of Cu evaporated onto 40  $\mu\text{g}/\text{cm}^2$  of carbon or 25  $\mu\text{g}/\text{cm}^2$  Cu on 5  $\mu\text{g}/\text{cm}^2$  cellulose nitrate (collodion). In the latter cases the targets were irradiated from the Cu side. Spherical focal spots of 1mm diameter and 7mm x 150  $\mu\text{m}$  line foci were produced with the f/12 NaCl lens as described above and in addition 15mm x 150  $\mu\text{m}$  line foci were obtained with a 4m focal length spherical mirror tilted about 10 degrees off axis.

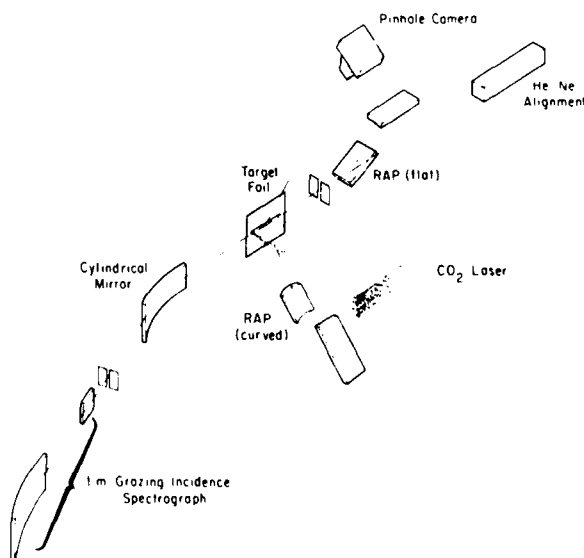


Figure 6. Experimental setup for studies of  $\text{CO}_2$  laser heated Cu plasmas in line focus geometry.

Diagnostics consisted of a flat crystal RAP spectrograph with 200  $\mu\text{m}$  wide entrance slit which viewed Cu L shell emission lines axially and could differentiate between emission from the front and rear sides of foil targets, a bent crystal RAP spectrograph in Von Hamos

geometry which viewed the same spectral lines from below and slightly in front of the target, and an x-ray pinhole camera with 50  $\mu\text{m}$  resolution filtered to detect x-rays near 1 keV viewed the focal region from above and slightly in front of the target. On some shots XUV spectra in the 50-300Å region were recorded on Kodak type 101 film with a 1 m grazing incidence spectrograph viewing the plasma axially. A grazing incidence cylindrical or toroidal mirror was used to image the plasma onto the spectrograph slit as shown.

As was the case with the Al targets described above, little difference in hard x-ray line emission was noticed between plasmas produced with the 1 mm diameter circular spot and the 150  $\mu\text{m}$  x 7 mm line. The plasmas produced by the line focus did however exhibit a significantly colder high energy bremsstrahlung spectrum. Typical continuum spectra for Cu-C targets are shown in Fig. 7 for 7mm line and 1mm spherical focus.

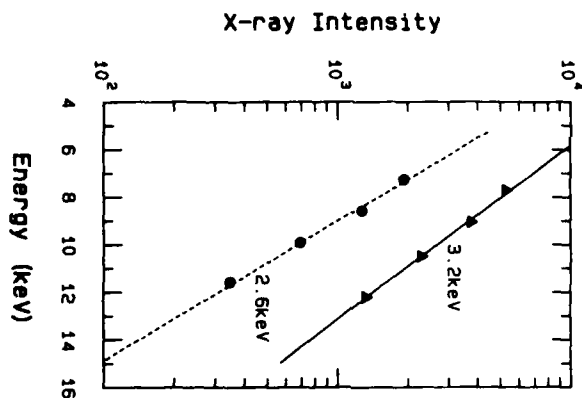


Figure 7. High energy x-ray continuum spectra from targets consisting of 45  $\mu\text{g}/\text{cm}^2$  Cu over 40  $\mu\text{g}/\text{cm}^2$  C. Triangles represent data from 1 mm diameter spherical focus and circles, data from 7 mm x 150  $\mu\text{m}$  line focus

Pinhole photographs of 1 keV x-ray emission from the targets irradiated with a line focus reveal a fairly uniform emission from the full length of the focal region. In most of the photographs of the foil targets, fine scale structure consisting of narrow (200  $\mu\text{m}$ ) dark bands appeared across the line focus. This problem was particularly evident with the thinner foils and is due to gaps in the Cu layer. As we improved our

foil preparation and storage technique this problem has been substantially reduced.

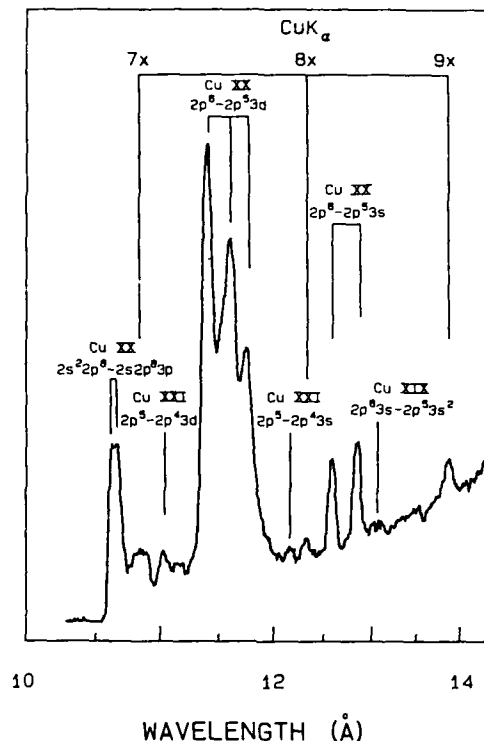


Figure 8. Cu L shell spectrum in region from 10.5-14Å recorded with bent crystal (Von Hamos) PET spectrograph.

The symmetry of the plasma expansion towards the front and rear of the target foil along the driving laser axis was studied with the spatially resolving flat crystal spectrograph shown in Fig. 6. Only the thicker (45  $\mu\text{g}/\text{cm}^2$  Cu plus 40  $\mu\text{g}/\text{cm}^2$  CH) were used in these shots. Although the spatial resolution was limited by the 200  $\mu\text{m}$  wide slit there was no evidence of Cu line radiation coming from the side of the foil opposite to the incoming laser beam. The copper line emission appeared to be largely restricted to a zone about 200  $\mu\text{m}$  wide on the front side of the target with a weaker "halo" of emission especially apparent in the  $2p^6-2p^5 3d$  CuXX transition extending out 500  $\mu\text{m}$  or more from the target surface. A microdensitometer scan of the spectrum recorded by the RAP, Von Hamos spectrograph focus in the region from 10.5-14Å from a target irradiated with a 7mm line focus is reproduced in Fig. 8.

It is interesting to compare the n-2 CuXX x-ray spectra observed in the present work to similar spectra [4] obtained

for 1  $\mu\text{m}$  laser target irradiation in line focus at an intensity of  $10^{13} \text{ W/cm}^2$ . In general terms, the spectra observed at the two wavelengths are more remarkable for their similarities than their differences, however in the NRL experiment much more symmetric (front to back) distribution of Cu XX lines viewed parallel to the target was observed even though their foils were approximately 2x thicker than those used here. This is an indication of somewhat greater thermal penetration in the case of the 1  $\mu\text{m}$  experiment. This is not surprising since the results of the layered AL, CH target experiment discussed above indicate a penetration of about 20  $\mu\text{gm/cm}^2$  in the 10  $\mu\text{m}$  case while the ablation depth for the 1  $\mu\text{m}$  experiment is estimated to be 70  $\mu\text{gm/nsec cm}^2$ . The ionization balance obtained in the two experiments is nevertheless quite similar with perhaps only slightly stronger fluorine like lines observed in the 1  $\mu\text{m}$  case. The line intensity ratios of neonlike Cu XX  $2p^6-2p^5$  nd series lines are very similar in the two cases implying about equal electron temperatures ( $\approx 300 \text{ eV}$ ) assuming local thermodynamic equilibrium. An interesting feature of the spectrum shown in Fig. 8 is the presence of several high orders (7,8,9) of the Cu  $K\alpha$  line at 1.54Å. This provides confirmation of the important role played by suprathreshold electrons in heating these plasmas.

We have obtained XUV spectra from 7 mm and 15mm long foils and solid Cu targets using the 1 m grazing incidence spectrograph (Fig. 6). A 1500Å Al filter was used to isolate the spectral region above about 170Å. The spectra are complicated by a number of oxygen lines and some yet unclassified Cu lines. We have been able to identify Cu XVIII, Cu XIX, and Cu XX lines. A typical spectrum is shown in Figure 9. The resolution of these spectra was limited by the rather wide (200  $\mu\text{m}$ ) entrance slit used on the grazing incidence spectrograph. The Cu XX  $J=2-1$  transitions for which gain has been reported in 1 $\mu\text{m}$  experiments are most prominent in the 15mm long line irradiations of the thin (25 $\mu\text{gm/cm}^2$  Cu on 5 $\mu\text{gm/cm}^2$  CH) foils. In this case, the  $J=1-1$  line at 296Å is also quite prominent. An attempt has been made to observe the off-axis emission by tilting the target 5° off the spectrograph axis. In this case, the Cu XX lines appear to be considerably reduced in intensity when compared to other Cu lines (Figure 10.) but the analysis

is complicated by an enhanced background

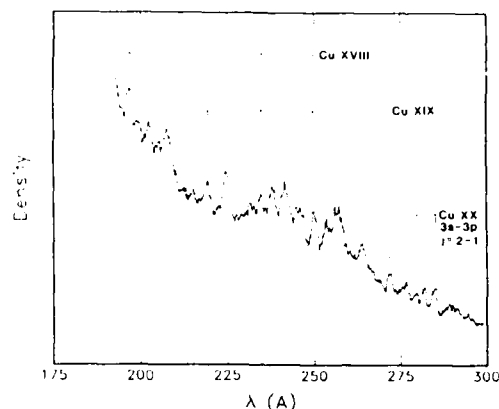


Figure 9. Axial VUV spectrum from Cu foil target (35 $\mu\text{gm/cm}^2$  Cu on 5 $\mu\text{gm/cm}^2$  CH).

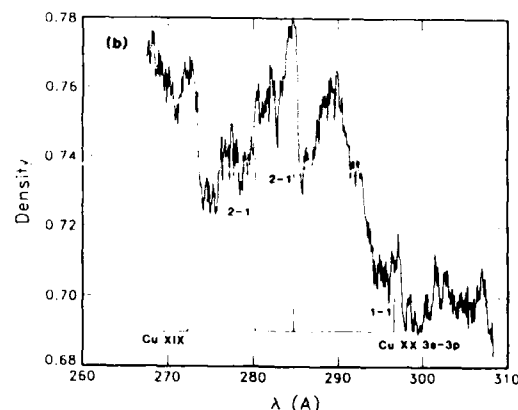
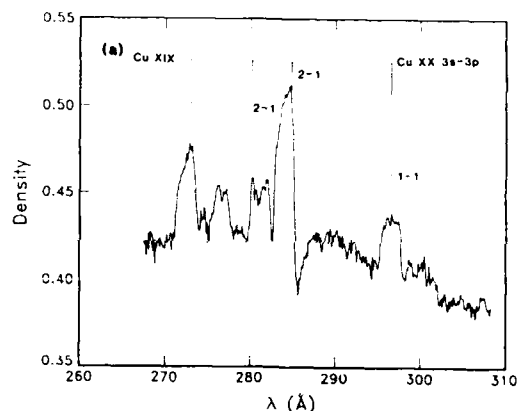


Figure 10. Axial, a), and 5 deg. off axis, b), spectra from 25 $\mu\text{gm/cm}^2$  Cu on 5 $\mu\text{gm/cm}^2$  CH in vicinity of 3p-3s Cu XX lines.

continuum presumably due to increased surface area exposed to the spectrograph. Nevertheless we interpret these results as evidence that gain is present for these Cu XX 3s-3p lines. We are presently making further optical modifications to produce a line focus up to 25 mm in length so that we may search for exponential growth in the emission on these transitions

### **Discussion:**

An attractive element in the possible use of 10  $\mu\text{m}$  lasers as drivers for electron collisionally pumped XUV lasers is the potential of benefitting from direct suprathermal electron excitation of the lasing ions. Several schemes for obtaining an enhanced population inversion by taking advantage of a superthermal electron population have been proposed [10],[11]. In one proposal [10], the 2p-3p collisional excitation rate for neonlike ions is enhanced on a transient basis by introducing electrons with energy optimally matched to the excitation potential and in another scheme [11], hot electron induced inner shell ionization of Na-like ions leads directly to a population inversion between the 3p and 3s levels of the neonlike ion. It seems likely that at practical limits to laser pump intensity for exploding foil targets (few  $\times 10^{13} \text{ W/cm}^2$ ) significant energy coupling to non-thermal electrons can be obtained only with a driving laser wavelength greater than 1  $\mu\text{m}$ . In the case of  $\text{CO}_2$  laser generated hot electrons, however, the maximum gain achievable by these means will be limited by the restriction on hot electron density imposed by the rather low critical electron density for 10  $\mu\text{m}$  radiation ( $10^{19} \text{ cm}^{-3}$ ). It seems unlikely that the hot electron density can exceed a few tenths of  $n_c$  so that to maintain for example a 10% fractional population of superthermal electrons would require working with laser plasmas in the  $10^{19} \text{ cm}^{-3}$  total electron density range. In this case achievable gains would likely be restricted to the order of one per cm and useful lasers relying on super-radiant operation would require gain lengths of the order of ten cm. For these purposes, it would be useful to explore various means of heating  $\sim 10 \text{ cm}$  long low density plasmas with 10  $\mu\text{m}$  light. Possible avenues include the heating of thin foils (or microstrips) at somewhat lower intensity than that used here or, perhaps guiding 10  $\mu\text{m}$  light at high intensity over this length

by means of a plasma waveguide.

In the present experiments, at an intensity of  $\sim 10^{13} \text{ W/cm}^2$ , we have identified the 3p-3s emission lines from Cu XX (neon-like). We have obtained strongest 3p-3s emission with thin foils ( $\sim 25 \mu\text{gm/cm}^2$  Cu over  $5 \mu\text{gm/cm}^2$  plastic). Under these conditions a comparison of on-axis to off-axis spectra provides evidence that gain is indeed achieved.

It is not clear whether hot electron reflexing plays any substantial role in the collisional excitation of these plasmas. In the present case, neon-like Cu has been chosen as a gain candidate because of the published data for 1  $\mu\text{m}$  target irradiation under similar conditions. No attempt has been made to choose a collisionally pumped system optimally matched to the thermal plasma parameters and hot electron temperature actually achieved.

### **References**

1. M.D. Rosen, P.L. Hagelstein, D.L. Mathews, E.M. Campbell, A.V. Hazi, B.L. Whitten, B. MacGowan, R.E. Turner, R.W. Lee, G. Charatis, Gar. E. Busch, C.L. Shepard, and P.D. Rockett, Phys. Rev. Lett. 54, 106 (1985).
2. D.L. Mathews, P.L. Hagelstein, M.D. Rosen, M.J. Eckart, N.M. Ceglio, A.V. Hazi, H. Medeck, B.J. MacGowan, J.E. Trebes, B. Whitten, E.M. Campbell, C.W. Hatcher, A.M. Hawryluk, R.L. Kauffman, L.D. Pleasance, G. Rambach and T.A. Weaver, Phys. Rev. Lett. 54, 110 (1985).
3. B.J. MacGowan, M.D. Rosen, M.J. Eckart, P.L. Hagelstein, D.L. Mathews, D.G. Nilson, T.W. Phillips, J.H. Scofield, G. Shimkaveg, J.E. Trebes, R.S. Walling, B.L. Whitten, and J.G. Woodworth, J. Appl. Phys. 61, 5243 (1987).
4. T.N. Lee, E.A. McLean, and R.C. Elton, Phys. Rev. Lett. 59, 1185 (1987).
5. R.L. Carman and G.F. Chapline, Proceedings of the International Conference on Lasers '81 (STS Press, McLean, VA 1982) p. 173.
6. V. Feldman, J.F. Seely and A.K. Bhatia, J. Appl. Phys. 56, 2475 (1984).

7. D.W. Forslund, J.M. Kindel, and K. Lee, Phys. Rev. Lett. 39, 184 (1977).
8. W.L. Kruer and K. Estabrook, Phys. Fluids 20, 1688 (1977).
9. D.W. Forslund and J.V. Brackbill, Phys. Rev. Lett. 48, 1614 (1982).
10. J.P. Apruzese and J. Davis, Phys. Rev. A28, 3686, (1983).
11. W.H. Goldstein and R.S. Walling, Phys. Rev. A36, 3482 (1987).
12. R.C. Elton, T.N. Lee, and W.A. Molander, J. Opt. Soc. Am. B, 4, 539 (1987).
13. A.J. Vinogradov, I. Yu Skobelev, and E.A. Yukov, Sov. J. Quant. Electron. 5, 630 (1975).
14. R. Fedosejevs, M.D.J. Burgess, G.D. Enright and M.C. Richardson, Phys. Fluids 24, 537, (1981).

## Ne-Like Ion X-Ray Laser Experiments in Plasmas Produced by 0.53- $\mu\text{m}$ and 0.35- $\mu\text{m}$ Laser Light

C. J. Keane,<sup>\*</sup> J. L. Bourgade,<sup>†</sup> P. Combis,<sup>†</sup> R. A. London,<sup>\*</sup> M. Louis-Jacquet,<sup>†</sup>  
B. J. MacGowan,<sup>‡</sup> D. L. Matthews,<sup>\*</sup> D. Naccache,<sup>†</sup> O. Peyrusse,<sup>†</sup>  
M. D. Rosen,<sup>\*</sup> G. Thiell,<sup>†</sup> and B. Whitten<sup>\*</sup>

<sup>\*</sup>Lawrence Livermore National Laboratory, University of California  
Livermore, California 94550

<sup>†</sup>Centre D'Etudes de Limeil-Valenton, B.P. 27, 94190 Villeneuve St. Georges, France

<sup>‡</sup>Lawrence Berkeley Laboratory, University of California, Berkeley, California 94720

### Abstract

Recent Ne-like ion x-ray laser experiments carried out at the Centre d'Etudes de Limeil-Valenton (CEL-V) with both 0.53- $\mu\text{m}$  and 0.35- $\mu\text{m}$  laser light will be described. This paper will concentrate primarily on the observation of amplification in Ne-like Sr ( $Z=38$ ) in plasmas produced by 0.53- $\mu\text{m}$  laser light. Small signal gains of 4.4  $\text{cm}^{-1}$  and 4.0  $\text{cm}^{-1}$  have been measured for the Ne-like Sr  $J=2-1$  transitions at 164.1 and 166.5 Å, respectively. In addition, the effects of pumping the Ne-like Se laser with 0.35- $\mu\text{m}$  light have been investigated. The resulting Se spectra do not differ significantly from those observed with 0.53- $\mu\text{m}$  light. A brief summary of other experiments carried out at CEL-V will also be given.

### Introduction

Since the demonstration of soft x-ray amplification in Ne-like Se in 1984,<sup>1</sup> significant progress has been made in characterizing, isoelectronically scaling, and boosting the output power of Ne-like x-ray lasing systems. In particular, up to 16 gain lengths have been observed in Ne-like Se,<sup>2,3</sup> and lasing has been demonstrated in Y ( $Z=39$ )<sup>1</sup> and Mo ( $Z=42$ ).<sup>4</sup> In addition to these experiments, which have been conducted with 0.53- $\mu\text{m}$  laser light, gain in Ne-like Ge ( $Z=32$ ) and Cu ( $Z=29$ ) has been reported in plasmas created by 1.06- $\mu\text{m}$  wavelength laser irradiation.<sup>5</sup>

In this paper, we present gain measurements for Ne-like Sr ( $Z=38$ ). This work was carried out as part of a

series of collaborative x-ray laser experiments between Lawrence Livermore National Laboratory (LLNL) and CEL-V. As part of this collaborative effort, Ne-like, Ni-like, and recombination x-ray laser systems were investigated. Table I summarizes the Ne-like ion x-ray laser experiments performed at CEL-V. In this paper, we will focus primarily on the results of the Ne-like Sr campaign; Ne-like Se x-ray laser spectra from plasmas produced by 0.35- $\mu\text{m}$  light will also be briefly described. Results from the other experiments listed in Table I will be presented in the near future.

Sr was chosen as an element to study for several reasons. First of all, it is of interest from the point of view of Ne-like kinetics. The reduced wavelength overlaps amongst the Ne-like lines of Sr as compared to other elements make this an attractive ion to study for purposes of identifying weak transitions. Identification of these weak lines may shed light on issues such as the unexplained relatively weak amplification of certain  $J=0-1$  transitions.<sup>1</sup> Secondly, a Ne-like Sr laser operating at 164.1 and 166.5 Å is a good candidate for use in x-ray optics related experiments, as discussed elsewhere in these proceedings.<sup>6</sup> Finally, recent experiments by Monier et al.<sup>7</sup> have demonstrated fluorescence of the  $2p^6-2p^53d$  line at 6.059 Å in Ne-like Sr due to photopumping of this transition by  $L\beta$  emission at 6.053 Å in H-like Al. This photopumping process may possibly be used to enhance the gain on transitions in the  $3p-3s$  manifold, and hence the measurement of gain in the non-photo-assisted case is of interest.

TABLE I: Ne-like Ion X-ray Laser Experiments Performed at CEL-V

Experiment	Target Thickness, Laser Conditions	Purpose
Ne-like Se Gain Optimization	35 $\mu\text{g}/\text{cm}^2$ ; $7 \times 10^{13} \text{ W}/\text{cm}^2$ ( $2\omega$ ) 46 $\mu\text{g}/\text{cm}^2$ ; $1.4 \times 10^{14} \text{ W}/\text{cm}^2$ ( $2\omega$ ) 58 $\mu\text{g}/\text{cm}^2$ ; $4 \times 10^{13} \text{ W}/\text{cm}^2$ ( $2\omega$ )	Examine behavior of Se gain as a function of target thickness, laser intensity
Ne-like Se J=0 Spectroscopy	70 $\mu\text{g}/\text{cm}^2$ ; $2 \times 10^{13} \text{ W}/\text{cm}^2$ ( $2\omega$ )	Attempt to maximize J=0 output by creating high density plasma
Ne-like Sr Gain Measurement and Spectroscopy	80 $\mu\text{g}/\text{cm}^2$ ; $1.4 \times 10^{14} \text{ W}/\text{cm}^2$ , $7 \times 10^{13} \text{ W}/\text{cm}^2$ ( $2\omega$ )	J=0-1 Gain measurements at 164.1, 166.5 Å; physics of J=0-1 transitions
Ne-like Ge Gain Measurement and Spectroscopy	27 $\mu\text{g}/\text{cm}^2$ ; $6 \times 10^{13} \text{ W}/\text{cm}^2$ ( $2\omega$ ) 34 $\mu\text{g}/\text{cm}^2$ ; $2 \times 10^{13} \text{ W}/\text{cm}^2$ , $5 \times 10^{13} \text{ W}/\text{cm}^2$ ( $2\omega$ )	Gain measurements and general spectroscopy
Ne-like Ag Spectroscopy	164 $\mu\text{g}/\text{cm}^2$ ; $2 \times 10^{14} \text{ W}/\text{cm}^2$ ( $2\omega$ )	Look for J=2-1 lasing transitions in Ag
Ne-like $3\omega$ Spectroscopy	Se, Mo, Ag; various thicknesses and intensities ( $3\omega$ )	Examine Ne-like lasing in plasmas produced by $3\omega$ light

### Experimental Setup

The experiments described in this paper were carried out at the Phebus laser facility located at the Centre d'Etudes de Limeil-Valenton, France<sup>8</sup>. The facility is similar in overall plan to the Nova Two-Beam chamber described elsewhere.<sup>4</sup> The Phebus laser consists of two laser chains, each of which is identical to a single arm of the Nova laser facility at Lawrence Livermore National Laboratory. For these experiments, Phebus provided up to 1400 J/arm of 0.53- $\mu\text{m}$  light in a 500-ps FWHM pulse.

Figure 1 shows a schematic of the Phebus target chamber with diagnostics in place. The radius of this chamber is 130 cm, as compared to 80 cm for the Nova Two-Beam vacuum chamber. The target was positioned at chamber center by a positioner capable of both translatory and rotational movement. Each laser beam was focused onto the

target by a pair of counterrotating cylindrical lenses and a single f/4.3 spherical lens. With this optical chain, a line focus continuously variable in length up to 2.7 cm was available. In an actual experiment, the line-focused beams were superimposed on the target. Target foils of 0.8, 1.7, and 2.2 cm length were used in these experiments. The alignment system for the targets was integral with that for the McPigs diagnostic and has been described previously.<sup>4</sup>

The diagnostics used in this work are shown in Fig. 1. The two principal instruments used to record soft x-ray spectra and measure gain were a McPigs soft x-ray spectrograph<sup>9</sup> and a transmission grating streaked soft x-ray spectrograph (SPARTUVIX).<sup>10</sup> The former provides high resolution ( $\Delta\lambda \sim 0.1\text{-}0.2 \text{ Å}$ ) time-gated spectra, while SPARTUVIX yields continuous time resolution of soft x-ray emission with less spectral resolution ( $\Delta\lambda \sim 1 \text{ Å}$ ). Details regarding



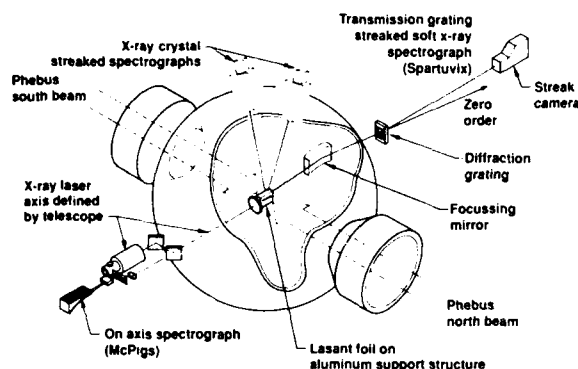


Figure 1: Experimental setup for X-ray laser research at the Phebus laser facility.

these diagnostics and their use in x-ray laser research have been given elsewhere.<sup>9,10</sup>

In addition to the SPARTUVIX and McPigs diagnostics that looked along the x-ray laser axis, a pair of streaked x-ray crystal spectrographs positioned off-axis were used to look at emission from 3-2 transitions. Time-integrated x-ray crystal spectrometers were also employed. A set of time-integrated x-ray pinhole cameras (filtered to look in the 1.5 keV region and used to measure the line focus width and verify beam super-position) completed the diagnostic suite.

## Experimental Results

For this work, exploding foil type targets similar to those employed in earlier Ne-like ion x-ray laser experiments<sup>1,3</sup> were used. The targets consisted of CH foils of areal density  $10 \mu\text{g}/\text{cm}^2$  overcoated with  $80 \mu\text{g}/\text{cm}^2$  of  $\text{SrF}_2$ . Line focus widths of  $150 \mu\text{m}$  or  $300 \mu\text{m}$  were used, corresponding to total on-target laser intensities of  $1.4 \times 10^{14} \text{ W}/\text{cm}^2$  or  $7 \times 10^{13} \text{ W}/\text{cm}^2$ . The  $1.4 \times 10^{14} \text{ W}/\text{cm}^2$  intensity was derived from a simple scaling model<sup>11</sup> for gain in Ne-like systems, and was estimated to be the optimum intensity for these targets. This intensity is midway between the  $7 \times 10^{13} \text{ W}/\text{cm}^2$  and  $4 \times 10^{14} \text{ W}/\text{cm}^2$  intensities used in previous work in  $\text{Se}^1$  ( $Z=34$ ) and  $\text{Mo}^4$  ( $Z=42$ ).

Figure 2 shows a simplified Grotrian diagram for Ne-like Sr and identifies the primary lasing transitions. Based on previous results in  $\text{Se}^1$  and  $\text{Mo}^4$ , the two  $J=2-1$  transitions at 164.1 and 166.5 Å are expected to have the highest gain.

(These transitions are analogous to the well known  $J=2-1$  transitions at 206.4 and 209.8 Å in Ne-like Se.<sup>1-3</sup>) Figure 3 shows a McPigs spectra from a 2.2-cm-long  $\text{SrF}_2$  target irradiated at a total intensity of  $1.4 \times 10^{14} \text{ W}/\text{cm}^2$ . For this shot, the spectrum was overexposed in order to allow weaker transitions to be viewed. The principal lasing transitions shown in Fig. 2 are identified. (The general features of the Sr soft x-ray and x-ray spectra were similar to those reported by other authors<sup>12-14</sup> and will be described in detail elsewhere.<sup>15</sup>)

The two  $J=2-1$  transitions are observed to be the brightest lines in the spectrum, in accord with expectations. Two other bright Ne-like lines may be seen (the Se analogous wavelengths<sup>16</sup> appear in parentheses): the  $J=1-1$  at 175.1 Å (220.8 Å), and the  $J=2-1$  at 224.9 Å (262.9 Å). The  $J=0-1$  line at 159.84 Å (182.4 Å), appears but is nearly coincident in wavelength with a bright sodium-like strontium line at 159.77 Å. This overlap will be seen to have consequences for measurement of gain on the 159.84 Å transition. The  $J=2-1$  and  $J=1-1$  Sr wavelengths quoted here are measured; the accuracy of these measurements is  $\pm 0.1$  Å. Our measurements for the wavelength of the 164.1 and 166.5 Å lines are in agreement with those performed by Wyart et al.<sup>12</sup>. The wavelengths of the  $J=0-1$  lines are semiempirical fits based on experimental data.<sup>17</sup>

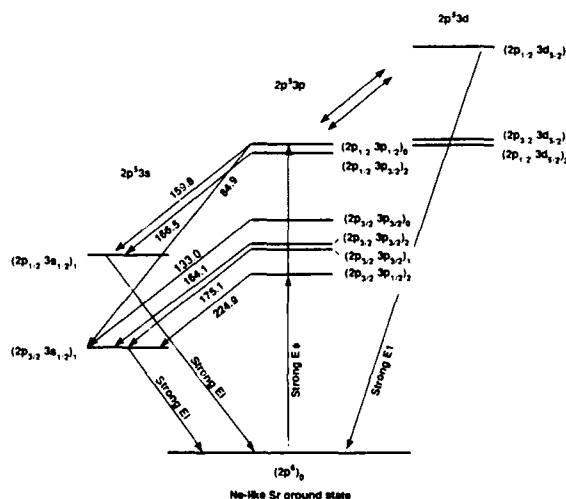


Figure 2: Grotrian diagram for Ne-like Sr, showing principal transitions of interest. (Position of Ne-like Sr ground state is not drawn to scale.)

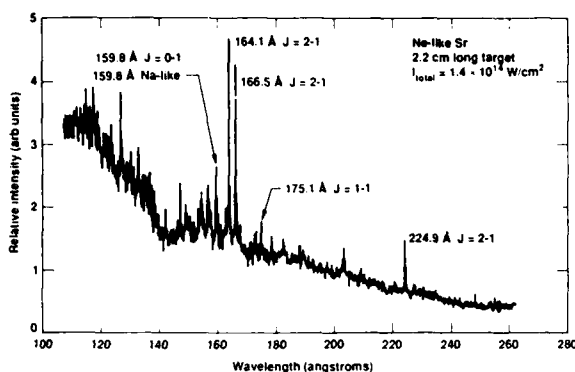


Figure 3: McPigs spectra from a 2.2-cm long  $\text{SrF}_2$  foil irradiated with  $0.53\text{-}\mu\text{m}$  light.

Figure 4 shows the behavior with target length of the  $164.1\text{ Å}$  transition as measured by McPigs for the high intensity case, along with the inferred gain coefficient. In this figure, the line intensity versus length has been fitted to the following formula:<sup>18</sup>

$$I = \frac{E}{\alpha} (e^{\alpha L} - 1)^{3/2} (\alpha L e^{\alpha L})^{-1/2}$$

where  $I$  is the intensity in  $\text{W/cm}^2\text{ sr}^{-1}$  integrated over the line profile,  $\alpha$  is the time-integrated line center gain coefficient,  $L$  is the target length, and  $E$  is the emissivity.

The increase in intensity of the  $164.1\text{ Å}$  line with target length as shown in Fig. 4 is consistent with a gain coefficient of  $4.4\text{ cm}^{-1}$ . The gain on the  $166.5\text{ Å}$  line was  $4.0\text{ cm}^{-1}$  for this case. In determining the measured gains, it was verified that the x-ray continuum scaled linearly with increasing target length as has been observed in other exploding foil type x-ray laser

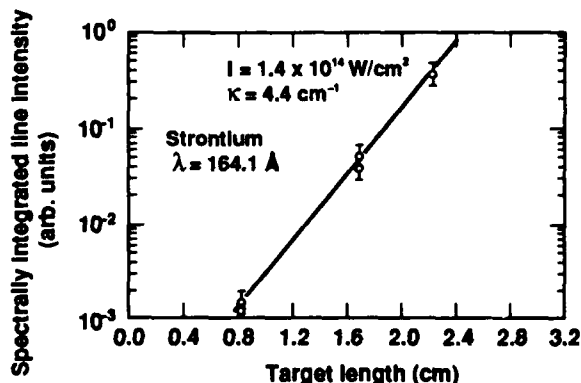


Figure 4: Intensity of the  $164.1\text{ Å}$  Sr  $J=2-1$  transition vs. target length for the  $1.4 \times 10^{14}\text{ W/cm}^2$  intensity case.

experiments. The detailed behavior of the gain coefficient at high and low intensity will be discussed in an upcoming paper.<sup>15</sup>

A definitive gain measurement was possible only for the two  $J=2-1$  transitions. The  $175.1$  and  $224.9\text{ Å}$  lines were observed, but their intensity on shorter targets was too low to provide a reliable gain measurement. The fact that these lines were observed, however, does indicate that they were probably being amplified. The  $159.8\text{ Å}$  transition was observed to grow slower than linear on all McPigs time strips. This type of behavior is well-known for Na-like<sup>1,4</sup> lines and occurs because such lines are generally optically thick. It thus appears that the observed  $159.8\text{ Å}$  spectral feature arises primarily from Na-like ion emission. The  $84.9\text{ Å}$  transition shown in Fig. 2 was not observed. At the moment, it appears that the other  $J=0-1$  line of interest at  $133.0\text{ Å}$  was also not observed. This region of the spectra is quite crowded, however, and further analysis of McPigs spectra in this wavelength region are underway.

In addition to these Sr experiments, several experiments were carried out with the Ne-like Se laser using  $0.35\text{-}\mu\text{m}$  laser light. Figure 5 shows the spectra from a  $1.6\text{-cm}$ -long Se target irradiated with  $0.35\text{-}\mu\text{m}$  light at an intensity of  $9 \times 10^{13}\text{ W/cm}^2$ . Note that the two  $J=2-1$  transitions at  $206.4$  and  $209.8\text{ Å}$  are observed to be the brightest lines in the spectrum. The relative intensities of the  $J=2-1$ ,  $J=1-1$ , and  $J=0-1$  lines in this spectrum are similar to those observed<sup>1-3</sup> with  $0.53\text{-}\mu\text{m}$  light. Further analysis of this data is underway and the results will be presented in the near future.

## Summary

A wide variety of experiments to investigate Ne-like ion x-ray laser physics issues have been carried out at the Centre d'Etudes de Limeil-Valenton, France, as part of a LLNL/CEL-V collaborative effort. In this paper, we have presented first results from a subset of these experiments. In particular, we have presented measurements of gain on several soft x-ray transitions in Ne-like Sr. Gains of  $4.4\text{ cm}^{-1}$  and  $4.0\text{ cm}^{-1}$  at an intensity of  $1.4 \times 10^{14}\text{ W/cm}^2$  were measured for the  $164.1\text{ Å}$  and  $166.5\text{ Å}$   $J=2-1$  transitions. (Note that it should be possible to demonstrate saturated output ( $\sim 20$  gain lengths) of the Ne-like Sr laser on the

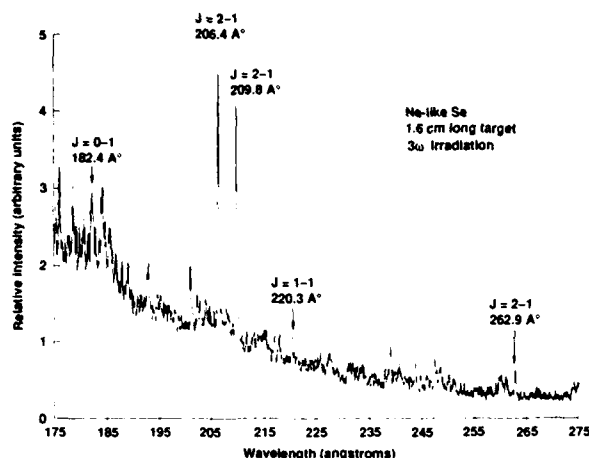


Figure 5: McPigs spectra from a 1.6-cm-long Se foil of 35- $\mu\text{g}/\text{cm}^2$  areal density irradiated by 0.35- $\mu\text{m}$  laser light.

Nova Two-Beam.) A wavelength overlap between a Na-like Sr transition at 159.77 Å and the Sr J=0-1 line at 159.84 Å prevented both positive identification and gain measurements for the latter. The J=0-1 line at 84.9 Å was not observed; this also appears to be true for the 133.0 J=0-1 transition. Initial experiments with 0.35- $\mu\text{m}$  laser light in Se have not resulted in any dramatic changes in the relative intensities of the Ne-like Se lasing lines as compared to the 0.53- $\mu\text{m}$  irradiation case.

### Acknowledgements

We would like to express our appreciation to the Phebus operations crew for their outstanding work during the entire series of LLNL/CEL-V x-ray laser experiments. We would also like to acknowledge J. Cox, D. Nilsen, and G. Stone of LLNL for their efforts in experimental setup and target preparation. This work was performed under the auspices of the U.S. Department of Energy by Lawrence Livermore National Laboratory under contract number W-7405-ENG-48.

### References

1. D.L. Matthews, et al., "Demonstration of a soft x-ray amplifier," *Phys. Rev. Lett.* **54**, 110 (1985); M.D. Rosen et al., "The exploding foil technique for achieving a soft x-ray laser," *Phys. Rev. Lett.* **54**, 106 (1985).
2. D.L. Matthews, M.D. Rosen, S.B. Brown, N.M. Ceglio, D.C. Eder, A.M. Hawryluk,

C.J. Keane, R.A. London, B.J. MacGowan, S. Maxon, D.G. Nilson, J.H. Scofield, and J.E. Trebes, 1987, "X-ray laser research at the Lawrence Livermore National Laboratory NOVA laser facility", *J. Opt. Soc. Am. B*, **4**, 575 (1986).

3. B.J. MacGowan, S. Brown, E.M. Campbell, M. Eckart, P. Hagelstein, C. Keane, R. London, D. Matthews, D. Nilson, T. Phillips, M. Rosen, J. Scofield, G. Shimkaveg, A. Simon, R. Stewart, J. Trebes, D. Whelan, B. Whitten, and J. Woodworth, (1986), "Lawrence Livermore National Laboratory X-ray laser research: recent results," in Multilayer Structures and Laboratory X-ray Laser Research, N. Ceglio, P. Dhez, Eds., *Soc. Photo-Opt. Instrum. Eng.* **688**, 36.
4. B. J. MacGowan, M.D. Rosen, M.J. Eckart, P.L. Hagelstein, D.L. Matthews, D.G. Nilson, T.W. Phillips, J.H. Scofield, G. Shimkaveg, J.E. Trebes, R.S. Walling, L. Whitten, and J.G. Woodworth, "Observation of soft x-ray amplification in neon-like molybdenum," *J. Appl. Phys.* **61**, 5243 (1987).
5. T.N. Lee, E.A. McLean, and R.C. Elton, "Soft x-ray lasing in neon-like germanium and copper plasmas," *Phys. Rev. Lett.* **59**, 1185 (1987).
6. N.M. Ceglio, "X-ray Optics for X-ray Laser Research and Applications," these proceedings.
7. P. Monier, C. Chenais-Popovics, J.P. Geindre, and J.C. Gauthier, "Demonstration of quiresonant X-ray photoexcitation in a laser created plasma," *Phys. Rev. A* **38**, 2508 (1988).
8. G. Thiell, A. Adolf, M. Andre, N. Fleurot, D. Friart, P. Juraszek, and D. Schirmann, "The Phebus experimental facility operating at 250 ps and 0.53  $\mu\text{m}$ ," *Lasers and Particle Beams* **6**, 93 (1988).
9. M.J. Eckart and N.M. Ceglio, "X-ray lasing: The diagnostics," in Energy and Technology Review, Lawrence Livermore National Laboratory, Livermore, CA, UCRL-52000-85-11, (Nov. 1985) p.25.
10. J.L. Bourgade, P. Combis, M. Louis-Jacquet, J.P. LeBreton, J. de Mascureau, D. Naccache, R. Sauneuf, G. Thiell, C.J. Keane, B.J. MacGowan, and D.L. Matthews, "Spartuvix: A time resolved XUV transmission grating spectrograph for x-ray laser research," *Rev. Sci. Instr.* **59**, 1840 (1988).

11. R.A. London and M.D. Rosen, "Hydrodynamics of exploding foil x-ray lasers," *Phys. Fluids* **29**, 3813 (1986); M.D. Rosen, R.A. London, and P.L. Hagelstein, "The scaling of Ne-like x-ray laser schemes to short wavelength," *Phys. Fluids* **31**, 666 (1988); B.L. Whitten, R.A. London, and R.S. Walling, "Scaling of Neon-like lasers using exploding foil targets," (submitted to *J. Opt. Soc. Am. B*).
12. J.F. Wyart, J.C. Gauthier, J.P. Geindre, N. Tragin, P. Monier, A. Klisnick, and A. Carillon, "Interpretation of a spectrum of laser irradiated strontium in the range 115-208 Å," *Physics Scripta* **36**, 227 (1987).
13. J.C. Gauthier, J.P. Geindre, P. Monier, C. Chenais-Popovics, J.F. Wyart, and E. Luc-Koenig, "X-ray spectroscopy of Ne-like and Na-like strontium ions," in Proceedings of the 3rd International Conference on Radiative Properties of Hot Dense Matter, B. Rozsnyai, C. Hooper, R. Cauble, R. Lee, J. Davis, Eds., (World Scientific Publishing, 1987), p. 154.
14. J.C. Gauthier, J.P. Geindre, P. Monier, E. Luc-Koenig, and J.F. Wyart, "Observation of electric quadrupole decays in the spectra of neon-like ions produced by laser irradiation," *J. Phys. B* **19**, L385 (1986).
15. C.J. Keane, et al., "Study of soft x-ray amplification in a laser produced Sr plasma," (to be submitted to *J. Opt. Soc. Am. B*).
16. M.J. Eckart, J.H. Scofield, and A.U. Hazi, "XUV emission features from the Livermore soft x-ray laser experiments," *Proceedings of the International Colloquium on UV and X-ray Spectroscopy*, Beaulieu-sur-Mer, France, September 1987, *J. Phys. (Paris)* **49**, C1-361 (1988).
17. J. Scofield, private communication, Lawrence Livermore National Laboratory, 1988.
18. G.J. Linford, E.R. Peressini, W.R. Sooy, and M.L. Spaeth, "Very long lasers," *Appl. Opt.* **13**, 379 (1974).

# Capillary Discharge Plasmas as Extreme Ultraviolet Laser Sources

J. J. Rocca, M. C. Marconi, M. Villagran Muniz, and D. C. Beethe

*Electrical Engineering Department, Colorado State University  
Fort Collins, Colorado 80523*

## Abstract

We propose the generation of XUV and soft X-ray laser radiation by electron-ion recombination in capillary plasmas excited by fast discharges. Highly ionized plasmas are created in a capillary geometry by a high current pulse; subsequently rapid cooling of the plasma occurs by electron heat conduction and radiation. Electron-ion recombination is expected to result in population inversion and gain in 3-2 transitions of hydrogenic ions with wavelengths ranging from the VUV to soft X-rays. We have generated nearly completely ionized helium and lithium capillary plasmas to study the possibility of amplification in the 3-2 hydrogenic lines during plasma recombination. Time resolved XUV spectra of a 500  $\mu\text{m}$  diameter lithium capillary discharge were obtained. The intensity of the LiIII 72.9 nm 3-2 line is observed to increase during the decay of the current pulse. The capillary discharge recombination scheme is expected to advantageously scale to soft X-rays wavelengths. A time dependent collisional-radiative model of the capillary plasmas predicts a gain of  $5\text{ cm}^{-1}$  in the 18.2 nm CVI transition.

## Introduction

Soft X-ray amplification has recently been demonstrated in highly ionized plasmas created by high energy laser pulses [1,2]. XUV lasers have also been demonstrated using laser excitation [3-5]. We propose the direct discharge excitation of XUV and soft X-ray recombination lasers using plasmas of capillary geometry. The capillary

advantages relate to the requirements for the generation of a dense highly ionized plasma as well as for its subsequent rapid cooling. In addition, the capillary limits the plasma radius, helping to avoid self absorption of resonant radiation.

In the proposed excitation scheme a nearly completely ionized plasma is created by a short (10-100 ns) high current pulse through a small diameter capillary. Capillary discharges can be used to create dense ( $10^{17}$  -  $10^{20}\text{ cm}^{-3}$ ) highly ionized plasmas with length-to-diameter ratio  $> 100$  [6,7]. Our experimental results show that in this geometry highly ionized plasmas with conditions appropriate to study short wavelength radiation amplification can be created with modest excitation energy. The capillary geometry favors plasma cooling by electron heat conduction at the termination of the discharge pulse as a consequence of the proximity of the plasma to the capillary walls. Heat conduction added to radiative losses from the highly charged ions results in rapid plasma cooling and a large three-body electron-ion recombination rate which is expected to result in population inversions and significant gain at XUV and soft X-ray wavelengths. Of particular interest are the 3 to 2 transitions of hydrogenic ions ranging in wavelength from 164 nm for HeII in a relatively low power density discharge, to 18.2 nm for CVI in high power density discharges. The scheme proposed is obviously not limited to these transitions, however hydrogenic ions simplify model calculations and plasma diagnostics. The experiments discussed in this work correspond to the study of highly ionized He and Li capillary discharges, and are relevant to the possibility of VUV and XUV

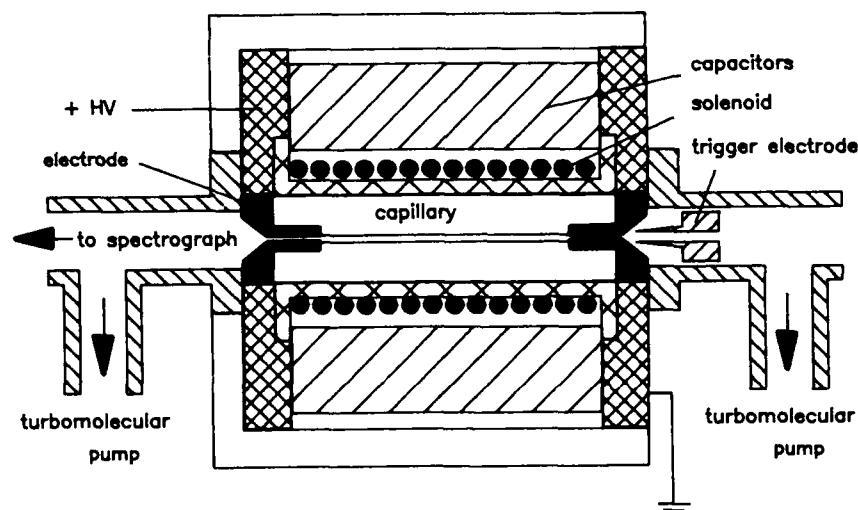


Figure 1. Capillary discharge set-up

amplification.

The concept we propose should scale advantageously to shorter wavelengths due to the favorable  $Z^7$  scaling of the optimum electron density [8]. We have developed a time dependent collisional radiative model of the capillary discharge which predicts that large gains should be obtainable at soft X-ray wavelengths. More specifically, the model predicts an exponential gain of  $e^{10}$  for the 18.2 nm transition of CVI in a capillary 100  $\mu\text{m}$  in diameter and 2 cm in length [9].

#### Capillary discharges experiments

To study the generation of highly ionized capillary plasmas in low  $Z$  elements we constructed the discharge arrangement schematically illustrated in figure 1. A 6.6 nF ring of ceramic capacitors which can be charged up to 100 kV surrounds a capillary channel. To keep the inductance at a very low value no switch is used in series with the discharge circuit. The capacitors are charged to a voltage below the capillary flashover value, and initiation of the discharge at the desired time is obtained by firing a smaller trigger discharge in proximity with one of the electrodes. After breakdown occurs rapid ablation and ionization of the wall material takes place due to extreme temperature loading of the capillary wall. A high temperature core plasma develops in the center of the capillary, surrounded by a cooler plasma in contact with the walls.

An electromagnet capable of generating an axial magnetic field of up to 100 kG with a half cycle of 170  $\mu\text{s}$  surrounds the capillary and provides additional control over the plasma evolution.

We have also constructed a modified version of this set-up that includes a spark-gap switch to study gas loaded capillary discharges. A high current pulse can create a magnetically self-confined plasma column, in which high temperature and a high degree of ionization are obtained. At the end of the excitation the plasma expands mixing with the surrounding cooler neutral gas. The electron gas rapidly loses energy in exciting and ionizing collisions, by heat conduction and in the volume change, causing plasma recombination.

The first experiments were conducted in Helium gas. The generation of a nearly totally ionized Helium plasma followed by three body electron-ion recombination when the plasma cools at the termination of the discharge pulse could result in gain in the VUV at 164nm. During the plasma recombination this line is excited predominantly by collisional and radiative decay of the population of levels of higher energy which are been pumped by electron-ion recombination. The HeII 4-3 transition at 486.5nm is of interest because feeds the  $n=3$  level and been in the visible region of the spectrum allows for convenient monitoring of the plasma evolution (figure 2).

Figure 3 illustrates the temporal

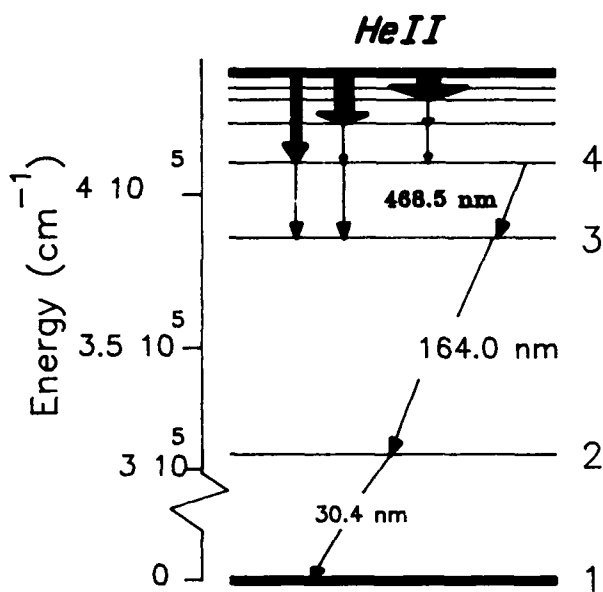


Figure 2. Simplified energy level diagram of HeII showing excitation following collisional recombination.

evolution of the discharge current and the corresponding 486.5nm HeII line emission in the radial direction from a 1 mm diameter, 30 cm long, 1 Torr capillary discharge excited by a 4nF capacitor charged to 25 kV. The 100 ns current pulse is well terminated, facilitating rapid cooling of the plasma at the end of the pulse. The most intense emission from the HeII 4-3 transition occurs 200 ns after the termination of the current pulse, indicating abundant excitation by electron-ion recombination.

The evolution of the electron density in the helium capillary plasma was measured by recording the Stark broadening of the HeII 486.5 nm line as a function of time. Figure 4 illustrates the measured line shape of this line at 86 ns and 293 ns after the initiation of the discharge current pulse. The evolution of the plasma density is plotted in figure 5. The measurements show that nearly complete ionization is achieved at the time of peak current. The plasma density at the time corresponding to the peak of the HeII recombination related line emission was measured to be  $3.4 \times 10^{16} \text{ cm}^{-3}$ . This electron density value is estimated to be several times larger than the value for which superelastic electron deexcitation of the n=3 level equals radiative decay through

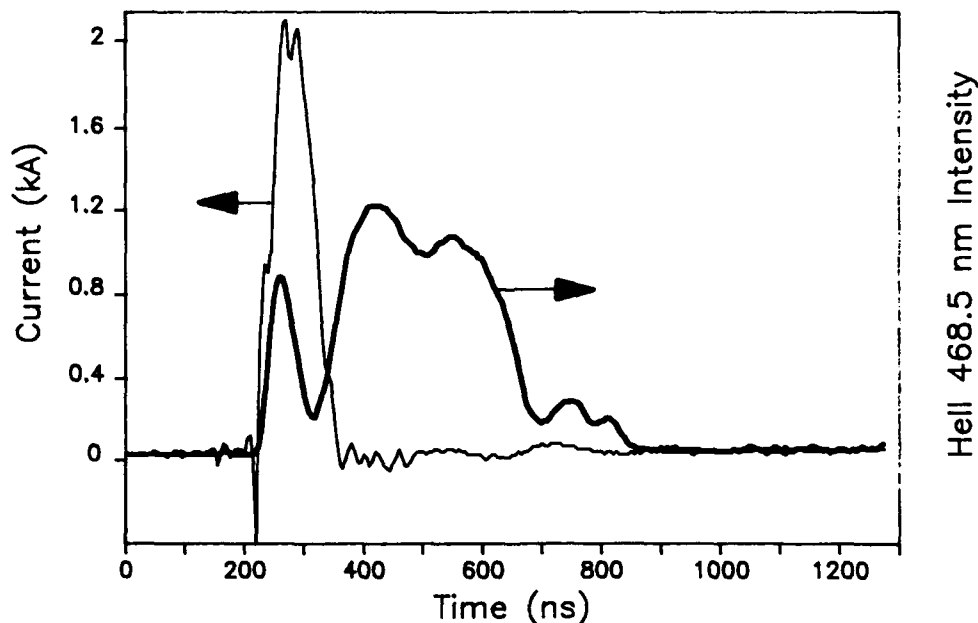


Figure 3. Current pulse and corresponding emission from the HeII 4-3 line in a 1 mm diameter, 30 cm long, 1 Torr, 25 kV He capillary discharge.

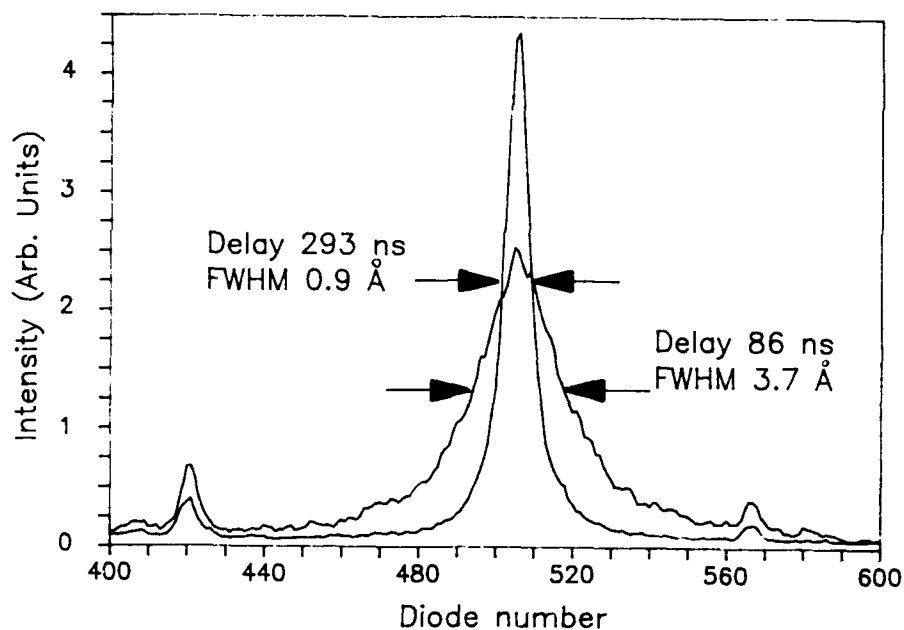


Figure 4. Stark broadened line shape of the HeII 468.5 nm line at 86 ns and 293 ns from the beginning of the discharge pulse of figure 3. The spectra correspond to radial emission from the He capillary discharge. The FWHM values had been corrected for instrumental broadening.

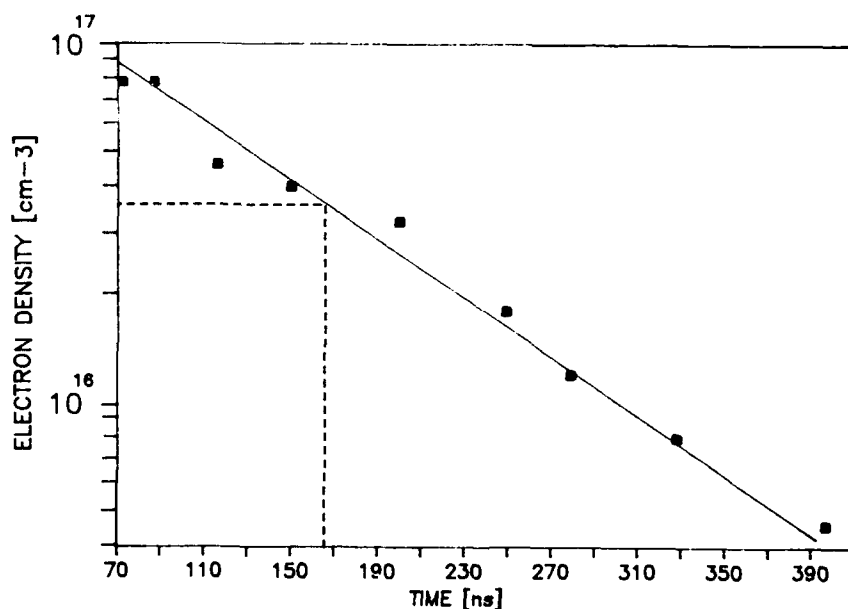


Figure 5. Measured evolution of the plasma density in a 20 kV, 1 Torr He capillary discharge. The dashed line indicates the density at the time of the recombination peak.

the emission at 164 nm [8,10]; and consequently is too high to obtain significant gain in this transition. Adjusting the discharge parameters to lower the plasma density is expected to lead to inversion of the 3-2 164 nm line.

#### *XUV emission from a lithium capillary discharge*

In a rapidly cooling lithium plasma, recombination of totally ionized atoms into high lying energy levels of LiIII followed by electron impact deexcitation, could result in a population



inversion between the  $n=3$  and  $n=2$  levels and amplification in the 72.9 nm transition (Figure 6). With the purpose of studying the excitation of this line by electron-ion recombination and the possibility of XUV amplification in lithium plasmas we constructed a lithium hydride capillary 500  $\mu\text{m}$  in diameter and 4 cm in length which was inserted in the set-up of figure 1. Lithium hydride was selected as the capillary material because its dielectric characteristic. The plasma is produced by ablation of the capillary walls following the discharge of the 6.6 nF ring of capacitors charged to voltages between 15 and 50 kV. The current pulse produced by a 40 kV discharge is illustrated in Figure 7. The peak current of the 50 ns FWHM pulse is 5 kA, corresponding to a current density of  $2.5 \times 10^6 \text{ A cm}^{-2}$ .

The set up illustrated in figure 8 was used to study the axial XUV emission from the capillary plasma. The radiation is focused into the entrance slit of a 1 m normal incidence vacuum monochromator by an aluminum coated spherical mirror, and is detected by a multichannel-plate intensified diode array detector. The current pulse was monitored with a Rogowski coil having a risetime of 2 ns, and was recorded by a 200 Mhz waveform transient digitizer. Time integrated XUV spectra do not show the 72.9 nm LiIII line when the discharge voltage is less than 20 kV, but when the discharge energy is increased by incrementing the charging voltage to 25 kV, the 72.9 nm line appears in the spectra and

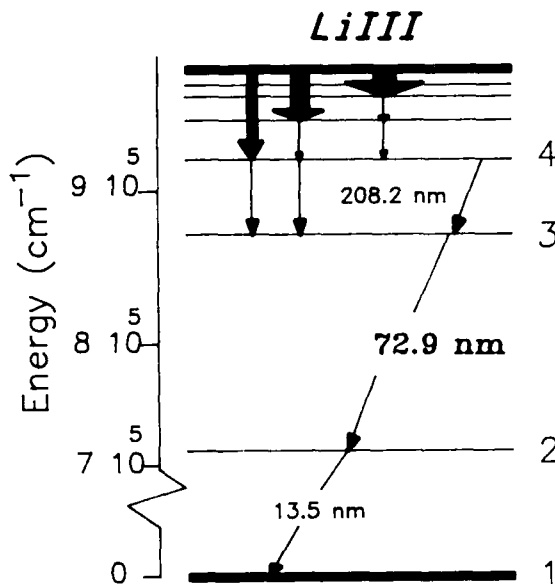


Figure 6. Simplified energy level diagram of LiIII showing excitation following electron-ion recombination.

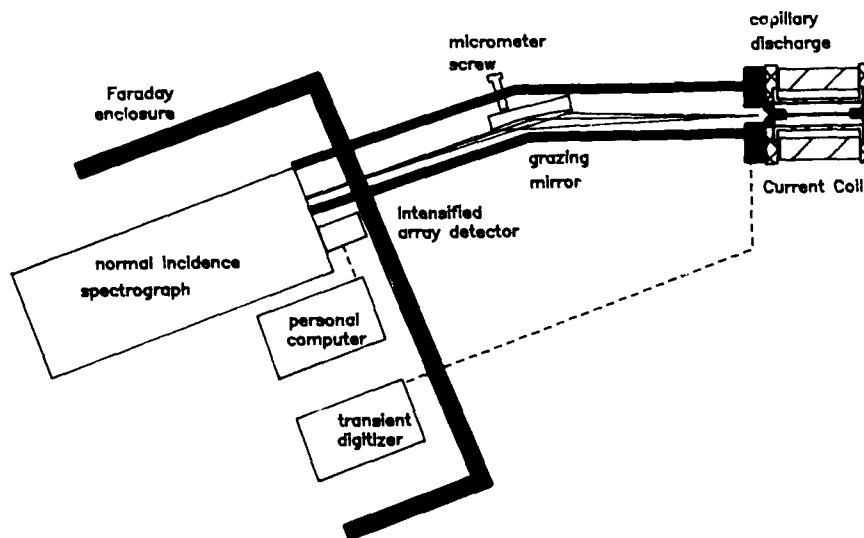


Figure 7. Experimental set-up used to study the XUV emission from a Li capillary discharge.

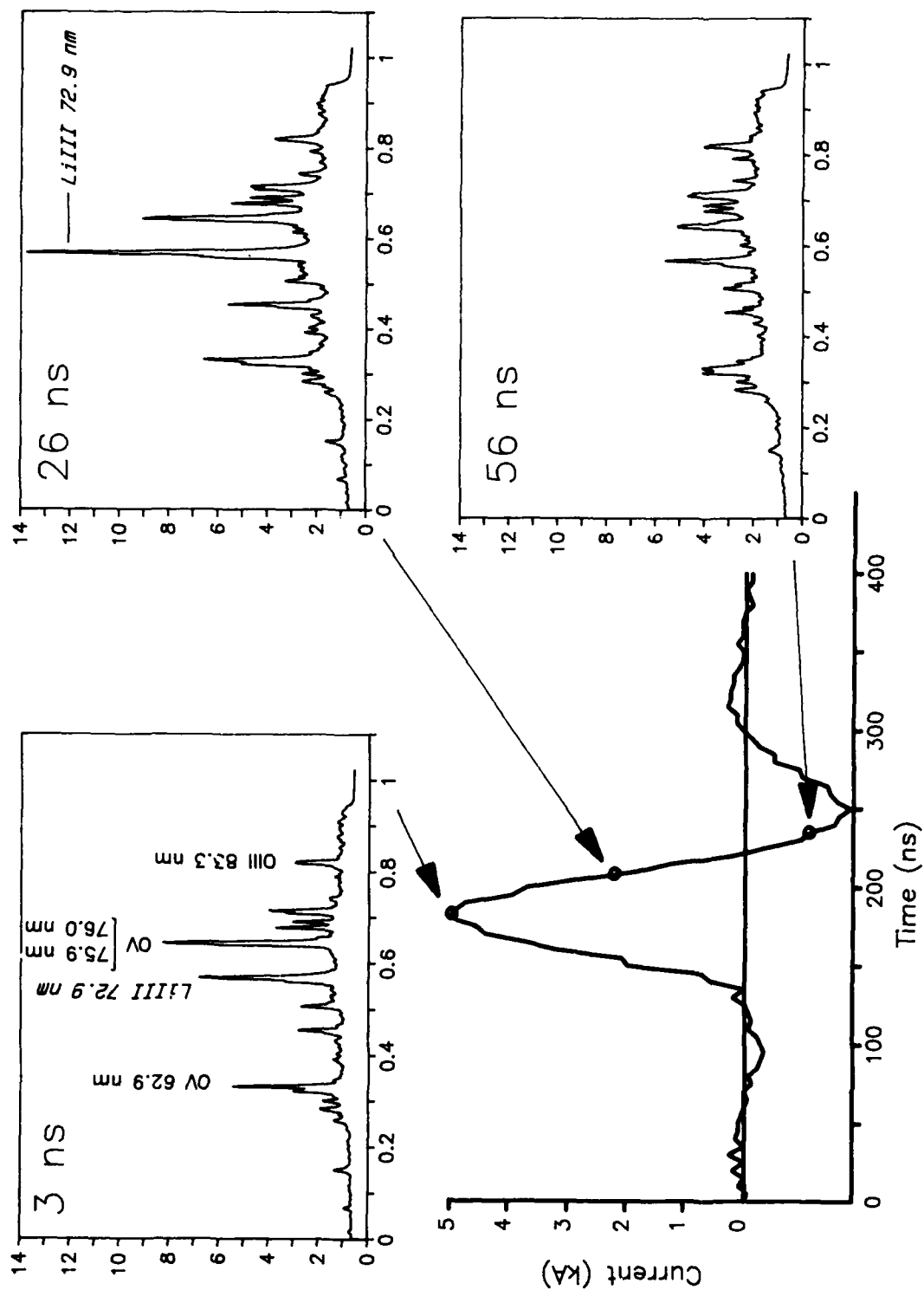


Figure 8. Time resolved XUV spectra of a 500  $\mu\text{m}$  diameter, 4 cm long L1 capillary discharge excited with the current pulse shown. The time delay with respect to the current peak is indicated in each spectrum.

at 40 kV (5 Joules of excitation energy) the emission from this line is strong.

Time resolved single shot XUV spectra were obtained by gating the multichannel plate intensifier with a 15 ns high voltage pulse. Triggering of the high voltage pulser was accomplished with the signal produced by the current coil. Three spectra corresponding to the time evolution of a 40 kV discharge pulse are illustrated in Figure 7. At the time of the peak current OV impurity lines are more intense than the LiIII 3-2 transition; OIV and OIII lines are also visible. During the decay of the discharge current pulse the intensity of the 72.9 nm line increases significantly with respect to the other lines and becomes dominant, reaching its maximum 26 ns after the peak of the discharge current pulse. Simultaneously, the ratio of the sum of the intensities of the OV to OIV lines is observed to decrease during the decay of the discharge current pulse. The observed increased emission of the 72.9 nm line is consistent with the pumping of the  $n=3$  level of LiIII by three-body electron-ion recombination as the plasma cools.

### Conclusions

Compact short wavelengths recombination lasers might possibly result from capillary plasmas created by discharge excitation. The capillary geometry allows: 1) Generation of highly ionized dense plasma with modest discharge energies, 2) rapid plasma cooling at the termination of the current pulse and 3) a plasma which is optically thin to the resonant radiation in the radial direction.

Highly ionized He and Li plasma were obtained in compact discharges. Hydrogenic lines, in which gain is expected to occur were observed to be significantly excited during plasma recombination. The concept should be scalable to soft X-ray wavelengths using available discharge technology.

### Acknowledgments

This research was supported by the National Science Foundation Grant No ECS-8606226 and a National Science Foundation Presidential Young Award (to J.J. Rocca). M.C. Marconi was supported by a fellowship from Universidad Nacional de Buenos Aires and Consejo de Investigaciones Cientificas y Tecnicas de la Republica Argentina. M. Villagran Muniz was partially supported by a post doctoral fellowship of Organization of American States.

### References

1. S. Suckewer, C.H. Skinner, H. Milchberg and D. Vorhees, Phys. Rev. Lett. 55, 1973 (1985).
2. D.L. Matthews, P.L. Hagelstein, M.D. Rosen, M.J. Eckart, N.M. Ceglio, A.V. Hazi, H. Medeck, B.J. MacGowan, J.E. Trebes, B.L. Whitten, E.M. Campbell, C.W. Hatcher, A.M. Hawryluk, R.L. Kauffman, L.D. Pleasance, G. Rambach, J.H. Scofield, G. Stone and T.A. Weaver, Phys. Rev. Lett. 54, 110, (1985).
3. K. Boyer, H. Egger, T.S. Luk, H. Pummer and C.K. Rhodes, J. Opt. Soc. Am. B 1, 3, (1984).
4. H.C. Kapteyn, R.W. Lee and R.W. Falcone, Phys. Rev. Lett. 57, 2939, (1986).
5. M.H. Sher, J.J. Macklin, J.F. Young and S.E. Harris, Opt. Lett. 12, 891, (1987).
6. R.A. McCorkle, Ann. N.Y. Acad. Sci. 342, 53, (1980); P. Bogen, H. Conrads, G. Gatti and W. Kohlhaas, J. Opt. Soc. Am. 58, 203, (1969).
7. D.R. Kania and L.A. Jones in Digest of the IEEE International Conference on Plasma Science (Institute of Electrical and Electronics Engineers, New York, 1984).
8. J.P. Apruzese, J. Davis, P.C. Kepple, M. Blaha, J. de Physique, Colloque C6-23, 47, (1986).
9. J.J. Rocca, D.C. Beethe and M.C. Marconi, Opt. Lett. 13, 565, (1988).
10. O. Wood and W. Silfast, Appl. Phys. Lett. 41, 121, (1982).

# High Power, Short Pulse Ultra-Violet Laser for the Development of a New X-Ray Laser

L. D. Meixler, C. H. Nam, J. Robinson, W. Tighe, K. Krushelnick, and S. Suckewer<sup>a</sup>

*Princeton University, Plasma Physics Laboratory, Princeton, New Jersey 08543*

J. Goldhar

*University of Maryland, College Park, Maryland*

J. Seely and U. Feldman

*Naval Research Laboratory, Washington, DC*

## Abstract

A high power, short pulse ultra-violet laser system (Powerful Picosecond-Laser) has been developed at Princeton Plasma Physics Laboratory (PPPL) as part of experiments designed to generate shorter wavelength X-ray lasers. With the addition of pulse compression and a final KrF amplifier the laser output is expected to have reached 1/3-1/2 TW levels. The laser system, particularly the final amplifier, will be described along with some initial soft X-ray spectra from laser-target experiments. The front-end of the PP-Laser provides an output of 20-30 GW and can be focussed to intensities of  $\sim 10^{16}$  W/cm<sup>2</sup>. Experiments using this output to examine the effects of a prepulse on laser-target interaction will be described.

## Introduction

One approach, which we consider as highly promising, is to use autoionizing metastable levels for storage of the pumping energy as proposed by S. Harris [1] for 207 Å lasing in Lithium. Other approaches are based on inner shell ionization [2,3] and Auger transitions [4,5].

It is our goal to demonstrate X-ray lasing significantly below 10 nm, perhaps as short as 1 nm. However, with present X-ray schemes (even those with extremely large pump lasers), these goals may be difficult to reach and a new approaches may be required.

In a recombination laser X-ray scheme the input pump intensity scales as severely as  $\lambda^{-4}$ . That is, to reduce the wavelength

by a factor of ten requires an increase in input laser power of four orders of magnitude. However, the pumping time required,  $\tau$ , actually decreases as  $\lambda^{-2}$ . So, the practical approach to shorter wavelength emission should make use of short pulse length, high power lasers. This is what has motivated our construction of the powerful, picosecond laser (PP-Laser).

For a number of years C. Rhodes and his group [6] proposed to use very high power density, short pulse lasers for multiphoton selective excitation of inner shell transitions in order to generate lasing in the 10 Å wavelength region.

## First Stage Of The System

The PP-Laser system which we have developed, [7] as well as systems developed by others, [8,11] have a large number of system components. The first stage of our system consists of a short pulse dye oscillator/amplifier whose output is frequency converted to obtain a wavelength of 248 nm, and then amplified by two KrF amplifiers to obtain output energy in the 20 - 30 mJ range. A detailed block diagram of the system showing the 1st stage, the optional pulse compression and the final KrF amplifier is given in Fig. 1.

The frequency doubled (523 nm) output of the mode-locked Nd:YAG pump is used to pump the cavity dumped dye oscillator, providing an output which is approximately 1 μs at 647 nm. Residual 1.06 μm from the YAG laser is directed through a pulse slicer, amplified, frequency doubled and used to synchronously pump a three stage dye amplifier. The output of the

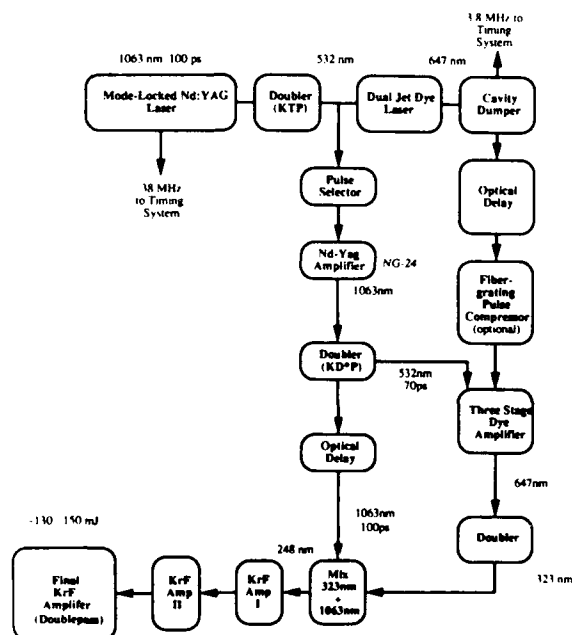


Figure 1. Picosecond Laser System - Block Diagram.

oscillator is delayed and then directed into this dye amplifier. Optionally, the pulse width of the pico-second pulse may be shortened to the 200-300 fs range with a fiber - grating compressor prior to amplification [12].

The non-compressed pulses, measured with an autocorrelator at the outputs of the Dye oscillator, and the Dye Amplifiers, and also at the output of KrF II (using the two photon fluorescence technique in Xe), were 1 psec, 1.3 psec, and 1.1 psec FWHM respectively (Fig. 2). The corresponding compressed pulse at the output of KrF II, measuring 250 fsec with the two photon fluorescence technique, is shown in Fig. 3.

The dye amplifier output is frequency doubled and then mixed with residual 1.063  $\mu\text{m}$  to yield the desired 248 nm seed pulse for the KrF\* excimer amplifiers. Without compression, the output beam from the 2nd KrF\* amplifier focal spot intensities of  $10^{16} \text{ W/cm}^2$ . This constitutes the output from the 1st stage of the PP-Laser System. A photograph of the 1st stage showing KrF AMP I and II in the foreground is shown in Fig. 4.

In Fig. 5 is presented intense spectral lines of hydrogen and helium like ions of oxygen and carbon in the wavelength region of 15 to 45 Å. It is remarkable

that the results look similar to the 1-2 keV high temperature tokamak plasmas, except that the lines are much broader [13].

### Results From The First Stage Of The Short Pulse Laser System

The output of the 1st stage (20-30 GW) was initially used in experiments with solid targets. Using a 3-m, high resolution XUV spectrometer [14], a number of spectra were recorded in the region from 10 to 300 Å. The highlights of the resulting spectra were the observation of highly ionized species (Fe XVI), Fig. 6, and very significant line broadening for certain transitions. The high resolution of the instrument can be seen from the narrowness of the LiII lines in Fig. 7. The observed broadening may be a result of either Stark broadening in high density ( $> 10^{22} \text{ cm}^{-3}$ ) plasma or the extremely high electric field associated with the laser pulse (10 V/Å). Modelling, based on Stark broadening, indicated that in some cases a mixing of wavefunctions and subsequent emission from otherwise forbidden transitions occurred, leading to observed asymmetry in certain lines (FVII 3d-2p, Fig. 8). This asymmetry, as recently was pointed out by K. Koshelev [15], may be the results of contribution to line intensities from satellite lines.

The effect of a prepulse [16] on the generation of plasma by a picosecond KrF\* laser has been examined. The prepulse preceding the picosecond pulse, arises from the amplified spontaneous emission (ASE) of the two KrF\* amplifiers. The amount of prepulse energy is varied by changing the injection timing of the seed pulse. Even though the ASE signal is a factor of  $10^4$  times longer in duration and more than  $10^5$  times weaker in intensity than the main picosecond pulse, it nevertheless significantly changes the condition of interaction of the main pulse with the target.

The spectra shown in Figs. 9 (a), (b), and (c) were obtained with a teflon target at injection times of  $t = -3, 0$ , and  $+3 \text{ ns}$  respectively, with respect to time  $t = 0$ , when the laser (1 ps) pulse energy is maximum. The estimated amount of prepulse energy in each case is 0.3, 7, and 15%, respectively, of the picosecond pulse energy. As the injection time is delayed (more prepulse) FVII, lines become broader. Also the forbidden transition 3p-2p of FVII, gets stronger with increasing prepulse.

This implies that the FVII ions are

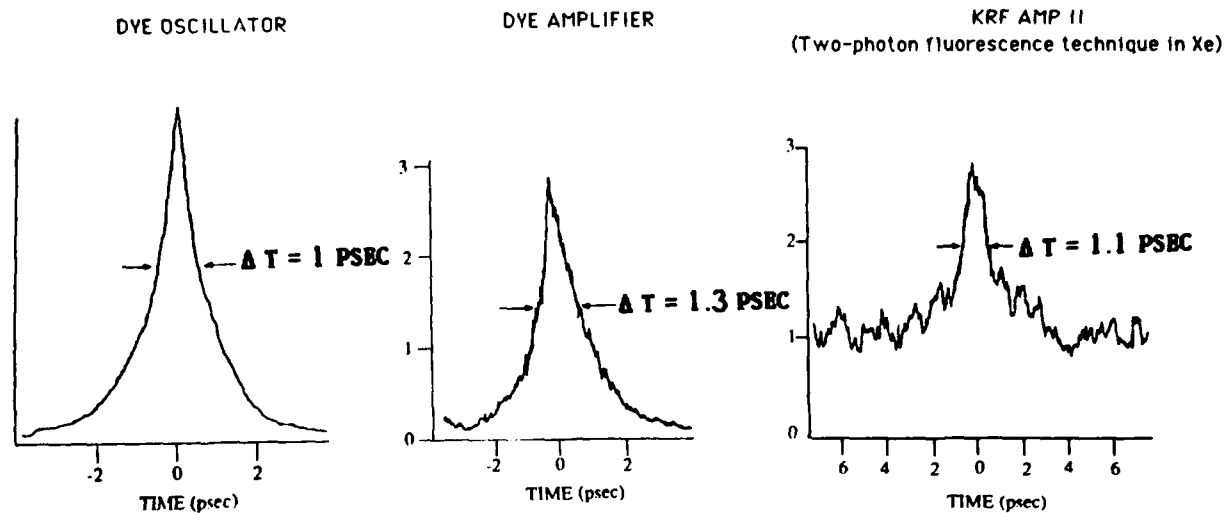


Figure 2. Autocorrelation traces of non-compressed pulses.

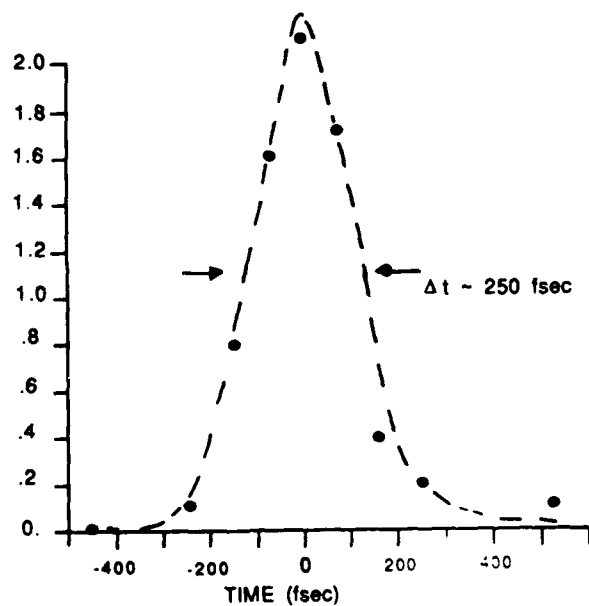


Figure 3. Compressed pulse at the output of the 2nd KrF\* amplifier.



Figure 4. First stage of Powerful Picosecond Laser System showing 1st and 2nd KrF amplifier.

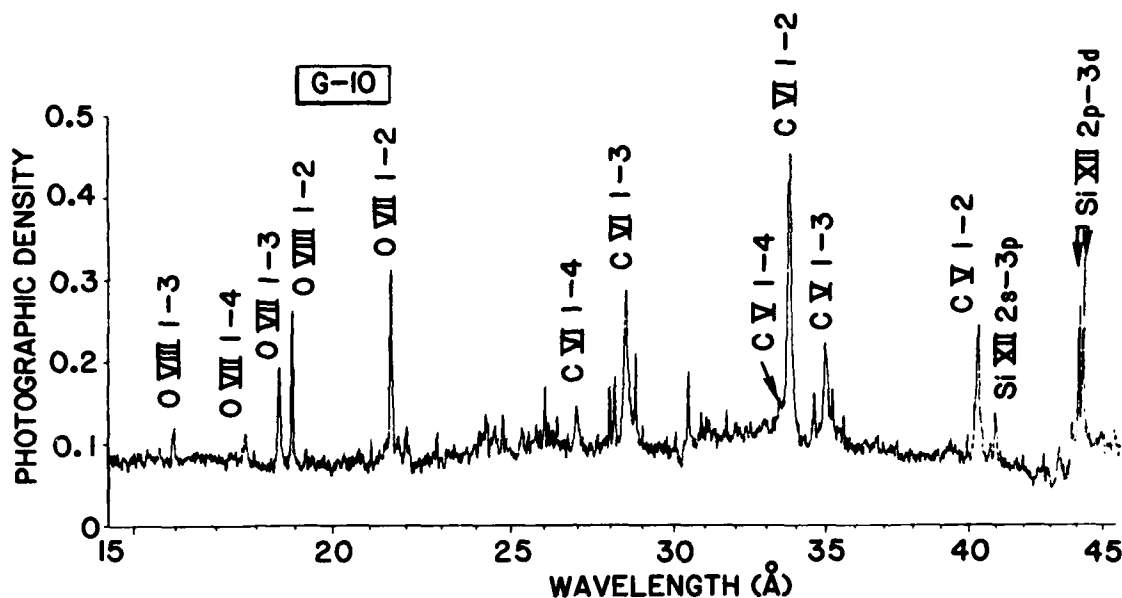


Figure 5. Densitometer trace of the spectrum from a G-10 target showing transitions in H-like and C VI and O VIII, He-like C V and O VII, and Li-like Si XII.

created at higher electron density closer to the peak of the picosecond pulse as the prepulse increases. Furthermore, narrower line widths of FVII in the case of a weak prepulse ( $t = -3$  ns, Fig. 9) means that FVII ions in this case are created at a lower density. Since the plasma created by the picosecond KrF\* laser freely expands, the observation of FVII ions at lower electron density implies that a significant part of the radiation from FVII ions is generated during the recombination phase after the laser pulse and there existed a plasma with higher electron density and higher electron temperature earlier in time. This may be indicated by the presence of much stronger resonance lines of CV and CVI (observed in third order) for the case of weak prepulse ( $t = -3$  ns) than those observed for a stronger prepulse ( $t = 0$  ns). Thus, the initial plasma in the case of  $t = -3$  ns is hotter than that at  $t = 0$  ns or  $t = +3$  ns.

The role of the prepulse can be modeled as follows. The prepulse is expected to create a low temperature plasma which will expand prior to the arrival of the picosecond pulse. As the amount and duration of prepulse increases, the number of ions interacting with the picosecond pulse will increase. Subsequently, the heat capacity of the plasma will increase with increasing prepulse because a larger number of particles are involved, with the result

that the peak electron temperature will decrease. Therefore a hotter plasma is created with less prepulse. This model is supported by calculations based on the observed spectral intensities and the linewidths of the Li-like FVII.

#### Final KrF\* Amplifier

Excimer Laser research is being vigorously pursued [17] because this class of lasers offered several advantages in comparison to other lasers; they can amplify sub-picosecond pulses [18], their short wavelength allows the output pulse to be focussed to a relatively small spot size, and their relatively high pumping efficiencies allow multi-terawatt power densities to be delivered to targets with small laboratory size facilities.

The final KrF\* excimer amplifier (KrF III) has as its seed pulse the 25 mJ, 248 nm output from the Picosecond Laser System first stage. The cross-sectional area of the laser cavity is 5 cm by 10 cm, and the active length is approximately 80 cm. The amplifier is UV preionized by a row of 41 pins which span the length of the laser active region. The amplifier has Brewster's angle window mounts on each end to minimize reflection from the quartz windows. The amplifier unit consists of the laser body and its associated high voltage circuitry contained in an aluminum enclosure to minimize EMI, and external high voltage power supplies and control electronics. Timing

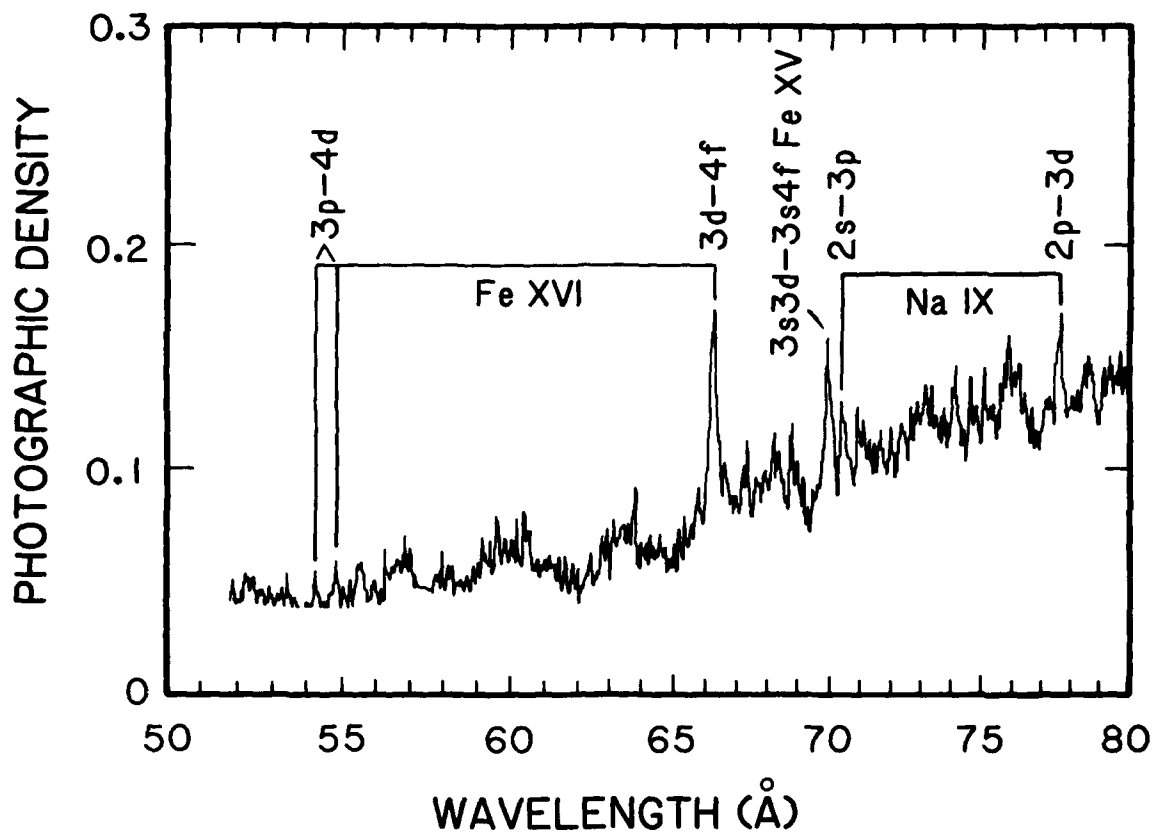


Figure 6. Iron spectrum showing Na-like Fe XVI and Mg-like Fe XV.

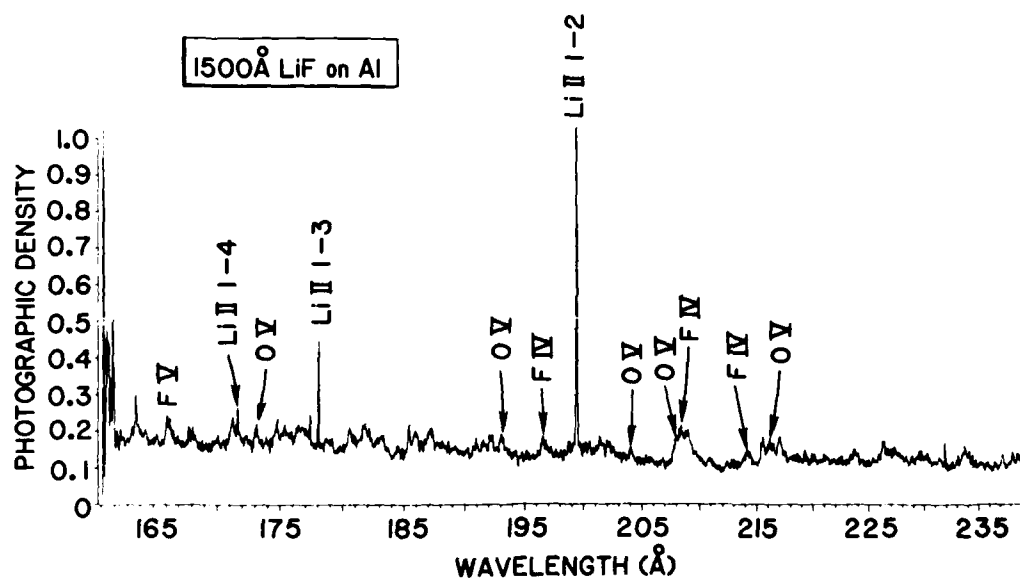


Figure 7. Densitometer trace of the spectrum from a 1500-Å LiF coating on aluminum target showing transitions in He-like Li II.



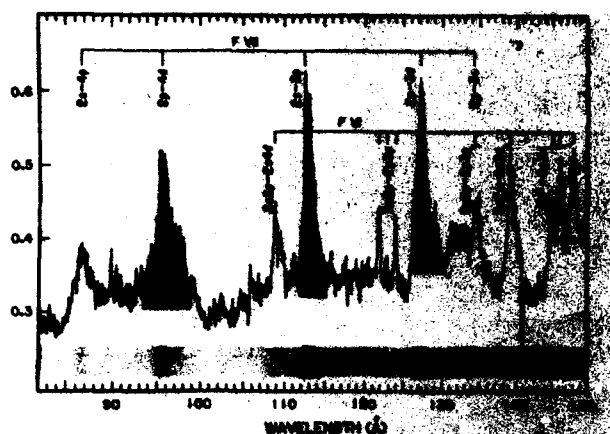


Figure 8. Fluorine spectrum obtained with teflon target.

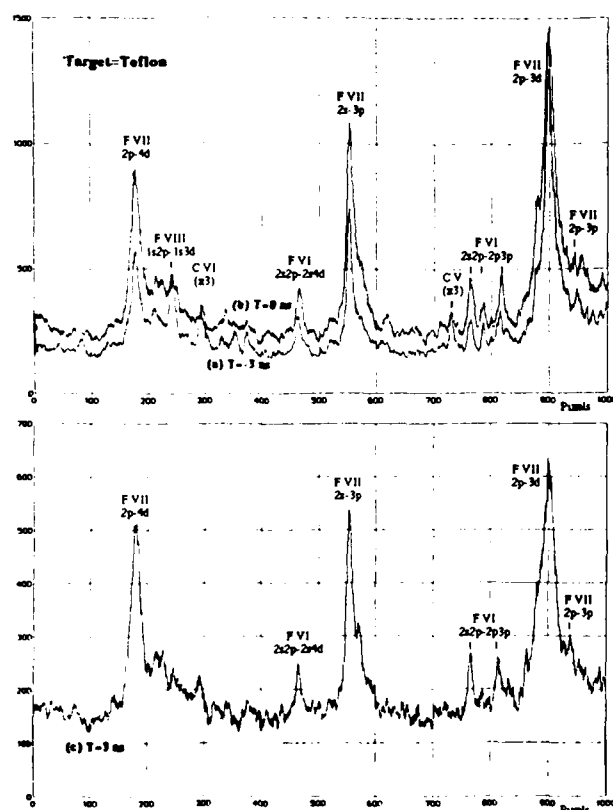


Figure 9. Fluorine and carbon spectra in the wavelength region 90-130 obtained with teflon target. The injection time of the picosecond pulse in each case (a)  $t = -3$  nsec, (b)  $t = 0$  nsec, and (c)  $t = +3$  nsec respectively.



Figure 10. End view of KrF amplifier.

is derived from the PPPL designed and constructed Fast Timing System and Master Timing System used to coordinate the rest of the experiment, which is locked to the 38 MHz clock derived from the mode locker of the Nd:YAG pump of the dye oscillator.

The main body of the amplifier is made of 1.25 inch thick G-10 epoxy fiberglass and the electrode ends are made from 3/4 inch thick aluminum. One electrode is machined from solid aluminum and the other electrode is similar but has a slot milled into it and then has a layer of stainless steel screening over it to allow the UV from the preionizer pins to pass through. The basic electrical circuit configuration of the laser is the capacitive discharge circuit, similar to those found in nitrogen, and CO<sub>2</sub> TEA lasers. The electrical circuits for excimer lasers, however, are characterized by very low inductance, very fast current and voltage rise-times and very high peak currents which means that circuit geometry, and component stresses are critical considerations in the development of a reliable laboratory scale 1 Joule excimer laser. Figure 10 shows an end view of the amplifier. The preionization circuitry is shown along the top of the amplifier, and the main discharge capacitors are mounted close to the laser body along each side.

A series of tests were run on the KrF\* final amplifier, first as an oscillator, and later as an amplifier in the Picosecond Laser System. In the oscillator configuration, a 1.5 meter radius spherical mirror was placed at one end of the laser, and a 5% reflective flat window at the other end so that a laser cavity was formed. In this

configuration a set of tests were run to determine the optimum gas mix to obtain maximum output energy. Based on these results, it was determined that the highest energy output was available using a mix of 50 torr krypton, 75 torr of 5% fluorine in a helium buffer gas mix, and then operating at 3 atm absolute with the balance of gas composed of neon. When the amplifier is part of the Picosecond Laser System, the amplifier is double passed. The pulse expands to fill the aperture as it traverses the amplifier on the initial pass, and is reflected by the 1.5 meter spherical mirror and slowly converges on its return trip before being focussed onto the target. In this configuration, output energy of 1 Joule has been measured using a 20 nsec seed pulse from the first two KrF amplifiers, and energy levels in the range of 150-200 mJ (with  $\sim 20\%$  ASE) have been recorded using the compressed seed pulse. Some recent results indicated that ASE has been reduced to  $\sim 10\%$  for 120-150 mJ output.

#### Initial Spectroscopic Results With The Final KrF Amplifier

The plasma is monitored by a grazing incidence soft X-ray spectrometer, (SOXMOS) [13] which uses a microchannel plate detection system for increased sensitivity over conventional spectrometers. Recently obtained spectra using the system with the large aperture final KrF\* amplifier, show results significantly different from the spectra obtained from the system without the final amplifier. The spectra of Fig. 11a was obtained from 200 non-compressed shots from the 1st part of the system, at an energy of approximately 20 mJ each and pulse duration 1 psec. The spectra of Fig. 11b was obtained from 5 shots at 100 mJ with compressed ( $\sim 300$  fsec) pulses. The latter spectra shows an increase of line broadening, and the onset of satellite lines in comparison to the former spectra. Spectra are being analyzed presently and the results will be published elsewhere.

Figs. 12 and 13 show the results obtained with a compressed 100 mJ pulse on a teflon target. Fig. 12 shows FVII lines which are very broadened, and have significant intensity, while Fig. 13, which corresponds to ASE only shots, shows no significant spectra, indicating that the FVII lines are a consequence of the shortened picosecond pulse.

#### Experimental Configuration For The New X-Ray Laser System

As mentioned earlier, the PP-laser has been developed as a high intensity pump source in the development of a shorter wavelength X-ray laser. In general, however, in order to obtain shorter wavelength emission, one must access transitions which arise from excited levels of highly ionized species. The laser characteristics which one needs to produce the relatively long-lived ionization stage required are very different from those needed to excite the short wavelength transition and produce a population inversion. While a single laser might be able to perform these tasks, a two-laser approach [19], which separates these processes promises to be a more efficient one.

The two-laser approach to produce a shorter wavelength X-ray laser (Fig. 14) consists of the following elements. A high energy CO<sub>2</sub> or Glass laser is fired onto a target producing a plasma column. A large magnet is used to confine the plasma and provide the desired plasma conditions. The short pulse, high power laser is used at the appropriate time (the occurrence of the correct ionization state), to create the inversion. The interaction is examined using various diagnostics, primarily axial and transverse XUV spectrometers. All the essential elements for this experiment are now in place. Temporal synchronization between the lasers, the magnetic field, and the diagnostics has been verified. Higher output power from the lasers may prove necessary but initial target experiments will be performed in the near future.

#### Conclusion

Initial tests have been conducted with a compressed laser pulse at 248 nm and have resulted in the spectra of plasma from teflon targets. The system appears to work reliably and is capable of being synchronized to other lasers, and diagnostics. Additional experiments will be performed to investigate the effects of the interaction of the powerful laser pulse on various targets.

#### Acknowledgement

We would like to acknowledge the help of J. Fujimoto (MIT) for his help with the pulse compression, and also M. Littman and R. Miles (both Princeton Univ.) and T. McIlrath (Univ. of Maryland) for their work and helpful suggestions on the

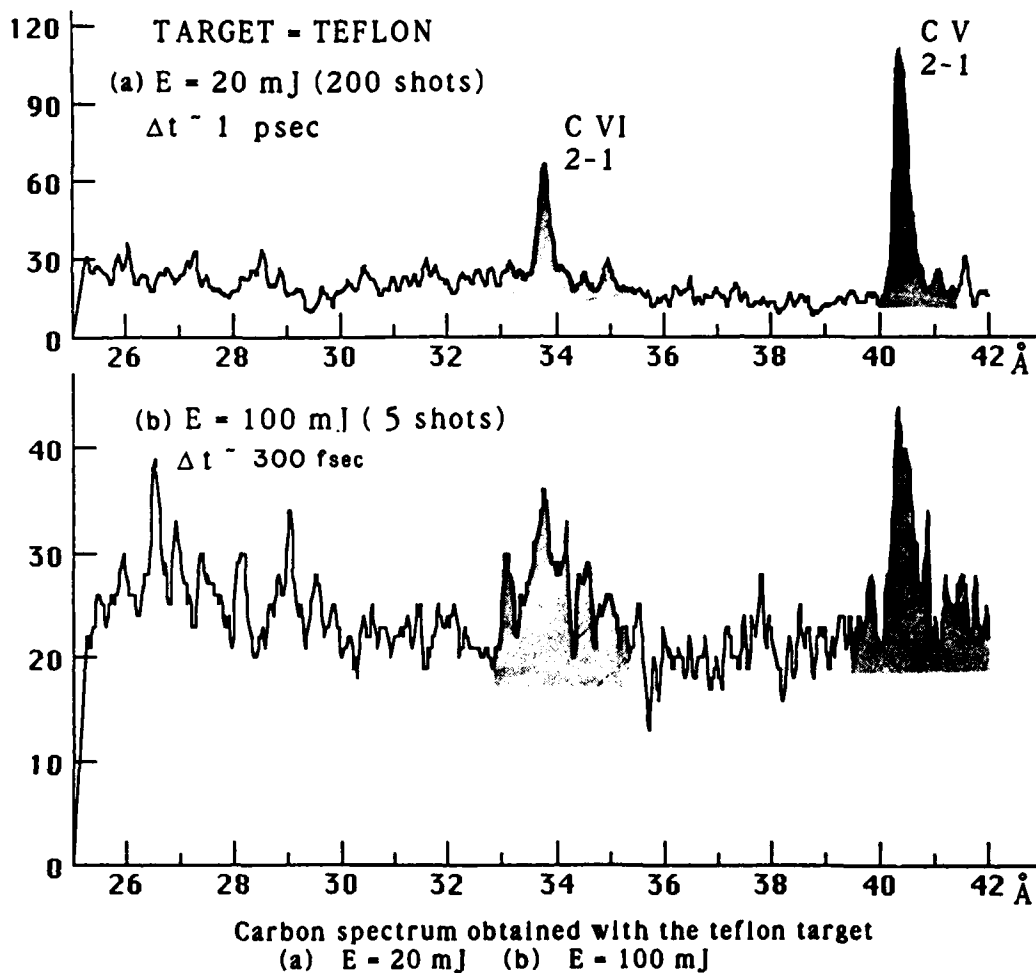


Figure 11. Carbon spectrum obtained with teflon target. (a) 200 shots at 20 mJ with  $\Delta t \sim 1 \text{ psec}$ , (b) 5 shots at 100 mJ with  $\Delta t \sim 300 \text{ fsec}$ .

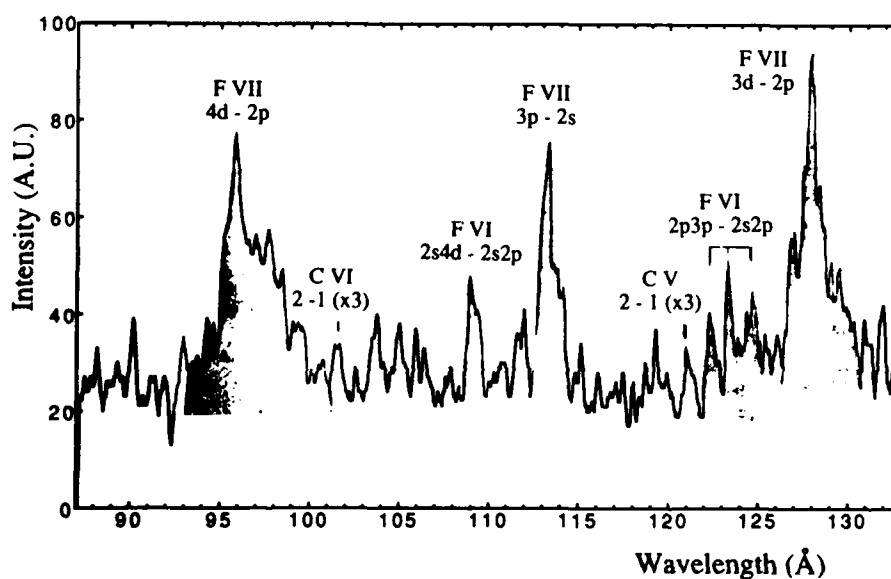


Figure 12. Fluorine and carbon spectra obtained with teflon target.

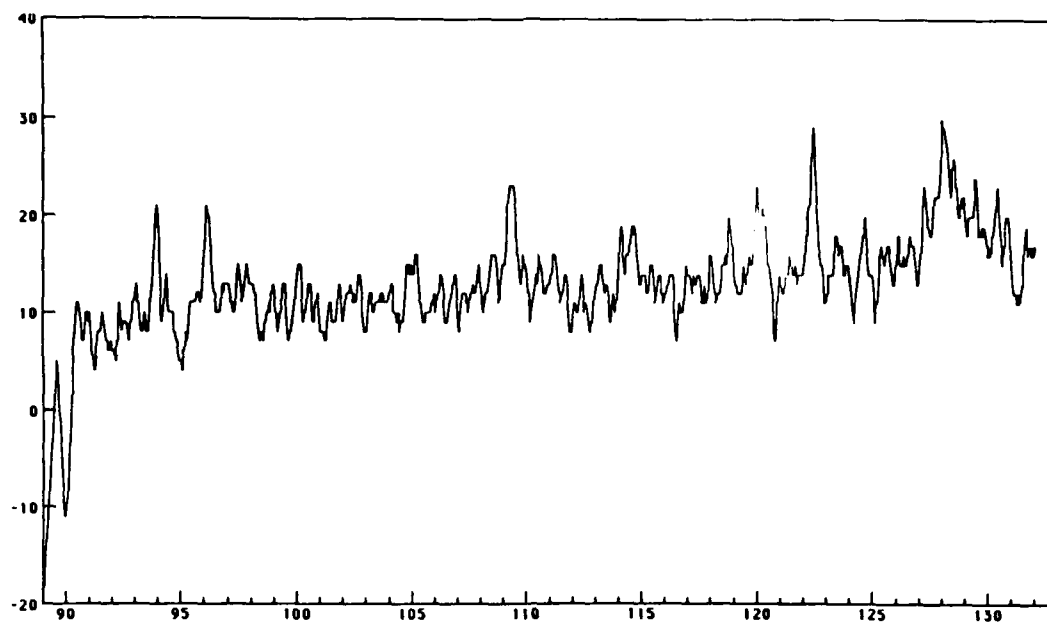


Figure 13. ASE ( $E = 20$  mJ) only output from final KrF amplifier - teflon target.

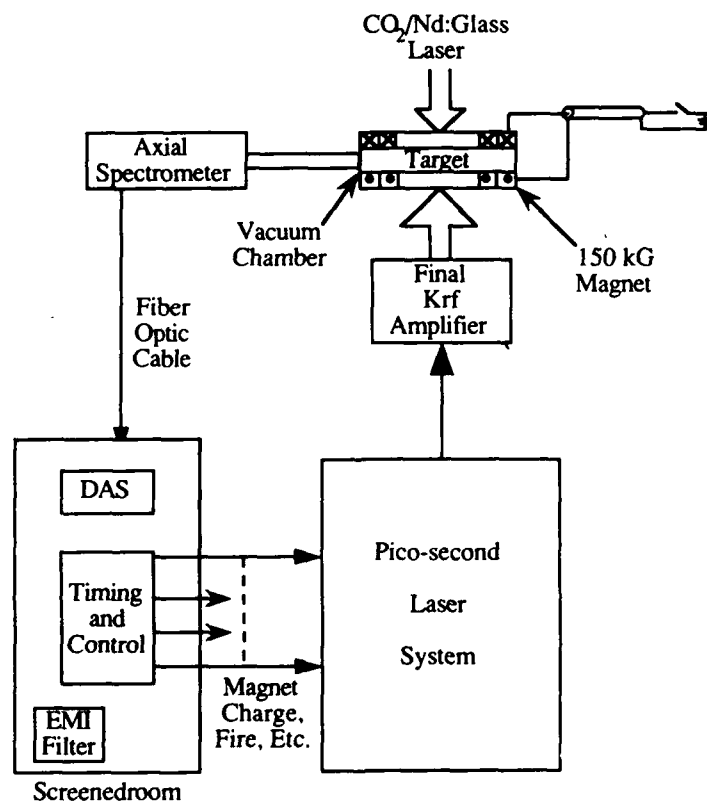


Figure 14. Schematic of arrangement of "Two-Laser Approach" to X-ray laser development.

PP-Laser system. We would additionally like to acknowledge the help of Nicholas Tkach in the electronics area, and John Schwarzmann and Andrew Schuessler for their help in mechanical construction. This research was supported by the U.S. Department of Energy, Advanced Energy Projects of Basic Energy Sciences, the U.S. Air Force Office of Scientific Research.

a. Also Mechanical & Aerospace Engineering Dept., Princeton University.

## References

1. S.E. Harris, "Proposal for a 207-Å Laser in Lithium," *Opt. Lett.* 5, 1 (1980).
2. M.A. Duguay and P.M. Rentzepis, "Some Approaches to Vacuum UV and X-Ray Lasers," *Appl. Phys. Lett.*, 10, 350 (1967).
3. E.J. McGuire, "Soft X-Ray Amplified Spontaneous Emission via the Auger Effect," *Phys. Rev. Lett.*, 35, 844 (1975).
4. R.W. Falcone, H.C. Kapteyn, and R.W. Lee, "Demonstration of a Short Wavelength Laser Pumped by Auger Decay," *J. Opt. Soc. Am. A*, 2, P 127 (1986).
5. W.T. Silvast and O.R. Wood, "Photoionization Lasers Pumped by Broadband Soft X-Ray Flux from Laser-Produced Plasmas," *J. Opt. Soc. Am. B*, 4, 609 (1987).
6. A. McPherson et al., "Studies of Multiphoton Production of Vacuum-Ultraviolet Radiation in the Rare Gases," *J. Opt. Soc. Am. B*, 4, 595 (1987).
7. W. Tighe, et al., "High Power Picosecond Laser System at 248 nm," *Rev. Sci. Instr.*, Vol. 59, No. 10, p. 2235-2240, Oct. 1988.
8. S. Watanabe, et al., "Multiterawatt Excimer Laser System," this proceedings.
9. A.P. Schwarzenbach, et al., "Subpicosecond KrF Excimer-Laser Source," *Opt. Lett.*, 2, 499 (1986).
10. P.H.Y. Lee, et al., "Collisionless X-Ray Generation from Picosecond Laser-Gas Interaction," this proceedings.
11. O. Willi, "Observations of High Density Plasmas Produced with a Picosecond High Power KrF Laser," this proceeding.
12. This work was done in conjunction with J. Fujimoto, M.I.T.
13. J.L. Schwob, et al., "High Resolution Duo-Multichannel Soft X-Ray Spectrometer for Tokamak Plasma Diagnostics," *Rev. Sci. Instrum.* 58, (9) p. 1601, Sept. 1987.
14. C.H. Nam, et al., "Observation of Asymmetric Stark Profiles from Plasmas Created by a Picosecond KrF Laser," *Phys. Rev. Lett.* 59, 2427 (1987).
15. K.N. Koshelev, "Asymmetric Line Profiles of Highly Charged Ions in Dense Plasmas and Dielectronic Satellites," *J. Phys. B*, 21, L 593.
16. C.H. Nam, Doctoral Thesis, "Spectroscopic Studies of Plasmas Created by a Powerful Picosecond KrF\* Laser," Princeton University, April 1988.
17. A. Endoh, et al., "Picosecond Amplification in Wide-Aperture KrF Lasers," *Optics Letters*, Vol. 12, No. 11, Nov. 1987.
18. S. Szatmari & Schafer, et al., "Picosecond Gain Dynamics of KrF\*," *Applied Physics B*, 33, 219-223 (1984).
19. S. Suckewer, et al., "Recent Progress in Soft X-Ray Laser Development at Princeton," *Journal de Physique*, Colloque C6, Supplement AU No DD, Tome 47, Oct. 1986.

## Soft X-Ray Amplification in a Magnetically Confined Recombining H-like and Li-like Plasma

D. Kim, C. H. Skinner, A. Wouters, E. Valeo, D. Voorhees, and S. Suckewer<sup>†</sup>

*Princeton University, Plasma Physics Laboratory, Princeton, New Jersey 08543*

### Abstract

A series of experiments with H-like carbon has been performed using a Nd/Glass laser ( maximum output energy is 100 J in 3 nsecs ) in a line focus configuration. The maximum gain observed was  $8.1 \text{ cm}^{-1}$  using 25 J laser energy. This work is an initial step toward the development of a soft x-ray amplifier for the presently operating C VI 182 Å soft x-ray laser in a CO<sub>2</sub> laser produced plasma confined in a magnetic field.

The possibility of lasing action at 187.2 Å in Li-like Mg X, 154.7 Å in Li-like Al XI, and 129 Å in Li-like Si XII in a magnetically confined recombining plasma has been also investigated. A CO<sub>2</sub> laser was focused onto a target assembly and the resulting plasma confined in a solenoidal magnet field up to 9 Tesla. Impurities such as iron or titanium were introduced to increase the cooling in the recombination phase to produce more favorable conditions for high gain. Gain-length products of  $1 \sim 2$  at 187.2 Å in Mg X,  $3 \sim 4$  at 154.7 Å in Al XI, and  $1 \sim 2$  at 129 Å in Si XII were observed. To better understand plasma dynamics, a one-dimensional hydro-atomic code has been developed to simulate the experiment. The comparison between experiments and computer simulation will be discussed.

### Introduction

The idea of creating a population inversion using the collisional recombination of ions dates back to 1960's when Gudzenko and Shelepin[1] proposed first this scheme in H-like ions. Since then, this scheme has been investigated both theoretically and experimentally. Adiabatic expansion was originally proposed

as a cooling method by Gudzenko and Shelepin. In 1974 Irons and Peacock[2] observed population inversions in H-like carbon ions between levels 3,4,5 and 2 in an expanding plasma created by laser irradiation of a slab target. However, the measured gain was low ( $\sim 10^{-5} \text{ cm}^{-1}$ ). Later higher gain was reported by Dewhurst *et al.*[3] but it was still too low to create a well collimated beam. In the late 1970's it was realized that the adiabatic expansion cooling may not be the most favorable means of producing significant gain because at the time of strongest recombination the plasma had already expanded so that the electron density was too low to produce high gain. To overcome this problem, Suckewer and Fishman[4] proposed a new configuration of confining a CO<sub>2</sub> laser produced plasma in a magnetic field. Using this new configuration, a gain-length product of 6.5[5], and later up to 8[6] at C VI 182 Å has been demonstrated.

The possibility of using soft x-ray lasers for microscopy of living cells has stimulated work to develop x-ray lasers operating in the wavelength region 23.3 Å to 43.7 Å, the so-called water window. An important point, however, that is rarely discussed, is the laser energy required for these applications. For instance, in order to record a high resolution image of a biological cell on photo-resist, a substantial laser beam energy is required. We have, therefore, dedicated a significant effort to increase the energy of the 182 Å soft x-ray laser. One approach has been to develop additional amplifiers.

### Experiments with H-like Carbon

The first step in developing such amplifiers is to generate gain in C VI at 182 Å. A gain medium was pro-

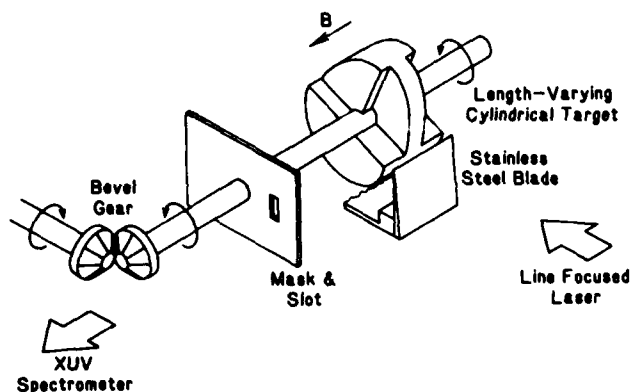


Figure 1. The rotatable target system

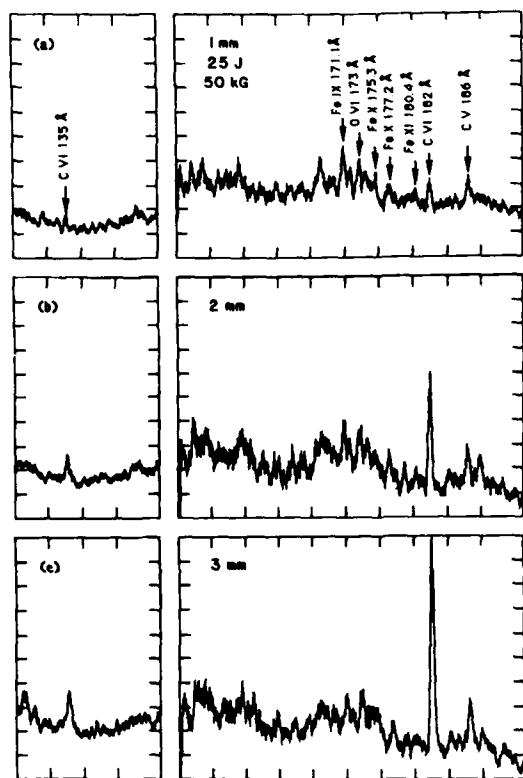


Figure 2. Experimental spectra obtained by XUV spectrometer for different plasma lengths, 1, 2, and 3 mm.

duced by Nd/Glass laser beam brought to a line focus on a solid carbon target in a strong magnetic field (field lines parallel to the line focus). The role of the magnetic field is less important here than in our work in generating gain at 182 Å using a CO<sub>2</sub> laser point-focused along the magnetic field axis because of much higher initial electron density for the

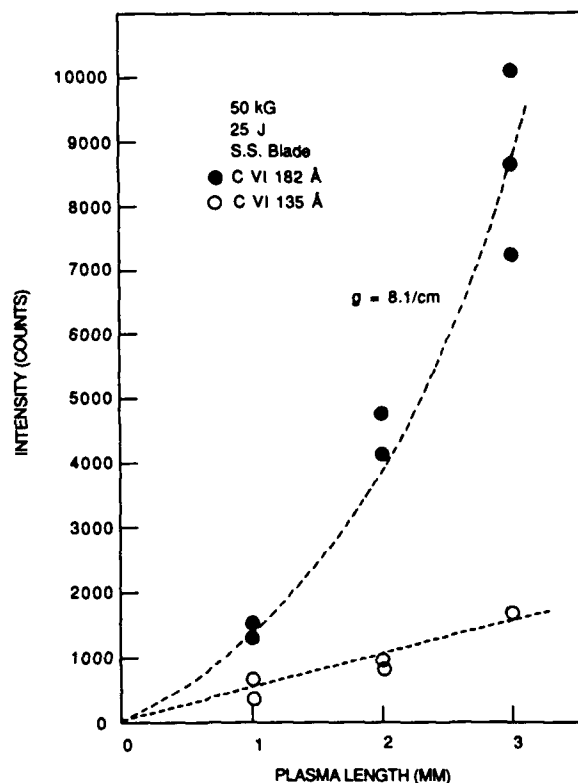


Figure 3. Intensities of C VI 182 and 135 Å vs. the plasma length. Theoretical curve of  $G = 8.1 \text{ cm}^{-1}$  is drawn.

1 μm wavelength Nd/Glass laser than for the 10 μm CO<sub>2</sub> laser. However, in the future, we plan to combine this amplifier with our CO<sub>2</sub> laser-pumped, magnetically confined soft x-ray laser; so, it is necessary that the Nd/glass laser pumped amplifier also work in a magnetic field and have a similar transverse dimension.

In the experiments the 2 in. diameter laser beam was line-focused onto the cylindrical target by the combination of a 67 cm focal length spherical lens and 450 cm focal length cylindrical lens (Figure 1). The dimensions of the line focus were ~ 100 μm by 5 mm. One of features of the target system is the capability of rotating the target so that for every shot a fresh target surface is exposed by the laser. Gain was measured by changing the target length and hence the plasma length, as shown in Figure 1. Another feature was the stainless steel blade 0.8 mm in front of the target. The 0.25 mm thick stainless steel blade is placed 0.8 mm away from the target surface. The function of the blade was to provide an additional cooling source: fully stripped carbon ions in the laser-produced plasma interact with the blade and cool down rapidly through thermal conduction and line radiation. Experiments with a target lacking the stainless steel blade showed signifi-

cantly lower gain. A limited spatial region is selected by a slot in a mask 1.5 cm away from the target in the axial direction and the plasma is viewed through the slot by an axial XUV spectrometer. For the data presented below, the slot size was  $0.8 \times 2$  mm and the near edge of the slot was 0.5 mm away from the target surface. Experiments in which the distance from the edge of the slot to the target surface was varied indicated a favorable condition for high gain in this region.

Figure 2 shows the experimental data recorded with an axial grazing-incidence soft x-ray spectrometer. The intensity dependence of the C VI 135 Å, C VI 182 Å, and C V 186 Å lines with respect to the plasma length are shown. The data were obtained with 25 J laser energy and the stainless steel blade and the slot dimensions as described above. The magnetic field was 50 kG. The plasma lengths were 1, 2, and 3 mm. Emission by iron is clearly seen in the spectra. The 182 Å line from C VI is blended with a similar wavelength line from iron. The line intensity of Fe XI 182 Å is known to be about the same as that of Fe XI 180.4 Å [7], hence, the small contribution of Fe XI 182 Å can be estimated and subtracted.

In Figure 3, the corrected line intensities of C VI 182 Å (integrated over time and frequency) are plotted with respect to the plasma length. The data have been fitted by the formula [8]

$$I \sim \frac{(e^{GL} - 1)^2}{(GLE^{GL})^{\frac{1}{2}}},$$

which describes the output intensity of a Doppler-broadened, homogeneous source of amplified spontaneous emission of gain-length product GL. The theoretical gain curve for  $G = 8.1 \text{ cm}^{-1}$  is drawn. It can clearly be seen that the C VI 182 Å line increases exponentially and the C VI 135 Å line linearly with the plasma length.

### Experiments with Li-like Ions and Computer Simulation

In this section the extension to Li-like ions of experiments with H-like C VI in a CO<sub>2</sub> laser produced magnetically confined plasma is presented. The Li-like sequence has several advantages over H-like sequence. As can be seen in Figure 4, Li-like ions have a lower ionization potential than H-like ions with a comparable lasing wavelength. For example, Si XII has an ionization potential of 523 eV for a  $4f - 3d$  transition at 129 Å, compared to H-like N VII which has an ionization potential of 667 eV for a 3-2 transition at 134 Å. The  $4f - 3d$  transition

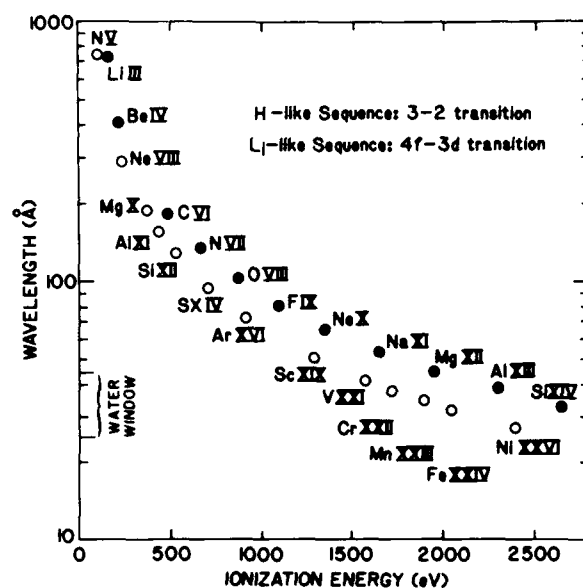


Figure 4. Potential lasing line vs. ionization energy for H-like sequence (3-2 transition) and Li-like sequence ( $4f - 3d$  transition)

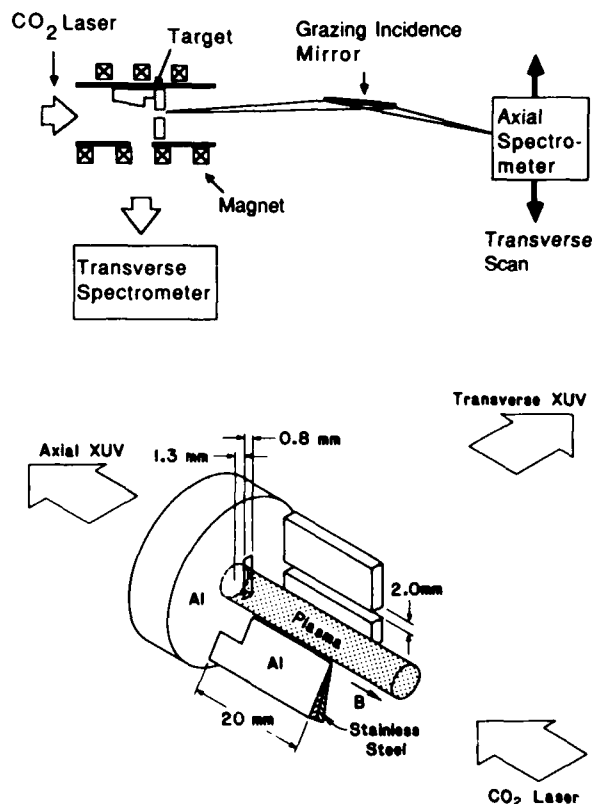


Figure 5. Experimental set-up and target assembly (Al in this case) used in the experiments with Li-like ions



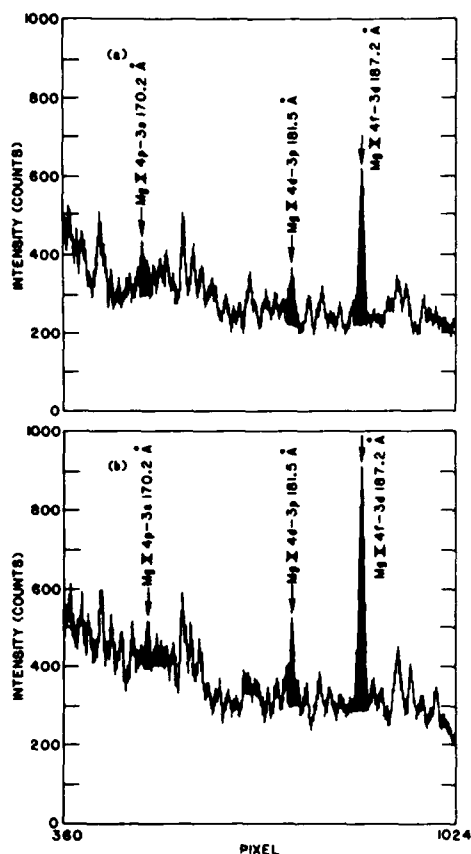


Figure 6. The axial spectra of Mg X in the non-gain region (a) and the gain region (b). The magnetic field strength used was 30 kG.

in Li-like sequence has a scaling of  $Z^{-2.4}$  with an atomic number  $Z$  which is more favorable than  $Z^{-2}$  scaling in H-like sequence. One of important atomic processes that create an population inversion is a fast depopulation process of the lower level. This is the  $L_{\alpha}$  radiative transition in H-like ions or the  $3d \rightarrow 2p$  radiative transition in Li-like ions. While the radiative transition rate in H-like ions scales as  $Z^4$ , the  $3d \rightarrow 2p$  transition in Li-like ions increases faster with  $Z$ ,  $Z^{f(Z)}$  with  $f(Z) > 5$  for  $Z < 30$ . Along the Li-like isoelectronic sequence, a higher gain at a shorter wavelength with a lower pumping laser power can be produced than along H-like isoelectronic sequence. This fact has been exploited in experiments with Al XI by Jaeglé *et al.*[9]

The experimental set-up is shown in Figure 5. A  $\text{CO}_2$  laser ( $\sim 500\text{J}$  in  $\sim 50\text{ nsec}$ ) is focused onto an aluminum or silicon target and creates a highly ionized plasma column confined in a strong axial magnetic field. A composite blade made from a sandwich of aluminum and stainless steel (or silicon and tita-

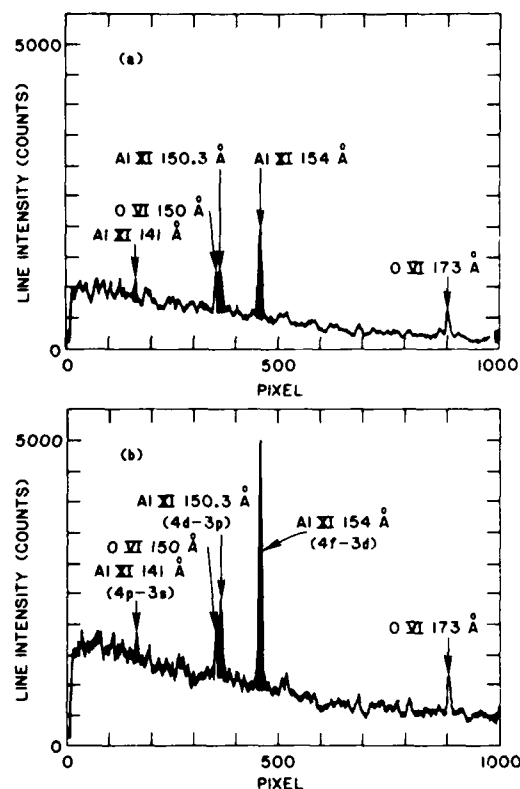


Figure 7. The axial spectra of Al XI in the non-gain region (a) and the gain region (b). The magnetic field strength used was 70 kG.

nium for silicon targets) is attached perpendicularly to the target surface (see Figure 5). The blade helps to create a more uniform plasma in the axial direction along the magnetic field and also provides a way to introduce impurities (stainless steel or titanium in our experiment) for additional cooling. The plasma is viewed in both axial and transverse directions by multichannel soft x-ray spectrometers[10], which produce time-integrated spectra. The axial emission is imaged by a grazing-incidence mirror onto the entrance slit of a multichannel soft x-ray spectrometer as shown in Figure 5. The geometry of the present experimental set-up allows us to adjust the spectrometer to view the  $\sim 200\mu\text{m}$  region with high gain (we refer to this region as the gain region) or the  $\sim 200\mu\text{m}$  region with little or no gain (we refer to this region as the non-gain region). On the spectrum recorded from the gain region, we expect to see the amplification of the potential lasing line by stimulated emission. This effect was clearly shown in the work on H-like CVI where extensive observations of absolute intensity and measurements of absolute divergence were the primary evidence for lasing[6].

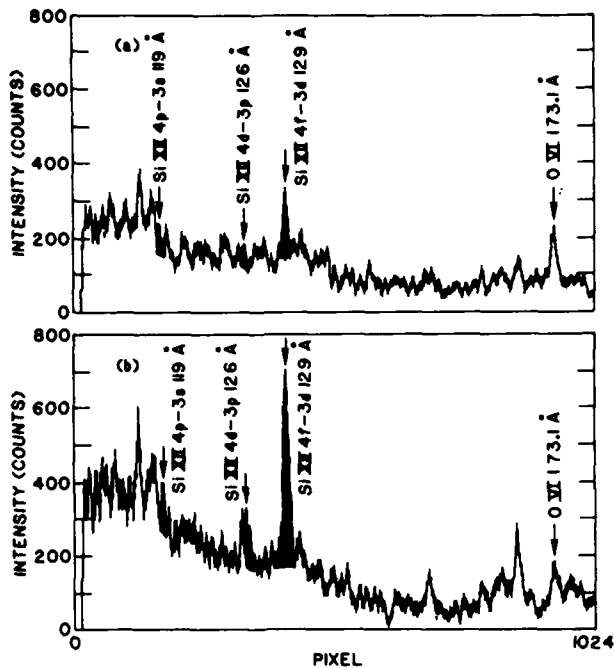


Figure 8. The axial spectra of Si XII in the non-gain region (a) and the gain region (b). The magnetic field strength used was 50 kG.

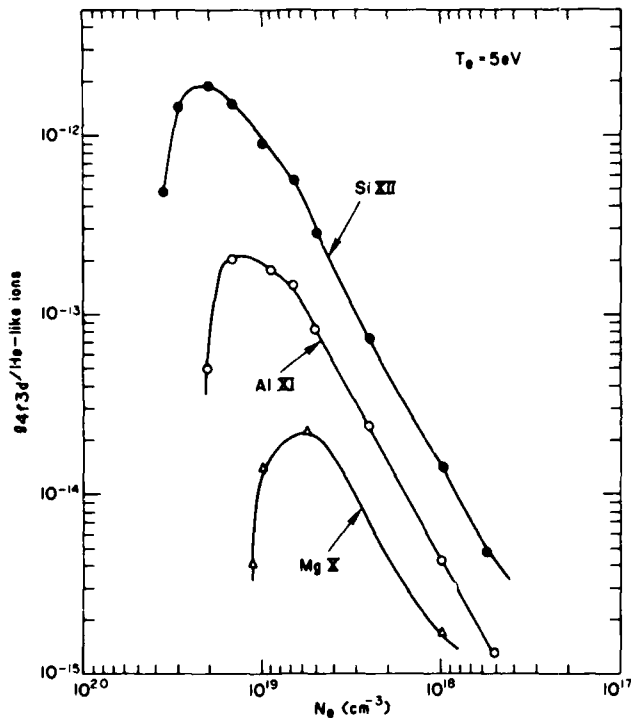


Figure 9. The normalized gain of the 4f-3d transition in Mg X, Al XI and Si XII vs. the electron density at  $T_e = 5$  eV.

Figures 6 - 8 are the spectra of Mg, Al and Si,

respectively, recorded by the axial XUV instrument at two different transverse positions corresponding to the gain and the non-gain regions as described in the previous paragraph. A convenient way of showing the amplification of the 4f-3d transition is to measure the change of the line intensity of this transition relative to that of the 4p-3s transition. This comparison, being based on lines in the same ion from upper levels with the same principal quantum number, is independent of uncertainties in the exact spatial distribution of different kinds of ions viewed by the spectrometer. For Mg case, the ratio of the line intensity of Mg X 187.2 Å to that of Mg X 170.2 Å in Figure 6(a) is 3:1 and the ratio in Figure 6(b) is 5:1. The change of the intensity ratio from one transverse position of the instrument (the non-gain region) to the other (the gain region) is  $5/3 = 1.7$ . The same analysis shows that the change of the ratio is 2.8 for Al case and 1.8 for Si case. This implies that a higher gain medium is created in Al plasma than in Mg and Si plasma. This can be understood with the help of Figure 9 which is produced by the atomic physics code for Li-like ions[11] for various electron densities at a given temperature. Unless the population of the He-like Mg is greater by a factor of about 10 than that of the He-like Al the gain on Mg X 187.2 Å line is not higher than the one on Al XI 154.7 Å line. In experiments, the comparable amounts of He-like Mg and Al might be produced and the better gain characteristic of Al produces a higher gain medium in Al than in Mg. However, in the case of Si, a smaller amount of He-like Si seemed to be produced due to the higher ionization energy of Si so that even though Si XII has a better gain performance than Al XI, a lower gain was observed in Si XII.

A one-dimensional hydro-atomic code[12], originally developed for C VI has been modified for Li-like ions in order to simulate the experiments. The code generated theoretical time-integrated spectra from the same plasma region as viewed by the spectrometers in experiment. Figure 10 shows the axial spectra generated by the computer along with the axial experimental spectra. The experimental spectra is also shown in Figure 7.

As observed in the experimental spectra, the ratio of the 154 Å to 141 Å line intensity is about three times larger in the calculated gain-region spectrum [Figure 10(b)] than in the calculated non-gain-region spectrum [Figure 10(d)] for a model plasma which has a gain-length product of  $GL = 3.7$ . The difference of a factor of 1.7 in the ratio of line intensity of 154 Å to 141 Å between experimental and theoretical spectra could be due to the variation of spectrometers

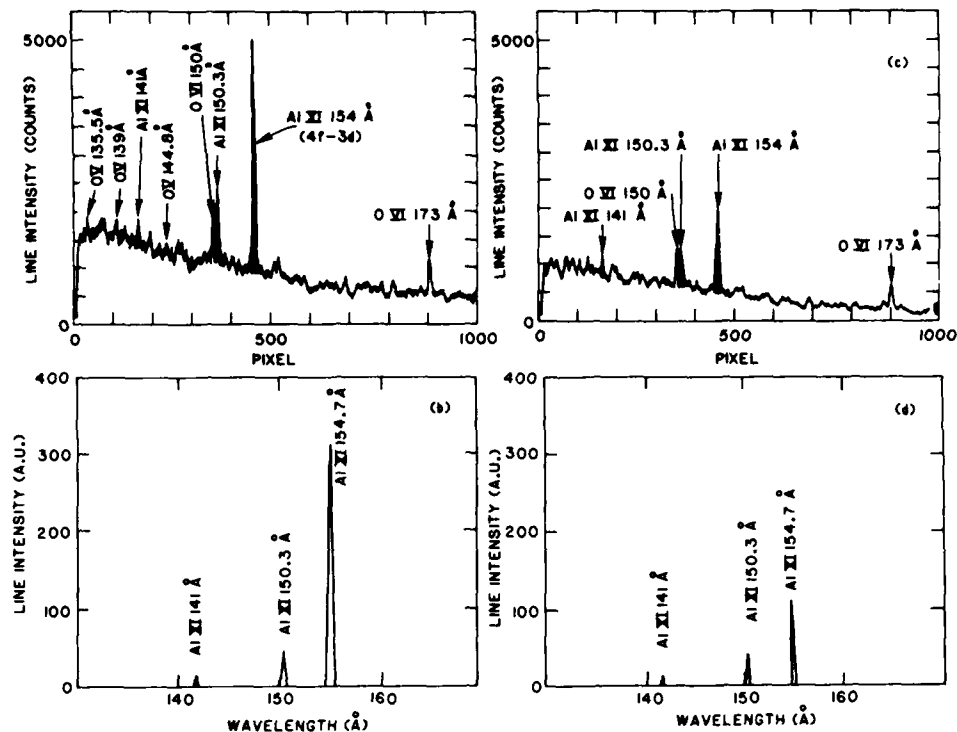


Figure 10. Axial spectra of Al XI; (a) and (c) are experimental data for the gain and the non-gain region, respectively; (b) and (d) are calculated time-integrated axial spectra over the gain region and the non-gain region, respectively.

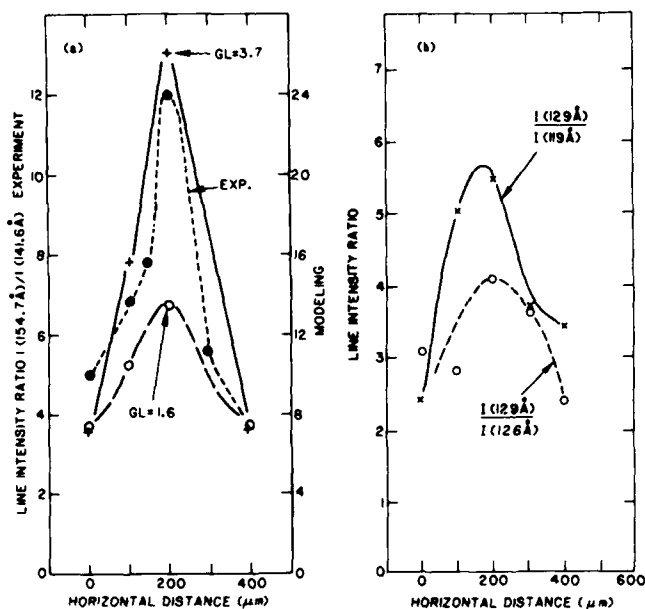


Figure 11. Observed and predicted line intensity ratio versus horizontal position of the axial spectrometer; (a) in Al XI experimental data (solid circle); modeling with peak  $GL = 1.6$  (open circle); modeling with peak  $GL = 3.7$  (cross); (b) observed line intensity ratio in Si XII.

ter detector sensitivity with wavelength. This has, of course, no effect on present results for relative values of line intensities in the gain and the non-gain region.

The experimentally observed change in the ratio of the 154 to 141 Å line intensity with respect to the transverse position of the axial spectrometer is shown in Figure 11(a), along with computational results. The use of the Al XI 150.3 Å line as a reference was avoided for two reasons. The intensity of the Al XI 150.3 Å line is unfortunately blended by the O VI 150.1 Å line. The relative intensities of O VI lines change with plasma conditions as shown in Figure 10(a) and (c) and it is difficult to unconvolute the intensity of the Al XI 150.3 Å line. The computations were performed for two plasma conditions with peak gain-length products  $GL=3.7$  and  $1.6$ , respectively. These two conditions were obtained by changing the amount of impurity, iron in our case, while maintaining a constant laser input energy. It can be seen that there is a good agreement between the shape of the curves for  $GL=3.7$  and the experimental data. The same analysis was done for cases of Mg and Si, where good agreements were observed for both Mg and Si for a  $GL=1.6$  model plasma.

## Future Development

Work to obtain the lasing action shorter wavelengths along the H-like or Li-like isoelectronic sequence is planned using the recombination scheme. The two laser approach[13] using the Kr- or Ar-like sequence is also underway. Meanwhile the work to combine the amplifier presented in this paper with the presently operating C VI 182 Å laser will be carried out to increase the output energy for application to x-ray microscopy.

## Acknowledgements

We thank H. Furth and W. Tighe for very helpful discussions. We greatly acknowledge G. Drozd, D. Diccio, A. Schuessler, J. Schwarzmann, and B. Micholvic for their technical support of making the new system and providing the length-varying cylindrical target.

This work was supported by the U.S. Department of Energy, Advanced Energy Projects of Basic Energy Sciences, the U.S. Air Force Office of Scientific Research.

† Also at Dept. of Mechanical and Aerospace Engineering, Princeton University

## References

1. L. I. Gudzenko and L. A. Shelepin, Sov. Phys. JEPT **18**, 998 (1964).
2. F. E. Irons and N. J. Peacock, J. Phys. B **7**, 1109 (1974).
3. R. J. Dewhurst, D. Jacoby, G. J. Pert, and S. A. Ramsden, Phys. Rev. Lett. **37**, 1265 (1976).
4. S. Suckewer and H. Fishman, J. Appl. Phys. **51**, 1922 (1980).
5. S. Suckewer, C. H. Skinner, H. Milchberg, C. Keane, and D. Voorhees, Phys. Rev. Lett. **55**, 1753 (1985).
6. S. Suckewer, C. H. Skinner, D. Kim, E. Valeo, D. Voorhees, and A. Wouters, Phys. Rev. Lett. **57**, 1004 (1986).
7. R. L. Kelly and L. J. Palumbo, in *Atomic and Ionic Emission Lines Below 2000 Angstroms; Hydrogen through Krypton*, NRL Report 7599, 1973.
8. G. J. Linford, E. R. Peressini, W. R. Sooy, and M. L. Spaeth, Appl. Opt. **13**, 379 (1974).
9. P. Jaeglé, G. Jamelot, A. Carillon, A. Klisnick, A. Sureau, and H. Guennou, J. Opt. Soc. Am. B **4**, 563 (1987) and references therein.
10. J. L. Schwob, A. Wouters, and S. Suckewer, Rev. Sci. Instrum. **58**, 1601 (1987).
11. D. Kim, C. H. Skinner, A. Wouters, E. Valeo, D. Voorhees, and S. Suckewer, PPPL-2502 (1988); to be published in J. Opt. Soc. Am. B.
12. E. Valeo, C. Keane, and R. M. Kulsrud, Bull. Am. Phys. Soc. **30**, 1600 (1985).
13. S. Suckewer, C. H. Skinner, C. Keane, D. Kim, J. L. Schwob, E. Valeo, D. Voorhees, and A. Wouters, in Proceedings of the First International Laser Science Conference. Dallas, Texas, 18-22 Nov., 1985.

# Calculation and Design of Ni-Like W Soft X-Ray Lasers<sup>†</sup>

S. Maxon, S. Dalhed, P. Hagelstein\*,  
B. MacGowan, R. London, and M. Rosen  
Lawrence Livermore National Laboratory  
P. O. Box 5508, Livermore, CA 94550, USA  
(415) 422-4091

## SUMMARY

Gain on 0-1 transitions has now been demonstrated in Ni-like  $\text{Eu}^{1,2}$  and  $\text{Yb}^3$  using targets between 60 and 100  $\mu\text{g}/\text{cm}^2$ . The intensities of the input laser were  $7 \times 10^{13} \text{ W}/\text{cm}^2$  (Eu) and  $1.4 \times 10^{14} \text{ W}/\text{cm}^2$  (Yb). The measured gain coefficient on the 71Å (Eu) and the 50.3Å line (Yb) was  $1 \text{ cm}^{-1}$ . Using a modified version of the Lagrangian hydrodynamics code LASNEX together with the kinetics code XRASER, the calculated gains are in reasonable agreement with experiment.<sup>2</sup>

In Ni-like W, the leading 0-1 transition has the wavelength 43.11Å. 1D calculations for 90  $\mu\text{g}/\text{cm}^2$  targets irradiated by a 3ω Gaussian pulse show an increase in the gain coefficient from 1 to  $2.6 \text{ cm}^{-1}$  as the intensity is increased from  $2.2 \times 10^{14}$  to  $2.6 \times 10^{14} \text{ W}/\text{cm}^2$ . The electron temperature, at the peak of the input pulse, increases from 0.8 to 0.95 keV.

A more dramatic effect is seen by using square pulses (3ω). The gain coefficient increases from 2 to  $6 \text{ cm}^{-1}$  when the intensity

is increased from  $1.8 \times 10^{14}$  to  $2.2 \times 10^{14}$  W/cm<sup>2</sup>. The electron density for the square pulse is a factor 2.5-3.0 times larger than the gaussian pulse.

The modified version of LASNEX which was used to run these problems radiates more energy producing lower temperatures in the plasma.

†Work performed under the auspices of the U.S. Department of Energy by the Lawrence Livermore National Laboratory under contract number W-7405-ENG-48.

\*Research Laboratory of Electronics, Massachusetts Institute of Technology, Cambridge, Massachusetts 02139

1. B. J. MacGowan, et.al., Phys. Rev. Lett. 59, 2157 (1987).
2. S. Maxon, et.al., Phys. Rev. A 37, 2227 (1988).
3. B. J. MacGowan, et.al., J. Opt. Soc. Am. B, to be published.

# Quantum-Mechanical Interference in Four-Wave Mixing

P. B. Chapple, K. G. H. Baldwin, and H.-A. Bachor

*Laser Physics Centre, Australian National University  
GPO Box 4, Canberra ACT 2601, Australia*

## ABSTRACT

Interference between two different quantum-mechanical pathways for 4 wave mixing in sodium vapor has been observed. The 4 wave mixing was enhanced by 2-photon resonance with the  $5s$  state, for one pathway, and the  $4d$  state, for the other. The phase of the interference could be varied continuously by varying laser frequencies, and constructive and destructive interference effects were studied. A model based on third-order perturbation theory gives a good description of the features observed.

## INTRODUCTION

Whenever a state can be coherently excited to another state by two or more different pathways, the complex amplitudes for the different processes must be added together, leading to constructive and destructive interference effects. We report here a novel 4 wave mixing experiment in which UV light was generated in sodium vapor via two different pathways, involving resonant enhancement from two different states. By appropriate choices of laser wavelengths, the processes could be driven separately or together. When they were driven together, both constructive and destructive interference effects were observed.

Recently there has been much interest in interference between, firstly, the atomic polarizations driven by laser light which is supplied to a nonlinear medium, and, secondly, those driven by light which is produced in the medium itself.<sup>1-5</sup> The effects reported here are simpler in that they involve only polarizations induced by the input laser fields. In fact the two interfering pathways are very similar, the only difference being the different resonances which were used to enhance the 4 wave mixing. Light at a wavelength of 195.5nm was generated by the action

of two photons of a red field at 602.2nm (frequency  $\omega_1$ ) and one photon of a green field at 557.0nm (frequency  $\omega_2$ ). The 4 wave mixing at  $2\omega_1 + \omega_2$  was resonantly enhanced by either (fig. 1): (i) a 2-photon resonance ( $2\omega_1$ ) with the  $5s_{1/2}$  state; or (ii) a 2-photon resonance ( $\omega_1 + \omega_2$ ) with the  $4d_{3/2}$  and  $4d_{5/2}$  states (which were unresolved in this experiment). The 4 wave mixing signal was recorded as a function of the red and green wavelengths in the vicinity of these 2-photon resonances.

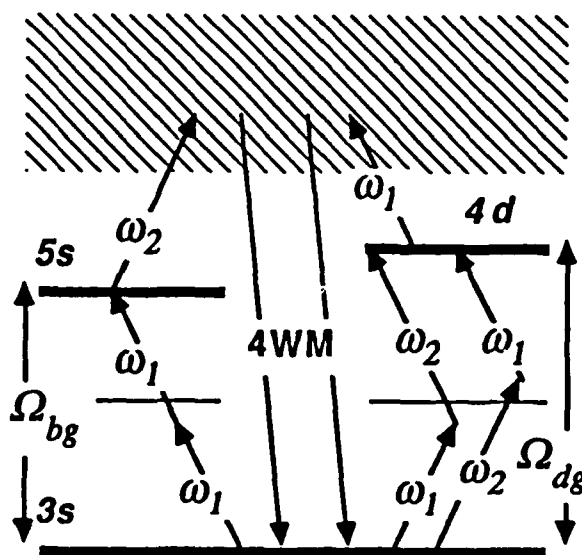


FIG. 1. Excitation pathways for the principal 2-photon-resonant, 4 wave mixing processes in this experiment.

## THEORETICAL MODEL

If the input fields have the same linear polarization, the lowest order (third-order) of perturbation theory which can describe the atomic polarization gives:

$$P^{(3)}(2\omega_1 + \omega_2) = \epsilon_0 \chi^{(3)}(-2\omega_1 - \omega_2; \omega_1, \omega_1, \omega_2) E(\omega_1)^2 E(\omega_2) \quad (1)$$

where the third-order susceptibility  $\chi^{(3)}(-2\omega_1 - \omega_2; \omega_1, \omega_1, \omega_2)$  can be written as the sum of two-photon resonant terms:

$$\chi^{(3)}(-2\omega_1 - \omega_2; \omega_1, \omega_1, \omega_2) = \frac{1}{\epsilon_0} \sum_{gbc} N_g \left[ \sum_b \frac{\mu_{gc} \mu_{cb} \mu_{bg} \mu_{gg}}{\Omega_{bg} - 2\omega_1 - i\Gamma_b} \cdot \frac{1}{\Omega_{cg} - \omega_1} \left( \frac{1}{\Omega_{cg} - 2\omega_1 - \omega_2} + \frac{1}{\Omega_{cg} + \omega_2} \right) \right. \\ \left. + \sum_d \frac{\mu_{gc} \mu_{cd} \mu_{dg} \mu_{gg}}{\Omega_{cg} - (\omega_1 + \omega_2) - i\Gamma_d} \left( \frac{1}{\Omega_{cg} - \omega_1} + \frac{1}{\Omega_{cg} - \omega_2} \right) \left( \frac{1}{\Omega_{cg} - 2\omega_1 - \omega_2} + \frac{1}{\Omega_{cg} + \omega_2} \right) \right]$$

Here the indices  $g, b$  and  $d$  stand for the degenerate components of the  $3s, 5s$  and  $4d$  states of sodium respectively (or almost degenerate components, if allowance is made for the fine and hyperfine splittings). These components must be summed over, to give the total resonant contribution to the nonlinear susceptibility. The sum over all odd parity states  $a$  and  $c$  accounts for the contribution of other states to the four wave mixing process, and includes an integral over the continuum states. The  $N_g$  values are the ground state atomic number densities, the  $\mu_{ij}$  values are electric dipole matrix elements in the direction of the applied fields, and  $\Omega_{ij}$  values are frequency intervals between states  $i$  and  $j$ .  $\Gamma_b$  and  $\Gamma_d$  determine the linewidths of the two-photon resonances.

If fine and hyperfine splittings are insignificant, then the polarization can be written simply as

$$P^{(3)}(2\omega_1 + \omega_2) = \frac{a_1}{\Omega_{bg} - 2\omega_1 - i\Gamma_b} + \frac{a_2}{\Omega_{dg} - (\omega_1 + \omega_2) - i\Gamma_d} \quad (2)$$

where the values  $a_1$  and  $a_2$  incorporate the dipole matrix elements and the nonresonant detunings. Since the laser frequencies are close to 2-photon resonance and  $\Gamma_b$  and  $\Gamma_d$  are small,  $a_1$  and  $a_2$  are regarded as being independent of frequency.  $P(2\omega_1 + \omega_2)$  does not include any linear polarization due to  $E(2\omega_1 + \omega_2)$  (small signal limit). The 4 wave mixing signal  $S$  is proportional to

$$S \propto |P(2\omega_1 + \omega_2)|^2 = \left| \frac{a_1/2}{(\Omega_{bg}/2 - \omega_1 - i\Gamma_b/2)} + \frac{a_2}{(\Omega_{dg} - \omega_1 - i\Gamma_d)} \right|^2 \quad (3)$$

The profile of  $S$  as a function of  $\omega_1$ , according to this

simple perturbative model, is thus the sum of two Lorentzians, plus an interference term. The two resonant frequencies are  $\Omega_{bg}/2$  and  $\Omega_{dg} - \omega_2$ . The two terms on the right-hand side of equation (3) may add together to produce constructive or destructive interference.

It is necessary to incorporate the effects of Doppler broadening of the 2-photon resonances by replacing their terms in equation (2) by convolutions with Doppler profiles. Further corrections are made by allowing for the fine structure splitting of the  $4d$  state (1.028 GHz), and the hyperfine splittings of the  $3s$  state (1.772 GHz) and the  $5s$  state (0.150 GHz).<sup>6</sup> Hyperfine splitting of the  $4d$  state is insignificant.

The 4 wave mixing signal produced is again proportional to  $|P(2\omega_1 + \omega_2)|^2$ . This theory is valid when the laser powers are low enough for third-order perturbation theory to give a correct description. When effects such as ac Stark shifting, saturation of resonances, self-focussing or nonlinear absorption of the input beams become significant, a considerably more complicated theory is required<sup>1,7-10</sup>.

## EXPERIMENT

The sodium was rf-heated in a stainless steel cell, under 25mbar of argon. Using hook interferometry,<sup>11</sup> the sodium density was determined to be  $3 \times 10^{14} \text{ cm}^{-3}$ , and the vapor length was 80mm. The two excimer-pumped dye lasers used Rhodamine 6G for the 602.2 nm beam and Coumarin 153 for the 557.0 nm beam. Each produced up to 30 mJ in ~20ns within a 1.2 GHz bandwidth. The beams were combined using a dispersing prism. The UV signal beam (collinear with the input beams) was separated using a Pellin-Broca prism, a UV-transmitting filter and a monochromator. The results presented here were obtained using unfocussed laser beams to reduce the complications which occur at high intensities. The central beam intensity in the cell was  $600 \text{ kW cm}^{-2}$  for the red beam, with 0.65 mJ per pulse in the cell, and  $1.4 \text{ MW cm}^{-2}$  for the green beam, with 2.7 mJ per pulse in the cell. The maximum signal produced at 195.5nm under these conditions was of the order of  $5 \times 10^{-15} \text{ J}$ .

## RESULTS AND DISCUSSION

Fig. 2 shows the recorded 4 wave mixing signal around 195.5nm, consisting of data obtained in a sequence of scans of the red laser frequency  $\omega_1$ . A slightly different green laser frequency  $\omega_2$  was chosen for each sequential scan. The larger peak, corresponding to the resonance  $\omega_1 = \Omega_{bg}/2$ , occurs in the same place for all of the scans, whereas the position of the smaller peak, for the resonance  $\omega_1 = \Omega_{dg} - \omega_2$ , depends on the green laser frequency.



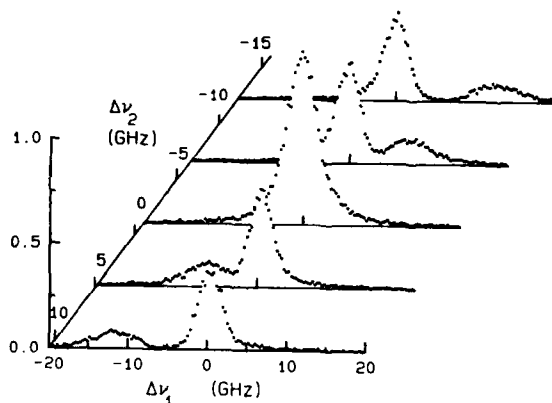


FIG. 2. Three-dimensional plot of the four wave mixing signal, in arbitrary units.  $\Delta\nu_{red}=0$  when  $\omega_1 = \Omega_{bg}/2$ , and  $\Delta\nu_{green}=0$  when  $\omega_2 = \Omega_{dg} - \Omega_{bg}/2$ .

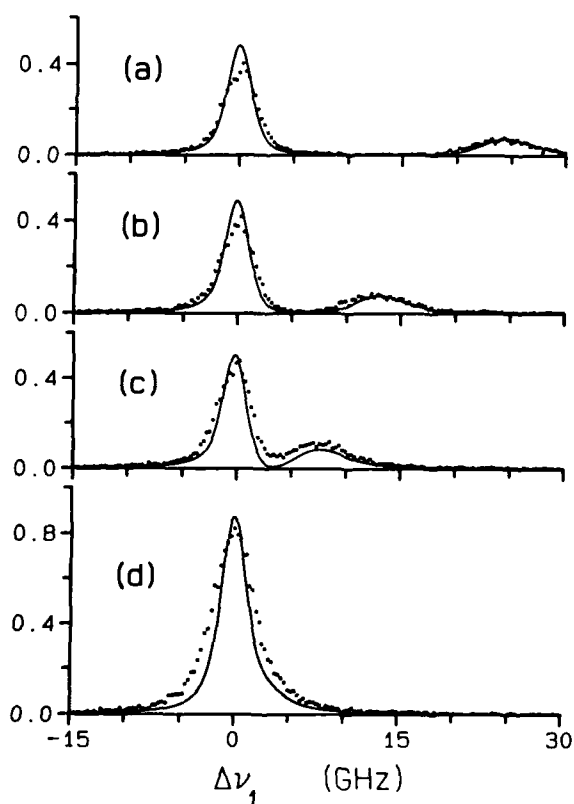


FIG. 3. Comparison of results (points) with theory (solid curves) for the 4 wave mixing output (arbitrary units) as a function of  $\omega_1$  (red laser). The green laser detuning  $\Delta\nu$  is  
(a)  $\Delta\nu = -1 \text{ GHz} - 4\delta$ , where  $\delta = 5.80 \text{ GHz}$   
(b)  $\Delta\nu = -1 \text{ GHz} - 2\delta$ . (c)  $\Delta\nu = -1 \text{ GHz} - \delta$   
(d)  $\Delta\nu = -1 \text{ GHz}$ .

Fig. 3 shows some of the red laser scans plotted with theoretical curves. The transverse damping terms  $\Gamma_b$  and  $\Gamma_d$  were calculated<sup>12</sup> to be give full collisional linewidths of 1.11 GHz and 0.98 GHz. From the number density measurement, a vapor temperature of 290 °C was inferred. The values  $a_1$  and  $a_2$  were determined by requiring that the peaks in the theoretical curve of Fig. 3 (a) have the same areas as the experimental ones. The ratio  $a_1/a_2$  was assumed to be real and positive, which agrees well with the experimental findings.

Constructive interference is clearly demonstrated in Fig 3(d), in which the peak height is greater than the sum of the peak heights of Fig 3 (a), for both theory and experiment. Destructive interference can be seen in Fig. 3 (b), in which the wings of the peaks have been suppressed slightly between the peaks. The observed profiles were slightly broader than the theoretical ones, probably because the effects of the nonzero laser bandwidths and the short duration of the pulse were not accounted for. Overall, however, the agreement between theory and experiment was good.

In order to check on the existence of competition and saturation effects, two other simultaneous emission processes were studied, using the same method of detection. Firstly, third harmonic generation due to the red laser, two-photon resonant with the 5s state, produced radiation at 200.8nm. This signal was found to have no dependence on the green laser beam. Secondly, 4 wave mixing produced radiation at  $\omega_1 + 2\omega_2$  (190.5nm), two-photon resonant with the 4d state. There was no evidence that this process varied when the red laser was two-photon resonant with the 5s state. These findings indicated that the different processes did not affect each other, giving some justification for the use of lowest order of perturbation theory in our discussion. In observations made at higher intensities, achieved by focussing the laser beams in the sodium vapor, saturation phenomena and the power broadening of peaks were observed. These were not evident in the case of unfocussed beams.

## CONCLUSION

In this work, a novel experiment was performed, in which two different quantum-mechanical pathways for 4 wave mixing in sodium vapor interfered with one another. Moreover, by varying the frequencies of the laser beams involved, the phase of this interference was varied continuously. In particular, constructive and destructive interference effects were observed. The pathways could also be isolated from one another to remove the interference. For low laser intensities, a simple theoretical model based on third-order perturbation theory gives a good description of the features observed. At higher intensities, saturation and other higher order processes make the situation considerably more complicated.

We wish to acknowledge the support of the Australian Research Grants Scheme.

## References

1. H. Kildal and S. R. J. Brueck, "Pump Depletion and Saturation of Two-Photon Resonant Third-Harmonic Generation Processes," *IEEE J. Quantum Electron.* **16**, 566-573 (1980).
2. J. C. Miller, R. N. Compton, M. G. Payne, and W. W. Garrett, "Resonantly Enhanced Multiphoton Ionization," *Phys. Rev. Lett.* **45**, 114-116 (1980).
3. J. J. Wynne, "Polarization Renormalization Due to Nonlinear Optical Generation," *Phys. Rev. Lett.* **52**, 751-754 (1984).
4. R. W. Boyd, M. S. Malcuit, D. J. Gauthier, and K. RzaKzewski, "Competition between amplified spontaneous emission and the four-wave-mixing process," *Phys. Rev. A* **35**, 1648-1658 (1987).
5. J. J. Wynne, "Nonlinear Optical Balance," in *Multiphoton Processes: Proceedings of the 4th International Conference on Multiphoton Processes, Boulder, Colorado, 1987*, edited by S. J. Smith and P. L. Knight, Cambridge University Press, Cambridge, U.K. (1988), pp. 318-327.
6. G. Grynberg and B. Cagnac, "Doppler-free multiphotonic spectroscopy," *Rep. Prog. Phys.* **40**, 791-841 (1977).
7. J. N. Elgin and G. H. C. New, "Semi-classical theory of two-photon resonant third-harmonic generation," *Opt. Commun.* **16**, 242-246.
8. A. T. Georges, P. Lambropoulos, and J. H. Marburger, "Theory of third-harmonic generation in metal vapors under two-photon resonance conditions," *Phys. Rev. A* **15**, 300-307 (1977).
9. P. M. Radmore and P. L. Knight, "Two-photon ionisation: interference and population trapping," *Phys. Lett.* **102A**, 180-185 (1984).
10. Z. Deng, "Line narrowing and photoelectron trapping in multiphoton ionization spectroscopy," *J. Opt. Soc. Am. B* **1**, 874-878 (1984).
11. M. C. E. Huber and R. J. Sandeman, "The measurement of oscillator strengths," *Rep. Prog. Phys.* **49**, 397-490 (1986).
12. F. Biraben, B. Cagnac, E. Giacobino, and G. Grynberg, *J. Phys. B* **10**, "Broadening and shift of the sodium 3S-4D and 3S-5S two-photon lines perturbed by noble gas," 2369-2374 (1977).

# Transversely Optically Pumped Ultraviolet Laser in the Range of 330-390 nm

Junhua Yu, Shangwen Sun, Yongkang Cheng, Chen Tang, and Zuguang Ma

*Institute of Opto-Electronics, Harbin Institute of Technology, Harbin, China*

## Abstract

A series of six laser lines at 330-390 nm on the  $B^3\Sigma^- \rightarrow X^3\Sigma^-$  transition in sulfur dimer vapor transversely-pumped by a XeCl laser at 308.1 nm was first observed and the corresponding absorption coefficient and small signal gain coefficient were measured. The mean gain is about  $0.30 \text{ cm}^{-1}$ .

## 1. Introduction

Sulfur dimer laser due to its high efficient, low pumping threshold and broad distributed spectrum was attractive as a blue-green laser for ocean-optics<sup>[1,2,3]</sup> but it is also a promising candidate for an efficient ultraviolet laser system. The shortest wavelength of UV lasing on the  $B \rightarrow X$  transition in  $S_2$  at 365 nm was achieved by S. R. Leone and K. G. Kosnik.

We realized the anticipated extending of the  $S_2$  UV lasing region towards the shorter wavelength for about 35 nm, while a XeCl excimer laser transversely pumped the T-shaped quartz cell with a plane-plane cavity. There are six UV lasing bands, spread in the range of 330-390 nm with corresponding peak wavelengths 330.92 nm, 337.73 nm, 340.18 nm, 344.81 nm, 353.16 nm and 380.42 nm. To verify the possibility to lase in near UV region for  $S_2$ , we measured the absorption coefficient and the small signal gain coefficient. And it was found that the gain coefficient is always larger than absorption coefficient in the above-mentioned UV spectral region. The mean value of gain coefficient in the whole UV region is about  $0.30 \text{ cm}^{-1}$ .

## II. Experiment

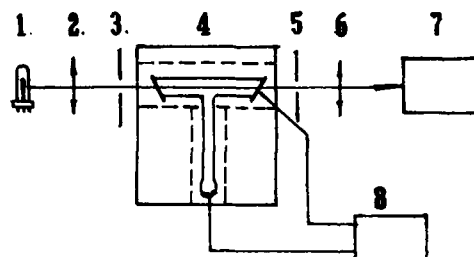


Fig.1 Setup for measuring absorption coefficient

1. Deuterium lamp 2. Spherical quartz lens ( $f=76.6\text{mm}$ ) 3, 5. Iris 4. T-shaped quartz cell 6. Cylindrical quartz lens ( $f=190\text{mm}$ ) 7. OMA-II 8. Temperature controller

Fig.1 shows the scheme of experiment set-up for measuring absorption coefficient of  $S_2$ . A Deuterium lamp was used as a cw light source at 190-500 nm. The spherical lens with a focal distance of 76.6 mm converts the point light source located in its focus into parallel light beam. The back iris may increase coaxiality of output beam. The emitted beam from the  $S_2$  cell via a cylindrical quartz lens is focused into the incident slit of the OMA-II polychromator. At 620°C in the high-temperature heating zone and at 180-230°C in the low-temperature heating zone the measured absorption coefficient of  $S_2$  can be expressed in the formula as follows,

$$\alpha(\lambda, T) = (1/L) \ln [I(\lambda, T_0) / I(\lambda, T)]$$

where  $I(\lambda, T_0)$  is the initial light intensity of the Deuterium lamp through the

cell which is heated at 115°C for reducing the influence of other gases in our experiment.  $I$  is the intensity of the lamp via the absorption medium.

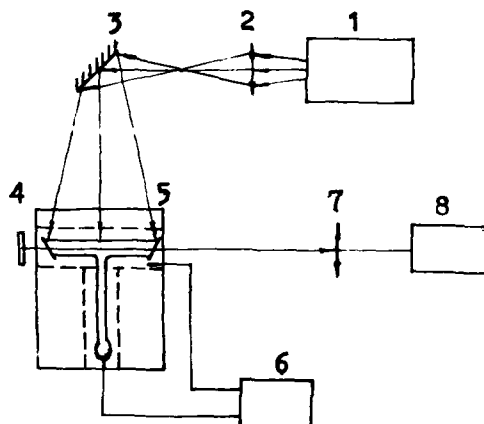


Fig. 2 Setup for gain measurement by the ASE technique of reflector-type  
1. EMG 201 MSC excimer laser 2. Cylindrical lens 3. Reflective mirror for 308.1nm 4. Al-coated reflector 5. T-shaped quartz cell 6. Temperature controller 7. Cylindrical lens 8. OMA-II

Fig. 2 illustrates the scheme of experimental setup for measuring small signal gain coefficient of  $S_2$  by means of amplified spontaneous emission (ASE) technique of reflector-type due to the high gain and the easy produced ASE in  $S_2$ . Using XeCl excimer laser as a pumping source and subtracting each other the light intensities with and without the pumping measured by OMA-II, while the aluminum coated reflector was covered, a single-pass intensity  $I_1$  is obtained without background noise. And in the same way, a round-trip intensity  $I_{21}$  with reflector of  $R=90\%$  is obtained. Substituting two values of  $I_1$  and  $I_{21}$  into the equation,

$$G_s(\nu) = (1/l) \ln [I_{21} / I_1 - 1] / R$$

where  $l$  is the active length of  $S_2$ . The small signal gain coefficient of  $S_2$  can also be calculated.

Fig. 3 demonstrates the scheme of  $S_2$  laser experimental setup for realization and measurement of UV laser oscillation on the  $B^2\Sigma_u^- \rightarrow X^2\Sigma_g^-$  transition. The transverse size of the pump beam from the XeCl excimer laser at 308.1 nm with a bandwidth of 3nm and pulse-duration of 28ns via two-cylindrical lenses is expended into  $l=16$  cm on the axis of the  $S_2$  cell. The output laser beam generated in the

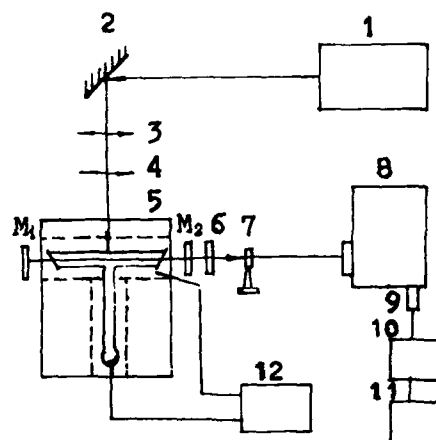


Fig. 3 Setup for realization and measurement of  $S_2$  UV laser oscillation on  $B \rightarrow X$  transition.  
1. EMG 201 MSC excimer laser 2. Reflective mirror 3, 4. Cylindrical lenses 5. T-shaped quartz cell 6. Neutral attenuator 7. Optical cable 8. SPEX monochromator 9. PMT(RCA 8852) 10. BOXCAR 11. X-Y recorder 12. Temperature controller

plane-plane cavity with an output coupler transmissivity of 50% and passing through neutral attenuators and optical quartz cable probe leads on to the slit of SPEX 1870 scanning monochromator calibrated by a He-Ne laser and then is detected by the PMT RCA 8852, processed by BOXCAR and recorded by a chart recorder.

### III. Results and discussion

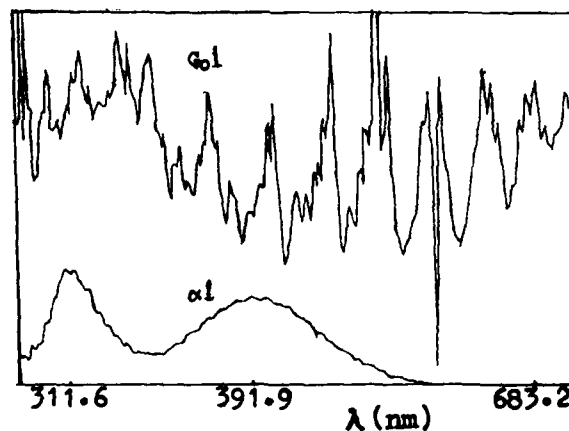


Fig. 4 Dependence of single-pass absorption and gain of  $S_2$  on the wavelength.

Fig. 4 shows the measured dependence of single-pass absorption and gain of  $S_2$  on the scanned wavelength at 600°C in the high-temperature zone and 220°C in the

low-temperature zone under the same pumping condition. From Fig.4, it can be seen that there exist two absorption peaks near 311.6 nm and 391.9 nm. The appearance of the latter results from the trimer  $S_3$ . This conclusion is also verified by the theoretical calculation. In point of absorption coefficient, it is more suitable to select the pumping wavelength corresponding higher absorption coefficient in the range of absorption spectrum. In our experiment, the  $\lambda=308.1$  nm corresponds to  $\alpha=0.083 \text{ cm}^{-1}$ . From the absorption spectrum we obtained absorption coefficient  $\alpha=0.026-0.052 \text{ cm}^{-1}$  at 290-305 nm and  $\alpha=0.034 \text{ cm}^{-1}$  at 337.1 nm. Therefore, using the XeCl excimer laser at 308.1 nm as pumping source is more efficient than the doubled-frequency dye laser and the  $N_2$  laser at 337.1 nm. The mean value of measured small signal gain coefficient in the UV spectral range is about  $0.30 \text{ cm}^{-1}$ .

Fig.5 shows the six-band UV laser spectrum on the B $\rightarrow$ X transition of  $S_2$ , which has threshold effect and optical cavity effect with laser intensity stronger than the fluorescence one by a factor of 1000. In this experiment the pumping wavelength of 308.1 nm with a bandwidth of 3 nm is very close to the resonant exciting wavelength on the X $\rightarrow$ B transition from the ground state  $X^3\Sigma_g^-, v''=1$  to the excited state  $B^3\Sigma_g^-, v'=4$  and from the  $X^3\Sigma_g^-, v''=2$  to the  $B^3\Sigma_g^-, v'=5$ . From the references 6 and 7, it can be concluded that at pumping wavelength of 308.1 nm with a bandwidth of 3 nm the stimulated absorption occurs between vibration-rotational levels as follows,  $X^3\Sigma_g^-, v''=1, J'' > 17$  and  $B^3\Sigma_g^-, v'=4, J' > 16$ ;  $X^3\Sigma_g^-, v''=2, J'' < 29$  and  $B^3\Sigma_g^-, v'=5, J' < 30$ . And the UV lasing occurs on the B $\rightarrow$ X transition from the higher rotational levels of vibrational level  $v'=4$  and the lower rotational levels of the vibration level  $v'=5$  to some of the vibration-rotational levels of the ground state. It means that every vibration transition contains a series of rotational transitions. The origins of six UV laser bands are listed in the Tab.1.

From Tab.1 and Fig.5, it is obvious that the value of the F-K factor corresponding to six UV bands are considerably large and the intensity of the laser output originated from the transitions  $v'=4 \rightarrow v''=10, 7, 6, 5$  are stronger than that from the transitions  $v'=5 \rightarrow v''=6, 5$  as a result of more population stored in the vibrational level of  $v'=4$  than the  $v'=5$ .

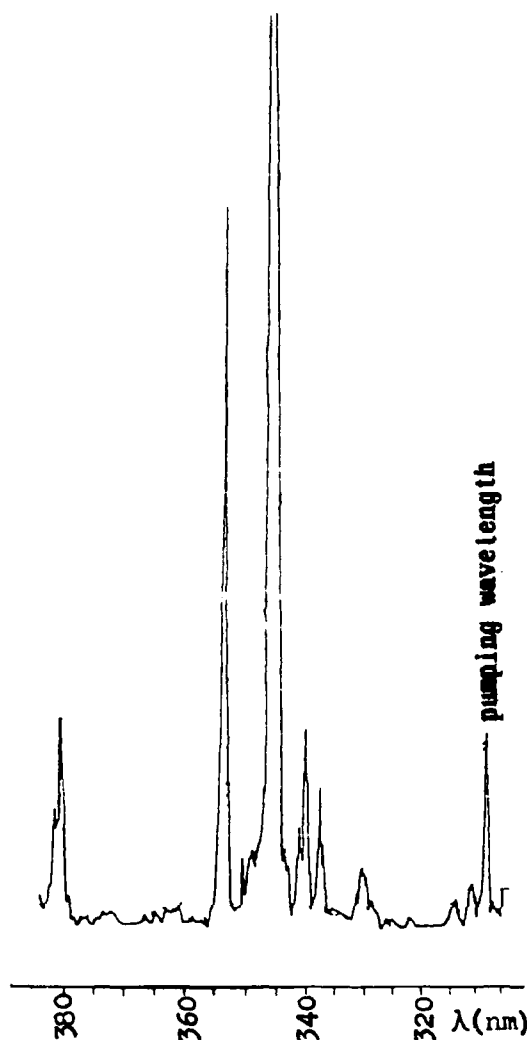


Fig.5  $S_2$  UV laser spectrum on the B $\rightarrow$ X transition

Table 1 Origins of the  $S_2$  six UV laser bands

Peak Wavelength(nm)		Laser transition	F-C Factors
Expt.	Calc.		
380.42	379.76	$v'=4 \rightarrow v''=10, 43 > J > 35$	0.062
353.16	352.74	$v'=4 \rightarrow v''=7, 55 > J > 33$	0.054
344.81	344.20	$v'=4 \rightarrow v''=6, 53 > J > 29$	0.061
340.18	338.72	$v'=5 \rightarrow v''=6, 28 > J > 13$	0.059
337.73	337.58	$v'=4 \rightarrow v''=5, 52 > J > 30$	0.011
330.92	330.76	$v'=5 \rightarrow v''=5, 20 > J > 5$	0.043

#### References

1. S. R. Leone and K. G. Kosnik, Appl. Phys. Lett., 30(7), 346(1977)
2. J. P. Girardeau-Montaut and G. Moreau, Appl. Phys. Lett., 36(7), 509(1980)
3. Yu Junhua, Sun Shangwen, Cheng Yongkang, Zhou Li and Ma Zuguang, Chinese J. Lasers, 15(2), 112(1980)

4. Ma Zuguang et al, Experimental Methods on Lasers(Chinese), 1987
5. K. A. Meyer and D.R. Crostey, J. Chem. Phys., 59(6), 3153(1973)
6. K. Kitten, IEEE J. Quant. Electron., QE-19, 1203(1983)
7. Zhou Li, MS Thesis (1986)

Spectra of Lead, Bismuth, Thorium and Uranium Relevant To A Neodymium-Like Soft X-ray Lasing Scheme, W.L. Hodge, High Energy Laser Associates, 6114 LaSalle Ave Oakland, Ca. 94611 Phone: (415) 658-8586, P.C. Filbert, D.A. Kohler, C.L. Navoda, and J.D. Perez, Applied Physics Laboratory, Palo Alto Research Laboratory, Lockheed Missile and Space Company, Palo Alto, Ca. 94304 Phone:(415) 424-2022, work supported by the Lockheed Independent Research Program, P.L. Hagelstein, Research Laboratory of Electronics, Massachusetts Institute of Technology Cambridge, Ma. 02139 Phone: (617) 253-0899, work supported by the Vinton-Hayes Foundation, S. Maxon, and J.H. Scofield, Lawrence Livermore National Laboratory, Livermore, Ca. 94550, Phone:(415) 447-8162, J.M. Peek, Los Alamos National Laboratory, Los Alamos, NM 87545, Phone: (505) 665-0542.

The Nd-like isoelectronic sequence (60 electrons) of high Z elements could provide the basis for a soft x-ray laser(1). Gain may be possible at approximately 70 Å for the 5f-5d transition in Nd-like Uranium. The potential advantage is that a medium power Nd:glass laser ( $10^{12}$  to  $10^{13}$  watts/cm<sup>2</sup>) is sufficient to create a soft x-ray laser. As a first step in this development, soft x-ray spectra from Pb, Bi, Th and U were taken. These results will be presented along with three different atomic structure computer calculations of transition energies.

The spectra were produced with  $10^{11}$  to  $10^{14}$  watt/cm<sup>2</sup> of laser power from the Lockheed Pulsed Laser Facility. Time integrated and theoretical spectra of Uranium are displayed in figure 1. The data is dominated by broad unresolved transition arrays (UTAs) from 5-5 and 6-5 transitions. The theoretical spectrum was created using calculated gf values and wavelengths for the Nd-, Pm- and Sm-like isoelectronic sequences. This comparison partially explains the gross features of the experimental data. Transitions from a large number of other ionization states will help form the broad UTAs.

1. P.L. Hagelstein and S. Dalhed, Phy. Rev. A, 37, 1358 (1988).

# Experimental and Theoretical Spectra of Uranium

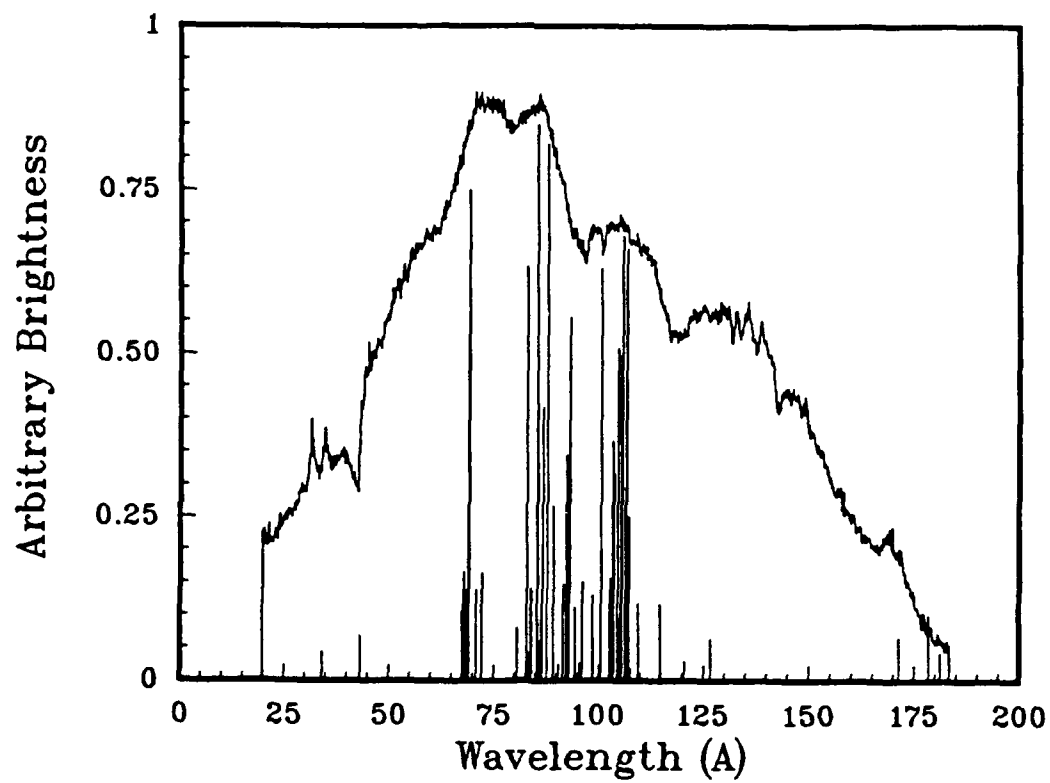


Figure 1



Soft X-Ray Lasing of Li-like Ions  
in Laser-Produced Plasmas\*

Yim T. Lee and W. M. Howard  
Lawrence Livermore National Laboratory  
Livermore, CA 94550

Several demonstrations of lasing in the extreme ultraviolet (XUV) wavelength region have been successfully achieved using either collision or recombination pumping. The first successful demonstration was reported for the 3p-3s transitions in Ne-like selenium ions. Laser transitions at shorter wavelengths have also been achieved by using the 4d-4p transitions in Ni-like ions. These schemes are based on collisional excitation pumping, while in other successful schemes the upper lasing levels are populated directly by recombination processes.

However, lasing using resonant photo-pumping in the XUV wavelength region has not yet been demonstrated. In resonant photo-pumping, the emission from one ion is used to pump a transition in the ion of a different element. A successful resonance scheme requires a close overlap between the wavelengths of these transitions. This concept for achieving population inversions of ions in plasmas was first proposed by Vinogradov et al. and by Norton and Peacock. Although several schemes for achieving laser amplification in the sub 100 Å wavelength region have been proposed, the shortest wavelength at which significant gain has been measured by using photo-pumping is 2163 Å.

Recently, we propose a new laser scheme based on resonant photo-pumping of Li-like ions using  $K\alpha$  radiation. In particular, we consider the lasing plasma to be a thin iron foil and the pump radiation source to be an aluminum slab. Both of these targets are assumed to be irradiated by a high-power optical laser. The radiation from the  $2p_{3/2}-1s_{1/2}$  transition of H-like aluminum ions in the source is used to pump the  $5p_{1/2}$  and  $5p_{3/2}$  levels of Li-like iron ions in the lasing plasma. Pumping of the 5p levels results in gains for the transitions between the  $n=5$  and  $n=4$  levels at the wavelengths of 70 Å.

In this paper we explore the possibility of designing a lasing medium in which population inversions between the  $n=5$  and  $n=3$  levels will occur in addition to that between the  $n=5$  and  $n=4$  levels. In our scheme, such transitions are between the  $5f$  and  $3d$  levels, giving the wavelengths at approximately  $23 \text{ \AA}$ . A source with this wavelength which lies inside the "water window" is needed for biological holography. Our calculation shows that population inversions between the  $5f$  and  $3d$  levels will occur if the lasing plasma after being ionized to Li-like state can be rapidly cooled down to a lower temperature. This results from the decrease in the collisional excitation contribution to the  $3d$  level populations and from the increase in the  $5f$  level populations by direct recombination. Rapid cooling of the lasing plasma will, in addition, enhance the gains for the  $n=5$  to  $n=4$  transitions. We will discuss experimental designs which can be used to demonstrate laser amplifications in these transitions.

In this paper we also present other resonance line pairs which can be applied to resonantly photo-excite Li-like ion of different elements other than iron. Discussion on the possibility of achieving laser amplification in some of these schemes by using laser-produced plasmas as a lasing medium will be presented.

\*Work performed under the auspices of the U.S. Department of Energy by the Lawrence Livermore National Laboratory under contract number W-7405-ENG-48.

# Time Development of Amplification in Na XI H $\alpha$ -Line at 54.19 Å

H. Nishimura, H. Shiraga, H. Daido, T. Tachi, P. R. Herman,  
E. Miura, H. Takabe, M. Yamanaka, and Y. Kato

*Institute of Laser Engineering, Osaka University, Suita, Osaka 565, Japan*

G. J. Tallents and M. H. Key

*Rutherford Appleton Laboratory  
Chilton, Didcot, Oxfordshire OX11 0QX, United Kingdom*

## Abstract

Temporal behavior of the Na XI Balmer- $\alpha$  (H $\alpha$ ) transition in a laser-produced NaF plasma is experimentally investigated. The time variation of the gain value was derived from the ratio of the H $\alpha$  intensities along and transverse to the x-ray laser axis. The Na XI H $\alpha$  line is amplified during 100-500 psec after laser irradiation with the maximum gain of 2-4 cm<sup>-1</sup>. The experimental result is in close agreement with a model calculation using a 2-dimensional hydrodynamic code.

## 1. Introduction

Research on extremely short wavelength laser is being proceeded not only because of attractive application to biological investigations but also interests in physical understandings of atomic processes which take place in highly excited dense matter. Extension of XUV lasers to shorter wavelengths are explored either with electron-collisional excitation scheme [1] or with recombining plasma scheme [2].

Recently, demonstration of soft x-ray gain in Balmer- $\alpha$  (H $\alpha$ ) transitions in Na XI at 54.1 Å, Mg XII at 45.5 Å and Al XIII at 38.8 Å has been reported on the basis of the recombining plasma scheme [3]. Details of this work are presented in this proceeding [4].

In this paper, we report time development of amplification in Na XI H $\alpha$  line measured in the above work. Observation was made by using two time resolving spectrographs. The experimental results are evaluated based on an isoelectronic scaling of the H $\alpha$  laser operating by recombination to hydrogenic ions, and the numerical calculation using a 2-dimensional fluid code.

## 2. Experiment

Major diagnostics apparatus were two time-resolving XUV spectrographs attaching streak cameras with the arrangement as shown in Fig. 1 [4]. One spectrograph aligned on the x-ray laser axis had a 1200 lines/mm variable periodicity flat-field diffraction grating. It gave spectra with a resolution of 0.2 Å at wavelengths around 50 Å with film recording, and 0.5 Å with a HAMAMATSU C2950 XUV streak camera. Rather poor spectral resolution resulted in line blending, requiring then deconvolution process in order to extract temporal behavior of the lasing line. Because this spectrograph was efficient in the long wavelength region (80-200 Å), a comparatively wide slit of 0.1mm in width was used as the photocathode in the streak camera. Time resolution in this case was 100 psec. A second similar spectrograph positioned 60 degrees with respect to the x-ray laser axis had a 2400 lines/mm grating blazed at a shorter wavelength. This transverse spectrograph gave

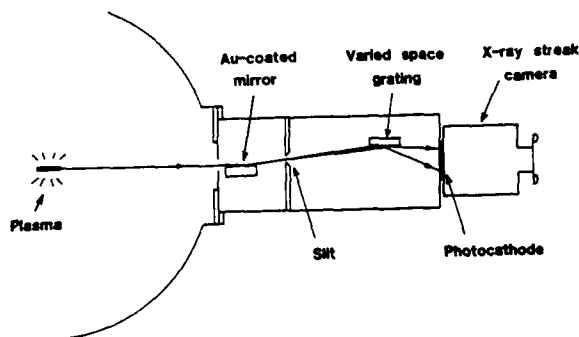


Figure 1. A schematic diagram of an XUV spectrograph equipped with an XUV streak camera.

spectra with 0.1 Å and 0.3 Å resolutions for film recording and KENTECK streak camera recording, respectively. Transmission type photocathodes were used in both streak cameras; photocathode for the HAMAMATSU was CuI of  $5.6 \times 10^{-5}$  g/cm<sup>2</sup> evaporated on an aluminum/parylene laminated substrate and that for the KENTECK was low-density CsI of  $2 \times 10^{-3}$  g/cm<sup>2</sup> evaporated on an aluminum/Formvar laminated substrate. Spectral sensitivities of these photocathodes [5,6] were taken into account in the data processing.

In the experiment, a stripe target was used; NaF was overcoated in a stripe shape of 30 μm in width and 6 mm in length on a parylene foil of 0.13 μm in thickness. Density-thickness product of the NaF was  $2.8 \times 10^{-4}$  g/cm<sup>2</sup>, which is thick enough to avoid the laser burn-through and to improve cooling of the ablated plasma via electron thermal conduction in addition to the adiabatic expansion.

Target was irradiated by one beam of frequency tripled light from the Gekko XII Nd:glass laser facility. The target normal was aligned on the laser axis. The laser pulse duration was 130 psec (FWHM) and the laser energy was  $150 \pm 15$  J. The focal spot was a line shape of 30 μm in width and 7 mm in length yielding  $5 \pm 0.5 \times 10^{14}$  W/cm<sup>2</sup> irradiance on the target.

A cross calibration target consisted of

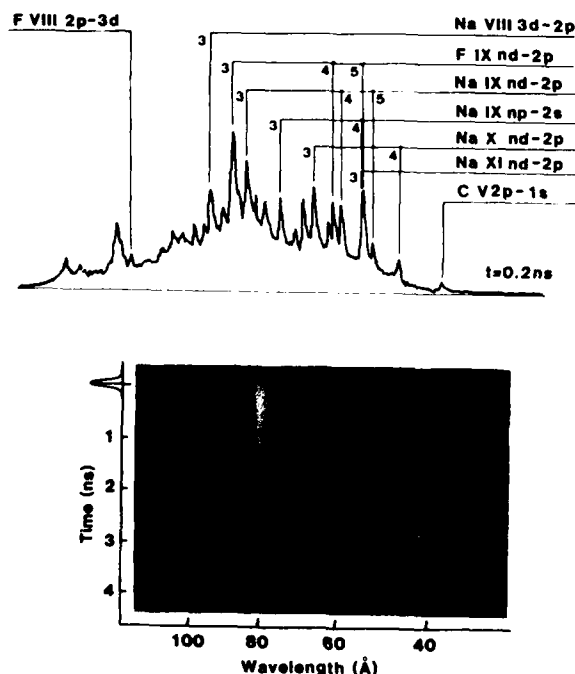


Figure 2. Streak camera record of the axial emission spectrum. The upper curve shows the spectrum at 200 psec after the laser peak.

0.2 μm-thick Na<sub>2</sub>B<sub>4</sub>O<sub>7</sub> evaporated on a 0.13 μm parylene film. The B V 2p<sup>2</sup>P<sup>0</sup>-1s<sup>2</sup>S line emission at 48.587 Å was used as a calibration source. This target was so aligned that the target normal was in the middle of the two spectrographs, and the size of the laser heated region was 30 μm × 0.65 mm providing spatially uniform source.

A time-resolved spectrum observed along the x-ray laser axis is shown in Fig. 2. Upper figure shows an instantaneous spectrum at 0.2 nsec after the laser peak. The Na XI Hα line (3d<sup>2</sup>D-2p<sup>2</sup>P<sup>0</sup> transition) is blended with the Na IX 4p<sup>2</sup>P<sup>0</sup>-2s<sup>2</sup>S and F IX 5d<sup>2</sup>D-2p<sup>2</sup>P<sup>0</sup> lines. These blended lines have to be deconvoluted using time variations of the other blending-free lines belonging to the same atomic species. First, fractions of blended lines were derived from the time-integrated spectrum with higher spectral resolution as shown in Fig. 3. A least-squares curve fitting numerical calculation program was used to extract the intensity of each line as given by the height of the stick spectrum. The Na XI Hα doublet line

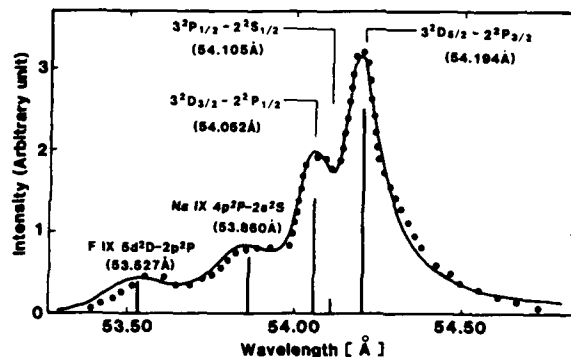


Figure 3. Time-integrated spectrum of the Na XI Hα line. The closed circles represent the spectrum obtained from the film recording and the solid curve shows the envelope of the deconvoluted lines whose heights and wavelengths are shown by the solid lines.

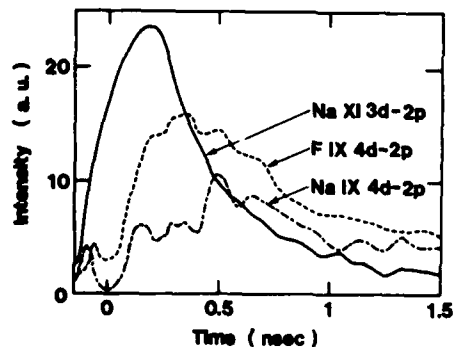


Figure 4. Time histories of the Na XI Hα, F IX 4d<sup>2</sup>D-2p<sup>2</sup>P<sup>0</sup> and Na 4d<sup>2</sup>D-2p<sup>2</sup>P<sup>0</sup> lines used for the deconvolution data processing.

consists of a stronger component at 54.194 Å ( $3d^2D_{5/2}-2p^2P_{3/2}$ ) and a weaker component at 54.052 Å ( $3d^2D_{3/2}-2p^2P_{1/2}$ ).

Second, time dependences of the blended lines were derived. The transition lines from the upper levels to the Na IX  $2s^2S$  level were blended with other lines. Therefore time resolved spectra of Na IX  $4d^2D-2p^2P^0$  and F IX  $4d^2D-2p^2P^0$  transition lines were used. Figure 4 shows the time dependences of Na IX  $4d^2D-2p^2P^0$  and F IX  $4d^2D-2p^2P^0$  transition lines for estimating the time dependences of the Na IX  $4p^2P^0-2s^2S$  and F IX  $5d^2D-2p^2P^0$ , respectively, together with the deconvoluted Na XI H $\alpha$  line. Emission intensities of the Na IX  $4d-2p$  and F IX  $4d-2p$  lines decrease at around the laser peak, in contrast to the time dependences of the Na XI H $\alpha$  line.

In order to extract time development of amplification, relative sensitivities of the axial and transverse spectrographs were calibrated using the cross calibration data [4] and the characteristic responses of the streak cameras together with the recording systems. Validity of this data processing procedure was checked using the B V  $2p^2P^0-1s^2S$  line emission from the Na<sub>2</sub>B<sub>4</sub>O<sub>7</sub> target. Temporal shapes of the B V  $2p-1s$  lines obtained from the two spectrographs agree quite well with each other.

Temporal variation of amplification coefficient  $g(t)$  was assessed by the time-dependent ratio  $R(t)$  of the H $\alpha$  intensity for the two spectrographs;  $R(t)=[\exp g(t)l-1]/g(t)l$ , where  $l$  is the length along the x-ray laser axis. Resulted time dependence of the gain coefficient is shown in Fig. 5. The gain starts  $\sim 100$  psec after the laser peak, becomes maximum at 150–200 psec and decays gradually as the emission intensity of the H $\alpha$  line decreases. The measured maximum gain coefficient of 2–4 cm<sup>-1</sup> is slightly higher than the time integrated data of  $g \sim 1.2$  cm<sup>-1</sup> obtained in the similar experimental conditions [3].

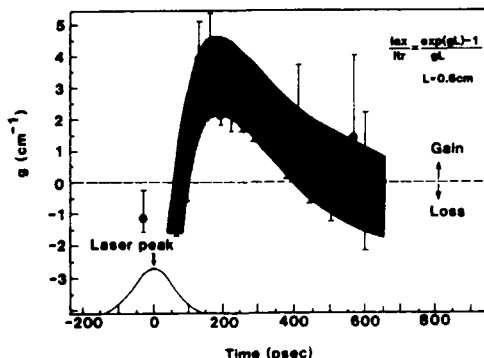


Figure 5. Time history of the gain coefficient of the Na XI H $\alpha$  line.

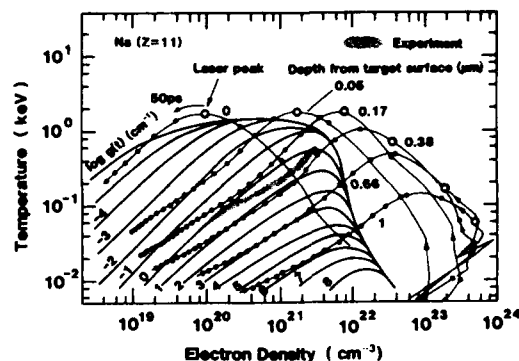


Figure 6. Dynamical behaviors of the NaF plasma and contours of the potentially available gain. Experimental data is represented by a shaded region.

### 3. Discussion

Isoelectronic scaling of highly ionized plasma XUV laser has been analyzed by M.H. Key [7]. A contour representation of the potentially available gain  $g$  for negligible ground state population is shown in Fig. 6 in terms of the electron density  $n_e$  and the electron temperature  $T_e$ . The initial plasma parameters and the cooling characteristic are quite important features determining the gain.

In order to follow the temporal behavior of the plasma density and temperature of a laser-created NaF plasma, computer simulation was made using a 2-dimensional Lagrangian fluid code ILESTA-2D [8]. Figure 7 shows plasma expansion behaviors expressed in terms of Lagrangean coordinate mesh, isodensity and temperature contours of a NaF target at 10 psec before and 110 psec after the laser peak. Laser is incident from the right-hand side and the x-ray laser axis is perpendicular to the figure plane. Lateral expansion along the target surface is noteworthy which contributes to plasma cooling.

Dynamical behaviors of plasma parameters obtained by this 2-D calculation are also plotted in Fig. 6. The initial depth from the surface of the plasma element is denoted on each curve in unit of  $\mu\text{m}$ . The times at the laser peak is marked by an open circle and each closed circle marks a time step of 50 psec. Experimentally obtained gain history is also represented by a shaded region. Simulation result indicates that the plasma component of  $n_e \sim 2 \times 10^{21} \text{ cm}^{-3}$  and  $T_e \sim 400 \text{ eV}$  mainly contributes to the amplification which is initially 0.22–0.26  $\mu\text{m}$  deep from the surface. The plasma component closer to the surface expands too fast for attaining optimum density. In contrast, the plasma component deeper from the surface does not reach to a temperature high enough to sustain sufficient ionization. At 50 psec after the laser peak, the temperature and the density

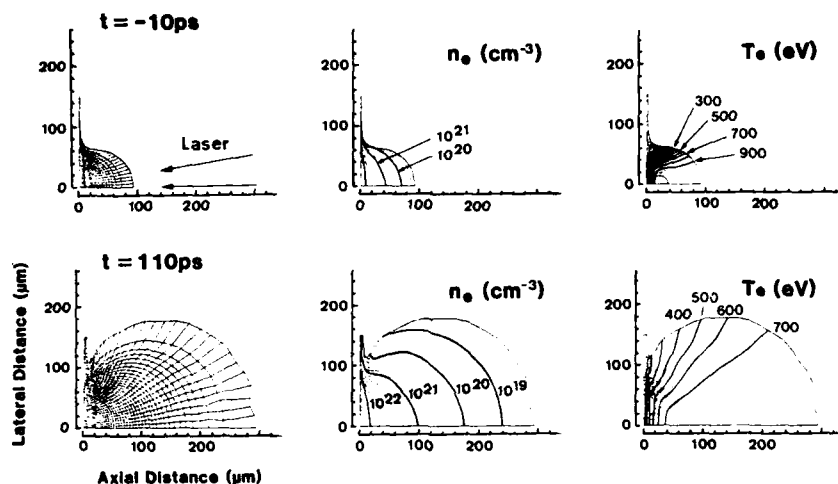


**Figure 7.** Plasma expansion behavior of the NaF target at 10 psec before and 110 psec after the laser peak calculated with a 2-dimensional fluid code.

of this depth region become respectively 1.5 keV and  $6.4 \times 10^{21} \text{ cm}^{-3}$  realizing ionization balance of  $nZ^{-1}/nZ=0.04$ . After this time, the plasma cools faster than by adiabatic expansion and results in maximum gain of  $g \sim 4 \text{ cm}^{-1}$  at 200 psec after the laser peak. At this time, the plasma component giving the maximum gain flows at  $\sim 80 \mu\text{m}$  away from the original position of the target surface.

#### 4. Conclusion

Time development of amplification of Na XI H $\alpha$  line in a laser-created NaF plasma was observed. The amplification starts at 100 psec after the laser peak and becomes maximum at 150-200 psec with the gain coefficient of 2-4  $\text{cm}^{-1}$ . Temporal behavior of the gain have been interpreted using the analytical and numerical evaluations for a 2-dimensionally expanding and recombining plasma generated by a short duration laser pulse.

#### Acknowledgements

The authors wish to acknowledge T.Jitsuno for laser operation and M.Takagi for target fabrication. Technical supports from the members of the Gekko Laser operation & development group, the optical technology group, the plasma diagnostics group, and the target fabrication group are gratefully acknowledged.

#### References

1. B.J.MacGowan, S.Maxon, P.L.Hagelstein, C.J.Keane, R.A.London, D.L.Matthews, M.D.Rosen, J.H.Scofield, and D.A.Wheeler, "Demonstration of soft x-ray amplification in Nickel-like ions" Phys. Rev. Lett., **59**, 2157-2160 (1987)
2. G.C.Popovics, R.Corbett, C.J.Hooker, M.H.Key, G.P.Kiehn, C.L.S.Lewis, G.J.Pert, C.Regan, S.J.Rose, S.Sadaat, R.Smith, T.Tomie, and O.Willi, "Laser amplification at 18.2nm in recombining plasma from a laser irradiated carbon fibre", Phys. Rev. Lett., **59**, 2161-2164 (1987)
3. Y.Kato, M.H.Key et. al., "Extension of recombining plasma laser with Balmer- $\alpha$  transition to shorter wavelength", in Proceedings of the International Quantum Electronics Conference(IQEC), Tokyo, 18-21 July, 1988.
4. Y.Kato, M.Yamanaka, H.Daido, T.Tachi, H.Nishimura, H.Shiraga, E.Miura, P.R.Herman, H.Takabe, T.Jitsuno, M.Takagi, S.Nakai, C.Yamanaka, M.H.Key, G.J.Tallents, S.J.Rose, and P. T.Ramsby, "Amplification of Na XI H $\alpha$ , Mg XII H $\alpha$ , and Al XIII H $\alpha$  transitions", in this volume.
5. B.L.Henke, J.P.Knauer, and K.Premaratne, "The characterization of x-ray photocathodes in the 0.1-10 keV photon energy region", J. Appl. Phys. **52**, 1509-1520 (1981).
6. E.B.Saloman, J.H. Hubbell, and J.H.Scofield, "X-ray attenuation cross sections for energy 100 eV to 100 keV and elements Z=1 to Z=92", in Atomic Data and Nuclear Tables **38**, 1-197 (1988).
7. M.H.Key, Rutherford Appleton Lab. Annual Rep. RAL 87-041, 100 (1987).
8. H.Takabe, "Two dimensional fluid simulation for implosion experiments with Gekko XII green laser system", Institute of Laser Engineering Quarterly Progress Report, ILE-QPR-87-22, P36-42 (1987).

# Gain Measurement on a 18.2-nm Carbon Recombination Laser Produced by an Intense CO<sub>2</sub> Laser

H. Daido, E. Miura, Y. Kitagawa, K. Nishihara, Y. Kato, C. Yamanaka,\* and S. Nakai

*Institute of Laser Engineering, Osaka University, Suita, Osaka 565, Japan*

*\*Institute for Laser Technology, 2-6 Yamada-Oka, Suita, Osaka 565, Japan*

## ABSTRACT

We propose a cylinder-type target as a carbon recombination laser medium made of 30- $\mu$ m thick parylene (C<sub>8</sub>H<sub>8</sub>) whose diameter and length are 3mm and 3mm-12mm, respectively. The high power CO<sub>2</sub> laser (500J in 50ns) irradiates a 2500- $\text{\AA}$  thick parylene foil attached to the end of the cylinder. Then the plasma from the thin foil and the cylinder wall produced by the scattered light expands and is confined in the cylinder, producing an almost uniform plasma without magnetic field. The plasma length of more than 1 cm was observed with x-ray pinhole camera. We measured the gain of CVI 3d-2p line (18.2 nm) using the axial and the transverse spectrometers. The maximum gain length product of 2.4 at cylinder length of 12 mm was obtained.

## 1. INTRODUCTION

Recently, several approaches to develop XUV (extreme ultra violet) to soft x-ray lasers have successfully demonstrated significant amount of gain and intense amplified spontaneous emission light[1]. Ne-like[2,3] and Ni-like[4] ions produced by line focused powerful lasers are excited by heated electrons and large gain length product of the order of ten has been achieved. The recombination pumped lasers have also demonstrated the significant gain length product[5-9]. The key issue to achieve high gain in recombination scheme is rapid cooling of highly ionized plasma via the thermal conduction, the expansion and the radiation.

In this paper, we propose the cylinder-type target as the Hydrogen-like Balmer-alpha carbon XUV laser medium[10-

12]. The expected scenario is as follows. The high power CO<sub>2</sub> laser hits a thin foil and the light is scattered back to the cylinder wall as shown in Fig.1. Almost uniform plasma is produced inside the cylinder during the early stage of the irradiation pulse. The successive laser pulse continues to heat the plasma and the fully ionized carbon plasma is generated in the long cylindrical heated region where the electron density is smaller than that near the cylinder wall due to the radial pressure balance. The radial density profile may satisfy the waveguiding structure[13]. The heated length is estimated with the scale length of the collisional absorption[14] to be several cm in our experimental condition. The cylinder wall should have sufficiently large heat capacity to cool the hot plasma efficiently and also have long inertial time to sustain the plasma pressure during the ionization and the recombination phases. When the laser stops or the plasma density exceeds the critical density of the CO<sub>2</sub> laser, the plasma cools rapidly due to strong heat conduction to the heavy thick cylinder wall and the population inversion occurs via the three body recombination process. The aim of this study is to obtain relatively large gain length product using relatively simple excitation laser system. We expect to obtain the MW level XUV coherent light using the XUV unstable resonator.

In the following sections, we describe the experimental setup, the gain measurements and discussions and the summary of this paper.

## 2. EXPERIMENTAL SETUP

We constructed the unstable resonator in

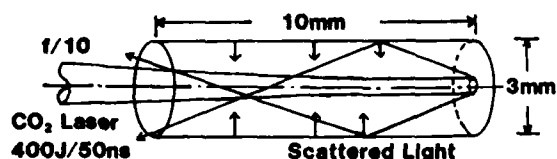


Fig.1 Schematic diagram of the cylinder target and laser irradiation geometry.

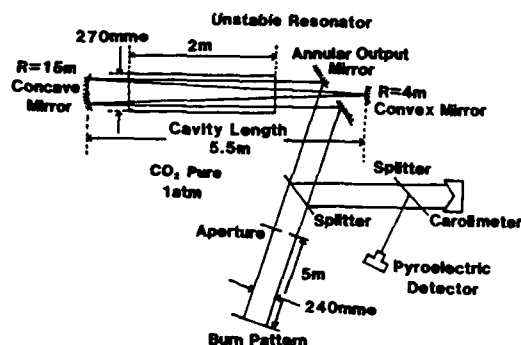


Fig.2 Large aperture CO<sub>2</sub> laser oscillator system in the LEKKO VIII system.

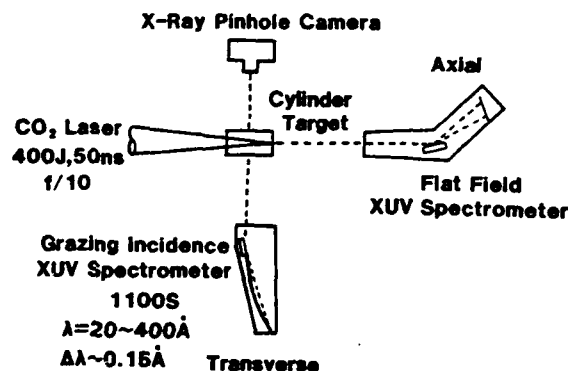


Fig.3 Schematic diagram of the target, the laser irradiation geometry and the observation system. The gain is measured with axial and transverse spectrometers.

the electron beam sustained discharge booster amplifier of the LEKKO VIII CO<sub>2</sub> laser system[15]. The optical parameters of the cavity are shown in Fig.2. The usual gold coated concave mirror was used as the cavity mirror. The pure molybdenum convex mirror whose damage threshold was about four times higher than the usual gold one[16] was used at the other side of the cavity. We have no damage problems on cavity optics. The diameter and the length of the medium are 27 cm and 2 m, respectively. The usual electrical input energy to the discharge was 16 kJ (maximum energy was 64 kJ) and the laser energies between 200 J and 500 J were stably obtained with a pulse width of 50 ns. The beam divergence was less than  $10^{-4}$  rad. We investigated the oscillation waveform changing the contents of CO<sub>2</sub>, N<sub>2</sub>, He gas mixture, but the waveforms did not change drastically. The booster amplifier has two main discharge chambers with only one electron beam gun chamber. One arm of discharge chamber was used as the oscillator. The other one is prepared to use as the amplifier to increase maximum laser energy and to optimize the waveform for XUV laser study.

The 400 J in 50 ns CO<sub>2</sub> laser light is focused with f/10 gold coated spherical mirror giving peak intensity of  $3 \times 10^{12}$  W/cm<sup>2</sup>. Schematic diagram of the irradiation and observation system are shown in Fig.3. We can measure two spectra simultaneously using the axial and the transverse grazing incidence XUV spectrometers. Spectral regions and resolutions of the axial and transverse spectrometers were 30-400 Å and 20-400 Å, 0.3 Å and 0.15 Å, respectively. The spectra were recorded on KODAK 101-07 film which was calibrated by Henke's group[17]. The x-rays whose energy was above 1 keV were imaged with 25 μm thick Be filtered x-ray pinhole camera. Heated plasma length of up to 1 cm was observed through the window at the cylinder wall. The focusing optics, targets (XUV laser medium) and diagnostic instruments are installed in the chamber which is evacuated to  $10^{-5}$  Torr by two turbo-molecular pumps.

### 3. GAIN MEASUREMENTS AND DISCUSSIONS

Typical XUV spectra in the axial and transverse directions are shown in Fig.4. The enhancement factor of CVI 3d-2p line are estimated with the axial and the transverse XUV fluences normalized by those of CVI 5d-2p line. CVI 3d-2p line in axial direction is obviously enhanced compared with the transverse one. Almost same results are obtained using CVI 6d-2p line



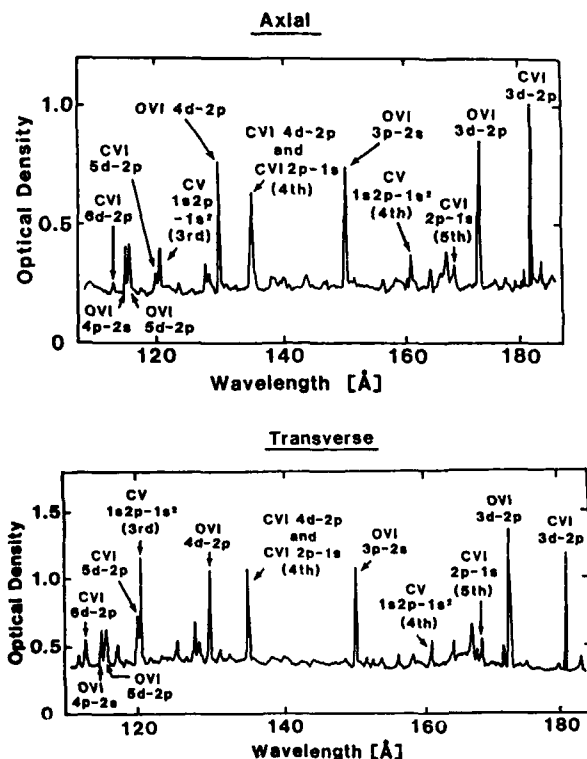


Fig.4 Observed axial and transverse XUV spectra. CVI 3d-2p line is enhanced in axial direction.

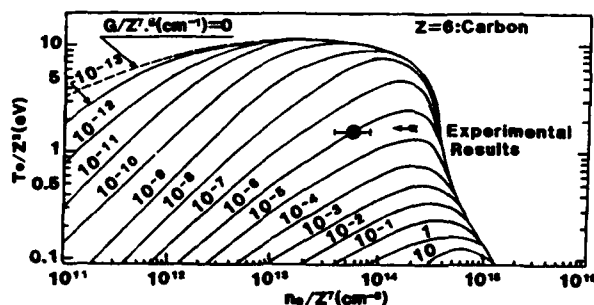


Fig.5 Iso-gain contour of the Hydrogen-like ions calculated with the quasi-steady state collisional-radiative model. Solid circle denotes the observed electron density and temperature, giving gain coefficient of an order of 1/cm for carbon ions.

as a reference line[5]. The maximum enhancement factor of 4.2 and corresponding gain length product of 2.4 were obtained with 12 mm long cylinder target. In our target, the gain coefficient was rather difficult to estimate. If we assume that the gain length is equal to the cylinder length because the plasma may cool strongly in the vicinity of the cylinder wall, the maximum gain coefficient is 3.8/cm at cylinder length of 6 mm.

We measured the electron temperature and density using the spectroscopic methods to be 50 eV and  $10^{19}/\text{cm}^3$ , details of which is described elsewhere[18]. The gain coefficient is predicted by the quasi-steady state collisional-radiative model assuming the fully striped carbon plasma at the initial stage of recombination[19]. Figure 5 shows the contour of the normalized iso-gain coefficient ( $G/Z^{0.5}$ ) of CVI 3d-2p line as functions of the normalized electron temperature ( $T_e/Z^2$ ) and the normalized electron density ( $n_e/Z^2$ ), where  $Z$  is the atomic number of the ions. Solid circle denote the measured density and temperature, giving gain coefficient of an order of 1/cm which agrees with the data of gain measurements. To obtain higher gain coefficient, the temperature should decrease during the recombination phase because the density is roughly limited by the critical density of the  $\text{CO}_2$  laser and the opacity of the Lyman-alpha line which pumps the lower lasing level to decrease the population inversion. Several improvements such as optimizations of cylinder parameters, wall materials, thickness of the foil and so on should be required for getting higher gain.

#### 4. SUMMARY

We propose a cylinder-type target as a carbon recombination laser medium. The long uniform carbon plasma up to 12 mm was produced by an intense  $\text{CO}_2$  laser irradiation. The measured gain length product of CVI 3d-2p line (18.2 nm) using the axial and transverse spectrometers was up to 2.4.

#### References

1. M. H. Key, "XUV lasers", *J. Mod. Optics* **35**, 575-585 (1988).
2. D. L. Matthews et al., "Demonstration of a Soft X-Ray Amplifier", *Phys. Rev. Lett.* **54**, 110-113 (1985).
3. T. N. Lee, E. A. McLean, and R. C. Elton, "Soft X-Ray Lasing in Neonlike Germanium and Copper Plasmas", *Phys. Rev. Lett.* **59**, 1185-1188 (1987).
4. B. J. MacGowan, S. Maxon, P. L.

- Hagelstein, C. J. Keane, R. A. London, D. L. Matthews, M. D. Rosen, J. H. Scofield, and D. A. Whelan, "Demonstration of Soft-X-Ray Amplification in Nickel-like Ions", *Phys. Rev. Lett.* **59**, 2157-2160 (1987).
5. S. Suckewer, C. H. Skinner, H. Milchberg, C. Keane, and D. Voorhees, "Amplification of Stimulated Soft-X-Ray Emission in a Confined Plasma Column", *Phys. Rev. Lett.* **55**, 1753-1756 (1985).
6. S. Suckewer, C. H. Skinner, D. Kim, E. Valeo, D. Voorhees, and A. Wouters, "Divergence Measurements of Soft-X-Ray Laser Beam", *Phys. Rev. Lett.* **57**, 1004-1007 (1986).
7. P. Jaegle, A. Carillon, A. Klisnick, G. Jamelot, H. Guennou and A. Sureau, "Soft-X-Ray Amplification in Recombining Aluminum Plasma", *Europhys. Lett.* **1**, 555-562 (1986).
8. C. Chenais-Popovics, R. Corbett, C. J. Hooker, M. H. Key, G. P. Kiehn, C. L. S. Lewis, G. J. Pert, C. Regan, S. J. Rose, S. Sadaat, R. Smith, T. Tomie, and O. Willi, "Laser Amplification at 18.2 nm in Recombining Plasma from a Laser-Irradiated Carbon Fiber", *Phys. Rev. Lett.* **59**, 2161-2164 (1987).
9. Y. Kato, P. R. Harman, T. Tachi, K. Shihoyama, K. Kamei, and H. Shiraga, "Amplification of XUV emission in H-like ions with thin foil targets", *Proc. SPIE*, **831**, 299-304 (1987).
10. E. Miura, H. Daido, and Y. Kitagawa, "Line Intensity Enhancement in Wall Confined Carbon Plasmas Produced by a CO<sub>2</sub> Laser", *ILF Quarterly Progress Report ILF-QPR-87-21*, 28-33 (1987).
11. H. Daido, E. Miura, Y. Kitagawa, Y. Kato, K. Nishihara, K. Sawai, S. Nakai and C. Yamanaka, "Study on XUV lasers produced by a CO<sub>2</sub> laser", in *Technical Digest, Conference on Lasers and Electro-Optics* (Optical Society of America, Washington, DC, 1988), paper THM20.
12. H. Daido, E. Miura, Y. Kitagawa, Y. Kato, K. Nishihara, S. Nakai, and C. Yamanaka, "Study on XUV lasers produced by a CO<sub>2</sub> laser", in *Proceedings of the International Symposium on Short Wavelength Lasers and Their Applications* (Springer-Verlag, Berlin) to be published.
13. J. G. Lunney, "Waveguiding in soft x-ray laser experiments", *Appl. Phys. Lett.* **48**, 891-893 (1986).
14. E. A. Crawford and A. L. Hoffman, "Investigation of highly ionized plasma plumes generated by CO<sub>2</sub> laser irradiation of solid targets in strong axial magnetic fields", in *Proceedings of Laser Interaction and Related Plasma Phenomena*, H. Hora and G. H. Miley, eds. (Plenum Press, New York, 1984) Vol.6, pp.353-367.
15. C. Yamanaka et al., "The LEKKO VIII CO<sub>2</sub> Gas Laser System", *IEEE J. Quantum Electron.* **QE-17**, 1678-1688 (1981).
16. Y. Ichikawa et al., "Highly damage-resistant Mo mirror for high-power TEA CO<sub>2</sub> laser systems", *Appl. Opt.* **26**, 3671-3675 (1987).
17. B. L. Henke, F. G. Fujiwara, M. A. Tester, C. H. Dittmore, and M. A. Palmer, "Low-energy x-ray response of photographic films. II. Experimental characterization", *J. Opt. Soc. Am.* **B1**, 828-849 (1984).
18. E. Miura, H. Daido et al., "Gain measurement of the CVI 3d-2p transition (182 Å) from the wall confined carbon plasmas produced by a CO<sub>2</sub> laser", to be published.
19. T. Fujimoto, "Kinetics of Ionization-Recombination of a Plasma and Population Density of Excited Ions. I. Equilibrium Plasma", *J. Phys. Soc. Jpn.* **47**, 265-272 (1979); T. Fujimoto, I. Sugiyama and K. Fukuda, "Collisional-Radiative Coefficients and Population Coefficients of Hydrogen Plasma", *Mem. Fac. Eng. Kyoto Univ.* **34**, 249-277 (1972).

# Narrow Line X-Ray Transition Radiation by Electron Beam Traversing a Solid-State Superlattice

A. E. Kaplan and C. T. Law

*Department of Electrical and Computer Engineering  
Johns Hopkins University, Baltimore, Maryland 21218*

## Abstract

Soft x-ray can be generated by low energy electron beams traversing a periodic layered medium with very short spatial period as was shown previously by Kaplan and Datta. We show that a combination of materials with high and low atomic number can produce an intense x-ray radiation with very narrow spectral peaks at the vicinity of K, L, ... atomic absorption edges of each of the materials. We propose selection rules for materials constituting the solid-state superlattice. Our results demonstrate that an inexpensive x-ray source with mega (or submega) electron volt energy of electron beam can be used to generate narrow-line x-ray radiation.

## Introduction

When an electron beam traverses the interface between two semi-infinite dielectric materials with different dielectric constants  $\epsilon_1$  and  $\epsilon_2$ , it emits electromagnetic radiation [1]. This phenomenon, which is called transition radiation, is different both from the Cerenkov radiation and from the Bremsstrahlung radiation. This electromagnetic radiation can be greatly enhanced by using a periodic multilayer medium (the so called resonant transition radiation) [2,3] instead of a single interface, see Fig. 1.

The spatial distribution of the intensity of transition radiation then has a conical pattern with most of the intensity at each particular wavelength  $\lambda$  concentrating about some certain angle  $\theta$  of emission measured from the path of the electron beam. Each spatial mode with a number  $r$  has a different resonant angle  $\theta_r$ , which is related to wavelength  $\lambda$  and to the speed of electron  $v$  by the resonant con-

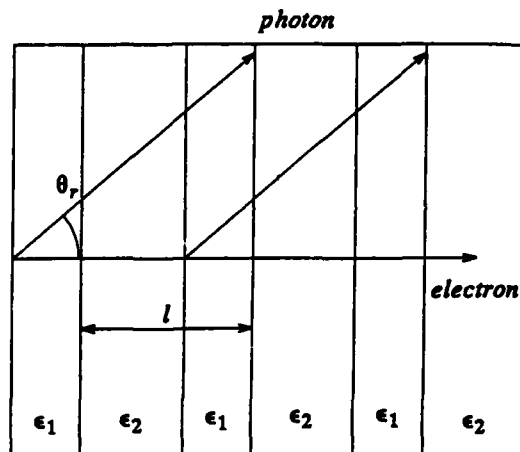


Fig. 1. The configuration of resonant transition radiation.

dition

$$\bar{\epsilon}^{1/2} \cos \theta_r = c/v - r\lambda/l \quad (1)$$

where  $\bar{\epsilon}^{1/2} = (\sqrt{\epsilon_1 l_1} + \sqrt{\epsilon_2 l_2})/l$  is the average refractive index,  $l_1$  and  $l_2$  are the thicknesses of the individual layers formed by two media, and  $l = l_1 + l_2$  is the spatial period of the periodic medium. This condition represents the constructive coherent interference of electromagnetic wave at a distance point; this fact was explicitly demonstrated in the recent experiment [4] with a small number of layers.

Usually [2,3,5-8]  $l \gg \lambda$ , so that ultra-relativistic electrons with energies 100MeV-50 GeV [5] are required to satisfy condition (1) for real  $\theta_r$ . However, with the advent of new technologies, periodic layered structures (and even superlattices) can be constructed with a spatial period less than 100 Å. These structure are widely used as x-ray

mirror [9,10]. It was recently proposed [11-13] to use these structures in order to obtain resonant transition radiation exploiting electron beams with very low energies. In solid-state structure, however, electron scattering and photoabsorption may be the main obstacles to achieving an effective source of x-ray radiation. More recently [14], we studied the losses due to photoabsorption and electron scattering and their effect on resonant transition radiation. We showed that a slightly increase of the electron beam energy will render insignificant the loss of electrons and photoabsorption imposes an energy ceiling above which an increase in electron beam energy produces no significant improvement.

For the transition radiation, electromagnetic field is generated due to the difference in dielectric constant between the neighboring layers and the power of the radiation is proportional to  $|\epsilon_1(\omega) - \epsilon_2(\omega)|^2$ . Therefore, dispersion of dielectric constants of the materials strongly affect the optimal radiation and the shape of the radiation spectrum. In this paper, we investigate the effect of anomalous dispersion in the dielectric constant on the radiation spectrum, and demonstrated that peaks with narrow spectral width can be generated. Based on this and our previous study on losses due to photoabsorption and electron scattering [14], we propose the rules for selection of materials constituting the solid-state superlattice. Usually, [5,6,8] light elements with small atomic number are used as radiators and air plays a role as a spacer in a system utilizing ultra-relativistic electrons. Since a solid-state structure [12-13] has to be used in order to employ low-energy electron beams and the value of  $\epsilon - 1$  is roughly proportional to the number of electrons which increases with atomic number of an atom, heavy elements with large atomic number become appropriate candidates as radiators and light elements as spacers in order to obtain a larger quantity  $|\epsilon_1 - \epsilon_2|$  (at least in a short-wavelength range). The use of materials with large atomic number is further justified by the fact that many [15] absorption lines of these materials fall within the soft x-ray range (0.1 - 2 keV).

### Transition radiation in a solid-state superlattice

The differential cross-section for transition radiation including photoabsorption in a multilayer system can be expressed in the following form [2,3,6-8]

$$\frac{d^2 N}{d\Omega d\omega} = F_1 F_2 F_3 \quad (2)$$

where  $F_1$  is the differential cross-section for one single interface,  $F_2$  denotes the coherent interference of radiation in a single plate (i.e. in two neighboring interfaces), and  $F_3$  represents the coherence summation of radiation from each layer. The unit of the differential cross-section is number of photon  $N$  per unit solid angle  $\Omega$  in steradian per frequency  $\omega$  per electron. The differential cross-

section for a single interface is given by [3]

$$F_1 = \frac{\alpha(\Delta\epsilon\beta)^2}{\pi^2\omega} |G|^2 \quad (3)$$

where  $\Delta\epsilon = \epsilon_1 - \epsilon_2$ ,  $\alpha = 1/137$  is the fine structure constant,  $\theta$  is the angle of emission,  $\omega$  is the frequency of the radiation,  $\beta = v/c$ , and  $G(\beta, \theta)$  is a radiation pattern of a single interface. If the electron energy is lower than that required for Cerenkov radiation (i.e., less than 100 - 500 MeV in our case),  $G(\beta, \theta)$  can be expressed as

$$G(\beta, \theta) = \frac{\sin\theta(1 - \beta^2 - \beta\cos\theta)}{2(1 - \beta^2\cos^2\theta)(1 - \beta\cos\theta)} \quad (4)$$

The factor  $F_2$  is attributable to coherent summation of radiation at two neighboring interfaces, and assumes the interference pattern of two sources

$$F_2 = 4 \sin^2[l_2\pi(1/\beta - \sqrt{\epsilon_2}\cos\theta)/\lambda] \quad (5)$$

where  $l_2$  is the thickness of the denser medium. This expression indicates that the power of radiation in a single plate is four times as large as that of single interface when the interference is constructive.

In order to include both photoabsorption and electron scattering into consideration, we note that both of them affect only "multilayer" factor  $F_3$ , whereas the factors  $F_1$  and  $F_2$  remain intact. To include photoabsorption into consideration, we assume that the emitted field decays exponentially as  $e^{-\bar{\mu}z/(2\cos\theta)}$  where  $\bar{\mu} = (\mu_1 l_1 + \mu_2 l_2)/l$  is the average absorption coefficient,  $z$  is the distance traveled by the electron and  $\theta$  is the angle of emission. For  $M$  period, we have

$$F_3 = \left| \sum_{s=0}^{M-1} \Phi_s \right|^2, \quad \Phi_s = e^{[-\sigma(M-s) + 2iXs]}, \quad (6)$$

where  $\sigma = \bar{\mu}l/(2\cos\theta)$  is dimensionless absorption parameter. The factor of  $\cos\theta$  in  $\sigma$  accounts for the longer path length traveled by the photon due to nonzero angle of emission.

Although both energies and momenta of electrons change as the electrons pass through a layer of the material, most of the transmitted electrons conserve their energies and momenta for films thinner than the mean free path [16]. In the first approximation, we consider only the radiation contribution of these electrons, and describe scattering in terms of the transmission of electron  $T$ . Interpreting  $T(z)$  as the probability of an electron to pass through a distance  $z$ , we can account for electron scattering by redefining  $\Phi_s$  in Eq. (6) as  $\Phi_s = \sqrt{T(sl)} e^{-\sigma(M-s) + 2iXs}$ . (The different, less rigorous, approach was used by us previously [17]. The results of [17] depart from the present calculations by less than an order of magnitude.) The dependence of  $T(z)$  on the thickness of the medium,  $z = sl$ , can be characterized by the so called critical length  $L_{cr} = (dE/dz)/E_0$  where

$dE/dz$  is the energy loss of electrons per path length, and  $E_0$  is the initial electrons energy.  $L_{cr}$  is defined as the length at which virtually all electrons are scattered and absorbed; it can be calculated by using Bethe's formula [18-20]. For  $L_{cr}$  longer than the total length of multilayer structure  $l$  (which is usually valid),  $T$  decays almost exponentially,  $T = \exp(-z/L_{cr})$ . It can be shown then that the factor  $F_3$  is expressed as

$$F_3 = e^{-(M-1)(\gamma+\rho)} [\cosh(M(\sigma-\rho)) - \cos(2MX)] / [\cosh(\sigma-\rho) - \cos(2X)] \quad (7)$$

where  $\rho = l/(2L_{cr})$ . Because of the rapid variation of  $F_3$  with respect to angle  $\theta$ , it is more meaningful to measure the radiation yield by integrating Eq. (2) over solid angle  $\Omega$  using Eqs. (3), and (7) under the condition that  $r=1$  and  $l_1 = l_2 = l/2$ :

$$\frac{dN}{d\omega} = \int_{-\infty}^{\infty} \left( \frac{d^2N}{d\omega d\Omega} \right) d\Omega = \frac{8\beta^2\lambda^2\alpha}{\pi^2 cl} \frac{\sinh(M(\sigma-\rho))}{(\sigma-\rho)} e^{-M(\sigma+\rho)} |\Delta\epsilon|^2 |G(\beta, \theta)|^2. \quad (8)$$

Eqs. (7) and (8) reduce to the known respective formulas [5-8] when only photoabsorption is present (i.e.  $\rho = 0$ ).

We now use Eq. (8) to find the optimal geometrical configuration (i.e. number of layers and thickness of each layer) so that the radiation is maximized in the desired frequency range. We maximize the right hand side of Eq. (8) with respect to  $\theta$ , and hence obtain  $\theta_r$  and optimal spatial period  $l_{opt}$ . We then maximize the term  $\sinh((\sigma-\rho)M)e^{-M(\sigma+\rho)}/(\sigma-\rho)$  with respect to  $M$ , and obtain the optimal number of periods as  $M_{opt} = [\ln(\sigma/\rho)]/[2(\sigma-\rho)]$ . We can now find the maximum radiation with angle  $\theta_r$ , period  $l_{opt}$ , and number of period  $M_{opt}$ . As a result, an "optimized" Eq. (8) can now be written as

$$\frac{dN}{d\omega} = \frac{\alpha}{2\pi^2 c} |\Delta\epsilon|^2 \frac{1}{\bar{\mu}} PQ \quad (9)$$

where

$$Q = (1-\beta l/\lambda)^2 [1 - (1/\beta - \lambda/l)^2] (1/\beta - \lambda/l),$$

$$P = (\rho/\sigma)^{M_{opt}}. \quad (10)$$

One can see that for sufficiently high electron beam energy (e.g.  $E_0 > 1$  Mev),  $Q_{opt}$  and respective  $l_{opt}$  can be approximated by a very simple formula:

$$Q_{opt} \simeq l_{opt}/\lambda \simeq \gamma^2 \quad (11)$$

For a fixed  $l$ ,  $Q$  is saturated [5-7] after  $Q_{opt}$  is reached even if electron energy keep on increasing. We discovered, however, that even when the period  $l$  is optimized for each particular  $E_0 = (\gamma-1)m_e c^2$ , there is some *maximal* meaningful energy ("ceiling") of electron beam related now

to photo-absorption. Indeed, it is obvious that using a multilayer structure thicker than  $1/\bar{\mu}$  will not yield a further increase in radiation. On the other hand, in order to still have a multilayer structure with reasonable number of layers (say  $M \geq 4$ ) [14] the condition for the maximum spatial period of the structure,  $l \leq 1/4\bar{\mu}$ , must be taken into account. Using this consideration as well as Eq. (11) for  $l = l_{opt}$ , we obtain the ceiling of the required  $\gamma$  as  $\gamma \leq 1/(2\sqrt{\lambda\bar{\mu}})$ . With the typical value of  $1/\bar{\mu} \simeq 1\mu m$  at  $\lambda \simeq 10\text{\AA}$ , we obtain  $\gamma \simeq 15$  corresponding to  $E_0 \simeq 7$  Mev. For light materials this ceiling may reduce to 2 Mev, and even lower.

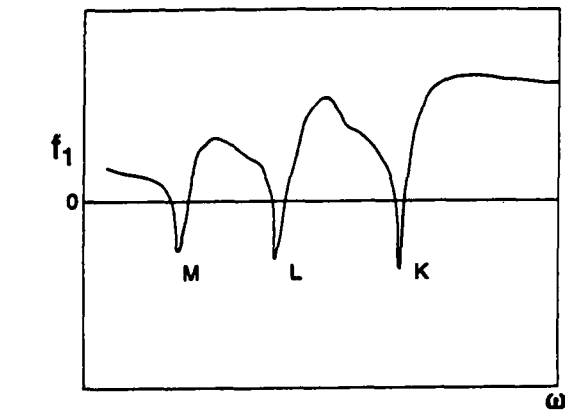
The *minimum* electron beam energy required to obtain appreciable intensity of radiation is achieved when electron scattering results in the same losses as photoabsorption, i.e.  $L_{cr}/e = 1/\bar{\mu}$ . The typical value of  $1/\bar{\mu}$  is of the order of microns around a wavelength of  $10\text{\AA}$ . For example when  $1/\bar{\mu} \simeq 5\mu m$ , the minimal electron energy is about 100 kev. Above this energy, photo-absorption begins to dominate over electron scattering.

### Resonances of dielectric constant

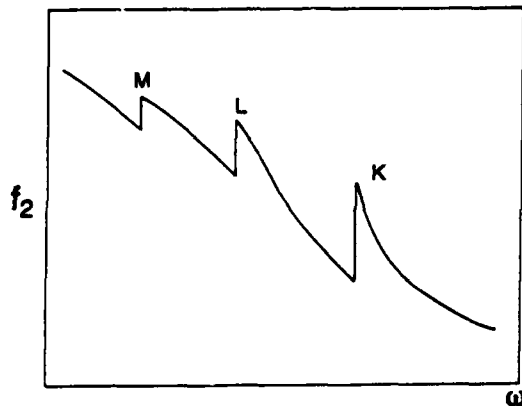
It is readily seen from Eq. (3) that the intensity of transition radiation is directly proportional to  $|\epsilon_1 - \epsilon_2|^2$  where  $\epsilon_{1,2}$  are respective dielectric constants of the both materials of periodic structure. Photoabsorption coefficient  $\bar{\mu}$  in Eqs. (7) also affects the intensity of radiation appreciably. Both of these parameters undergo large change near so called atomic absorption edges at which the absorption rises sharply. In Figs. 2a and 2b the atomic scattering factors  $f_1$  [related to dielectric constant by Eq. (16) below] and  $f_2$  [related to absorption by Eq. (17) below] versus photon energy are depicted.

Because of the sharp changes in  $f_1$  and  $f_2$ , one must expect a significant resonant increase of radiation intensity in the vicinity of these atomic absorption edges of either of two materials. For each particular element, these atomic absorption edges (and related resonances of refractive index) are pertinent to the photo-ionization of bounded electrons [21] from their respective atomic shells (K, L, M ...) to the ionization continuum.

The most known effect related to this electron transition, is almost discontinuous jump of absorption  $\mu$  (or  $f_2$ , see below) as the photon energy increases in the vicinity of resonance. The points at which absorption increases almost discontinuously due to photo-ionization of K, L, M or N electrons are called K, L, M, N absorption edges respectively. The most pronounced absorption edges correspond to inner atomic shells. Most of the elements have at least one absorption edge in the soft x-ray range. This situation is depicted in Fig. 3 which shows the location of absorption edge in photon energy versus atomic number for various atomic shells.



a)



b) Fig. 2. Typical behavior of a) atomic scattering factor  $f_1$  and b) atomic scattering factor  $f_2$  versus frequency  $\omega$ .

The less known (or rather less used) phenomenon is a resonant anomalous dispersion of a real component of dielectric constant at absorption edges, which can result in quite a drastic change of refractive index. For example, although the common notion is that the refractive index  $n$  for x-rays is slightly less than unity, the resonant dispersion at absorption edges can result in  $n$  being significantly greater than 1 [22]. It can readily be noticed though that anomalous dispersion in the x-ray range must have a major importance as far as the Cerenkov and transition radiations are concerned since the behavior of  $n(\omega)-1$  (in the Cerenkov radiation) or  $n_1^2(\omega)-n_2^2(\omega)$  (in the case of the transition radiation), determines the very existence of these phenomena.

In order to take the anomalous dispersion into account, we use atomic scattering factors to calculate the dielectric constant and absorption.

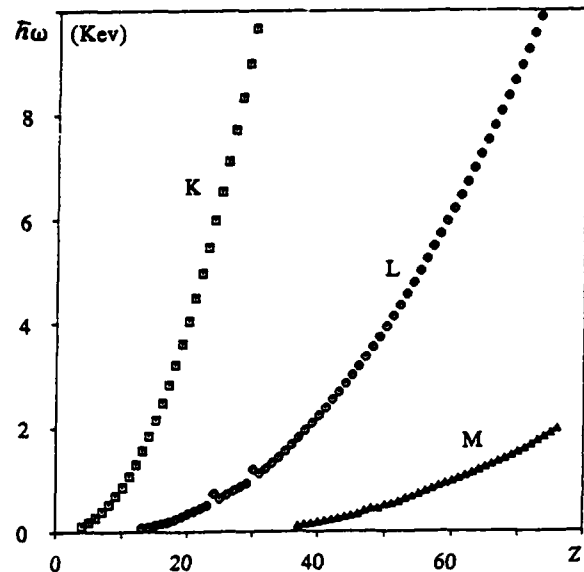


Fig. 3. Location of absorption edges in photon energy  $h\omega$  versus atomic number  $Z$ , with curves K, L, and M corresponding to the respective absorption edges.

The total (complex) dielectric constant can be expressed then in terms of the complex atomic scattering factor

$$\epsilon = (1 - f_r \lambda^2 N_A / (2\pi))^2; \quad f = f_1 + if_2 \quad (12)$$

where factors  $f_1$  and  $f_2$  are real and can be expressed as [15,22]

$$f_1 = Z + \frac{2}{r_0 c} \sum_q \int_{\omega_q}^{\infty} \frac{\nu^2 (\omega^2 - \nu^2) Z_q \mu_q(\nu) d\nu}{(\omega^2 - \nu^2)^2 + \Gamma_q^2 \omega^4} \quad (13)$$

and

$$f_2 = \frac{2}{r_0 c} \sum_q \int_{\omega_q}^{\infty} \frac{\Gamma_q \omega^2 \nu^2 Z_q \mu_q(\nu) d\nu}{(\omega^2 - \nu^2)^2 + \Gamma_q^2 \omega^4} \quad (14)$$

where  $Z_q$  is the number of q-shell electrons,  $\mu_q$  is the cross-section for photo-ionization of q-shell electrons by a photon with a frequency  $\nu$ ,  $\omega$  is the frequency of incident photon,  $\Gamma_q$  is the damping factor, and  $\omega_q$  is the threshold frequency (i.e. absorption edge frequency). The damping constant  $\Gamma_q$  can be determined experimentally. In the ideal case, the damping is due to radiation damping only [22],

$$\Gamma_q = \Gamma_0 = 2e^2 \omega_q / (3m_0 c^3) = 2r_0 k_q / 3. \quad (15)$$

Eqs. (13) and (14) are the counterparts of the Kramers-Kronig relations for atomic scattering factors. Each bound electron in an atom can be treated as an oscillator and the summation of the scattering factors from each electron gives the resulting atomic scattering factor in Eqs. (13) and (14). Far from absorption edges, Eqs (13) and (14) can be reduced to

$$f_1 = Z + \frac{2}{r_0 c} \int_0^{\infty} \frac{\nu^2 \mu_a(\nu) d\nu}{\omega^2 - \nu^2} \quad (16)$$

$$f_2 = \frac{\omega \mu_a(\omega)}{4\pi r_0 c} \quad (17)$$

where  $\mu_a = \mu/(N_A) = \sum \mu_q Z_q$  is the atomic cross-section. Since usually  $f_1 \gg f_2$  and  $1 \gg r_0 \lambda^2 N_A f_1 / (2\pi)$ , we can further simplify Eq. (12) as

$$\epsilon \approx 1 - \frac{f_1 r_0 \lambda^2 N_A}{\pi} \quad (18)$$

With experimental and theoretical data for atomic scattering factors in Ref [15], we can readily calculate absorption coefficient and dielectric constant with Eqs. (16) and (17), and make the following observations. As expected, we find  $f_1 \approx Z$  at the frequencies higher than the frequency of K absorption edge since all the electrons can then be considered as free. Elements with  $Z = 1$  to 4 have their K absorption edges below 0.2 keV, Fig. 3. However, there are many absorption edges of elements of high  $Z$  falling within the soft x-ray range as depicted in Fig. 3. As a result, Eq. (18) has to be used for calculation of dielectric constant which can be larger than unity around the absorption edges owing to anomalous dispersion.

Unfortunately, the known experimental data (see e.g. Ref[15]) do not provide any significant information on the atomic scattering factor  $f_1$  in the very close vicinity of absorption edges, i.e. in the range being of the most interest for our purposes. Apparently this is related basically to the fact that so far, there were no immediate practical needs for this kind of data. Therefore, in order to obtain the data on the resonances of real part of refractive index, we have to make a theoretical estimates based on Eq. (13) using some reasonable assumptions. Assuming, in a rough approximation, in Eq. (13) [15,22,23]

$$\mu_q \approx \frac{r_0 c}{2\omega_q} \left( \frac{\nu}{\omega_q} \right)^{p_q} \quad \text{for } \nu < \omega_q \quad (19)$$

where increment  $p_q$  varies [22,23] for different shells (and frequencies) remaining basically between  $p = 3$  and  $p = 2$ , we rewrite Eq. (13) in the form

$$f_1 = \sum_q Z_q J_q \quad (20)$$

where

$$J_q = (p_q - 1) s^2 \int_1^{\infty} \frac{(x^2 - s^2) dx}{x^{p_q} [(x^2 - s^2)^2 + \Gamma_q^2 x^4]} \quad (21)$$

where  $s = \omega/\omega_q$ . Using  $p = 3$  which is approximately valid for K-electrons [23], one readily obtains that in this case

$$J_K = 1 + \frac{1}{4x} \ln \left[ \frac{(x-1)^2 + \Gamma^2/4}{(x+1)^2 + \Gamma^2/4} \right] \quad (22)$$

whereas for  $p = 2$  (which is approximately the case for L-electrons)

$$J_L = 1 + \frac{1}{2x^2} \ln \left[ \frac{(x^2 - 1)^2 + \Gamma^2}{1 + \Gamma^2} \right] \quad (23)$$

For M-electrons  $p$  is close [24,25] to 2.5; calculations for this and some other fractional quantities of  $p$  with  $2 < p < 3$  [which result in much more complicated functions compared with Eqs.(22) and (23)] can be found in Ref.[22]. At the present stage, however, it does not seem justifiable to go into too detailed picture of the resonances, since  $p$ -factor in general depends not only on the kind of shell, but also on frequency, and, quite possible, on many other factors. Therefore, in our further calculations in this paper, for all shells other than K-shell we will use Eq. (23) for  $p = 2$ , which results in slightly reduced quantity for the magnitude of  $|f_1|$ , and therefore, in reduced maximum intensity of radiation.

All solid elements have sharp resonance at K-edge, beginning from  $Z=3$ , i.e. from lithium, whose K-absorption edge corresponds to  $\lambda_K \approx 226.5 \text{ \AA}$ ;  $\lambda_K$  decreases as  $Z$  increases. Since the photo-ionization gives rise to sharp resonances only when electrons are excited from the inner-atomic shells, the L-shells can be used beginning from  $Z = 14$  (Silicon, with the L-absorption edge at  $\lambda_L \approx 123 \text{ \AA}$ ), M-shells beginning from  $Z = 48$  (cadmium, with  $\lambda_M \approx 28,13 \text{ \AA}$ ), and N-shells beginning from  $Z = 58$  (cerium with  $\lambda_N \approx 100 \text{ \AA}$ ; in this particular case, the N-shell resonance according to data [15] becomes very sharp even before N-shell is completely filled up). For all these shells and elements, the factor  $f_1$  at the absorption edge, according to Eqs. (20) - (23), can approximately be written as

$$f_1 \approx Z - A_q + B_q [J_q (\omega/\omega_q) - 1] \quad (24)$$

where subscript  $q$  labels the type of shell (K, L, M, N), and  $A_q = 0, 2, 10, 28$  and  $B_q = 2, 8, 18, 32$ , for the K, L, M and N shells respectively. The Eq. (24) and Eqs. (20) - (23) were used by us to calculate parameters of the system for a few specific examples of materials. Although the increment  $p$  is not very well defined for L, M and N shells, the total error in the peak intensity of radiation with  $p = 2$  does not exceed 10 - 20 %. The important factor that needs further detailed investigation, is the splitting of resonance for the higher shells (L, M, N) into sub-shell levels, which should reduce somehow the resonance peak of  $|f_1|$  and therefore, the peak intensity of the transition radiation. It must be noted though that all the results using Eqs. (22) and (24) should be valid for K-shell lines. One can also note, that the peak resonant magnitude of  $f_1$  determined by Eqs. (22) or (23) is very insensitive to the variation of damping parameter

$\Gamma$  compare with radiation damping Eq. (15), since this magnitude at the point of resonance ( $x=1$ ) depends on  $\Gamma$  as  $\approx \ln(\Gamma)$ .

### Selection of materials

Proposed method of x-ray generation is suitable to obtain radiation in the entire range of wavelengths 1 - 200 Å. Using various combination of materials, a broad spectrum of x-ray radiation can be obtained. This method, however, can be envisioned as the most efficient way of generation of narrow x-ray lines radiation in the vicinity of absorption edges of various elements where dielectric constant  $\epsilon$  varies drastically. The idea is that for each desired frequency the alternating layers are chosen in such a way that one of the materials of the multilayer structure has its resonant frequency (i.e. frequency of one of its absorption edges) in the vicinity of the desired frequency. We will call such material (or layer) a "radiator". The other material must be chosen in such a way that its absorption edges are far from the chosen frequency of radiation. We will call such layers "spacers". Another requirement for the spacer is that its absorption in the vicinity of desired frequency be minimum. This brings us to the condition that for the most of frequencies of radiation the spacer must be a light element with a low atomic number. Yet another "technological" requirement is for each material to form stable layers with smooth surfaces. All these requirements single out three light elements ("island of light elements"): B, Be, and C as the best candidates. It is worth noting that carbon is conventionally used in multilayers mirrors for x-ray range [10].

The radiator candidates can be chosen from the elements in the periodic table with one of their absorption edges close to the desired frequency. This procedure is illustrated by Fig. 3. In Fig. 3 (which is based on data from Ref [15]), the photon energies corresponding to K, M, L absorption edges are plotted against the atomic number of elements which embrace almost the entire periodic table. One can see that for photon energy within the soft x-ray range (up to 2 keV), elements for the radiator can be chosen from K, L, or M branches. The further selection of one of these groups is based on the absorption factor as well as the dielectric constant factor  $|\epsilon_1 - \epsilon_2|^2$ . At high photon energy ( $\geq 0.3$  keV or  $\lambda \leq 44$  Å), the rule of thumb is to choose the heaviest elements as the radiator because their dielectric constants differ the most from the light spacer. To illustrate that, consider desired photon energy  $\approx 0.88$  keV corresponding to  $\lambda \approx 14$  Å. One can see from Fig. 3 that the radiator candidates are Ni and Ce (leaving aside Ne as a gas). Obviously, the best candidate is Ce.

The procedure described above enables one to select couples of elements each one consisting of a heavy element (radiator) + a light element (spacer) for generation of narrow line radiation with rela-

tively high photon energy or short wavelengths (down to a few angstroms). At low photon energies, though, the light element may occur to be a good candidate as radiator. Consider an example when the desired photon energy of radiation is 100 eV which corresponds to  $\lambda \approx 110$  Å. One can see from Fig. 3 that the radiator candidates are Be, Al and Rb (with different shells). Since at low photon energy the absorption factor is larger for elements with high atomic number, Be is the best candidate. It is obvious, therefore, that in order to design a narrow line radiator for longer wavelengths ( $\approx 44$  Å and longer) one has to use couples of two elements out of the "island of light elements", i.e. B, Be, and C. A combination of either two of these elements will form a system which would radiate at two frequencies out of three: 43.68 Å or 284.84 eV (C), 66.0 Å or 188.0 eV (B), and 111.0 Å or 111.0 eV (Be). Based on the results from previous section, the energy of electron beam required for these structures to generate, are very low and can vary from 200-300 keV to 1 MeV.

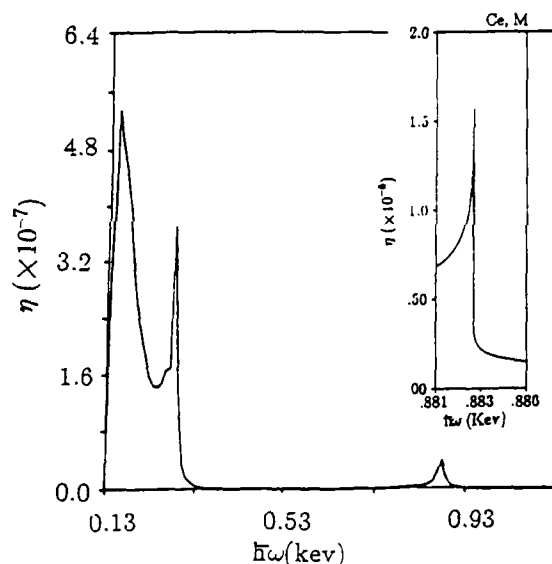


Fig. 4. Radiation efficiency  $\eta$  in number of photon / eV-electron-Mev versus photon energy  $\hbar\omega$  in keV for the periodic structure with combinations of Be/Ce when electron beam energy  $E_0$  is 1 MeV and the spatial period  $l$  and total length  $L$  are optimized at the absorption edges of heavy elements. Inset: Actual peak of Ce

We consider some combinations of different media that constitute the periodic structure. In these examples, our choice of spacers will be Carbon (C). The advantages of C is its surface smoothness and stable boundary separation. The K absorption edges of C is at 0.283 keV. For the illustration sake, we choose Barium (Ba), Cerium (Ce), and Europium (Eu) as radiators (this choice being somewhat arbitrary). For practical applications, the choice of radiator depends on the fre-



quency range desired. The absorption edges of Ba, Ce, and Eu are at 0.78 kev (M edge), 0.883 kev (M edge), and 1.11 kev (M edge) respectively. These elements with high atomic number have the characteristic of large  $f_1$  and  $f_2$  compared to elements with low atomic number. The results of the previous sections indicate that in a soft x-ray range one should expect the resulting spectral density to have two peaks. The peak at low frequency is due to the element with low atomic number (which act then as a radiator) while the peak at higher frequency is due to the element with higher atomic number. As a demonstration, we use electron beam energy of 1 Mev which is readily available in university laboratories.

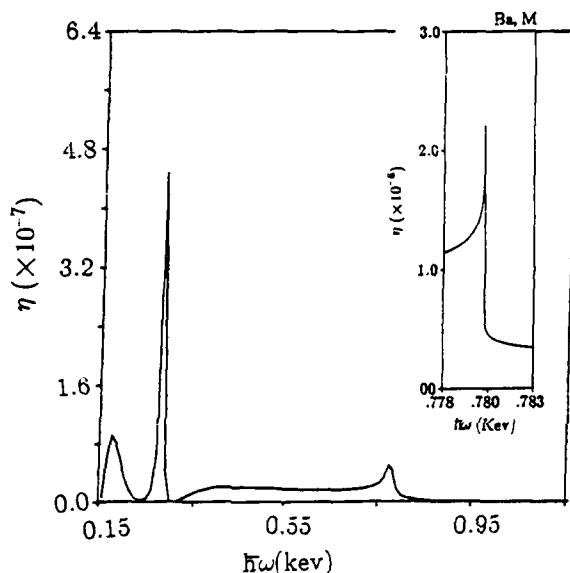


Fig. 5. The same as Fig. 4 except Be/Ba as the materials constituting periodic structure. Inset: Actual peak of Ba

Figs. 4-6 shows the plots of radiation efficiency  $\eta = E_0^{-1} dN/d\omega$  versus photon energy for the cases with C as a spacer and Ba, Ce, or Eu as a radiator. The plots in Figs. 4-6 show the radiation from each structure optimized at the absorption edge frequency of each radiator. Note that we plotted the actual height and width of the peaks from heavy materials in the inset of Figs. 4-6 instead of drawing them in the main figures because these peaks are too high and too narrow to be depicted in the main figures. Indeed, the actual relative width of each peak is about  $10^{-6}$  with radiation damping accounted for [see Eq. (15)], and its height is on the order of  $10^{-6}$  which is about two order of magnitude larger than the scale of the main figure. It is obvious that the spectrum are maximum at the absorption edge frequency of each radiator. Since  $|\Delta\epsilon|^2$ , which determines the intensity of radiation in direct proportion, decreases as  $\omega$  increases, the peaks at high frequency have lower intensities than those peaks at

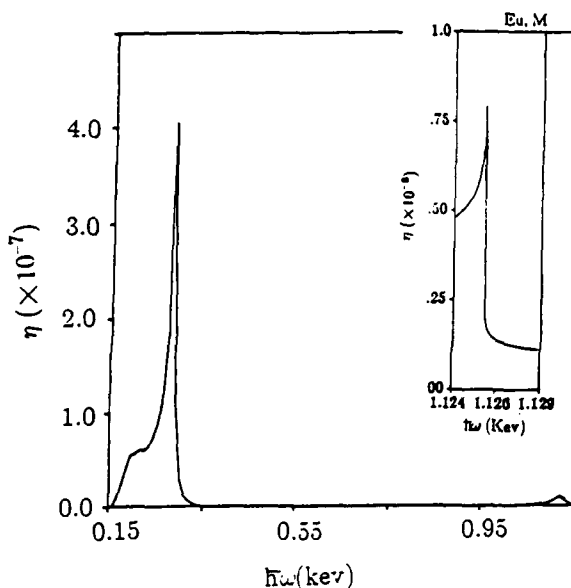


Fig. 6. The same as Fig. 4 except Be/Eu as the materials constituting periodic structure. Inset: Actual peak of Eu

low frequency. Based on the same reasoning, we expect the radiation at lower frequency generated by the light elements to be stronger than that of heavier elements emitted at high frequency. We also notice the abrupt decrease of radiation at frequency higher than the absorption edge frequency due to the discontinuous jump of absorption near the absorption edge.

The total length  $L$  of the structure and its spatial period  $l$  required for the maximum radiation for the C/Ba, C/Ce, and C/Eu structures when  $E_0 = 1$  Mev are listed in Table 1. The value of parameters  $L$  and  $l$  for the structures in Tables 1 correspond to the structure used in Figs. 4-6, i.e. to the optimum structure at the absorption edge of the heavy elements. We observe from the tables that the period of the structure does not depend on the kind of materials whereas the total length of the structure varies a lot with different media. The variation in total length is due to the dependence of  $L$  on absorption coefficient. The angle of emission which depends on the electron beam energy is approximately  $17.7^\circ$  for the case of  $E_0 = 1$  Mev.

## Conclusions

We have investigated the role of photoabsorption and electron scattering in x-ray emission by electrons with low energies. We showed that energy of electron beam  $E_0$  from 100 - 200 kev to a few Mev is sufficient to give rise to the narrow line transition radiation (with a relative linewidth  $\sim 10^{-4}$ - $10^{-5}$ ) in a multilayer structure with a short spatial period (50  $\text{\AA}$  to 2000  $\text{\AA}$ ). We developed a procedure which allows us to choose appropriate

Table 1. The optimal spatial period  $l_{opt}$  and optimal total length  $L_{opt}$  for period structure with combination of Be/Ge, Be/Ce, Be/Ba, and Be/Eu for  $E_0 = 1$  Mev around the radiation peak for higher frequencies corresponding to various transitions of different heavier elements (the M edges - for the Ba, Ce, and Eu).

Radiator	$\lambda$ (Å)	$l_{opt}$ (Å)	$L_{opt}$ (μm)
Ce	14 (0.88 kev)	1297	5.97
Ba	16 (0.77 kev)	1396	9.07
Eu	11 (1.11 kev)	982	9.48

materials (both for radiator and spacer) in order to obtain radiation with narrow resonant peaks at the frequencies of absorption edges of various elements which are due to photo-ionization electron transitions from inner-atomic shells. We have developed a numerical procedure to optimize parameters of the periodic structure required to obtain maximum radiation. In this procedure, the spatial period, optimal total length, and resonant angle are evaluated. This completely specifies the design of the system.

This research was supported by AFOSR.

## References

1. V. L. Ginzburg and I. M. Frank, "Radiation of a uniformly moving electron due to its transition from one medium into another," *Zh. Eksp. Theor. Fiz.* vol. 16, pp. 15-28, No. 1, 1946 ( *J. of Phys.*, vol. 9, pp. 353-62, No. 5, 1945).
2. G. M. Garibyan, "Contribution to the theory of formation transition x-ray radiation in a stack of plates," *Zh. Eksp. Theor. Fiz.*, vol. 60, pp. 39-52, 1971 ( *Sov. Phys. JETP*, vol. 33, pp. 23-9, July 1971).
3. M. L. Ter-Mikaelian, *High Energy Electromagnetic Processes in Condensed Media*. New York: Wiley Interscience, 1972.
4. M. J. Moran, B. A. Dahling, P. J. Ebert, M. A. Piestrup, B. L. Berman and J. O. Kephart, "Measurement of coherent transition X rays," *Phys. Rev. Lett.*, vol. 57, PP. 1223-6, 1986.
5. M. L. Cherry, G. Hartmann, D. Muller and T. A. Prince, "Transition radiation from relativistic electrons in periodic radiators," *Phys. Rev.*, vol. D10, pp. 3594-607, Dec. 1974.
6. P. J. Ebert, M. J. Moran B. A. Dahling, B. L. Berman, M. A. Piestrup, J. O. Kephart, H. Park, R. K. Klein and R. H. Pantell, "Transition X rays form medium-energy electrons," *Phys. Rev. Lett.*, vol. 54, pp. 893-6, March 1985.
7. C. W. Fabjan and W. Struczinski, "Coherent emission of transition radiation in periodic radiators," *Phys. Lett.*, vol. 57B, pp. 483-486, Aug. 1975.
8. M. A. Piestrup, P. F. Finman, A. N. Chu, T. W. Barbee, Jr., R. H. Pantell, R. A. Gearhart, F. R. Buskirk, "Transition Radiation as an x-ray source," *IEEE J. Quan. Elect.* vol. QE-19, pp. 1771-81, 1983.
9. T. W. Barbee and D. C. Keith, in *Workshop on Instrumentation for Synchrotron Radiation Research*, H. Winick and G. Brown, eds. Stanford Synchrotron Radiation Laboratory 78/04, III-36 (May 1978).
10. E. Spiller, "Evaporated multilayer dispersion elements for soft x-rays," in *Topical Conference on Low-Energy x-ray Diagnostics*, D. T. Attwood and B. L. Henke, eds. AIP Conf. Proc., vol. 75, 1981, pp. 124-130.
11. A. E. Kaplan and S. Datta, "Extreme-ultraviolet and x-ray emission and amplification by non-relativistic electron beam traversing a superlattice," *Appl. Phys. Lett.*, vol. 44, pp. 661-3, 1984.
12. A. E. Kaplan and S. Datta, "Extreme-ultraviolet and x-ray emission and amplification by non-relativistic electron beam traversing a superlattice," in *Second Topical Meeting in Laser Technique in the Extreme Ultraviolet*, S. E. Harris and T. B. Lucatorto, eds. AIP Conf. Proc., vol. 119, 1984, pp. 304-10.
13. S. Datta and A. E. Kaplan, "Quantum theory of spontaneous and stimulated resonant transition radiation," *Phys. Rev.*, vol. A31, pp. 790-6, Feb. 1985.
14. C. T. Law and A. E. Kaplan "x-ray transition radiation in a solid-state superlattice: photo-absorption, electron scattering, and radiation optimization," *Opt. Lett.*, vol. 12, pp. 900-902, Nov. 1987.
15. B. L. Henke, P. Lee, T. J. Tanaka, R. L. Shimabukuro and B. K. Fujikawa, *Atomic Data and Nuclear Data Tables*, vol. 27, pp. 1-144, Jan. 1982.
16. H. Raether, "Solid state excitations by electrons (plasma oscillations and single electrons transition)," in *Springer Tracts in Modern Physics*, G. Hohler, ed. vol. 38, New York: Springer-Verlag, 1965, pp. 84-157.
17. C. T. Law and A. E. Kaplan "Low relativistic electron beams traversing a superlattice as x-ray source," in *Third Topical Meeting on Wavelength Coherent Radiation Generation and Applications*, D. T. Attwood and J. Bokor, eds. AIP Conf. Proc. No. 147, 1986, pp. 27-33.
18. L. Pages, E. Bertel, H. Joffre and L. Sklavenitis, "Energy loss, range, and Bremsstrahlung yield for 10 kev to 100 Mev electrons in various elements and chemical compounds," *Atomic Data*, vol. 4, pp. 1-127, March 1972.
19. J. Ashkin and H. A. Bethe, "Passage of radiation through matter," in *Experimental*

- Nuclear Physics*, E. Sigre, ed. vol. 1, New York: Wiley, 1953.
20. B. Rossi, *High-Energy Particles*. Englewood Cliffs: Prentice-Hall, 1961.
  21. E. Fermi, *Nuclear Physics*. rev. ed., Chicago: University of Chicago Press, 1950.
  22. L. G. Parratt and C. F. Hampstead, "Anomalous dispersion and scattering of x-rays," *Phys. Rev.*, vol. 94, pp. 1593-60, 1954.
  23. D. R. Hartee, "Calculation of atomic structure," *Repts. Progr. in Phys.*, vol. 11, pp. 113-143, 1946.

## VUV Amplification of Neon-Like Titanium Ion

Hidehiko Yashiro,\* Tamio Hara, Kozo Ando, Yoshinobu Aoyagi,  
Toshihiko Dote,\* and Susumu Namba

*The Institute of Physical and Chemical Research, Hirosawa 2-1, Wako, Saitama 351-01, Japan*

*\*Department of Electrical Engineering, Faculty of Engineering  
Saitama University, Shimo-ohkubo 255, Urawa, Saitama 338, Japan*

### ABSTRACT

Amplified spontaneous emission of the  $2p^5 3s^3 P_1 - 2p^5 3p^3 D_2$  transition at 50.8 nm in neon-like titanium ion has been observed in a line-shaped plasma produced by focusing a long laser pulse of 5 ns on a slab target for keeping population inversion for a long time.

### INTRODUCTION

Laser produced plasmas have been applied to short wavelength laser studies because of including high density multiply charged ions. The electron collisional excitation of neon-like ions in the laser produced plasma is one of the pumping schemes of the short wavelength laser. The radiative decay of the  $2p^5 3p$  levels to the ground state  $2p^6$  of neon-like ion are forbidden, while the  $2p^5 3s$  levels decay very rapidly to the ground state. Consequently, the population inversion between  $2p^5 3s$  and  $2p^5 3p$  takes place. D.L.Mattews and co-workers have reported ASE ( Amplified Spontaneous Emission ) of neon-like selenium ion using a selenium coated film target [1]. B.J.MacGowan and co-workers also reported ASE of neon-like molybdenum ion using a molybdenum coated film target [2]. T.N.Lee and co-workers reported ASE of neon-like germanium ion using a coated film, and also observed ASE of copper ions using a coated film, a foil and a slab as a target [3]. The electron collisional excitation is essentially a continuous pumping scheme, so that the population inversion is maintained while this pumping scheme exists. We have observed ASE of the  $2p^5 3s^3 P_1 - 2p^5 3p^3 D_2$  transition of neon-like titanium ion at 50.8 nm. The Nd-glass laser with the pulse width of 5 ns is focused on a slab target in a

line shape for producing population inversion.

### EXPERIMENT

The experimental setup is illustrated in Fig.1. This system is mainly consisted of the target chamber equipped with a focusing lens system and a Seya-Namioka type monochromator to observe the VUV emission from the laser produced plasma. The Nd-glass laser ( 1.05  $\mu\text{m}$ , 5 ns ) was focused on a target in a line shape of maximum 18 mm

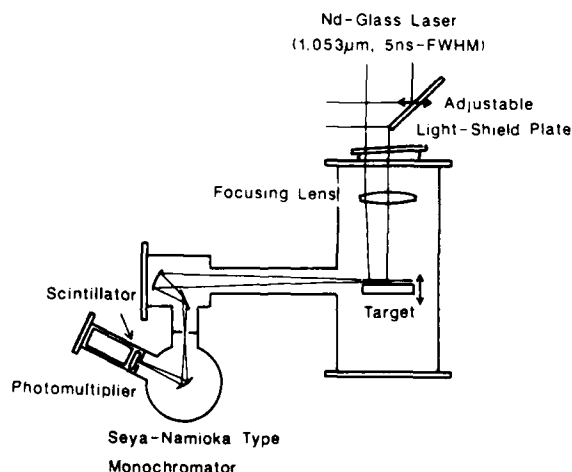


Fig.1 Schematic of the experimental setup.

length and 40  $\mu\text{m}$  width by the focusing lens system. The width of line focus is defined as a FWHM ( Full Width at Half Maximum ) of the depth profile of a scar on a target. At the laser energy of 40 J, the laser power density was about  $1.0 \times 10^{12} \text{ W/cm}^2$ . In order to vary the plasma length without any change of other parameters, an adjustable light-shield plate was set in front of the focusing lens system. A titanium target was a slab of the 1 mm thickness with 99.9 % purity. In this experiment, the Seya-Namioka type monochromator was set to observe the emissions along the long side of a line plasma ( the axis of the plasma ) as shown in Fig.1. This monochromator was used with a grating of 1200 lines/mm and 2 Å resolution. A concave mirror and a plane mirror which were coated with platinum were set to focus a image of the plasma on the entrance slit of the monochromator. We observed the plasma at distance of 100  $\mu\text{m}$  from the target surface, because the spatial resolution of this optical system was about 100  $\mu\text{m}$  and the emission from the plasma was not cut by the edge of the target. This position has the strongest intensity although the intensity was not able to be measured inside of this position. The emission from the laser produced plasma was detected by the photomultiplier with the scintillator of dimethyl-POPOP deposited on a plane glass plate uniformly. The response time of the detector system was about 3 ns.

## RESULTS & DISCUSSION

Spectra around 50.8 nm are shown in Fig.2 for the plasmas of 18 mm and 9 mm length. The wavelength of 50.8 nm corresponds to the  $2p^3s^3P_1 - 2p^3p^3D_2$  transition of neon-like titanium ion. The line intensity of this transition for the plasma of 9 mm length is buried in the background level. But for the plasma of 18 mm length the line intensity at 50.8 nm is clearly higher than the background. The measured intensities at 50.8 nm and 50.6 nm are shown as a function of the plasma length in Fig.3, where the intensity of 50.6 nm was used as a monitor of the background. It is clear that the line intensity at 50.8 nm increases nonlinearly with the plasma length. On the other hand, the intensity at 50.6 nm does not increase. It is considered from these results that the spontaneous emission at 50.8 nm is amplified in the laser produced plasma. However, the amplification at 50.8 nm was not detected at the laser energy less than 40 J.

From the measurement of time-resolved spatial distribution of the emission, the expansion velocity of the plasma was obtained to be about  $1.6 \times 10^7 \text{ cm/s}$ . The time of flight through the distance of 100

$\mu\text{m}$  which is the spatial resolution of measurement is 0.63 ns. This time is so short compared with 5 ns of the laser pulse. It is obvious that if a target is sufficiently thick, the plasma is ejected continuously during the laser irradiation.

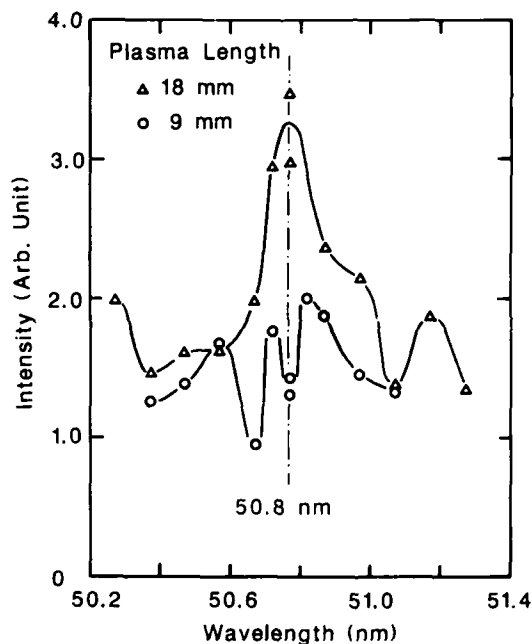


Fig.2 Spectra for plasma lengths of 9 mm and 18 mm. These spectra were observed at 40 J laser energy.

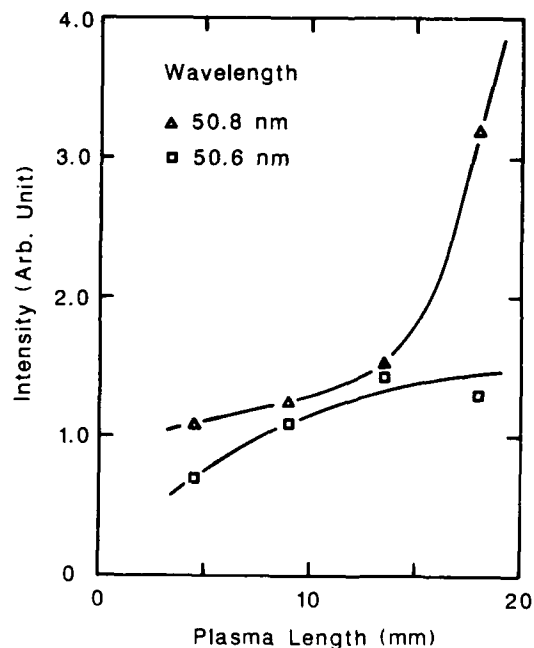


Fig.3 Intensity variations at 50.6 nm and 50.8 nm as a function of the plasma length. The laser energy is 40 J.

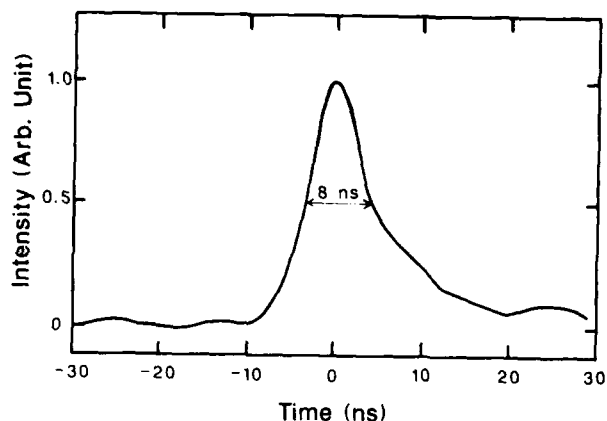


Fig.4 Time variation of the intensity at 50.8 nm.

The depth of a ditch created by the laser was about 16  $\mu\text{m}$ , which was negligible compared with the distance of 100  $\mu\text{m}$  from the target.

A typical example of ASE signal at 50.8 nm is shown in Fig.4. The time variation of the line intensity at 50.8 nm has a FWHM of about 8 ns. This time width can be explained as the combination of the laser pulse width and the response time of the detector. Because the response time is about 3 ns, the duration time of 50.8 nm emission is estimated to be about 5 ns, which is equal to the laser pulse width. Therefore, it is considered that long time duration of population inversion is realized by using the long pulse laser for irradiating a slab target. Recently, mirrors with high reflectivity in VUV region has been developed by use of a multilayer structure [4]. And besides, the observation of a large effect of the cavity mirrors on VUV ASE signal in the plasma produced by a short pulse laser was reported [5]. In our experiment using a longer pulse laser, it is expected that the effect of cavity mirrors on ASE signal becomes more significant.

#### SUMMARY

We produced a plasma by focusing a long pulse Nd-glass laser in a line shape on a slab target. ASE of the neon-like titanium ion transition  $2p^5 3s^3 P_1 - 2p^5 3p^3 D_2$  at 50.8 nm along the axis of the plasma has been observed. From the time variation of 50.8 nm emission, we conclude that amplification will continue during irradiation of the Nd-glass laser. It is greatly expected that by using cavity mirrors in long pulse operation, VUV laser oscillation with high efficiency can be achieved.

#### REFERENCES

1. D.L.Matthews, P.L.Hagelstein, M.D.Rosen, M.J.Eckart, N.M.Ceglio, A.U.Hazi, H.Medecki, B.J.MacGowan, J.E.Trebes, B.L.Whitten, E.M.Campbell, C.W.Hatcher, A.M.Hawryluk, R.L.Kauffman, L.D.Pleasant, G.Rambach, J.H.Scofield, G.Stone and T.A.Weaver, "Demonstration of a Soft X-Ray Amplifier," *Phys. Rev. Lett.* **54**, 110-113 (1985).
2. B.J.MacGowan, M.D.Rosen, M.J.Eckart, P.L.Hagelstein, D.L.Matthews, D.G.Nilson, T.W.Phillips, J.H.Scofield, G.Shinkaveg, J.E.Trebes, R.S.Walling, B.L.Whitten and J.G.Woodworth, "Observation of soft x-ray amplification in neonlike molybdenum," *J. Appl. Phys.* **61**, 5243-5248 (1987).
3. T.N.Lee, E.A.McLean and R.C.Elton, "Soft X-Ray Lasing in Neonlike Germanium and Copper Plasmas," *Phys. Rev. Lett.* **59**, 1185-1188 (1987).
4. N.M.Ceglio, D.G.Stearns, D.P.Gaines, A.M.Hawryluk and J.E.Trebes, "Multipass amplification of soft x rays in a laser cavity," *Optics Lett.* **13**, 108-110 (1988).
5. J.A.Trail, R.L.Byer and T.W.Barbee,Jr., "Measurement of soft x-ray multilayer mirror reflectance at normal incidence using laser-produced plasmas," *Appl. Phys. Lett.* **52**, 269-271 (1988).

## X-Ray Laser Research at Physics International

C. Deeney, J. Levine, T. Nash, P. D. LePell, and M. Krishnan

*Physics International Company  
2700 Merced Street, San Leandro, California 94577*

### Abstract

Photopumped and recombination X-ray laser schemes are under investigation at Physics International, on the DNA/PITHON 3 TW facility. For the sodium-neon resonant photopumped scheme, DNA/PITHON is used to implode a sodium-bearing plasma, the pump, and a secondary capacitor bank is used to drive a neon gas puff Z-pinch, the lasant. The characterization of the pinched sodium plasma is reported in this paper, as are pump power measurements, which showed 65 GW in the Na X  $1s^2-1s2p$   $^1P$  line. In earlier experiments, neon gas was imploded onto sodium-fluoride coated targets, on-axis, but insufficient sodium pump powers were obtained. However, some very interesting spectral features, which could be an indication of recombination pumping, were observed in the neon plasmas formed when neon was imploded onto aluminum targets. These results are also presented in this paper.

### Introduction

The energy levels for the sodium-neon photopumped (1) X-ray laser scheme are shown in Fig. 1. The Na X  $1s^2-2p$   $^1P$  line at 11.0027 Å pumps the Ne IX  $1s^2-1s4p$   $^1P$  line, at 11.0003 Å. This pumping could result in inversions in the 4-3, 4-2, and 3-2 lines. Apruzese and Davis (2) predict a gain on the 4-3 line, at 230 Å, of  $1\text{ cm}^{-1}$  when the sodium and neon plasmas are 4 cm apart and the sodium radiates 200 GW in the pump line. This gain estimate assumes a neon ion density of  $10^{18}\text{ cm}^{-3}$ .

This photopump scheme has been investigated experimentally using laser-produced plasmas (3) and Z-pinch (4); however, there has as yet been no demonstration of gain. At Physics International, the sodium-neon scheme is being investigated using pulse-power-driven Z-pinch to produce both the lasant and

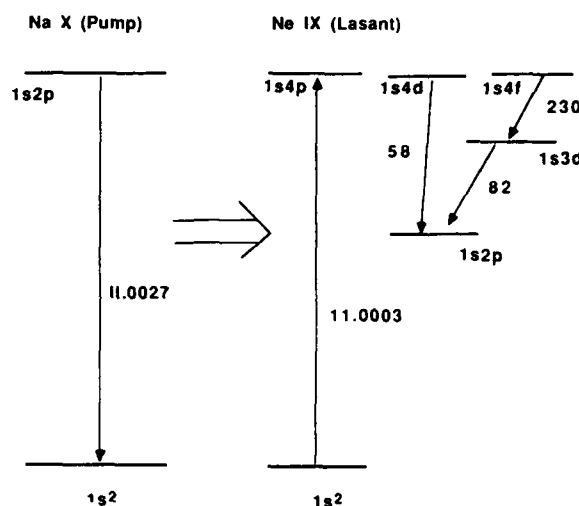


**Figure 1. Energy level diagram for the sodium-neon photopump X-ray scheme.**

pump plasmas. In a gas puff Z-pinch, a large current, 100 kA - 5 MA, is passed through either a gas jet or an annular gas shell. The interaction of the current with its self-magnetic field results in a Lorentz force that is directed radially inwards. This force compresses the plasma. When the sheath or imploding shell assembles on-axis, the directed radial kinetic energy is thermalized and a hot, dense plasma is formed, which is subsequently heated by the current.

Gas puff Z-pinch and imploding wire arrays are copious X-ray sources. When imploded with small, <10 kJ, slow, 1-μs risetime banks, 10% of the stored energy is radiated in the 100-1000 eV region over 500 ns or so, and the plasmas formed typically have electron densities in the range of  $10^{19}$  to  $10^{20}\text{ cm}^{-3}$  and electron temperatures less than 100 eV (5,6). On large pulse-power-driven Z-pinch, which operate at the

multi-TW level, greater than 1% of the stored energy is radiated at keV photon energies in 10-20 ns timescales (7), and the plasmas have electron densities in the mid  $10^{20} \text{ cm}^{-3}$  and electron temperatures in the range of 400-1000 eV (7,8,9,10).

Based on the performance of Z-pinchs under different driver conditions, the approach shown in Fig. 2 was adopted to perform sodium-neon photopump experiments. The DNA/PITHON generator, whose parameters are given in Table 1, is used to implode a sodium bearing plasma. This should provide the high pump power. The cooler, 50-eV, less dense,  $n_e = 5 \times 10^{19} \text{ cm}^{-3}$ , neon plasma will be formed using a 27-kJ, 9- $\mu\text{F}$  capacitor bank, which generates 500 kA with a 2- $\mu\text{s}$  quarter period. The geometry of these two Z-pinchs is designed to allow them to be brought to within 4 cm of each other. The advantage of this approach is that the two plasmas can be independently controlled and optimized to the correct size, temperature, and densities. Also, length scaling can be examined without having to change the actual plasma length, which could alter the plasma parameters. The variation of intensity with length can be achieved by baffling the

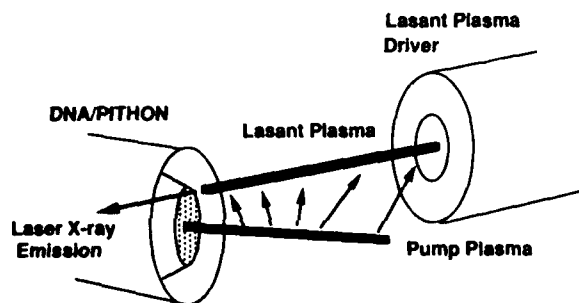


**Figure 2. Physics International's approach to photopumped X-ray laser scheme. Two separate, optimized drivers are used to produce the lasant and the pump plasma.**

**Table 1. PITHON parameters.**

Machine Parameters:

Peak Current = 2 to 3 MA  
Inductance = 20 to 30 nH  
 $t_{\text{rise}} = 50 \text{ ns}$   
E<sub>stored</sub> = 3/4 MJ

Pinch Plasma Parameters:

$n_e \approx \text{mid } 10^{20} \text{ cm}^{-3}$   
 $T_e \approx 400 \text{ to } 1000 \text{ eV}$   
 $l \approx 3 \text{ cm}$   
 $d \approx 2 \text{ mm}$   
Yield  $\approx 10 \text{ kJ}$  of 1 keV X-rays  
 $t \approx 10 \text{ to } 20 \text{ ns}$

neon plasma so that different lengths of the lasant plasma are pumped by the sodium plasma.

In this paper, the preliminary efforts to produce the sodium plasma, and the pump yield measurement on DNA/PITHON, are described. The development of the neon plasma is also briefly described. Early experiments on the sodium-neon scheme involved imploding neon gas onto aluminum and sodium fluoride coated targets. Although the sodium pump line yield was low, some interesting spectral features were observed, which could indicate recombination pumping, and these are also discussed.

**Sodium Source Development.**

The reactivity of pure sodium makes it difficult to use in Z-pinchs, compared to ordinary metals that can be made into wires and imploded as arrays. Techniques do exist which allow sodium compounds to be vaporized and puffed, similar to a gas. An electrical discharge passed through a NaF capillary (11) has been shown to produce a sodium containing jet, and this jet was used as a Z-pinch load on Gamble II to produce 35 GW in the Na X  $1s^2-1s2p \ ^1P$  line (12,13). Other work performed by Gazaix (14) has demonstrated highly collimated jets of aluminum and sodium.

In the source used in the Physics International experiments, sodium chloride was packed into a fixed annular volume. The mass loading was  $100 \pm 10 \text{ mg}$ . The driver bank was a 28- $\mu\text{F}$  capacitor, charged to 15 kV, which discharged through a 58- $\mu\text{H}$  inductor into the sodium chloride load. The capacitor was crowbarred after 40  $\mu\text{s}$  to allow the inductor-driven current to decay slowly in the sodium chloride plasma. Typically the main PITHON current would be fired between 30 and 50  $\mu\text{s}$  after the current was initiated in the sodium chloride load. No detailed measurements were performed of the mass distribution or the control of the sodium chloride vapor source. Future work will improve and characterize the sodium source.

**Pump Line Yield Measurements.**

The sodium source was mounted onto the DNA/PITHON generator and sodium chloride vapor puffs were imploded. A range of X-ray diagnostics, as shown in Fig. 3, was employed to measure the X-ray yield and the collapse dynamics. The pump line

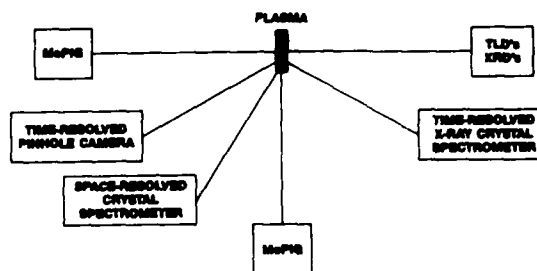


**Figure 3. Diagnostic layout.**



temporal behavior was measured using a germanium-filtered, copper cathode X-ray diode (15) (XRD) and a time-resolved (3 gated frames) crystal spectrometer. A 12-frame X-ray pinhole camera filtered with 8  $\mu\text{m}$  of Kapton was used to study the spatial extent of the X-ray emitting regions in time. A time-integrated crystal spectrometer was used to measure the relative yield from one shot to another.

The time-resolved pinhole camera shows that the sodium plasma is 3 mm in diameter and 2 cm long; however, it is not very homogeneous or uniform. This is acceptable, in this case, since there is sufficient separation of the pump and lasant plasma to compensate for non-uniformities in the sodium plasma. However, gross plasma instabilities in the sodium plasma should be avoided. The sodium plasma radiates typically for 40 ns, with the most intense period being 15 ns in duration. The axial variation in time to pinch—the so-called *zipper effect*—is of the order of 10 ns. A typical time-integrated spectrum, Shot #4706, is shown in Fig. 4. The ratio of the  $L_{\alpha}$  to the  $He_{\alpha}$  of the sodium indicates a temperature of 600-800 eV, which is hotter than the optimal temperature estimated to maximize the  $He_{\alpha}$  intensity. As can be seen from the spectrum, there is a significant fraction of radiation in aluminum impurity lines and some in zinc and copper lines. The source of these impurities are the puff nozzle, which is made from aluminum, and the current return cage, which is made from brass. Using a graphite nozzle, the aluminum radiation was eliminated but the pump line yield was not significantly increased.

In Fig. 5, the germanium-filtered, copper cathode XRD signal is shown superimposed on the pinch current for Shot # 4706. The peak power measured in the pump line was 65 GW with a 14-ns FWHM. The total yield in the line was 2 kJ. The filtering on this diode rejects the  $Na L_{\alpha}$  line and the aluminum radiation. From the published cathode sensitivities and known filter transmissions, the signal was analyzed to give the absolute power in the pump line. Further analysis of the data, to study the yield variation with puff driver and pulsed power parameters, is underway. The germanium filter does pass the copper and zinc impurities, which are seen on the spectra shown in Fig. 5; however, their magnitudes are low for this shot. In

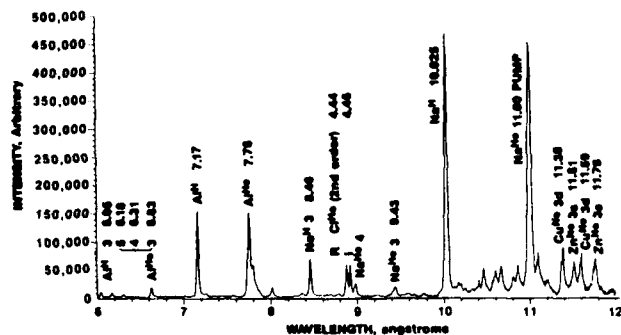


Figure 4. Time integrated X-ray crystal spectra.

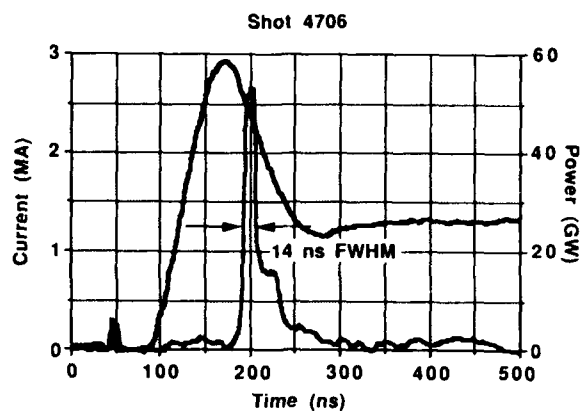


Figure 5. Germanium-filtered, copper cathode XRD: Signal and Pinch Current.

shots where the pump line yield was low, the impurity emission was comparable with the pump line. This is demonstrated in the time resolved spectra, shown in Fig. 6.

#### The Neon Plasma Source.

As described above, a 27-kJ capacitor bank was used to drive the neon plasma. Some preliminary shots were taken with this source, and the time resolved XUV images obtained show that the plasma is 5 cm long and 1 mm in diameter. There were problems with insulator breakdown under UV illumination; therefore, the neon bank was redesigned. As yet, this redesigned version has not been tested and the neon plasma has not been diagnosed.

#### Implosions onto Targets and Evidence for Recombination Pumping.

There have been some other tests performed at Physics International to either implement the sodium pump or produce a uniform neon plasma. These tests involved imploding a neon gas shell onto a target placed on-axis, as pioneered by Sandia (16) and shown schematically in Fig. 7. Targets of 3-cm length and 1.6-mm diameter

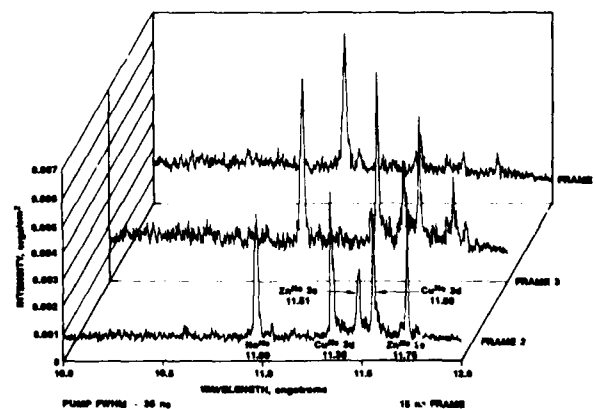
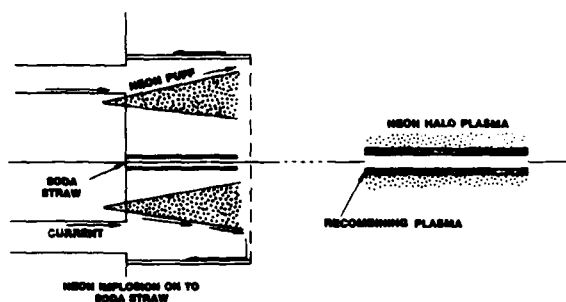


Figure 6. Time-resolved X-ray crystal spectra.



**Figure 7. Schematic drawings of experimental configuration which produced aluminum and neon plasmas.**

were used, and these were 2- $\mu\text{m}$ -thick parylene coated with 3000 Å of sodium fluoride or sometimes 3000 Å of aluminum as a comparison. With the sodium-fluoride-coated targets only 100 joules was emitted in the sodium pump line, which is an insufficient yield. With the target in place, a uniform neon plasma some 3 cm long and 200  $\mu\text{m}$  thick was produced on the surface, as shown in the 5-ns X-ray framing camera pictures in Fig. 8, but the neon plasma was of too high a temperature and had too short a lifetime to be usefully pumped by a sodium plasma.

Thus the use of targets did not seem to be a fruitful way of approaching the sodium-neon scheme. But targets may be of interest in another way. When a collapsing gas shell stagnates onto a target, only a few thousand angstroms of the target are heated enough to radiate in the K-shell, so the bulk of the target remains cold and dense. Thus there can be two mechanisms by which three-body recombination can take place. After the initial pinch onto the target, the plasma can expand and cool, which would result in three-body recombination in the dense plasmas near the target surface, or secondly, stripped ions in the thermalised neon plasma which propagate towards the cool dense target can then undergo three-body recombination. As previously stated, the neon was ionized to the H-like and He-like states when imploded onto a target, and therefore there may be evidence of recombination producing inversions. On-axis and off-axis XUV spectra

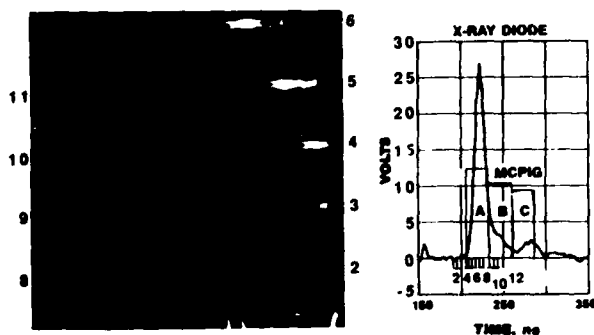


**Figure 8. 5-ns time-resolved X-ray pinhole photographs from Shot 4436, neon imploding onto 1.8- $\mu\text{m}$  Al.**

were taken, using the time-resolved MCPIGS and time-integrated McDonald spectrometers, so that it was possible to look for inversions which could indicate three-body recombination pumping.

In Fig. 9, the radial and axial spectra taken from a 25-ns long MCPIG time frame are shown. The target was again coated with 3000 Å aluminum. There is a known candidate laser line, 4f-3d in Li-like aluminum (17), and this line is seen in both the on- and off-axis spectra. Its intensity relative to the non-lasing, 150.1 Å, Li-like oxygen 3p-2s line is the same in both the on- and off-axis spectra. This indicates that there is no inversion, probably due to severe optical trapping in the 3d-2p transition in Li-like aluminum since the  $n=2$  level is the ground state.

Spatial anomalies have been observed, however, in the XUV emissions from H-like neon when the neon was imploded onto 1.8- $\mu\text{m}$  thick aluminum cylindrical targets. These more massive, 1.8- $\mu\text{m}$  aluminum targets may serve as better heat sinks to induce recombination. In Fig. 10, the spatial profiles of the 4-2 and 3-2 (Balmer  $\alpha$ ) of H-like neon are shown. These line profiles were taken from a 25-ns-long time frame of a MCPIG. The time frame was timed to be coincident with the stagnation of the bulk plasma on the target. The radial spatial resolution, due to a cross slit, is 1.5 mm at the source. The 4-3 line emission peaks on-axis but the spatial resolution is comparable to the target size; therefore, this emission is probably peaked in the vicinity of the outer target surface. By contrast, the 3-2 line emission peaks at some 6-mm diameter annulus. In Fig. 11, the spatial radial profiles of the 3-2 and 4-2 lines in H-like neon are compared when neon is imploded onto targets coated with a large amount of magnesium. The use of magnesium avoids the problem of the blending of the neon 4-2 line with an aluminum line. The line emission in both these lines is similar. If it is assumed that the 4-2 line behaves similarly for a aluminum target, then the H-like neon 4-2 line and the 4-3 line have different radial spatial profiles. Any gain on the 4-3 line would be an order of magnitude greater than that for the 4-2 line. Thus the 4-3 line could be lasing on-axis while the 4-2 does not.

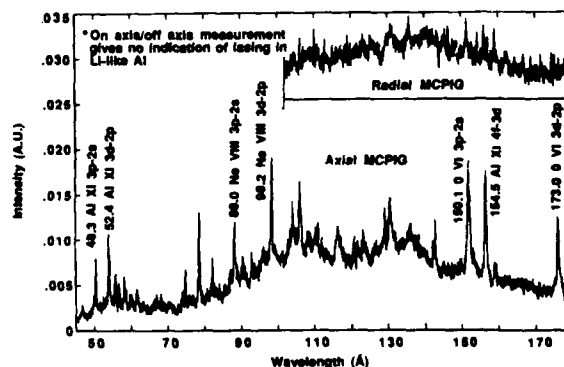


**Figure 9. Shot 4519, MCPIGs spectra, neon on 3000 Å Al on 2- $\mu\text{m}$  parylene.**

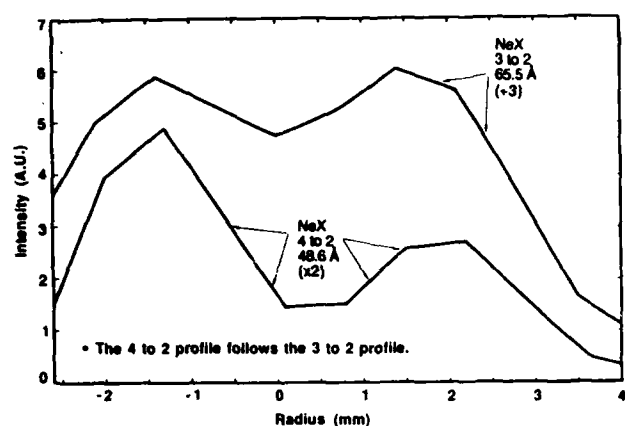


**Figure 10. Shot 4452, radial profiles of lines of H-like neon, neon on 1.8  $\mu$ m Al.**

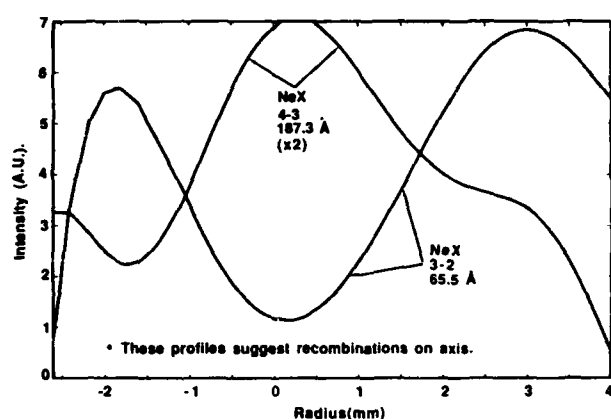


**Figure 11. Shot 4438, neon on magnesium, radial profiles of lines of H-like neon.**

An interpretation of the spatial line profile data is that, at stagnation, the neon within a 2 to 3 mm radius is in the H-like stage, and within a 1 to 2 mm radius the neon is predominantly fully stripped. As these fully stripped ions come into contact with the dense and cool aluminum plasma, three-body recombination can take place which populates the  $n=4$  level in H-like neon. This would result in the maximum 4-3 emission emanating close to the outer target surface. These features are only observed with the more massive, 1.8- $\mu$ m Al targets, probably due to increased cooling, hence recombination. The fact that the emission occurs at the time of stagnation, not expansion, would seem to contradict any interpretation based on plasma expansion.

The optical trapping should be less for the 3-2 transition in H-like neon, where the  $n=1$  level is the ground state, by approximately a factor of 10 compared to the 3-2 transition in the Li-like aluminum. This may explain why there was no evidence of inversion in the Li-like aluminum but some in the neon. On- and off-axis measurements have yet to be performed with the more massive targets. Although inversion and

lasing have not been substantiated, it is clear that there is substantial recombination occurring in the neon at the target surface.

## Conclusions and Future Work.

X-ray laser research on gas puff Z-pinchs, focussing on the sodium-neon photopump scheme, is in progress. The results, to date, of this study can be summarized as follows:

- Sodium implosions using a 3-TW generator have resulted in 65 GW, 2 kJ being emitted in the Na X  $1s^2-1s2p$  line.
- A neon gas puff Z-pinch has been designed and constructed to produce a neon plasma in the correct ionization stage to be pumped by the sodium pump radiation.
- Anomalies in the spatial profiles of the 4-3 H-like neon line, seen when neon is imploded onto aluminum targets, could be explained by three-body recombination pumping of the  $n=4$  level at the target surface.

Future work will require the optimization of the sodium source so that the goal of 200-250 GW in the sodium He $\alpha$  can be met. The neon plasma has to be characterized and optimized into the desired ionization stage; then fluorescence and length scaling experiments will be performed to look for gain in the He-like 4-3 line at 230 Å. A concentrated effort will be directed towards the sodium-neon X-ray laser scheme, but if there is an opportunity, on- and off-axis time-resolved measurements will be performed, with implosions onto targets, to further investigate the three-body recombination in H-like neon.

## Acknowledgements

The assistance of N. Knobel, G. James and the DNA/PITHON team is gratefully acknowledged.

F. Young, J. Davis and J. Apruzese are also thanked for their contributions to this work. This work was supported by SDIO/IST and directed by NRL. Additional support was given by the Defense Nuclear Agency, and the encouragement of Mr. J.Z. Farber is gratefully acknowledged.

## References

1. J.P. Apruzese, J. Davis & K.G. Whitney, J. Appl. Phys., 53(6), 4020, (1982).
2. J.P. Apruzese & J. Davis, Phys. Rev. A, 31(5), 2976, (1985).
3. J.G. Lunney et al., Optics Comm., 50(6), 369, (1984).
4. J.P. Apruzese et al., SPIE "Short and Ultrashort Wavelength Lasers" vol. 875, 2, (1988).
5. P. Choi, A.E. Dangor and C. Deeney, SPIE "Soft X-ray Optics and Technology," vol. 733, 53, (1986)

6. G. Nave, "Soft X-ray Spectroscopy of a Gas Puff Z-Pinch.", PhD Thesis, University of London, (1986).
7. R.B. Spielman et al., J. Appl. Phys., 57(3), 830, (1985).
8. C. Stallings et al., Appl. Phys. Lett., 35(7), 524, (1979).
9. W. Clark et al, J. Appl. Phys., 53(8), p5552, (1982).
10. P. Burkhalter et al., J. Appl. Phys., 50(2), 705, (1979).
11. F.C. Young et al., Record of IEEE Conf. on Plasma Sciences, Cat. No. 86CH2137-6, 87, (1986).
12. F.C. Young et al., Appl. Phys. Lett., 50(16), 1053, (1987).
13. J.P. Apruzese et al., Phys. Rev. A, 35(11), 4896, (1987).
14. M. Gazaix et al., J. Appl. Phys., 56(11), 3209, (1984).
15. F.C. Young, S.J. Stephanakis and V.E. Scherrer, Rev.Sci. Instrm., 57(8), 2174, (1986).
16. R.B. Spielman et al., Appl. Phys. Lett., 47(3), 229, (1985).
17. P. Jaegle et al., Opt. Soc. Am. B., 4(4), 563, (1987).

# Continuous Anti-Stokes Raman Laser Operation

A. Feitisch and B. Wellegehausen

*Institut für Quantenoptik, Universität Hannover  
Welfengarten 1, 3000 Hannover 1, Federal Republic of Germany*

## Abstract

The non parametric anti-Stokes Raman process provides a possibility for the efficient upconversion of infrared or visible laser radiation into the uv and vuv spectral range. Especially for cw operation the active materials in discharge excited gas laser systems may be used. A first cw system has been operated in an argon ion laser, where 648.3 nm radiation of a dye laser could be converted into 437.5 nm radiation, with a conversion efficiency of more than 20 % and a maximum output power of 150 mW.

## Introduction

The realization of continuous short-wavelength coherent radiation is a special and difficult task. So far, no cw operating primary laser system below 200 nm exists. By third order frequency mixing cw radiation down to 135 nm has been produced with output powers in the 100 nanowatt range /1/. From basic principle, the anti-Stokes Raman process should allow more powerful cw operation. So far powerful pulsed operation of anti-Stokes Raman lasers (ASRL) with a shortest wavelength around 146 nm has been demonstrated /2/.

A necessary requirement for operation of an ASRL is a population inversion on a two photon transition. For the pulsed systems the two photon inversion has been generated by photodissociation of molecules /3/ and by innershell photoionisation of atoms /4/. Inversion densities in the order of  $10^{15} \text{ cm}^{-3}$  have been produced, which were necessary to operate the systems as transient systems without any feedback. If optical resonators can be applied, as for the cw systems, the necessary two photon inversion densities may be reduced to the order of  $10^{10} \text{ cm}^{-3}$  or less. Consequently, naturally existing two photon inversions in cw operating normal laser systems, especially discharge pumped lasers, may be used for ASRL purposes. Two schemes described in Fig. 1 may be used.

First, a natural two photon inversion is expected between two levels of same parity, where the upper level 2 is a metastable or long living level, which should be well populated in a discharge, and the lower level 1 is a short living, lowly populated level, for example the final level of an operating laser transition.

Second, a natural two photon inversion is evident in a cascade laser scheme (Fig. 1b). Instead of the cascade laser ( $\nu_{24}, \nu_{41}$ ) an ASRL may be operated, converting pump laser radiation of frequency  $\nu_p$  into anti-Stokes radiation of frequency  $\nu_{as}$ .

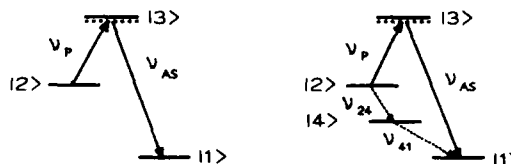


Fig 1. : Anti-Stokes Raman laser upconversion schemes

## Experimental

In case of the argon ion excited in the discharge of an argon ion laser, a two photon inversion exists between the long living quasi metastable  $3d^2P_{3/2}$  level and the  $4s^2P_{3/2}$  level, which is the final level of the well known 488 nm and 515 nm laser transition (Fig. 2). With the next available resonance  $4p^2S_{1/2}$ , this inversion allows the conversion of 648 nm radiation into 437 nm radiation.

With a Spectra Physics 2025 argon ion laser discharge as active material and a single frequency DCM - dye laser as pump source, a maximum output power of 150 mW at 437.5 nm could be achieved for a pump power of 650 mW. No saturation could be

observed at this pump power level, so that much higher output powers appear feasible. Different resonator configurations, involving standing wave and running wave ring configurations have been investigated. In the ring resonator unidirectional oscillation (in pump direction) of the ASRL is obtained, which is due to an intrinsic gain asymmetry of the Raman amplification process. This unidirectional oscillation and a so far possible tuning of the ASRL of more than 20 GHz around the resonance are a proof of the Raman nature of the process. Further experimental details can be found in /5/.

With the argon ion laser discharge and the described method chances for ASRL down to 200 nm and even below exist, starting from higher lying levels and using higher lying intermediate resonances as indicated in Fig. 2. In first experiments with a blue dye laser as pump source on the  $4s^2D_{5/2} - 4p^2P_{3/2}$  transition (427.8 nm), strong laser induced fluorescence on the  $4p^2P_{3/2} - 4s^2P_{3/2}$  transition at 294 nm has already been observed. Instead of the argon ion other ionic species such as the cadmium ion or the copper ion may be used for short-wavelength ASRL. For example, in the He-Cd hollow cathode discharge ASRL down to 200 nm seem to be possible, using the two photon inversion between the  $6g^2G$  and the  $5d^2D$  states, which drives oscillation of the well known red-green cascades (636 nm, 537 nm) /6/.

## References

1. J. Nolting, H. Kunze, I. Schütz, R. Wallenstein: Appl. Phys. B, to be published
2. K. Ludewigt, W. Pflingsten, C. Möhlmann, B. Wellegehausen: Opt. Lett. 11,39, (1987)
3. J.C. White: in "Tunable Lasers", Springer Series: Topics in applied Physics 59 p 181ff, (1987)
4. M. Hube, M. Dieckmann, H. Welling, B. Wellegehausen: submitted to J. Opt. Soc. Am. B
5. A. Feitisch, D. Schnier, T. Müller, B. Wellegehausen IEEE J. Quant. Electr., Vol 24, No 3, 507, (1988)
6. CRC Handbook of Laser Science and Technology, Vol II, p. 178 ed. M.J. Weber, CRC Press Inc. 1982

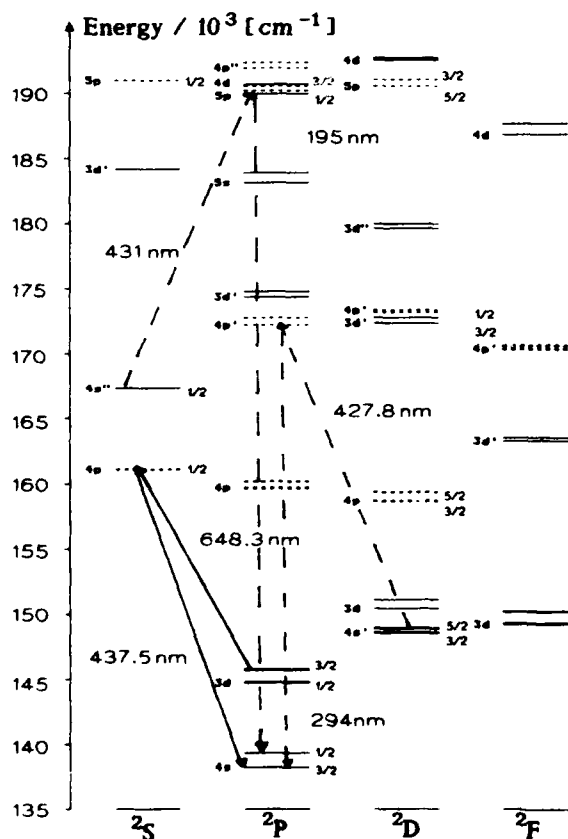


Fig. 2 :  $Ar^+$  level scheme with realized ( — ) and proposed ( ---- ) anti-Stokes Raman lasers

# ULTRAHIGH PEAK POWER PULSES PRODUCED BY CHIRPED PULSE AMPLIFICATION

P. Maine, D. Strickland, B. Bado, and G. Mourou

LABORATORY FOR LASER ENERGETICS  
University of Rochester  
250 East River Road  
Rochester, NY 14623-1299

Chirped Pulse Amplification (CPA)<sup>1</sup> allows the amplification of short laser pulses in amplifying media with good storage properties (low transition cross section) like Nd:glass<sup>1,2</sup> or Alexandrite.<sup>3-4</sup> In these media, straight amplification cannot be performed well, because of the large input flux necessary to reach efficient energy extraction. This condition leads to unacceptable peak powers. To minimize the intensity effects, the pulse is stretched, amplified, and recompressed. This technique allows an efficient energy extraction while maintaining a good beam quality. The intensity is kept below the onset level of small-scale focusing, occurring when values of the B integral are larger than three. We recall that the B integral is given by the expression.

$$B = \frac{2\pi}{\lambda} \int_0^L n_2 I(z) dz.$$

where  $\lambda$  is the laser wavelength,  $n_2$  the nonlinear index of refraction,  $I(z)$  the laser intensity, and  $L$  the optical element lengths.

Using this technique, we have been able to amplify single picosecond pulses to the joule level using a table-top system. The beam divergence has been measured to be two times the diffraction limit at the output of the system.

A 50 ps pulse is produced by a cw mode-locked YLF laser. The pulses are coupled into a single mode optical fiber and are spectrally broadened by self-phase modulation and stretched by group velocity dispersion. Additional stretching up to a nanosecond can be obtained by using a pair of gratings between the focal points of telescope.<sup>5-6</sup> The pulses are then injected into a regenerative amplifier, which brings their energy from the nanojoule to the millijoule level. The regenerative amplifier output is successively amplified to 100 mJ and 1 J by two Nd:glass amplifiers of 9 mm and 16 mm diameters respectively. After amplification, the pulses are recompressed to 1 ps by a double-pass grating-pair compression system. At this point the laser energy 0.6 J.

We have shown that amplification over nine orders of magnitude can be achieved with this technique. Presently, we are exploring the possibility of scaling up the pulse energy with Nd:glass systems to the 1 kJ level, while maintaining the pulse duration of 1 ps. Also, we will describe current efforts based on CPA to produce ultrahigh peak power pulses in the picosecond domain with material such as Ti:sapphire or Alexandrite.

## ACKNOWLEDGMENT

These authors wish to thank Lawrence Livermore Laboratory for the loan of the Nd:YLF laser and the diffraction gratings, ENSTA/Ecole Polytechnique for the loan of the Nd:Glass amplifier head, and Corning Glass Works for the single mode optical fiber.

This work was supported by the United States Air Force Office of Scientific Research under contract F49620-87-C-0016 to the Ultrafast Optical Electronics Center at the Laboratory for Laser Energetics of the University of Rochester; by SDIO/IST and managed by ARO under contract #DAAL03-86-K0152; and by the Laser Fusion Feasibility Project at the Laboratory for Laser Energetics which has the following sponsors: Empire State Electric Energy Research Corporation, New York State Energy Research and Development Authority, Ontario Hydro, and the University of Rochester. Such support does not imply endorsement of the content by any of the above parties.

## REFERENCES

1. D. Strickland and G. Mourou, Opt. Commun. **56**, 219 (1985).
2. D. Strickland, P. Maine, M. Bouvier, S. Williamson, and G. Mourou, Ultrafast Phenomena V, eds., G. R. Fleming and A. Siegman (Springer Verlag, 1986), p. 38.
3. P. Bado, M. Pessot, J. Squier, G. Mourou, and D. Harter, IEEE J. Quant. Electron. (accepted for publication).
4. M. Pessot, J. Squier, P. Bado, G. Mourou, and D. Harter, submitted to IEEE J. Quant. Electron.
5. O. E. Martinez, IEEE J. Quant. Electron. **OE-23**, 59 (1987).
6. M. Pessot, P. Maine, and G. Mourou, Opt. Commun. **62**, 419 (1987).



# Multiterawatt Excimer Laser System

S. Watanabe, A. Endoh, M. Watanabe, and N. Sarukura

*Institute for Solid State Physics, University of Tokyo  
Roppongi 7-22-1, Minato-ku, Tokyo 106, Japan*

## Abstract

A peak power of 4 TW has been obtained in KrF with an output energy of 1.5 J in 390 fs from an electron-beam-pumped amplifier with an active cross section of  $320 \text{ cm}^2$ . The amplified spontaneous emission was as low as 1.8% in energy. The pulse width was measured by the newly-developed third-order autocorrelation technique based on the XeF C-A transition. An initial pulse width of 210 fs was increased to 390 fs through amplifiers. The process of the pulse width broadening was investigated in detail through dummy optics, the thickness of which coincides with the entire system. The broadening was attributed mainly to the linear dispersion of thick optics for near-transform-limited input pulses. Nonlinear absorption and self-phase modulation were not significant in the output window of a  $2.25\text{-cm}$ -thick  $\text{CaF}_2$  at an intensity of  $13 \text{ GW/cm}^2$ .

## Introduction

There are considerable interests in the development of multiterawatt excimer lasers for applications of an extremely high intensity optical field to multiphoton processes and XUV lasers.[1,2] A peak power of 1 TW was obtained recently in a XeCl discharge laser with a pulse width of 310 fs.[3] KrF is an attractive medium for a much higher peak power due to the possibly shorter pulse width and the capability of employing larger aperture electron-beam-pumped amplifiers. The shortest pulse of 45 fs was achieved by compressing the chirped pulse from a KrF amplifier with a 4-mJ energy.[4] An electron-beam-pumped amplifier was employed to produce 2.5 J with a 3.5-ps-

duration at KrF.[5] On the other hand, two-photon absorption at 248 nm in UV materials has been discussed at intensities of 10 to  $100 \text{ GW/cm}^2$  because of its potential limit to an achievable peak intensity.[6] In this paper, we report the results of multiterawatt amplification of a subpicosecond (sub-ps) KrF laser. A sub-ps KrF pulse was amplified in an electron-beam-pumped laser up to 4 TW, which is the highest peak power ever obtained in excimer lasers. The final pulse width was measured to be 390 fs by using the newly developed method.[7]

A block diagram of an amplification system is shown in Fig.1. The system was composed of three stages, namely the front end including dye lasers and high repetition rate amplifiers, two discharge amplifiers with a  $7 \text{ cm} \times 7 \text{ cm}$  aperture and an electron-beam-pumped amplifier with a  $23 \text{ cm} \times 23 \text{ cm}$  aperture.

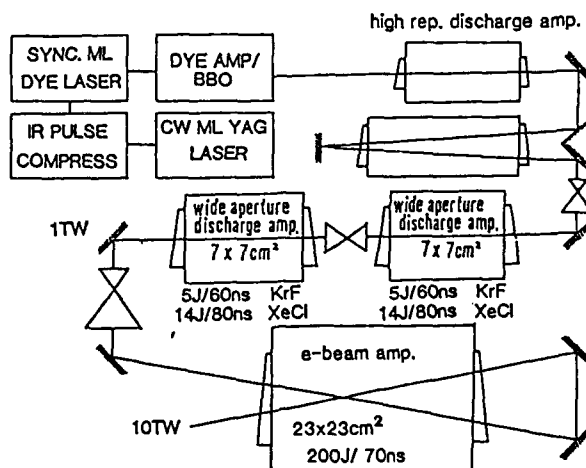


Fig.1 Block diagram of a multiterawatt excimer laser system.

## §1. Subpicosecond generation at 248nm

The schematic diagram to generate 248-nm pulses is shown in Fig.2. The hybrid synchronously pumped mode-locked dye laser generated sub-ps pulses at 745nm. The mixed solution of Pyridine 2 / DDI [8] was used in a single jet as the combination of a gain medium and a saturable absorber. The average power was 30mW. The frequency-doubled output of a mode-locked cw Nd:YAG laser (Spectra Physics series 3000, PRF 82MHz) with a fiber-grating pulse compressor (Spectra Physics 3690) was used to pump the dye laser with a pulse width of 3.5ps at 530nm. Autocorrelation measurement showed the pulse width at 745nm to be 290fs with some temporal wings present in Fig.3(a). The spectral width was 2.1nm, as shown in Fig.3(b). The time-bandwidth product is 0.33, which is very close to the value for a transform-limited sech pulse. Amplification of a single selected pulse in the train was accomplished by a four-stage dye amplifier chain, which was pumped by a 5.5-ns, 75-mJ XeCl laser. In the amplifier chain, LD-700 was used in all stages. Conventional side-pumped cells were used for the first three stages and a prismatic cell with a bore of 2mm was used for the final stage. The dye concentration was  $1.3 \times 10^{-3}$  M in methanol for the first and second cells. The third and fourth cells were used with the concentration of  $6.5 \times 10^{-4}$  and  $3.5 \times 10^{-4}$  M in methanol, respectively. To

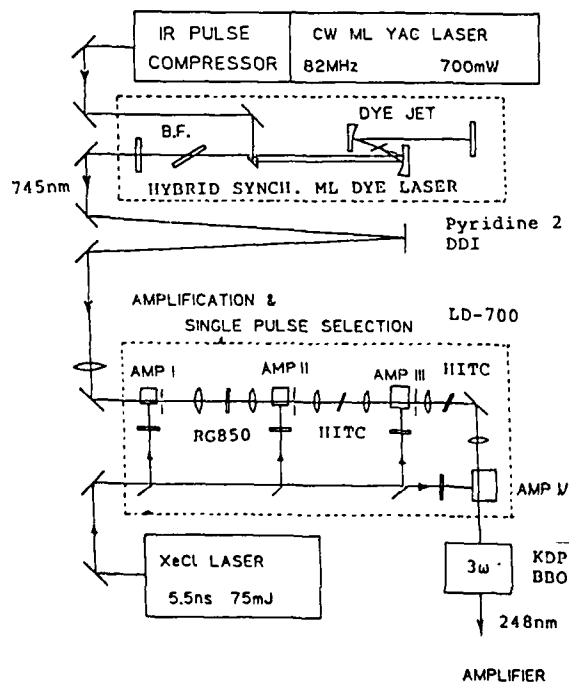


Fig.2 Schematic diagram to generate sub-ps pulses at 248nm.

reduce ASE, saturable absorbers were inserted between every stage. The solid saturable absorber (Schott glass RG850) was placed between the first and second stages, and HITC saturable absorber dye jets were used among the later stages. The amplified energy was 480μJ. The total gain through the chain was more than  $10^6$ . Explicit difference in a pulse width and spectrum was not observed after the amplifier chain. But the temporal wings almost disappeared during amplification. The autocorrelation trace and spectrum are shown in Fig.4(a), (b), respectively. The amplified 745-nm pulse was frequency-doubled in a 1mm-thick KDP crystal and then sum-frequency mixed with its second harmonic in a 1mm-thick BBO crystal. The energy of the 248-nm seed pulse was a few microjoules. The uv pulses were amplified

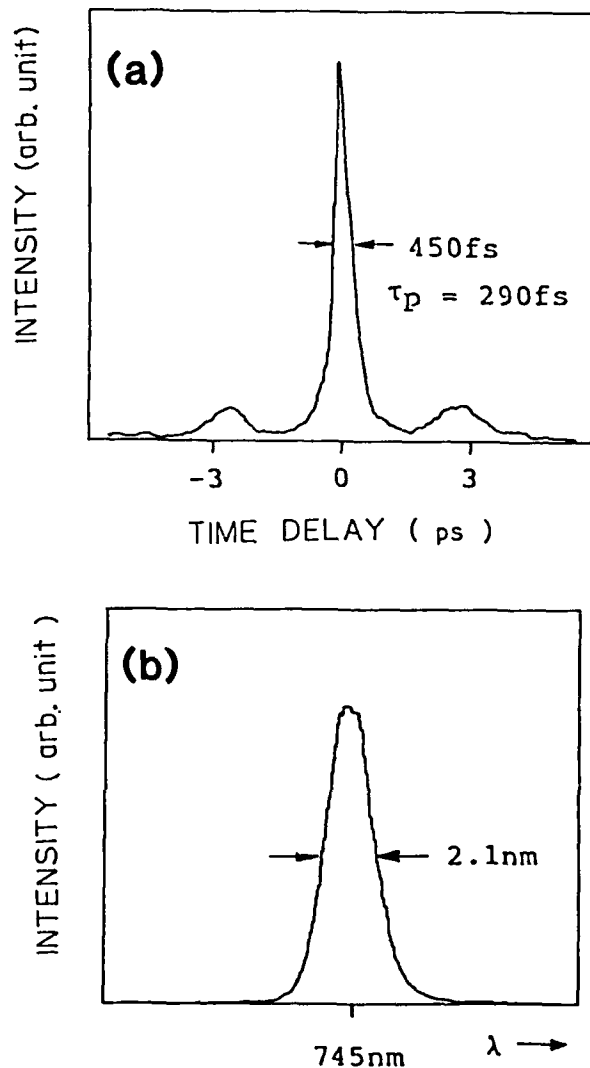


Fig.3 (a) Background-free autocorrelation and (b) corresponding spectrum of 745-nm pulses at the oscillator.

by two high repetition rate KrF preamplifiers, which have the same aperture size of 2cm x 1cm, and active lengths of 30cm and 60cm, respectively. First, the pulses were amplified in the 30-cm laser and then amplified in the 60-cm laser with the double pass configuration employing a vacuum spatial filter between each pass. A typical output energy was 10mJ with a negligible small content of an ASE background. The beam divergence was 50 $\mu$ rad, which is twice for the diffraction limit.

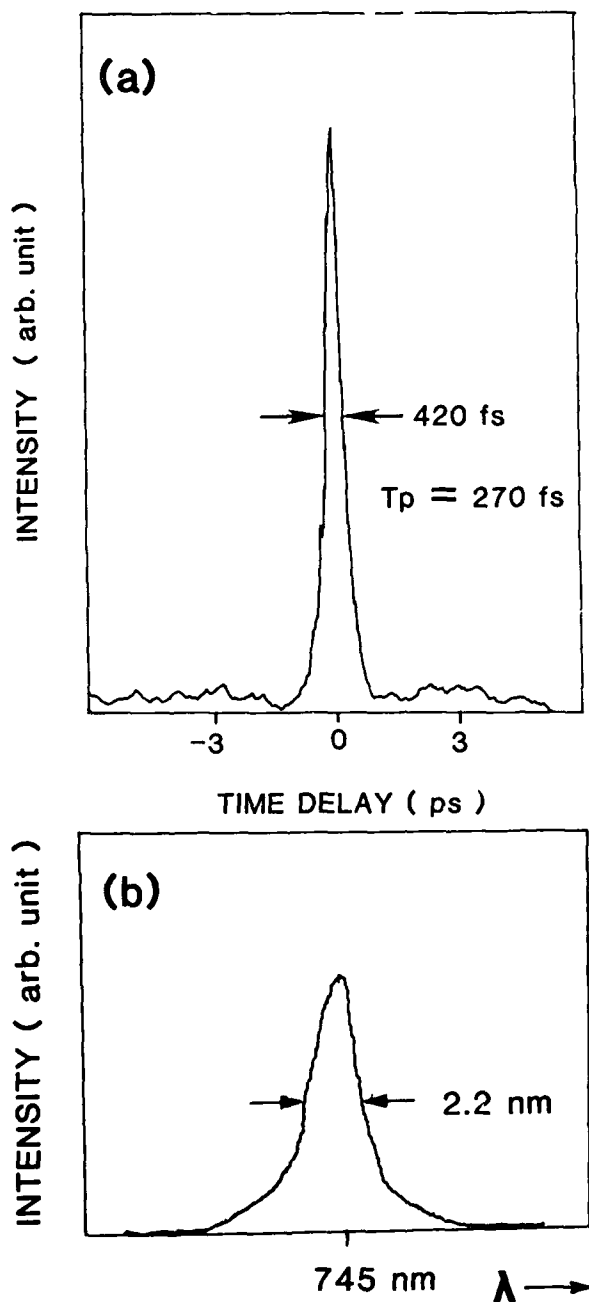


Fig.4 (a) Background-free autocorrelation and (b) corresponding spectrum of 745-nm pulses after the dye amplifier chain.

## §2 Single shot measurement of subpicosecond pulse width

In a multiterawatt system, a pulse width measurement of a single shot is required. The pulse width measurement for a sub-ps KrF laser using two-photon fluorescence of Xe<sub>2</sub> excimers was reported by Hutchinson et al [9]. In this method, a vuv lens along with a vuv image detector must be handled in a vacuum chamber. Furthermore to obtain high resolution, the lens must be well aberration-corrected for the given field size and spectral width. From this point of view, visible fluorescences are obviously desirable both for higher resolution and easier handling. The intensity of the XeF C-A transition (480nm) induced by a sub-ps KrF laser was found to show a cubic dependence on KrF laser intensity (Fig.5), while it showed a quadratic dependence at a low intensity of 30-ns pulses. There is shown in Fig.6 the kinetic pathway to form XeF B and C states. In a high intensity region, the three-photon ionization of Xe atoms may become dominant, as observed using the fourth harmonic of a

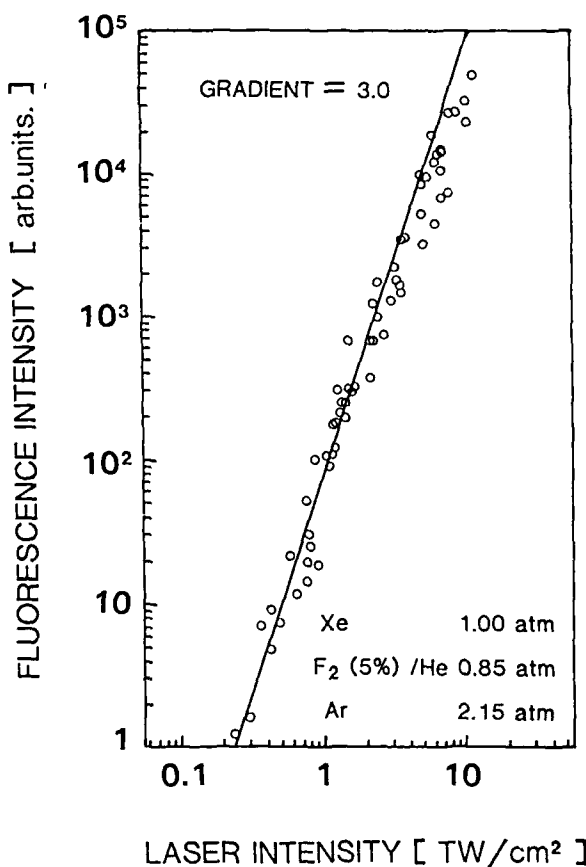


Fig.5 The dependence of the XeF C-A fluorescence on intensity of the subpicosecond KrF laser.

Nd:YAG laser [10]. In this case, the XeF B state is produced through the reaction of  $\text{Xe}^+$  with  $\text{F}_2$  which is created electron attachment of  $\text{F}_2^-$ . The XeF C state is known to be collisionally mixed with the XeF B state. [11,12] Both state radiate 352nm and 480nm, respectively, and relax with almost the same decay time. The  $\text{Xe}_2\text{F}$  trimer is also produced from the C state and emits a 600-nm photon. The time durations of these fluorescences were found to be a few nanoseconds from measurements made with the biplanar phototube for the typical gas mixture with 1.00 atm of Xe, 0.85 atm of 5%  $\text{F}_2$  in He, and 2.15atm of Ar. This value is short enough that the spatial diffusion of XeF excimers does not affect the resolution of autocorrelation measurements even in the sub-ps region. The typical arrangement with a triangular configuration was employed to measure the pulse width of the KrF laser by the three-photon fluorescence of the XeF C-A transition. An input pulse was focused by a 60-cm focal-length lens and divided by a beam splitter into two beams, which were reflected by two turning mirrors and collided precisely at the focal point in the gas cell. The fluorescence image was enlarged by a factor of 5 - 10 with a reversely mounted camera lens (Nikon 55mm F3.5), and detected by a SIT camera with a multichannel analyzer. The pulse width after the preamplifier was measured to be 180 fs by using this method. The width of autocorrelation trace was divided by 1.29 with regards to three-photon fluorescence by assuming a  $\text{sech}^2$  pulse. The single shot autocorrelation trace and spectrum are shown in Fig.7 (a), (b), respectively. The observed contrast ratio was close to the theoretical value of 10:1.

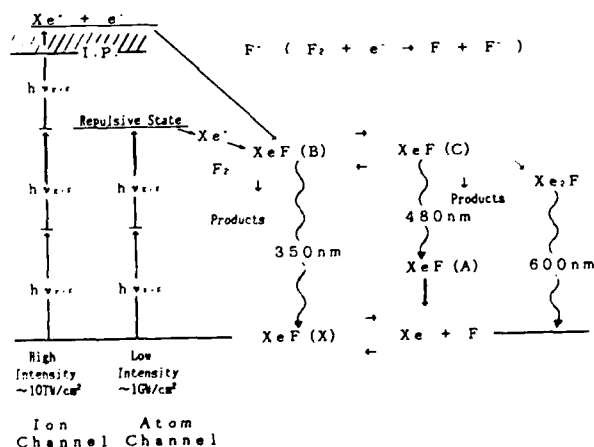


Fig.6 Kinetic pathway to form XeF excimers.

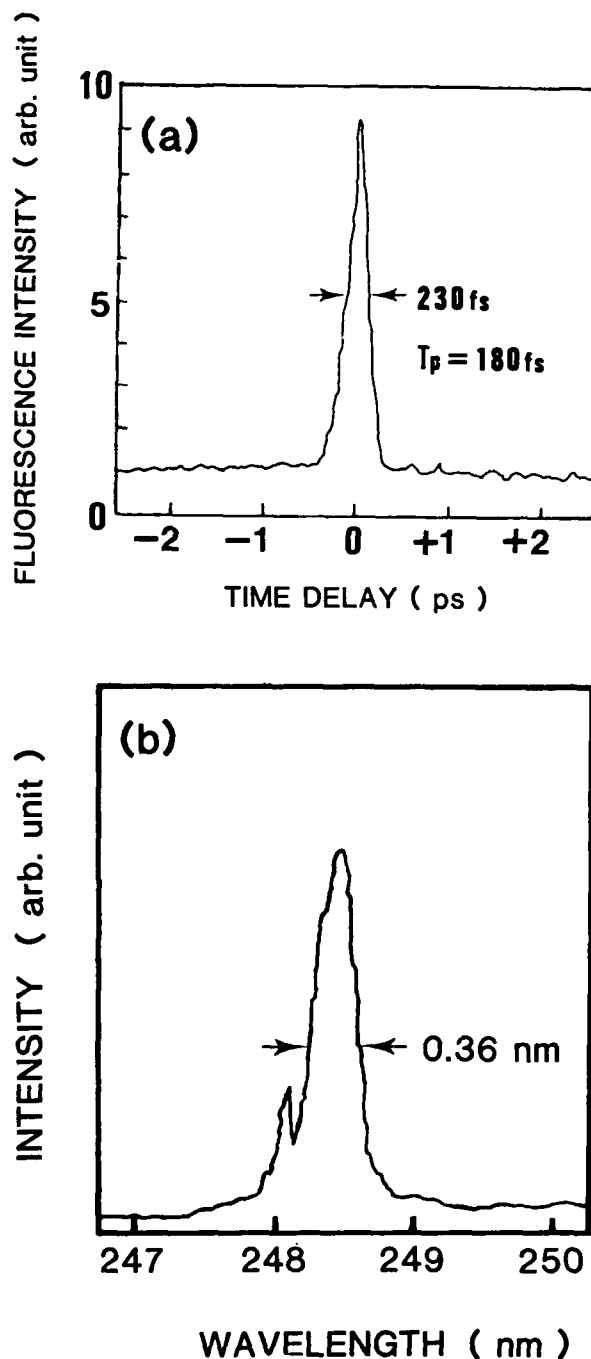


Fig.7 (a) Autocorrelation trace and (b) corresponding spectrum of a single 248-nm pulse after the the front end.

### §3 Multiterawatt amplification

The experimental set up is shown in Fig.8. The beam was expanded by a telescope combined with the spatial filter to a  $25\text{-cm}^2$  cross section to feed to the next discharge laser stage. A vacuum spatial filter with a  $100\text{-}\mu\text{m}$  pinhole was used to suppress ASE. An input energy to the preamplifier was decreased to the  $5\text{-mJ}$  level due to losses by inserted optics.

A preamplifier in the system was an UV-preionized discharge laser with a  $7\text{cm} \times 7\text{cm}$  cross section. Amplification characteristics were studied earlier in detail by using  $20\text{-ps}$  pulses.<sup>[13]</sup> The active volume was  $4$  liter with an  $80\text{-cm}$  length. The amplifier was operated with a gas mix of  $0.3\% \text{F}_2$  and  $5\% \text{Kr}$ , diluted by  $\text{Ne}$  at  $4.5$  atm. The electrical pumping density of discharge was about  $2.5 \text{ MW/cm}^3$  at its peak. The small signal gain was measured to be  $3.9 \text{ %/cm}$ . The amplifier was double passed to provide a typical output of

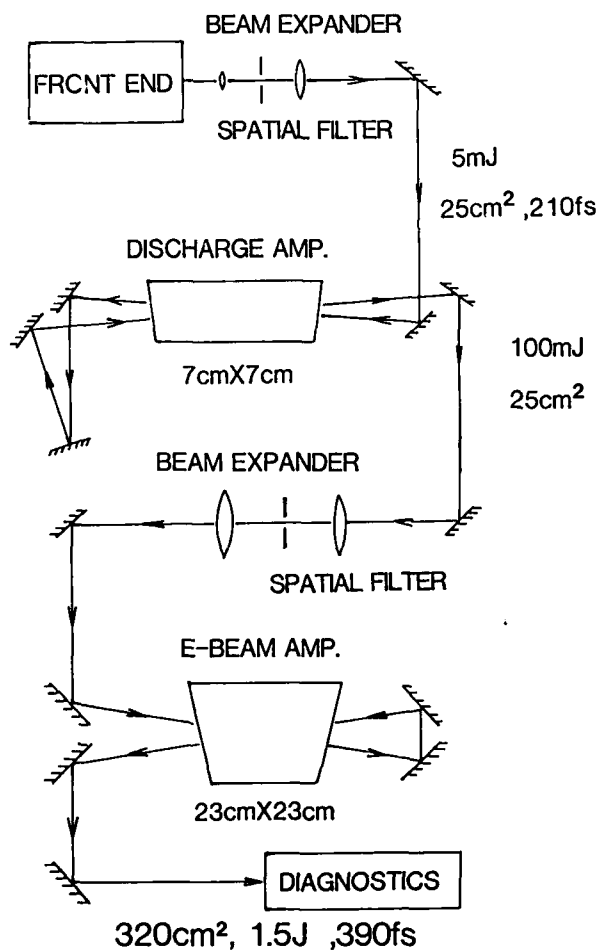
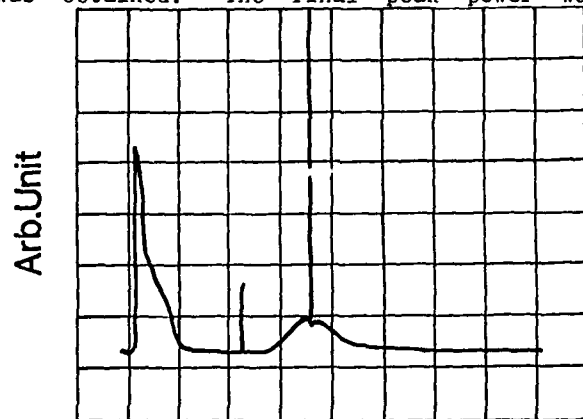


Fig.8 Experimental setup of multiterawatt amplification.

$100 \text{ mJ}$ . The maximum output energy was  $160 \text{ mJ}$  at a relatively high gain and input energy. The extracted energy was the same between sub-ps and  $20\text{-ps}$  pulses.<sup>[13]</sup> The windows were antireflection-coated,  $10\text{-mm-thick}$   $\text{CaF}_2$  crystals. The intensity at the output window was  $16 \text{ GW/cm}^2$  with a cross section of  $25 \text{ cm}^2$  and an estimated pulse width of  $250 \text{ fs}$ . No color center formation was observed in the window material after several hundred shots. The output beam of the preamplifier was spatially filtered with a  $300\text{-}\mu\text{m-diameter}$  pinhole and expanded in vacuum to fill the entire aperture of the main amplifier. The ASE accompanying the pulse was negligibly small after the spatial filter. The input energy to the main amplifier was decreased to  $50 \text{ mJ}$  by losses due to optical components such as the spatial filter and turning mirrors.

The main amplifier was an electron-beam-pumped laser with an active volume of  $23\text{cm} \times 23\text{cm} \times 80\text{cm}$  ( $42$  liter).<sup>[14]</sup> When operated as an oscillator,  $160 \text{ J}$  in  $70 \text{ ns}$  was obtained. The laser was developed as a picosecond amplifier with attentions to spatially uniform gain distribution, low ASE, and low jitter timing. The inside wall of the laser chamber was processed in black to avoid reflection. The gas mix used was  $0.5 \text{ % } \text{F}_2$ ,  $14\% \text{ Kr}$ , diluted by  $\text{Ar}$  at  $1$  atm. The deposited energy was  $1.8 \text{ kJ}$  in  $70 \text{ ns}$ , thus the pump rate being  $0.6 \text{ MW/cm}^3$ . The output window was a  $25\text{-mm-thick}$ ,  $250\text{-mm-diameter}$   $\text{CaF}_2$ , while a  $30\text{-mm-thick}$ ,  $300\text{-mm-diameter}$  fused quartz was used for the other window. In the separate measurement, the transmission of  $\text{CaF}_2$  was investigated at an intensity range of  $10$  to  $100 \text{ GW/cm}^2$  with sub-ps pulses. The measurement indicated that the transmittance of the  $\text{CaF}_2$  window was over  $90\%$  even at  $30 \text{ GW/cm}^2$ , while the transmittance of the quartz window was only  $40\%$ . The transmittance of  $\text{CaF}_2$  was substantially higher than the previous data. The quartz window must be used at a low intensity of a few  $\text{GW/cm}^2$ . The limited diameter of  $\text{CaF}_2$  slightly restricted the active cross section to  $320 \text{ cm}^2$ . The beam was double passed through the amplifier, and nearly  $60\%$  of the active volume was utilized in the final pass. The time interval between the first and second passes was determined to be  $20 \text{ ns}$  by the requirements of the optical arrangement. The amplified pulses and the spontaneous emissions from the amplifiers were observed simultaneously through UV fibers (Fig.9).<sup>[13]</sup> The pulse widths of spontaneous emissions were  $40 \text{ ns}$  for the discharge laser and  $60 \text{ ns}$  for the electron-beam-pumped amplifier, respectively. Strong gain depletion was observed after the passage of the saturating pulse especially in the case of the main amplifier. The output beam was relayed by mirrors to the diagnostic

section. The amplified beam was characterized on pulse width, spectrum, ASE background and output energy. The spectrum of the final output was essentially the same as that of the front end (Fig.10). This shows that self-phase modulation did not occur after the front end. The pulse width of 390 fs was much wider than 210 fs in the front end (Fig.11). The process of the pulse width broadening is described in the next section. ASE was measured at the diagnostic section 15m apart from the output window to be 27 mJ (1.8% of the total energy). With an input energy of 50 mJ, an output energy of 1.5 J was obtained. The final peak power was



50ns/div

(a)



50ns/div

(b)

Fig.9 Time sequences of the trigger-laser lights and the spontaneous emissions from (a) the discharge-pumped and (b) the electron-beam-pumped amplifiers. Strong gain depletion was observed in (b).

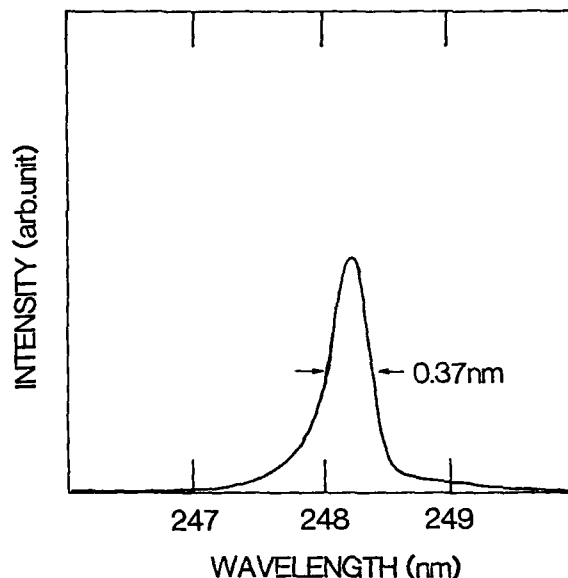


Fig.10 Spectrum of the 4-TW KrF laser.

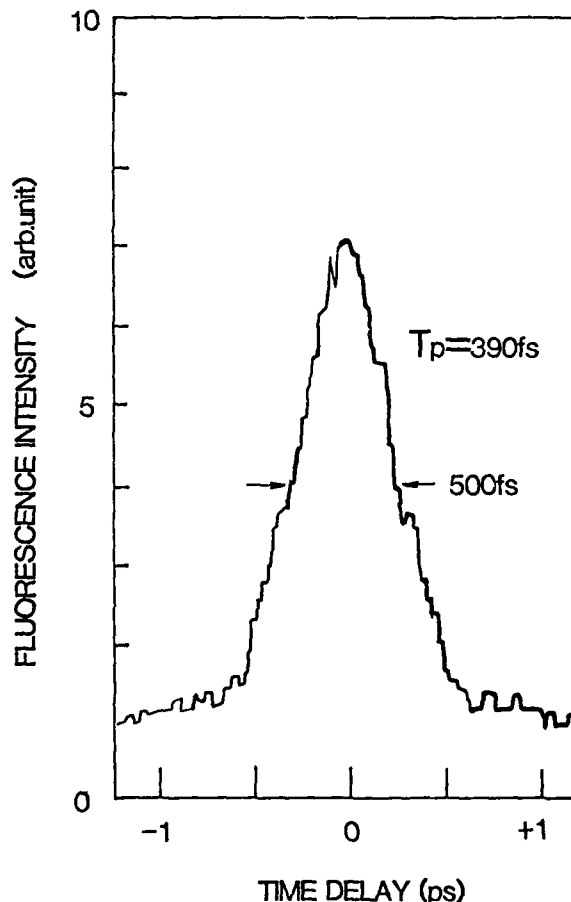


Fig.11 Single shot autocorrelation trace of the 4-TW KrF laser. The  $\text{sech}^2$  pulse shape was assumed.

deduced to be 4 TW (390 fs, 1.5 J) with a 320-cm<sup>2</sup> cross section. The fluence and the intensity were 4.7 mJ/cm<sup>2</sup> and 13 GW/cm<sup>2</sup>, respectively. Two-photon absorption in the CaF<sub>2</sub> window of a 25-mm thickness was not significant within the experimental errors. It was reasonable to assume the small signal gain of 5%/cm at a pump rate of 0.6 MW/cm<sup>2</sup> [5]. Then the maximum extractable energy  $E_{\text{max}} = g_0 I E A$  was calculated as 2.5 J ( $g_0$ : the small signal gain of 5%/cm, 1; the active length of 80 cm,  $E$ : the saturation fluence of 2 mJ/cm<sup>2</sup>,  $A$ : the cross section of the beam of 320 cm<sup>2</sup>). Losses in the output window due to reflection and absorption were around 10%, thus the obtained energy was 65% of  $E_{\text{max}}$ . This value was quite reasonable with regards to high absorption in the electron-beam-pumped medium [15]. The obtained fluence of 4.7 mJ/cm<sup>2</sup> was low compared with the ASE-limited value of 10 mJ/cm<sup>2</sup> [13]. The measured intensity of 13 GW/cm<sup>2</sup> was well below the region where nonlinear absorption was considerable. Then 10 TW would be possible in the present system both by increasing a gain of the final amplifier and by compensating pulse width broadening.

#### §4 Process of pulse width broadening [17]

The pulse width after the final amplifier was measured to be 390 fs when the pulse width at the preamplifier was 210 fs. Self-phase modulation was not observed from the final spectrum. In order to investigate the pulse broadening due to the dispersion of optical element in the KrF system, the change of a pulse width was measured through quartz and CaF<sub>2</sub> blocks as dummy optics. The thicknesses of quartz and CaF<sub>2</sub> were 100 mm and 74 mm, respectively, which almost coincide with those of the entire system. The autocorrelation traces of the pulses before and after the dummy optics were obtained simultaneously by the single shot technique. The spectra were also monitored before and after the dummy optics simultaneously. The explicit change of a spectral width and shape was not observed between them at an energy of 1 mJ with a cross section of 2 cm x 1 cm. The input pulse width was varied by small changes in the adjustment of the hybrid mode-locked dye laser resonator. The pulse width after dummy optics is plotted versus the input pulse width in Fig. 12. The pulses around 200 fs were almost transform-limited when assuming a sech<sup>2</sup> pulse while the pulse width around 500 fs was near twice of the transform-limited value. The time-bandwidth products of all data were within twice for transform-limited pulses. At the input pulse of 210 fs, the pulse was broadened to 360 fs. This result is close to the pulse

width obtained after the final amplifier. At the shortest input pulse of 180 fs, the output pulse width was 330 fs. The pulse width broadening was previously analyzed in a CPM ring laser with regards to a frequency sweep and a dispersion by assuming a gaussian pulse shape [16]. The theory with no regards to a frequency sweep is relatively in good agreement with the measurements above an input range of 300 fs, but predicts a larger broadening than the observation below 300 fs. The reason of this difference is not so clear within the scope of this experiment. This difference would arise from the nature of the input pulse such as a pulse shape and a frequency sweep. But in this experiment the frequency sweep in the input pulse is small because the observed time-bandwidth product is very close to the transform-limited value for a sech<sup>2</sup> pulse. Then, the observed pulse width broadening would be explained by the linear dispersion of the optical elements for near-transform-limited pulses.

#### Conclusion

Sub-ps pulses as short as 180 fs have been generated by the system based on the hybrid synchronously pumped dye laser. The pulse width was measured in each shot by the newly-developed third-order autocorrelation technique with the XeF visible transition. A 210-fs KrF pulse was amplified to 4 TW with a 390-fs pulse width by using the 23 cm x 23 cm-aperture electron-beam-pumped laser. The output energy was 1.5 J with the 1.8% ASE background. The fluence was 4.7 mJ/cm<sup>2</sup> and the intensity was 13 GW/cm<sup>2</sup>. Two-photon

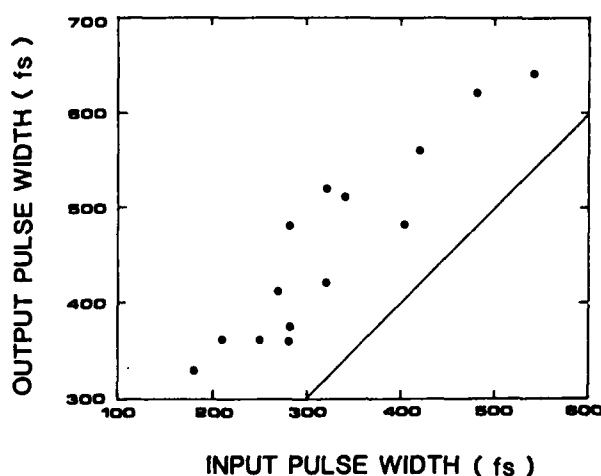


Fig.12 The pulse width after dummy optics versus the input pulse width. The straight line corresponds to the case without broadening.

absorption was not significant in the 25-mm-thick  $\text{CaF}_2$  window at an intensity level in this experiment. Self-phase modulation was not observed from the spectrum of the final output. The process of pulse width broadening was investigated in detail through dummy optics. The broadening was attributed mainly to the linear dispersion for near-transform-limited pulses. The peak power of excimer lasers was improved by almost one order of magnitude compared with the previous report by sub-ps amplification of the electron-beam-pumped laser. The system will contribute to the physics at a high intensity optical fields.

### Acknowledgement

The authors would like to acknowledge to K.Sajiki for the development of high repetition rate discharge lasers.

### References

1. C.K.Rhodes, Science 229, 1345 (1985)
2. S.Szatmari, F.P.Schäfer, E.Müller-Horche, and W.Münchenheim, Opt.Comm. 63, 305 (1987)
3. S.Watanabe, A.Endoh, M.Watanabe, and N.Sarukura, Opt.Lett. 13, 580 (1988)
4. F.P.Schäfer, G.Künle, S.Szatmari, and M.Styer, in digest of Technical Papers, IQEC 88, Tokyo, Japan, paper MM-1. (Japan Society of Applied Physics, Tokyo, 1988)
5. J.R.M.Barr, N.J.Everall, C.J.Hooker, I.N.Ross, M.J.Shaw and W.T.Toner, Opt. Commun. 66, 127 (1988)
6. A.J.Taylor, T.R.Gosnell, J.P.Roberts, C.S.Lester, R.B.Gibson, S.E.Harper, and C.R.Tallman, in Digest of Technical papers, IQEC 88, Tokyo, Japan, paper ThF3 (Japan Society of Applied Physics, Tokyo, 1988)
7. N.Sarukura, M.Watanabe, A.Endoh, and S.Watanabe, to be published in Opt. Lett.
8. M.D.Dawson, T.F.Boggess and A.L.Smirl, Opt.Lett. 12, 254 (1987)
9. M.H.R.Hutchinson, I.A.McIntyre, G.N.Gibson and C.K.Rhodes, Opt.Lett. 12, 102 (1987)
10. N.Morita and T.Yajima, Appl.Phys.B, 25 (1982)
11. W.Walter, R.Sauerbery, F.K.Tittel and W.L.Wilson, Jr., Appl.Phys.Lett. 41, 387 (1982)
12. R.Sauerbery, W.Walter, F.K.Tittel and W.L.Wilson, Jr., J.Chem.Phys. 78, 737 (1983)
13. A.Endoh, M.Watanabe, and S.Watanabe, Opt.Lett. 12, 906 (1987)
14. A.Endoh, M.Watanabe, and S.Watanabe, Fusion Tech. 11, 492 (1987)
15. F.Kannari, M.J.Shaw, and F.O'Neill, J.Appl.Phys. 15, 476 (1987)
16. W.Dietel, E.Döpel, D.Kühle, and B.Wilhelmi, Opt. Commun. 43, 433 (1982)
17. M.Watanabe, A.Endoh, N.Sarukura and S.Watanabe, submitted to Appl.Phys.B



# Narrowband Tunable VUV/XUV Radiation Generated by Frequency Mixing of Pulsed and CW Laserradiation

G. Hilber, A. Lago and R. Wallenstein  
Institut für Quantenoptik, Universität Hannover  
3000 Hannover, FRG

Four- and six-wave mixing of pulsed and cw laser radiation in gases generates coherent radiation in the spectral region of the VUV/XUV at 60 - 200 nm.<sup>1</sup> Recently considerable experimental progress has been achieved towards the development of powerful coherent VUV/XUV light sources based on these nonlinear optical methods.

The third-order resonant sum- and difference frequency mixing in Kr, for example, generates broadly tunable VUV/XUV radiation at wavelengths in the region of 70 - 200 nm. Because of the high efficiency, the reliability, and the experimental simplicity the conversion in Kr has the potential to become a standard method for the generation of frequency tunable VUV/XUV light.<sup>2</sup>

The frequency mixing of cw laser radiation produces frequency stable VUV radiation (at 140-200 nm) of narrow spectral width ( $\Delta E < 3 \cdot 10^{-5} \text{ cm}^{-1}$ ).

In contrast to the extensive experimental investigations the theoretical treatment of frequency mixing in gases was restricted mostly to special conditions (like homogeneous medium, equal confocal parameters, focii of the laser beams located at the same position, etc.)<sup>3</sup>.

Using the integral method to solve the inhomogeneous Maxwell equation we were able to perform a rigorous theoretical analysis of the frequency mixing in gases.<sup>3</sup> This analysis provides a general description of optical frequency mixing of  $n$  different laser beams in gases of arbitrary density distribution. Besides the conversion in pulsed gas jets, the frequency mixing using Gaussian laser beams with different confocal parameters and the

frequency conversion of crossed beams have been analyzed in detail. These results provide new, important information for the optimization of the conversion efficiency. Possible improvements indicated by theory exceed one order of magnitude. First experiments confirm these predictions.

Because of the enhanced efficiency frequency mixing of pulsed radiation generated with laboratory-size laser systems will produce tunable VUV light of narrow spectral width ( $\Delta E < 10^{-2} \text{ cm}^{-1}$ ) and pulse powers of at least 10-50 KW.

- 1 R. Hilbig, G. Hilber, A. Lago, B. Wolff, and R. Wallenstein  
Comments At.Mol.Phys. part D18, 157 (1986), and references therein
- 2 G. Hilber, A. Lago and R. Wallenstein, JOSA B4, 1753 (1987)
- 3 A. Lago, G. Hilber, and R. Wallenstein, Phys.Rev.A 36, 3827 (1987), and references therein.

# High Efficiency, Scalable, 130 nm Coherent Source by Four-Wave Mixing in Hg Vapor

C. H. Muller, III, C. E. Hamilton, and D. D. Lowenthal

*Spectra Technology, Inc., 2755 Northup Way, Bellevue, Washington 98004*

A. V. Smith

*Sandia National Laboratories, Albuquerque, New Mexico 87185*

## ABSTRACT

Coherent vacuum ultraviolet (VUV) pulses with energy 1.1 mJ, 3 ns pulse length ( $1.3 \text{ MW cm}^{-2}$  unfocused), and measured bandwidth  $<0.1 \text{ cm}^{-1}$  have been achieved using four-wave sum-frequency mixing in mercury vapor. High energy conversion efficiencies of 5 percent have been demonstrated in a collimated beam geometry over 1 meter interaction lengths. The 130 nm radiation is tunable over  $2.5 \text{ cm}^{-1}$ . The experimental facility assembled to produce this efficient VUV laser source will be described, and comparison between experimental measurements and theory are provided.

## INTRODUCTION

Recent measurements<sup>1,2</sup> and calculations<sup>3-5</sup> have shown that two-photon-resonant sum-frequency mixing in Hg vapor is an efficient process for the production of coherent VUV radiation in the 120-140 nm region. In contrast to earlier experimental work, which utilized a tightly focused geometry and very high pump intensities,<sup>6-8</sup> these new results show that efficient conversion is possible with relatively low input laser intensities ( $5\text{-}10 \text{ MW cm}^{-2}$ ) and collimated non-focused beams. The collimated geometry is very important because it allows tractable modeling, area scaling of the processes to higher energies per pulse, and high optical quality of the output wave. In the collimated geometry we have demonstrated 5 percent conversion efficiencies in the production of 130 nm radiation. VUV

output energies of 1.1 mJ have been achieved. The laser system and mixing cell constructed for this demonstration are described, and comparisons between experimental results and predictions are presented.

## SUM-FREQUENCY MIXING IN HG VAPOR

A thorough discussion of efficiency limiting mechanisms, nonlinear phase matching conditions, and input wave flux considerations for 130 nm generation is given in Ref. 5. A simplified energy level diagram for Hg is shown in Fig. 1. One approach for 130 nm generation with collimated beams in pure Hg involves input energies  $\omega_1 = 39220 \text{ cm}^{-1}$  (255 nm),  $\omega_2 = 24710 \text{ cm}^{-1}$  (405 nm), and  $\omega_3 = 12870 \text{ cm}^{-1}$  (777 nm). As shown in Fig. 1, the  $7^1S$  state is used for two-photon resonant enhancement and  $\omega_1$  and  $\omega_2$  are chosen to index match the process. In this case the nonlinear susceptibility is very large since the detuning from the  $6^3P_1$  and  $8^1P_1$  states is  $200 \text{ cm}^{-1}$  and  $68 \text{ cm}^{-1}$ , respectively. For sum-frequency mixing ( $\omega_1 + \omega_2$ ) are chosen to be in exact resonance with the  $7^1S$  state of  $^{202}\text{Hg}$  and  $\omega_4 = \omega_1 + \omega_2 + \omega_3$ . In the exact resonance case, amplified spontaneous emission (ASE) at 1014 nm ( $7^1S\text{-}6^1P$ ) and 408 nm ( $7^1S\text{-}6^3P$ ) is expected to limit conversion efficiencies to approximately 10%. Other considerations such as absorption of the 130 nm output wave by the wings of Hg ( $8^1P$ ), Stark effects, impurities in the Hg vapor mixing cell, and photoionization may also contribute to reduced conversion efficiencies. It is possible that losses due to

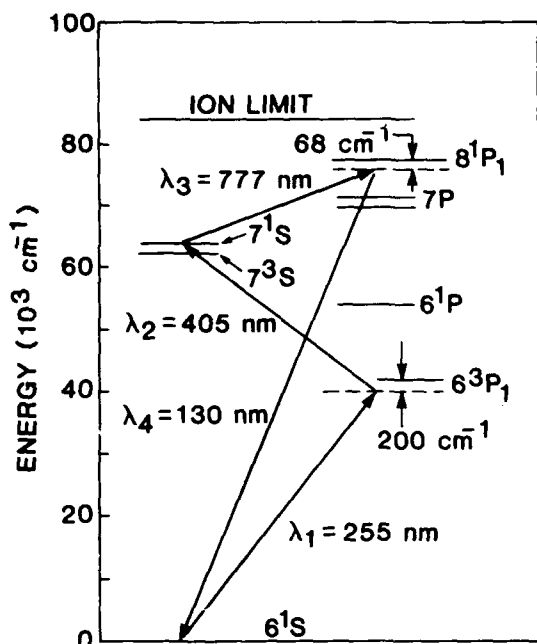


Figure 1. Simplified energy level diagram for Hg showing the states used for sum-frequency mixing to 130 nm.

ASE may be eliminated by tuning  $\omega_1 + \omega_2$  slightly to the red of the  $7^1S$  state of  $^{202}\text{Hg}$  ("near-resonance" condition), however, in this case, hyper-Raman scattering<sup>5</sup> may still limit conversion efficiencies at 130 nm. We expect to look into this question in the near future. Optimum flux rates for mixing at 130 nm are approximately  $\phi_1/\phi_2/\phi_3 = 1/1/1$  with parallel polarized input beams.

### 130 nm LASER SYSTEM

Efficient generation of 130 nm radiation in a collimated nonfocused four-wave-mixing process requires single-frequency, near diffraction limited, spatially uniform laser sources. Our mixing scheme employs input wavelengths at 255, 405, and 777 nm. One distinct advantage of the 255/405/777 nm approach is that ultimately it could be implemented with an all solid state Ti:Sapphire laser system. At the present time, however, the laser system used to produce these wavelengths is shown schematically in Fig. 2. Three fundamental wavelengths at 765, 810 and 777 nm are generated with single frequency ring dye oscillators. These cw beams are amplified into nanosecond pulse widths

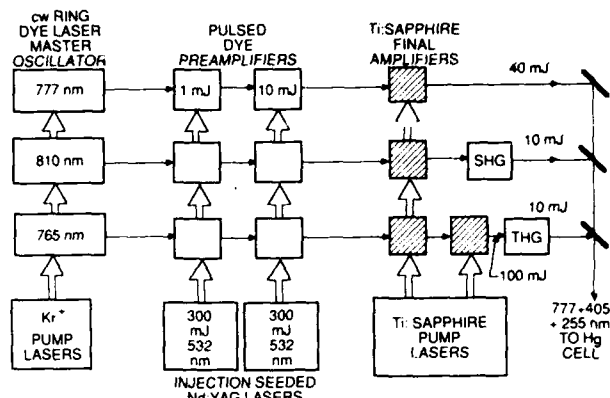


Figure 2. Schematic of the 130 nm laser system.

using dye amplifiers (PDA) pumped by frequency doubled Nd:YAG. Two stages of PDAs are used: the first stage is a 3 dye cell transversely pumped PDA; and the second is a modified unit with only a single transversely pumped dye cell. These two stages of dye amplification provide approximately 10 mJ per pulse outputs at the three fundamental wavelengths with single frequency diffraction limited beam quality.

The Nd:YAG pump laser system for the PDAs is critical to obtaining smooth, repeatable, nsec pulse outputs. The pump arrangement uses two Spectra-Physics DCR-3A Nd:YAG laser systems. The first DCR-3A is employed as a standard oscillator, but is injection seeded with another commercial device manufactured by Light Wave Electronics. The seeded DCR-3A provides a smooth temporal pulse output that is completely free of longitudinal mode beating. This in turn produces a temporally smooth pulse out of the pulsed dye amplifiers. The frequency doubled output from this Nd:YAG oscillator is used to pump the first stage of three PDA units; leftover 1.06  $\mu$  radiation is then amplified in the second DCR-3A Nd:YAG system and used to pump the second stage of three PDA units. Thus, each of the six PDA's is pumped with approximately 100 mJ of single mode 532 nm radiation. This approach avoids intensity modulations from the pump waves modulating the dye waves, which would increase the bandwidth and cause conversion fluctuations.

The next stage of laser amplification is generated by Nd:YAG pumped Ti:Sapphire. We have chosen Ti:Sapphire because of its higher demonstrated conversion efficiency, compared to

dye amplifiers, and its demonstrated higher pulse energy when pumped with commercial based, frequency doubled, Nd:YAG hardware. Also, because of its simplicity, no dye solution, and its ability to store energy on a microsecond time scale. The ability of Ti:Sapphire to store energy has advantages in terms of reducing the possibility of damaging the material with the pump beams. For example: the pump beam, a doubled Nd:YAG laser, need not be a few nsec in length but instead can be up to several hundred nsec in length.

As shown in Fig. 2, an actively mode locked, Q-switched train from a commercial Quantronix Nd:YAG laser system is used to pump the Ti:Sapphire. The mode locked output train is composed of 100 ps pulses spaced at 10 ns intervals for a total train length of 200 nsec. This Quantronix output train is pre-amplified in a DCR-2A Nd:YAG laser system; the output is then split equally into two beams and each of these beams amplified further in two more DCR-2A Nd:YAG units. The final configuration delivers two beam lines each with 400 mJ of frequency doubled Nd:YAG output. The first of these two beam lines is divided equally into three parts and is used to pump the first three stages of Ti:Sapphire amplification for the 765, 810, and 777 nm fundamental wavelengths. This amplification stage brings these wavelengths up to a maximum of 40 mJ/pulse. The second mode locked beam line is used to pump a fourth Ti:Sapphire amplifier in the 765 nm wavelength train, bringing this energy per pulse up to 120 mJ.

The pump geometry for a single Ti:Sapphire amplifier is shown schematically in Fig. 3 for the 765 nm beam. As shown, a collinear "end" pump configuration is employed in which the pump and extraction beams are overlapped in the Ti:Sapphire brick and they are counterpropagating. The 765 nm extraction beam follows the 532 nm mode locked pump beam in time by approximately 200 ns. Dichroic splitters are used to separate the pump, extraction, and amplified beams. Typical energy gains are 4 per Ti:Sapphire amplifier stage.

Following the Ti:Sapphire amplifiers, the 765 nm radiation is tripled (doubled and mixed) in frequency to 255 nm, while the 810 nm wavelength is doubled in frequency to 405 nm.

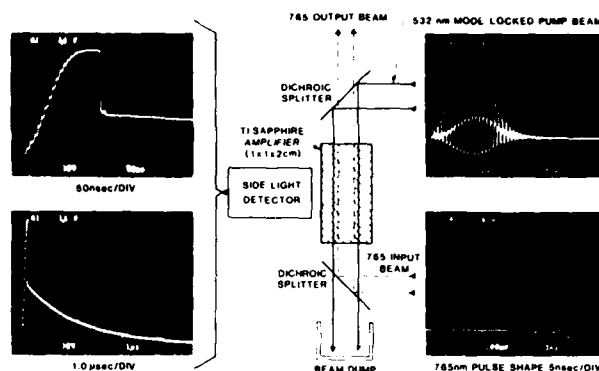


Figure 3. Arrangement of a single pass Ti:Sapphire amplifier. The fluorescence temporal profile is shown on the left. The sudden decrease in the fluorescence signal is due to the extraction pulse. The pump beam temporal behavior is shown on the right.

The harmonic generators and geometry used are nearly identical to the standard configuration used in doubling and tripling pulsed Nd:YAG lasers. The nonlinear materials are KDP, KD P, and BBO, which are angle tuned for phase matching. Both one and two dimensional physical optics models of the doubling and tripling scheme have been run to determine predicted conversion efficiencies. Reasonable conversion efficiencies are achieved even at low energies due to the short pulse length, single mode, and high beam quality input. Our calculations show that doubling efficiencies, at 810 nm, of  $\approx 40$  percent are achievable and that tripling of 765 nm could occur at the 40-50 percent level. Presently, typical pulse energies are 10 mJ at 255, 405, and 777 nm. These beams are overlapped by using dichroic mirrors prior to mixing in the Hg cell.

Temporally smooth, spatially uniform pump beams are required in order to obtain high mixing efficiencies in a collimated geometry. As a result of this requirement, we have paid a great deal of attention to the quality of the 255, 405, and 777 nm input laser beams. A typical spatial profile for the 405 nm pump beam is shown in Fig. 4: The 255 and 405 nm spatial profiles are similar. This spatial profile was obtained at the input to the Hg vapor cell following the dye and Ti:Sapphire amplifiers. The energy per pulse was approximately 10 mJ, the bandwidth was  $<400$

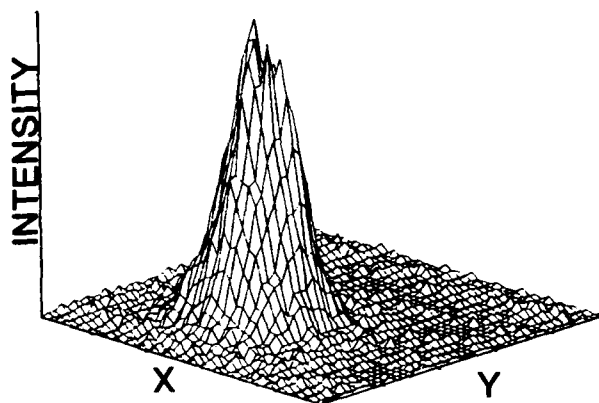


Figure 4. Typical spatial profile for the 405 nm pump beam. The measured diameter ( $1/e^2$ ) is approximately 8 mm.

MHz, and the beam diameter ( $1/e^2$ ) was 8 mm.

The laboratory arrangement for the complete laser system is shown pictorially in Fig. 5. The 21 oscillators or amplifiers lasers described previously are arranged in three beam lines on six optical tables. The Hg vapor four-wave-mixing cell and VUV diagnostic chamber occupy the seventh optical table.

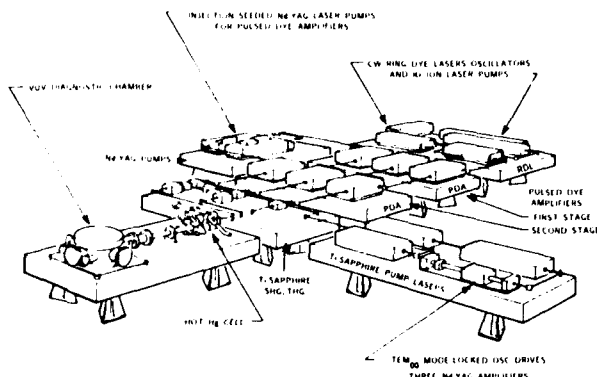


Figure 5. Pictorial of the laboratory layout.

#### FOUR-WAVE-MIXING CELL

Fig. 6 shows a schematic of the 1.1 m long Hg vapor four-wave-mixing cell. This Hg cell is a "hot cell" design where the windows, cell body, pressure transducers, etc. are maintained at a constant temperature of 200 C. The ultrahigh vacuum stainless steel cell is assembled from standard conflat parts.

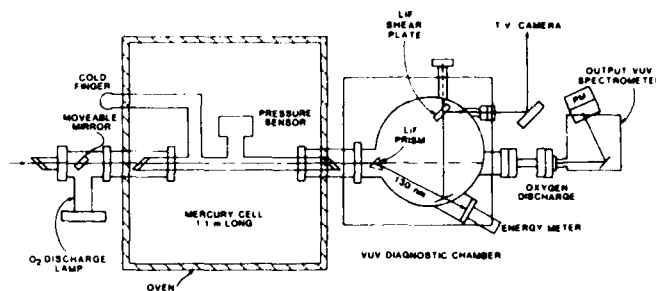


Figure 6. Schematic representation of the Hg vapor cell and VUV diagnostics.

However, the copper gaskets are silver plated to prevent reaction with Hg vapor. The Hg vapor pressure is controlled with an external "cold finger." Three inch diameter  $MgF_2$  input and output Brewster windows are sealed to the stainless steel cell with a silicon-based cement. As used, the cement maintains vacuum integrity above 250 C. The output end of the Hg cell is interfaced to a vacuum diagnostics box which contains a VUV prism for separating the 130 nm radiation from the 777 nm, 405 nm, and 255 nm input pump wavelengths. Both ends of the Hg cell outside the oven are evacuated in order to prevent heat loss. The 130 nm energy,  $E_{130}$ , is measured with a Laser Precision energy monitor. This device is located in a small nitrogen-purged cavity connected to the vacuum diagnostics box. A  $MgF_2$  window separates the two regions.

Accurate knowledge of the window and prism transmission at 130 nm is critical to determining energy conversion efficiency. The percent transmission,  $T$ , of the 6 mm thick  $MgF_2$  windows at 130 nm, (250 C,  $T=46\%$  and 20 C,  $T=50\%$ ), was measured with the oxygen discharge lamp and the input VUV spectrometer shown in Fig. 6. Transmission through a 1 cm path in the VUV prism was measured to be 38%. Absorption in the Hg cell at 130 nm due to impurities such as  $H_2O$  vapor or organics is negligible. Consequently, 91.3% of the generated 130 nm energy is absorbed in the two partially transmitting  $MgF_2$  windows and in the VUV prism prior to measurement. In other words, 130 nm energy produced as a result of the four-wave-mixing process in the Hg cell is a factor of 11.4 greater than the measured energy after transmission through two  $MgF_2$  windows and a VUV prism.

## 130 nm MEASUREMENTS

A natural isotopic mixture of Hg was used for the results reported in this paper, and the mass 202 two-photon resonant  $7^1S$  transition was excited in exact resonance. The Hg  $7^1S$ - $6^1P$  structure is shown in Fig. 7. This plot was obtained by scanning  $\omega_2$  (with  $\omega_1 = 39212.01 \text{ cm}^{-1}$ ) across the  $7^1S$  level while observing the 1014 nm  $7^1S$ - $6^1P$  emission signal. The Hg isotope structure is clearly discernible. Note that each peak is labeled with the isotope number and the excitation wavelength. The measured Doppler width of  $0.06 \text{ cm}^{-1}$  ( $2 \times 0.03 \text{ cm}^{-1}$ ) for the  $^{202}\text{Hg}$  isotope is in good agreement with a calculated value of  $0.07 \text{ cm}^{-1}$ . In addition, the emission signal for each line in Fig. 7 fairly accurately represents the fraction of the isotope in natural Hg. Substantial Rabi broadening of the  $7^1S$ - $6^1P$  transition occurs for the input power levels necessary to mix efficiently. Consequently, for exact resonance experiments, it is necessary to tune  $\omega_1 + \omega_2$  to the exact two-photon wavelengths prior to higher power mixing experiments.

Both one dimension  $\omega_2$  (plane) and two-dimension (Gaussian) codes<sup>2</sup> have been written to simulate the four-wave-mixing process in Hg

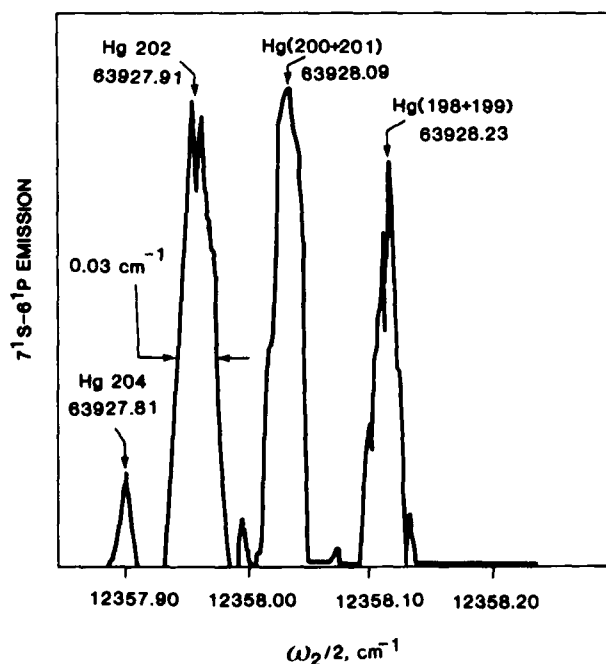


Figure 7. Emission scan of the Hg ( $7^1S$ - $6^1P$ ) transition obtained by varying  $\omega_2$  with  $\omega_1$  fixed.

vapor. These codes assume a temporally flat pulse shape and monochromatic radiation. For laser input energies of  $E=7.0/8.5/5.5 \text{ mJ}$  per pulse at  $\lambda = 255/405/777 \text{ nm}$ , Hg vapor pressure of 5 torr, and 8 mm diameter beams, the measured  $E_{130}$  was  $0.1 \text{ mJ}$  per pulse. This corresponds to  $1.1 \text{ mJ}$  per pulse in the Hg cell due to the four-wave-mixing process when allowances are made for optical losses as discussed above. The energy conversion efficiency is 5.2%. These results are in good agreement with calculations from the two-dimensional code which predict 7.8% conversion efficiency. Further increases in conversion efficiency may be possible once experimental conditions have been optimized.

A typical spatial profile for the 130 nm beam is shown in Fig. 8. The input pump beams were near-Gaussians (as shown in Fig. 4) with a pump pulse energy  $E=9/7/5 \text{ mJ}$  at  $\lambda=255/405/777 \text{ nm}$ . The pressure in the Hg cell was 3.84 torr. The 130 nm spatial profiles were recorded by using a sodium salicylate coated window and observing fluorescence at 420 nm. The 130 nm beam diameter is approximately 6 mm and is in good agreement with a calculated beam diameter of 6.6 mm.

An upper limit to the 130 nm bandwidth has been determined by scanning the VUV source through the  $^3P_2$  -  $^3S_0$  oxygen atom absorption profile at  $76795 \text{ cm}^{-1}$ . The oxygen atoms were produced by dissociating  $\text{O}_2$  in a

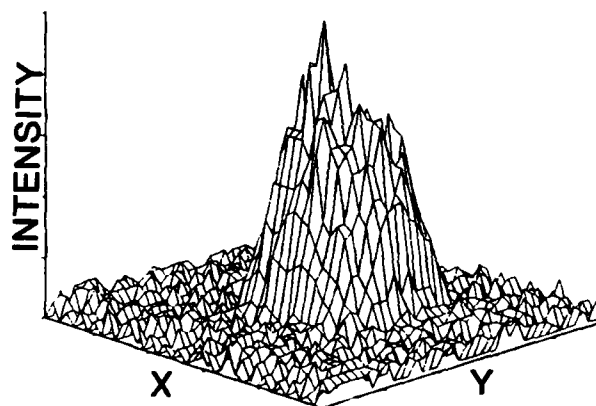


Figure 8. Spatial profile of the 130 nm VUV beam. The beam diameter ( $1/e^2$ ) is approximately 6 mm.

low current discharge. Absorption was measured downstream from the discharge in the cold flowing afterglow. As shown in Fig. 9, the absorption profile corresponds to a 330 K Doppler width. If we assume a room temperature (300 K) oxygen atom temperature, then the 130 nm source bandwidth would be less than  $0.075 \text{ cm}^{-1}$ .

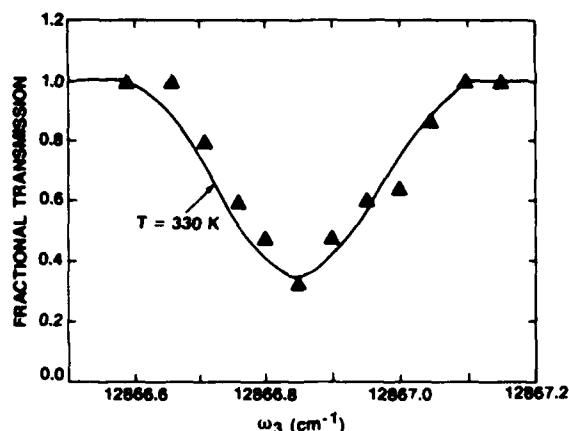


Figure 9. Oxygen atom absorption scan. The data were obtained by tuning the VUV beam through the  $^3P_2 - ^3S_1$  transition. The best fit shown by the solid line corresponds to a 330 K doppler temperature.

The 130 nm wavefront quality has been measured by using the LIF lateral shearing interferometry shown in Fig. 10. The fringe patterns for three consecutive laser shots shown in Fig. 11 correspond to an estimated wavefront distortion of  $< \lambda/2$ . Additional experiments are planned to investigate the dependency of wavefront quality on the input laser conditions.

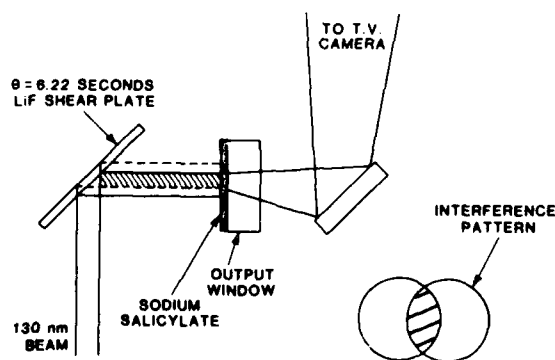


Figure 10. Schematic of VUV lateral shearing interferometer.



Figure 11. Shearing interference pattern at 130 nm for three consecutive laser shots.

Sum-frequency-mixing in Hg vapor should be tunable between 120 and 140 nm by setting the wavelength of the input beams for proper phase matching conditions.<sup>4</sup> In our case, with  $w_1$  and  $w_2$  fixed, however, it is still possible to obtain limited tunability at 130 nm by scanning  $w_3$  over the width of the index matching peak. The range of tunability depends on the product of the Hg vapor density and cell length  $[\text{Hg}]L$ . For  $[\text{Hg}]L = 10^{19} \text{ cm}^{-2}$  ( $\text{Hg} = 5 \text{ torr}$  and  $L = 100 \text{ cm}$ ), we calculate, using the one-dimensional codes, approximately  $2 \text{ cm}^{-1}$  tunability around 130 nm. As shown in Fig. 12, the measured tuning range is roughly  $2.5 \text{ cm}^{-1}$  for these conditions. Note that the measured and calculated signals have been normalized to the same intensity for  $\Delta w_3 = 0$ , and  $w_1$  and  $w_2$  are fixed in wavelength. A greatly increased tuning range can be obtained by scanning  $w_1$  and  $w_2$  while maintaining index match with  $w_3$ .

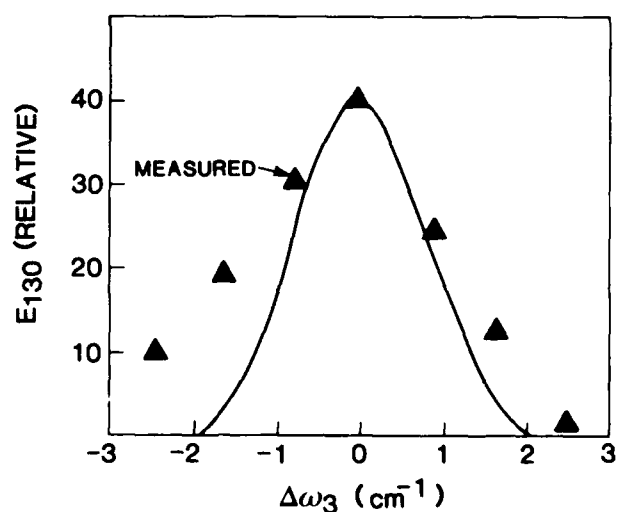


Figure 12. Phase matching curve for 130 nm production with  $w_1$  and  $w_2$  fixed.



The 130 nm output energy (and thus the four-wave-mixing efficiency) is strongly dependent on the Hg vapor pressure. This dependency is shown in Fig. 13 for the conditions noted. The solid triangles represent calculations based on the 2-dimensional codes. Note that the agreement between experiment and theory is good up to a Hg vapor pressure of approximately 4 torr. At this point, however, the measured VUV energies begin to decrease and the discrepancy between experiment and calculations begins to widen. At 9 torr the measured 130 nm energy has decreased by a factor of almost four. The mechanism leading to this rollover in energy has been identified. We have found that the rollover is due to absorption of the 130 nm photons followed by a  $4.18\ \mu\text{m}$  stimulated Raman transition to the  $8^1S_1$  state in Hg. This process will be discussed in detail in a subsequent publication.

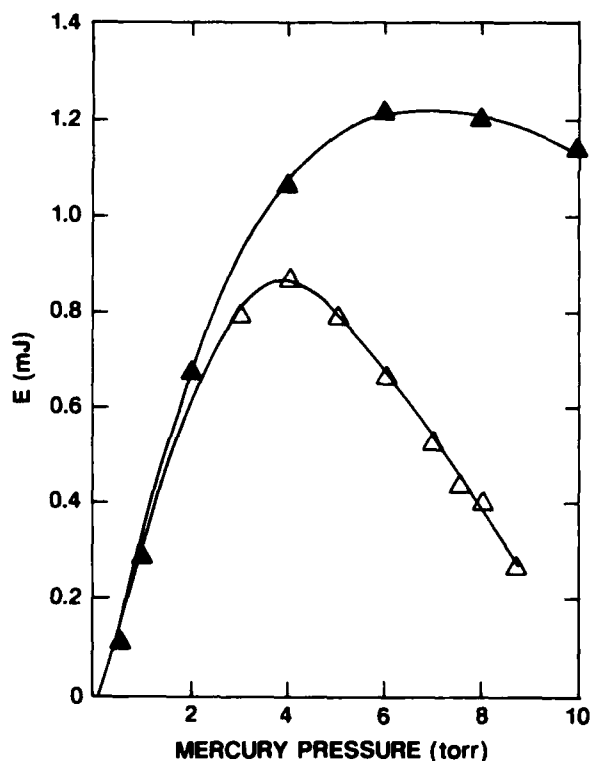


Figure 13. Energy per pulse at 130 nm vs. Hg vapor pressure. The solid triangles are calculations while the open triangles are measurements. The pump energies were 8/4/4 mJ at 255/405/777 nm. The beam diameter ( $1/e^2$ ) was 8 mm. The rollover in measured energy is due to a stimulated Raman process.

## CONCLUSIONS

We have obtained efficient two-photon-resonant sum-frequency mixing in Hg vapor for the production of 130 nm VUV coherent radiation. Collimated nonfocused power densities exceeding  $1\ \text{MW cm}^{-2}$  have been produced at 130 nm. At the present time mixing efficiencies are  $>5\%$ . The 130 nm radiation is tunable over  $2.5\ \text{cm}^{-1}$  with  $\omega_1$  and  $\omega_2$  fixed. Measurements and calculations are in good agreement, indicating that "exact resonance" conversion efficiencies of 10% may be possible. Additional experiments to investigate near-resonance mixing efficiencies are planned.

## References

1. C.H. Muller, III, D.D. Lowenthal, M.A. DeFaccio, A.V. Smith, "High efficiency, energy-scalable, coherent 130-nm source by four-wave mixing in Hg vapor," *Opt. Lett.* **13**, 651 (1988).
2. C.H. Muller, III, D.D. Lowenthal, M.A. DeFaccio, M. Cimolino, J.P. Hauch, "Coherent VUV laser at 130 nm: Experiment" in *Proceedings of SPIE, Pulsed Single-Frequency Lasers: Technology and Applications*, Volume 912, 106 (1988).
3. A.V. Smith, G.R. Hadley, P. Esherick, and W.J. Alford, *Opt. Lett.* **12**, 708 (1987).
4. A.V. Smith and W.J. Alford, "A practical guide for 7S resonant frequency mixing in Hg: Generation of light in the 230-185 and 140-120 nm ranges," to be published *J. Opt. Soc. Am. B*.
5. A.V. Smith, W.J. Alford, and G.R. Hadley, "Optimization of two-photon resonant four-wave mixing: Application to 130.2 nm generation in Hg vapor," submitted to *J. Opt. Soc. Am. B*.
6. R. Mahan and F.S. Tomkins, *I.E.E.E. J. Quantum Electron.* **QE 18**, 913 (1982).
7. R. Hillig and R. Wallenstein, *I.E.E.E. J. Quantum Electron.* **QE 19**, 1759 (1983).
8. P.R. Herman and B.P. Stoicheff, *Opt. Lett.* **10**, 502 (1985).
9. C.H. Muller, III and M.W. Barrett, "High Temperature Seals for VUV Experiments," in press, *Rev. Sci. Instrum.*, August, 1988.

# Intense Coherent Radiation in the VUV and XUV Region with Electron Beam Pumped Rare Gas Excimer Lasers

Wataru Sasaki and Kou Kurosawa

*Department of Electronics, University of Osaka Prefecture  
4-804, Mozu-umemachi, Sakai, Osaka 591, Japan*

Peter R. Herman, Kunio Yoshida, and Yoshiaki Kato

*Institute of Laser Engineering, Osaka University  
2-6, Yamada-Oka, Suita, Osaka 565, Japan*

Rare gas excimer lasers are attractive sources for applications in laser spectroscopy, plasma diagnostics and photolytic pumping of other lasers. Since 1981, we have developed high-power rare-gas excimer lasers pumped by a pulsed electron beam and studied their performance using tunable cavities [1,2].

This report presents an overview of intense coherent sources in the VUV and XUV spectral region based on such excimer lasers and frequency conversion techniques of stimulated Raman scattering and anti-Stokes Raman laser pumping to extend the wavelength coverage.

Three topics are emphasized:

- 1) Present status of rare gas excimer lasers in our laboratory;
- 2) Extension of the excimer laser wavelength

coverage by stimulated Raman scattering in hydrogen molecules.

- 3) Discussion of anti-Stokes Raman lasing in group VI atoms with the aim to generate XUV radiation.

Lasing conditions of rare gas excimer lasers are summarized in Table 1. Our efforts have been focused on the Ar and Kr excimer lasers which oscillate in the vicinity of 126nm and 146nm, respectively. Finding high reflectance cavity mirrors and efficient transmitting optics in this wavelength region posed serious problems. Good multi-layered dielectric mirror are not well developed, necessitating a systematic test of efficiencies and damage thresholds of several materials for the cavity mirrors, namely, Al film, quartz glass plate, single crystal Si, Mo, and SiC, and  $MgF_2$ .

Table 1: Present status of rare gas excimer lasers

	Wavelength [nm]	Peak power [MW]	Band width [nm]	Resonator
Ne	80			SiC-SiC USR
Ar	126	16	1	SiC-MgF <sub>2</sub>
	124-128(tuned)	>1	0.3	16 MgF <sub>2</sub> (prism)
Kr	146	7	1	Si-MgF <sub>2</sub>
	145.5(tuned)	3.5	0.1	32 MgF <sub>2</sub> (prism)
Xe	172*	400	-	-
	170-176**	1	0.1	MgF <sub>2</sub>

\* E.R.Ault et al.:Unpublished.

\*\* C.B.Edwards et al.:Rev. Sci. Inst., 50, 1201 (1978).

Although the Mo and SiC mirrors were found to have high damage threshold, (much better than deposited Al film mirrors), output powers were finally limited by damage to the  $\text{MgF}_2$  output mirror.

The maximum peak output power of the Ar excimer laser was 16MW with 1nm band width when using a SiC back mirror and  $\text{MgF}_2$  output mirror. A Si back mirror and  $\text{MgF}_2$  output mirror worked best for the Kr excimer laser, yielding 7MW in a 1nm band width. The largest peak power Xe excimer laser, developed by Ault et al. [3], yielded 400MW, but details of this laser have not been published. Ne excimers fluoresce near 80nm[4], but have not been made to lase due to high threshold power requirements and poor optical quality of cavity mirrors in the XUV region. However, the recently developed SiC mirror was measured to have a high reflectance of 40% at 80 nm. An unstable resonator composed by SiC-SiC mirrors is presently being developed.

Broad band gain profiles of the rare gas excimer lasers permit laser wavelength tuning by using dispersive optics. A  $\text{MgF}_2$  prism with 16 apex angle was inserted in the cavity of the Ar excimer laser to yield a tuning range of 124nm to 128nm at a line width of 0.3 nm. A larger apex angle  $\text{MgF}_2$  prism (32°) was used in the Kr excimer laser to provide the same dispersion. The tuning range was not fully tested, but a peak power of 3.5MW in a narrow linewidth of 0.1 nm was produced. Tunable oscillation has also been demonstrated for the Xe excimer laser [5].

The limited spectral coverage of rare gas excimer lasers in the VUV spectral region has stimulated efforts to expand the spectral tuning range and permit wider spectroscopic applications of these sources. Stimulated Raman scattering, a popular frequency converting technique of longer wavelength laser radiation, is somewhat limited in application to the VUV due to the lack of non-absorbing molecules. Only hydrogen and deuterium gases have been found suitable as Raman medium for rare gas excimer lasers.

A typical stimulated Raman scattering spectrum of Kr excimer laser radiation in hydrogen molecules is shown in Fig. 1. The Kr excimer laser output at 145.8nm was converted into 1st (154.8nm) and 2nd (165.4nm) order Stokes radiation and also 1st order anti-Stokes radiation (137.5nm). Calibration lines at 116.5 and 123.6nm were produced by a Kr discharge lamp.

The dependence of Raman line power with hydrogen gas pressure is plotted in Fig. 2 as a function of total output power. Also included is the fraction of reduced fundamental laser power. The intensities

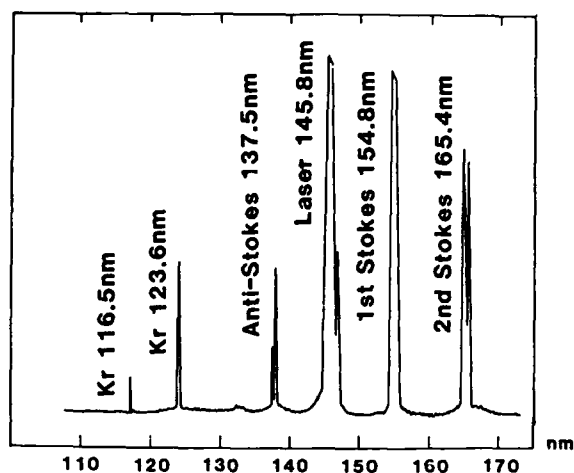


Figure 1: Stimulated Raman scattering spectrum of the Kr excimer laser source using molecular hydrogen. Calibration lines at 116.5 and 123.6nm were produced by a Kr discharge lamp.

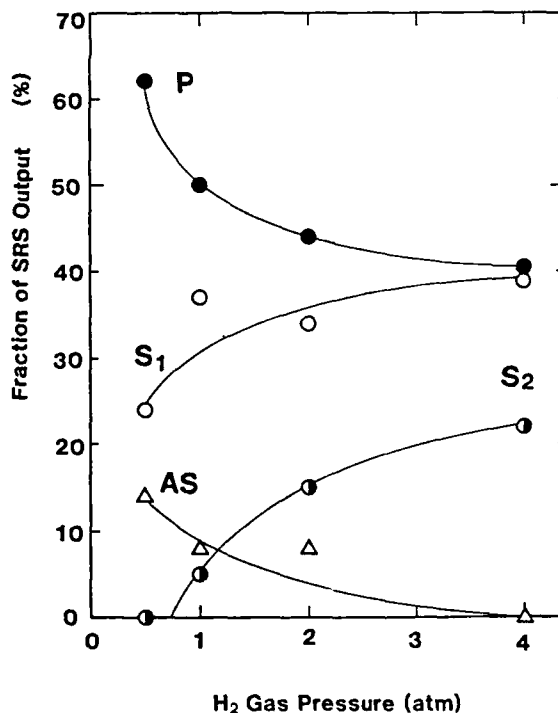


Figure 2: Fractional stimulated Raman scattering output power as a function of  $\text{H}_2$  pressure. Laser power was 2.5MW. Fraction of fundamental laser power is shown by P.

are seen to increase with increasing  $H_2$  pressure to 40% efficiency for the 1st Stokes line and 20% efficiency for the 2nd Stokes line at 4atm of  $H_2$  pressure. However, the 1st anti-Stokes line intensity decreases with increasing  $H_2$  pressure from a peak conversion efficiency of 15% at 0.5atm pressure.

The stimulated Raman scattering power and reduced fundamental laser power are plotted in Fig. 3 as a function of pumping laser power at 145.8nm. Note that the onset of 1st anti-Stokes radiation occurs at lower pumping power than that for the 2nd Stokes radiation.

The tunable VUV ranges provided by rare gas excimer lasers and the hydrogen Raman shifter are summarized in Fig. 4 together with the expected tuning range using a deuterium Raman shifter. In addition to the 1st and 2nd Stokes lines and the 1st anti-Stokes line, 3rd Stokes radiation was also generated in  $H_2$  gas with the Kr excimer output. Anti-Stokes radiation could not be generated with the Ar excimer laser, but 1st and 2nd Stokes lines were observed. Raman conversion of Xe excimer laser radiation was not tested but the expected tuning ranges are included in Fig. 4. Stimulated Raman scattering provides a convenient technique for efficient wavelength conversion in the VUV spectral region, reaching limitations only at the shortest wavelengths, near 100nm, due to the dispersion and absorption by  $H_2$  gas.

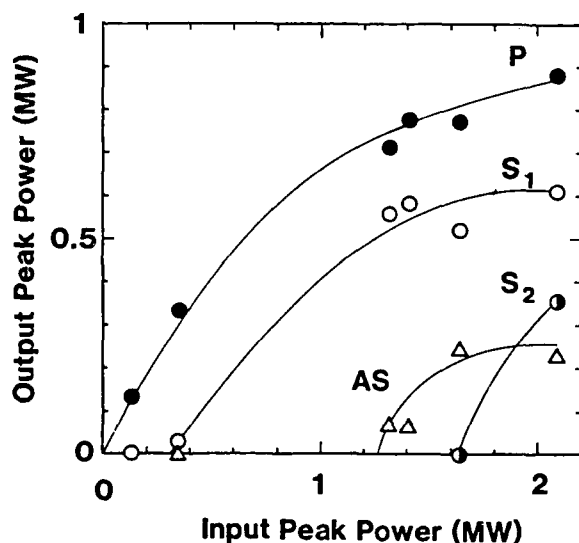


Figure 3: Peak power of stimulated Raman scattering lines as a function of pumping laser power for a  $H_2$  pressure of 2atm.

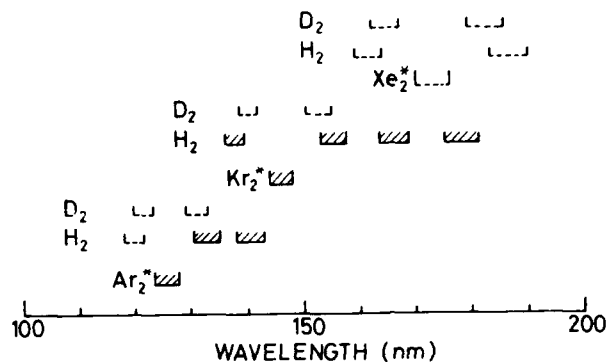


Figure 4 Tuning ranges available in the VUV region with rare gas excimer lasers and their Raman shifted output using  $H_2$  and  $D_2$  gas. Hatched regions show wavelengths generated in this laboratory.

In order to generate shorter wavelengths reaching into the XUV spectral region, new techniques must be considered. One possible scheme is the anti-Stokes Raman laser (ASRL), which unlike anti-Stokes stimulated Raman scattering, requires a population inversion between the initial and final state of the Raman transition.

White[6] proposed several ASRL transitions based on population inversion in group VI atoms, O, S and Se, and lasing has been successfully demonstrated at a few VUV wavelengths[7]. In the case of group VI atoms the population inversion can be formed by photodissociation of molecules using excimer laser radiation.  $N_2O$  gas can be dissociated with Ar excimer laser radiation as follows:

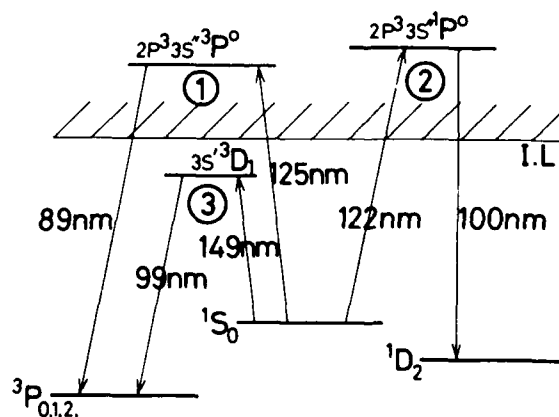


Figure 5: Energy level diagram of atomic oxygen showing relevant states and wavelengths for three possible pathways of ASRL.

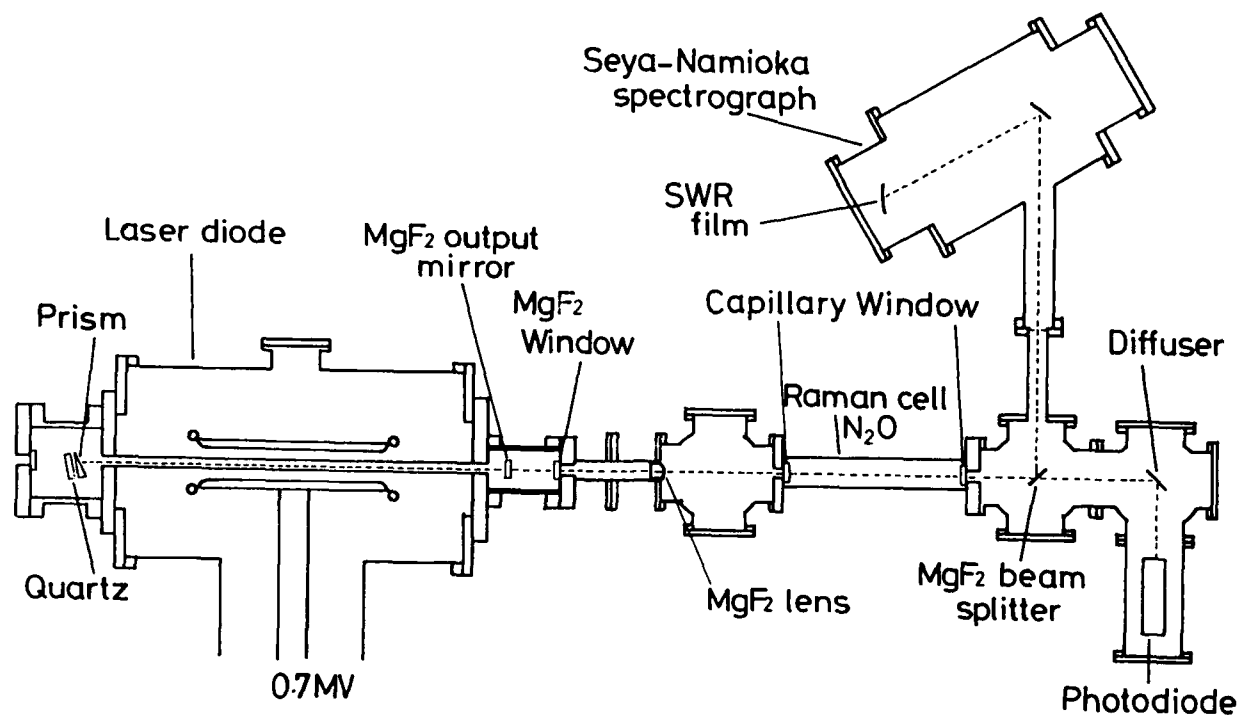
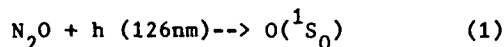


Figure 6: Experimental arrangement for an XUV anti-Stokes Raman laser pumped with an Ar excimer laser.



The quantum yield for the metastable state  $^1\text{S}_0$  is approximately 0.8[8], resulting in a population inversion with the ground  $^3\text{P}_{2,1,0}$  or  $\text{D}_2$  states. A similar population inversion can be produced in  $\text{S}(^1\text{S}_0)$  and  $\text{Se}(^1\text{S}_0)$  by photodissociation of COS gas with Kr excimer laser radiation and COSe gas by Xe excimer laser radiation respectively. The maximum possible frequency shift occurs between the  $^1\text{S}_0$  and  $^3\text{P}_{2,1,0}$  states, yielding  $22446\text{ cm}^{-1}$  for Se,  $22181\text{ cm}^{-1}$  for S, and  $33791\text{ cm}^{-1}$  for O. We are interested in the large frequency shift available in oxygen to generate the shortest possible wavelength. An energy level diagram of initial, intermediate, and final states relevant to ASRL in oxygen atoms is shown in Fig. 5. One can tune to near resonances  $2\text{p}^3\text{s}^3\text{p}^0 - ^1\text{S}_0$  (scheme 1),  $2\text{p}^3\text{s}^3\text{p}^0 - ^1\text{S}_0$  (scheme 2, and  $3\text{s}^3\text{d}^1 - ^1\text{S}_0$  (scheme 3), using pump wavelengths of 124.8nm, 121.8nm, and 148.5nm, respectively, to finally produce ASRL wavelengths of 88.9nm, 100.0nm, and 99.0nm, respectively.

Estimates of threshold lasing condition (Gain  $\times$  Length = 30) are given in Table 2 for each ASRL scheme. Ar excimer laser radiation is focused into a Raman cell to

fully breach the  $\text{N}_2\text{O}$  gas. In schemes 2 and 3, auxiliary sources based on anti-Stokes shifted Ar excimer laser radiation in  $\text{D}_2$  gas (121/8nm) and Kr excimer laser radiation (148.5), respectively, are needed to pump the ASRL.

However, the first ASRL scheme is much simpler, requiring only Ar excimer radiation to both photodissociate  $\text{N}_2\text{O}$  and resonantly photopump  $\text{O}(^1\text{S}_0)$  at 124.8nm. Also, this scheme produces the shortest wavelength at 89nm. The major drawback is the small ASRL cross-section of  $9.7 \times 10^{-27}\text{ cm}^4/\text{W}$  which arises from the weak oscillator strength of the intercombination transition  $2\text{p}^3\text{s}^3\text{p}^0 - ^1\text{S}_0$ .

Table 2 also lists the expected laser pumping intensities at the Raman cell focus, which give rise to threshold population inversions in the range of  $5 \times 10^{14}$  to  $3 \times 10^{17}\text{ cm}^{-3}$  for the various scheme. The large population inversion of the first scheme, namely  $3 \times 10^{17}\text{ cm}^{-3}$ , can be generated in the laser focal volume with a modest 10mJ of the Ar excimer laser output energy.

The experiments arrangement of test ASRL in  $\text{N}_2\text{O}$  using Ar excimer radiation is shown in Fig.6. The Ar excimer laser output is focused with a 1500mm focal length  $\text{MgF}_2$  lens into the center of a 30cm long Raman cell containing 1-2torr of  $\text{N}_2\text{O}$  gas. Multi-capillary arrays are used as efficient

Table 2: Threshold conditions for three ASRL schemes in atomic oxygen.

Photo-dissociation laser	Power [MW]	Pump radiation source	Pump intensity [ $\text{W}/\text{cm}^2$ ]	ASRL cross section [ $\text{cm}^4/\text{W}$ ]	Threshold population inversion [ $\text{cm}^{-3}$ ]
$\text{Ar}_2^*(\text{tuned})$ 124.8nm	10	$\text{Ar}_2^*(\text{tuned})$ 124.8nm	$3.3 \times 10^8$	$9.7 \times 10^{-27}$	$3.1 \times 10^{17}$
$\text{Ar}_2^*(\text{tuned})$ 126.4nm	5	AS in $\text{D}_2$ 121.8nm	$1.7 \times 10^7$	$1.2 \times 10^{-22}$	$4.9 \times 10^{14}$
$\text{Ar}_2^*$ 126nm	5	$\text{Kr}_2^*(\text{tuned})$ 148.5nm	$3.3 \times 10^8$	$1.7 \times 10^{-25}$	$1.7 \times 10^{16}$

and high damage resistant input and output windows. A differential pumping arrangement maintains vacuum of  $10^{-4}$  mmHg outside of the Raman cell.

To date, threshold ASRL conditions were not met due largely to the poor beam divergence of the pump laser. The stable resonator consists of a pair of flat mirrors having low cavity Q, which together prevents a tight focus of 0.2mm diameter to occur in the Raman cell. An unstable resonator based on SiC mirrors is proposed to solve this problem. Also, intracavity dispersion optics are necessary to reduce the Ar excimer laser bandwidth and therefore tune more closely to resonance.

In summary, powerful and tunable Ar and Kr excimer lasers operating at VUV wavelength were developed. Hydrogen Raman shifters were demonstrated to widely expand the tuning range of these excimer lasers within the VUV spectral region (i.e. 124nm to 200nm) with high conversion efficiencies.

A proposal to operate an XUV ASRL at 89nm was described.

#### References

- [1] Y. Uehara et al.: Opt. Lett. 10, 487 (1985).
- [2] K. Kurosawa et al.: IEEE, J. Quantum Electron., QE-24, No.9 (1988).
- [3] E. R. Ault et al.: ARPA Contract No.0014-72-C-0456 (1975).
- [4] Y. Tanaka et al.: J. Opt. Soc. Am., 45, 663 (1955).
- [5] C. B. Edwards et al.: Rev. Sci. Instrum., 50, 1201 (1979).
- [6] J. C. White: Opt. Lett., 9, 38 (1984).
- [7] K. Ludewigt et al.: IEEE, J. Quantum Electron., QE-22, 1967 (1986).
- [8] G. Black et al.: J. Chem. Phys., 62, 4266 (1975).

## X-Ray Emission Studies of Sub-Picosecond Laser Produced Plasmas

M. M. Murnane, H. C. Kapteyn, and R. W. Falcone

*Department of Physics, University of California at Berkeley  
Berkeley, California 94720*

### Abstract

We report on both experimental and theoretical studies of high-temperature, high-density plasmas produced when a solid is illuminated with intense, 160 femtosecond laser pulses. Time resolved measurements have determined the x-ray pulsewidth from the plasma to be  $2 \pm 2$  psec in all spectral regions up to a kilovolt. Spectroscopic observations demonstrate that the x-ray emission comes from regions of density higher than those found in a conventional laser produced plasma. Finally reflectivity measurements indicate that the laser is absorbed at the surface of the solid before it expands.

With the advent of high power, short pulse laser systems, it is now possible to extend psec pulse generation into the x-ray regime.[1-10] This is achieved by focusing the laser onto the surface of a solid, thus producing a high temperature x-ray emitting plasma. Provided the laser pulse is short and has a rapid rising edge, energy can be absorbed by the electrons at solid densities in an optical skin depth, before significant ablation of the solid occurs.[1] Rapid cooling of these hot electrons is expected due to rapid thermal conduction into the underlying cold material, electron energy loss to ions, and expansion into the surrounding vacuum.[1,2,8,9,10] This can lead to rapid recombination in the plasma, thus terminating the x-ray emission.

The laser system used for these studies consisted of a colliding pulse mode-locked laser at 616nm, amplified in a series of five dye amplifiers to give a final output energy of 3.5mJ at a repetition rate of 10 Hz, with a pulselength of 160 fsec.[11] The focusing optic was an aberration free, off-axis parabolic mirror which focused the laser pulses at intensities exceeding  $10^{16}$  Wcm<sup>-2</sup> onto a solid target mounted on a scanning stage. Plasma temperatures of greater than 230 eV were obtained as estimated from both the intensities of the

emission lines from various ionization stages and reflectivity measurements; this temperature is consistent with predictions of one-dimensional (1-D) heat flow models describing the laser-solid interaction.[1,2] Emission from the plasma extended over a broad spectrum up to photon energies of at least 1 keV.

The theoretical model employed to model the laser energy absorption by the solid involves a set of coupled equations in 1-D which describe the temperature evolution of the electrons ( $T_e$ ) and ions ( $T_i$ ) as a function of time -

$$c_e \left( \frac{dT_e}{dt} \right) = K \left( \frac{d^2 T_e}{dz^2} \right) - G(T_e - T_i) + (1 - R)\alpha I e^{-\alpha z}$$

$$c_i \left( \frac{dT_i}{dt} \right) = G(T_e - T_i)$$

where  $c_e$  and  $c_i$  are the electron and ion heat capacities,  $K$  is the thermal conductivity of the electrons,  $G$  is the electron-ion coupling constant,  $R$  is the laser reflectivity and  $\alpha$  is the absorption length. In this model the electrons are heated by the laser while the ions are heated only due to collisions with the hotter electrons. With increasing temperature the system changes from an ordered solid to a high-temperature, high-density plasma and hence the physical parameters in the above expression will change as a function of time - by several orders of magnitude in some cases. Inelastic and expansion cooling have not been included, which results in a slower predicted cooling than expected experimentally. Since the plasma is in local thermodynamic equilibrium, inelastic cooling is not the dominant cooling mechanism at the temperatures reached for these experiments, but expansion cooling is significant and can cause the electron temperature to drop by a factor of 2 - 4 in 1 psec under our experimental conditions. Figure 1 shows the model

prediction for the electron temperature as a function of time. The peak electron temperature is 350 eV, whereas the ions attain temperatures of only 20 eV during the same period. However, even without considering expansion cooling the electron temperature drops rapidly after the laser pulse and the x-ray emission from this hot plasma is expected to decay even more rapidly.

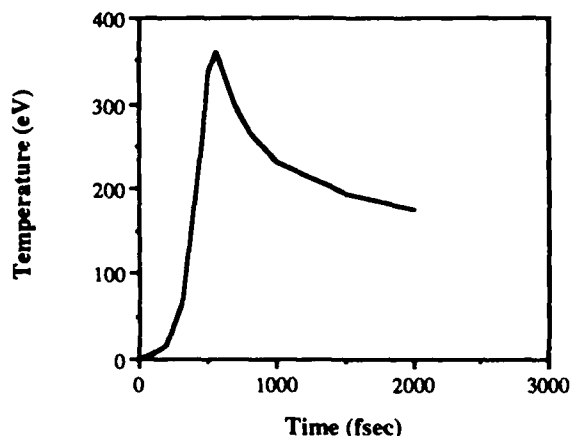


**Figure 1** Results of theoretical model for the electron temperature of silicon as a function of time for a 160 fsec FWHM excitation pulse with a peak intensity of  $10^{16} \text{ Wcm}^{-2}$ .

A Kentech x-ray streak camera with a  $100 \mu\text{m}$  slit and 35 kV/cm extraction field was used to measure the emission pulsewidth; the composite photocathode consisted of lexan (100 nm), aluminum (25 nm) and potassium bromide (150 nm). This photocathode has good quantum efficiency [12] at photon energies exceeding 30 eV. An estimate of the time resolution and sweep speed calibration of the x-ray streak camera was obtained using two 500 fsec laser pulses at 308 nm, separated by a known time delay. The ultraviolet (uv) pulses had to be focused on the photocathode to obtain a response, due to the extremely low photoelectron yield at this wavelength. A CCD camera and computer system were used to record the streak camera output with a precision of 0.3 psec and with a sensitivity of a single photoelectron.

Figure 2 shows streak camera traces of the plasma x-ray emission from a silicon target (Fig. 2(a)), and the response to the uv laser pulse (Fig. 2(b)). The full-width at half-maximum intensity pulsewidths are 6.0 psec and 5.6 psec respectively, and are repeatable within 10 %. These measurements give a deconvolved x-ray pulsewidth of  $2 \pm 2$  psec. We note that it is not strictly correct to deconvolve the x-ray and uv curves in order to obtain the true x-ray pulselength since the secondary electron energy distribution is not the same for x-ray and uv wavelengths. Under uv illumination, electrons are emitted from a well defined F-center[13] in the photocathode and have a narrower distribution and extent than those emitted as a result of x-ray

illumination. Temporal dispersion through the streak camera[10] will then lead to a slightly different impulse response in the two different wavelength regions, with a faster response in the uv. Thus deconvolution yields only an upper limit of 2 psec for the x-ray emission pulsewidth. For silicon, the x-ray pulsewidth was measured both with and without a 100 nm thick filter of aluminum between the plasma and the photocathode; no change in pulsewidth was observed using the aluminum filter, which eliminated all radiation below 50 eV.

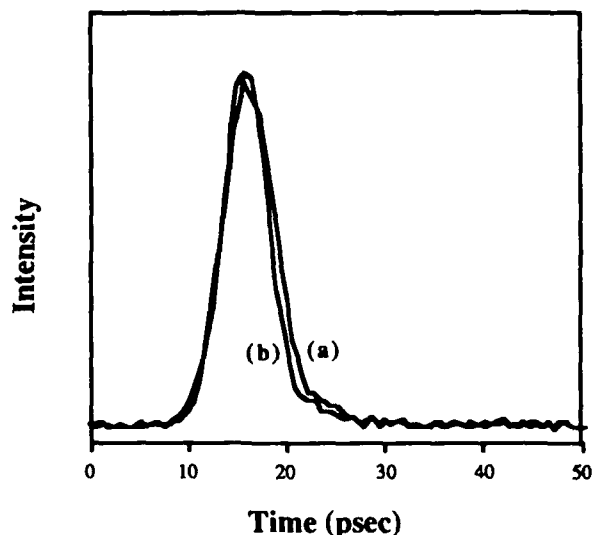


**Figure 2** (a) Streak camera measurement of the soft x-ray pulsewidth from a silicon plasma showing a FWHM of 6.0 psec.

(b) Streak camera response using a 500 fsec, 308 nm pulse incident on the same photocathode, showing a FWHM of 5.6 psec.

A tantalum target was also used to investigate the plasma emission in the keV region of the spectrum, by placing an  $8 \mu\text{m}$  beryllium filter in the path of the x-rays to eliminate all radiation below 800 eV. A slightly shorter emission pulsewidth was observed under these conditions, since the high energy states giving rise to this radiation recombine rapidly. The tantalum target yielded signals at least 5 times more intense than silicon for all energy ranges. At very high intensities, space charge effects in the streak camera lead to broadening of the measured pulse duration both in the uv and x-ray regions, with almost identical saturation characteristics.[14,15]

Very different results were obtained when the short laser pulse was preceded by laser energy on a nanosecond time scale resulting from amplified spontaneous emission (ASE) originating in the dye laser amplifiers.[11] Figure 3(a) shows a 77 psec x-ray decay time from a silicon target obtained when the ASE energy was about 10% of the energy in the short laser pulse. As shown in Fig. 3(b), this reduced to 40 psec



when an additional aluminum filter was used to eliminate all radiation below 50 eV. Figure 3(c) shows the short pulse x-ray emission obtained when the ASE was less than  $10^{-4}$  of the short pulse energy (normal conditions), for comparison. In all cases the fast risetimes are streak camera limited at 2.7 psec, but the decay time is much longer when ASE is present. When the ASE energy was reduced to 5% the decay time was reduced to 10 - 20 psec; the ASE threshold for observable x-ray pulse broadening was  $4\mu\text{J}$ . ASE alone did not generate any detectable short wavelength radiation.

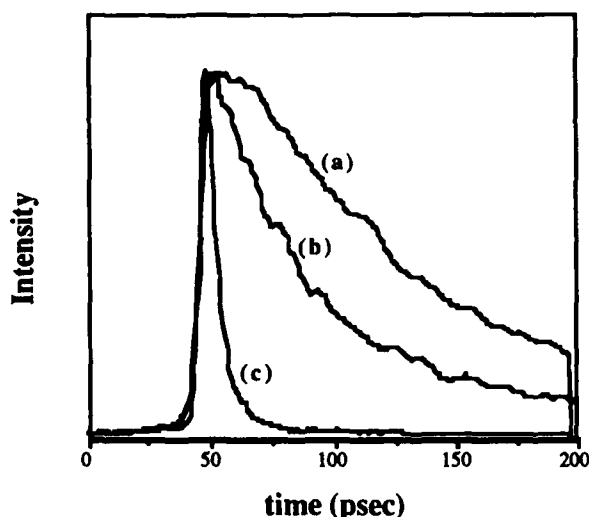


**Figure 3** Soft x-ray pulsewidths obtained from a silicon plasma under various conditions; peak intensities have been normalized.

- (a) Short pulse excitation with 10% ASE energy present.
- (b) As in 3(a) but filtered to show response above 50eV only. (intensity multiplied by 4)
- (c) Short pulse excitation with less than  $10^{-4}$  ASE energy background. (intensity multiplied by 3)

We interpret the long measured decay time in the presence of ASE prepulse as emission coming from a lower density plasma compared to the case of no ASE. The ASE energy which precedes the short pulse laser can vaporize the solid and create a region of lower electron density away from the solid surface which will effectively absorb the short pulse laser at the critical density, where the plasma frequency equals the optical frequency.[3,16] In this lower density plasma, two and three body recombination rates will be reduced; also, reduced thermal conduction and slower expansive cooling will result from the decreased temperature and density gradients due to longer scale-lengths. These conditions lead to an expected increase in the x-ray emission decay time, which is consistent with our observations. These experiments explained the increase in efficiency observed by other groups with the presence

of a prepulse.[7] The streak camera data indicates that a great portion of the increased efficiency comes from radiation emitted at later times.

Time resolved measurements can also explain the increase in intensity observed when a target is irradiated several times on the same spot. As shown in Fig. 4, when several laser pulses are incident on the same spot, a second peak in intensity appears which is delayed later in time with increasing number of shots. However the initial peak remains short in duration but changes in intensity with repeated shots. The large increase in intensity observed when time-integrated experiments are performed arises mainly due to radiation emitted at later times. With increasing number of shots on target, a deeper crater is drilled, starting at  $10\mu$  diameter for a single shot and reaching  $50\mu$  after 10 shots. The radiation at later times is probably due to confinement of the plasma by the walls of the crater. The increase in intensity of the initial peak with increasing irradiation may be due to surface roughness which can increase the absorption of the laser light.

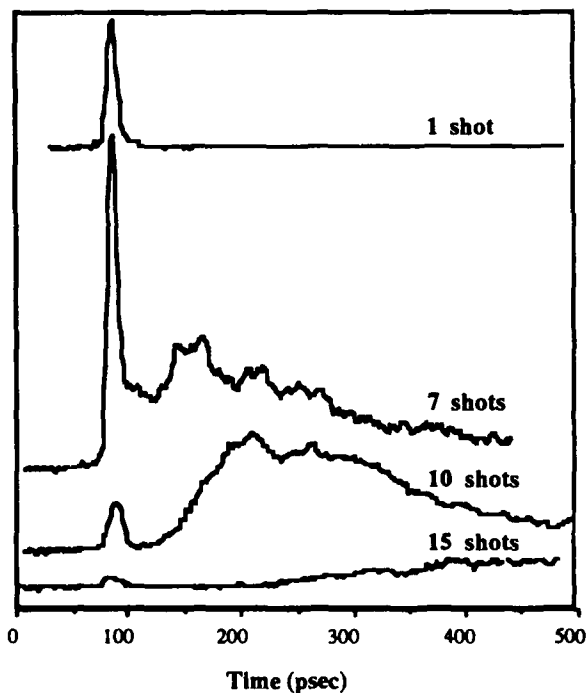


**Figure 4** Streak Camera measurements of the time-history of the emission from a silicon target irradiated on the same spot for different numbers of shots.

Additional evidence for the presence of a high density, rapidly quenched plasma was obtained from time-integrated high resolution plasma spectroscopy experiments. As shown in Fig. 5(a), when the ASE prepulse background energy is simultaneously incident on the target with the short laser pulse we observe both singlet and triplet lines of the Si V ( $2p^6 - 2p^5 3s$ ) transitions at 11.79 nm and 11.90 nm. We do not

observe the triplet line in the absence of the ASE background, as shown in Fig. 5(b). Similar behavior is seen for the case of the Al IV ( $2p^6 - 2p^5 3s$ ) transitions at 16.01 nm and 16.17 nm. In silicon (aluminum), the lifetime of the singlet excited state is 33 psec (59 psec) while the triplet state lifetime is 300 psec (770 psec). [17] We attribute the absence of the long lived triplet emissions under short pulse illumination only to rapid quenching in the plasma. Assuming the mechanisms populating the levels are the same for both experiments, in the case of the short pulse plasma the density is sufficiently high that the levels remain coupled during the entire emission. Thus the radiation from the singlet dominates since the radiative rate of this state is 10 times faster than that of the triplet state. For the lower density plasma created when ASE is present as a prepulse, the levels become uncoupled during the expansion so that both lines are observed.

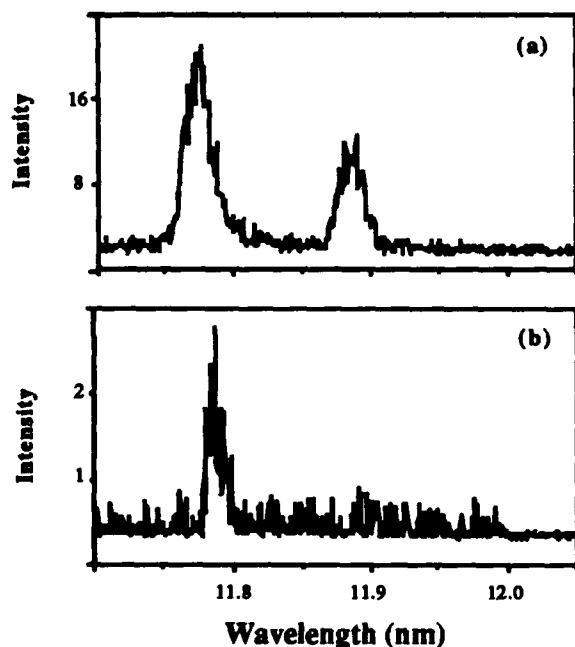


Figure 5 Plasma emission at the Si V ( $2p^6 1S - 2p^5 3s^1 P, ^3P$ ) transitions at 11.79 nm and 11.9 nm. (a) Short pulse laser illumination with 10% ASE energy background. (b) Short pulse laser illumination only.

Figure 6 shows the reflectivity of the short pulse laser from the silicon target (measured at an angle of incidence of 5 degrees to the normal), as a function of incident laser fluence. The results can be compared with model calculations of the reflectivity of the solid versus electron temperature, shown in Fig. 7. At low temperatures, the reflectivity in Fig. 7 is computed from data [18] on room temperature and liquid silicon. In the intermediate temperature, cross-hatched region the reflectivity was not calculated because a plasma model

is not expected to apply. At high temperatures, the calculations assume a Drude model for the dielectric constant [19] of the ionized material and equilibrium ionization conditions computed as a function of electron temperature.

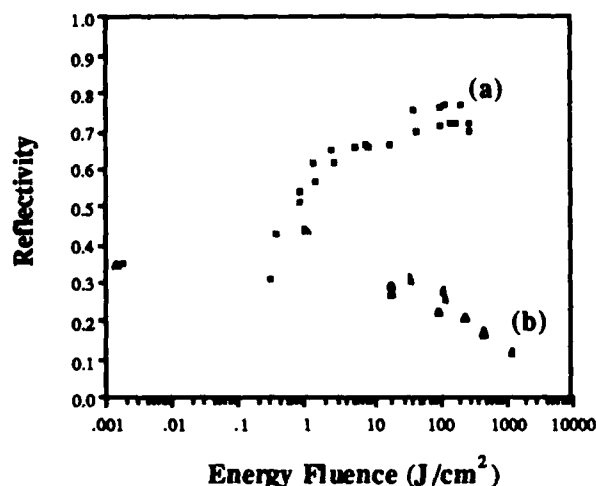


Figure 6 Experimental values for the reflectivity of a silicon as a function of energy fluence on target at an angle of incidence of 5 degrees to the normal.

(a) Short pulse laser illumination.  
(b) 7 nsec long laser pulse illumination.

Figure 6(a) shows the reflectivity ( $R$ ) of silicon as it evolves from a room temperature solid at low laser fluence, with  $R = 35\%$ , to a high temperature, partially ionized plasma, with  $R = 75\%$ . The high reflectivity data is consistent with the model at temperatures of approximately  $230 \pm 20$  eV, when both spatial and temporal averaging of the reflected beam are taken into account. This value is to be compared with the predicted peak temperature of 350 eV from Fig. 1. The reflected short pulse laser beam is specular and image-preserving, even at incident intensities of  $10^{16} W/cm^2$ . However, after the short pulse is incident on the surface, a several micron deep crater is produced as a result of the shock.

Previous measurements [20,21] have determined the increasing reflectivity of silicon up to fluences of about  $2 J/cm^2$  and are in agreement with Fig. 6(a). Figure 6(b) shows the reflectivity of a typical long pulse (7 ns) 532 nm laser pulse. In this case, the reflectivity is significantly lower for a given energy fluence due to efficient coupling between the laser and the lower density material formed by vaporization of the solid during the rising edge of the pulse.[3,16] In addition, the reflected portion of the 7 ns pulse is completely diffuse with no retention of beam structure. The reflectivity in the long pulse experiment was measured using a large area lens to sample a known solid angle, from which the total reflectivity could be deduced since the reflected beam was reasonably uniform over the half

sphere. For all measurements both input and output beams were sampled on each shot and were repeatable to 10%.

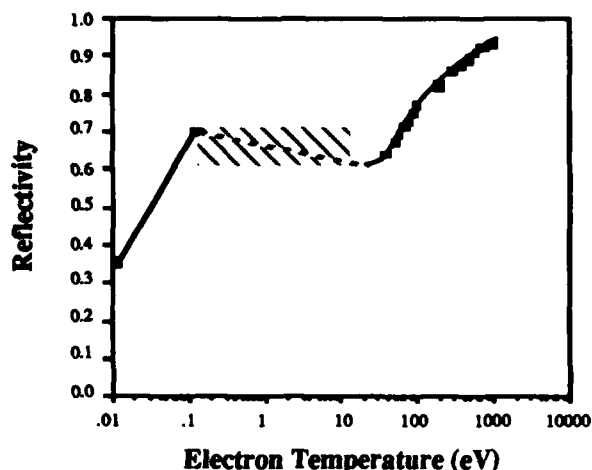


**Figure 7** Model values for the reflectivity of a silicon target as a function of temperature using a Drude model of a solid density, ionized plasma.

## Conclusion

In summary, we measured soft x-ray emission from a 160 fsec laser produced plasma to be less than  $2 \pm 2$  psec duration. We demonstrated that for plasmas heated by a short pulse laser in conjunction with a long pre-pulse the x-ray duration is at least an order of magnitude longer in time. Targets irradiated several times on the same spot resulted in an initial short x-ray pulse followed by a second x-ray emission burst as the plasma recombined at the walls of the crater. Spectroscopy experiments confirmed the presence of rapidly quenched plasma when a solid is illuminated at high intensity by a sub-picosecond laser without a pre-pulse of laser energy. Finally, reflectivity measurements are consistent with absorption of the short pulse laser at solid densities, in contrast to longer pulse illumination for which the coupling is into a preformed lower density plasma.

The authors wish to thank Brad Wargelin for the loan of the streak camera photocathode. This work was supported by the National Science Foundation, AT&T Bell Laboratories, E.I. Du Pont de Nemours and Company, Newport Corporation and through a collaboration with Lawrence Livermore National Laboratory under the auspices of the U.S. Department of Energy under contract #W-7405-ENG-48.

## References

1) R.W. Falcone and M.M. Murnane, "Proposal for a Femtosecond X-Ray Light Source" in *Short Wavelength Coherent Radiation: Generation and*

- Applications, D.T. Attwood and J. Bokor, eds. (AIP 147, New York, 1986).
- 2) M.M. Murnane and R.W. Falcone, "Plasmas Produced by Short Pulse Lasers", to be published in *Proceedings of the Conference on Atomic Processes in Plasmas*, Santa Fe, NM, September 1987.
- 3) O.L. Landen, E.M. Campbell and M.D. Perry, *Opt. Com.* 63, 253 (1987); D.G. Stearns, O.L. Landen, E.M. Campbell and J.H. Scofield, *Phys. Rev. A* 37, 1684 (1988).
- 4) H.M. Milchberg, R.R. Freeman and S.C. Davey, "Measurements of Subpicosecond Laser Produced Plasmas," in *Advances in Laser Science II*, M. Lapp, W.C. Stwalley and G.A. Kenney-Wallace, eds. (AIP, New York, 1987).
- 5) C.H. Nam, W. Tighe, S. Suckewer, J.F. Seeley, U. Feldman and L.A. Woltz, *Phys. Rev. Lett.* 59, 2427 (1987).
- 6) D. Kuhlke, U. Herpers and D. von der Linde, *Appl. Phys. Lett.* 50, 1785 (1987).
- 7) O.R. Wood II, W.T. Silfvast, H.W.K. Tom, W.H. Knox, R.L. Fork, C.H. Brito-Cruz, P.J. Maloney and C.V. Shank, *J. Opt. Soc. Am. B* 4 #13, P24 (1987).
- 8) S.E. Harris and J.D. Kmetec, *Phys. Rev. Lett.* 61, 62 (1988).
- 9) A. Caruso and R. Gratton, *Plasma Phys.* 11, 839 (1969).
- 10) D.J. Bradley, A.G. Roddie, W. Sibbett, M.H. Key, M.J. Lamb, C.L.S. Lewis and P. Sachsenmaier, *Opt. Com.* 15, 231 (1975).
- 11) M.M. Murnane and R.W. Falcone, *J. Opt. Soc. Am. B* 5, 1573 (1988).
- 12) O.H. Siegmund, D.E. Everman, J.V. Vallergera and M. Lampton, *Appl. Opt.* 27, 1568 (1988).
- 13) H. R. Philipp and H. Ehrenreich, *Phys. Rev.* 131, 2016 (1963).
- 14) H. Niu and W. Sibbett, *Rev. Sci. Instrum.*, 52, 1830 (1981).
- 15) M.M. Murnane, H.C. Kapteyn and R.W. Falcone, to be published.
- 16) C.E. Max, "Physics of the Coronal Plasma in Laser Fusion Targets," in *Laser Plasma Interactions*, R. Balian and J.C. Adam, eds. (North Holland, Amsterdam, 1982).
- 17) S.O. Kastner, K. Omidvar and J.H. Underwood, *J. Astrophys.* 148, 269 (1967).
- 18) K.D. Li and P.M. Fauchet, *Appl. Phys. Lett.* 51, 1747 (1987).
- 19) L. Spitzer, "Physics of Fully Ionized Gases" (Interscience, New York, 1962).
- 20) C.V. Shank, R. Yen and C. Hirlimann, *Phys. Rev. Lett.* 50, 454 (1983).
- 21) D. Hulin, M. Combescot, J. Bok, A. Migus, J.Y. Vinet and A. Antonetti, *Phys. Rev. Lett.* 52, 1998 (1984).

## Observations of High Density Plasmas Produced with a Picosecond High Power KrF Laser

O. Willi, G. Kiehn, J. Edwards, V. Barrow, and R. Smith

*Blackett Laboratory, Imperial College of Science and Technology  
Prince Consort Road, London SW7 2BZ, England*

### ABSTRACT:

The interaction of a single picosecond, high power KrF laser pulse with solid targets has been studied using time integrated and time resolved x-ray spectroscopy. Fully ionized aluminum plasmas with temperatures of about 400 eV and densities well above  $10^{23} \text{ cm}^{-3}$  were observed when the ASE prepulse was less than  $10^{-5}$ .

### 1. INTRODUCTION:

The recent development of high power picosecond lasers have opened up exciting possibilities of producing very hot high density plasmas. This is because the laser energy is absorbed very close to the initial target surface since no significant hydrodynamic motion can occur on a subpicosecond time scale. It is crucial however that the contrast ratio between the prepulse and the main pulse is high so that the target surface is not damaged by the prepulse and no plasma is produced ahead of the main pulse. Otherwise the laser energy of the short pulse is deposited close to the critical density resulting in plasmas which are only hot close to the critical density layer.

This paper describes experimental observations and computational modeling on the interaction of a 3.5 ps high power KrF laser pulse with solid targets at irradiances up to  $10^{17} \text{ Wcm}^{-2}$ . Fully ionized Al plasmas close to solid density with temperatures of 400 eV were observed when the prepulse level was low. The results were modeled by a 1-D hydrodynamic computer code.

### 2. EXPERIMENTAL ARRANGEMENT:

The experiments were carried out at the SERC Central Laser Facility (Rutherford Appleton Laboratory) using the recently developed short pulse, high power KrF laser system SPRITE [1]. The short pulse is generated by a mode-locked dye laser which operates at 746 nm and is amplified in a three stage dye amplifier system. It is then frequency tripled in two KDP crystals resulting in a wavelength of 248 nm. Finally, the 3.5 ps pulse is amplified to energies up to 2.5 J in one discharge and two electron beam pumped KrF amplifiers. The laser beam was focused onto target with an  $f/2.5$  aspheric lens to a  $20 \mu\text{m}$  focal spot. Irradiances up to  $10^{17} \text{ Wcm}^{-2}$  were achieved. The focal spot size was monitored using an x-ray pinhole camera with  $15 \mu\text{m}$  resolution while the focal spot distribution was recorded with an equivalent plane monitor using a similar lens. A fast optical diode was used to measure the ASE prepulse level. The total laser energy was recorded with an energy calorimeter.

The primary diagnostic used to study the plasma was a time resolved crystal spectrograph. A flat TLAP crystal was coupled to an x-ray streak camera operating in the 5-7 Å spectral window. The spectral and temporal resolutions were  $15 \text{ mÅ}$  and 15 ps respectively. Time integrated spectra were recorded with a PET crystal. Figure 1 shows the experimental arrangement.

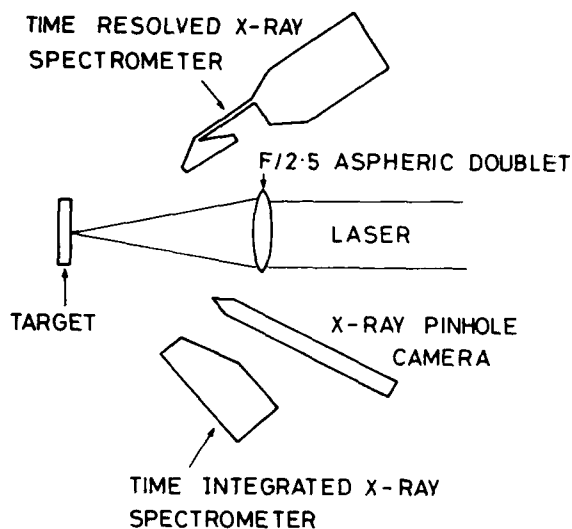


Figure 1. Experimental arrangement.

### 3. EXPERIMENTAL RESULTS:

#### 3.1. Measurements of the prepulse level:

A high contrast ratio between the main pulse and the ASE is crucial for the production of fully ionized plasmas with densities close to solid. Otherwise a large cold plasma corona is formed by the ASE pulse resulting in the heating of the plasma at the critical density by the short pulse. This leads to a sharp fall-off of the temperature above critical.

Various observations were made to investigate the level of the ASE pulse incident on the target surface. Optical diodes were used to measure the contrast ratio. Energy levels of less than one per cent were measured for low prepulse shots resulting in a contrast ratio of less than  $10^{-5}$  in power since the ASE is emitted during 20 ns.

Secondly, targets irradiated with large ASE pulses showed craters up to 200  $\mu\text{m}$  in diameter on the target surface in contrast to the 20  $\mu\text{m}$  focal spot of the main pulse. This is an indication that the divergence of the ASE pulse is larger than that of the main short pulse but this is not a quantitative measurement since lateral energy flow may have occurred during the 20 ns time interval. Thirdly, a time resolved VUV spectrograph was used to study the emission from the preformed plasma produced by the ASE pulse. For large prepulses (10% or more of the total energy), transitions in the XUV/VUV spectral region were clearly observed. When the ASE pulse was small no plasma emission was seen ahead of the 3.5 ps laser pulse.

Finally, titanium targets overcoated with layers of plastic 0.5 to 4  $\mu\text{m}$  in thickness were used to study the x-ray emission of titanium. A large  $K\alpha$  signal as well as the He-like resonance spectrum was seen for large prepulses. When the prepulse was small only the  $K\alpha$  emission was seen on targets with plastic layers thinner than 2  $\mu\text{m}$  demonstrating that the small ASE pulse did not damage the plastic coating of the target.

#### 3.2. High density observations:

A number of features typical of ultra high density plasmas such as Stark broadening and continuum lowering were seen in x-ray spectra from shots with a low ASE prepulse. Figure 2 shows an x-ray streak spectrum from an Al foil target irradiated with a  $3 \times 10^{16} \text{ Wcm}^{-2}$  laser pulse. The Al He $\beta$  (1s2-1s3p) transition is very wide and intense, completely dominating the spectrum. Higher series transitions from H and He like ions are faint and start to turn on some 15 ps after the He $\beta$  transition. In contrast, a distinctly different spectrum was obtained when there was a large ASE prepulse.

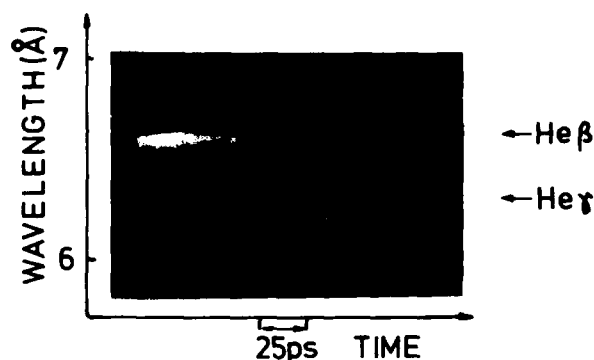


Figure 2. Streak image of an aluminum target which was irradiated with a 3.5 ps laser pulse with a small ASE prepulse.

Figure 3 shows a spectrum taken on an Al target irradiated by a pulse with an ASE energy of 30% of the total laser energy. The spectrum contains the full H and He like series. The width of the He $\beta$  transition is much smaller and the lines are emitted for several hundred picoseconds without significant change in brightness indicating a large plasma corona.

The electron density is obtained by comparing the Stark widths of the He $\beta$  and He $\gamma$  transitions with profiles predicted by the atomic physics codes RATION and SPECTRA[2]. Figure 4 shows densitometer traces of the He $\beta$  and He $\gamma$  line profiles of figure 2 taken about 15 ps after the start of the emission. Superimposed are two line profiles predicted by RATION and SPECTRA for an electron density of  $1.6 \times 10^{23} \text{ cm}^{-3}$ . The simulations of the spectra used a temperature of 400 eV and made corrections for opacity broadening.

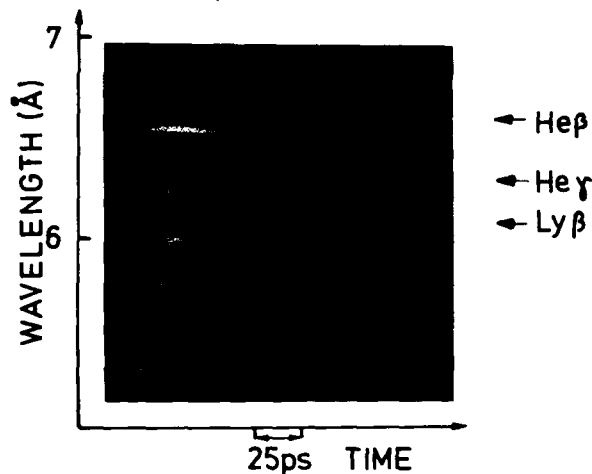


Figure 3. Streak image recorded on an Al target which was irradiated with 3.5 ps laser pulse superimposed on a large ASE prepulse.

A further indication of high electron density is that the higher series transitions are missing. At close to solid density the number of bound states is reduced because of the close proximity of the ions [3]. In addition, Stark broadening also causes the lines to merge into a continuum [4].

The temporal evolution of the spectral lines is illustrated in figure 5. Microdensitometer traces of the streak image of figure 2 are shown at two different times. Initially the He transition is very broad and intense, peaking after the start of the emission. The width changes in time and is asymmetric towards higher energies. At about 25 ps after the start of the emission, the profiles decrease in width and become weak at about 45 ps. The Heγ line switches on after about 15 ps. After about 30 ps the Lyα transition is observable coincident with the decrease in width of Heβ.

The electron temperature was obtained from the ratio  $\text{Al Ly}\alpha / \text{Al He}\alpha$  of time integrated spectra. A temperature of  $400 \pm 50$  eV was found by using small opacity corrections.

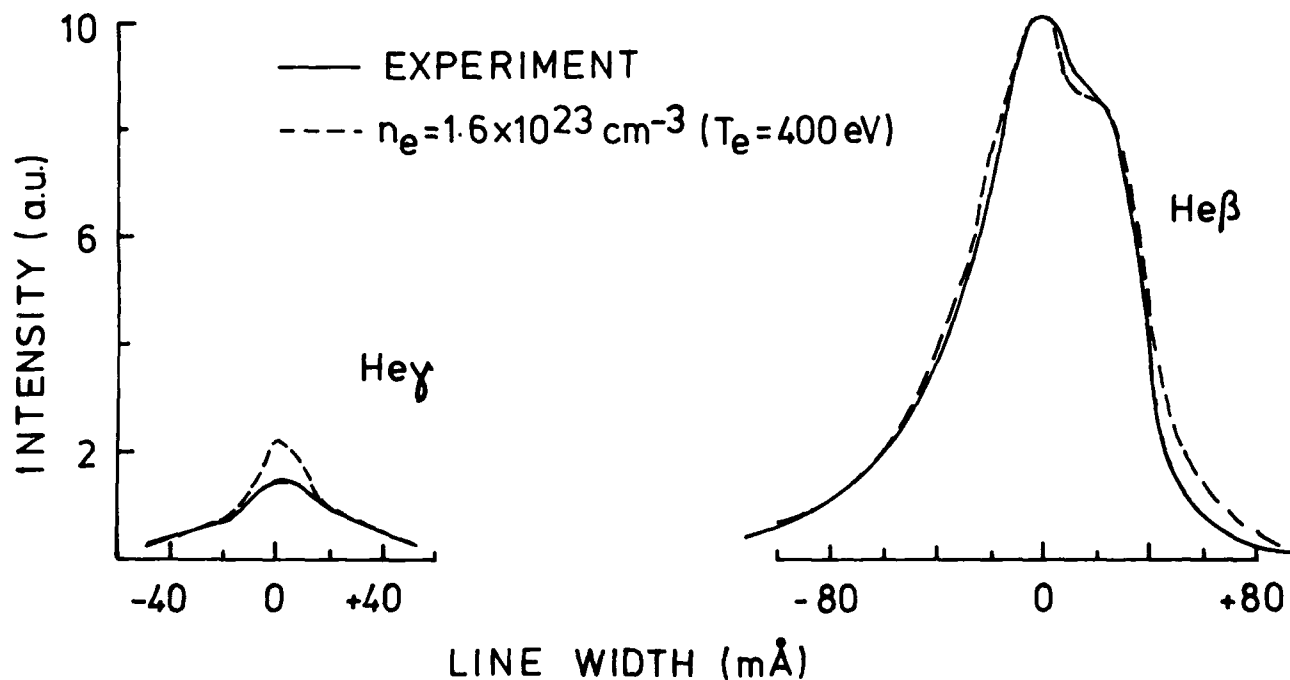


Figure 4. Comparison of experimental line profiles of Al Heγ and Al Heβ with predicted profiles calculated with  $T_e = 400$  eV and  $n_e = 1.6 \times 10^{23} \text{ cm}^{-3}$ .

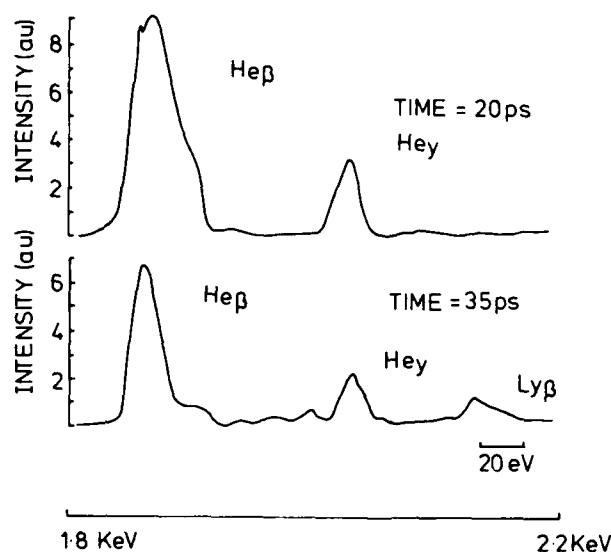


Figure 5. Microdensitometer traces of the experimental spectrum shown in figure 2 at 20 ps and 35 ps after the beginning of the emission.

The electron density was also obtained for spectra recorded on targets with large ASE prepulses. The Stark width was again compared with synthetic spectra produced by RATION and SPECTRA and good agreement was found for  $n_e = 3 \times 10^{22} \text{ Wcm}^{-2}$ . This is consistent with x-ray emission from densities close to critical ( $1.6 \times 10^{22} \text{ cm}^{-3}$ ) for 248 nm laser light.

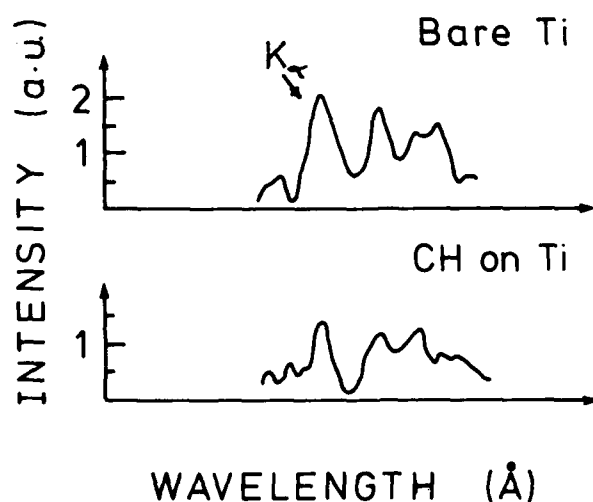


Figure 6. Ti  $K\alpha$  emission from a bare and a  $0.5 \mu\text{m}$  plastic coated Ti target.

### 3.3. Ti K Alpha Measurements:

Titanium foil targets overcoated with various thicknesses of plastic were used to investigate the level of hot electron production in shots with and without a large ASE prepulse. The  $K\alpha$  signal was measured with time integrated x-ray crystal spectrometers. Figure 6 shows microdensitometer traces of  $K\alpha$  spectra taken on a bare titanium and a titanium target overcoated with  $0.5 \mu\text{m}$  of plastic. No  $K\alpha$  signal was seen with  $2 \mu\text{m}$  of plastic overcoats when the prepulse level was very low. From the  $K\alpha$  intensity of these shots it was found that about 20% of the incident laser energy was deposited in hot electrons with energies larger than 4.5 keV. In contrast, when the prepulse level was large a strong  $K\alpha$  signal and He-like lines were observed indicating that several microns of plastic were ablated by the prepulse.

### 4. MODELING OF THE EXPERIMENTAL DATA:

Detailed hydrodynamic simulations were carried out using the 1-D hydrocode MEDUSA. All the simulations were performed with a laser wavelength of 248 nm and aluminum and plastic coated titanium target material. The low prepulse simulations were run for a 0.55 J, 3.5 ps (FWHM) gaussian pulse to model the experimental shot shown in figure 2.

The laser energy was absorbed via inverse bremsstrahlung up to the critical density. 20% of the remaining energy was dumped at the critical density surface to simulate resonance absorption. The fraction of resonantly absorbed energy producing hot electrons was assumed to be 0.9. A flux limiter of  $0.1 \times$  classical free streaming limit was used. The simulations show that only up to 0.5 per cent of the laser energy is absorbed via inverse bremsstrahlung. This is because very little sub-critical plasma is formed during the 3 ps laser pulse. Figure 7 shows MEDUSA outputs of  $N_e$ ,  $T_e$  and  $Z$  the average ionization stage for an Al slab target during and after the laser pulse. The code predicts higher densities during the pulse than are seen experimentally and this is due to the 15 ps resolution of the x-ray spectrometer resulting in temporal smearing. After the laser pulse the predicted temperature and density are better in agreement with the experiment.

The simulations indicate that the laser pulse might have interacted with the solid but due to the low temporal resolution of the spectrograph the solid density could not have been observed.

The effect of laser prepulse was also simulated. A 20 ns gaussian pulse containing 30% of the short pulse energy was superimposed on a 3 ps 0.8 J pulse. During the prepulse several microns of plastic was ablated resulting in a large preformed plasma corona with a temperature of about 100 eV. The short pulse was completely

absorbed via inverse bremsstrahlung in the large underdense plasma corona resulting to electron temperatures up to several keV in the 1-D calculations. Due to these large temperatures a flux limiter of  $0.03 \times$  classical free streaming limit has to be used in the code. Otherwise the overdense plasma temperature becomes unrealistically large. Figure 8 shows the simulation results for the prepulse case. 2-D Fokker-Planck simulations clearly show that most of the absorbed laser energy is transported laterally across the target surface leading to a 1 keV plasma close to the critical density when a large underdense plasma is present. Consequently the 1-D hydrocode simulations overestimated grossly the temperature invoking a small flux limiter. On the other hand when no preformed plasma was present the total absorbed energy is transported into the target, i.e., towards higher electron densities justifying the large flux limiter ( $0.1 \times$  free streaming limit for the prepulse free conditions).

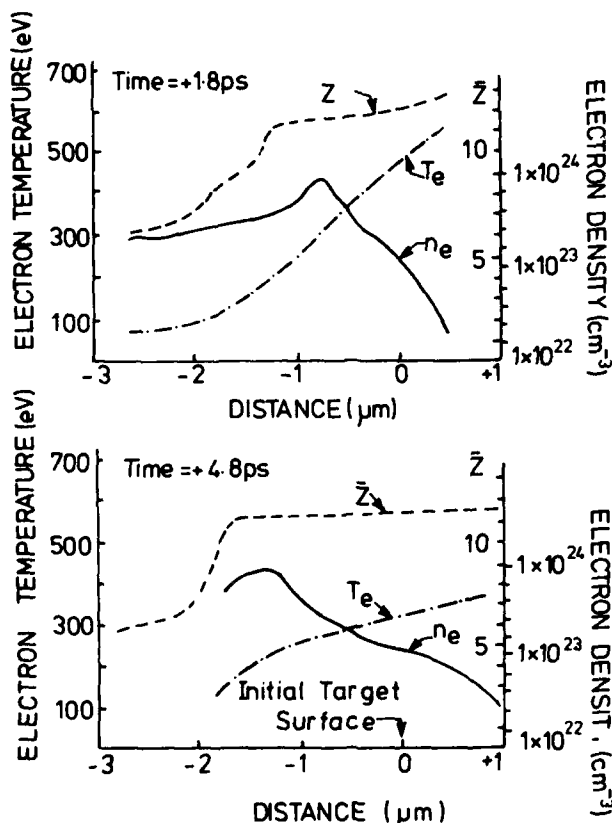


Figure 7. Hydrodynamic simulations of a 3.5 ps laser pulse without prepulse showing the evolution of the electron density, temperature, and average ionization during and after the laser pulse.

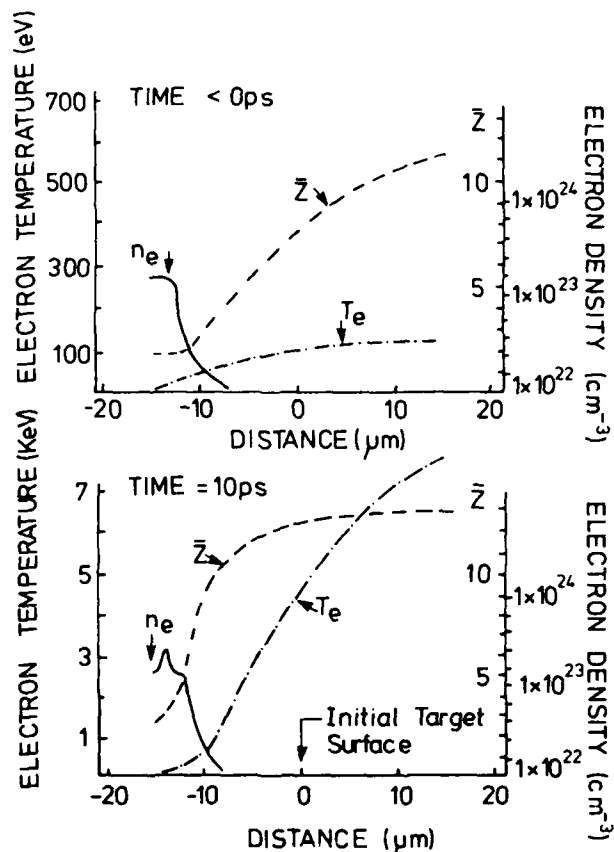


Figure 8. Hydrodynamic simulation of a 3.5 ps pulse with a 30% prepulse showing the evolution of the electron density, temperature and average ionization before and after the interaction of the short laser pulse.

## 5. CONCLUSIONS:

Fully ionized aluminum plasmas with electron densities close to solid and temperatures of about 400 eV have been produced by a single picosecond high power KrF laser pulse with a high contrast ratio. The density was inferred from Stark widths and continuum lowering while the temperature was obtained from line ratio measurements.  $K\alpha$  measurements on Ti targets indicated that about 20 % of the total laser energy was coupled into suprathermal electrons. 1-D hydrodynamic code simulations were in good agreement with the experimental observations.

## ACKNOWLEDGMENT:

We would like to acknowledge the contributions made to this work by the CLF staff.



#### REFERENCES:

1. J.M. Barr et al., Opt. Comm., 60, 127 (1988).
2. R.W. Lee, B.L. Whitten and R.E. Stout II, J. Quant. Radiat. Transfer, 32, 91 (1984).
3. J.C. Stewart and K.D. Pyatt, Astrophysics J., 144, 1203 (1966).
4. D.R. Inglis and E. Teller, Astrophysics J., 90, 439 (1939).
5. G. Rickard, I. Williams and A. Bell, Proc. of ECLIM, Madrid 1988

## **Current Prospects for Free-Electron Lasers in the Extreme Ultraviolet\***

Brian E. Newnam  
Chemical and Laser Sciences Division, MS J564  
Los Alamos National Laboratory  
Los Alamos, New Mexico 87545  
505/667-7979

In the last few years, free-electron laser (FEL) oscillators and amplifiers have produced coherent radiation over a broad spectral range extending from 463 nm in the visible to millimeter wavelengths as summarized graphically in Fig. 1. These successful demonstrations have encouraged a number of research centers to boldly consider extension of this electron-accelerator-based technology to the extreme ultraviolet (XUV) below 100 nm where no powerful, tunable, coherent-radiation source presently exists. Here, the peak- and average-power output of FEL oscillators and amplifiers should surpass the capabilities of any existing, continuously tunable photon sources by many orders of magnitude.

Extending FELs to ever shorter wavelengths, however, is inherently difficult since the gain decreases monotonically with the square-root of the wavelength, and below 100 nm the available mirrors for resonators have comparatively low reflectance, generally  $\leq 50\%$ . With such mirrors, the small-signal power gain for a single pass through the magnetic undulator must exceed 400% just to reach the threshold for oscillation. Increased gain can be attained with long undulators comprising several hundred periods and peak current of  $\geq 100$  A. However, long undulators have reduced homogeneous gain bandwidth equal to  $1/4N$ , where  $N$  is the number of periods. Since the gain is decreased by transverse beam emittance and longitudinal energy spread, it is essential that the accelerators deliver very bright electron beams. Storage rings and rf-linear accelerators, as indicated in Fig. 2, appear to be the only sources of electron beams with brightness adequate for XUV FELs.

The proposed FEL schemes include oscillators using optical resonators, single-pass amplifiers based on self-amplification of spontaneous emission (SASE), multiple-pass regenerative amplifiers, and optical klystrons in which electrons bunched by external lasers radiate coherent harmonics. We review the features and output parameters of several of these active or proposed programs and the technological challenges that must be met to guarantee their successful operation.

---

\* This work was supported by the Division of Advanced Energy Projects of the U. S. Dept. of Energy Office of Basic Energy Sciences and by Los Alamos National Laboratory (ISR&D).

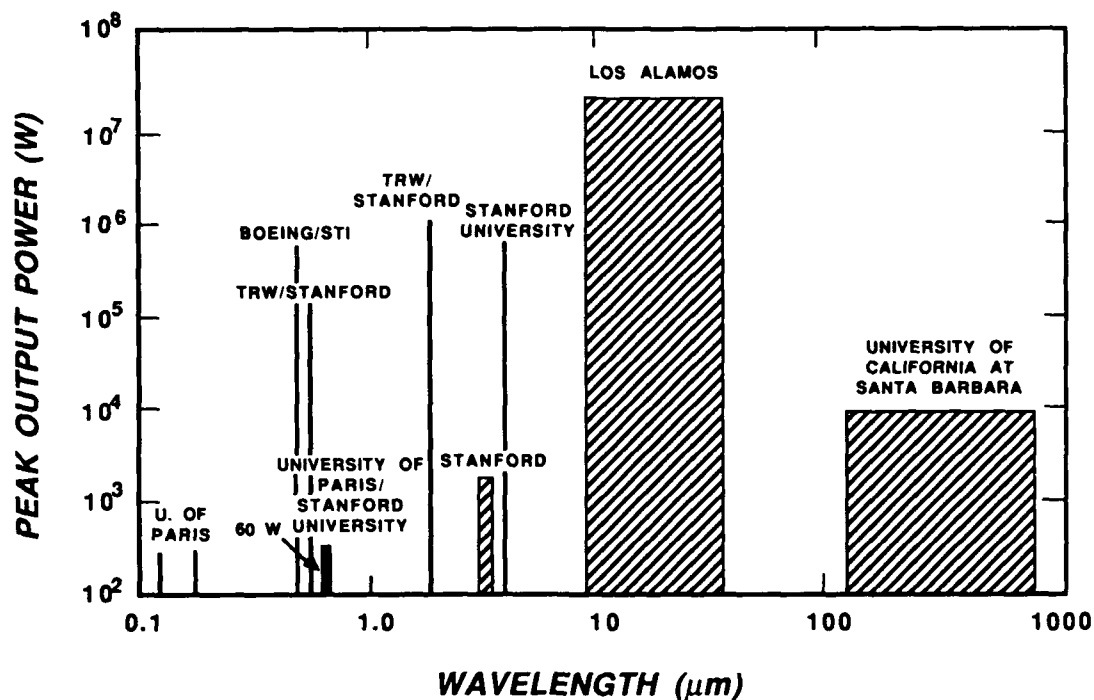


**Figure 1.** FEL oscillators presently span a broad wavelength range from the visible to the far-ir. Devices to operate in the 10 - 100 nm range have been designed for demonstration experiments.

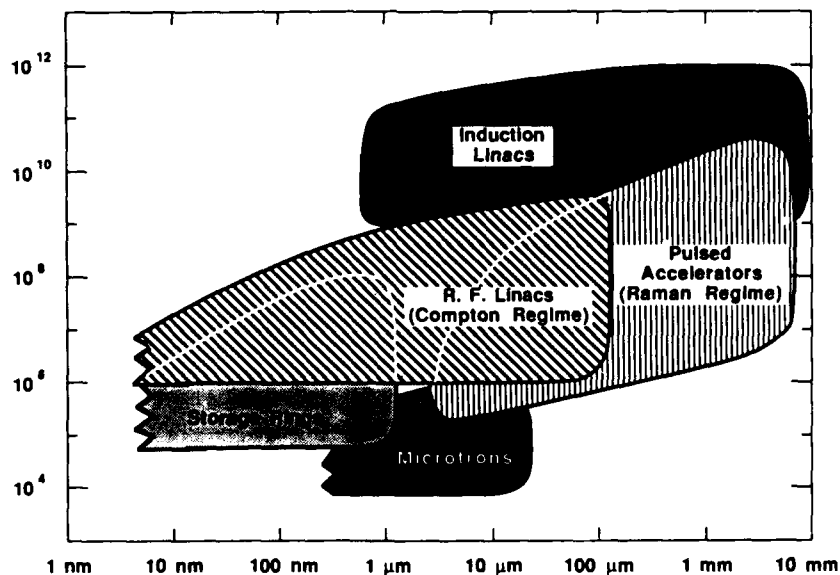


**Figure 2.** FELs for different wavelength regimes use different accelerator technologies. The FEL resonance equation states that wavelength depends inversely as the square of the electron energy. Thus, low-voltage machines such as diode pulsers and electrostatic accelerators are generally used for the far-infrared and millimeter wave regions. To reach shorter wavelengths, higher electron energy with high beam brightness is required. Storage rings and rf linacs with advanced injectors appear capable of extending FEL operation to 100 nm and below.

# Compact X-Ray Free-Electron Laser

W. Barletta,<sup>†</sup> M. Atac,<sup>\*</sup> A. Bhowmik,<sup>\*</sup> B. Bobbs,<sup>\*</sup> D. B. Cline,<sup>\*</sup> R. A. Cover,<sup>\*</sup>  
F. P. Dixon,<sup>\*</sup> J. Gallardo,<sup>†</sup> J. Kolonko,<sup>\*</sup> C. Pellegrini,<sup>†</sup>  
G. Rakowsky,<sup>\*</sup> X. Wang,<sup>†</sup> and G. Westenskow<sup>‡</sup>

<sup>\*</sup>Center for Advanced Accelerators, University of California, Los Angeles, California 90024

<sup>†</sup>Brookhaven National Laboratory, Upton, New York 11973

<sup>‡</sup>Lawrence Livermore National Laboratory, University of California  
Livermore, California 94550

<sup>\*</sup>Rockwell International Corporation, Rocketdyne Division, Canoga Park, California 91303

## ABSTRACT

We present a design concept and simulation of the performance of a compact x-ray, free electron laser driven by ultra-high gradient rf-linacs. The accelerator design is based on recent advances in high gradient technology by a LLNL/SLAC/LBL collaboration<sup>†</sup> and on the development of bright, high current electron sources by BNL and LANL. The GeV electron beams generated with such accelerators can be converted to soft x-rays in the range from 2 – 10 nm by passage through short period, high field strength wigglers as are being designed at Rocketdyne. Linear light sources of this type can produce trains of picosecond (or shorter) pulses of extremely high spectral brilliance suitable for flash holography of biological specimens *in vivo* and for studies of fast chemical reactions.

## 1. Introduction

Over the past decade the material, chemical, and biological science research communities have demonstrated an ever increasing interest in using sources of radiation of XUV and soft x-ray radiation. The most important sources in this spectral region are storage ring facilities which produce broad band, incoherent synchrotron radiation. The spectral brilliance of storage ring sources is restricted both by the incoherence of the radiation process and by limitations in beam density. Moreover, the minimum pulse lengths available exceed 20 ps.

<sup>†</sup>Work performed under the auspices of the U.S. Dept. of Energy by LLNL under contract W-7405-ENG-48.

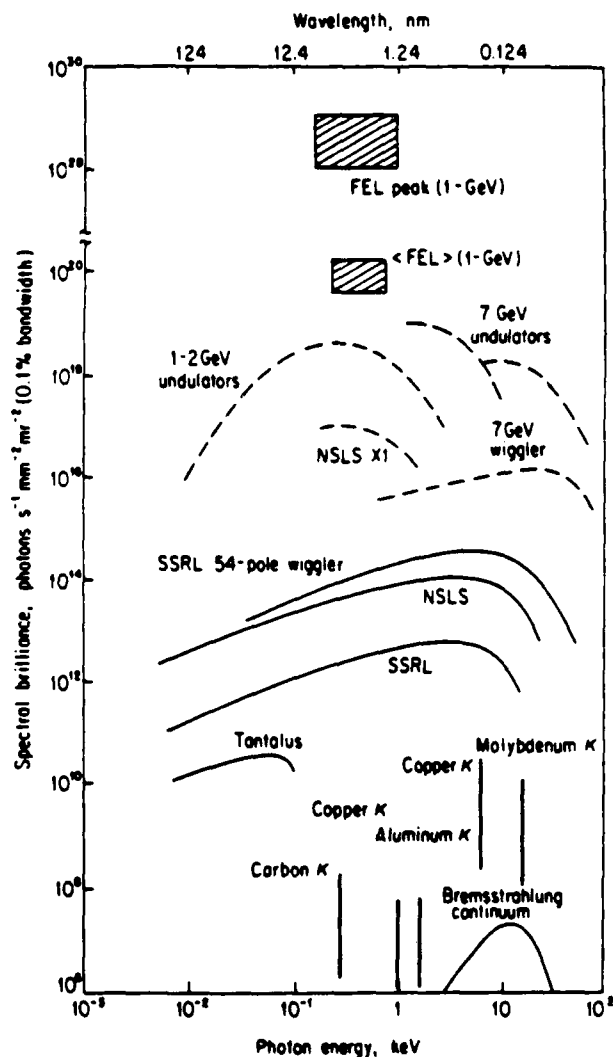


Figure 1

As an alternative to storage ring sources, it is now feasible to develop compact sources of intense, coherent soft x-rays with extremely high peak and time average spectral brilliance (Figure 1), very short pulse duration (picosecond or less), and broad frequency tunability. The x-rays are generated by self-amplified spontaneous emission from an intense electron beam traversing a wiggler in a single-pass free electron laser (FEL) architecture. X-ray FEL's driven by ultra-high gradient, rf-linacs, should find a wide range of uses due to the possibility of constructing instruments with unique characteristics tailored to the specific needs of the user.

The basic elements of the linear x-ray source as illustrated in Figure 2 are, 1) a laser driven, high gradient r.f. electron gun plus a conventional S-band post accelerator, 2) an ultra-high gradient linac to produce a GeV beam, 3) and a high field strength, short wavelength wiggler with a precision beam control system.

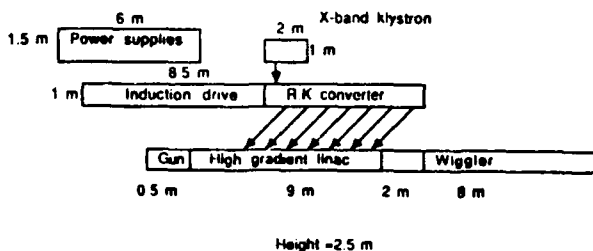


Figure 2

This report describes the prospects for the design of a compact, X-ray FEL and of the various component sub-systems. It includes recent simulations plus rules for scaling the FEL performance to other wavelengths. Finally, the critical issues for the construction of an instrument in the near future are addressed.

## II. Scaling Basis For the X-Ray FEL Design

Building a compact, soft x-ray FEL presents two main design difficulties: a) producing a high energy electron beam with sufficiently high density and sufficiently small momentum spread as required to generate high gain, b) producing high precision, high field strength wigglers. The architecture for the FEL relies on single pass growth from self-amplified spontaneous emission (SASE) starting from beam noise in a long undulator<sup>1,2</sup>. This process can be viewed as the natural extension of the emission of synchrotron radiation from an undulator. If the undulator is long enough and if the beam intensity is high enough, the spontaneous emission will be amplified by the beam itself, and the output radiation will grow exponentially until

the FEL amplifier saturates. This process has been demonstrated in a quasi-optical experiment with 2 mm radiation in the ELF experiment at LLNL<sup>3</sup>.

The usual resonance condition connecting the beam energy,  $\gamma$ , the wiggler wavelength,  $\lambda_w$ , and the signal wavelength,  $\lambda$ , is

$$\lambda = \left( \frac{\lambda_w}{2\lambda^2} \right) (1 + a_w^2) \quad (1)$$

where  $a_w$  is the dimensionless vector potential of the planar wiggler,

$$a_w = \frac{e\lambda_w B_0}{2\sqrt{2}\pi m_e c^2} \quad (2)$$

A simple expression for the amplification in a planar wiggler can be estimated in the cold beam limit of the one-dimensional FEL theory<sup>1</sup>. The power grows exponentially with an e-folding length of

$$L_g = \frac{\lambda_w}{4\pi\rho}, \quad (3)$$

where

$$\rho = \left( \frac{a_w \omega_p}{4\omega_w} \right)^{\frac{2}{3}}. \quad (4)$$

In Equation (4),  $\omega_p$  is the beam plasma frequency divided by  $\gamma^3$  and  $\omega_w$  is the wiggler frequency. The power at saturation will be  $P_{FEL} = \rho P_{beam}$ ; for the parameters of interest for x-ray FELs the efficiency at saturation can be approximately 0.1%. At this point additional energy can be extracted from the electron beam by tapering the wiggler, or the electrons can be diverted to a second converter for the production of harder, incoherent x-rays.

The resonance condition constrains the allowable spread of longitudinal velocities of the electrons in the beam such that the electrons do not slip more than a small fraction of an optical wavelength per gain length. This consideration leads to constraints on the beam emittance,  $\epsilon_n$ , and energy spread; namely,

$$\frac{\Delta\gamma}{\gamma} = \frac{\rho}{4}, \quad (5)$$

and

$$\epsilon_n \leq \frac{\lambda\gamma}{2\pi}. \quad (6)$$

Equation (5) should be applied in the restrictive sense of a constraint on the spread in the longitudinal component of  $\gamma$ . Another design condition for the FEL comes from requiring that diffraction does not take energy out of the beam in a distance equal to a gain length,  $L_g$ . Hence, the gain length of

the laser must be shorter than the Rayleigh range,  $Z_R$ ;

$$Z_R = \frac{\pi a^2}{\lambda_s}. \quad (7)$$

Hence,

$$a^2 > \frac{\lambda_s \lambda_w}{4\pi^2 \rho}, \quad (8)$$

where  $a$  is the size of the beam in the wiggler. If the wiggler employs natural focussing, the betatron wavelength in the wiggler and the beam size are related by

$$\lambda_\beta = \frac{\lambda_w \gamma \sqrt{2}}{a w} \quad (9)$$

Additional focussing may be employed to increase  $\rho$  as long as the constraints on longitudinal velocity spread remain satisfied. If enough focussing can be added to keep  $\lambda_\beta$  constant with increasing energy, then one can show that

$$\rho \sim \gamma \lambda^{\frac{1}{2}}, \quad (10)$$

a far more favorable scaling with wavelength than obtains for atomic lasers.

### III. Simulation of the X-Ray FEL Performance & Undulator Design

To go beyond the estimate of FEL performance based on scaling laws, the Rocketdyne simulation code, FELOPT, was used to calculate the performance of a 2.5 nm SASE amplifier and to assess the sensitivity of the gain to energy spread, emittance, and wiggler errors. Two sets of parameters, listed in Table I, were chosen that differ in the assumed electron beam energy and in the wiggler magnetic field strength and period. In both cases, the wiggler poles are assumed to be curved so as to provide natural focussing in both transverse planes. The electron beam has a parabolic radial distribution of charge and is uniformly distributed in transverse phase space with 90 % of the electrons in the energy interval  $\pm 0.05$  %.

As illustrated in Figures 3 and 4, both amplifiers saturate in  $\approx 800$  wiggler periods to yield powers of a few hundred megawatts. The sensitivity of the performance to increase in energy spread or emittance is indicated in Table II. Doubling  $\epsilon_n$  or  $\Delta\gamma$  significantly decreases the saturated output. Still, the output is adequate for most purposes. Sensitivity to wiggler phase errors is presented in Table III. Steering errors are neglected; i.e., perfected corrections to the trajectory are assumed.

The results indicate that an rms field error of  $\approx 0.1$  % is adequate.

PARAMETERS		
	CASE I	CASE II
Wavelength (Å)	25	25
Energy (GeV)	1.02	1.44
Wiggler Wavelength (cm)	1.0	2.0
Magnetic Field (T)	1.514	0.757
Wiggler Length (m)	8.1	11.5
Current (A)	400	400
Energy Spread (%)	0.1	0.1
Normalised Emittance (mm-mrad)	1.0	1.0

Table I

As the simulations show, efficient conversion of the high energy electron beam to soft x-rays requires the fabrication of long, high accuracy, high field strength wigglers with precision beam control. Considerable progress in precision wiggler design using diverse magnet technologies has been made over the past four years. For example, the 25-m long Paladin wiggler at LLNL - a hybrid electro-magnet design with curved pole faces<sup>4</sup> and 8 cm period - has  $\approx 300$  periods with a measured uncorrelated field error of  $< 0.1$  %. An alternative approach, especially attractive for wigglers with a periodicity shorter than 4 cm, is a pure permanent magnet (PPM) structure.

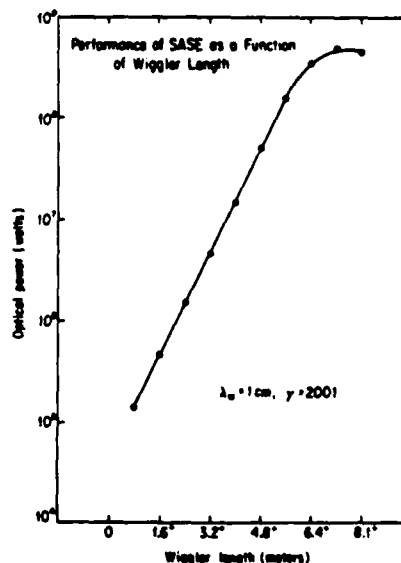


Figure 3

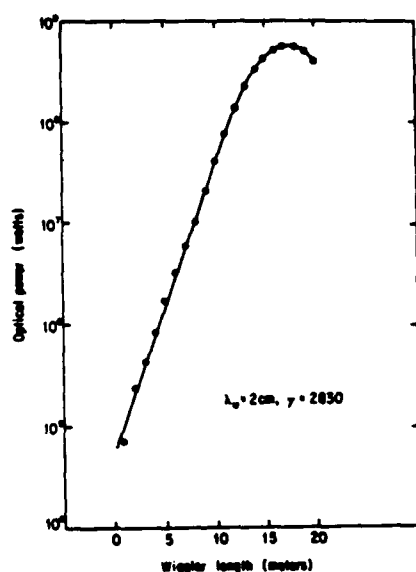


Figure 4

An 80 period, 2 m long, PPM wiggler built by Rocketdyne for experiments at the Stanford Mark III accelerator<sup>5</sup> has demonstrated precision control of electron trajectories equivalent to an uncorrelated field error of 0.055 %. A photograph of the functioning wiggler is given in Figure 5.

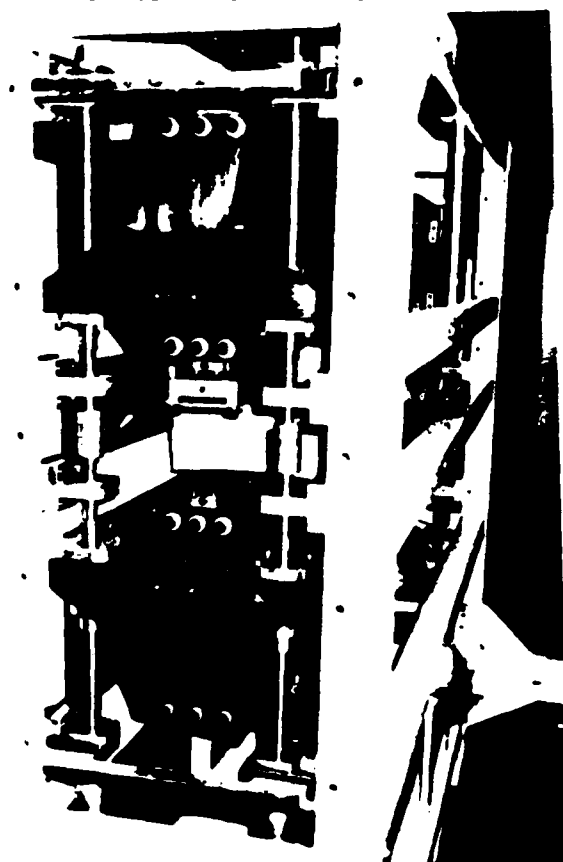


Figure 5

The design used an innovative optimisation algo-

rithm, "simulated annealing"<sup>6</sup>, to compensate for normal production tolerances in the field strength and polarisation angle of individual magnets.

Rocketdyne is now extending this technique to minimise phase errors between the electrons and the optical field in the design of new higher field PPM arrays for retrofit into the 2-m wiggler.

SENSITIVITY TO CHANGES IN ELECTRON EMITTANCE AND ENERGY SPREAD		
$\gamma = 2830$ , WIGGLER LENGTH, $L_w = 20$ m		
ENERGY SPREAD (%)	NORMALIZED EMITTANCE (mm - mr)	POWER OUT (W)
0.1	1	$5.8 \times 10^6$
0.1	2	$3.0 \times 10^6$
0.2	1	$3.8 \times 10^7$

Table II

The high field wiggler design has been validated in full-scale laboratory models. Special magnet module assembly fixtures and insertion/extraction tools have been developed for safe handling and accurate positioning of magnets in the presence of strong magnetic forces. Improved magnet measurement procedures have in turn lead to improved field models and improved wiggler optimisation algorithms.

EFFECT OF PHASE ERRORS RESULTING FROM WIGGLER FIELD ERRORS				
Power at Peak of Gain Curve (8 m & 17 m, Respectively)				
WFE (%)	0	0.3	0.5	1.0
Case 1 ( $\gamma = 2001$ ) ( $\times 10^6$ W)	4.9	4.2	3.6	
Case 2 ( $\gamma = 2830$ ) ( $\times 10^6$ W)	5.8	5.7	5.5	4.0

Table III

The basic PPM wiggler design is readily scalable subject to some practical limitations. First, all magnet dimensions scale directly with  $\lambda_w$ . Hence, the minimum period is limited to  $\approx 1$  cm by the difficulties in handling, assembling, and clamping fragile wafers of powerful SmCo<sub>5</sub> magnets. The replacement arrays for the 2-m wiggler have a period of 2.4 cm. This high field configuration has been extended in a detailed design to even shorter periods (1.2 cm). Another critical dimension, the minimum gap,  $g$ , between the poles may be set by optical aperture requirements or by mechanical

limitations in the vacuum chamber design. Since  $B_0 \sim \exp(-g/\lambda_w)$ , the minimum practical gap height constrains the choice of  $B_0$  and  $\lambda_w$  for a given beam energy.

The PPM wiggler for the x-ray FEL will have several hundred periods and an overall length from several to twenty meters. The wiggler could be built in sections to be assembled and aligned on site. The structure will consist of a series of linked, kinematically mounted space frames (Figure 6) or tables depending on the desired orientation of the wiggle plane (and consequent polarisation of the x-rays).

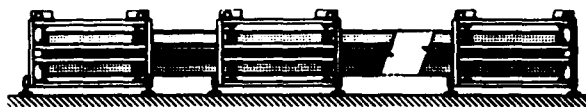


Figure 6

The magnet arrays themselves will also be built in optimised sections of 100 periods and joined in a way that maintains the prescribed periodicity and field strength across each joint. Mechanical support and gap adjustment are also provided at each joint. Beam position monitors and steering correction coils are also provided at 100 period internals. Since the PPM array is iron-free and the relative permeability of  $\text{SmCo}_5$  is near unity, fields superimpose linearly. Therefore, steering coils and additional distributed quadrupole focusing coils can be mounted externally along the wiggler.

The separate aluminum vacuum chamber will consist of extruded segments in the shape of an I-beam with an elliptical beam aperture through the center of the web. The I-beam shape is sufficiently strong that the chamber can be supported independently of the magnet arrays. Wigglers longer than a few meters will require vacuum joints in the beam tube welded in situ. Access ports drilled through the web to the beam aperture allow for diagnostic access and provide vacuum ports.

#### IV. Description of Accelerator Components

Although the use of SASE eliminates the need for mirrors, single pass architectures will require  $> 10^6$  small signal gain to yield x-ray beams of high spectral brilliance. A pre-requisite for such high gains is the generation of extremely bright, high current electron beams. Recent advances at LANL, BNL, and other laboratories in developing electron guns with a brightness exceeding that of operating storage rings such as the SLC damping ring (greater than  $10^{10}$  A/m<sup>2</sup>-rad<sup>2</sup>). These electron injectors are based on the technology of laser

driven photo-cathodes (both metallic and semiconductor) in cavities with very high accelerating fields (10 to 100 MeV/m) followed by magnetic compression to reduce space charge effects at low beam energy. For example, the rf-gun built at Los Alamos<sup>7</sup>, using a  $\text{Cs}_3\text{Sb}$  cathode in a 1.3 GHz cavity, has produced a beam of  $\sim 300$  A with a normalised rms emittance of  $10^{-6}$  m-rad at a beam energy of 1.1 MeV and a pulse length of  $\approx 50$  ps.

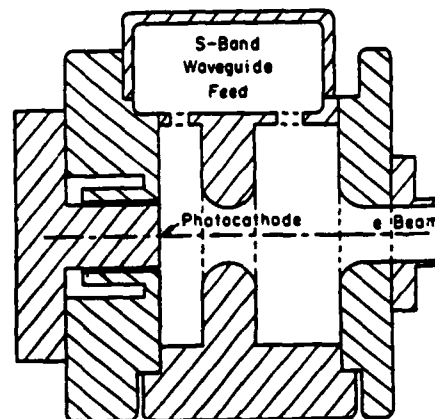


Figure 7

Limitations on the emittance of an electron gun are imposed by several physical effects: the maximum current density available from the cathode, non-linear electro-magnetic forces in the rf-cavity and space charge forces. One means of reducing the space charge forces is to apply a very strong rf-field at the cathode surface in order to accelerate the beam rapidly to relativistic velocities. This approach is being followed in an injector now being built at BNL. The BNL gun, illustrated in Figure 7, is expected to produce a beam of 200 A in 3 ps with a normalised rms emittance of  $\approx 3 \times 10^{-6}$  mrad with a pulse length of  $< 5$  ps. In the BNL gun a mode locked, frequency doubled Nd:YAG laser is used to drive a metallic photocathode in a 2.87 GHz cavity ( $1\frac{1}{2}$  cells) to emit a beam with a current density  $< 600$  A/cm<sup>2</sup>. A single master oscillator locks the phase of the electron bunch with the rf-power drive of the injector. Accelerating fields as high as 100 MeV/m raise the beam energy to 4.8 MeV in  $< 8$  cm. Such a gun could produce a useful x-ray FEL based on SASE in the range from 5 - 10 nm. Combining this approach with magnetic compression at high energies, it should be practical to construct guns with  $\approx 1$  kA of peak current in 1 ps at a normalised rms emittance of  $10^{-6}$  m-rad. Such a bright gun should extend the accessible wavelength range to 1 nm.

The GeV-class linear accelerator that drives the x-ray FEL can be made far more compact than present rf-linacs through the use of the ultra-high gradient structures now under investigation by a



SLAC/LLNL/LBL collaboration for a linear collider at TeV energies. The performance goals<sup>8</sup> for these structures are gradients exceeding 200 MeV/m and cost < 1 M\$/GeV. The peak currents will be ~ 1 kA at a normalized brightness of about  $10^{12} \text{ A}/(\text{m}^2\text{-rad}^2)$  in a train of ~ 20 micro-pulses each of ~ 1 ps duration and spaced by 0.1 to 1 ns. The pulse train is repeated at a frequency of 100 – 1000 Hz; the rms energy spread through the macro-pulse must be < 0.1 %.

The physical phenomenon which forms the basis for scaling the gradient in rf-linacs from the 17 MeV/m of the Stanford Linear Collider to the desired ~ 200 MeV/m for compact linear light sources, is the increase in peak electric field that can be sustained without breakdown<sup>9</sup> with increasing rf-frequency and with shortening duration of the rf-power. For disk-loaded waveguide structures the peak field that can be maintained is

$$E_{pk} = 120 \text{ MV/m} \left( \frac{f}{2.87 \text{ GHz}} \right)^{\frac{1}{2}}. \quad (11)$$

The accelerating field is a factor of ~ 2 less than the peak value. The total peak rf-power needed to drive the accelerator based on a  $2\pi/3$  disk-loaded waveguide can be estimated as

$$P_{rf} \approx 6 \text{ GW} \left( \frac{E_a}{200 \text{ MeV/m}} \right)^2 \left( \frac{L}{2000} \right) \left( \frac{\lambda_{rf}}{105 \text{ mm}} \right)^{\frac{1}{2}}. \quad (12)$$

For compact 1 GeV linacs to be practical and affordable a new class of rf-power sources is needed. One of the most promising approaches to power compact linacs is the relativistic klystron<sup>10</sup> driven by an induction linac, as illustrated in Figure 8.

Schematic of a relativistic klystron

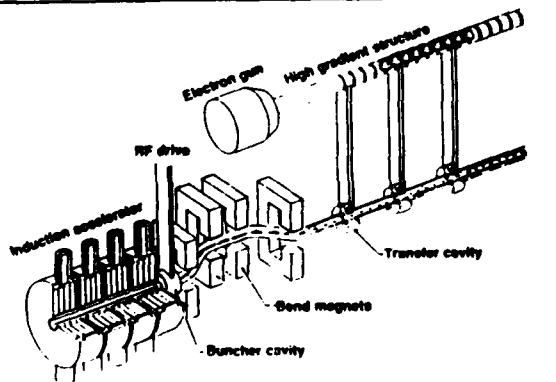


Figure 8

In the relativistic klystron a multi-kA, multi-MeV beam produced with a linear induction accelerator (LIA) is modulated at the desired rf-frequency (10 to 15 GHz); the modulated high current beam then excites an rf-generating transfer structure. The

high peak power rf is then fed via waveguides to the miniaturised rf-cavities of the high gradient rf-linac.

Initial experiments<sup>11</sup> at LLNL have extrapolated a conventional, high gain klystron design using velocity modulation to < 1 MV operation to produce a source of more than 200 MW of rf-power at 11.4 GHz (X-band). This source has been used to power a 25 cm long section of X-band, disk loaded waveguide structure to obtain an accelerating gradient exceeding 135 MeV/m in a demonstration earlier this year.

Characteristics of drive for x-ray FEL			
Beam parameters		Accelerator	
Beam Energy (GeV)	1	Frequency (GHz)	11.49
Peak Current (A)	1000	rf-efficiency	50 %
Pulse Length (ps)	1.2	Iris a (mm)	4.35
Pulse Length (mm)	0.4	Fill T/atten. T	0.15
Norm Emit (mm-rad)	0.001	Bunch (*full phase)	5.1
N-part	$7.2 \times 10^6$	v-group/c	0.049
Size in Linac (μm)	24.1	Energy/m (J/m)	28.9
$\Delta\gamma/\gamma$ (%)	0.1	E-max (MV/m)	375
n Bunches	5	Grad (MeV/m)	155.1
Bunch Space (ns)	0.26	Length (m)	6.59
Rep Rate	200	Cavity Size (mm)	10.7
Induction Drive		Fill Length (m)	0.44
		Fill Fraction	0.98
I-induction (A)	3000	rf P (MW/m)	1128
Overall length (m)	9.5	Loading %	0.8
V-induction (MeV)	5.4	Beam Efficiency (%)	3.1
Length Induction Drive	7.1	rf-supply (ns)	28

Table IV

For the 1 GeV linac needed to drive the FEL described by the FELOPT simulation, one injects the beam from a photo-cathode gun into a linac at a conventional gradient which acts as a matching section for bringing the beam into the high gradient structure operating at 11.4 GHz. The characteristics of the X-band linac with its relativistic klystron power supply can be determined from well known scaling laws<sup>8,12</sup> and are listed in Table IV. This linac would produce a train of five micropulses spaced by 0.46 ns. Operating at a repetition rate of 200 Hz, the FEL driven by such an accelerator would produce x-rays with a peak spectral brilliance  $\approx 3 \times 10^{28}$  (photons-sec<sup>-1</sup>-mm<sup>2</sup>-mrad<sup>-2</sup>) per 0.1 % bandwidth. The time average brilliance for this design is  $\approx 4 \times 10^{19}$ .

## V. Critical Issues and Conclusions

The x-ray FEL relies on the performance of components that have been shown to operate well, although not necessarily in the required parameter range. The ultimate performance of the laser will depend not just on the component level performance, but also on the integrated system of high precision beam generation, guidance, and control. The issue most critical to the extension of free electron laser technology to the x-ray regime can be summarised as

- 0) generation of extremely high brightness electron beams and preservation of beam quality during the acceleration and energy conversion process

In addition to the difficulties of beam generation, the following four areas will be critical to the ultimate performance of the FEL in that they profoundly affect beam quality:

- 1) pulse-to-pulse reproducibility and stability of the electron beam
- 2) phase and amplitude stability of the relativistic klystron power drive with respect to the electron pulses from the photo-injector
- 3) beam transport into and through the wiggler
- 4) wake-field suppression in the high gradient rf-linac

Each of these areas must be studied in the laboratory at the component level and eventually in integrated sub-scale tests at longer wavelengths.

Compact x-ray FELs will require precise mechanical alignment of the cavities, beam tube, magnetic centerline, and optical axis. Laser alignment techniques used for large optical systems may be useful. Insertable screens and steering correction may provide initial alignment of magnetic mechanical axes. In the wiggler, the beam should not deviate from the centerline by more than a fraction of the beam size. A key to the success of this program will be the development of fast beam position monitors with an accuracy of  $\approx 20$  microns.

Industrial applications of compact sources of coherent x-rays with very high time average brilliance include integrated circuit lithography using imaging masks and soft x-ray (4 - 5 nm) reflective optics. This technique offers ultimate feature size of about 50 - 150 nm, well below that currently achieved ( $\frac{3}{4}$  to 1 microns).

X-ray FELs driven by compact linacs could also provide sources of extremely high peak brilliance. Imaging of biological samples with x-rays in the wavelength range of 4 - 5 nm will allow resolution of cellular sub-structures in the natural

state without dehydration or staining. This wavelength regime is also the most suitable for holographic imaging of proteins *in vivo*. Moreover, the picosecond duration exposures at multi-GHz rates, obtainable with linear light sources, will allow dynamic measurements of specimens. Such studies of samples in a normal physiological environment would be complementary to ordinary scanning electron microscopy. X-ray spectroscopy in the range of 2 - 4 keV accesses the K-edges of P, S, Na, K, Ca, and Cl - all elements of considerable biological significance. Based on the cost algorithm of Reference 11, the expected cost of such high brilliance x-ray instruments is expected to be under 10 M\$.

## References

1. R. Bonifacio, C. Pellegrini, L. M. Narducci, Opt. Comm., **50**, 373 (1984)
2. J.B. Murphy and C. Pellegrini, J. Opt. Soc. Am., **B2**, 259 (1985)
3. A.L. Throop, et al.; "Experimental results of a high-gain microwave FEL operating at 140 GHz"; LLNL, UCRL-97706, presented at the Ninth International FEL Conference, Williamsburg, VA, Sept 14 - 18, 1987; to be published in Nuclear Instrumentation Methods.
4. G. Deis, et al, "A Long Electromagnetic Wiggler for the Paladin Free-Electron Laser Experiments", IEEE Transactions on Magnetics, Vol 24, No. 2, March 1988.
5. A. Bohwmik, et. al., "First Operation of the Rocketdyne/Stanford Free Electron Laser", Proc. IX International Free Electron Laser Conference, Williamsburg, VA, Sept 1987.
6. A.D. Cox and B.P. Youngman, Proc. SPIE, Vol. 582, pp 91 - 97, 1985.
7. J.S. Fraser and R.L. Sheffield, J. Quantum Electronics QE-23, 1489 (1987)
8. R. Palmer, Interdependence of Parameters for TeV Colliders, SLAC-4295.
9. J.W. Wang, V.Nguyen-Tuong, and G.A.Loew, RF Breakdown Studies in a SLAC Disk-loaded Structure, Proceedings of the 1986 Linear Accelerator Conference, SLAC-303 (1986)
10. A.M. Sessler and S.S. Yu, Phys. Rev. Lett. **58**, 2439 (1987)
11. M. Allen, et al, Proceedings of the European Particle Accelerator Conference, (1988)
12. W.A. Barletta, High Gradient Accelerators for Linear Light Sources, LLNL report UCRL-99268, Rev I, to be published in Nuc. Instruments and Methods, (1988)

# Targets for Efficient Femtosecond-Time-Scale X-Ray Generation

J. D. Kmetec and S. E. Harris

*Edward L. Ginzton Laboratory, Stanford University  
Stanford, California 94305*

## Abstract:

High power femtosecond lasers can be used to generate bright x-ray sources. The choice of element for the laser-produced-plasma target strongly affects the nature of the emitted x-rays. Combining low  $Z$  and high  $Z$  elements results in the brightest femtosecond x-ray radiators. Examples of lithium and tin combinations yielding  $3.6 \text{ \AA}$  x-rays with up to several percent conversion efficiencies are given.

## Introduction:

For many years, the output of pulsed laser systems have been focussed onto solid targets to generate plasmas. It is well known that a laser-produced-plasma can efficiently radiate in the XUV to x-ray regions of the spectrum. The recent development of very high peak power femtosecond lasers promises to yield even brighter plasmas emitting at even shorter wavelengths (1). We have studied the role of the laser target in a femtosecond-time-scale plasma and suggest several configurations which maximize the x-ray conversion efficiency while retaining the short pulse nature of the laser.

The dominant radiative processes in a laser-produced-plasma are line emission and two-body recombination. There have been experiments using picosecond and femtosecond lasers to drive x-ray-emitting plasmas (2-5), and also some measurements which show x-ray pulse lengthening well into the picosecond range (6). Both because of the relatively low power density on target, and because the targets were heavy metals, the electron temperatures were low, and the rise and fall times of the x-ray pulse were dominated by avalanche stripdown and two-body

radiative recombination. Characteristic recombination times are slow compared to currently available femtosecond lasers. We propose conditions which maximize line radiation excited by hot electrons. The radiative rates and the heating and cooling times of the electrons can be much faster than recombination times.

The electrons are heated by the high power density of the laser, and cooled by inelastic ionizing collisions with the ions and by thermal diffusion. On a femtosecond time scale, ablation is negligible and thus very little cooling is achieved by plasma expansion. High  $Z$  elements have low thermal conductivity but very high inelastic cooling rates which prevent the laser from heating the electrons to high temperatures. Low  $Z$  elements quickly ionize completely and lose all inelastic

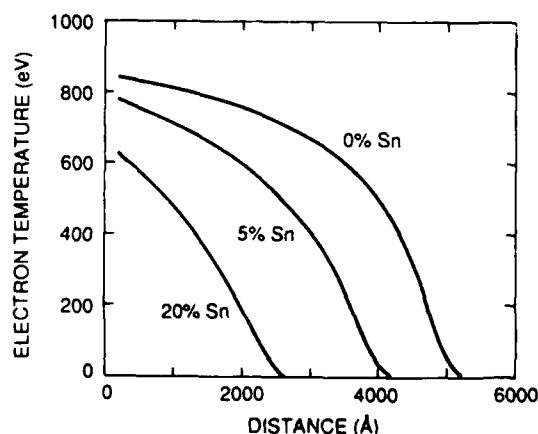


Figure 1: Electron temperature vs. distance for a solid Li-Sn mixed target at an absorbed energy of  $1 \text{ kJ/cm}^2$ , for different values of Sn density. The profiles are evaluated 50 fs after the peak of the laser pulse. Reproduced with permission from Ref. 7. Copyright 1988, American Physical Society.

cooling power, allowing the plasma to heat to temperatures required for efficient x-ray line excitation. High Z elements are clearly necessary for x-ray line emission, thus proper combinations of low Z and high Z elements can maximize the x-ray yield. Using an example of tin (Sn) and lithium (Li), we present three cases: solid Sn-Li mixed species, a thin foil of Sn-Li mixed species, and a thin film of Sn on solid Li. The x-ray spectrum under our conditions will be dominated by Sn L-M radiation at 3.6 Å. For a given absorbed laser energy each of these cases can provide greater than an order of magnitude increase in Sn L-M emission over that of a solid Sn target.

#### Model:

A description of the model can be found elsewhere (7). Briefly, we assume that a tightly focussed 100 fs laser pulse (gaussian in time) is incident on the surface of a target and that some fraction of the laser energy is absorbed in a skin depth of about 150 Å. Electrons in the interior of the metal are heated by electron-electron

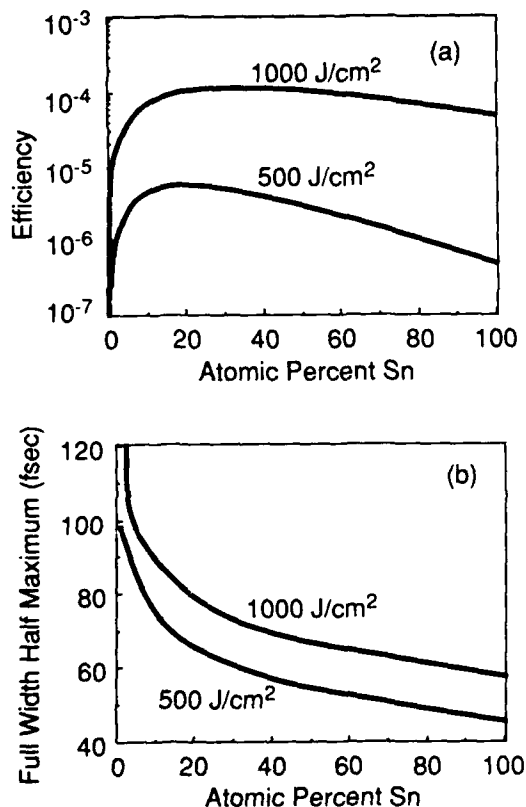


Figure 2: Solid Li-Sn mixed-species target results: (a) X-ray peak power conversion efficiency ( $\lambda=3.6$  Å) as a function of percent Sn. (b) X-ray pulse width for a 100 fs laser pulse.

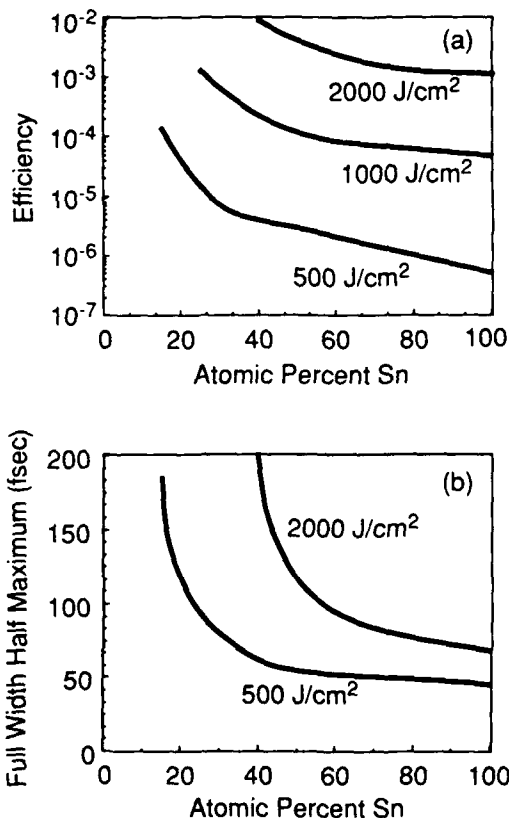


Figure 3: Thin (1000 Å) foil of Li-Sn mixed-species results: (a) X-ray peak power conversion efficiency ( $\lambda=3.6$  Å) as a function of percent Sn. (b) X-ray pulse width for a 100 fs laser pulse.

diffusive energy transfer and are cooled by ionizing collisions with heavy metal atoms and also by thermal diffusion further into the interior. The diffusion is determined from an inelastic loss-modified thermal conductivity (7). X-ray line emission arises from electron impact ionization of L-shell electrons or, after Sn has stripped enough to have vacancies in the M-shell, by electron impact L-M excitation (8). In both cases, the x-ray yield is weighted by a radiative branching ratio (9). Reference (7) did not contain the latter mechanism of x-ray generation. The plasma remains optically thin to the L-M radiation.

#### Results:

A computer code was written to evaluate the thermal diffusion and ionization subject to an incident absorbed energy. Figure 1 shows the electron temperature as a function of distance for different values of Sn density in a Sn-Li solid. The absorbed energy is 1 kJ/cm<sup>2</sup> and the

profiles are evaluated 50 fs after the peak of the laser pulse.

Figure 2 (a,b) shows the conversion efficiency (absolute) from peak absorbed laser power to peak 3.6 Å x-ray power and the resulting x-ray pulse width as a function of atomic percent Sn. This target is solid Sn-Li mixed species and the cooling necessary for rapid termination of the x-rays is achieved by both inelastic and diffusive cooling.

Figure 3 (a,b) is similar, except the target is a thin (1000 Å) foil of a Sn-Li mixture. The thin foil prevents diffusive cooling, thus inelastic processes provide all the cooling. Sufficiently low Sn densities are not able to cool the hot electrons following the laser heating. In these cases, the Sn is severely ionized and two-body radiative recombination becomes the dominant mechanism to generate x-ray photons. The expected x-ray pulse length is then likely to be in excess of several picoseconds.

Figure 4 (a,b) are the results for a thin layer of Sn on solid Li. A layer that is thinner than the heated region represents a smaller inelastic cooling rate to the hot electrons, since these electrons spend a fraction of their time in Li, which has little inelastic cooling. Thus higher electron temperatures are achieved; while the presence of Li behind the layer allows for diffusive cooling, ensuring that the x-ray pulse remains short. This target configuration is likely to be the brightest x-ray radiator, with absorbed laser power to x-ray power conversion efficiencies exceeding one percent.

#### Conclusion:

We have shown that the inelastic cooling rate of a heavy metal, together with diffusive cooling, allows an x-ray pulse to replicate a laser pulse on a femtosecond time scale; and to achieve such an x-ray pulse, the quantity of heavy metal must be reduced to a level commensurate with the absorbed laser energy. Greater available laser energy allows conversion to x-rays of shorter wavelength than the example given here. Similar efficiencies are obtained for 1.5 Å L-M radiation from lithium-tungsten combinations, at absorbed energies in the 20 to 50 kJ/cm<sup>2</sup> range.

For a 10<sup>-13</sup> sec, 10<sup>12</sup> W (peak) laser driver, and 30 percent absorption (inverse bremsstrahlung of 2 kJ/cm<sup>2</sup> on pure Sn), a 200 Å Sn film on Li will allow the generation of femtosecond 3.6 Å x-ray pulses with a peak power of 10<sup>10</sup> W. At ten hertz this will produce a point source with an average power of 10 milliwatts.

This work has been supported by the U.S. Air Force Office of Scientific Research, the U.S. Army Research Office, and the U.S. Office of Naval Research.

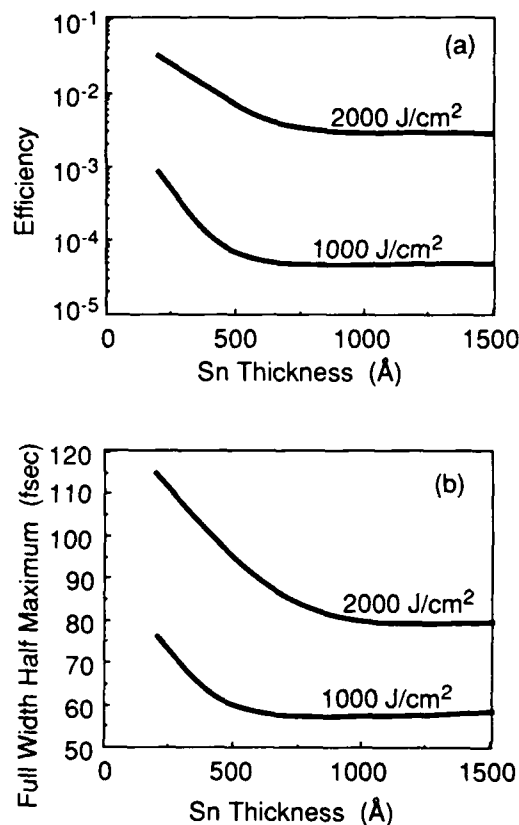


Figure 4: Thin film of pure Sn on solid Li results: (a) X-ray peak power conversion efficiency ( $\lambda=3.6$  Å) as a function of percent Sn. (b) X-ray pulse width for a 100 fs laser pulse.

#### References:

1. R. W. Falcone and M.M. Murnane, "Proposal for a femtosecond x-ray light source", in *Short Wavelength Coherent Radiation: Generation and Applications*, edited by D.T. Attwood and J. Bokor, AIP Conference Proceedings No. 147 (American Institute of Physics, New York, 1986), pp. 81-85.
2. O.R. Wood, II, W.T. Silfvast, H.W.K. Tom, W.H. Knox, R.L. Fork, C.H. Brito-Cruz, M.C. Downer, and P.J. Maloney, "Effect of pulse duration on short wavelength emission from femtosecond and picosecond laser-produced Ta plasmas", *Appl. Phys. Lett.* 53(8), 654-656 (1988).
3. D. Kuelke, V. Herpers, and D. Von der Linde, "Soft x-ray emission from subpicosecond laser-produced plasmas", *Appl. Phys. Lett.* 50, 1785-1787 (1987).

4. D.W. Phillion and C.J. Hailey, "Brightness and duration of x-ray line sources irradiated with intense 0.53  $\mu\text{m}$  laser light at 60 and 120 ps pulse width", Phys. Rev. A34, 4886-4896 (1986).
5. D.G. Stearns, O.L. Landen, E.M. Campbell, and J. Scofield, "Generation of ultrashort x-ray pulses", Phys. Rev. A37, 1684-1690 (1988).
6. N. Nakano and H. Kuroda, "Energies and time-resolved spectroscopy of 10-2000  $\text{\AA}$  emissions from laser plasmas produced by a picosecond laser", Phys. Rev. A35, 4719-4728 (1987).
7. S.E. Harris and J.D. Kmetec, "Mixed-species targets for femtosecond-time-scale x-ray generation", Phys. Rev. Lett. 61, 62-65 (1988).
8. M. Rosen, Lawrence Livermore National Laboratory, Livermore, CA; private communication.
9. E.J. McGuire, "Atomic L-shell Coster-Kronig, Auger, and radiative rates and fluorescence yields for Na-Th", Phys. Rev. A3, 587-594 (1971).

---

**Part 2**  
**High Intensity Laser Interaction with Matter**

---

## The Stark Effect in Atoms at Extremely High Intensities: Ponderomotive Potentials and All That

Richard R. Freeman

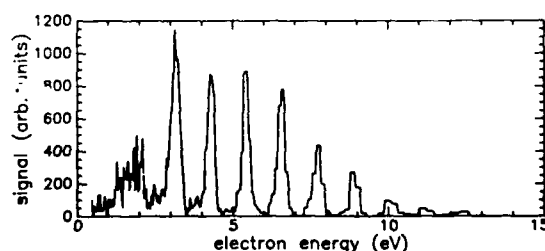
*AT&T Bell Laboratories, Murray Hill, New Jersey 07974*

### ABSTRACT

Recent measurements of the kinetic energies of photoelectrons produced in multiphoton ionization of the rare gases for ultra-short ( $\leq 250$  femtosec), high intensity ( $\approx 10^{14}$  W/cm<sup>2</sup>) light near 616 nm reveals a complex spectra, rich in structure with some features so narrow in energy that they are limited by the spectrometer resolution. In this paper I show that this thoroughly unanticipated result is a signature of a general phenomena, one that is present (but often hidden) in all multiphoton experiments regardless of the pulse length employed in the particular experiment. Further, I argue this phenomena is directly related to the ponderomotive potential associated with the "wiggle" motion that an electron executes under the influence of an intense optical field.

At intensities exceeding approximately  $10^{13}$  W/cm<sup>2</sup>, most atoms and molecules begin to ionize, regardless of the wavelength of light. Under these conditions, simple threshold ionization processes become replaced with "higher-order" ones, the most prominent being the occurrence of multiple electron peaks separated by the photon energy. This phenomena, first reported by Agostini *et al.* in 1979 [1], is now called "above threshold ionization" (ATI). Far from being a singular occurrence, ATI has since been observed in many different atoms and molecules by investigators using lasers with widely differing

wavelengths [2]. Indeed, ATI can be quite pronounced: Fig. 1 shows ATI in xenon for 1.06  $\mu$ m laser light at  $\approx 2 \times 10^{13}$  W/cm<sup>2</sup> and 100 psec pulse duration. The threshold ionization electron peak, the only peak that would be in the spectrum at lower energies, is dwarfed in magnitude by the higher order peaks which occur at energies separated by 1.16 eV, the energy of a 1.06  $\mu$ m photon.



1. The ATI spectrum in xenon for 1.06  $\mu$ m laser light at  $\approx 2 \times 10^{13}$  W/cm<sup>2</sup> and 100 psec pulse duration.

In an effort to understand the origins of ATI, the experimental efforts of a number of groups have concentrated on the behavior of these higher order peaks as a function of laser intensity [3], polarization [4] and pulse width [5]. Initial experiments were performed with relatively long laser pulses, and while the spectra were found to be insensitive to the nominal pulse width, they were critically dependent not only on the laser polarization, but on the intensity of the laser as well [6]. Recently ATI has been investigated using



ultra-short laser pulses [5], and to the amazement of all concerned, the observed spectra bore virtually no resemblance to those recorded with long pulses. However, analysis of all the experimental data, both long and short pulse, reveals that one physical concept plays a substantial, if not dominant role in all of the observed phenomena: the ponderomotive potential of free and bound electrons in an intense electromagnetic field.

At low intensities, the only interaction between an electron and an electromagnetic wave is spontaneous Thompson scattering. Extrapolating the linear spontaneous Thompson scattering rate to high field intensities yields the prediction that an electron will scatter virtually no photons from a laser pulse and in turn suffer no changes in either momentum or energy. However, Bucksbaum and coworkers [7] have recently shown that a 1 eV electron attempting to traverse a focused Nd:YAG beam with  $10^{13}\text{W/cm}^2$  peak intensity will actually be backscattered! The resolution to this apparent contradiction is that electrons interact with high intensity light via *stimulated* scattering, a coherent process in which the effective cross section is immensely larger than the normal spontaneous process. Within the context of quantum electrodynamics, the interaction of an electron with a high intensity electromagnetic wave is completely described in terms of this coherent photon picture [8]. Often referred to as "stimulated Compton scattering", it makes use of differential photon occupation in the various spatial and frequency modes of the focused, short pulsed laser. For example, at some physical position within the laser beam focus the electron can absorb a photon from one spatial mode  $k_1$  and scatter this photon preferentially into another mode,  $k_2$ , whose photon occupation is higher. The difference in photon momentum,  $\hbar(k_2 - k_1)$ , is given to the electron in the direction of the gradient of the intensity.

As mathematically complete as the stimulated scattering picture is, when it comes to one's intuition about the result of experiments, or to the calculation of the effect of a real laser beam on an atom, it is far more useful to convert to a classical field picture of the interaction. Indeed, the classical manifestation of the stimulated scattering of a very large number of coherent photons is the

sinusoidal motion of the electron driven by the E and B fields of the light beam. The interaction energy of an electron in an optical field with peak value  $E_0$  is

$$U_p = \frac{e^2 E_0^2}{4m_e \omega^2} \quad (1)$$

Note that the interaction energy scales as the intensity of the light, and inversely with the square of the frequency. For an electron irradiated with  $1.064\mu\text{m}$  light,  $U_p$  has a value of 1 eV for  $10^{13}\text{W/cm}^2$ .

The total energy of the electron [9] is equal to the instantaneous value of  $U_p$  plus its energy of directed motion; that is

$$E_{\text{total}} = U_p + E_{\text{kinetic}} \quad (2)$$

where  $E_{\text{kinetic}}$  is the energy associated with the time averaged motion. When the laser beam is constant, or changes so slowly that there is no appreciable change in its amplitude during the passage of the electron through it, then  $E_{\text{total}}$  is a constant of the motion and Eq. (2) may be used to predict the average motion of an electron in the vicinity of or within a high intensity laser beam. On the other hand, if the electron passes through the laser beam in times comparable to the duration of the laser pulse, Eq. (2) still describes the total energy of the electron, but  $E_{\text{total}}$  becomes a function of time and the total energy of the electron is no longer conserved. There have been several recent experiments showing the effects of ponderomotive forces (the spatial gradient of Eq. (1) arising from the Gaussian distribution of electric field intensities within the laser focus) [6], and the energy nonconservation of the total energy of electrons arising from the finite pulse width of laser pulse [10].

We now turn our concern to the effects of high intensity fields on electrons bound in atoms. The highly excited Rydberg states are particularly easy to understand: they have wavefunctions that differ only slightly from the continuum states just above them in energy, so they are expected to behave nearly identically. Thus the states near the ionization limit will increase by  $U_p$  in a field with peak intensity  $E_0$  and frequency  $\omega$ . For deeply bound states, however, the answer is quite different. Here the wavefunction is

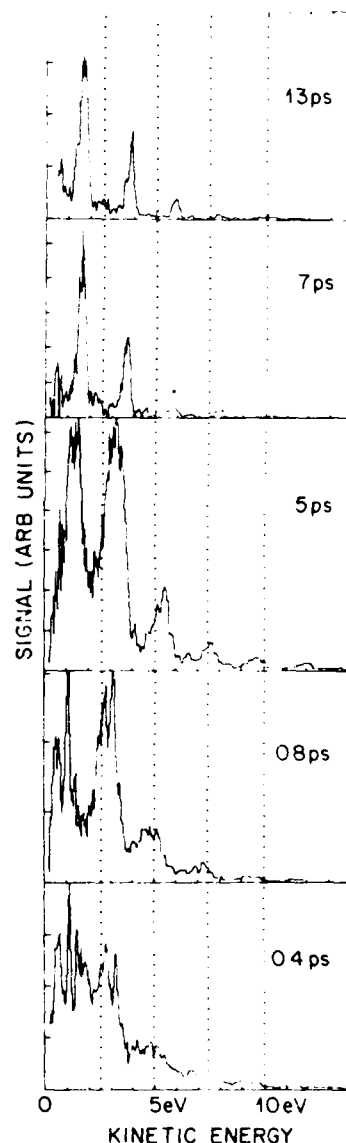
pulled into the core, and contains high values of momenta due to the strong pull of the core. Classically one can immediately estimate the effect of an outside field at frequency  $\omega$  driving an electron bound with a characteristic frequency  $\omega_0$  by solving the electric force equation. After averaging over an optical cycle, the effective potential,  $U_{p'}$  of the deeply bound electron is given by  $U_{p'} = U_p(\omega/\omega_0)^2$ . For example, in heavy rare gases ground states are bound with an energy of approximately 10 eV, while the energy of a Nd:YAG photon is on the order of 1 eV. Thus while the states nearly at the ionization limit are increasing in energy with  $U_p$ , the ground state is increasing by only 1% as much. Thus we are led to the amusing, and at first glance quite surprising, result that the ionization potential of an atom increases approximately as  $U_p$ , at least in the limit of long wavelengths and deeply bound ground states. Upon reflection, however, this result is entirely physical, for more work is required to ionize an atom in an intense field, and the extra work is just the ponderomotive energy the newly created free electron must possess at the value of field where it leaves the atom [11].

In nearly all of the original ATI experiments, the effects of ionization potential changes were nearly impossible to detect. This is due to energy conservation for all photoemission processes that employed laser pulses with relatively long duration: The ionization potential of the atom increases by  $U_p$ , thus decreasing the initial directed energy of the photoemitted electron by the same amount. However, the photoemitted electron is created with  $U_p$  worth of oscillatory energy so if it leaves the beam before the light intensity changes, it converts this oscillatory energy back into directed energy, just compensating for the original decrease in initial kinetic energy due to the raised ionization potential [11].

Quite clearly this energy conservation depends upon the electron leaving the laser beam before the light intensity changes appreciably. In the opposite extreme limit the laser pulse is so short that the electron does not have a chance to sample any significant variation in the laser intensity. Under these circumstances the oscillatory energy of the photoemitted electron, that is,  $U_p$ , is given back to the optical field and the electron arrives at the detector with the velocity and direction it had

at the moment of ionization. Freeman *et al.* [5] and Agostini *et al.* [12] have demonstrated how the ATI peaks shift as the pulse length of the ionizing laser is reduced from the "long pulse" limit through the intermediate regime to the onset of the "short pulse" limit.

Figure 2 shows the effect of pulse length on ATI peaks for 616 nm light in xenon as originally reported by Freeman *et al.* [5]. The expected shift of the peaks to lower energy as

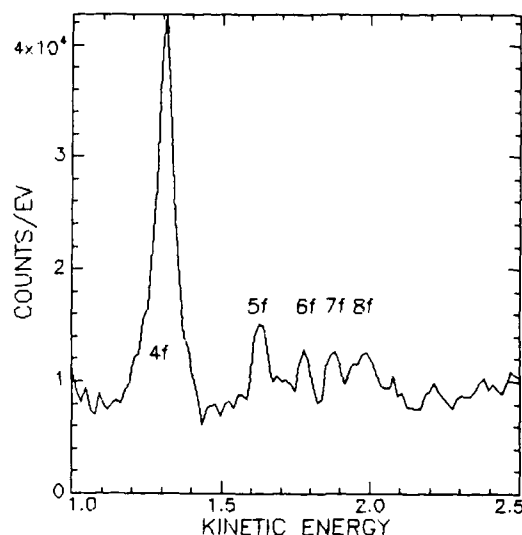


2. The effect of pulse length on ATI peaks for 616 nm light in xenon.

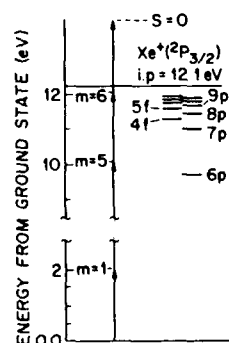
the pulse length passes from the long pulse regime at 13 psec to the short pulse regime at less than 5 psec is clearly visible. The remarkable, and totally unexpected, results obtained for pulse lengths shorter than 5 psec are shown in the bottom two spectra: For the shortest pulses the ATI peaks break up into a narrow fine structure. This fine structure was found to be reproducible and independent of the spatial and temporal modes of the laser pulse. The fine structure is quite narrow in energy width, in fact much of the apparent width of the structure in Fig. 2 is simply the resolution of the electron energy analyzer employed in these original investigations.

The spectrum for xenon using a pulse width of approximately 200 femtosec at 616nm with a peak intensity of approximately  $10^{14} \text{W/cm}^2$  is shown on Fig. 3. For these measurements the detector electronics were adjusted to record spectra according to the total energy in the pulse: thus for each run we recorded 7 separate spectra binned according to the total energy within the pulse (and assuming no pulse-to-pulse changes in the pulse width, according to the peak intensity as well). For a typical run the laser had 100% energy fluctuations, so the individual bins contained variations of less than 15%. We also employed a new high sensitivity electron energy analyzer which is capable of collecting over  $2\pi$  sr in a field-free environment while maintaining high energy resolution. (This device is described by Van Woerkom *et al.* elsewhere in this volume.)

The explanation of this structure lies in the ponderomotive energy that Rydberg states possess in the optical field. Consider the schematic energy level diagram shown in Fig. 4. Highly excited states shift *up* in energy with increasing intensity approximately as the ponderomotive energy  $U_p$  given in Eq. 1. Because the ground state effectively does not change its energy, the excited states will come into resonance with a harmonic of the optical field at some intensity. When this resonance occurs, the ionization rate is increased and an increased photoelectron yield is recorded. In the case where the excited states increase their energy precisely as  $U_p$  (an approximation that is excellent for high lying states and less so for more deeply bound ones), this model makes specific predictions for the energies of the increased photoelectron yield arising from resonance with any state; viz,  $E = \hbar\omega - E_{\text{binding}}$ , where  $E_{\text{binding}}$  is the



3. The high resolution ATI spectrum for xenon using a pulse width of approximately 200 femtosec at 616 nm with a peak intensity of approximately  $10^{14} \text{W/cm}^2$ .



4. Schematic level diagram of xenon; also shown is the  $n=6$  resonance for 616 nm laser radiation.

absolute value of the binding energy of the atomic state in question. The recorded energies at which the increases in the photoelectron yield occur for a given atomic state is independent of the position of the atom within the laser focus, or of the temporal nature of the ionizing beam. That is, if the beam is long in duration, the exact process described above goes on, only the electrons produced have a chance to slide down the ponderomotive hill of the laser beam on their way to the detector: the amount of initial directed kinetic energy a photoelectron at any given location within the laser focus is missing is precisely made up for by the height of the ponderomotive hill at the location of the atom. Thus all electrons arrive at the detector with the same energy; however, they will indeed be inhomogeneous in the sense that they were produced by different resonances within the atom. In the short pulse case, the electrons' energy is recorded as they were ionized and the influence of the structure of the atom of the photoelectron process is uncovered. In *both* cases, the atomic levels of the atom determine the photoemission process.

Also shown in Fig. 3 is the simple prediction for f states according to the "theory" of  $E = \hbar - E_{\text{binding}}$ . The match is striking indeed. We have also recorded spectra using a high angular resolution detector at an angle that reduces the contributions of the f states. Under these circumstances it is possible to identify d, p and even s states in the spectra. From this kind of data we have been able to assign energies to individual states and to measure the Stark effect of these states at these extremely high intensities.

These results suggest that for sufficiently high intensities *all* multiphoton excitation or ionization processes become resonant—at least in the sense that the resonances within the atom or molecule contribute directly to the result. From the discussion presented above it is possible to estimate rather simply the intensity level for a given experiment that will produce this "resonance" behavior. For energy levels that are removed  $\Delta E$  from an n photon potential resonance of the appropriate parity, the intensity that will produce a resonance contribution from this level is approximately

$$I(W/\text{cm}^2) = 10^{13} \Delta E \left( \frac{1}{\lambda} \right)^2$$

where  $\lambda$  is in microns, and  $\Delta E$  in eV. Thus regardless of the length of the laser pulse, just the fact that high intensities are employed in the experiment is usually all that is required to guarantee that the atomic structure of the atom will play a role. Certainly this work calls into question the usual assumption of multiphoton ionization that only the ground state and some general potential is enough to specify the problem.

## REFERENCES

1. P. Agostini, F. Fabre, G. Mainfray, G. Petite and N. Rahman, *Phys. Rev. Lett.* **42**, 1127 (1979).
2. T. J. McIlrath, P.H. Bucksbaum, R.R. Freeman, and M. Bashkansky, *Phys. Rev. A* **35**, 4611 (1987); T.S. Luck, T. Graber, H. Jara, U. Johann, K. Boyer, and C.K. Rhodes, *J. Opt. Soc. Am. B* **4**, 847 (1987).
3. P. Kruit, J. Kimman, and M. van der Wiel, *Phys. Rev. A* **28**, 248 (1983); L.A. Lompre, A.L. Huillier, G. Mainfray, and C. Manus, *J. Opt. Soc. Am. B* **2**, 1906 (1985).
4. P.H. Bucksbaum, M. Bashkansky, R.R. Freeman, T. J. McIlrath, and L. DiMauro, *Phys. Rev. Lett.* **56**, 2590 (1986).
5. R.R. Freeman, P.H. Bucksbaum, H. Milchberg, S. Darack, D. Schumacher, and M.E. Geusic, *Phys. Rev. Lett.* **59**, 1092 (1987).
6. R.R. Freeman, T.J. McIlrath, P.H. Bucksbaum, and M. Bashkansky, *Phys. Rev. Lett.* **57**, 3156 (1986).
7. P.H. Bucksbaum, M. Bashkansky, and T.J. McIlrath, *Phys. Rev. Lett.* **58**, 349 (1987).
8. J.H. Eberly, *Progr. Optics VII*, E. Wolf, Ed., Amsterdam, North Holland, 1969, pp 361-415, and references therein.
9. T.W.B. Kibble, *Phys. Rev.* **150**, 1060 (1966).

10. H.G. Muller, H.B. van Linden van den Heuvell, P. Agostini, G. Petite, A. Antonetti, M. Franco, and A. Migus, *Phys. Rev. Lett.* **60** 565 (1988).
11. P.H. Bucksbaum, R.R. Freeman, M. Bashkansky, and T.J. McIlrath, *J. Opt. Soc. Am. B* **4**, 760 (1987).
12. P. Agostini, J. Kupersztych, L.A. Lompre, G. Petite, and F. Yergeau, *Phys. Rev. A* **36**, 4111 (1987).

## Strong-Field Processes in the Ultraviolet Region

K. Boyer, G. Gibson, H. Jara, T. S. Luk, I. A. McIntyre, A. McPherson  
R. Rosman, J. C. Solem,<sup>†</sup> and C. K. Rhodes

*Laboratory for Atomic, Molecular, and Radiation Physics, Department of Physics  
University of Illinois at Chicago, P.O. Box 4348, Chicago, Illinois 60680*

### Abstract

A laboratory means for the generation of ultrahigh energy density states of matter, corresponding approximately to 0.1 – 1.0 W/atom at solid density, appears within technological reach. This capability enables the production, in a convenient laboratory environment, of energy densities comparable to those occurring in stellar interiors. The use of this technology will permit the study of a new realm of atomic phenomena involving (1) the behavior of matter in very strong fields, (2) the properties of highly stripped ions, (3) the characteristics of dense highly non-equilibrium plasmas, (4) high-field modes of electromagnetic propagation, and (5) the possibility of a new laser-driven means for the excitation and control of nuclear reactions.

### Introduction

The availability of a technology [1,2] capable of producing subpicosecond ultraviolet pulses with energies at the joule level in low divergence beams at high repetition rates is making possible a new regime of laboratory-scale physical study concerning the behavior of matter exposed to extremely high energy densities and field strengths [3,4]. With this new experimental means, a maximum electric field strength  $E$  on the order of 100 ( $e/a_0^2$ ) should be attainable, a condition that should permit the generation of energy densities comparable to, or possibly exceeding, those characteristic of stellar environments. Moreover, an electric amplitude of this magnitude at ultraviolet wavelengths will cause the development of strongly relativistic [5–8] electronic motions with an energy scale comparable to typical nuclear binding energies.

Several important implications stem directly from the technical capability to generate such unusually high energy densities and strong electromagnetic forces. Foremost, it is expected

that atomic and molecular material will respond in very unusual ways to such severely perturbed conditions and it has been conjectured, in contrast to interactions associated with weak fields, that fundamentally different types of electronic motions [9] may be driven under such circumstances. At the outset, therefore, we expect, in comparison to the normal weakly excited conditions, significant modifications of (1) the properties of electromagnetic interactions with free atoms, (2) the behavior of dense plasmas, and (3) the modes of electromagnetic propagation [10] occurring through such highly excited material.

Considerable data support the conclusion that very high energy deposition rates can be achieved in materials as a consequence of the strong electromagnetic perturbations associated with laser intensities significantly exceeding  $10^{16}$  W/cm<sup>2</sup>. This view is based on the accumulating evidence, derived from both experimental findings [4,11] and theoretical analyses, [12] that extremely high peak energy transfer rates can be achieved. For example, recent studies [13] of the kinetic energy distributions of ionic fragments, produced by multiphoton ionization of N<sub>2</sub> and other molecules, [14] clearly indicate that a considerable fraction of the energy transfer occurs over a maximum time interval bounded by a few cycles of the wave. For the case of N<sub>2</sub>, at an intensity of  $\sim 10^{16}$  W/cm<sup>2</sup> with 248-nm radiation, [13] a peak rate on the order of a few milliwatts/molecule was inferred from this work. It is projected [12] that for higher intensities, in the range of  $10^{18}$  –  $10^{20}$  W/cm<sup>2</sup>, the rate may approach a value of  $\sim 1$  W/atom, particularly for heavy materials. The implication is a transferred energy in the range of  $\sim 100$  keV/atom, a magnitude sufficient to lead to ionization of electrons in the L-shell of uranium ( $\sim 21$  keV).

It is important to realize that this estimate is not an enormous extrapolation from existing experimental results. As described elsewhere in this volume, [15] radiation from Ar<sup>30+</sup> produced in

a gaseous target has been observed from the (2s2p<sup>6</sup>) state, a level that lies more than 1.1 keV above that of the neutral atom ground state. Ionization [16] of the L-shell of Ar<sup>8+</sup> alone requires 0.42 keV.

Overall, the evidence points overwhelmingly to the conclusion that states of matter involving very high energy densities, on the order of  $\sim 1$  W/atom at solid density ( $\sim 10^{22}$  W/cm<sup>3</sup>), can be studied at a high data rate by relatively simple laboratory means. Furthermore, since the time scale for the production of these conditions is extremely short ( $\sim 100$  fs), unusual plasma states far from equilibrium conditions are expected. The study of such physical conditions is anticipated to lead to insights on the non-equilibrium properties of extremely high energy density states of matter.

The availability of an ultrahigh brightness ultraviolet laser technology will serve the study of (1) the fundamental behavior of atomic material in very strong fields ( $E \gg e/a_0^2$ ), (2) the properties of highly stripped ions, (3) the characteristics of dense non-equilibrium plasmas, and (4) the modes of electromagnetic propagation occurring under extreme conditions of material excitation. These four topics all represent frontiers in the realm of atomic phenomena. In addition to these four areas, there is a fifth subject, although not strictly limited to the atomic domain, in which important fundamental information should be forthcoming. It involves the coupling of atomic and nuclear degrees of freedom with the possible outcome that a new means for the control of nuclear reactions would become available. A range of possibilities exists for various nuclear systems, [17–20] including that of fission. [21]

## Discussion

**Ultrahigh Brightness Subpicosecond Laser Technology.** Since the feasibility of this new realm of physical research is fundamentally predicated on the availability of bright high-peak-power ultraviolet sources, we describe the development of those sources and the performance limits that can be achieved.

The presently operating KrF\* (248-nm) system, which incorporates a large aperture (100 cm<sup>2</sup>) power amplifier, is illustrated in Fig. (1). Currently, the output energy is measured to be  $\sim 350$  mJ in a pulse length of  $\sim 600$  fs. These are the parameters delivered at the end of the beam line at the experimental stations. The pulse width of  $\sim 365$  fs measured [22] in a previous instrument [2] has been broadened to some extent by the effect of group velocity dispersion arising from the additional optical elements associated with the large aperture power amplifier. This pulse broadening effect can be eliminated by known techniques [23] of compensation using either prisms or gratings.

An essential parameter governing the brightness of the 248-nm source is the focal spot size that can be achieved. Therefore, the ability to produce a small focal volume was one of the

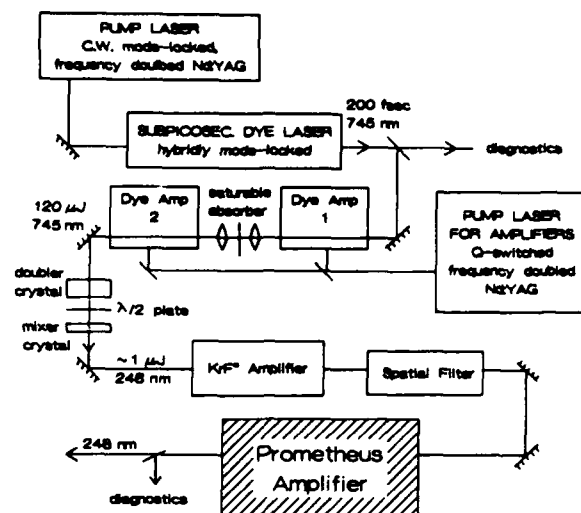


Figure 1. Schematic of high brightness subpicosecond source incorporating a large aperture (100 cm<sup>2</sup>) power amplifier (Prometheus).

chief design criteria for the large aperture system. The result of a measurement [24] on part of the beam profile, (the diagnostic equipment could only accept a beam 3 cm in diameter) at a point after the power amplifier, is illustrated in Fig. (2). A focal diameter of  $\sim 1.4$   $\mu$ m, produced with an f/2 optical system, is shown, a value very close to the diffraction limit ( $\sim 0.9$   $\mu$ m). Further refinement of the system may enable this diameter to be reduced to the  $\sim 1.0 - 1.2$   $\mu$ m range.

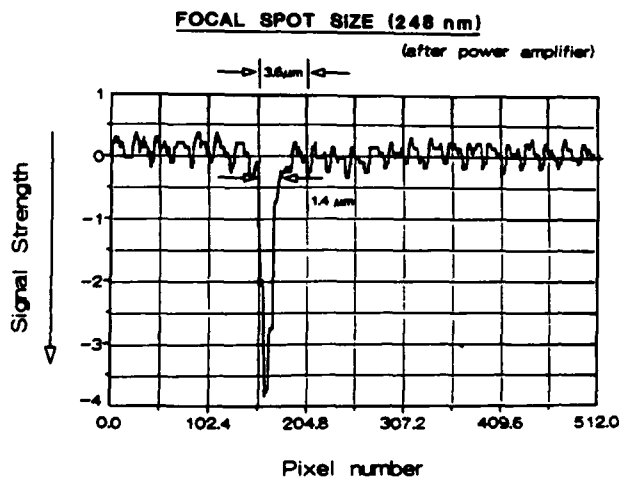


Figure 2. Spatial profile of focal spot recorded for the seed beam after the power amplifier with an f/2 optical system. A spot diameter of  $\sim 1.4$   $\mu$ m is measured.

The present capabilities of the source, based on the measurements described above, are summarized in Table 1. Assuming the total 350 mJ is focusable to 1.4  $\mu$ m, then a maximum intensity  $I \approx 3.8 \times$

$10^{19}$  W/cm<sup>2</sup> is derived, a value only slightly below the Compton Intensity, [5,7]  $I_{co} \approx 4.5 \times 10^{19}$  W/cm<sup>2</sup>.

These parameters of performance can be compared with the values believed to be the limiting achievable figures for the system being developed. The comparisons are presented in Table 2. In terms of the maximum electric field, or equivalently, the force that can be exerted on a charged particle, the present system is within a factor of six of the limiting value.

Table 1. Summary of Current Operating Parameters of 248-nm System

Measured Quantities:

- $E \approx 350$  mJ (output energy)
- $\tau \approx 600$  fs (pulse width after power amplifier)
- $d = 1.4$   $\mu$ m (seed beam diameter after power amplifier)

Derived Quantity:

- $I \approx 3.8 \times 10^{19}$  W/cm<sup>2</sup>

Table 2. Comparison of Current and Projected Operating Parameters for the 248-nm System

Parameter	Current Measured Value	Projected Developed Value
Pulse Energy (J)	$\sim 0.350$	1.0
Pulse Width (fs)	$\sim 600$	100
Focal Spot Diameter ( $\mu$ m)	$\sim 1.4$	1.0 - 1.2
Maximum Intensity (W/cm <sup>2</sup> )	$3.8 \times 10^{19}$	$\sim 10^{21}$
Maximum Electric Field (V/cm)	$\sim 1.5 \times 10^{11}$	$\sim 9 \times 10^{11}$
Pulse Repetition Rate (s <sup>-1</sup> )	0.5	1.0

**Behavior of Atomic and Molecular Matter in Very Strong Fields.**

A research effort is currently underway in several laboratories whose goal is the understanding of the nonlinear processes governing the coupling of intense radiation to atomic and molecular matter. The general amplitude under study is

$$NY + X \rightarrow X^q + qe^- + Y, \quad (1)$$

a process which, overall, produces ions, electrons and photons. Although certainly far from complete, this work has revealed several important characteristics of the strong field interaction.

In the effort to understand the coupling represented by process (1), the properties of ion charge state distributions, [25] electron energy spectra, [26,28] and both fluorescence and harmonic radiation [4,11] produced by irradiation of atoms with intense ultraviolet radiation have been investigated. The substantial body of information contained in earlier work concerning the ion and electron distributions is documented extensively in references [3,4,25-28] and associated citations.

Theoretically, the picture is diverse and controversial. The models describing the electronic motion under strong fields range from those involving sequential electron emission [29] on one hand to others which consider the consequences of more organized multi-electron motions. [9,30,31] The role of screening has been evaluated [32] and analogies with atomic, [30] ionic, [33] and electronic [34] collisions have been discussed.

At the present, for the most interesting regime in which the external field is far larger than an atomic unit, no comprehensive theory exists and the experimental capability is just now, as discussed above, permitting the study of that important region.

**Conclusions**

A high-data-rate laboratory-scale capability for the exploration of matter at energy densities comparable to those characteristic of a stellar environment would greatly enhance the ability to understand the complex behavior associated with those extreme conditions. Such experimental methods now appear within our technological reach. The use of this new technology should permit the study of new realms of atomic phenomena. Specifically, the areas involve (1) the behavior of matter in very strong fields, (2) the properties of highly stripped ions, (3) the characteristics of dense highly non-equilibrium plasmas, (4) high-field modes of electromagnetic propagation, and (5) the possibility of a laser-driven means for the excitation and control of nuclear reactions.

**Acknowledgements**

The authors would like to thank Paul Noel, Rick Siagle, and Jim Wright for their technical assistance. This work was supported by AFOSR, LLNL, ONR, and SDI.

† permanent address: Theoretical Division, MS-B210, Los Alamos National Laboratory, Los Alamos, NM 87545

**References and Notes**

1. J. H. Glowia, G. Arjavalingham, P. P. Sorokin, and J. E. Rothenberg, "Amplification of 350 fsec Pulses in XeCl Excimer Gain Modules,"



- Opt. Lett. **11**, 79 (1986).
2. A. P. Schwarzenbach, T. S. Luk, I. A. McIntyre, U. Johann, A. McPherson, K. Boyer, and C. K. Rhodes, "Subpicosecond KrF\*-Excimer-Laser Source," Opt. Lett. **11**, 499 (1986).
3. C. K. Rhodes, "Multiphoton Ionization of Atoms," Science **229**, 1345 (1985).
4. C. K. Rhodes, "Ordered Many-Electron Motions in Atoms and X-Ray Lasers," in Giant Resonances in Atoms, Molecules, and Solids, ed. J.-P. Connerade, J. M. Esteve, and R. C. Karnatak (Plenum Press, New York, 1987) p. 533.
5. M. J. Feldman and R. Y. Chiao, "Single-Cycle Electron Acceleration in Focused Laser Fields," Phys. Rev. **A4**, 352 (1971).
6. E. S. Sarachik and G. T. Schappert, "Classical Theory of Scattering of Intense Laser Radiation by Free-Electrons," Phys. Rev. **D1**, 2738 (1970).
7. F. V. Bunkin et al., "Interaction des Electrons avec un Champ Intense de Rayonnement Optique," in Polarisation, Matière et Rayonnement, édité par La Société Française de Physique (Presses Universitaires de France, Paris, 1969) p. 157.
8. I. A. McIntyre and C. K. Rhodes, "High Power Excimer Lasers," submitted to Appl. Phys. Rev.
9. M. Pont, N. R. Walet, M. Gavril, and C. W. McCurdy, "Dichotomy of the Hydrogen Atom in Superintense, High-Frequency Laser Fields," Phys. Rev. Lett. **61**, 939 (1988).
10. J. C. Solem, T. S. Luk, K. Boyer, and C. K. Rhodes, "X-Ray Charge Displacement Self-Channelling as a Method for Energy Concentration," this volume.
11. C. K. Rhodes, "Physical Processes at High Field Strengths," Physica Scripta, **T17**, 193 (1987).
12. K. Boyer, H. Jara, T. S. Luk, I. A. McIntyre, A. McPherson, R. Rosman, and C. K. Rhodes, "Limiting Cross Sections for Multiphoton Coupling," Revue Phys. Appl. **22**, 1793 (1987).
13. K. Boyer, T. S. Luk, J. C. Solem, and C. K. Rhodes, "Kinetic Energy Distributions of Ionic Fragments Produced by Subpicosecond Multiphoton Ionization of N<sub>2</sub>," Phys. Rev. A., in press.
14. L. J. Fransinski, Conference on Atoms in Strong Fields, Grainau, West Germany, 5-9 September 1988, private communication.
15. G. Gibson, R. Rosman, T. S. Luk, I. A. McIntyre, A. McPherson, G. Wendin, K. Boyer, and C. K. Rhodes, "Characteristics of a Non-Equilibrium Picosecond Laser Plasma," this volume.
16. R. L. Kelly and L. J. Palumbo, "Atomic and Ionic Emission Lines Below 2000 Angstroms," NRL Report 7599 (USGPO, Washington, D.C., 1983).
17. L. C. Biedenharn, G. C. Baldwin, K. Boyer, and J. C. Solem, "Nuclear Excitation by Laser Driven Coherent Outer Shell Electron Oscillations", in AIP Conference Proceedings No. 146, Advances in Laser Science - I, edited by W. C. Stwalley and M. Lapp (AIP, New York, 1986) p. 52.
18. L. C. Biedenharn, K. Boyer, and J. C. Solem, "Possibility of Grating by Laser-Driven Nuclear Excitation", in AIP Conference Proceedings No. 146, Advances in Laser Science - I, edited by W. C. Stwalley and M. Lapp (AIP, New York, 1986) p. 50.
19. G. A. Rinker, J. C. Solem, and L. C. Biedenharn, "Nuclear Interlevel Transfer Driven by Collective Outer Shell Electron Oscillations", LA-UR-86-4187, Los Alamos National Laboratory Report, October, 1987.
20. M. S. Weiss, private communication.
21. K. Boyer, T. S. Luk, and C. K. Rhodes, "Possibility of Optically Induced Nuclear Fission," Phys. Rev. Lett. **60**, 557 (1988).
22. M. H. R. Hutchinson, I. A. McIntyre, G. N. Gibson, and C. K. Rhodes, "Measurements of 248 nm, Subpicosecond Pulse Durations by Two-Photon Fluorescence of Xenon Excimers," Opt. Lett. **12**, 102 (1987).
23. S. Szatmári, F. P. Schäfer, E. Müller-Horsche and W. Mückenheim, "Hybrid Dye-Excimer Laser System for the Generation of 80 fs, 900 GW Pulses at 248 nm," Opt. Commun. **63**, 305 (1987).
24. Preliminary measurement of seed beam profile, X.-J. Pan, private communication.
25. T. S. Luk, U. Johann, H. Egger, H. Pummer, and C. K. Rhodes, "Collision-Free Multiple Photon Ionization of Atoms and Molecules at 193 nm," Phys. Rev. **A32**, 214 (1985).
26. U. Johann, T. S. Luk, H. Egger, and C. K. Rhodes, "Rare-Gas Electron-Energy Spectra Produced by Collision-Free Multiquantum Processes," Phys. Rev. **A34**, 1084 (1986).
27. T. S. Luk, T. Graber, H. Jara, U. Johann, and C. K. Rhodes, "Subpicosecond Ultraviolet Multiphoton Electron Spectroscopy of Rare Gases", J. Opt. Soc. B **4**, 847 (1987).
28. R. R. Freeman, P. H. Bucksbaum, H. Milchberg, S. Darack, D. Schumacher, and M. E. Geusic, "Above-Threshold Ionization with Subpicosecond Laser Pulses," Phys. Rev. Lett. **59**, 1092 (1987).
29. P. Lambropoulos, "Mechanisms for Multiple Ionization of Atoms by Strong Pulsed Lasers," Phys. Rev. Lett. **55**, 2141 (1985).
30. K. Boyer and C. K. Rhodes, "Atomic Inner-Shell Excitation Induced by Coherent Motion of Outer-Shell Electrons," Phys. Rev. Lett. **54**, 1490 (1985).
31. A. Szöke and C. K. Rhodes, "Theoretical Model of Inner-Shell Excitation by Outer-Shell Electrons," Phys. Rev. Lett. **56**, 720 (1986).
32. G. Wendin, L. Jönsson, and A. L'Huillier, "Screening Effects in Multielectron Ionization of Heavy Atoms in Intense Laser Fields," Phys. Rev. Lett. **56**, 1241 (1986).
33. K. Boyer, G. Gibson, H. Jara, T. S. Luk, I. A. McIntyre, A. McPherson, R. Rosman, J. C. Solem, and C. K. Rhodes, "Corresponding Aspects of Strong-Field Multiquantum Processes and Ion-Atom Collisions," IEEE Transactions on Plasma Science, in press.
34. K. Boyer, H. Jara, T. S. Luk, I. A. McIntyre, A. McPherson, R. Rosman, J. C. Solem, and

C. K. Rhodes, "Discussion of the Role of Many-Electron Motions in Multiphoton Ionization and Excitation," in *Multiphoton Processes*, edited by S. J. Smith and P. L. Knight (Cambridge University Press, Cambridge, 1988) p. 58.

# Multiphoton Ionization for the Production of X-Ray Laser Plasmas

P. B. Corkum and N. H. Burnett

*National Research Council of Canada, Division of Physics  
Ottawa, Ontario K1A 0R6, Canada*

## Abstract

In the long wavelength (or high intensity) limit, above threshold ionization (ATI) is primarily the result of the interaction of a newly freed electron with the laser field. A classical model of ATI predicts that the energy of a newly released electron can be controlled by varying the laser wavelength and polarization. Similar predictions are made by Keldysh-style theories. Measurements, performed using both linearly and circularly polarized picosecond 10  $\mu\text{m}$  pulses, confirm these conclusions.

Cold, high-Z plasmas for recombination XUV lasers can be produced by multiphoton ionization with linearly polarized visible or UV radiation. Hot electrons, potentially suitable for electron-pumping of ionization-phase XUV lasers can be produced using longer wavelength or circularly polarized light.

## 1 Introduction:

Efficient production of highly ionized plasmas for laboratory XUV laser studies is a problem of much contemporary interest [1]. Impressive progress has been made in demonstrating gain from highly ionized plasmas in both the electron collisionally pumped [2] and recombination [3] regimes. However, experiments reported to date are noteworthy for the extremely poor efficiency in transferring visible laser pump energy into the upper level of the XUV laser. In this paper we will discuss the possibility of efficiently producing XUV laser plasmas by optical field induced

ionization of high-Z ions using subpicosecond visible or uv laser pumps.

One of the earliest concepts proposed for the production of laboratory XUV laser plasmas was to produce ionization disequilibrium in recombining plasmas by rapid cooling [4]. A related but little noted proposal was to produce ionization disequilibrium using multiphoton ionization to make cold, fully ionized plasmas on a time scale less than the recombination time [5]. We shall refer to these as recombination lasers. Ionization disequilibrium can also be produced by introducing a small fractional population of superheated electrons into an equilibrium or supercooled plasma [6]. We will refer to these as ionization or excitation schemes.

The application of optical field induced ionization to the production of plasmas for recombination schemes requires that highly stripped ions be produced on a sub-picosecond time scale and that the resulting plasma have an electron temperature much colder than the ionization potential of the final ionization state of the recombining ion. We will show that this is possible, using linearly polarized UV laser light as the ionizing source.

We will also discuss the possibility of producing plasmas for ionization or excitation phase XUV lasers by partially stripping a high-Z ion with high intensity laser radiation and then using either the coherent oscillation energy or incoherent drift energy (in the case of circularly polarized light) of the optical field produced electrons to induce further ionization or excitation. Considerable choice of hot

electron energy is afforded by varying the ionization potential of the intermediate ionization state and the wavelength and polarization of the optical laser.

## II A Semi-Classical Model of ATI:

It is clear that the precise control of ionization and the resulting electron velocity distribution is important for the X-ray laser schemes discussed above. If the laser medium is to be an optically produced low density plasma, then it is essential to understand the process of multiphoton ionization (MPI) and in particular the energy distribution of the electrons that are produced. In recent years there has been considerable research on MPI [7] and there are now some well established concepts. In the short pulse, high power or the long wavelength limits the internal structure of the atom can play little role in determining the overall ionization rate [8]. In these cases the purely atomic physics aspects of multiphoton ionization will be the simplest.

Keldysh-style theories [9] should be applicable to these cases. This is confirmed with picosecond [10] and subpicosecond [8] 0.6  $\mu\text{m}$  pulses by observation of ion spectra. Although these low intensity 0.6  $\mu\text{m}$  experiments are strongly suggestive of the physics that should be expected with higher intensity or longer wavelength pulses, appropriate experiments have not been performed. We will describe some measurements of the energy of electrons produced during multiphoton ionization of xenon with long wavelength ultrashort pulses. Long wavelength pulses produce an ionization regime which is analogous to that encountered in the ionization of high ionization potential ions with shorter wavelength lasers. We will show that the results of the long wavelength experiments are also closely described by Keldysh-style theories but first we will introduce a classical, quasi-static theory of ATI, which accurately describes the experimental results and agrees, over a wide parameter range with Keldysh theories. The classical theory gives a simple physical picture of ATI and allows us to derive electron temperature distributions for the resulting plasma.

Consider an electron released from rest at  $t=t'$  into a strong laser field. The electron will experience a force which, in

the nonrelativistic limit, is proportional to the electric field given by  $\mathbf{E} = E_0 \cos(\omega t) \mathbf{e}_x + \alpha E_0 \sin(\omega t) \mathbf{e}_y$ , where  $\alpha < 1$  allows for arbitrary polarization.

The electron motion in the field of the laser is given by:

$$v_x = v_0 \sin(\omega t) + v_{0x} \quad v_y = -(\alpha v_0) \cos(\omega t) + v_{0y} \quad (1)$$

where  $v_0 = qE_0/m\omega$  and  $v_{0x}$  and  $v_{0y}$  can be evaluated from the initial conditions. If the electron is produced with  $t'=0$  by linearly polarized light, we see that  $v_{0y}=0$ . In general the drift velocity of the electron is given by  $v_{0x} = -v_0 \sin \omega t'$  and  $v_{0y} = \alpha v_0 \cos \omega t'$ . The probability of ionization as a function of time can be calculated in the quasi-static limit using DC tunnelling theory [11]:

$$w(t) = 4\omega_0 \left( \frac{E_i}{E_h} \right)^{5/2} \frac{E_a}{E(t)} \exp \left( - \frac{2}{3} \left( \frac{E_i}{E_h} \right)^{3/2} \frac{E_a}{E(t)} \right) \quad (2)$$

where  $\omega_0 = me^4/\hbar^3$  is the atomic frequency unit,  $E_h$  and  $E_i$  are the ionization potentials of hydrogen and the atom under consideration and  $E_a = m^2 e^5/\hbar^4$  is the atomic unit of electric field. By substituting  $E(t) = E_0 \cos(\omega t)$ , and integrating over one cycle, it is possible to obtain a distribution of drift energy for the linearly polarized case,

$$F(\xi) \propto \frac{W(E_0(1-\xi/\xi_0))^{1/2}}{(\xi/\xi_0)^{1/2}(1-\xi/\xi_0)^{1/2}} \quad (3)$$

where  $\xi_0 = q^2 E_0^2 / 2m\omega^2$ . If this distribution is multiplied by the phase averaged ionization rate as a function of laser intensity and integrated over the laser pulse shape, the electron distribution shown in Fig. 1 (solid curve) is obtained for a 2.5 psec, 10  $\mu\text{m}$  pulse with a peak intensity of  $1 \times 10^{14}$  W/cm<sup>2</sup>, ionizing a hydrogen like ion with  $E_i = 12.1$  eV.

For circularly polarized light ( $\alpha=1$ ), we can always orient the co-ordinate system so that  $t'=0$ . The initial conditions then give a drift velocity of  $v_{0x}=0$  and  $v_{0y}=v_0$ . That is, the electron drifts in a direction perpendicular to the field in which it was released (ionized). The electron distribution shown in Fig. 1 (dashed curve) is obtained for circularly polarized light with a peak intensity of  $2 \times 10^{14}$  W/cm<sup>2</sup> and other parameters the same as above. Whereas the width of the distribution for linearly polarized light is primarily determined by the phase angle at which the electron is

produced, the width for circularly polarized light is characteristic of the pulse envelope.

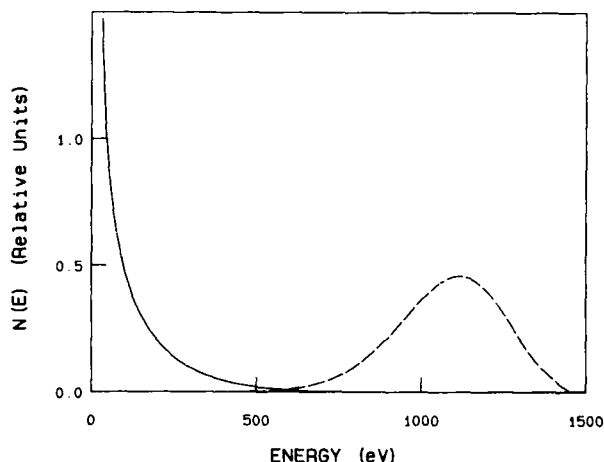


Figure 1. Electron energy distribution calculated using the classical theory of above threshold ionization for a hydrogen-like ion with an ionization potential of 12.1 eV. Linear polarized (solid curve, peak intensity of  $10^{14}$  W/cm<sup>2</sup>) and circularly polarized (dashed curve, peak intensity of  $2 \times 10^{14}$  W/cm<sup>2</sup>) 10  $\mu$ m radiation and 2.5 psec pulses were assumed.

### III ATI with Picosecond 10 $\mu$ m Pulses:

To confirm these predictions, an experiment was performed using a picosecond, 9.3  $\mu$ m pulse produced in a laser system described elsewhere [12]. For the present experiment the maximum pulse energy was approximately 60 mJ. The coherent structure of the pulse is such that approximately 65 % of the energy is in a 2.5 psec pulse [13]. Most of the remainder appears 25 psec later in a second 2.5 psec pulse. Thus the peak laser power was as high as  $2.5 \times 10^{10}$  W.

The laser was designed to produce linearly polarized light. The plane of polarization was changed by adding an additional reflecting surface along the path followed by the beam as it was transported from the laser to the target chamber. Circularly polarized light was produced by passing the beam through a Fresnel rhomb. The beam was focused into a target chamber with either a 25 cm (linearly polarized) or a 12.5 cm (circularly polarized) focal length lens to a beam waist of 170 or 85  $\mu$ m.

The target chamber could be pumped to a background pressure of  $10^{-9}$  Torr. A xenon pressure of  $10^{-6}$  Torr was used

for all measurements. The beam was focused between parallel electrodes that could be biased (with an extraction potential) so as to extract either electrons or ions which were measured with an electron multiplier. Time of flight was used to establish the ion species. Only Xe<sup>+</sup> was present in the measurements described herein.

The electron energy spectrum was determined by collecting those electrons with sufficient energy to pass through a grid biased with a retardation potential. Any detected electron possessed sufficient drift energy in the direction of the electron multiplier to overcome the retardation potential minus that portion of the extraction potential seen by the electron. The detected signal is  $S(E_0) = \int_0^\infty n(E) dE$  where  $n(E)$  is the number of electrons with drift energy  $E$ .

Figure 2(a) is a graph of the electron energy observed with the electric field of the 10  $\mu$ m radiation perpendicular to the direction of the extraction and retardation fields. Classically the drift energy in this direction should be zero. This fact can be used to calibrate the extraction potential as seen by the electron at 240 V (the applied extraction potential was 400 V, the focus was approximately half way between the electrodes). If 240 eV is subtracted from the electron energy we obtain a typical electron energy in the direction perpendicular to the laser field of <10 eV. Considering the electrical noise in the vicinity of the measurement and the mechanical stability of the apparatus, we cannot be sure that this is not the resolution limit of the experiment. However, there are additional sources of electron energy. Although the 10  $\mu$ m pulse is short, the ponderomotive potential ( $E_p = q^2 E_0^2 / 4m\omega^2$ ) is very large (approximately 500 eV). An electron needs to travel only a very small distance in the direction of the electron multiplier to gain a few electron volts of energy from the ponderomotive potential. Alternately, if the electromagnetic field has a slightly elliptical component ( $\alpha=0.1$ ), 10 eV electrons would be produced.

Figure 2(b) shows the distribution of electron energies measured with the electric field of the ionizing radiation pointing in the direction of the extraction and retardation potentials. The 240 V extraction field has been subtracted from the measured electron energy. It is clear from a comparison of Fig. 2 (a) and (b)

that the electrons drift primarily along the direction of the laser field.

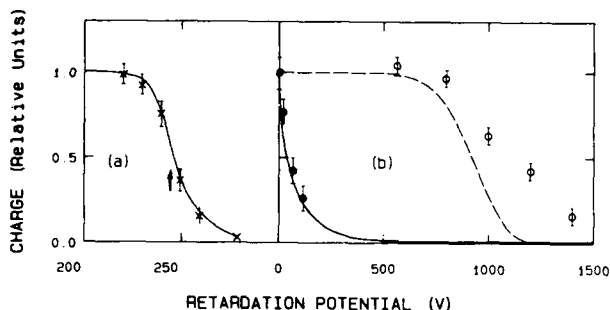


Figure 2. Relative number of ATI electrons with energy in excess of the retardation potential plotted as a function of the retardation potential. A 2.5 psec, 9.3  $\mu\text{m}$  pulse was used to ionize  $10^{-6}$  Torr of xenon. (a) Electron energy measured in the direction perpendicular to the electric vector of the laser field. The laser focus was at a potential of 240 volts as noted by the arrow. (b) Electron energy measured (solid data points) and calculated (solid curve) in the direction of the laser electric field. Also shown are experimental data (open data points) and calculated (dashed curve) obtained with circularly polarized light.

The intensity at which ionization occurs, for linearly polarized light, is approximately  $5 \times 10^{13} \text{ W/cm}^2$ . Thus for our 2.5 psec pulse, the electron is left with  $<10\%$  of the oscillatory energy after the laser pulse has passed. As we shall show in the next two sections, this is an important observation for recombination lasers. Fig. 2(b) (solid curve) is a plot of the calculated value of  $S(E_0)$ , using the quasi-static model described above with a DC ionization rate modified to agree with the expression given by Perelomov et al [14] (this gives a value very nearly equal to Eq. 2 for Xe I).

Fig. 2(b) (open circles) shows the electron energy distribution obtained with circularly polarized light. A typical electron energy is 1200 eV. With that energy, an electron will travel approximately 5 wavelengths in the smaller focal spot of

the 12.5 cm lens. Considering the random distribution of ionization sites and the random direction of the electrons the ponderomotive potential will significantly broaden the electron spectrum relative to what it would have been in its absence and add a significant fraction of the ponderomotive energy to the most favourably directed and positioned electrons. The ponderomotive contribution probably accounts for the differences between experiment and the predictions of the quasi-static model (Fig. 2(b) dashed curve).

The approach that we have taken is very reminiscent of Keldysh-style theories. Keldysh theories dress the outgoing wave function to account for the main effects of the optical field. The ionization rate is then determined by a first order perturbation calculation of the transition probability from the ground state to the dressed free state of the electron. In our classical theory of ATI we have dressed the electron classically for the main effects of the laser field rather than quantum mechanically.

#### IV Plasma Requirements for Recombination XUV Lasers:

The problem of producing population inversions in recombining hydrogen-like ions has been the subject of considerable analysis especially under conditions where ionization disequilibrium is produced by a rapid cooling of the plasma. The possibility of producing gain in plasmas which start off in ionization disequilibrium has been studied in a series of papers by Jones and Ali [15,16]. Although they do not elaborate methods for producing such a situation, their simulations follow the recombination of initially fully stripped ions in an electron reservoir of arbitrary initial temperature. They point out that under such conditions, it is possible to obtain gain on the ground state ( $n=2-1$ ) transition of the hydrogen-like ion as well as the more usual ( $n=3-2$ ) transition. Such a ground state laser is particularly attractive from the point of view of scaling recombination lasers to shorter wavelengths but has been ruled out, in recombination schemes relying on adiabatic expansion of an initially near equilibrium plasma, by the extremely rapid cooling requirement. Using optical field induced ionization, a cold fully stripped ion can be allowed to recombine on a time scale of hundreds of femtoseconds

resulting in just the situation described by Jones and Ali. The threshold-like nonlinearity in ionization rates from tunnelling in an optical field will ensure complete evacuation of the ground state of the hydrogen-like ion at the start of the recombination process.

The initial electron density required for optimum gain in recombining ions is determined by the twin requirements that three body recombination populates the upper laser level but that the electron density is not so high as to collisionally quench the population inversion. In the case of carbon, the desired electron density for the  $L_{\alpha}$  laser is in the range from  $10^{21}$ - $10^{22}$   $\text{cm}^{-3}$ , while for the carbon  $n=3-2$  laser electron densities in the range from  $10^{19}$ - $10^{20}$   $\text{cm}^{-3}$  are required. An indication of the time scales required for an initially fully stripped plasma to develop maximum gain on these transitions can be obtained from the calculations of Jones and Ali. These times are one to two hundred femtoseconds and one to two picoseconds at optimum density on the carbon 2-1 and 3-2 transitions respectively.

### V Cold Plasmas from Multiphoton Ionization :

Having introduced a simple model of ATI we now show that electron distributions produced by UV ionization of helium or carbon should lead to gain on a number of XUV transitions. We will also show that the wavelengths and intensities required of the ionizing laser fall within the domain of the classical model and are accessible to current ultrashort pulse laser technology.

The ionization potential of hydrogen-like ions with  $Z$  in the range from 2 to 6 varies from 54.4 eV for  $\text{He}^+$  to 490 eV for  $\text{C}^{5+}$ . The optical intensity required to remove the last electron can be estimated from Keldysh theory (Eq. (1) in Ref. 9). The laser intensity for an ionization rate of  $10^{12} \text{ sec}^{-1}$  is plotted in Fig. 3 for ionization potentials in the range from 100 to 500 eV and optical wavelengths in the range from 0.1- $10\mu\text{m}$ . The ionization rate is very nearly frequency independent over this parameter range. This is the tunnelling limit of Keldysh theory ( $\gamma \ll 1$ , where  $\gamma$ , the Keldysh parameter  $\gamma = \omega (2mE_i)^{1/2} / qE_0$ ). This is also the domain of the quasi-static assumption of Sec 2.

In fact, when Eq. (2) is averaged over a complete optical cycle, one obtains [14]

$$W_{ac} = \left(\frac{3}{\pi}\right)^{1/2} \left(\frac{E_0}{E_a} \left(\frac{E_h}{E_i}\right)^{3/2}\right)^{1/2} W(E_0) \quad (4)$$

This expression yields an ionization rate that is virtually identical to that predicted using Eq. (1) of Ref 9 for hydrogen-like ions over the range shown in Fig. 3.

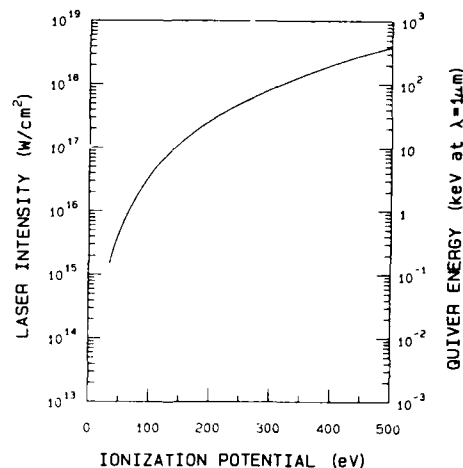


Figure 3. Light intensity required to give an ionization rate of  $10^{12} \text{ sec}^{-1}$  from Ref 9. For ionization potentials greater than 50 eV the theory predicts no wavelength dependence of the ionization rate for optical frequencies.

For nonhydrogen-like atoms, static field calculations indicate that the ionization rate will be greatly increased. Ionization of more complex atoms or ions is described by a static ionization rate of [14]

$$W_{st} = \frac{\omega_0^2 C_{n^* \ell}^2 E_i}{2E_h} \frac{(2\ell+1)(\ell+|m|)!}{2^{|m|} (|m|)! (\ell-|m|)!} \left(2 \left(\frac{E_i}{E_h}\right)^{3/2} \frac{E_0}{E} \right)^{2n-|m|-1} \exp\left(-\frac{2E_0}{3E} \left(\frac{E_i}{E_h}\right)^{3/2}\right) \quad (5)$$

where  $n^*$  is the effective principal quantum number ( $n^* = Z/(E/E_h)^{1/2}$ ),  $\ell$  is the orbital angular momentum quantum number and  $Z$  is the charge state of the resulting ion.  $C_{n^* \ell}$  is a constant approximately equal to two.

Using Eq. (5) in the quasi-static approximation, the intensity necessary to give an ionization rate of  $10^{12}$  for various ions of potential XUV laser interest is plotted in Fig. 4. It is apparent that optical intensities in the range from  $10^{18}$   $\text{W/cm}^2$  to  $10^{19}$   $\text{W/cm}^2$  are required.

As described in Sec (2), in the quasi-

static limit the ionization current will be restricted to narrow intervals near the peak of the electromagnetic wave because of the exponential dependence of the ionization rate on the electric field amplitude. The average ATI energy then becomes

$$\langle \epsilon \rangle = \frac{\int_0^{\pi/2} 2E_q W_{st}(E, E_i) \cos^2 \theta d\theta}{\int_0^{\pi/2} W_{st}(E, E_i) d\theta} \quad (6)$$

where  $E = E_0 \sin \theta$ .

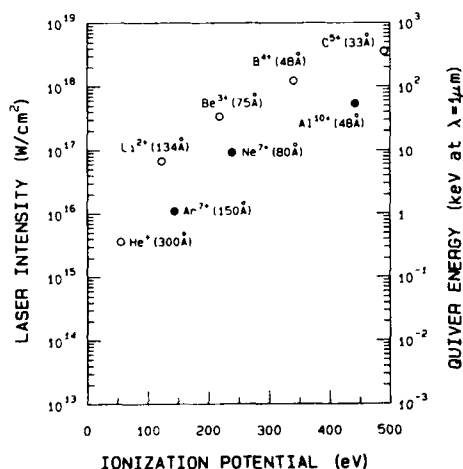


Figure 4. Laser intensity required to yield an ionization rate of  $10^{12} \text{ sec}^{-1}$  using the quasi-static approximation for various ions of potential XUV laser interest. Wavelengths for transitions between the ground state and the first excited state of these ions are indicated. The open circles are obtained from Eq. (2) and the closed circles from Eq. (5), both averaged over one period.

The average energy is plotted in Fig. 5 for a variety of laser wavelengths at a laser intensity corresponding to an ionization rate of  $10^{12}$  as calculated using Eq. (6). Clearly the average ATI energy can be kept below the ionization potential for ionization potentials up to about 500 eV by employing UV laser radiation. (Fig. 5 considerably overestimates the average electron energy of an MPI produced high-Z plasma since the majority of the free electrons come from the lower ionization stages. This point will be discussed more fully below.)

It is apparent that the coherent

oscillatory energy of the electrons will be much larger than the final state ionization potential for practical ionizing lasers. In order to have a cold dense plasma at the end of the pulse it is essential, therefore, that the electrons produced in the optical field interact with it adiabatically as the pulse is extinguished.

Strong field electron heating by inverse bremsstrahlung is discussed in Ref 17. Inverse bremsstrahlung heating is most concern at the high densities required for a carbon 2-1 lasers. In this limit the electron heating rate is given by

$$\frac{d\epsilon}{dt} = \frac{2Ze^4 n_e}{E_q^{1/2} m_e^{1/2}} \ln \left( \frac{4ZE_q}{kT} \right) \ln \left( \frac{4E_q}{kT} \right) \quad (7)$$

Assuming that the electron density is obtained by hydrogen doping, the Z dependence of Eq. (7) can be ignored. In that case ATI dominates for pulse durations less than about 100 fsec at electron densities of  $10^{22} \text{ cm}^{-3}$ .

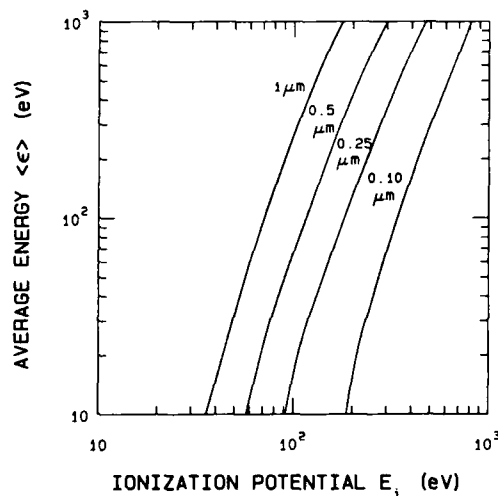


Figure 5. The average ATI energy obtained when hydrogen-like ions are ionized at a rate of  $10^{12} \text{ sec}^{-1}$  as a function of the ionization potential and ionizing laser wavelength.

Another limitation is imposed by the motion of electrons in the large ponderomotive potential gradients surrounding the laser focus. The time for free electrons to leave the focus, thereby acquiring an energy equal to the



ponderomotive potential is on the order of  $(2\pi/\omega)(d/\lambda)(c/v_{osc})$  where  $d$  is the focal spot diameter and for intensities of relevance to the XUV laser problem,  $v_{osc}/c$  is of the order of 0.1. The time for ponderomotive heating can be short, especially since  $d$  will be restricted by the need to limit the optical power. The situation is alleviated in sufficiently dense plasmas where the electrons will be electrostatically coupled to the massive ions. The spatial scale length of such coupling will be  $\lambda_d = (E_c/4\pi n_0 e^2)^{1/2}$ . For  $d \gg \lambda_d$  the time scale for ponderomotive heating will be increased by  $(m_i/zm_e)^{1/2}$ . The laser pulse durations required to avoid ponderomotive electron heating are not incompatible with the time scale required in any event to produce population inversion in recombining high-Z ions.

It is apparent that the average intrinsic electron drift energy scales approximately as the ponderomotive energy in the optical field at threshold for ionization. If one then considers the ionization of a high-Z ion in a short optical pulse, the initial stages of ionization will occur at low laser intensity and the resulting electrons will have much less drift energy than will electrons produced by the final stage of ionization. Provided that all of the electrons interact adiabatically with the optical laser pulse, the average electron drift energy will be considerably less than that shown in Fig. 5. In the case of carbon for example, the average electron energy  $\xi_{av}$  will be decreased by a factor of three to four from the drift energy carried by the final electron. Immediately after the extinction of the optical pulse the electron distribution will be highly non-Maxwellian with an excess of electrons at very low energy. Although, in principle, this situation is highly advantageous from the point of view of obtaining population inversion, the electrons will relax towards an equilibrium (Maxwellian) distribution through electron-electron collisions on a time scale less than the time scales involved in recombination. Under these conditions, the most conservative assumption of a Maxwellian electron distribution with temperature given by  $T_e \approx 0.667 \xi_{av}$  is likely to provide a reasonable starting point for calculations of recombination kinetics.

## VI Requirements for Ionization and Excitation XUV Lasers:

Although the number of possible schemes for ionization and excitation XUV lasers

pumped by electrons from optical field induced ionization is probably only limited by one's imagination, it is possible to speculate about general requirements. One should look for stable ionization states (closed shells) where the last surplus electron is produced into an optical field with  $E_c$  large enough that the electron can ionize or excite the closed shell configuration. In the case of circularly polarized light, the drift energy will be equal to the coherent component and will remain with those electrons produced in the final ionization stage even after the optical pulse is extinguished. In the case of linearly polarized light, and negligible electron-ion scattering, the coherently oscillating electrons will return their energy to the optical field as the ionizing laser pulse is extinguished. Both cases are of potential interest.

It is interesting to note that a number of short wavelength schemes presently being developed [1] use electron excitation. The independent control of the electron energy and the ionization state that is possible through multiphoton ionization by varying the polarization and the wavelength of the ionizing laser will be important for these and similar approaches.

## VII Lasers for MPI:

The development of short pulse lasers over the last 5 years has been very favourable to the above approach to XUV lasers. The main energy storage lasers ( $\text{CO}_2$  and Nd:glass) can now be efficiently operated with picosecond pulses and promise to scale to very high powers [18]. However, it is not necessary to develop ultra-high power lasers, to reach conditions that are compatible with gain in Helium II ( $L_\alpha$  transition at 30nm), for example. Both XeCl and KrF lasers can be operated with pulses of approximately 100 fsec duration and peak powers in excess of  $10^{12}$  W have already been achieved [19]. Such a pulse could reach an intensity of  $10^{16}$  W/cm<sup>2</sup> (in excess of that needed to produce  $\text{He}^{++}$ ) over an interaction length of 1 cm. For longitudinal pumping, beam defocusing due to plasma induced index of refraction changes would limit the plasma density to less than approximately  $5 \times 10^{17}$  cm<sup>-3</sup> (a  $\pi/4$  phase change over one cm) [20]. This density is near optimum for gain on the  $L_\alpha$  line in HeII.

## VIII Conclusions:

In conclusion we have introduced a semiclassical description of ATI which agrees, in the tunnelling limit, with the description of ATI implicit in Keldysh type theories. ATI allows considerable control of the plasma conditions produced by multiphoton ionization. This control will be an important new parameter in plasma experiments. It appears possible, using linearly polarized UV radiation, to ionize ions with ionization potential up to the 500 eV level and maintain an adequately cold electron energy distribution for recombination type XUV laser schemes.

#### Acknowledgements:

The authors wish to acknowledge discussions with C. Rolland, S.L. Chin, and F. Brunel. We especially wish to thank S.L. Chin for the use of the electron spectrograph for these measurements and D. Joines for his continued technical assistance.

#### References:

1. See papers at this conference.
2. D.L. Mathews et al. Phys. Rev. Lett. 54, 110 (1985).
3. C. Chenais-Popovics et al., Phys. Rev. Lett. 59, 2161 (1987).
4. L.I. Gudzenko and L.A. Shelepin, Sov. Phys. JETP 18, 998 (1964).
5. J. Peyraud and N. Peyraud, J. Appl. Phys. 43, 2993 (1972).
6. For a review, see F.V. Bunkin, V.I. Derzhiev, and S.I. Yakovlenko, Sov. J. Quantum Electron. 11, 981 (1981).
7. See for example papers in Atomic and Molecular Processes with Short Intense Laser Pulses, NATO ASI Series B: Physics, Vol. 171, A.D. Bandrauk editor, Plenum Press (1988).
8. S.L. Chin, C. Rolland, P.B. Corkum and P. Kelly, Phys. Rev. Lett. 61, 153 (1988).
9. L.V. Keldysh, Sov. Phys. JETP 20, 1307 (1965).
10. M.D. Perry, A. Szoke, O.L. Landen and E.M. Campbell, Phys. Rev. Lett. 60, 1270, (1988).
11. L.D. Landau and E.M. Lifshitz, Quantum Mechanics, 2nd Ed., Pergamon Press, (1965), p. 276.
12. P.B. Corkum and C. Rolland, SPIE 664, High Intensity Laser Processes, 212 (1986).
13. P.B. Corkum, IEEE J. Quantum Electron. QE-21, 216 (1985).
14. A.M. Perelomov, V.S. Popov and M.V. Terent'ev, Sov. Phys. JETP 23, 924 (1965).
15. W.W. Jones and A.W. Ali, Appl. Phys. Lett. 26, 450 (1975).
16. W.W. Jones and A.W. Ali, J. Phys. B: At. Mol. Phys. 11, 187, (1978).
17. G.J. Pert, J. Phys. A: Gen Phys. 5, 506 (1972).
18. P.B. Corkum, Laser Acceleration of Particles, C. Joshi and T. Katsouleas editors, AIP Conference Proceedings No. 130, p. 493, (1985).
19. see S. Watanabe, et. al. in this volume.
20. P.B. Corkum and C. Rolland, NATO ASI Series B: Physics, Vol. 171, A.D. Bandrauk editor, Plenum Press (1988) p. 157.

# Charge-Displacement Self-Channeling as a Method for Energy Concentration

K. Boyer, T. S. Luk, J. C. Solem,<sup>†</sup> and C. K. Rhodes

*Laboratory for Atomic, Molecular, and Radiation Physics, Department of Physics  
University of Illinois at Chicago, P.O. Box 4348, Chicago, Illinois 60680*

## Abstract

The concentration of energy arising from charge-displacement self-channeling is discussed. Since high energy deposition rates are expected to arise from multiphoton coupling and the channel can also serve as an effective waveguide for secondary radiation, such circumstances are ideal for generating coherent short wavelength radiation.

## Channeled Propagation

Amplification in the x-ray region requires prodigious energy deposition rates [1] spatially organized in a high-aspect-ratio volume of material. The fundamental question, therefore, centers on the controlled deposition of energy at high specific powers. We show that the use of extremely intense ( $10^{19} - 10^{22}$  W/cm<sup>2</sup>) short pulse ( $\sim 100$  fs) radiation may be able to produce both the necessary deposition rates and spatial control by combining (1) the energy deposition [2,3] arising from high-order multiphoton processes with (2) a new mode of channeled propagation involving a charge-displacement mechanism. A significant point that will emerge is that the conditions needed for the strong multiphoton coupling are identical to those found required for the confined propagation.

It appears [4-6] that a fundamentally new regime of electromagnetic propagation will develop in plasmas for subpicosecond radiation of sufficient intensity. In the high intensity case of interest, in which processes generating ionization dominate the coupling, multiphoton ionization is expected to produce a substantial reduction of both the linear and nonlinear refractive indices of the medium. For a suitably ionized plasma, this combination of high charge state ions with the electron density produced by the multiphoton coupling appears capable of producing a new mode of radiative channeling.

Indeed, preliminary analysis [7] supports the presence of the following mechanism. For a sufficiently short pulse ( $\sim 100$  fs), the massive ions remain spatially fixed while the relatively mobile electrons are expelled by the ponderomotive force from the high intensity zone. Thereby, a state of equilibrium can be established between the ponderomotive and the electrostatic force densities owing to the charge displacement. Since the electrons, which embody a negative contribution to the index, are expelled, an on-axis region of relatively high refractive index is formed which supports the channeling. In a limiting case, it appears that the behavior approaches that characteristic of a metallic waveguide. Interestingly, a focusing mechanism of this type is not describable in terms of the conventional [8] nonlinear index parameter  $n_2$ . A further unusual aspect of this process, since there is a strong tendency to locally reduce the plasma frequency  $\omega_p$  in the region where the intensity is high, is that it may enable propagation for appreciable distances in plasmas that would normally be considered as overdense.

The essence of the idea can be understood in the following manner. The steady-state force balance between the radially outward ponderomotive force and the oppositely directed electron-ion attraction is represented, in cylindrical symmetry for a completely ionized tenuous ( $\omega \gg \omega_p$ ) plasma, by

$$\frac{2\pi e^2}{m\omega^2 c} \nabla I(r) + e^2 n_e \int \frac{\rho(r') (r - r')}{|r - r'|^3} d^3 r' = 0. \quad (1)$$

For a cylindrical gaussian intensity distribution  $I(r)$ , the total charge density  $\rho(r)$  can be written in exact form as

$$\rho(r) = 2B (1 - r^2/r_0^2) \exp(-r^2/r_0^2) \quad (2)$$

In which  $B = I_0(m\omega^2 c n_e r_0^2)^{-1}$  and  $m$ ,  $c$ ,  $n_e$ , and

$r_0$  denote the electron mass, speed of light, quiescent plasma density, and radius (HWHM) of the assumed gaussian intensity profile, respectively. The form of this solution is shown in Fig. (1) for a value of  $B = 0.4$ . The expulsion of the electrons from the central region is apparent.

A charge distribution of this nature can lead to channeled propagation. An estimate of the condition necessary can now be made by describing the charge displacement by two regions, such that  $\rho(r < r_0\sqrt{2}) = \rho(0)$  and  $\rho(r \geq r_0\sqrt{2}) = \rho(r_0\sqrt{2})$ , and equating the angle of total internal reflection to the angle corresponding to the first minimum of diffraction. This procedure yields a critical intensity

$$I_c = \frac{\pi m \omega^2 c}{64(1 + e^2)r_0} \approx (4.3 \times 10^{-2}) \frac{m \omega^2 c}{r_0}, \quad (3)$$

in which  $r_0$  denotes the classical electron radius. Significantly, this intensity is independent of the electron density  $n_0$  and contrasts with the power threshold [8] normally arising from induced index charges in transparent dielectrics. Analytic approximations extending to high electron density show a significant dependence of  $I_c$  on  $n_0$  only quite near the critical density. Furthermore, it is easily demonstrated that  $I_c$  normalized to the Compton intensity [9] is a constant (0.54) independent of frequency, a finding which shows that the charge-displacement mechanism is associated with relativistic conditions. For a wavelength of 248 nm,  $I_c = 2.4 \times 10^{19}$  W/cm<sup>2</sup>. Finally, a striking aspect of the analysis [7] is the extremely strong frequency dependence favoring the use of ultraviolet wavelengths to establish the conditions for channeling. Scaling laws are derived [7] indicating variations as rapid as  $\omega^9$ .

**Charge-Displacement Focusing**  
(Low Density Plasma)

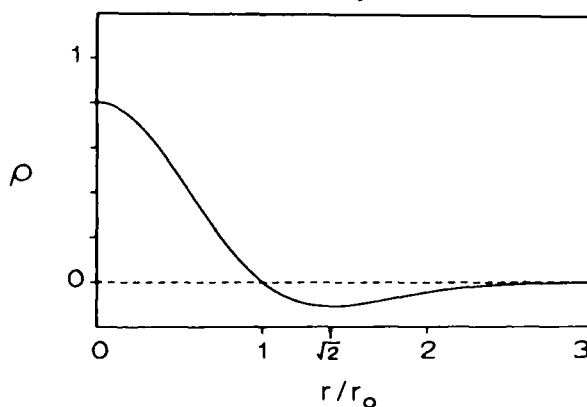


Figure 1. Illustration of the total charge density  $\rho$  as a function of normalized radial distance  $r/r_0$  for  $B = 0.4$ .

## Controlled Energy Concentration - Summary

In terms of the basic question of the controlled deposition of energy at high specific powers, the answer that emerges from these considerations involves three separate components. They are (1) a new ultraviolet pulsed power technology, [10] (2) an energy deposition mechanism based on highly nonlinear coupling, [11] and (3) a condition for channeled propagation. [7] It can be seen that these three elements, which appear capable of producing conditions comparable to, or possibly exceeding those of a thermonuclear environment, [10] fit together in a remarkably congenial way. Figure (2) illustrates these relationships. A principal finding is that the radiative conditions needed for the strong multiphoton coupling governing the energy transfer rate [11] are essentially identical to those required for the channeled propagation [7] and that the laser technology [10] can readily produce the regime of irradiation necessary. The compatibility of these three factors is a key feature of this method for the attainment of very high energy density states of matter.

## Multiphoton Energy Transfer Cross Section

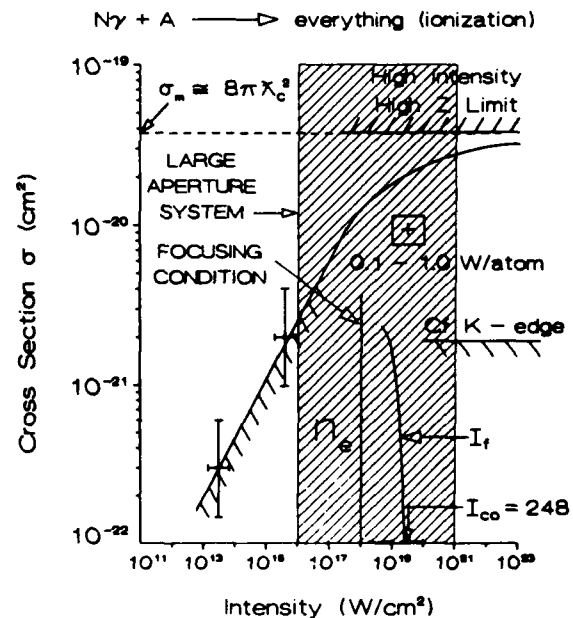


Figure 2. Illustration of how (1) the energy transfer cross section  $\sigma$ , (2) the channeling condition, and (3) the pulse power technology all fit together. The significant fact is that the conditions needed for the strong multiphoton coupling governing the energy transfer ( $I \approx I_{co} \approx 10^{19}$  W/cm<sup>2</sup>) are identical to those required for the channeled propagation ( $I_t \approx I_{co} \approx 10^{19}$  W/cm<sup>2</sup>), and that the developing large aperture ultraviolet laser technology moves us into the desired range.

## Acknowledgements

This work was supported by AFOSR, LLNL, ONR, and SDI.

† permanent address: Theoretical Division, MS-B210, Los Alamos National Laboratory, Los Alamos, NM 87545

## References and Notes

1. A. V. Vinogradov and I. I. Sobel'man, "The Problem of Laser Radiation Sources in the Far Ultraviolet and X-Ray Region," *Sov. Phys.-JETP* **36**, 1115 (1973).
2. C. K. Rhodes, "Physical Processes at High Field Strengths," *Physica Scripta* **T17**, 193 (1987).
3. C. K. Rhodes, "Multiphoton Ionization of Atoms," *Science* **229**, 1345 (1985).
4. W. B. Mori, C. Joshi, J. M. Dawson, D. W. Forslund, and J. M. Kindel, "Evolution of Self-Focusing of Intense Electromagnetic Waves in Plasma," *Phys. Rev. Lett.* **60**, 1298 (1988).
5. G.-Z. Sun, E. Ott, Y. C. Lee, P. Guzdar, "Self-Focusing of Short Intense Pulses in Plasmas," *Phys. Fluids* **20**, 526 (1987).
6. Ya. L. Bogomolov, S. F. Lirin, V. E. Semenov, and A. M. Sergeev, "Ionization Self-Channeling of Extremely Intense Electromagnetic Waves in a Plasma," *Pis'ma Zh. Eksp. Teor. Fiz.* **45**, 532 (1987) [Engl. transl.: *Sov. Phys. - JETP Lett.* **45**, 680 (1987)].
7. J. C. Solem, T. S. Luk, K. Boyer, and C. K. Rhodes, "X-Ray Amplification with Charge-Displacement Self-Channeling," *Phys. Rev. Lett.*, submitted.
8. P. L. Kelley, "Self-Focusing of Optical Beams," *Phys. Rev. Lett.* **15**, 1005 (1965).
9. The Compton intensity is given by  $I_{co} = m\omega^2 c / 4\pi \lambda_c \alpha$  with  $\lambda_c$  the Compton wavelength of the electron and  $\alpha$  the fine structure constant. The intensity is defined by the condition that the average nonrelativistically calculated quiver speed of the electron be equal to the speed of light.
10. K. Boyer, G. Gibson, H. Jara, T. S. Luk, I. A. McIntyre, A. McPherson, R. Rosman, J. C. Solem, and C. K. Rhodes, "Strong-Field Processes in the Ultraviolet Region," this volume.
11. K. Boyer, H. Jara, T. S. Luk, I. A. McIntyre, A. McPherson, R. Rosman, and C. K. Rhodes, "Limiting Cross Sections for Multiphoton Coupling," *Revue Phys. Appl.* **22**, 1793 (1987).

# Stimulated Compton Backscattering and the High Intensity Kapitza-Dirac Effect

D. W. Schumacher, P. H. Bucksbaum, and M. Bashkansky\*

AT&T Bell Laboratories, Murray Hill, New Jersey 07974

## Abstract

We report the scattering of low energy free electrons from an optical standing wave at intensities of  $10^{13}$  to  $10^{14}$  W/cm<sup>2</sup>.<sup>1</sup> This interaction is the high intensity limit of the Kapitza-Dirac effect,<sup>2</sup> wherein electrons Bragg scatter from the standing wave "lattice". In this regime, the momentum exchanged exceeds the reciprocal lattice vector by a factor of 500 or more, and the scattering rate is comparable to the optical frequency. The electron motion is most easily analyzed by classical mechanics.

## Introduction

The Kapitza-Dirac (K-D) effect is the wave-particle dual of Bragg scattering: a particle beam scatters from a periodic lattice of light, exchanging integer multiples of momentum  $\hbar G = 2\hbar k$ , where  $G$  is the reciprocal lattice vector of an optical standing wave, and  $k$  is the optical wave vector. For electrons, the K-D effect comes from stimulated Thomson scattering, in which virtual photo-absorption from one of the two traveling wave modes in the standing wave is accompanied by stimulated emission into the opposing mode (see figure 1a). The Bragg condition (see equation 5 below) is equivalent to simultaneous conservation of energy and momentum for electron-photon backscattering.

Here we report on the K-D effect for electrons in very high intensity light, where the momentum transferred to the electrons by the light exceeds the Bragg condition by a factor of five hundred or more. This is the first experimental study of the *high intensity* K-D effect.<sup>3</sup> The large momentum transfer can be understood in terms of the classical motion of the electron in a spatially periodic effective potential.

## Low intensity scattering rate

The steady state rate  $\Gamma$  for K-D scattering by a nonrelativistic electron in a standing wave produced by two counterpropagating lasers, is given in lowest order perturbation theory by

$$\Gamma = n\rho \left. \frac{\partial \sigma_T}{\partial \Omega} \right|_{\theta=\pi}, \quad (1)$$

where  $n$  is the number of photons per mode in the standing wave,  $\rho$  is the photon flux from either laser beam, and  $\partial \sigma_T / \partial \Omega$  is the differential Thomson cross section, evaluated in the backscattering direction. For two equal linearly polarized counterpropagating plane waves, this yields

$$\Gamma = \left[ \frac{c^2}{\hbar v^3} \frac{I}{\Delta v} \right] \left[ \frac{I}{\hbar v} \right] \left[ \frac{e^4}{m_e^2 c^4} \right] = \frac{U_0^2}{\hbar^2 \Delta v}, \quad (2)$$

where

$$U_0 = \frac{e^2 I}{2\pi m_e c v^2} \quad (3)$$

is the ponderomotive potential (essentially, the electron "quiver" energy) due to each laser beam alone,<sup>4</sup>  $I$  is the intensity of each beam,  $v$  its frequency, and  $\Delta v$  its bandwidth. This is identical to Kapitza and Dirac's original result,<sup>2</sup> except for an enhancement factor of two due to polarization (they assumed that the light in the standing wave was unpolarized).

For example, if the standing wave is made from counterpropagating Nd:YAG laser beams ( $v=2.8 \times 10^{14}$  Hz) with a temporal coherence of 100 psec ( $\Delta v=5$  GHz), then the scattering rate into the +1 or -1 Bragg order is

$$\Gamma = 5.2 \left[ \frac{I}{1 \text{ MW/cm}^2} \right]^2 \text{ MHz}. \quad (4)$$

The Bragg condition is

$$a = \lambda \cos \theta, \quad (5)$$

where  $a$  is the electron DeBroglie wavelength, the lattice spacing is  $\lambda/2$ , and the electron angle with respect to the laser direction is  $\theta$ .

## Modifications at higher intensities

These formulae hold for intensities low enough that  $\Gamma$  does not exceed the bandwidth of the light, or for  $I < 30 \text{ MW/cm}^2$

in the example above. Current pulsed laser beams can exceed this intensity by a factor of  $10^7$  or more. We wish to examine how equation 2 is modified in an intense laser field. For intensities above  $30 \text{ MW/cm}^2$ , equation 2 breaks down because the number of photons per mode depends on the coherence time  $1/\Delta\nu$  of the light. If the mean time between scatterings is less than this time, the phase of the electron is interrupted early, so that the relevant coherence time is no longer  $1/\Delta\nu$ , but the time since the last scattering. This suggests the substitution  $\Delta\nu \rightarrow \Gamma$ , leading to a high intensity formula

$$\Gamma = \frac{U_0}{\hbar} = 160 \left[ \frac{I}{1 \text{ GW/cm}^2} \right] \text{GHz} \quad (I > 30 \text{ MW/cm}^2). \quad (6)$$

Thus we arrive at an important difference between the high and low intensity regimes: for low intensities, the stimulated scattering rate depends on the *product* of the two laser intensities in the standing wave; for higher intensities, the rate is linear in intensity, and therefore linear in the ponderomotive potential.

As the intensity increases still further, the rate increases until the simple analogy to Bragg scattering breaks down. At  $I \approx 10 \text{ GW/cm}^2$ , the scattering length approaches a single wavelength, so that the electron wave function is no longer sensitive to the periodicity of the light lattice. Then equation (5) no longer applies.

The rate continues to increase with intensity, and for intensities greater than  $10^{13} \text{ W/cm}^2$ ,  $\Gamma$  in equation (6) exceeds the laser frequency! Then the K-D effect becomes considerably more complicated than the simple picture just given. In addition to the lowest order process suggested by figure 1a, higher order diagrams leading to the same net momentum transfer also contribute, as shown in figure 1b. Furthermore, scattering into higher Bragg orders (figure 1c), and multiple scattering (figure 1d) also must be taken into account. There have been several attempts to deal with the theory for high intensities.<sup>5-7</sup> Here we present the first experimental study of the high intensity K-D effect, carried out in standing waves with peak intensities of  $10^{13}$  to  $10^{14} \text{ W/cm}^2$ .

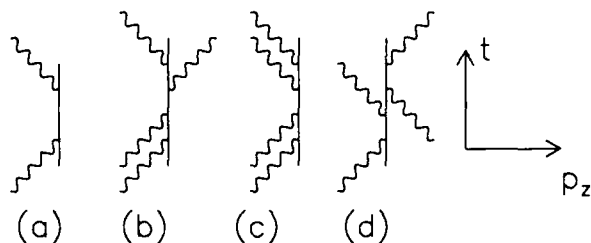


Figure 1. Feynman graphs for K-D scattering. (a): lowest order diagram, for net momentum transfer of  $+2\hbar k$ . (b): higher order corrections to the lowest order Bragg peak in (a). (c): lowest order diagram for scattering into the next order Bragg peak. (d): multiple scattering; in the case shown, there is no *net* momentum transfer. (From reference 1)

## Experimental apparatus

Our high intensity standing waves were made by colliding two focused  $1064 \text{ nm}$  laser pulses (see figure 2). The pulses were  $100 \text{ psec}$  long, and approximately fourier-transform limited, to insure a uniform stationary standing wave during the  $\approx 10\text{--}20 \text{ psec}$  transit of the electrons through the focus. To form the standing wave, a single amplified pulse is split by a dielectric beamsplitter, and each arm is focused to  $15 \mu\text{m}$  at a common point, from opposite directions. The intensity, polarization, and arrival time of each beam may be adjusted independently.

The electrons in this experiment come from above-threshold ionization (ATI) of low density ( $10^8\text{--}10^{10} \text{ cm}^{-3}$ ) xenon and krypton *in the standing wave itself*.<sup>8</sup> The highly nonlinear intensity dependence of ATI (at least 11 photons are required to ionize xenon, 12 for krypton) insures that the electrons have maximum spatial and temporal overlap with the high intensity standing wave. The ATI electron energies range from zero to  $20 \text{ eV}$ .

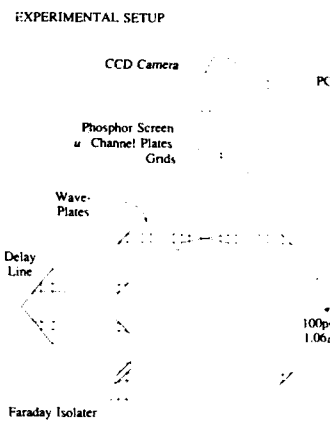


Figure 2. Experimental geometry, showing laser beam lines. The layout is essentially a Mach-Zender interferometer. In fact, we used the interferometric alignment to measure the temporal coherence length of the laser pulses. A Faraday isolator was used to keep light from re-entering the laser amplifier chain. (From reference 1)

The detector used to observe electrons under these conditions is shown schematically in figure 3. Each electron scatters from the focused standing wave for up to  $20 \text{ psec}$  as it drifts out of the light. After leaving the focus, electrons traverse a  $5 \text{ cm}$  field-free region to an image intensified detection screen subtending  $0.08 \text{ sr}$  ( $66^\circ$  opening angle), bisecting the polarization plane. Retarding grids at the screen can select electrons at specific energies. Arrival angles are detected by a television camera and collected over many laser pulses, resulting in two-dimensional histograms in  $\theta$  (the polar angle with respect to  $k$ ) and  $\phi$  (the azimuthal angle).

## Data

Figure 4 is a histogram of the photoelectron angular distribution from a *single* focused laser beam (no standing wave).

The detection region is centered on the polarization, and most photoelectrons are emitted near this direction. The elongation in azimuthal ( $\phi$ ) angles is due to ponderomotive scattering from intensity gradients as the electrons leave the focus.<sup>9</sup> This distribution is typical of above-threshold linearly polarized multiphoton ionization in rare gases.<sup>8</sup>

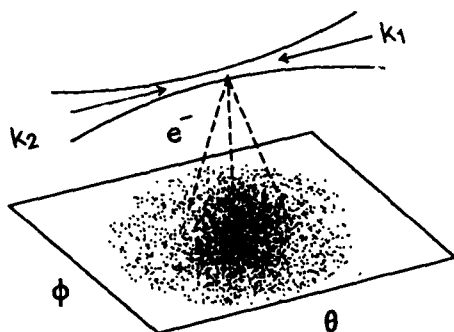


Figure 3. Experimental geometry. Photoelectrons produced in a standing wave scatter out of the focus, and are detected on a screen. (From reference 1)

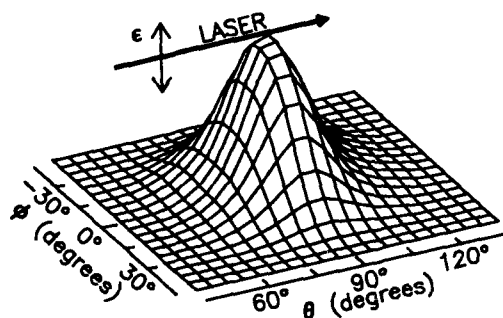


Figure 4. Typical electron angular distribution for electrons with 9 to 12 eV of energy, from ATI in xenon produced by a single 1064 nm laser beam (no standing wave). The peak laser intensity is approximately  $8 \times 10^{13} \text{ W/cm}^2$ . (From reference 1)

Figure 5 shows electrons emitted from a standing wave with the same geometry and polarization as the traveling wave focus in figure 4. The angular distribution splits to form two peaks symmetric with respect to the polarization plane. This is the K-D effect. It is, however, quite unlike the single Bragg scattering case in magnitude; for these electrons have absorbed on the order of 1000  $\hbar k$  of momentum.

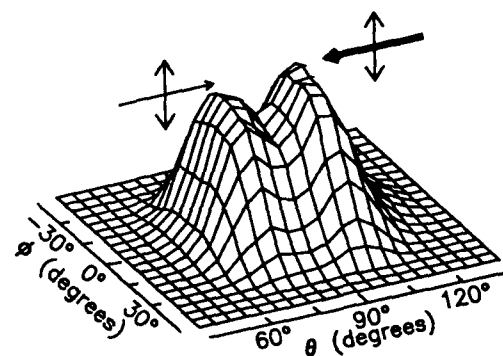
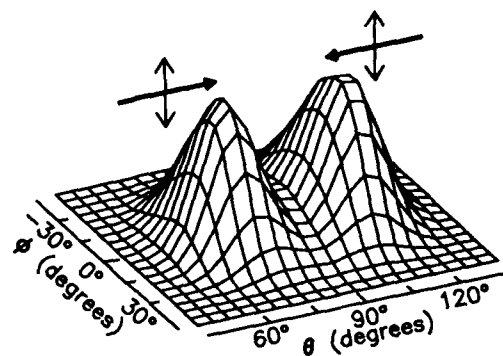


Figure 5. Top: K-D effect in a linearly polarized standing wave, for 9 to 12 eV electrons. As in figure 4, the peak laser intensity is approximately  $8 \times 10^{13} \text{ W/cm}^2$ . Bottom: Reduced contrast standing wave, made from beams of unequal intensities. (From reference 1)

If the contrast of the standing wave is reduced by using laser beams with unequal intensities, the two peaks move together, indicating a reduction in the K-D scattering (bottom of figure 5).

We have investigated the dependence of the scattering angle on electron energy, laser polarization, and on the contrast of the standing wave. Most interesting is the effect for a circularly polarized standing wave, shown in figure 6. If the two light pulses have the opposite helicity (hence equal angular momentum), then K-D scattering is quite pronounced. (upper figure in 6). If the beams have equal helicity, hence the opposite angular momentum, then all diagrams in figure 1 are forbidden by angular momentum conservation. No K-D scattering is expected, or observed (lower figure 6).



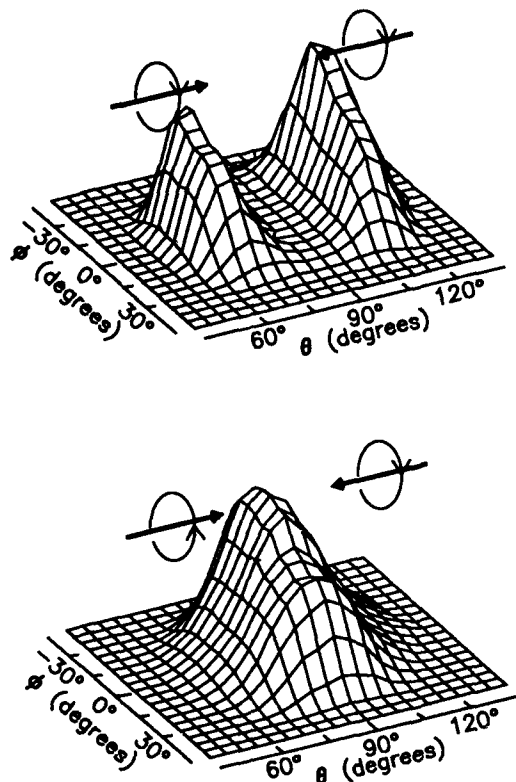


Figure 6. Top: K-D effect in a circularly polarized standing wave, with opposite helicities in the two beams. Bottom: K-D effect is absent in a circularly polarized standing wave with equal helicities in the beams. (From reference 1)

#### Electron energy effects

The rate of above-threshold ionization is an extremely strong function of intensity of the electric field. The ionization probability varies from negligible to near unity over a rather small range of intensity. In fact, a reasonably successful simple model assumes that all ionization for a particular atom occurs at roughly the same intensity, depending only on the laser wavelength and the work function of the atom. If the KD effects using two different atomic sources are compared, for example xenon (I.P.=12.128 eV) vs. krypton (I.P.=13.996 eV), any changes should be due to the different laser intensity where electrons are formed in the standing wave. On the other hand, distributions of electrons with different energies, but from the same atom, should start at about the same laser intensity. The next two figures demonstrate this effect.

Figure 7 shows the scattering distribution for xenon as a function of electron energy. Lower energy electrons are scattered at larger angles, but the net momentum transfer is roughly independent of electron energy.

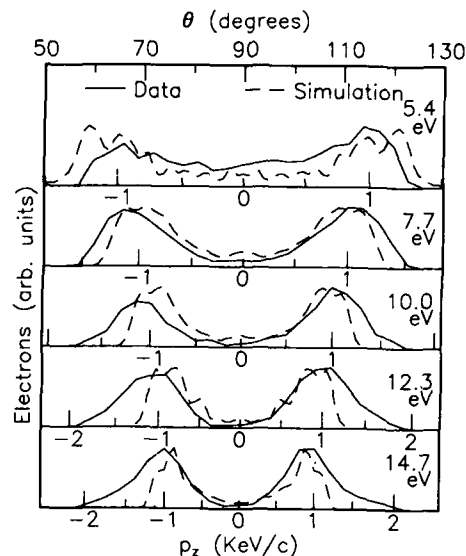


Figure 7. Polar angle distributions for electrons of different energies from ATI in xenon in the same standing wave. All distributions are plotted vs. polar angle (top scale). Bottom scale shows the momentum transfer for each energy. Solid lines are data, collected in a 2 eV window bracketing the energy shown. Dashed lines are results of Monte Carlo electron trajectories. (From reference 1)

Figure 8 shows the same distributions, but for krypton. Here the momentum transferred to the electrons by the standing wave is still independent of electron energy, but is uniformly higher than for xenon. This indicates that these electrons may have come from higher intensities in the standing wave.

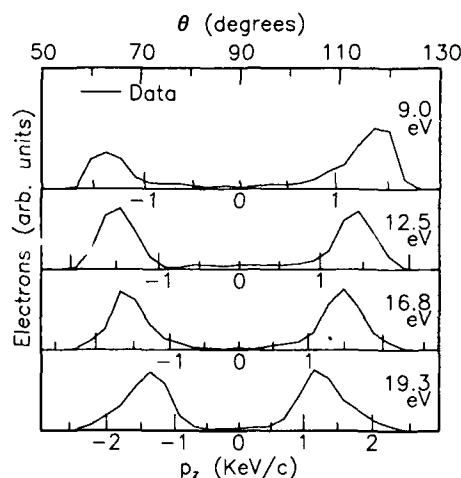


Figure 8. Polar angle distributions for krypton ATI electrons of different energies in the same standing wave, plotted as in figure 7.

Another way to change the momentum transfer is to lessen the contrast of the standing wave, as in figure 5 (bottom). As one laser beam is attenuated, the net scattering in the polar direction is reduced, approaching the distribution for a single laser beam (figure 4).

### Analysis

For these high intensities, perturbation theory is quite unwieldy.<sup>5</sup> More appropriate methods treat the light as a time varying potential.<sup>6,7</sup> In the non-relativistic plane wave approximation, Schrodinger's equation may be written:

$$\frac{(P - \frac{e}{c} A(x,t))^2}{2m_e} \psi(x,t) = i\hbar \frac{\partial \psi(x,t)}{\partial t} \quad (7)$$

where  $A(x,t)$  is the classical (non-quantized) time-dependent vector potential for a standing wave produced by two counterpropagating plane waves along  $\hat{z}$ :

$$A(x,t) = A_0(\hat{e}_1 \cos(kz - \omega t) + \hat{e}_2 \cos(kz + \omega t)) \quad (8)$$

If  $A$  were a *traveling* plane wave, the solution to equation (7) would be a Volkov state;<sup>10</sup> but for the standing wave, no analytic solution to equation (7) has been found. Since the scattering rate is so large, we resort to a classical approximation,<sup>6</sup> in which the Hamiltonian operator on the left side of equation (7) becomes a classical Hamiltonian  $H$  describing the motion of a nonrelativistic spinless electron in a standing light wave.

For slowly moving electrons, the rapidly oscillating portion of  $H$  may be replaced by a time-averaged spatially periodic effective potential. If  $\hat{e}_1$  and  $\hat{e}_2$  are identical linear polarizations, then the effective potential takes the form  $U_F(z) = 4U_0 \cos^2(kz)$ . Thus the K-D effect is simply potential scattering from a periodic grating of height  $4U_0$ . Equation (6) must be replaced by a position dependent scattering rate

$$\Gamma_{1 \rightarrow 2}(z) = \frac{2U_0}{\hbar} \sin(2kz), \quad (9)$$

where  $1 \rightarrow 2$  means that this is the *net* scattering rate of photons from beam 1 to beam 2. This rate can be positive or negative. Quantum calculations in the high intensity limit yield similar results (reference 7, equations 46-49).

This classical Hamiltonian is identical to that of a simple pendulum of mass  $m_e$  and length  $1/(2k)$  under a uniform force  $4kU_0$ .<sup>11</sup> Electrons whose total energy  $E$  is less than the antinodal maximum potential  $4U_0$  are localized in a sinusoidal potential well centered on an electric field node of the standing wave, where they oscillate in the  $\hat{z}$  direction with angular frequency

$$\Omega = \omega \frac{\pi}{\chi(E)} \left\{ \frac{2U_0}{m_e c^2} \right\}^{1/2}. \quad (10)$$

Here  $\chi(E)$  is a complete elliptic integral of the first kind

$$\chi(E) = \int_0^{\frac{\pi}{2}} \frac{dx}{[1 - (E/4U_0)^2 \sin^2 x]^{1/2}}. \quad (11)$$

For example, the oscillation period for a 1 eV electron in a peak potential of 10 eV (corresponding to  $\approx 10^{14}$  W/cm<sup>2</sup> for Nd:YAG radiation) is 0.3 psec.

In order to compare our results to the predictions of this classical approximation, we have calculated electron trajectories with a time varying spatially periodic ponderomotive potential appropriate for a standing wave formed by two perfectly overlapped 100 psec pulses meeting in a TEM<sub>00</sub> gaussian focus. Electrons were launched in the simulation according to a very simple model, in which all ionization takes place at a single threshold intensity of approximately  $3 \times 10^{13}$  W/cm<sup>2</sup>. This is the ionization intensity appropriate for xenon.<sup>9</sup> The photoelectrons are initially directed along the laser polarization, but immediately begin to oscillate in the  $\pm k$  direction under the influence of the ponderomotive spatial grating. Eventually they migrate to the edges of the beam, where the standing wave intensity is lower. At some point, after several oscillations, the electrons reach a part of the focus with a low enough potential to convert from bound to unbound motion. This is shown for a single trajectory in figure 9. Histograms for Monte Carlo generated electron distributions at several energies are shown along with the xenon data in figure 7. Results are quite consistent with the data, and lend strong support to the ponderomotive hypothesis.

### Conclusion

We have demonstrated the Kapitza-Dirac effect at light intensities where the scattering rate equals or exceeds the

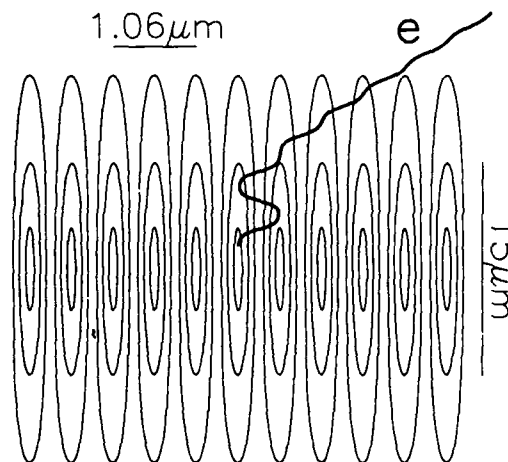


Figure 9. The calculated trajectory of an ATI electron drifting out of the standing wave, showing one cycle of bounded motion in a potential trough, followed by a transition from bounded to unbounded motion along  $\hat{z}$ . (From reference 1)

optical frequency. The results resemble classical scattering of point electrons from a ponderomotive grating. This ponderomotive approach is expected to break down at still higher intensities, when the oscillation frequency of an electron bound in the standing wave potential well approaches an optical cycle. This regime also corresponds to the onset of relativistic effects in the electron motion. Intensities of this magnitude will be available in the near future.

## References

\*Permanent address: Naval Research Laboratories, Washington, D.C.

1. P.H. Bucksbaum, D.W. Schumacher, and M. Bashkansky, *Phys. Rev. Lett.* **61**, 1182 (1988).
2. P. L. Kapitza and P. A. M. Dirac, *Proc. Cambridge Philos. Soc.* **29**, 297 (1933).
3. Attempts to observe the K-D effect for electrons at low intensities include L. S. Bartell, R. R. Roskos, and H. B. Thompson, *Phys. Rev.* **166**, 1494 (1968); H. Schwarz, *Phys. Lett.* **43A**, 457 (1973); Y. Takeda and I. Matsui, *J. Phys. Soc. Jpn.* **25**, 1202 (1968); H. C. Pfeiffer, *Phys. Lett.* **26A**, 326 (1968). The K-D effect in atoms has been studied by P. J. Martin, B. G. Oldaker, A. H. Miklich, and D. E. Pritchard, *Phys. Rev. Lett.* **61**, 515 (1988); and P. L. Gould, G. A. Ruff, and D. E. Pritchard, *Phys. Rev. Lett.* **56**, 827 (1986).
4. R. R. Freeman, T. J. McIlrath, P. H. Bucksbaum, and M. Bashkansky, *Phys. Rev. Lett.* **57**, 3156 (1986).
5. E. A. Coutias and J. K. McIver, *Phys. Rev. A* **31**, 3155 (1985); R. Gush and H. P. Gush, *Phys. Rev. D* **3**, 1912 (1971); L. S. Bartell, *J. Appl. Phys.* **38**, 1561 (1967).
6. Y. W. Chan and W. L. Tsui, *Phys. Rev. A* **20**, 294 (1979).
7. M. V. Fedorov, *Sov. Phys. JETP* **25**, 952 (1967).
8. T. J. McIlrath, P. H. Bucksbaum, R. R. Freeman, and M. Bashkansky, *Phys. Rev. A* **35**, 4611 (1987).
9. R. R. Freeman, T. J. McIlrath, P. H. Bucksbaum, and M. Bashkansky, *Phys. Rev. Lett.* **57**, 3156 (1986).
10. D.M. Volkov, *Z. Physik* **94**, 250 (1935).
11. See any standard mechanics text, for example, A. Sommerfeld, *Mechanics*, New York: Academic Press, pp. 87-90 (1952).

# Search for X-Rays Generated by Collisionless Multiphoton Processes

Peter H. Y. Lee, Donald E. Casperson, and Gottfried T. Schappert

*Physics Division, Los Alamos National Laboratory  
P.O. Box 1663, Mail Stop E526, Los Alamos, New Mexico 87545*

## ABSTRACT

We have conducted photon counting experiments to search for x rays which may be generated by either collisionless multiphoton induced inner-shell processes or bremsstrahlung at high laser irradiance. Using KrF light at an irradiance  $\sim 3 \times 10^{17}$  W/cm<sup>2</sup> on low density Xe gas targets, we detect no prompt photons which are characteristic of these processes.

## INTRODUCTION

For some time, Boyer and Rhodes[1] have advocated that at very high laser irradiance (i.e., such that the optical field strength exceeds an atomic unit  $e/a_0$ ), the outer shell electrons of an atom can be driven into coherent motion, resulting in strong coupling of the laser energy to the atoms by inducing inner-shell excitation. The consequence of this is that x rays may be emitted from relaxation of the excited states. On the other hand, collective quivering of an entire shell in the vicinity of the parent ion may also generate bremsstrahlung. We shall call these collisionless multiphoton processes of x ray generation.

Although Lambropoulous[2] doubts that an entire atomic outer-shell can be excited and Wendin et al.[3] pointed out that screening by outermost shells will make it very difficult to create inner-shell vacancies, Biedenharn et al.[4] have suggested that the collective outer-shell motion may offer a method of achieving collisionless nuclear excitation. This idea of laser-atom-nucleus coupling

mechanism is presently being tested by Dyer et al.[5]

In order to directly test the idea of whether or not multiphoton processes at very high laser irradiance can drive outer-shell electrons into coherent motion and induce inner-shell excitation or generate bremsstrahlung, we have used the Los Alamos Bright Source (LABS) laser to irradiate low-density Xe gas targets at  $I > 10^{17}$  W/cm<sup>2</sup> and have conducted photon counting experiments to search for "prompt" radiation, i.e., photons characteristic of the relaxation of collisionless inner-shell excitations or bremsstrahlung due to collective electron quiver. In the present context, "inner-shell" means the shells adjacent to the outermost shell. The radiation which is characteristic of multiphoton inner-shell excitation in Xe appears as photons in the 90-140 eV range for transitions between the N and O levels and photons in the 500-1000 eV range for transitions between the M and N levels. Bremsstrahlung is a continuum. Since the electron quiver energy is  $E = (e^2/\pi mc^3)I\lambda^2$ , peak energies over 1 KeV are possible for a KrF laser at  $I > 10^{17}$  W/cm<sup>2</sup>. Photons generated by either the inner-shell process or bremsstrahlung are, in principle, spectrally distinguishable.

## EXPERIMENTAL

The LABS laser consists of a mode-locked visible dye laser heterodyned to 248 nm and amplified in two KrF amplifiers. Output is typically 20 mJ of 0.7 ps pulses at a repetition rate of 3 Hz. The pulse can be focused, using an f/1 parabolic

mirror, to a minimum spot size of  $\sim 5 \mu\text{m}^2$ . A detailed description of LABS is published elsewhere.[6] Figure 1 shows the schematic of the experimental configuration. Laser pulses from LABS are directed into the target chamber by a turning mirror, while a small fraction of the light passes through the mirror to a fast photodiode providing a trigger reference in the detector electronics. A 50 mm diameter f/1 parabolic mirror focuses the beam down to best focus at the center of the target chamber. The target chamber is filled with Xe at low pressure. Average peak irradiance on target, accounting for all measured mirror and target chamber window losses, is  $\sim 3 \times 10^{17} \text{ W/cm}^2$ ; the optical field strength corresponding to this irradiance is  $\sim 3$  atomic units. X-ray photons generated in the focal region (i.e., the laser-atom interaction region) are detected through a thin-foil filter by a photon counting system consisting of either a fast, high-gain microchannel-plate (MCP) detector or a slower, high-gain MCP/phosphor/photomultiplier detector assembly; the detectors subtend a variety of solid angles with respect to the interaction region. Three different filters were used for the experiments: Filter-1 consists of  $1 \mu\text{m}$  of Parylene ( $\text{C}_8\text{H}_8$ ) and  $1000 \text{ \AA}$  of aluminum ( $500 \text{ \AA}$  evaporated on each side of the Parylene); Filter-2 consists of  $2 \mu\text{m}$  of Parylene and  $2000 \text{ \AA}$  of aluminum; Filter-3 consists of  $5 \mu\text{m}$  of beryllium. The filter transmissions are plotted in Figure 2 using data of Henke et al.[7]

For photon detection, a fiducial at "zero-time" is established by measuring the "prompt" x rays generated from a solid target when irradiated by KrF pulses. A multichannel analyzer with 1-ns resolution provides temporal discrimination between "prompt" ( $< 1 \text{ ns}$  delay) and delayed x rays. Spectral discrimination is provided by the set of different thin-foil filters described above.

The zero-time fiducial measurement is made each time a new experimental configuration is used, and checked often between experimental runs. A typical 200-shot zero-time fiducial measurement using the fast MCP detector establishes the  $t_0$  (prompt) bin of the multichannel analyzer with a FWHM of  $1.4 \text{ ns}$ , which is indicative of the temporal resolution of the photon counting system electronics. Background calibrations of both types of detectors at a variety of solid

angles were obtained at a background target chamber pressure of  $1 \times 10^{-7}$  Torr, for a total of  $3.4 \times 10^4$  laser shots. The background count rate is found to be  $0.3$  per  $10^3$  shots for the fast MCP and  $< 0.7$  per  $10^3$  shots for the slower MCP/phosphor/PMT, regardless of filter used.

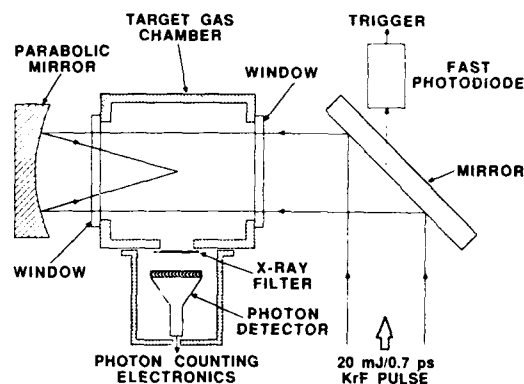


Figure 1. Schematic of experiment. The vacuum on the detector side is maintained at  $\sim 10^{-7}$  Torr while the target chamber gas pressure can be varied between  $3 \times 10^{-8}$  to  $0.3$  Torr. The thin x-ray filter serves as a vacuum window as well as a uv (5 eV laser photons) shield. Photon counting data are accumulated by a 1024-channel multichannel analyzer with 1-ns resolution.

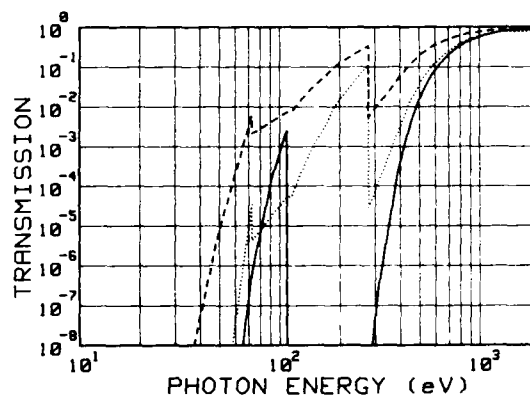


Figure 2. Transmission of thin-foil filters used in the experiments. Dashed line: Filter-1 ( $1 \mu\text{m}$  Parylene +  $0.1 \mu\text{m}$  Aluminum); dotted line: Filter-2 ( $2 \mu\text{m}$  Parylene +  $0.2 \mu\text{m}$  Aluminum); solid line: Filter-3 ( $5 \mu\text{m}$  Beryllium). The experimental results indicate that the energy range immediately below the Be K-edge ( $111 \text{ eV}$ ) is the region where delayed photons are observed.

## RESULTS & DISCUSSION

Four photon counting experiments using the fast (FWHM = 1.4 ns) MCP and Xe gas at 0.124 Torr gave the following results:

1) With the detector subtending a solid angle  $\Omega$  of  $7.85 \times 10^{-3}$  Sr and using Filter-1, a  $1.2 \times 10^4$ -shot run produced a total of 60 counts between the zero to 1000 ns bins. For this run, the earliest count was recorded at 6 ns after the  $t_0$  fiducial. We note that there are many delayed photons but no prompt ones. The 1000 Å of aluminum on the filter serves as a uv shield; in its absence the detector would record scattered 5 eV laser photons at  $t_0$  from every laser shot.

2) At  $\Omega = 7.85 \times 10^{-3}$  Sr with Filter-3, a  $2.8 \times 10^4$ -shot run recorded a total of 69 counts. Again there are delayed photons, with the earliest count recorded at 2 ns after  $t_0$ .

3) Using Filter-1 and changing to a larger solid angle ( $\Omega = 2 \times 10^{-2}$  Sr), a  $1.2 \times 10^4$ -shot run recorded 120 counts, with the earliest count occurring at 3 ns after  $t_0$ .

4) At  $\Omega = 2 \times 10^{-2}$  Sr with Filter-2, a  $10^4$ -shot run provided only 3 delayed counts, which, incidentally, is the background count rate. This means that the delayed photons are practically not transmitted through Filter-2.

From the experimental results, we note the following: Filter-1 is more transmissive (by more than a factor of 2) than Filter-3, while Filter-2 is not transmissive. The count rate peaks at  $\sim 8$  ns after  $t_0$  followed by a gradual decay over several hundred nanoseconds. A typical count histogram is shown in Figure 3.

With the null result of prompt photons in Experiments 1 to 3 described above, we can estimate an upper limit for the probability (P) that a prompt x ray will be generated in a Xe atom by either the multiphoton inner-shell excitation or bremsstrahlung mechanism. The number density of Xe atoms at 0.124 Torr is  $4.38 \times 10^{15} \text{ cm}^{-3}$  and the focal volume (focal spot area  $\times$  Rayleigh range) is  $\sim 100 \mu\text{m}^3$ ; hence, there are  $N = 4.38 \times 10^5$  atoms in the focal volume. The detector solid angle is  $\Omega = 7.85 \times 10^{-3}$  Sr (we will use the smaller value for a conservative estimate). A filter transmission of  $T = 10^{-3}$  is assumed (again being conservative, since P will be smaller if T is larger), and the MCP efficiency for sub-keV photons is  $\eta \sim 0.1$ . The total number of shots was  $N_s = 5.2 \times 10^4$ .

Folding in all these parameters we arrive at an upper limit for P:

$$P < (N_s \Omega T \eta)^{-1} = 5.6 \times 10^{-5}.$$

The probability of quivering electrons producing bremsstrahlung can be estimated from the thermal bremsstrahlung emission formula:

$$\epsilon = 1.4 \times 10^{-27} \sqrt{T_e} n_e n_i Z^2 g_B \text{ (erg s}^{-1} \text{ cm}^{-3}\text{)}$$

where  $g_B$  is a frequency average of the velocity averaged Gaunt factor. Using reasonably high electron densities ( $n_e > n_i$ ),  $Z \sim 10$ , and an unrealistically large electron temperature (i.e.,  $T_e$  corresponding to peak electron quiver energy of 1 keV) still yields negligible values of  $\epsilon$ . Since the filters do not transmit any photons with energy less than  $\sim 50$  eV, we may say that at  $I \sim 3 \times 10^{17} \text{ W/cm}^2$  of KrF light, there are no measurable prompt photons of energy  $> 50$  eV, regardless of the generating mechanism.

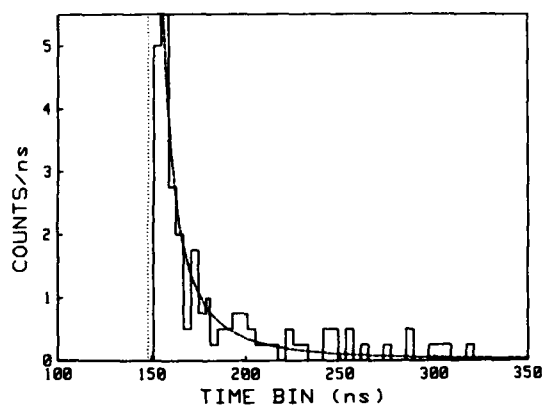


Figure 3. A typical count histogram displaying channels 100 to 350. This was recorded from a  $1.2 \times 10^4$ -shot run with Xe gas at 0.124 Torr using the fast MCP detector at a solid angle of  $\Omega = 2 \times 10^{-2}$  Sr and the compound filter of 1  $\mu\text{m}$  Parylene + 1000 Å Aluminum. The dotted line marks the  $t_0$  fiducial, i.e., the time at which prompt x rays should arrive. The earliest count for this run was recorded at 3 ns after  $t_0$ . Common to all the data, no prompt counts were recorded and peak count rate occurred at  $\sim 8$  ns after  $t_0$ . Although the multichannel analyzer has 1-ns resolution, this histogram is bin-averaged (4 ns-wide bin) for easier visualization. The model constant/ $[1 + (t - t_p)/\tau]^2$ , with  $\tau \sim 15$  ns gives the best fit (dashed curve) to the "decay" of count rate with respect to time.

On the other hand, the probability of generating a delayed photon per atom in the focal volume is  $\sim 10^{-2}$ , as derived from our measurements. The energy of the delayed photons can be determined by noting that Filter-1 is more transmissive than Filter-3, while Filter-2 does not transmit the delayed photons. Examining Figure 2, we find that such a condition can only be satisfied in the energy range of 80-110 eV. We need to point out, however, that the transmission values of thin foils below  $\sim 70$  eV are not well characterized and subject to great uncertainty. In any case, we can conservatively claim that the delayed photons are in the energy range below 110 eV.

From the experimental results, we believe that delayed photons are generated by "collisional" processes, e.g., recombination of electrons with the more highly stripped ions, or charge exchange between these ions and lower charge-state ions or neutrals. In both instances the relaxation of excited states could produce the observed photons. However, these mechanisms are convolved with the expansion and cooling of the laser-atom interaction region, so that the detailed processes are not easily unraveled. An additional experimental detail is provided to emphasize this point. The previously described Experiment 3 which recorded 120 counts provides reasonable statistics for a curve to be fit to the "decaying" portion of the count histogram. The best fit for the decay rate is obtained not with an exponential which would be expected if charge exchange were the dominant mechanism, but a curve with the functional form which is characteristic of radiative recombination, i.e.,  $[1+(t-t_p)/\tau]^{-2}$ , where  $t_p$  is the time bin of peak count rate, and  $\tau \sim 15$  ns the value of best fit (see Figure 3). However, the rate constant  $\kappa$  derived from using the upper limit of  $n_1 \leq 4.4 \times 10^{15} \text{ cm}^{-3}$  and the curve-fitted value of  $\tau$  gives  $\kappa \sim (n_1 \tau)^{-1} \geq 1.5 \times 10^{-8} \text{ cm}^3/\text{s}$ , which is too large (by orders of magnitude) compared to computed values of rate constants for radiative recombination in uniform plasmas. In another experiment a  $10^4$ -shot run using the MCP/phosphor/PMT detector at  $\Omega = 3.75 \times 10^{-2}$  Sr, with the  $5 \mu\text{m}$  Be filter and Xe at 0.124 Torr, produced a total of 141 counts. Again the best fit to the "decaying" portion of the histogram is a radiative-recombination-type function, but the rate constant derived from the fit is again too large compared to computed

values. These results clearly indicate that the generation of delayed photons is not a simple process. In any case, we are certain that delayed photons are not generated by collisionless multiphoton processes.

## CONCLUSION

In conclusion, based on the results of detecting no prompt photons, we believe that even if the mechanism of laser driven coherent outer-shell oscillation were possible, it is not capable of inducing inner-shell excitation at  $I \sim 3 \times 10^{17} \text{ W/cm}^2$ . Perhaps the mechanism will become effective at significantly higher irradiances ( $I \gg 10^{17} \text{ W/cm}^2$ ) and significantly shorter pulses ( $\ll 1$  ps), but this remains to be seen.

## ACKNOWLEDGEMENT

We gratefully acknowledge the contributions of S. Harper, A. Taylor, and J. Roberts for operating LABS; K. Stetler for technical assistance; and L. Jones and Prof. H. Griem for useful discussions. This work was performed under the auspices of U.S. Department of Energy under contract W-740-ENG-36.

## REFERENCES

1. K. Boyer and C. K. Rhodes, Phys. Rev. Lett. 54, 1490 (1985).
2. P. Lambropoulos, Phys. Rev. Lett. 55, 2141 (1985).
3. G. Wendin, L. Jönsson, and A. L'Huillier, Phys. Rev. Lett. 56, 720 (1986).
4. L. C. Biedenharn, G. C. Baldwin, K. Boyer, and J. C. Solem, AIP Conf. Proc. No. 146, 52 (1986), New York. G. A. Rinker, J. C. Solem, and L. C. Biedenharn, AIP Conf. Proc. No. 160, 75 (1987), New York.
5. P. Dyer, J. A. Bounds, R. C. Haight, and T. S. Luk, Proc. SPIE, Vol. 875. "Short and Ultrashort Wavelength Lasers" (C. R. Jones, Ed.), p. 88, January (1988), Los Angeles, CA.
6. J. P. Roberts, A. J. Taylor, P. H. Y. Lee, and R. B. Gibson, Optics Lett. 13, 734 (1988).
7. B. Henke, P. Lee, T. J. Tanaka, R. L. Shimabukuro, and B. K. Fujikawa, Atomic Data and Nuclear Data Tables, Vol. 27, No. 1, Academic Press, New York (1982).

## Characteristics of a Non-Equilibrium Picosecond Laser Plasma

G. Gibson, R. Rosman, T. S. Luk, I. A. McIntyre, A. McPherson,  
G. Wendin,<sup>†</sup> K. Boyer, and C. K. Rhodes

*Laboratory for Atomic, Molecular, and Radiation Physics, Department of Physics  
University of Illinois at Chicago, P.O. Box 4348, Chicago, Illinois 60680*

### Abstract

VUV spectra of a highly ionized argon plasma produced by a high-power subpicosecond laser are analyzed to determine the electron temperature. The calculated electron temperature is too low to support the highest observed charge state, showing the plasma charge state distribution to be out of Saha equilibrium.

### Introduction

Unusual states of highly ionized plasmas can be generated over a wide range of electron densities with the use of high-power subpicosecond ultraviolet lasers. Plasmas created by such means should have characteristics quite different from those produced by traditional techniques involving current-pinches or laser radiation in the much longer nanosecond time regime. Generally, the conventional approaches involve electron collisions over a considerable time period (e.g.  $\sim 10^{-9}$  sec) as the main mechanism producing the higher charge states. Consequently, this process often can be well described in thermodynamic terms. In contrast, plasmas produced by multi-photon ionization on a subpicosecond time scale involve a high level of ionization, low electron heating, negligible ion heating, and insignificant heavy-body hydrodynamic motion. This type of plasma is perfectly suited to recombination laser schemes: the low electron temperature leads to rapid recombination, the low ion temperature reduces doppler broadening, and, most importantly, the initial charge state distribution can be substantially out of thermal equilibrium.

This work presents VUV spectra of argon plasmas produced by a high power subpicosecond ultraviolet laser over a wide range of laser power (10–300 GW) and electron density ( $2 \times 10^{19}$  –  $2 \times 10^{20}$  cm<sup>-3</sup>). Most of the observed spectral

lines can be identified from Ar<sup>5+</sup>, Ar<sup>6+</sup>, and Ar<sup>7+</sup> as well as a doublet from Ar<sup>8+</sup>. From the Ar<sup>7+</sup> spectrum an electron temperature can be deduced by comparing the line intensities to calculated values. A value of 20 eV is obtained and found to be inconsistent with the observed Ar<sup>8+</sup> radiation.

### Experiment

As the laser, target, and spectrometer used in this experiment have been described in detail elsewhere [1,2,3,4], only a brief summary is presented here. Subpicosecond pulses at 745 nm are extracted from a hybridly mode-locked dye laser. These pulses are frequency tripled to 248 nm, pre-amplified by a commercial KrF\* excimer and spatially filtered. The pulses are then amplified by 1) a second commercial excimer to 10–20 mJ and focused with an F/14 spherical lens to a peak intensity  $\sim 10^{16}$  Wcm<sup>-2</sup> or 2) the Prometheus amplifier system [4] to  $\sim 300$  mJ and focused with an F/15 spherical lens to an estimated peak intensity of  $\sim 5 \times 10^{16}$  Wcm<sup>-2</sup>. The rather small increase in peak intensity for the more powerful beam is due to severe spherical aberration in the F/15 focusing lens. The target is produced by a pulsed valve giving densities of  $2 \times 10^{18}$  –  $2 \times 10^{19}$  cm<sup>-3</sup>. The radiation is observed by a McPherson grazing incidence spectrometer recording from 25–750 angstroms. The spectrometer was calibrated with a HeNe discharge lamp and fluorescence lines to an absolute accuracy of  $\pm 0.3$  angstroms.

### Results

Fig. 1 shows a typical region of the spectrum produced by the 10 GW beam with identified transitions from various charge states as well as some possible new identifications. Almost all the lines were identified from published results for the Ar<sup>1+</sup>, Ar<sup>2+</sup>, Ar<sup>3+</sup>, Ar<sup>4+</sup>, and Ar<sup>7+</sup> spectra [5,6,7,8].





from  $\text{Ar}^{8+}$  to  $\text{Ar}^{7+}$  was neglected [12] because of the closed shell structure of  $\text{Ar}^{8+}$ . Rate coefficients were obtained from a variety of sources [9,13,14].

The plasma electron temperature was calculated by comparing ratios of experimental line intensities for isolated transitions in the  $\text{Ar}^{7+}$  spectrum with numerical predictions of the plasma model. The results are shown in Fig. 4. Since the model had no free parameters, except the electron temperature and initial charge state distribution, the agreement between the data and the model for a temperature of 20 eV is remarkable. The discrepancy for the  $\text{Ar}^{7+}(3d-4f)$  transition could be explained by its wavelength as it is rather different from the other transitions and so could be susceptible to systematic errors in the spectrometer. It is also possible that other processes are playing a role in determining the emission from this level. Further study of this matter is required. This value of 20 eV compares well with an electron spectrum taken with the 10 GW laser beam under collision free conditions at a somewhat lower intensity [15]. The data are shown in Fig. 5 and suggest an average electron kinetic energy of about 20 eV for the highest charge states. This would imply that no additional electron heating occurs in the gas target at the densities used in the present experiment.

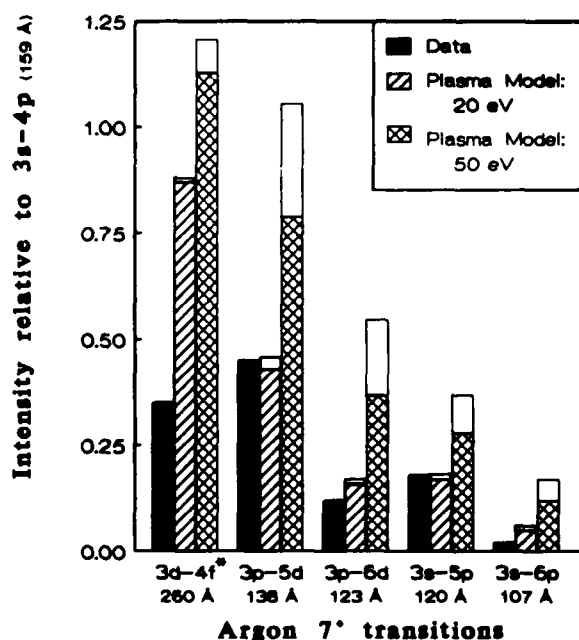


Fig. 4. Line intensities for selected  $\text{Ar}^{7+}$  lines normalized to the  $\text{Ar}^{7+}(3s-4p)$  transition. Open regions in the bar correspond to varying the initial conditions in the plasma model. \*All  $3d-4f$  intensities are divided by 10.

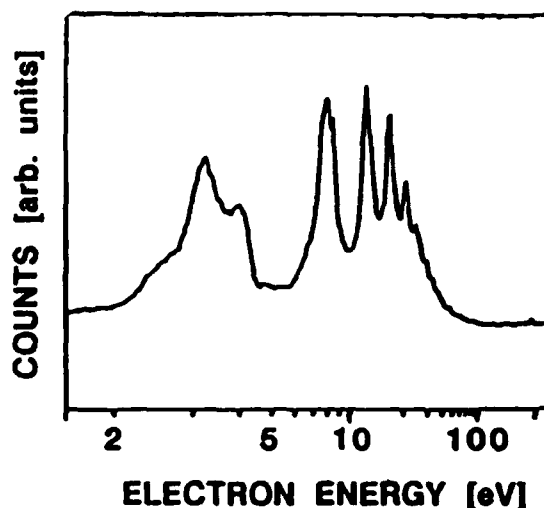


Fig. 5. Electron energy spectrum for argon at  $7 \times 10^{15} \text{ Wcm}^{-2}$ , from Ref. 15.

In addition to determining the electron temperature, the plasma model can predict the density dependence of the  $\text{Ar}^{7+}$  transitions. The results of the calculations and the experimental data from the 300 GW beam are compared in Fig. 6. Besides an overall scaling factor, the model had no free parameters except the electron temperature determined previously. However, one additional effect needed to be considered in order for the model to match the observed pressure dependence [10]. The spectral data are time integrated and, hence, the line intensities

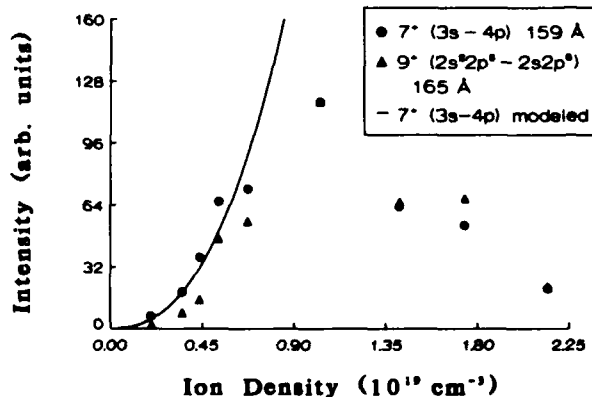


Fig. 6. Pressure dependences of various lines, both experimental (300 GW beam) and modeled ( $T_e = 20 \text{ eV}$ ). Turn over at higher densities is due to non-resonant absorption of the fluorescence by the surrounding gas.

depend on the lifetime of the plasma. The lifetime of the plasma, in turn, depends on the cooling rate of the plasma. Under these conditions, electron conduction cooling is the dominant cooling mechanism. As the thermal conductivity is inversely proportional to gas density, the lifetime of the plasma will be directly proportional to the gas density. Taking this effect into account, the plasma model correctly predicts the density dependence of the  $\text{Ar}^{7+}(3s-4p)$  transition. Thus, the line radiation from  $\text{Ar}^{7+}$  is consistent with a collisional-radiative model with an electron temperature of  $\sim 20$  eV.

The  $\text{Ar}^{3+}$  line in Fig. 6 is similar to the  $\text{Ar}^{7+}$  line in that it is a ground state transition and has about the same excitation energy [6,8] and transition probability [9]. Thus, it is not surprising that it has a similar density dependence. However, the origin of the  $\text{Ar}^{3+}$  ions is not so clear. Although they could have been produced by multi-photon ionization, preliminary ion measurements with the same laser system and focusing lens did not detect any  $\text{Ar}^{3+}$  ions [16]. On the other hand, an electron density of  $5 \times 10^{19} \text{ cm}^{-3}$  and temperature of 20 eV cannot support  $\text{Ar}^{3+}$  in Saha equilibrium [14]. The ratio of  $\text{Ar}^{3+}$  to  $\text{Ar}^{7+}$  ions under these conditions would be less than  $10^{-5}$ . Thus, 20 eV is not a high enough temperature to substantially ionize  $\text{Ar}^{3+}$ . The  $\text{Ar}^{3+}$  radiation could have been produced earlier in time at a higher temperature. However,  $\text{Ar}^{3+}$  radiation would have been produced at the same time, and none was observed. Alternatively, the  $\text{Ar}^{3+}$  ions may be in a different region of space, perhaps at a higher temperature. The region of  $\text{Ar}^{3+}$  is most likely surrounded by  $\text{Ar}^{7+}$  and calculations of electron conduction cooling [10] show that spatial variations in temperature rapidly decay. The electrons in the  $\text{Ar}^{3+}$  region would quickly equilibrate with the surrounding electrons.

The most consistent explanation is that the laser pulse creates a plasma, through a process not yet understood, containing  $\text{Ar}^{7+}$ ,  $\text{Ar}^{3+}$ , and  $\text{Ar}^{2+}$  with an initial electron temperature of 20 eV. This temperature can excite the  $\text{Ar}^{7+}$  states, the first excited state of  $\text{Ar}^{3+}$ , but nothing in  $\text{Ar}^{2+}$ . This situation is consistent with all the experimental and calculated results presented in this paper and shows that it is possible to create a higher charge state than can be supported in Saha equilibrium.

## Conclusion

VUV spectra of a highly ionized argon plasma produced by a high power subpicosecond laser are presented along with calculations from a plasma model. Comparison of the two show that the observed  $\text{Ar}^{7+}$  radiation is fully consistent with a collisional-radiative model of the plasma with an electron temperature of 20 eV. Furthermore, comparing this electron temperature with a collision-free electron energy spectrum shows that little additional heating of the electrons occurred in the dense gas target. Finally, observation of  $\text{Ar}^{3+}$

radiation indicates that the charge state distribution is not in Saha equilibrium as the electron temperature and density of the plasma can not support the  $\text{Ar}^{3+}$  charge state.

## Acknowledgements

The authors would like to thank J. Peek for providing the Cowan code and indispensable help in implementing it, and P. Noel, R. Slagle, and J. Wright for their technical assistance. This work was supported by AFOSR, LLNL, ONR, NSF, and SDI.

† permanent address: Institute of Theoretical Physics, Chalmers Institute of Technology, Fysikgränd 3, S-412 90 Göteborg, Sweden

## References

1. A. McPherson, G. Gibson, H. Jara, U. Johann, T. S. Luk, I. A. McIntyre, K. Boyer and C. K. Rhodes, "Studies of Multiphoton Production of Vacuum Ultraviolet Radiation in the Rare Gases," *J. Opt. Soc. Am.* **B4**, 595 (1987).
2. C. K. Rhodes, "Physical Processes at High Field Strengths," *Physica Scripta*, **T17**, 193 (1987).
3. A. P. Schwarzenbach, T. S. Luk, I. A. McIntyre, U. Johann, A. McPherson, K. Boyer and C. K. Rhodes, "Subpicosecond KrF\* Excimer-Laser Source," *Optics Letters* **11**, 499 (1986).
4. I. A. McIntyre, T. S. Luk, G. Gibson, H. Jara, A. McPherson, X. J. Pan, K. Boyer and C. K. Rhodes, "Ultrahigh Intensity KrF\* Laser," to be submitted to *Optics Letters*.
5. I. Lesteven-Vaïsse, M. Chantepie, J. P. Grandin, D. Hennecart, X. Husson, D. Leclerc, J. P. Buchet, M. C. Buchet-Poullizac, J. Desesquelles, and S. Martin, "VUV Spectra of Multicharged Recoil-Ions: Neon and Argon," *Physica Scripta* **34**, 138 (1986).
6. R. L. Kelly and L. J. Palumbo, "Atomic and Ionic Emission Lines Below 2000 Å," N.R.L. Report 7599 (1973).
7. B. C. Fawcett, A. Ridgeley and G. E. Bromage, "The Spectrum ArIX and Extended Spectral Classification in ArV to ArVIII and ArX," *Physica Scripta* **18**, 315 (1978).
8. R. Engleman, Jr., D. B. Thomson and D. A. Monaghan, "Vacuum Ultraviolet Emission from Argon, Krypton, and Xenon in a Radial-Viewed Theta Pinch," LANL Report LA-6275-MS (1976).
9. R. D. Cowan, *The Theory of Atomic Structure*

and Spectra (University of California Press, Berkeley, 1981) and J. Peek, private communication.

10. G. Gibson, et al., "Recombination Lasers Using Multiphoton Ionization," to be submitted.
11. D. R. Bates, A. E. Kingston, and R. W. P. McWhirter, "Recombination between Electrons and Atomic Ions," *Proc. Roy. Soc. A*267, 297 (1962).
12. J. M. Shull and M. van Steenberg, "The Ionization Equilibrium of Astrophysically Abundant Elements," *Astrophys. J. Suppl. Ser.* 48, 95 (1982).
13. R. U. Dalta, H.-J. Kunze, and D. Petrini, "Collisional-Rate Coefficients for Sodiumlike ArVIII Ions," *Phys. Rev. A*6, 38 (1972).
14. H. R. Griem, Plasma Spectroscopy (McGraw-Hill, New York, 1964).
15. U. Johann, T. S. Luk, I. A. McIntyre, A. McPherson, A. P. Schwarzenbach, K. Boyer and C. K. Rhodes, "Multiphoton Ionization in Intense Ultraviolet Laser Fields," in Proceedings of the Topical Meeting on Short Wavelength Coherent Generation, ed. D. T. Attwood and J. Bokor, AIP Conference Proceedings No. 147 (AIP, New York, 1986) p. 202.
16. T. S. Luk, private communication.

# Investigations of Multiphoton Excitation and Ionization in a Short Range Potential

S. M. Susskind, S. C. Cowley, and E. J. Valeo

*Princeton University, Plasma Physics Laboratory  
P.O. Box 451, Princeton, New Jersey 08543*

## Abstract

We introduce an approach to the study of excitation and ionization for a system containing a model confining potential consisting of a set of  $\delta$ -functions. In particular, analytical and numerical results are presented for the multiphoton ionization rate, under strong field conditions, of an electron confined by a  $\delta$ -function potential.

## 1 Introduction

Recently, there has been an increase of interest in the study of methods to calculate the excitation and ionization of atoms in the presence of strong electromagnetic fields. This interest stems from the availability in the laboratory of very powerful lasers capable of delivering a focused intensity on the order of and beyond the typical intensity felt by an electron in the atom ( $\sim 10^{16}$  Watt/cm<sup>2</sup>). Such strong fields make the problem of calculating rates non-perturbative in character whereas traditional methods which are based on a perturbation expansion in the applied field over the atomic field,  $F/F_{\text{atom}}$ , are of limited applicability.

In many of the experiments the photon energy  $\omega$  (we adopt atomic units everywhere) is much smaller than the typical ionization potential  $I_p$  (or the typical energy difference between the atomic levels of interest,  $\Delta E$ ). For instance, for a CO<sub>2</sub> laser  $\omega \sim 0.1$  eV and for a Nd laser  $\omega \sim 1$  eV but ionization potentials are usually tens of eV. Clearly, one way to proceed is to formulate a theory in which  $\omega/I_p$  (or  $\omega/\Delta E$ , for excitation) is treated as small[1]. Note that, for small fields,  $I_p/\omega$  ( $\Delta E/\omega$ ) is roughly the number of photons involved in the ionization (ex-

citation). This type of approach was pioneered by Keldysh[2], who studied the ionization of a hydrogen atom. Perelomov, Popov and Terentev[3] in an alternative way studied the ionization of an electron from a  $\delta$ -function potential. Several authors[4, 5] have studied the excitation of a two-level system when  $\omega/\Delta E$  is considered a small parameter. Non-perturbative methods should eventually provide a way of studying the competition between excitation and ionization and understanding the possibility of obtaining in the laboratory population inversions due to multiphoton pumping, between levels with an energy difference in the X-ray region[6].

In recent experiments on the ionization of atoms the outgoing electron was analyzed in energy[7, 8]. Several features like ponderomotive corrections to the ionization potential and above-threshold ionization, where the electron absorbs more than the minimum number of photons necessary for ionization, were observed. These features were already predicted qualitatively in the above-mentioned approaches.

The purpose of the present work is to examine some aspects of the strong field, many photon limit in a class of models that represent the atom (or energy levels of interest) with model potentials consisting of a sum of  $\delta$ -functions. The analytic results given here are derived using a new method which is asymptotically correct when the number of photons goes to infinity. The results are quite good, however, for a few photons. We compare some analytic results with direct numerical integration of the equations. The agreement is good.

## 2 The Model

We will represent our atom by the following binding potential:

$$V(x) = - \sum_{i=1}^M B_i \delta(x - x_i). \quad (1)$$

$V(x)$  is clearly a short-range potential and has the following properties: 1) The number of bound states that it can have lies between 1 and  $M$  (number of  $\delta$ -functions). 2) It has a continuum spectrum for all energies above zero. 3) By adjusting the parameters  $B_i$  and  $x_i$  we can make the energy levels of the model coincide with any  $M$  levels of a real atom we are interested in studying. We will concentrate here in presenting our numerical and analytical results for the simplest potential of this class, the one  $\delta$ -function potential ( $M=1$ ), studied by Perelomov *et al.* This potential has one bound state and a continuum and hence will allow us to study ionization. Detailed derivations of the formulas will be presented elsewhere. We will also relegate the study of the next simpler member of the class of potentials (1),  $M=2$ , in which already the competition between excitation and ionization can be studied, to a future publication[9].

## 3 Multiphoton Ionization in a Delta function potential

### 3.1 Analytical Treatment

We are going to study, then, an electron bound by the potential

$$V(x) = -B\delta(x). \quad (2)$$

This potential has only one bound state, of energy  $-B^2/2$  ( $I_p = B^2/2$ ), where the electron is going to be at  $t = 0$ . We will subject this system to the linearly polarized field (we choose to work in the  $F \cdot x$  gauge)

$$V_{ext} = Fx \cos(\omega t), \quad (3)$$

$F$  is the amplitude of the applied field (all the expressions will be given in atomic units). Schrödinger's equation for this system is then

$$i \frac{\partial \psi(x, t)}{\partial t} = -\frac{1}{2} \frac{\partial^2 \psi(x, t)}{\partial x^2} - B\delta(x) \psi(x, t) + Fx \cos(\omega t) \psi(x, t). \quad (4)$$

It proves to be more convenient to work with the following integral form of Eq. (4).

$$\psi(x, t) = \psi_0(x, t) - \frac{i^{1/2}}{\sqrt{2\pi}} \int_0^t \frac{dt'}{\sqrt{(t-t')}} \int_{-\infty}^{\infty} dx'$$

$$\times \exp[iS_{cl}(x, t; x', t')] V(x') \psi(x', t'). \quad (5)$$

The inhomogeneous term is the wavefunction  $\psi_0(x, t)$  which coincides with the bound state at  $t = 0$  and which at later times evolves with the hamiltonian of the electron in the external field only.  $\exp(iS_{cl})/\sqrt{2\pi i(t-t')}$  is the Green's function[10] for, and  $S_{cl}(x, t; x', t')$  is the classical action of, an electron subject to the potential (3) which starts at  $x', t'$  and ends at  $x, t$ . In our case  $V(x')$  is given by Eq. (2) and then the  $x'$  integral is straightforward. Specializing the equation to  $x = 0$  we obtain an integral equation, now in time only, for  $\chi(t) = \psi(0, t)$ :

$$\chi(t) = \chi_0(t) + \frac{i^{1/2}B}{\sqrt{2\pi}} \int_0^t \frac{dT}{\sqrt{T}} e^{iS(t, t-T)} \chi(t-T), \quad (6)$$

where  $S(t, t-T) = S_{cl}(0, t; 0, t-T)$  and is given by

$$S(t, t-T) = \frac{1}{2T} [x_0(t) - x_0(t-T)]^2 - \frac{1}{2} \int_{t-T}^t \dot{x}_0^2(\tau) d\tau. \quad (7)$$

$x_0(t)$  is the classical position of an electron subject to the external field only.

Note that we have eliminated in this way the space dependence from the problem. From the solution  $\chi(t)$  of Eq. (6), we can reconstruct  $\psi(x, t)$  by means of Eq. (5). However, this is unnecessary for computing the ionization rate.

We look for a solution of the integral equation (6) in the eikonal form

$$\chi(t) = \exp\left[i \int_0^t \Omega(\tau) d\tau\right], \quad (8)$$

where  $\text{Re } \Omega(\tau)$  is the eigenvalue of the bound state plus its a.c. shift and  $\text{Im } \Omega(\tau)$  is half of the instantaneous ionization rate. With this form of the solution we can calculate, basically by a steepest descents method in the complex  $T$ -plane, the time-averaged ionization rate  $w$ . The assumptions used in the derivation are that the number of photons be large,  $B^2/2\omega \gg 1$ , and at the same time  $\gamma^2 \ll$  number of photons, where  $\gamma = \omega B/F$  is Keldysh's parameter. The result is

$$w = \frac{2}{\pi} \gamma^2 F \sum_{p \geq \nu} k_p^{-1} [\beta^2 + \frac{4k_p^2 \gamma^4}{B^2}]^{-1/4} \times \exp\left\{ \frac{B^2}{\omega} \left[ \left(1 + \frac{k_p^2}{B^2} + \frac{1}{2\gamma^2}\right) v_0 + \frac{1}{2\gamma} \left(-\frac{3k_p}{B} v_1 - u_1\right) \right] \right\} \times \left\{ 1 + (-1)^p \cos\left\{ \frac{B^2}{\omega} \left[ \left(1 + \frac{k_p^2}{B^2} + \frac{1}{2\gamma^2}\right) u_0 + \frac{1}{2\gamma} \left(\frac{3k_p}{B} u_1 + v_1\right) + \frac{1}{2} \arctan\left(\frac{2k_p \gamma^2}{B\beta}\right) \right] \right\} \right\}, \quad (9)$$

where the  $u_0, v_0$  have the following definitions:

$$\begin{aligned} u_0 &= \arccos \sqrt{\frac{\alpha}{2} + \sqrt{\frac{\alpha^2}{4} + \gamma^2}}, \\ v_0 &= \operatorname{arcsinh} \sqrt{-\frac{\alpha}{2} + \sqrt{\frac{\alpha^2}{4} + \gamma^2}}, \end{aligned} \quad (10)$$

with  $\alpha$  defined by

$$\alpha = 1 - \gamma^2 - \frac{k_p^2 \gamma^2}{B^2}, \quad (11)$$

$u_1, v_1$  defined by

$$\begin{aligned} u_1 &= \sqrt{\frac{\beta}{2} + \sqrt{\frac{\beta^2}{4} + \frac{k_p^2 \gamma^4}{B^2}}}, \\ v_1 &= -\sqrt{-\frac{\beta}{2} + \sqrt{\frac{\beta^2}{4} + \frac{k_p^2 \gamma^4}{B^2}}}, \end{aligned} \quad (12)$$

and  $\beta$  defined by

$$\beta = 1 + \gamma^2 - \frac{k_p^2 \gamma^2}{B^2}. \quad (13)$$

$k_p^2/2$  is the kinetic energy of the electron ejected by absorbing  $p$ -photons which satisfies the energy conservation relation

$$-\frac{B^2}{2} - \frac{F^2}{4\omega^2} + p\omega = \frac{k_p^2}{2}. \quad (14)$$

$-B^2/2$  is the ionization potential of the atom in the absence of the external field,  $-F^2/4\omega^2$  is the correction to the ionization potential due to the field, the so-called ponderomotive shift.

The sum in formula (9) expresses the fact that the rate is a sum of processes involving the absorption of an integer number  $p$  of photons, where  $p \geq \nu \equiv B^2/2\omega + F^2/4\omega^3$ . This is the so-called above-threshold ionization[7, 8].

If we expand Eq. (9) up to  $k_p^2/B^2$ ; that is, to first order in the kinetic energy of the ejected electron over the 'bare' ionization potential, we obtain the expression for  $w$  due to Perelomov, Popov and Terentev[3]:

$$\begin{aligned} w &= \frac{2F}{\pi} \frac{\gamma^2}{(1 + \gamma^2)^{1/2}} \\ &\times \exp \left\{ -\frac{B^2}{\omega} \left[ \left(1 + \frac{1}{2\gamma^2}\right) \operatorname{arcsinh} \gamma - \frac{1}{2\gamma} \sqrt{1 + \gamma^2} \right] \right\} \\ &\times \sum_{p \geq \nu}^{\infty} \left[ 1 + (-1)^p \cos \left( \frac{2Bk_p}{\omega\gamma} \sqrt{1 + \gamma^2} \right) \right] \\ &\times \frac{1}{k_p} \exp \left[ \frac{k_p^2}{\omega} \left( \frac{\gamma}{\sqrt{1 + \gamma^2}} - \operatorname{arcsinh} \gamma \right) \right]. \end{aligned} \quad (15)$$

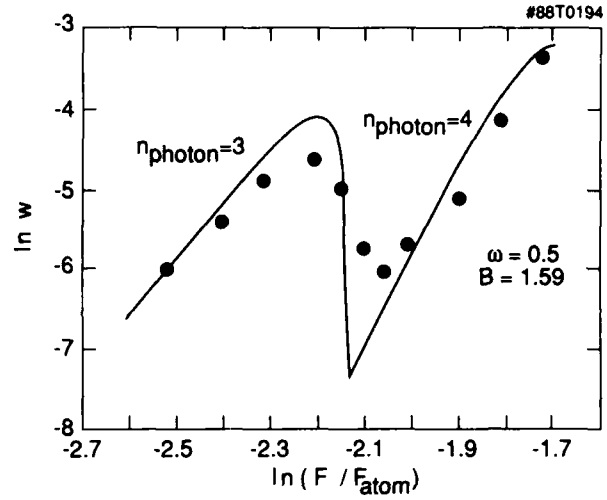


Figure 1: Log-log plot of the ionization rate versus the relative field.

The two formulas, Eqs. (9) and (15), are qualitatively the same but differ substantially in cases where the higher terms beyond the first are important; that is towards the tunneling limit in Keldysh's nomenclature ( $\gamma \simeq 1$  or lower).

### 3.2 Numerical Treatment

We have developed a code that solves the integral equation (6), by advancing in time the wavefunction at  $x = 0$ ; that is  $\psi(0, t) = \chi(t)$ . From it, one could reconstruct the wavefunction  $\psi(x, t)$  using Eq. (5). However, we are only interested here in calculating the average ionization rate. The average decay rate of  $|\chi(t)|^2$  is the ionization rate; this can be obtained from a plot of  $\ln|\chi(t)|^2$  versus time. The results obtained from the code are compared with the analytic results of Eq. (9) in Figs. 1 and 3 for a variety of cases. In Fig. 1, the logarithm of the ionization rate  $w$  given by Eq. (9) is plotted against the logarithm of the relative field  $F/F_{\text{atom}}$ . The range of intensities in the graph corresponds in hydrogen to  $1.6 \cdot 10^{14} \text{ W cm}^{-2}$  to  $1.2 \cdot 10^{15} \text{ W cm}^{-2}$ . The atomic field seen by the electron in the bound state of the potential (2) is  $F_{\text{atom}} = B^3$ . We choose for the calculations a value of  $B = 1.59 \text{ a.u.}$ , which corresponds to  $I_p = 1.27 \text{ a.u.}$ . By choosing the photon energy  $\omega = 0.5 \text{ a.u.}$ , we have that the number of photons necessary to reach the continuum is  $[I_p/\omega] + 1 = 3$  for small fields (the notation  $[ ]$  denotes 'integer part of'). As the ponderomotive term  $F^2/4\omega^2$  starts to increase by going to higher field amplitudes, we see a dramatic change in the slope of the log-log curve. This change corresponds

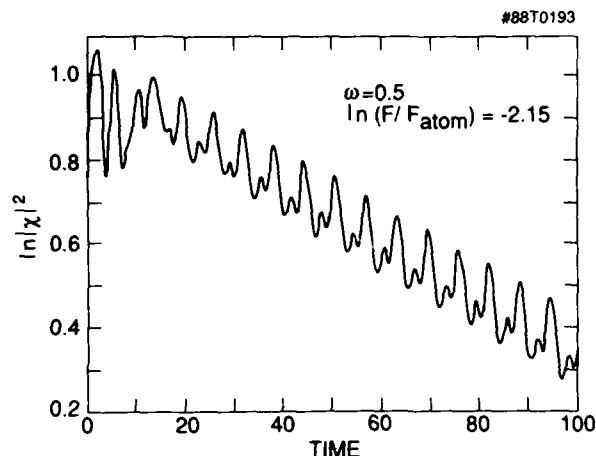


Figure 2: Natural logarithm of the probability of remaining at the origin versus time.

to the transition from a 3-photon process to a 4-photon process because the field is so high that the corrected ionization potential is larger by one photon energy than the 'bare' ionization potential and the system requires one more photon to ionize. One can verify that the two slopes in Fig. 1 are in a 3 to 4 ratio. The dots in the figure indicate the results of a numerical evaluation of the integral equation (5) to obtain  $\chi(t)$ . We determine  $w$  from the average slope of the plot of  $\ln|\chi(t)|^2$  versus  $t$ . An example of this kind of plot is shown in Fig. 2. Each dot in Fig. 1 is determined in this way from the  $|\chi(t)|^2$  versus  $t$  plots for the different values of  $F$ . We can see that the comparison between the asymptotic result and the numerical result is very good, even for the small number of photons involved (remember that the analytical result is better the larger the number of photons).

In Fig. 3, we do the same comparison between analytical and numerical ionization rates but for a photon energy of  $\omega = 0.25$  a.u.. Now, the 'bare' atom needs 7 photons to ionize and, as we can see from the figure, the number of photons needed goes up to 15 for the higher fields in the graph. We can see also a lot of structure due to the change in character, from  $p$  to  $p + 1$  photons, in the ionization with relatively little change in the field. The numerical results reproduce this structure. For the lowest field values, where the ionization rate is so low that an average slope has to be computed over longer running times of the code, the numerical evaluation is inaccurate.

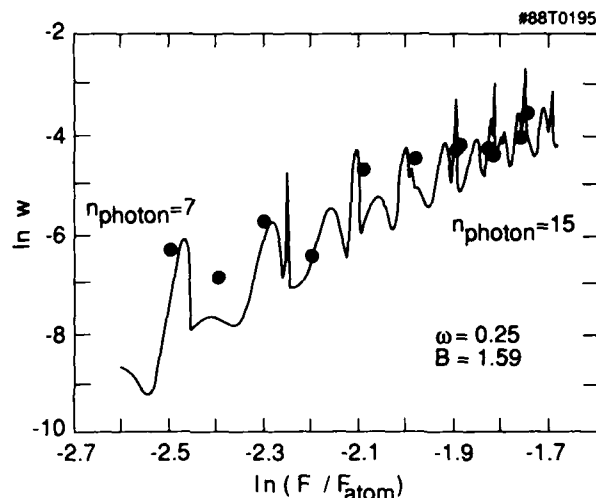


Figure 3: Log-log plot of the ionization rate versus the relative field.

#### 4 Acknowledgments

We thank Carl Oberman and Russell Kulsrud for many useful discussions and Szymon Suckewer for his constant support of this effort. This work was supported by the United States Department of Energy (USDOE), Division of Advanced Energy Projects of the Office of Basic Energy Sciences under Contract No. KC-05-01 and by the USDOE under Contract No. DE-ACO2-76-CHO3073.

#### References

- [1] N. B. Delone and V. P. Krainov, *Atoms in Strong Light Fields* (Springer, Berlin, 1985), Chapter 4.
- [2] L.V. Keldysh, *Zh. Eksp. Teor. Fiz.* **47**, 1945 (1964) [*Sov. Phys. JETP* **20**, 1307 (1965)].
- [3] A.M. Perelomov, V.S. Popov and M.V. Terentev, *Zh. Eksp. Teor. Fiz.* **50**, 1393 (1966) [*Sov. Phys. JETP* **23**, 924 (1966)].
- [4] D.F. Zaretskii and V.P. Krainov, *Zh. Eksp. Teor. Fiz.* **66**, 537 (1974) [*Sov. Phys. JETP* **39**, 257 (1974)].
- [5] R.E. Duvall, E.J. Valeo and C.R. Oberman, *Phys. Rev. A*, **37**, 4685 (1988).
- [6] C. W. Clark, M. G. Littman, R. Miles, T. J. McIlrath, C. H. Skinner, S. Suckewer, and E. Valeo, *J. Opt. Soc. Am. B* **3**, 371 (1986).



- [7] P. Agostini, F. Fabre, G. Mainfray, G. Petite and N.K. Rahman, *Phys. Rev. Lett.*, **42**, 1127 (1979)
- [8] T.J. McIlrath, P.H. Bucksbaum, R.R. Freeman and M. Bashkansky, *Phys. Rev. A*, **35**, 4611 (1987).
- [9] S. M. Susskind, S. C. Cowley and E. J. Valeo, *in preparation*.
- [10] R. P. Feynman and A. R. Hibbs, *Quantum Mechanics and Path Integrals* (McGraw Hill, New York, 1965).

## Multiphoton Spectroscopy of Multielectron Atoms and the Quest for Direct Two-Electron Ejection

P. Lambropoulos

*University of Southern California, Los Angeles, California 90089-0484*

### Abstract

I present a brief review of recent high intensity experiments showing the participation of multiphoton resonances with bound atomic states. The results compare favorably with some of our calculations on rare gases and alkaline earths.

Until about a year ago, it was generally accepted that multiphoton ionization under strong lasers (say above  $10^{12}$  W/cm<sup>2</sup>) were insensitive to the details of atomic structure. Recent experiments<sup>1-4</sup>, however, have shown that, even at intensities as large as  $5 \times 10^{14}$  W/cm<sup>2</sup>, resonance with bound atomic states have a profound effect on the process. Not only does the ionization signal show pronounced enhancement, but the position, width and height of the resonance can be correlated surprisingly well with the properties of specific atomic states.

Consider, for example the results of Landen et al<sup>1</sup>, and Perry and Landen<sup>2</sup> who have reported resonant enhancement via a 3-photon resonance (in 4-photon ionization) with states such as  $4d(J=1)$  and  $4d'(J=3)$  in Kr. From their data, these authors have extracted values for AC Stark shifts and ionization cross sections (for the resonant states), as well as for the 3-photon Rabi frequency between the ground and the resonant state. We have performed calculations for these processes, employing multichannel quantum defect theory (MQDT) which we have recently expanded<sup>5</sup> so as to include states with angular momentum up to  $J=4$ . The resulting values of the atomic parameters for the  $4d(J=1)$  state of Kr are: Photoionization cross section  $4.42 \times 10^{-18}$  cm<sup>2</sup> as compared to the experimental  $8 \times 10^{-18}$  cm<sup>2</sup>, AC Stark shift 639 cm<sup>-1</sup> per  $10^{13}$  W/cm<sup>2</sup>

as compared to the experimental 644.8 cm<sup>-1</sup>, and 3-photon Rabi frequency  $3 \times 10^{-7}$  I<sup>3/2</sup> as compared to the experimental  $2.16 \times 10^{-7}$  I<sup>3/2</sup>. Considering the complexities of both theory and experiment (which can not be discussed in detail here), the agreement is excellent.

The proximity of bound atomic states to multiphoton resonance appears to play a significant role even when resonance structure is not obvious or has not been examined in detail experimentally. I take here as a brief example 6-photon ionization of Xe with radiation of two different wavelengths, namely  $\lambda_1=532$  nm and  $\lambda_2=583$  nm. Measurements<sup>6,7</sup> of the saturation intensity at these wavelengths seems to suggest (after adjusting for differences in pulse duration etc.) that ionization at 532 nm is much more efficient than at 583 nm. A calculation<sup>8</sup> of the relevant 6-photon generalized cross sections reveals that at 532 nm the cross section is of the order of  $10^{-74}$  cm<sup>12</sup> sec<sup>5</sup> while at 583 nm it is of the order of  $10^{-80}$  cm<sup>12</sup> sec<sup>5</sup>. The difference between these two cross sections more or less accounts for the difference between the observed saturation intensities. The reason can be traced to a 5-photon near resonance with the 7s state for 583 nm and with 8d for 532 nm. The 8d has an ionization cross section larger by more than an order of magnitude than the 7s, and the corresponding 5-photon Rabi frequency is more than two orders of magnitude for the 8d. Also the AC Stark shifts play their role in this case.

Further evidence on the influence of bound states shifting through resonance during fast (sub-picosecond) pulses has been provided in very recent experiments by Freeman et al<sup>9</sup> and by Muller et al.<sup>10</sup>

Calculations that we have performed most recently<sup>9</sup> on models with realistic atomic parameters confirm the role of such resonances and suggest an even larger variety of phenomena.

At somewhat lower intensities ( $\sim 10^{12}$  W/cm<sup>2</sup>), experiments<sup>10</sup> on Sr have produced a wealth of experimental data showing resonances not only with intermediate bound states but also with doubly excited bound and autoionizing states. The simultaneous excitation of the electrons above the first threshold has certainly been observed and the absorption of at least one additional photon above the first threshold has also been confirmed. As a result of such additional photon absorptions, the ion (Sr<sup>+</sup>) has been left to excited states such as 4d and 5p. It has, however, been impossible to observe the direct two-electron ejection. It appears that competition from decays into single-electron autoionization channels still dominates<sup>11</sup> at pulses longer than 20 ps or so. With shorter pulses becoming now readily available, it may well be that two-electron ejection will be more favorable, especially if wavelengths producing resonances with selected doubly excited states can be chosen.

#### Acknowledgments

This work was supported by the NSF Grant No. PHY-8609966.

#### References

1. O. L. Landen, M. D. Perry and E. M. Campbell, Phys. Rev. Lett., 59, 2558 (1987).
2. M. D. Perry and O. L. Landen, Phys. Rev. A 38, 2815 (1988).
3. R. R. Freeman, P. H. Bucksbaum, H. Milchberg, S. Darack, D. Schumacher and M. E. Gersic, Phys. Rev. Lett. 59, 1092 (1987).
4. H. G. Muller, H. B. van Linden van den Heuvell, P. Agostini, G. Petite, A. Antonetti, M. Franco and A. Migus, Phys. Rev. Lett. 60, 565 (1988).
5. Anne L'Huillier, X. Tang and P. Lambropoulos, Phys. Rev. A, in press (February 15, 1989).
6. M. D. Perry, O. L. Landen, A. Szöke and E. M. Campbell, Phys. Rev. A 37, 747 (1988).
7. Anne L'Huillier, L. A. Lompre, G. Mainfray and C. Manus, Phys. Rev. A 27, 2503 (1983).
8. X. Tang and P. Lambropoulos, unpublished.
9. X. Tang, A. Lyras and P. Lambropoulos, submitted to Phys. Rev. Lett.
10. For an up to date review of the status of this problem see P. Lambropoulos, X. Tang, P. Agostini, G. Petite and Anne L'Huillier, Phys. Rev. A in press (December 15, 1988).
11. For a thorough discussion of this question, see P. Lambropoulos and X. Tang, JOSAB 4, 821 (1987).

# Symmetries and Asymmetries in Above-Threshold Ionization

P. H. Bucksbaum, M. Bashkansky,\* and D. W. Schumacher

*AT&T Bell Laboratories, Murray Hill, New Jersey 07974*

## Abstract

Angular distributions of atomic electrons photoionized above threshold by intense elliptically polarized light contain strong asymmetries with respect to reflection about either principal polarization axis.<sup>1</sup> These observations, which contradict Keldysh-Faisal-Reiss theory predictions,<sup>2,3,4</sup> point to the significant role of the long range electrostatic potential of the ion in shaping the wave function of the outgoing electron. The experimental evidence for this phenomenon is reviewed for helium, krypton, and xenon photoelectron spectra, as a function of laser intensity, polarization, and electron energy.

## Introduction

Nearly ten years after the discovery of above-threshold ionization (ATI),<sup>5</sup> there is still considerable controversy about the correct theoretical description of this ubiquitous high intensity phenomenon. ATI, also called "excess photon" ionization, is multiphoton ionization (MPI) in which the final kinetic energy of the photoelectrons exceeds  $h\nu$ . The electron spectra generally contain a series of sharp peaks or groups of peaks, separated by  $h\nu$ . ATI becomes the dominant feature of MPI spectroscopy when six or more photons are required to ionize, and seems to nearly always occur when laser intensities exceed about  $5 \times 10^{12} \text{ W/cm}^2$ . ATI has been linked to the breakdown of minimum-order perturbation theory in the interaction of atoms with a laser field.<sup>6</sup>

The ATI experiments with elliptically polarized light described here disagree with predictions of theories proposed by Reiss<sup>4</sup> and Faisal,<sup>3</sup> based on older work by Keldysh<sup>2</sup> (so-called Keldysh-Faisal-Reiss, or KFR theories). These theories have risen to prominence in recent years because of their success in describing photoionization with circularly polarized light.<sup>7</sup> At the same time, the KFR approach is generally less successful in accurately predicting spectra obtained with linearly polarized light.<sup>8</sup> The examination of the intermediate case (elliptical polarization) in the current

set of experiments helps to explain this difference, and also reveals the role of the static potential of the ion in controlling the evolution of photoelectrons.

After a brief introduction to KFR theories, the experiments on elliptically polarized light will be discussed in detail. By bringing together all of our data in one publication, we hope to provide a useful guide to theorists interested in this problem.

## Keldysh-Faisal-Reiss Theories

KFR theories depart from perturbative treatments of the radiation field, by viewing the laser interaction as a classical time-varying potential in which the electron wave function evolves from a localized packet around the ion core, to an outgoing free electron in the presence of the laser field. The most straightforward, if inelegant, path to solving this problem involves direct computer integration of Schroedinger's equation. Although much progress has been made recently, full three dimensional treatments have not been done.

The KFR approach considers photoionization as a scattering problem. The ansatz that distinguishes KFR treatments from the exact problem is that the final state electron is dominated by the classical electric field of the laser, with the coulomb field of the ion playing a negligible role, whereas the initial state is dominated by the static potential of the ion. Schroedinger's equation for the final state electron can be written (in the  $\mathbf{A} \cdot \mathbf{p}$  gauge)

$$\frac{[\mathbf{p} - \frac{e}{c} \mathbf{A}(\mathbf{x}, t)]^2}{2m_0} \psi(\mathbf{x}, t) = i\hbar \frac{\partial \psi(\mathbf{x}, t)}{\partial t} \quad (1)$$

where  $\mathbf{A}(\mathbf{x}, t)$  is the classical (non-quantized) vector potential, usually expressed in the electric dipole approximation as:

$$\mathbf{A}(\mathbf{x}, t) \approx \mathbf{A}(t) = \hat{\mathbf{e}} A_0 \sin \omega t \quad (2)$$

The solutions, called Volkov states, are the quantum-mechanical versions of free wiggling electrons.<sup>9</sup> When described in the  $A \cdot p$  gauge, they are plane waves whose time dependence has been modified by the electromagnetic vector potential. For example, in the case of linear polarization  $\hat{\epsilon}$ , the Volkov solution is:

$$\Psi_{\text{Volkov}}(\mathbf{x}, t) = \exp \left[ \frac{i}{\hbar} \mathbf{p} \cdot \mathbf{x} - \frac{i}{\hbar} \frac{p^2}{2m_e} t - \frac{i}{\hbar} \frac{e^2 A_0^2}{4m_e c^2} t \right. \\ \left. - \frac{i}{\hbar} \frac{e^2 A_0^2}{8\omega m_e c^2} \sin(2\omega t) + \frac{i}{\hbar} |\hat{\epsilon} \cdot \mathbf{p}| \frac{e A_0}{m_e \omega c} \sin(\omega t) \right] \quad (3)$$

Like plane waves, these solutions are eigenstates of the canonical momentum with eigenvalue  $\mathbf{p}$ . The extra time-dependent phases are periodic energy fluctuations caused by the oscillating field. The three extra phase factors are: the average kinetic energy change due to wiggling in the presence of the laser electric field; the periodic fluctuations about this value with frequency  $2\omega$ ; and oscillation at  $\omega$  (the  $\hat{\epsilon} \cdot \mathbf{p}$  term), due to the component of the driving force in the direction of the drift.

It is useful to compare these wave functions to classical electrons. These solutions are not eigenstates of energy, just as a classical charged particle in a classical oscillating electric field does not have constant energy. However, while classical wiggling particles have a continuous but finite energy range, between a minimum and a maximum value, the Volkov state is a superposition of plane wave energy eigenstates that are distributed over an infinite energy range, but are separated by discrete amounts equal to integer multiples of  $\hbar\omega$ . This can easily be demonstrated by expanding equation 3 in plane waves:

$$\Psi_{\text{Volkov}}(\mathbf{x}, t) = e^{\frac{i}{\hbar} (\mathbf{p} \cdot \mathbf{x} - \frac{p^2}{2m_e} t - U_p t)} \\ \times \sum_{n=-\infty}^{\infty} \sum_{m=-\infty}^{\infty} J_m \left( \frac{U_p}{2\hbar\omega} \right) J_{n-2m} (|\hat{\epsilon} \cdot \mathbf{p}| \frac{e A_0}{\hbar\omega m_e c}) e^{i n \omega t} \quad (4)$$

Here  $J_m$ 's are cylindrical Bessel functions, whose arguments are the coefficients of the oscillating terms in the Volkov phase in equation 3; and  $U_p$  is the time-averaged wiggling kinetic energy, or ponderomotive potential, of the electron. Thus Volkov states have at least one feature in common with ATI final states: they both consist of a series of energy peaks separated by  $\hbar\omega$ .

#### ATI in Circularly Polarized Light

An example of the success of the KFR approximation in reproducing circularly polarized ATI spectra is shown in figure 1. The laser intensity is the only adjustable parameter.<sup>7,10</sup>

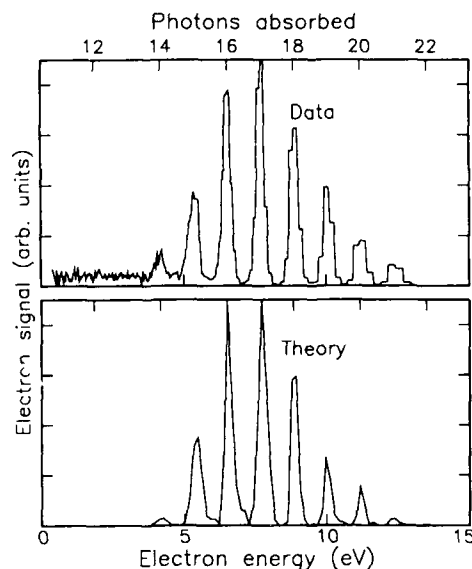


Figure 1. Top: ATI spectrum for circularly polarized 1064 nm light in xenon (from reference 10). Bottom: A computer simulation of the experiment, using ionization rates from the Keldysh theory of H. Reiss (reference 7), integrated over the measured temporal and spatial profile of the laser pulse.

Much poorer agreement is achieved for linear polarization (figure 2) However, the principal features are there: a series of energy peaks, separated by  $\hbar\omega$ , decreasing gradually at higher energies.

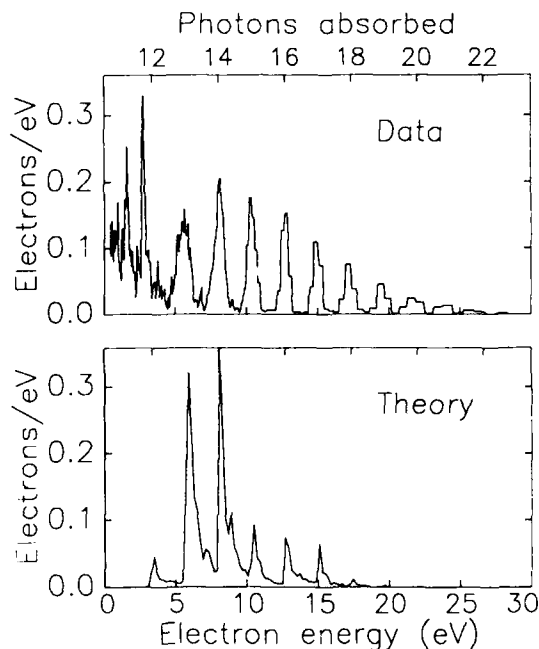


Figure 2. Comparison between KFR calculation and data, as in figure 1, but for linearly polarized light.

The Volkov wave function is more complicated for linear polarization than for circular. For example, for linear polarization, the wave function is usually quite sharply peaked along the polarization axis, while it is isotropic in the polarization ( $\phi$ ) plane for circular polarization. However, there may be an even more straightforward explanation for the systematic failure of KFR theories to deal as effectively with linear polarization as with circular polarization: Since the final state electrons in a circularly polarized ATI experiment must remove the angular momentum gained by absorbing many photons, they must possess high angular momentum wave functions. These are excluded from the vicinity of the ion core by the centrifugal barrier. Therefore, the final states only sample regions of space where the KFR approximation neglecting final state coulomb forces is approximately valid, i.e. regions where the ion potential is weak. For linear polarization, this is not the case, and the coulomb potential of the ion substantially modifies the escaping electron wave function.

### KFR predictions for Elliptically Polarized Light

These arguments motivated the current investigation of ATI for *elliptical* polarization. Here Keldysh theories make definite predictions about angular distributions as well as spectra. The predictions may be obtained easily from a generalization of equation 3 to elliptical polarization. If the atomic ground state wave function is spherically symmetric, the distribution for the electron peak due to  $k$  photon absorption, apart from an overall factor, is given by

$$dW/d\Omega \propto \left| \sum_{m=-\infty}^{\infty} J_m(\alpha) J_{k+2m}(\beta) e^{i(k+2m)\chi} \right|^2, \quad (5)$$

where

$$\alpha = \frac{U_p}{2\hbar\nu} \cos(\xi),$$

$$\beta = \frac{2}{\hbar\nu} \sin(\theta) \sqrt{U_p(k\hbar\nu + E_G - U_p)(1 + \cos\xi \cos 2\phi)},$$

$\xi$  is related to helicity  $h$  by  $\xi = \arcsin(h)$ ,  $E_G$  is the atomic ground state energy, and  $\chi = \arctan(\tan(\phi)\tan(\xi/2))$ .

These four-fold symmetric patterns in the polarization plane, which range from butterfly-shapes to clover leaves to figure-eights, are the result of wave-mechanical interference in the outgoing electron wave, as it is driven back and forth by the time-varying electric field.

### Lasers and Data Collection

The data in these studies were obtained using an amplified mode-locked Nd:YAG laser and its second harmonic. The pulsewidth was variable between 0.10 and 0.15 nsec, and was monitored by standard autocorrelation techniques. The spatial profile of the beam was a truncated central airy disk, focused to an area 20  $\mu\text{m}$  in diameter at half intensity. The focus was measured with a simple achromatic microscope imaged onto a television camera. Ionization occurred in a magnetically and electrically shielded vacuum with a base

pressure of  $1 \times 10^{-9}$  torr, seeded with  $10^8$  to  $10^{11}$  atoms/cm<sup>3</sup> of xenon, krypton, or helium.

Electrons were collected by two methods: The first was a time-of-flight spectrometer subtending a solid angle of 0.003 sr in the polarization plane. In this device, angular distributions were obtained by rotating the polarization, which was set as follows: First, the laser light passed through a linear polarizer, then through a half wave-plate, a quarter wave-plate, and a second half wave-plate. The retardation plates were all crystalline quartz, multiple order, anti-reflection coated, and commercially supplied. Although only one half-wave and one quarter-wave-plate are required to fix any polarization, the additional half-wave-plate provides more control. Here the first half-wave-plate may be moved while the quarter-wave-plate remains fixed, to establish the helicity without moving the orientation of the major and minor polarization axes. The second half-wave-plate then rotates the polarization ellipse to the desired orientation. The scheme is imperfect, because wave-plates are seldom manufactured to the required tolerance, and are also extremely sensitive to alignment in the mount. To combat these problems, the polarization was analyzed at each orientation. We were thus able to maintain the retardation and orientation to within  $\pm 2^\circ$ . The *sign* of the helicity (i.e. right- vs. left-handed polarization) was determined by a zero-order circular analyzer, constructed using stretched polyethylene film and a linear polarizer.

A different detector has been employed more recently to obtain higher angular resolution, at the expense of energy resolution, or to view angles away from the polarization plane. This second device consisted of a set of retarding grids, followed by microchannel electron multipliers subtending 0.08 sr (66° opening angle), centered in the polarization plane perpendicular to  $k$ . Electrons from the channel plates impinged onto a phosphor-coated conductive glass plate, which was viewed from behind by a television camera. Electrons were collected over many laser pulses, resulting in two-dimensional histograms in  $\theta$  (the polar angle with respect to  $k$ ) and  $\phi$  (the azimuthal angle). By rotating the polarization to different orientations, a mosaic was constructed consisting of the full angular distribution between  $\theta=60^\circ$  and  $\theta=120^\circ$ , over all angles in  $\phi$ .

### Early work

In early work, electrons were collected over one quadrant in the azimuthal ( $\phi$ ) plane perpendicular to the laser direction  $k$ , spanning angles between the polarization semi-major and semi-minor axes.<sup>12</sup> The polarization was nearly (but not quite!) circular (helicity  $h=0.985$ ). Fits were made to a general four-fold symmetric function

$$\sum_{n=-\infty}^{\infty} a_n \cos 2n\phi, \quad (6)$$

where  $\phi$  is the azimuthal angle (with respect to  $\hat{x}$  in the  $\hat{x}$ - $\hat{y}$  plane). These resemble the KFR predictions, although a number of systematic discrepancies were noted. Ponderomotive effects are evident in the lower energy electron peaks; in addition, it was usually necessary to adjust the helicity in order to obtain the best fit (see figure 3).

### Asymmetric distributions

The KFR predictions contain more symmetry than the electric dipole Hamiltonian, because they do not distinguish the sense of rotation of the light. Reversal of helicity affects the phase, but not the amplitude, of the Volkov state, and therefore has no effect on the energy spectrum. However, an extension of the measurements to the full azimuthal plane reveals that equation 6 is generally inadequate to fit the data. Instead, it must be expanded to

$$\sum_{n=0}^{\infty} a_n \cos 2n\phi + b_n \sin 2n\phi. \quad (7)$$

This is the most general angular distribution consistent with

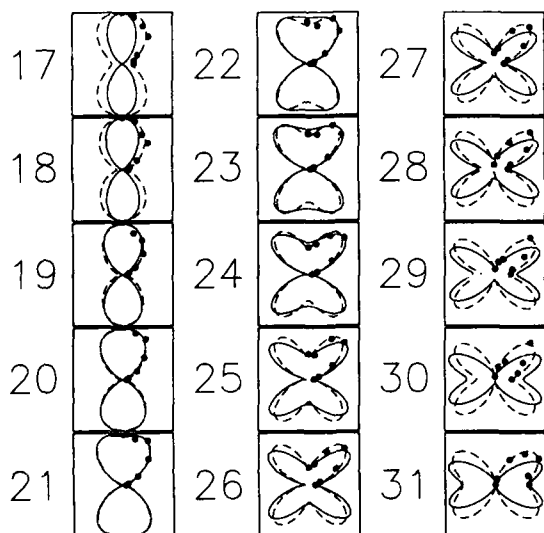


Figure 3. ATI in krypton with nearly circularly polarized light ( $lh=0.985$ ). Points are data collected over one quadrant. Solid lines are fits to a series in  $\cos(2n\phi)$  for  $\phi=0,1,2,3$ . Dotted lines are predictions of the KFR theory for  $lh=0.94$ . (From reference 11)

invariance under rotation about  $\mathbf{k}$  ( $\hat{z}$  axis) by  $\pi$ . The light-atom system must be invariant with respect to this rotation in order to satisfy spatial isotropy; however, the four-fold invariance of equation 1 is lost.

A typical example is shown in figure 4, which displays the full angular distribution of the ATI electrons from krypton ionized by 19, 1064 nm photons. In this example, the laser was "right elliptically polarized" (negative helicity), with  $h=-0.82$  ( $\xi=-55^\circ$ ). The dotted line is the KFR prediction, neglecting all ponderomotive effects. The obvious discrepancy is the strong asymmetry with respect to reflection about either the major or minor axes. Simultaneous reflection  $\hat{x} \rightarrow -\hat{x}$ ,  $\hat{y} \rightarrow -\hat{y}$  is symmetric, as expected.

These azimuthal asymmetries depend on the ATI peak, the atom, the laser wavelength and intensity, the sign and magnitude of the retardation, and on the laser focus parameters. Figure 5 shows how angular distributions for xenon evolve from low to high energy electrons at fixed laser intensity. The solid lines are fits to a Fourier series of the form in expression (7).

Figure 5 and the figures that follow also show that the distributions invert when the helicity is reversed. Along with symmetry under  $\hat{x} \rightarrow -\hat{x}$ ,  $\hat{y} \rightarrow -\hat{y}$ , this feature helps to rule out a large class of potential experimental systematic errors, such as stray magnetic fields.

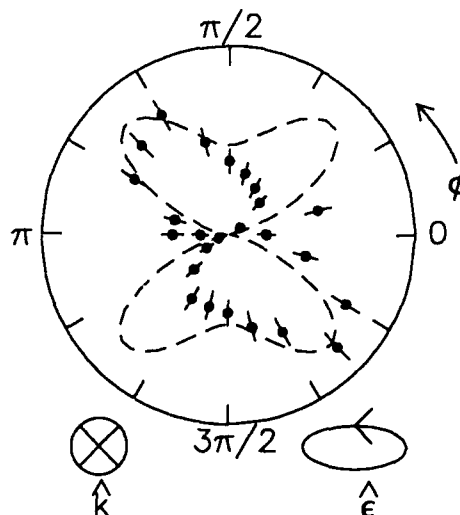


Figure 4. Azimuthal angular distribution for 19 photon ionization of krypton by 1064 nm light of 150 psec duration, focused to approximately  $2 \times 10^{15} \text{ W/cm}^2$ , and elliptically polarized with helicity  $h=-0.82$ . Dashed line is prediction of the Keldysh-Faisal-Reiss theory, with no ponderomotive effects included. Data fail to display fourfold symmetry predicted by this and other ATI theories. (From reference 1)

Krypton, which has a higher ionization potential than xenon (13.996 eV vs. 12.128 eV), produces similar asymmetric distributions, as shown in figure 6 Helium, with twice the ionization potential of xenon, has been studied using photons with twice the energy ( $\lambda=532 \text{ nm}$ ,  $h\nu=2.330 \text{ eV}$ ). The results are shown in figure 7.

We have also investigated the polar angle dependence and find that electrons are nearly all emitted in the polarization plane, symmetric with respect to the forward and backward hemispheres (Figure 8). The only unexpected asymmetry is in the azimuthal angles.

The asymmetry is nearly always present for elliptical polarization, but has never been observed for either linear or circular. (For circular polarization, such an asymmetry is forbidden by spatial isotropy.) As the absolute value of the helicity increases, starting from  $h=0$  (linear polarization), the asymmetries gradually appear. This can be seen in the series of distributions for krypton in figure 9. This figure also shows the gradual change in the distributions with the ATI peak, and a change with laser intensity. The latter is somewhat obscured by the well-known ponderomotive scattering effects which tend to smear out the angular distributions for slower electrons at high intensities.<sup>12</sup>

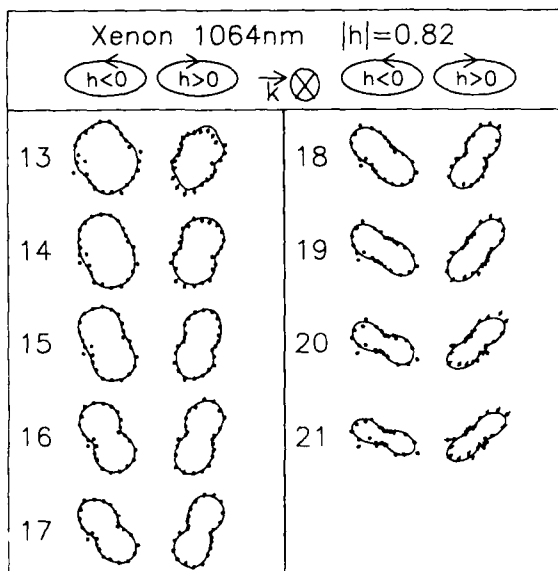


Figure 5. ATI for elliptical polarization in xenon. The laser pulsewidth was 0.10 to 0.12 nsec, and its helicity is  $\pm 0.82$ .  $I_{\text{peak}}=4 \times 10^{13} \text{ W/cm}^2$ .  $P_{1/2}$  and  $P_{3/2}$  final states were not resolved, so numbers indicate photons absorbed for the  $P_{3/2}$  final state. (From reference 1)

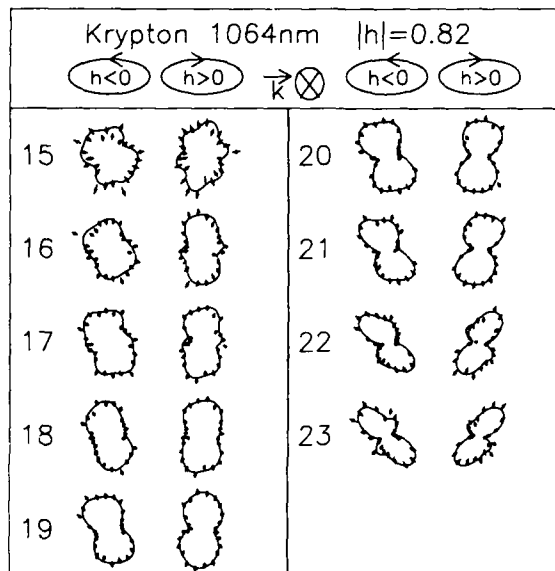


Figure 6. Kr 1064nm:  $I_{\text{peak}}=4 \times 10^{13} \text{ W/cm}^2$ ;  $P_{3/2}$  final states only. (From reference 1)

While the asymmetries appear to be quite general phenomena, it is clear that specific atomic structure does play a role. This is most obvious in the case of xenon ionized by six 532nm photons to the  $P_{3/2}$  ion final state, shown in figure 10. Here the sign of the asymmetry is reversed relative to all other cases studied, including higher ATI peaks in the same atom. Analysis

A semi-classical argument provides a qualitative understanding of this phenomenon. An electron that ionizes by absorbing many elliptically polarized photons carries off several units of angular momentum. In helium, for example, where the initial atom and final ion are both s states, the electron carries off about  $n\hbar$  units of angular momentum, where  $h$  is the light helicity and  $n$  is the number of photons absorbed. If the electron and ion were classical particles, the electron-ion system would have a classical impact parameter  $b$  (neglecting internal degrees of freedom), of

$$b = \frac{n\hbar}{\sqrt{2m_e(n\hbar\omega + E_G - U_P)}} \quad (8)$$

Here  $E_G$  is the (negative) ground state energy, and  $U_P$  is the ponderomotive potential energy of the electron, which subtracts from its drift kinetic energy.<sup>13</sup> The quantum-mechanical manifestation of the classical impact parameter is the exclusion of the final state wave function from the ion by a centrifugal potential barrier.

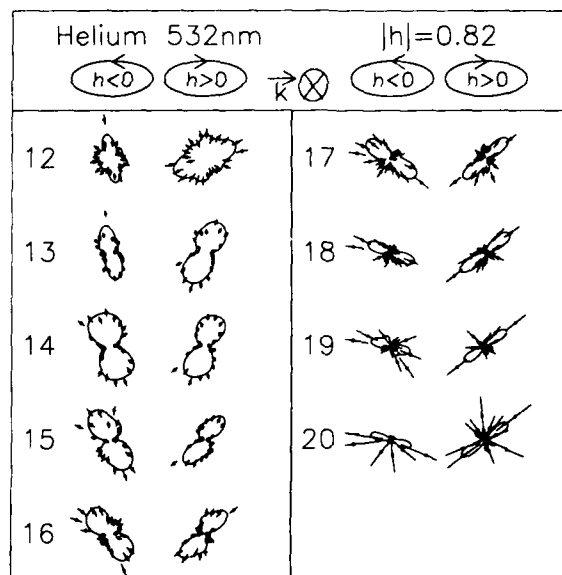


Figure 7. Helium 532nm:  $I_{\text{peak}}=1 \times 10^{14} \text{ W/cm}^2$ . (From reference 1)

During the escape of the electron from the ion field, the angular momentum is constant (neglecting further interactions with the laser field), but linear momentum is not. For a coulomb potential, a classical electron describes a hyperbolic trajectory. The asymptotic momentum deviates from



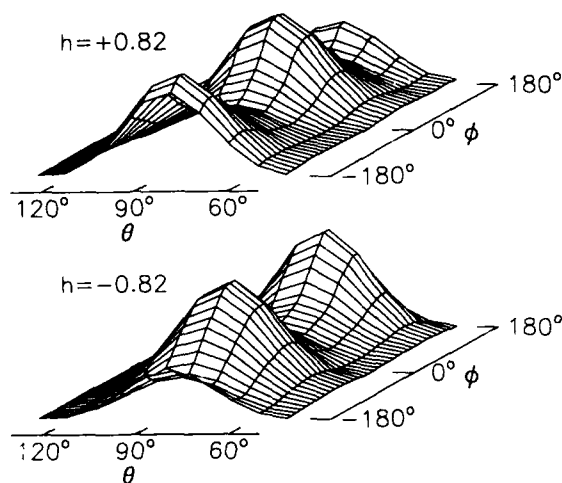


Figure 8. Angular distributions in the azimuthal ( $\phi$ ) and polar ( $\theta$ ) directions, for xenon photoionized by 1064 nm light with helicity  $h=+0.82$  (top) and  $h=-0.82$  (bottom). Data set contains all ATI peaks with energies of 9 eV and higher, summed together. The laser wave vector  $\mathbf{k}$  lies along  $\theta=0$ . This view emphasizes the fore-aft symmetry about the polarization plane defined by  $\theta=\pi/2$ . The only observed asymmetry is in the azimuthal direction. (From reference 1)

the momentum at the point of closest approach by an angle given by

$$\Phi_{\text{DEV}} = \frac{h}{|h|} \sin^{-1} \left[ \left( 1 + \frac{2(n\hbar)^2 (n\hbar\omega + E_G - U_P)}{m_e c^4} \right)^{-1/2} \right] \quad (9)$$

For example, consider negative helicity 532 nm light, retarded to  $\xi = -55^\circ$  ( $h=-0.82$ ), incident on helium (shown in figure 7). Electrons ejected after absorbing 14 photons have an energy of approximately 8 eV, and for the peak intensity in figure 7, approximately 2.5 eV of this total is in the form of ponderomotive potential energy. These numbers imply an angular deviation during the electrons transit out of the ion potential, of  $-8^\circ$ , i.e. *counterclockwise* when viewed along  $+z$ . The helium spectra for  $h=-0.82$  in figure 7 do appear to be distorted counterclockwise from the distributions predicted by the KFR theory. These classical ideas do not explain all of the observations, but they may suggest a physical principle responsible for the broken symmetry.

#### Final State Effects

Recently, it has been noted<sup>14</sup> that the quantum-mechanical origins of these deviations are phase shifts imposed on the outgoing electron wave. Although such shifts have several sources, such as bound state resonances, or continuum-continuum transitions, the principal contribution may be sim-

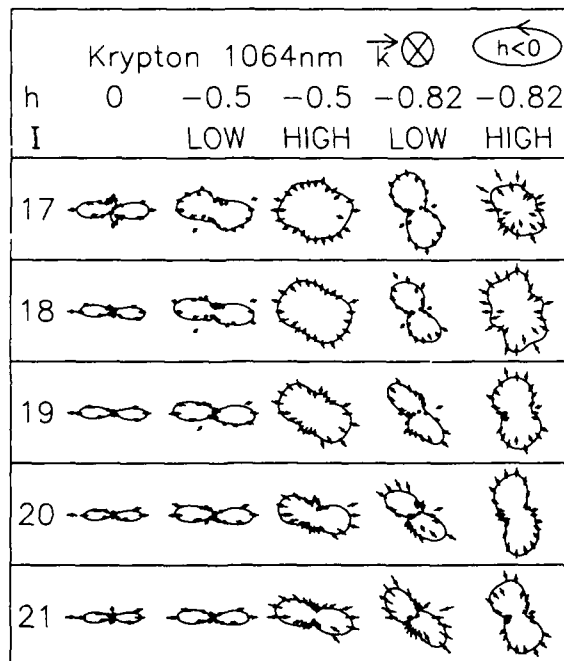


Figure 9. Azimuthal distributions for various retardations and laser intensities, for krypton photoionized by 1064 nm light. Numbers to the left of each row designate photons absorbed to the  $P_{3/2}$  ion final state for each ATI peak. First column: linear polarization,  $I_{\text{peak}}=2.5 \times 10^{13} \text{ W/cm}^2$ . Second column:  $h=-0.5$ ,  $I_{\text{peak}}=2 \times 10^{13} \text{ W/cm}^2$ . Third column:  $h=-0.5$ ,  $I_{\text{peak}}=4 \times 10^{13} \text{ W/cm}^2$ . Fourth column:  $h=-0.82$ ,  $I_{\text{peak}}=2 \times 10^{13} \text{ W/cm}^2$ . Fifth column:  $h=-0.82$ ,  $I_{\text{peak}}=4 \times 10^{13} \text{ W/cm}^2$ . (From reference 1.)

ply the ion potential phase shift itself. This is precisely the quantum analog of the curved trajectory of a classical electron climbing out of an ion potential.

The interaction between the outgoing electron and the ion potential leads to a complex phase  $e^{i\delta_l}$  multiplying the ordinary complex azimuthal dependence of spherical waves with definite angular momentum  $l$  and  $z$ -component  $m_l$ . For potentials that fall off *faster* than  $1/r$ , the asymptotic wave can always be written in the form:<sup>15</sup>

$$u_{lm}(r, \theta, \phi) = e^{i\delta_l} R_{lm}(r) P_{lm}(\theta) e^{im\phi} \quad (10)$$

Here  $E$  is the electron energy, and  $P_{lm}(\theta)$  is an associated Legendre polynomial. For a free outgoing spherical electron wave,  $\delta_l$  vanishes, and  $R_{lm}(r)$  is (except for a normalization) a spherical Bessel function  $j_l(pr/\hbar)$ . ( $p$  is the electron radial momentum.) For a Coulomb potential, the asymptotic phase shift is not well defined, because it continues to increase as  $\log(pr/\hbar)$ ; however, this logarithmic  $r$ -dependent phase

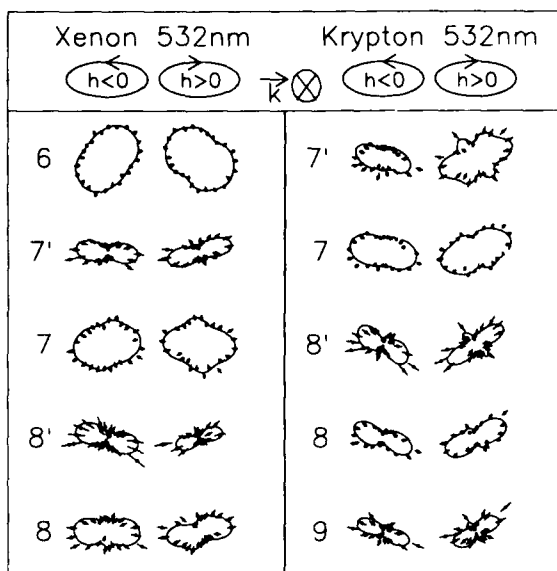


Figure 10. ATI in xenon and krypton using 532nm light with peak intensity of  $1 \times 10^{13} \text{ W/cm}^2$  (Xe); and  $1.5 \times 10^{13} \text{ W/cm}^2$  (Kr), with helicity  $h = \pm 0.82$ . Note the relative reversal of the asymmetry for 6 photon ionization of xenon. (From reference 1)

affects all partial waves equally, and therefore cannot give rise to asymmetries through interference. On the other hand, there is also an  $l$ -dependent phase shift, given by

$$\delta_l = \arg \Gamma(l+1 + \frac{i\hbar}{pa_0}), \quad (11)$$

where  $a_0$  is the Bohr radius. Since this phase factor depends on  $l$  rather than  $m_l$ , it cannot affect azimuthal distributions either, unless the final state is a superposition of partial waves with different  $l$  and  $m_l$ . However, this is precisely the case for ATI using elliptically polarized light.

We should therefore expect asymmetries of the form

$$\sum_n c_n \cos(2n\phi + \delta_n), \quad (12)$$

where the  $\delta_n$ 's are linear combinations of the  $\delta_l$ 's in equation (10). The scale of the angular distortion is set by the size of the phase shifts, which are on the order of radians for these ATI experiments. In the case of linear polarization, the asymmetries vanish, since partial waves with the same  $l$  but opposite  $m_l$  contribute equally, and interfere to form wave functions with an overall phase shift, but no angular shift.

Several attempts to incorporate these shifts into ATI calculations are now underway. Modifications to Keldysh theory, straightforward perturbation calculations, and calculations involving resonant intermediate states, have all been

suggested. Since this subject is still only a few weeks old, the outcome and significance of these observations and new speculations are not yet known.

We gratefully acknowledge spirited discussions with M. Mittleman, and comments by T. J. McIlrath, who suggested we study helium.

## References

\*Present address: Naval Research Laboratory, Washington, D.C.

1. M. Bashkansky, P.H. Bucksbaum, and D.W. Schumacher, Phys. Rev. Lett. **60**, 2458 (1988).
2. L. V. Keldysh, Sov. Phys. JETP **20**, 1307 (1965).
3. F. H. M. Faisal, J. Phys. B **6**, L89 (1973).
4. H. R. Reiss, Phys. Rev. A **22**, 1786 (1980).
5. P. Agostini, F. Fabre, G. Mainfray, G. Petite, and N. Rahman, Phys. Rev. Lett. **42**, 1127 (1979).
6. A representative compilation of recent theoretical and experimental work is the feature issue on Multielectron Excitations in Atoms, Jour. Opt. Soc. B **4**, ed. by W. E. Cooke and T. J. McIlrath, 701-862 (1987).
7. H.R. Reiss, J. Phys. B **10**, L79 (1987).
8. P.H. Bucksbaum, M. Bashkansky, and D.W. Schumacher, Phys. Rev. A **37**, 3615 (1988).
9. D.M. Volkov, Z. Physik **94**, 250 (1935).
10. M. Bashkansky, P.H. Bucksbaum, and D.W. Schumacher, Phys. Rev. Lett. **59**, 274 (1987).
11. P. H. Bucksbaum, M. Bashkansky, R. R. Freeman, T. J. McIlrath, and L. F. DiMauro, Phys. Rev. Lett. **56**, 2590 (1986).
12. R. R. Freeman, T. J. McIlrath, P. H. Bucksbaum, and M. Bashkansky, Phys. Rev. Lett. **57**, 3156 (1986).
13. T. J. McIlrath, P. H. Bucksbaum, R. R. Freeman, and M. Bashkansky, Phys. Rev. A **35**, 4611 (1987).
14. This has been suggested by: X. Tang and P. Lambropoulos, for perturbative calculation of three photon ionization of hydrogen, private communication; by S. Basile, F. Trombetta, and G. Ferrante, for non-perturbative ionization of helium, preprint and private communication; and by H. Muller, G. Petite and P. Agostini, preprint and private communication.
15. H.A. Bethe and E. Salpeter, *Quantum Mechanics of One- and Two-Electron Atoms*, Springer-Verlag: Berlin, sect. 54 (1957).

## Multiphoton Ionization with Femtosecond Laser Pulses

H. G. Muller, FOM Institute, Amsterdam

### Temporary Address:

Service de Physique des Atomes et des Surfaces  
Centre Etudes Nucleaire Saclay  
91191 Gif-sur-Yvette Cedex  
France

There are a number of reasons to use subpicosecond pulses in multiphoton ionization experiments. Pulses with shorter risetimes make it possible to study processes with higher rates before one runs into the problem of depletion of target atoms. Furthermore the momentum of the electron does not change between the point of ionization and the detector if the pulse expires before the electron has time to sample the spatial inhomogeneity of the light intensity. This makes it possible to identify the intensity at which an electron was formed from the energy with which it reaches the detector.

Yet another advantage is the fact that the primary ionization products are subject to the ionizing radiation for only a short amount of time, thus reducing the probability of sequential ionization as compared to direct processes. In this paper the experimental results on the multiphoton ionization of xenon with pulses of 100 fs, that were obtained during the preceding year at ENSTA, Palaiseau, will be presented.

# High-Order Harmonics in Light Scattering by Atomic Electrons Above Threshold

J. H. Eberly and Q. Su

*Department of Physics and Astronomy, University of Rochester  
Rochester, New York 14627*

J. Javanainen

*Department of Physics, University of Connecticut, Storrs, Connecticut 06268*

## Abstract

We report on light scattering in multiphoton ionization (MPI) computer experiments at high laser intensity. The plateau and cut-off features recently reported in laboratory experiments on high-order harmonic generation by McPherson, et al., and by Ferray, et al., are corroborated. We report scattered light spectra in four different cases and exhibit the corresponding ATI photoelectron spectra. We propose a connection between ATI and high-order harmonics.

## 1 Nonlinear Optics, a Quick Review

The usual problem in nonlinear optics is to determine the susceptibility that governs the wave-mixing process of interest. In the present case we will be interested in nonlinear light scattering accompanying multiphoton ionization (MPI) at high incident intensities. There is typically only one incident field in an MPI experiment, and so the relevant wave-mixing process is harmonic generation. At low light intensities the first harmonic order of any interest is generally the third, so for reference we reproduce here the expression for the nonlinear susceptibility responsible for third harmonic generation:

$$\chi(-3\omega, \omega, \omega, \omega) = (N / \epsilon_0 \hbar^3) \times \sum_{l,m,n} \mu_{g l} \mu_{l m} \mu_{m n} \mu_{n g} A_{l m n} \quad (1.1)$$

Here  $\mu$  denotes a dipole matrix element,  $N$  is the density of scatterers, and  $A_{l m n}$  contains resonance denominators:

$$A_{l m n} = (\omega_{l g} - 3\omega)^{-1} \times (\omega_{m g} - 2\omega)^{-1} (\omega_{n g} - \omega)^{-1} + (\dots) \quad (1.2)$$

where (...) means counter-resonant (and therefore smaller) terms with the signs of the  $\omega$ 's in the various factors reversed.

We can use this expression for susceptibility to make a dimensional analysis of the third order polarization density which is given by:

$$P^{(3)}(3\omega) = \epsilon_0 \chi^{(3)}(-3\omega, \omega, \omega, \omega) \mathcal{E}^3(\omega) \quad (1.3)$$

We see that  $P^{(3)}$  has the generic form:

$$P^{(3)} = N \mu (\kappa)^3 \quad (1.4)$$

where the dimensionless parameter  $\kappa$  is defined to be

$$\kappa = (\mu \mathcal{E} / \Delta E). \quad (1.5)$$

Expression (1.4) indicates that  $P^{(3)}$  equals a typical polarization density  $N \mu$  times a dimensionless factor taken to the power corresponding to the order of the harmonic to be generated. Here we have denoted all dipole matrix elements by  $\mu$  and all resonance

denominators by  $\Delta E$ . Of course the range of actual values for both  $\mu$ 's and  $\Delta E$ 's is very large, but we are interested mainly in "average" values that will define a typical "critical" value of  $\mathcal{E}$  when we put  $\kappa \approx 1$ .

This critical value of field strength can have key significance in nonlinear optical phenomena because it defines the incident laser intensity above which the usual perturbative susceptibility analysis must be regarded as unreliable. For example, if  $\kappa > 1$  the lowest (third order) contribution to third harmonic generation, given above in Eq. (1.1), will be smaller than the higher order (5th, 7th, ..... ) contributions to the third harmonic. This is related to the physical meaning of the term "breakdown of perturbation theory," since perturbation theory is founded on the assumption of the opposite behavior, namely that higher order contributions and processes are progressively smaller.

It is easy to show<sup>1a</sup> that sensible average values of  $\mu$  and  $\Delta E$  lead to a critical value of the incident field strength equal to about 1% of the atomic unit, which gives  $I_{crit} \approx 10^{13}$  watts/cm<sup>2</sup>. This is the same conclusion about the critical intensity that has also been reached in several other ways.<sup>1b</sup>

Thus, in the intensity range of interest ( $10^{13} - 10^{15}$  W/cm<sup>2</sup>) in recent MPI work on above-threshold ionization(ATI),<sup>2</sup> it is doubtful whether perturbation theory is usable at all. This means there is no appropriate expression for susceptibility available, which creates an important theoretical question: how to make reliable calculations about nonlinear optical phenomena accompanying ATI. It appears to us best to return to first principles and recall that all coherent stimulated atomic radiation (in the dipole approximation) is governed by the oscillations of the atomic dipole moment  $D(t)$ . For example, we could compute its Fourier transform to determine the coherent part of the scattered light spectrum. While this procedure is certainly non-perturbative and exactly correct, it usually cannot be carried out, even numerically, because  $D(t)$  is not known for any real atom in the presence of a radiation field, not even for hydrogen. Our approach is to calculate numerically the atomic wave functions needed to compute  $D(t)$  for a simplified but "representative" model atom instead.

## 2 Representative Model Atom and Its Wave Functions

Our model atom is defined by the one-dimensional bare Hamiltonian (in atomic units)

$$H_0 = - (1/2) \partial^2 / \partial x^2 - 1/\sqrt{(1+x^2)} \quad (2.1)$$

There is no fundamental basis for our specific choice of "representative" binding potential  $V(x) = -1/\sqrt{(1+x^2)}$ , but it is simple and satisfies these elementary requirements that are shared by all real atoms:

- (a)  $V(x) = V(-x)$ , to ensure that parity is a good quantum number; and
- (b)  $V(x) \approx 1/|x|$  for large  $x$ , to ensure coulombic behavior near to and above ionization threshold; and
- (c)  $V(x)$  is monotonic increasing.

The absence of a singularity at  $x = 0$  is, in one dimension, the analog of a three-dimensional atom's reduced severity of singularity at  $r = 0$ . To this bare Hamiltonian we add the laser-atom interaction in dipole approximation:

$$H' = - xE(t) = - x\mathcal{E}_0(t) \sin\omega t \quad (2.2)$$

where  $\mathcal{E}_0(t)$  is a pulse-shape function. We will show results for both square and smooth pulse shapes.

Using  $H_0$  we compute numerically the bare atomic eigenvectors  $|E_m\rangle$ , and using the full Hamiltonian we numerically compute the time-dependent state vector  $|\Psi(t)\rangle$ , assuming ground-state initial conditions. Our numerical methods have been reported elsewhere.<sup>3a</sup> We show a bare energy-level diagram, drawn to scale for our representative atom, in Fig. 1 for later reference.

With the state vector  $|\Psi(t)\rangle$  we can evaluate the atomic dipole moment:  $D(t) = \langle \Psi(t) | x | \Psi(t) \rangle$ . The frequencies at which  $D(t)$  oscillates will appear in the scattered light spectrum. The number of photons coherently scattered at a given frequency is proportional to the square of  $D(\omega)$ , the Fourier transform of  $D(t)$ . Thus we take  $|D(\omega)|^2$  to represent the scattered light spectrum.

If we label the positive-energy eigenstates of  $H_0$  by their kinetic energy  $W$ , then the probability that the electron, following a laser pulse, has kinetic energy  $W$  in the range  $dW$  is  $P(W) dW = |\langle W | \Psi(t) \rangle|^2 dW$  and

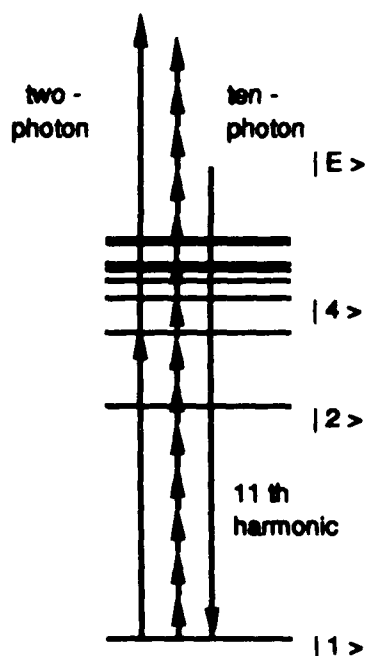


Figure 1. Energy level diagram for model atom used in this paper. The high-lying Rydberg levels are not shown. The vertical arrows indicate to scale the 2-photon and 10-photon ionization processes discussed in Secs. 3 and 4.

the total ionized fraction is given by  $P^{(I)} = \int dW P(W)$ . A plot of  $P(W)$  vs.  $W$  gives the ATI (above-threshold ionization) spectrum for the multiphoton process. Clearly the ATI spectrum is just as easily obtained from our numerical wave functions as is  $D(t)$ , and we have previously reported a number of ATI results.<sup>3b,c</sup>

### 3 Multiphoton Ionization and High-Order Harmonics

We now present the results of four multiphoton ionization computer experiments. The first three experiments are for relatively long-wavelength incident light. In each of them we chose a square laser pulse of  $16\frac{1}{4}$  cycles duration with photon frequency  $\omega = 0.07$  a.u. Since the ground state of our model is at  $-0.670$  a.u., this frequency corresponds to (nominal, weak-field) 10-photon ionization. The experiments employ field strengths of  $\mathcal{E}_0 = 0.04, 0.05$ , and  $0.06$  a.u. (intensities

in the range  $10^{13} - 10^{14}$  W/cm<sup>2</sup>). The fourth experiment uses shorter wavelength incident light corresponding to 2-photon ionization, with  $\mathcal{E}_0 = 0.05$  a.u. and a smooth envelope given by  $\sin^2(\pi t/T)$  where  $T$  is 96 cycles long.

In Figs. 2-4 we show both the ATI photoelectron spectra and the scattered light spectra from the 10-photon MPI experiments. There are many well-resolved peaks in the light spectra. The most prominent peaks occur exactly at the positions of the harmonics  $q\omega$  of the incident light, but there are other subsidiary and intermediate peaks and a continuous background as well, of much lower intensity. The ATI peaks have the same spacing as the harmonic peaks, and several are labelled by the number  $q$  of photons required to create them from

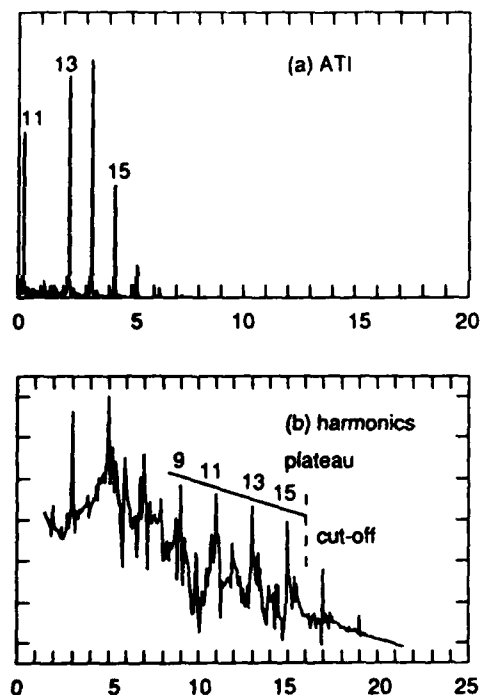


Figure 2. (a) ATI spectrum and (b) light scattering spectrum computed for the same  $16.25$  cycle square laser pulse. The vertical axes are linear in (a) and logarithmic (base 10) in (b), normalized to fit the graph window. The horizontal axes measure photon energy and electron kinetic energy, respectively, in units of the incident laser photon energy  $\omega = 0.07$  a.u. Various peaks are labelled with their  $q$ -number. Here  $\mathcal{E}_0 = 0.04$  a.u., ATI peak-13 height =  $0.077$ , and third harmonic peak height =  $7.70$ , in arbitrary units that are held the same in all figures below.

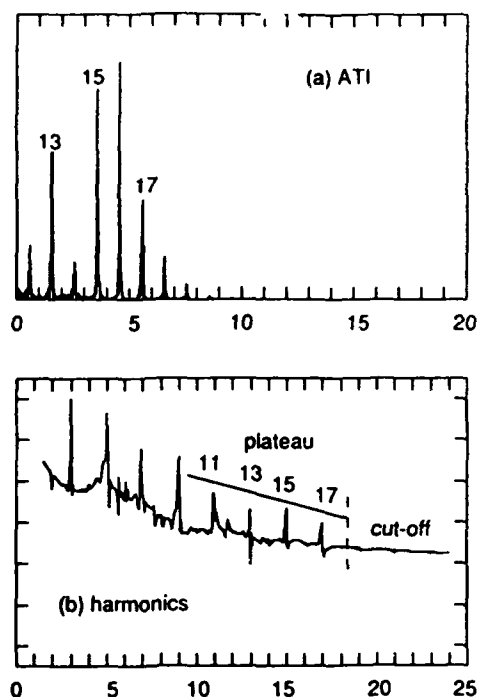


Figure 3. Same as Fig. 2, except  $\mathcal{E}_0 = 0.05$  a.u., ATI peak-13 height = 0.116, and third harmonic peak height = 54.2.

the ground state. The  $q$ -value (or "multiphoton index") of the lowest ATI peak increases by one unit from figure to figure. This is due to the upward shifting of the ionization threshold to higher energy as a function of the increased laser intensity, because of the ac Stark effect:

$$\Delta E = \mathcal{E}_0^2/4\omega^2, \quad (3.1)$$

which is the same as the so-called ponderomotive potential energy.

In the light scattering spectra we call attention to the appearance of the "cut-off" phenomenon identified for the first time by Ferray, et al.,<sup>4</sup> in laboratory experiments on harmonic generation and to the appearance of the "plateau" of slowly-changing harmonic intensities observed by Ferray, et al., and earlier by McPherson, et al.<sup>5</sup> A plateau of relatively high harmonics with a fairly abrupt cut-off is evident<sup>6</sup> in Figs. 2 and 3. Only a plateau appears in Fig. 4.

However, the cut-off is evidently intensity-dependent and we assume it is also present but outside the computed range in Fig. 4. Note that for this model atom the strength of the background grows rapidly with increasing incident light intensity.

The peaks in the ATI spectra of Figs. 2-4 are located as expected at the energies  $W_q = q\omega - E_I$  (where  $E_I$  is the effective ionization potential) and in each figure several peaks are prominent and easily identified above the background.

In Fig. 5 we show the results of our 2-photon ionization computer experiment. There are many differences compared to the 10-photon case. An obvious cause of some of the differences, of course, is the frequency scale change. However, three other differences are (1) the practical absence of any harmonics — only the third harmonic occurs, (2) the appearance of sharp well-resolved non-harmonic lines in the light-scattering spectrum, and (3) the much richer structure in the photoelectron spectrum, which has been reported before.<sup>3c</sup>

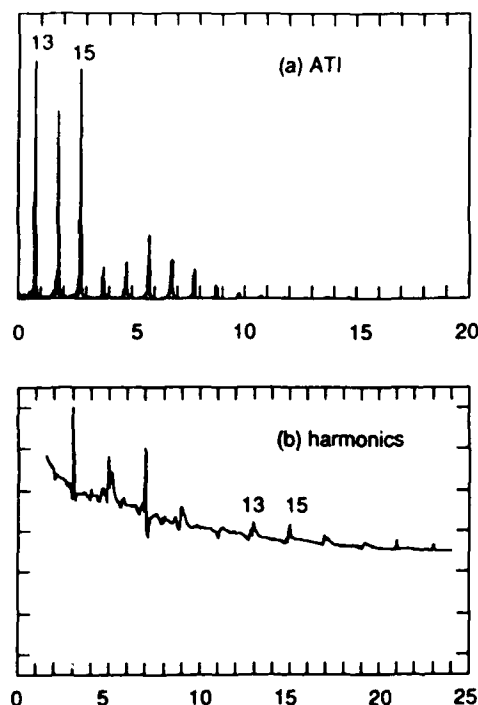


Figure 4. Same as Fig. 2, except  $\mathcal{E}_0 = 0.06$  a.u., ATI peak-13 height = 1.11, and third harmonic peak height = 282.

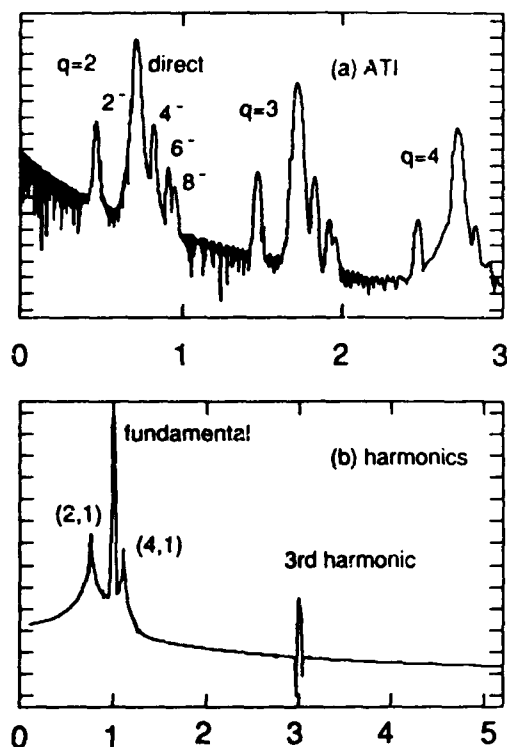


Figure 5. Same as Fig. 2, except that  $\mathcal{E}_0 = 0.05$  a.u.,  $\omega = 0.52$ , the pulse is 96-cycles and smooth, and the ATI vertical scale is logarithmic. ATI 2-photon peak height = 0.0675, third harmonic peak height =  $5.0 \times 10^{-5}$ .

#### 4 Conclusions

We now briefly explain how we presently understand the phenomena shown in Figs. 2-5. We think that plateau and cut-off features in harmonic spectra will be consistently reproduced in the corresponding ATI spectra, and at closely corresponding  $q$  values. Consider Fig. 3 as a good example. From  $q = 11$  to  $q = 17$  there is a "plateau" of approximately equal-strength harmonic peaks, and after  $q = 17$  there is an abrupt cutoff. Comparison with the corresponding ATI spectrum shows essentially the same behavior — approximately equal ATI peaks for  $q = 13, 15$  and  $17$ , and a clear drop in strength beyond  $q = 17$ . Note that one extra peak

appears in the harmonic plateau (the 11th) than appears in the ATI plateau. We believe this is because the Rydberg region of our model atom cannot resolve electron energies very well in  $16 \frac{1}{4}$  cycles and the "missing" ATI peak is present below the threshold.

Does this explanation also hold for the two-photon results in Fig. 5, even though only the third harmonic appears there, about three orders of magnitude above the background? We believe that it does, since the missing 5th harmonic would be associated with a  $q = 5$  ATI peak. While we can guess from the lower ATI peaks that a  $q = 5$  peak will be clearly evident if we compute for slightly higher ATI energies, it will be 5-6 orders of magnitude weaker than the  $q = 3$  peak. For this reason the 5th harmonic peak falls below the background and is not seen.

The presence of the "extra" lines in the light-scattering spectrum of Fig. 5 have not been obtained theoretically previously. They simply show the presence of population transiently but coherently excited into various low-lying bound states. These states all have dipole matrix elements with the initial state, and so the transition frequencies show up in the dipole spectrum. Thus the high-order harmonics are a reflection of above-threshold electron excitation, and the lower non-harmonic frequencies arise from below-threshold excitation. In an actual experiment these excitations would be much more likely to appear as line radiation, not coherent scattering, and so we have labelled them in the figure by the initial and final atomic states involved.

#### 5 Summary

We propose that the "plateau" and "cut-off" features of laboratory harmonic spectra<sup>4,5</sup> should be understood as parallel expressions<sup>7</sup> of the fundamental photon-electron interaction process previously probed in ATI experiments. We suppose that this is true of any atomic species, not only noble gases. Since our model is intrinsically one-electron in nature, our data suggests that (despite the non-negligible gas pressures employed) the laboratory experiments have observed fundamental single-atom phenomena in light scattering. A more complete discussion of the correspondence of high harmonics and ATI, including a non-perturbative non-numerical analysis of the electron state vector, has been submitted elsewhere.<sup>7</sup>



## Acknowledgements

We thank S.L. Chin, L.A. Lompre and G. Mainfray for discussions, and the Allied-Signal Corporation and the John Von Neumann Center for support of computing resources, and K. Kulander and B.W. Shore for sharing their results before publication.

## References and Notes

1. (a) S.E. Harris, Phys. Rev. Lett. **31**, 341 (1973); (b) Y. Gontier, M. Poirier and M. Trahin, J. Phys. B **13**, 1381 (1980), M. Aymar and M. Crance, J. Phys. B **14**, 3585 (1981), and L. Pan, K.T. Taylor and C.W. Clark, Phys. Rev. Lett. **61**, 2673 (1988).
2. Several reviews of above-threshold ionization are now available: P. Agostini and G. Petite, in Contem. Phys. **29**, 57 (1988), J.H. Eberly and J. Javanainen, Eur. J. Phys. **9**, \_\_\_\_ (1988), and P.W. Milonni, in Atoms in Strong Fields, edited by M.H. Nayfeh (Academic Press, in press)
3. (a) J. Javanainen, Q. Su and J.H. Eberly, Phys. Rev. A **38**, 3430 (1988), and J. Javanainen, Q.C. Su and J.H. Eberly, in Atomic and Molecular Processes with Short Intense Laser Pulses, edited by A.D. Bandrauk (Plenum, 1988), p. 243; (b) J. Javanainen and J.H. Eberly, in Multiphoton Processes, edited by S.J. Smith and P.L. Knight (Cambridge, 1988), p. 88; J.H. Eberly, J. Javanainen and Q. Su, Kvant. Elek. **15**, 1157 (1988); J.H. Eberly and J. Javanainen, Phys. Rev. Lett. **60**, 1346C (1988); and (c) J. Javanainen and J.H. Eberly, J. Phys. B **21**, L93 (1988), and J. Javanainen and J.H. Eberly, Phys. Rev. A (in press).
4. M. Ferray, A. L'Huillier, X.F. Li, L.A. Lompre, G. Mainfray and C. Manus, J. Phys. B **21**, L31 (1988), and X.F. Li, A. L'Huillier, M.Ferray, L.A. Lompre and G. Mainfray (preprint).
5. C.K. Rhodes, Phys. Scripta T17, 193 (1987), and A. McPherson, G. Gibson, H. Jara, U. Johann, I.A. McIntyre, K. Boyer, and C.K. Rhodes, JOSA B **4**, 595 (1987).
6. Plateau and cut-off features have been found in a computer simulation of harmonic generation by xenon atoms by K. Kulander and B.W. Shore (private communication).
7. J.H. Eberly, Q. Su and J. Javanainen, J. Opt. Soc. Am. B (submitted).

---

**Part 3**  
**Microscopy and Holography**

---

## X-Ray Microscopy for the Life and Physical Sciences

D. Attwood,<sup>\*</sup> Y. Vladimirovsky,<sup>\*‡</sup> D. Kern,<sup>†</sup> W. Meyer-Ilse,<sup>‡</sup> J. Kirz,<sup>•</sup> S. Rothman,<sup>\*‡</sup>  
H. Rarback,<sup>§</sup> N. Iskander,<sup>•</sup> K. McQuaid,<sup>‡</sup> H. Ade,<sup>•</sup> and T. H. P. Chang<sup>†</sup>

<sup>\*</sup>*Center for X-Ray Optics, Lawrence Berkeley Laboratory  
University of California, Berkeley, California 94720*

<sup>†</sup>*Nanostructure Technology Group, IBM T. J. Watson Research Center  
Yorktown Heights, New York 11974*

<sup>‡</sup>*Universität Göttingen, Forschungsgruppe Röntgenmikroskopie, Geiststrasse II  
D-3400 Göttingen, Federal Republic of Germany*

<sup>•</sup>*Department of Physics, State University of New York, Stony Brook, New York 11974*

<sup>§</sup>*National Synchrotron Light Source, Brookhaven National Laboratory, Upton, New York 11973*

<sup>‡</sup>*University of California, San Francisco, California 94143*

<sup>‡</sup>*IBM East Fishkill Development Center, Hopewell Junction, New York 12553*

Advances in x-ray microscopy coupled with the development of bright, partially coherent radiation at x-ray wavelengths, herald a new period in which scientists in diverse disciplines will use x-ray imaging and probing techniques to see ever smaller structures, write ever smaller patterns, and study physical, chemical and biological systems, not only with an elemental sensitivity, but in many cases with a sensitivity to details of bonding. The combination of x-ray microscopy and various emission spectroscopies will permit the study of surfaces, thin films and material interfaces, as well as biological samples in their natural, unaltered and hydrated state<sup>1,2</sup>.

In this brief report we describe two recent x-ray microscopy experiments which demonstrate achievement of significant milestones in the development of high spatial resolution x-ray microscopy for the life and physical sciences. In one series of experiments it was clearly demonstrated that x-ray optical systems are capable of forming images of nanostructure patterns associated with future microelectronic devices, to a spatial resolution better than 0.1 microns. In the second set of experiments, unaltered biological material was imaged in its natural state without recourse to sectioning, staining, fixing or drying, at a spatial resolution well beyond that of the optical microscope, and with a delivered energy dose well below that of an electron microscope.

The series of experiments<sup>3</sup> in which it was shown that x-ray optical systems are capable of imaging microelectronic circuits, to a spatial resolution better than 0.1 microns, were performed by collaborators from LBL's Center for X-Ray Optics, IBM's Nanotechnology Group, and the Universität Göttingen's Forschungsgruppe Röntgenmikroskopie. The microelectronic pattern imaging experiments were performed using a new 400Å (outer zone width) gold Fresnel zone plate objective lens<sup>4</sup>, in the Göttingen group's x-ray microscope<sup>5</sup>, operated at 45Å wavelength at the Berlin Electron Synchrotron facility (BESSY). The new 400Å zone plate lens was fabricated at IBM as part of a collaborative agreement with the Center for X-Ray Optics. The theoretical resolution of such a lens is 500Å, a value which appears to have been achieved or closely approached in these experiments<sup>3</sup>. Figure 1 shows an SEM photograph of the gold Fresnel zone plate lens.



Figure 1. The gold Fresnel zone plate lens used to image nanostructure electronic patterns at BESSY. The lens has 500 zones, with a nominal outer zone width of 400Å, a gold thickness of 700Å, and a bar to space ratio in the outer region of 2:1. The lens has an outer diameter of 80µm, and a focal length of 0.71 mm at the 45Å wavelength used for pattern imaging. The effective aperture is F/9.

Figure 2 shows x-ray images of nanostructure patterns associated with a developmental, fast gating time FET of interest to IBM<sup>6,7</sup>. The opaque gold pattern is supported by a thin (~1,000Å), x-ray transmissive silicon nitride membrane. Pattern features well below 0.1 micron (1,000Å) are clearly resolved, demonstrating an ability to "see" such features albeit on a relatively small transverse field (~30 microns wide). The next step is to "write" patterns with this scale of detail, and then to devise a combination of methods for doing so on a larger transverse field.

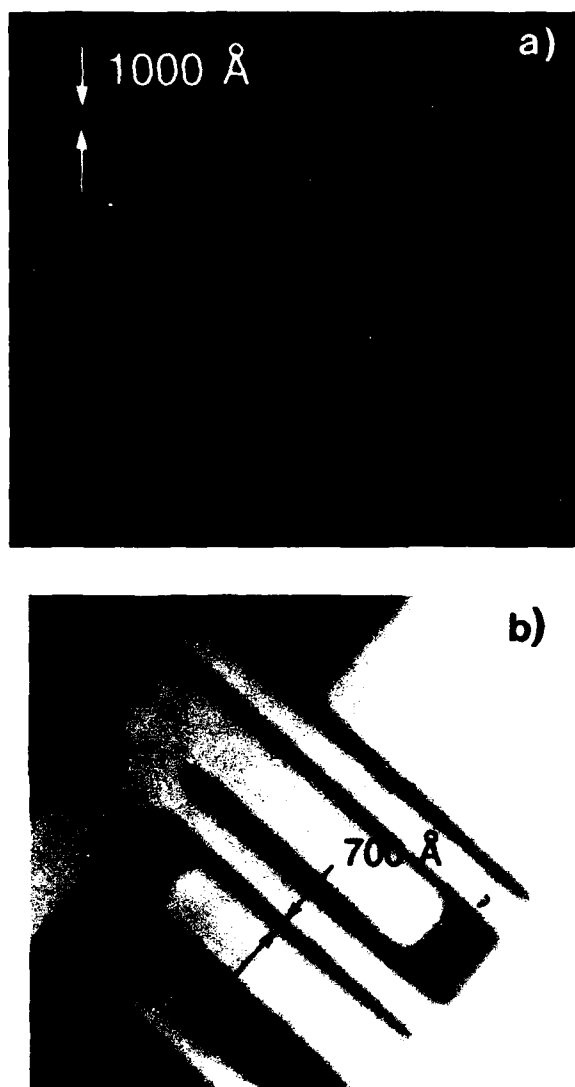


Figure 2.(a) A soft x-ray image, taken at  $45\text{\AA}$  wavelength, of the gate level pattern associated with an experimental  $0.1\text{ micron}$  MOSFET under development at IBM. The  $1,000\text{\AA}$  ( $0.1\text{ micron}$ ) gold bars are clearly resolved. The gold pattern is supported by an x-ray transmissive silicon nitride membrane of approximately  $1,000\text{\AA}$  thickness. The image shown is one portion of a repetitive pattern which is approximately  $30\text{ microns}$  across. (b) A soft x-ray image of two levels of the same MOSFET showing further pattern detail, including a clearly resolved  $700\text{\AA}$  gap ( $0.07\text{ micron}$ ) between gold fingers.

In the second series of experiments<sup>8</sup>, a significant milestone was achieved in that for the first time unaltered biological material, in its wet and natural environment, was imaged with a spatial resolution well beyond that of the optical microscope. In these experiments approximately  $1\text{ micron}$  diameter vesicles containing digestive enzymes were imaged at a spatial resolution better than  $1,000\text{\AA}$ , using IBM-CXRO Fresnel zone plates similar to those discussed above<sup>4</sup>, but having a thick apodized central region, and outer zone widths of  $500\text{\AA}$  or  $700\text{\AA}$ , depending on the particular experiment. These experiments,

involving damage sensitive biological material, were performed with the Stony Brook/NSLS scanning x-ray microscope at Brookhaven National Laboratory's National Synchrotron Light Source (NSLS)<sup>9</sup>, as a part of a collaboration involving SUNY Stony Brook, Brookhaven National Laboratory, UC San Francisco, IBM's Nanotechnology Group, and LBL's Center for X-Ray Optics. Figure 3 shows an image obtained at  $32\text{\AA}$  wavelength of a pancreatic secretion granule, separated from a male Sprague-Dawley rat, but maintained whole and otherwise unaltered in a specifically constructed fixture capable of maintaining an aqueous environment, with thin x-ray transmissive windows suitable for use with soft x-rays, and designed for use with the Stony Brook/NSLS scanning microscope<sup>10</sup>. This particular image was obtained with a  $700\text{\AA}$  outer zone width lens. Image formation in the scanning microscope is obtained on a pixel by pixel basis, by recording variations in transmitted x-ray flux as a function of position as the sample is rastered past the lens focal spot. In figure 3, a color image has been formed from the resultant array of numbers. The quantitative color assignment provides a mechanism for feature recognition through x-ray absorption. Low count rates, and thus high absorption, are represented by red, while blue represents low absorption. The chemical nature of this experiment and the wavelength used, suggest that red to orange appearance indicates varying concentrations of carbon containing proteins, while blue areas indicate prevalence of water. Comparison to electron microscope data is discussed in reference 8. Although the radiation dose was relatively high for this sample, approximately one megarad, the specimen was observed about  $20\text{ minutes}$  later in a second image, and except for small scale spatial variations near the resolution limit of the microscope, appeared to be unchanged. Future experiments will attempt to study not only structural integrity and elemental mapping<sup>11</sup>, but will also attempt to study biological function as well, through variation of chemical environment between exposures.

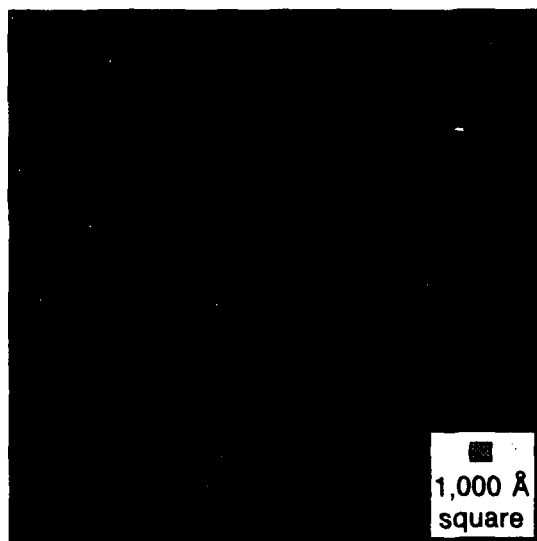


Figure 3. The image of a one micron diameter zymogen granule, obtained at  $32\text{\AA}$  wavelength with the scanning absorption microscope at NSLS. Protein content, indicated by higher absorptivity at this wavelength, is shown in reddish orange. Water, indicated by relatively low x-ray absorption is shown in blue. Color is quantitatively related to count rate, and thus absorption. Spatial resolution in this particular image, is approximately equal to the  $1,000\text{\AA}$  by  $1,000\text{\AA}$  square shown in the figure.

In conclusion, it is evident that x-ray optics and x-ray microscopy are making regular progress in the development of new tools for science and technology. The authors are pleased to acknowledge assistance from the staffs at NSLS and BESSY, use of the Göttingen microscope developed by G. Schmahl and D. Rudolph, and financial support from the U.S. Department of Energy, Office of Basic Energy Sciences, Division of Material Sciences, through contracts DE-AC03-76SF-00098 and DE-AC02-76-CH00016, the U.S. Department of Defense, Air Force Office of Scientific Research through University Research Initiative contract F49620-87-K-0001, the German Federal Ministry for Research Technology, and the U.S. National Science Foundation through grant BBS 8618066.

#### References

1. G. Schmahl and D. Rudolph, Eds., X-Ray Microscopy (Springer - Verlag, Berlin, 1984).
2. D. Sayre, M. Howells, J. Kirz and H. Rarback, Eds., X-Ray Microscopy II (Springer - Verlag, Berlin, 1988).
3. Y. Vladimirovsky, D. Kern, W. Meyer-Isle and D. Attwood, "X-Ray Imaging of Nanostructure Patterns", Appl. Phys. Lett. (to be published).
4. Progress in Fresnel lens fabrication, electron beam writing, and subsequent etching, plating and monitoring techniques is discussed in: Y. Vladimirovsky, D. Kern, T.H.P. Chang, D. Attwood, H. Ade, J. Kirz Vac. Sci. Technol. **6**, 311 (1988); Y. Vladimirovsky et al., Nucl. Instr. Meth. **A266** 324 (1988). Additional descriptions of micro Fresnel zone plate developments are given in several papers in references 1 and 2.
5. D. Rudolph, B. Niemann, G. Schmahl and O. Christ, in X-Ray Microscopy, op. cit., p. 192.
6. G. Sai-Halasz, M. Wordeman, D. Kern, E. Ganin, S. Rishton, D. Zicherman, H. Schmid, M. Polcari, H. Ng, P. Restle, T.H.P. Chang and R. Dennard, IEEE Electron Device Lett. **EDL-8**, 463 (1987).
7. T.H.P. Chang, D. P. Kern, E. Krauschmer, K.Y. Lee, H. E. Luhn, M. A. McCord, S.A. Rishton and Y. Vladimirovsky, "Nanostructure Technology", IBM J. Res. Dev. **32**, 462 (1988).
8. S.S. Rothman, N. Iskander, D. Attwood, Y. Vladimirovsky, K. McQuaid, J. Grendell, J. Kirz, H. Ade, I. McNulty, D. Kern, T.H.P. Chang and H. Rarback, "Advances in High Resolution X-Ray Microscopy - Imaging the Interior of a Whole and Unmodified Biological Object (to be published); S.S. Rothman et al. in X-Ray Microscopy II, op. cit., p. 372.
9. H. Rarback, D. Shu, S.C. Geng, H. Ade, J. Kirz, I. McNulty, D. Kern, T.H.P. Chang, Y. Vladimirovsky, N. Iskander, D. Attwood, K. McQuaid and S. Rothman, Rev. Sci. Instrum. **59**, 52 (1988).
10. N. Iskander, Senior Honors Thesis, Department of Physics, University of California, Berkeley, 1987.
11. C. Jacobsen, J.M. Kenney, J. Kirz, R. Rosser, F. Cinotti, H. Rarback and J. Pine, Phys. Med. Biol. **32**, 431 (1987).

## Contact Microscopy with a Soft X-Ray Laser

D. S. DiCicco,<sup>a</sup> D. Kim, R. J. Rosser,<sup>a</sup> C. H. Skinner, and S. Suckewer<sup>b</sup>

*Princeton University, Plasma Physics Laboratory, Princeton, New Jersey 08543*

A. P. Gupta

*Department of Entomology, Rutgers University, New Brunswick, New Jersey 08903*

J. G. Hirschberg

*Physics Department, University of Miami, Coral Gables, Florida 33124*

### Abstract

A soft X-ray laser of output energy 1-3 mJ at 18.2 nm has been used to record high resolution images of biological specimens. The contact images were recorded on photoresist which was later viewed in a scanning electron microscope. We also present a Composite Optical X-Ray Laser Microscope "COXRALM" of novel design.

### Introduction

The emerging technology of X-ray lasers [1,2] will have increasing impact in a number of fields. Microscopy using soft X-ray lasers offers the exciting prospect of imaging live cells at high resolution, thereby bridging the gap between electron microscope images of non-live cells that have undergone extensive specimen preparation, and low resolution but high fidelity images of live cells recorded with light microscopes [3,4]. In this paper we present high resolution images of several different biological specimens obtained with a soft X-ray laser. The soft X-ray laser at Princeton is well suited to contact microscopy as the pulse length (10-30 nsec) and pulse energy (1-3 mJ) are sufficient to record a flash image of a biological specimen on photoresist in a single shot. At the laser wavelength of 18.2 nm the absorption cross section of oxygen is three times that of carbon, providing good contrast between carbon in the cell proteins and oxygen in the surrounding water.

To be of maximum utility to biologists a soft X-ray laser contact microscope should be suitable for everyday use

on fragile, living biological specimens. We are developing a novel microscope design which will enable the operator to view and manipulate the specimen just prior to exposure (see later).

### X-Ray Laser Development at Princeton

The soft X-ray laser at Princeton is based on a rapidly recombining plasma confined in a magnetic field. A commercial CO<sub>2</sub> laser with maximum energy 1 kJ and duration 70 nsec, is focussed onto a carbon disc located in a strong (up to 90 kG) magnetic field, creating a plasma of sufficient temperature that a substantial fraction of the ions are stripped of electrons. Radiation cooling after the laser pulse produces rapid three-body recombination into highly excited states in hydrogen-like carbon. The  $m = 2$  level is rapidly depopulated by the strong  $2 \rightarrow 1$  radiative transition and in this way a population inversion is built up between levels 3 and 2, leading to amplified spontaneous emission and lasing at 18.2 nm (Fig. 1). The strong confining magnetic field provides several advantages. It enables the electron density to be controlled to the optimum value and forms the plasma into a long thin geometry suitable for a laser. The geometry is also suited to fast radiation cooling, and the radiation cooling can be enhanced by the addition of high Z materials.

The CO<sub>2</sub> laser is focussed onto a target chamber inside a solenoidal magnet that is surrounded by diagnostic spectrometers (see Fig. 2). The spectrometers are calibrated absolutely and measure the soft X-ray gain by measuring the directionality of the emitted radiation.

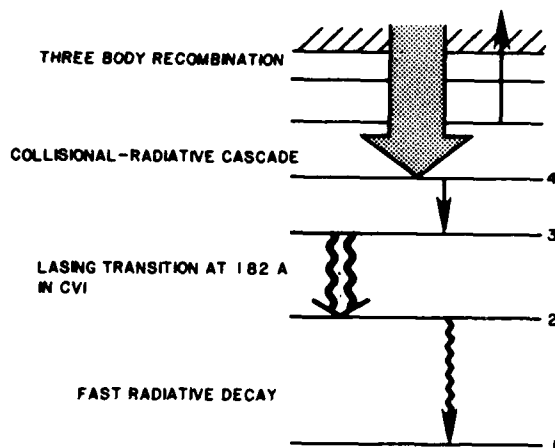


Figure 1. Principle of generation of population inversion and lasing action in hydrogen-like ions in a rapidly recombining plasma.

In a long thin plasma most of the stimulated emission is along the plasma axis and the gain is measured by comparing the axial to transverse intensity.

The target is a carbon disc with one to four blades attached perpendicular to the target surface. The blades help to generate an elongated plasma. They also help to cool the plasma by thermal conduction and additional radiation losses. An important feature is the radial profile of the plasma. The plasma pressure is balanced by the magnetic field pressure so that on axis there is a high temperature due to heating by the laser, and corresponding low density. In the outer cooler regions the density is higher and it is in these outer regions that the conditions are most favorable for fast recombination. The gain is generated in an annular region around the center of the cylindrical plasma. An off-axis slot in the target transmits the stimulated emission to the axial spectrometer. The system has a very accessible output beam, can be fired every three minutes and operated by only two people.

A gain-length of  $GL \approx 8$  on the 3-2 transition at 18.2 nm has been achieved with an output energy of 1-3 mJ in a low divergence, (5 mrad), beam. This system has been described previously in a number of publications, see e.g. [5] - [7]. More recently efforts to obtain gain at wavelengths shorter than 18.2 nm have resulted in measurements of gain-length  $GL \approx 3-4$  at 15.4 nm in AlXI and  $GL \approx 1-2$  at 12.9 nm in SiXII [8]. Current research is focussed on

Table 1

#### Soft X-Ray Laser Output Parameters

Gain - Length	8
Wavelength	18.2 nm
Energy	1-3 mJ
Power	100 kW
Duration	10-30 nsec
Divergence	5 mrad
Efficiency	$10^{-5}$
Shortest Wavelength	12.9 nm
Repetition Time	3 min.

increasing the output energy of the 18.2 nm laser by additional amplifiers [9] and exploring a new approach to developing X-ray lasers in the wavelength region from 5 nm down to 1 nm [10].

#### Contact Microscopy Using a Soft X-Ray Laser

Much progress has been made in Biology and Medicine due to the high resolution images obtained from electron microscopes. However, in order to be viewed by an electron microscope the specimen must be dried, stained and sectioned and it is clear that some information about the living cell is lost in the process. One can view a live cell with a light microscope with high fidelity but the resolution is of course limited. Soft X-ray contact microscopy offers a new method to obtain high resolution images of live cells. The specimen is contained in an environmental cell isolated from the X-ray laser vacuum system by a 120 nm thick silicon nitride window. The image is recorded on photoresist which is later viewed by an electron microscope [11]. This approach has been used recently with plasma light sources and synchrotrons [3,12]. The highly collimated output beam of the soft X-ray laser compared to a conventional plasma light source has the advantage of less penumbral blurring of the image and more flexible microscope design. The soft X-ray laser also has the advantage of a 10-30 nsec exposure time enabling flash images of live cells to be recorded, unlike the several minutes needed for synchrotron

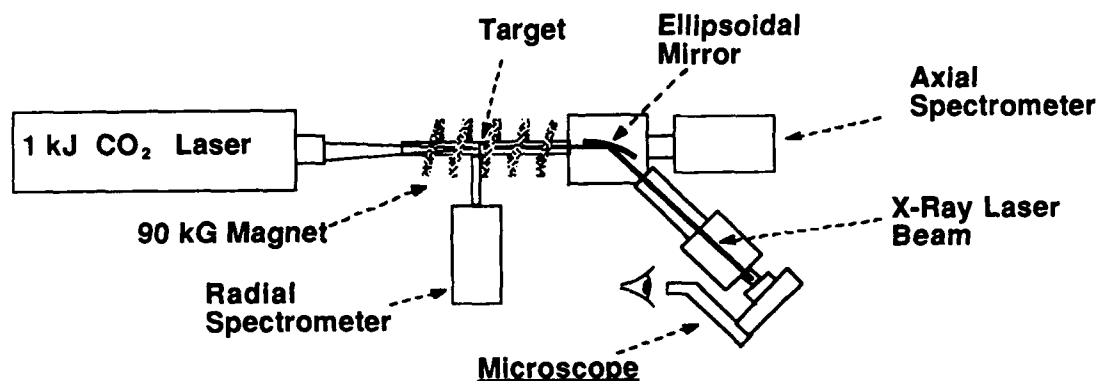


Figure 2. Contact microscope installed on the soft X-ray laser.

sources which effectively prevents the imaging of live cells with synchrotrons.

The soft X-ray laser output beam originates from an annular gain region 50-100  $\mu\text{m}$  wide in the plasma. The beam is emitted along the magnetic field axis and is normally detected with a grazing-incidence spectrograph equipped with a multichannel detector. For microscopy experiments, an ellipsoidal mirror is used to deflect the soft X-ray beam to the photoresist in a contact microscope. The mirror is a diamond turned, post polished, rhodium coated ellipsoid which provides an image of the soft X-ray gain region in the plasma on the photoresist.

In the first experiments a contact image of # 100 mesh was made on both Kodak 101 film and copolymer photoresist P(MMA co MAA). While the film was much more sensitive, the inevitable grain structure degraded the resolution to a few microns. Much higher resolution was obtained on the photoresist. Noteworthy here is that although the photoresist is much less sensitive than film, needing of the order of 100 mJ  $\text{cm}^{-2}$  for exposure, the available energy in the soft X-ray laser beam was sufficient to expose the resist in one shot.

In contact microscopy the shadow of the specimen is recorded in the resist in the following way. Exposure to X-rays produces chain scission in the long polymer molecules in the photoresist and hence the exposed areas dissolve faster in a suitable solvent. After development, a relief map of the X-ray absorption by the specimen is formed on the surface of the resist. The resist is then coated with a thin layer of Au/Pd and viewed at high resolution in a scanning electron microscope.

A suspension of diatoms (silicified skeletons of planktonic algae) was placed on photoresist and left to dry. After exposure in vacuum by the soft X-ray laser the copolymer photoresist was developed for one minute in a mix of equal parts methyl isobutyl ketone and isopropyl alcohol and viewed in a scanning electron microscope (SEM). The SEM image is shown in Fig. 3 and a resolution of 0.1  $\mu\text{m}$  is apparent. Since the diatoms are high contrast objects this technique can also be described as microlithography and illustrates the potential application of X-ray lasers to micro-electronics.

It was found that the photoresist PBS (polybutene-1-sulfone) was a factor of three more sensitive than the copolymer resist and was therefore used for subsequent exposures of biological specimens. The PBS resist was developed in methyl ethyl ketone (2 parts) and isopropanol (1 part) for 15 seconds. In initial experiments with biological specimens placed in contact with the resist, it proved difficult to remove the specimens from the resist after the exposure. This opened the possibility of confusion of remnants left on the resist with the relief image formed in the resist [13]. In order to avoid this problem the biological specimens were mounted on a thin (5 nm) carbon film supported on a standard TEM grid (Fig. 4). This was placed in contact with the resist for the exposure and could be easily removed and if necessary reused in later exposures.

One topic of considerable current interest in biology is immunology and since this involves the dynamic response of immune cells to foreign matter it is a natural subject for investigation by soft X-ray laser microscopy. One of the most primitive and hence simplest,



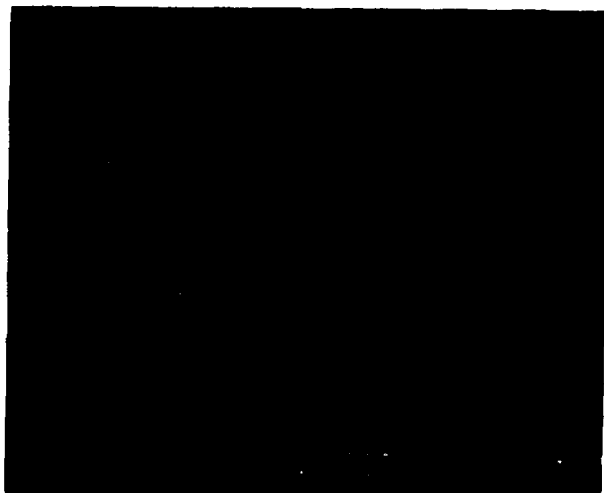


Figure 3. SEM image of replica of Diatom fragment (silicified skeleton of planktonic algae).

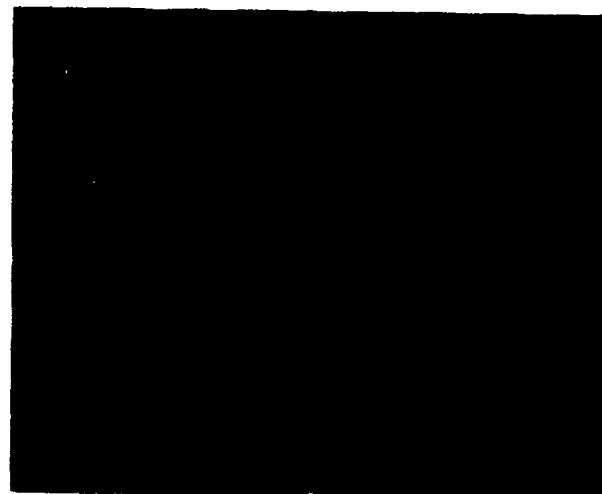


Figure 5. SEM image of replica of Granulocytes from *Limulus Polyphemus* (Horseshoe Crab).

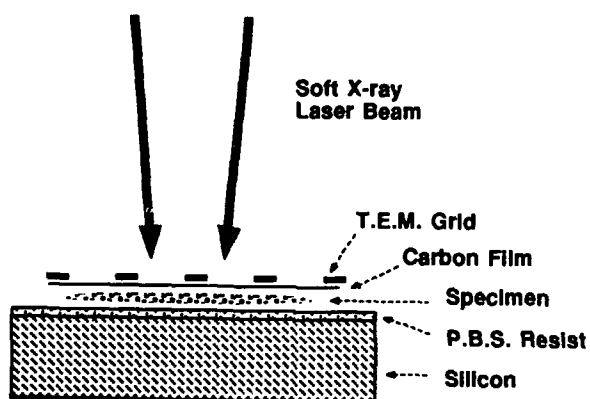


Figure 4. Contact Microscopy of biological specimens.



Figure 6. SEM image of replica of hela cells (Helen Lane cervical cancer cell).

# COMPOSITE X-RAY LASER MICROSCOPE (COXRALM)

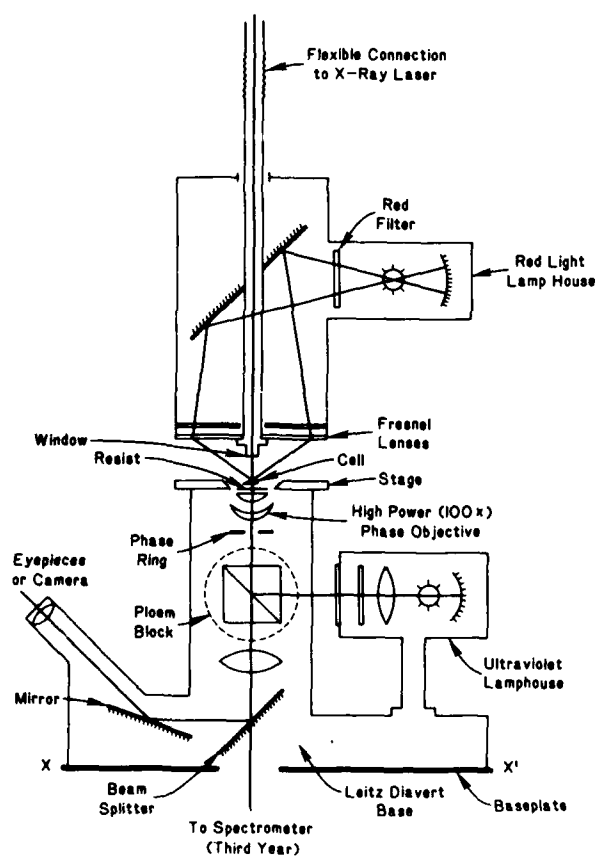


Figure 7. Schematic of Composite X-Ray Laser Microscope.

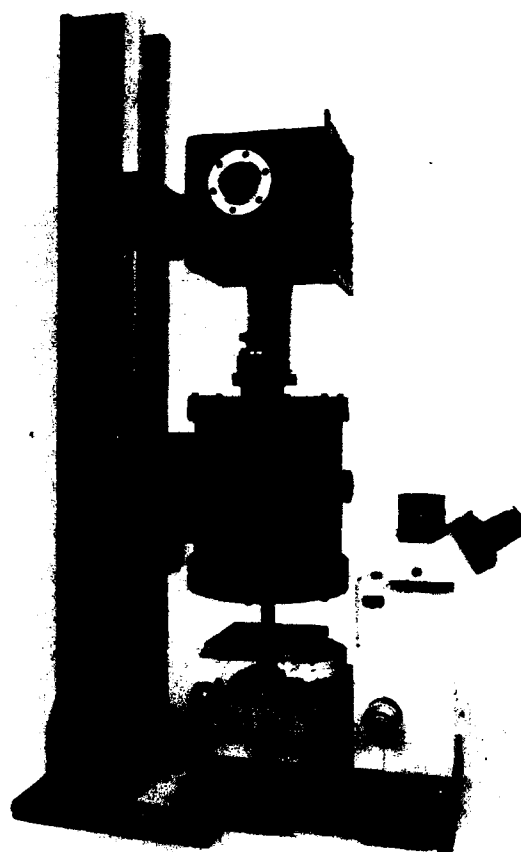


Figure 8. Composite X-Ray Laser Microscope.

immune systems is found in the horseshoe crab (*Limulus Polyphemus*) where there is only one type of immune cell to fulfill several functions. A sample of blood from the horseshoe crab was dehydrated in an ethanol series and critical point dried using the standard procedure but was not fixed or stained and an exposure was taken with the soft X-ray laser contact microscope. The resulting images viewed in an JEOL 840 scanning electron microscope are shown in Fig. 5. The depressions apparent in the granulocyte are known to exhibit immune functions from work in conventional electron microscopy. The smaller white features covering the cell are new and were not apparent on images obtained in conventional electron microscopy. Their identity and function is presently unknown.

One of the difficulties of reading a relief pattern in a photoresist with a SEM is that the electron beam in the SEM is capable of writing a raster pattern in the resist and destroying the image. In the above images the accelerating voltage was reduced to 5 kV to avoid this effect but the resulting readout process is lengthy. We have developed a technique which enables the resist image to be quickly acquired and read out at a much lower beam current ( $2 \times 10^{-12}$  A compared to the  $2 \times 10^{-11}$  A used previously). In this technique the resist has a 1000 Å thick gold underlayer which increases the flux of backscattered electrons. The SEM image is then predominantly formed by backscattered electrons rather than secondary electrons from the surface. There is a minor decrease in the ultimate achievable resolution of the SEM with this technique but this does not appear to be a significant factor at present.

This technique was used in the image of Hela cells shown in Figure 6. This is an embedment-free section of a monolayer of extracted Hela cells on a carbon/formvar base. Hela cells are cultured human cervical cancer cells and the clumping feature apparent in the irregularly shaped nuclei are the result of invasion by a virus.

#### Microscope Development

Perhaps the greatest potential for soft X-ray laser microscopy is in the study of dynamic processes in live cells. To maintain and manipulate cells in a living state is a considerable experimental challenge and for novel

microscopic techniques to have a significant impact in biology they must be practical and convenient to use. To this end we have developed a Composite Optical Soft X-ray Laser Microscope, "COXRALM" Figs. 7, 8. This is a new type of microscope combining an inverted phase contrast optical microscope with a soft X-ray laser contact microscope. The inverted optical microscope has already been used [14] as a microspectrofluorometer for the study of transient coenzyme fluorescence changes in living cells as a result of the intracellular microinjection of metabolites. This research is aimed at understanding the pathology and physiology of cancer cells. However the inevitable limitations in resolution of the optical microscope meant that many features of the metabolic processes inside the cells remained obscure.

COXRALM offers the possibility of making an X-ray contact image of these cells while preserving the ability to select and observe through the optical microscope and perform microinjection of metabolites and/or inhibitors and xenobiotics just prior to X-ray exposure.

The cells will be mounted on resist on a transparent substrate. When a contact X-ray image is desired the X-ray laser beam tube will be lowered until the silicon nitride vacuum window at the tip is in contact with the cell and then the X-ray laser is triggered. The system has been installed on the X-ray laser and was used in initial experiments without the optical microscope to generate the contact images shown in Figs. 5 and 6.

#### Acknowledgements

We would like to thank Scott Orenberg and David Ornelles for preparation of the biological specimens and Elaine Lenk for the Electron Microscopy, and acknowledge significant contributions from E. Kohen, L. Meixler, T. Bennett, and P.C. Cheng. The silicon nitride windows and copolymer resist were provided by the IBM Watson Research Center. COXRALM was fabricated by Princeton X-Ray Laser Inc. This work was made possible by financial support from the U.S. Department of Energy, Advanced Energy Projects of Basic Energy Sciences.

- a. PXL Inc., 1-H Deerpark Drive, Monmouth Jt., NJ 08852.
- b. Also at Mechanical & Aerospace Engineering Dept., Princeton University.

## References

1. Proceedings of International Colloquium on X-Ray Lasers Eds: P. Jaegle and A. Sureau, Journal de Physique, Tome 47, Colloque C6, Octobre 1986. Les Editions de Physique, Les Ulis Cedex, France.
2. Special Issue on X-Ray Lasers, IEEE Transactions on Plasma Science, 16, (5) October 1988.
3. X-Ray Microscopy II - Proceedings of the International Symposium, Eds: D. Sayre, M. Howells, J. Kirz, H. Rarback, Brookhaven, Aug. 31-Sept. 4, 1987, Springer-Verlag 1988.
4. X-ray Microscopy, Instrumentation and Biological Applications, Eds: P.C. Cheng and G.J. Jan, Springer-Verlag, Berlin, Heidelberg, (1987).
5. S. Suckewer, "X-Ray Related Experiments and Theory at Princeton," this volume.
6. C.H. Skinner, D. DiCicco, D. Kim, L. Meixler, C.H. Nam, W. Tighe, and S. Suckewer, "Toward Shorter Wavelength Lasers and Soft X-ray Microscopy," IEEE Transitions on Plasma Science 16, 5, 512-519 (1988).
7. S. Suckewer, C.H. Skinner, D. Kim, E. Valeo, D. Voorhees, and A. Wouters, "Divergence Measurements of Soft X-ray Laser Beam," Phys. Rev. Lett. 57, 1004-1007, (1986).
8. D. Kim, C.H. Skinner, A. Wouters, E. Valeo, D. Voorhees, and S. Suckewer, "Soft X-ray Amplification in Lithium-like AlXI (154 Å) and SiXII (129 Å)," JOSA B, in press (1988).
9. D. Kim, C.H. Skinner, G. Umesh, and S. Suckewer, "Gain Measurements at 182 Å in CVI Generated by a Nd/Glass Laser" submitted to Optics Letters.
10. L. Meixler, C.H. Nam, J. Robinson, W. Tighe, K. Krushelnick, S. Suckewer, J. Goldhar, J. Seely, and U. Feldman, "High Power, Short Pulse Ultraviolet Laser for the Development of a New X-ray Laser," this volume.
11. P.C. Cheng, R. Feder, D.M. Shinozaki, K.H. Tan, R.W. Eason, A. Michette, and R.J. Rosser, "Soft X-ray Contact Microscopy," Nucl. Instrum. Methods A246, 668-674 (1986).
12. R. Feder, V. Banton, D. Sayre, J. Costa, M. Baldini, and B. Kim, "Direct Imaging of Live Human Platelets by Flash X-ray Microscopy," Science 227, 63-64 (1984).
13. P.C. Cheng, D.M. Shinozaki, and K.H. Tan, "Recent Advances in Contact Imaging of Biological Materials" in X-Ray Microscopy, P. 65-104, Eds. P.C. Cheng and G.J. Jan, Springer-Verlag Berlin Heidelberg 1987.
14. J.G. Hirschberg, A.W. Wouters, E. Kohn, C. Kohen, B. Thorell, B. Eisenberg, J.M. Salmon and H.S. Ploem, "A High Resolution Grating Microspectrofluorometer with Topographic Option for Studies in Living Cells," ACS Symposium Series No 102 Ed: Y. Talmi, American Chemical Society 1979.

## X-Ray Fourier-Transform Holographic Microscope

W. S. Haddad, D. Cullen, J. C. Solem,<sup>†</sup> K. Boyer, and C. K. Rhodes

MCR Technology Corporation, P.O. Box 10084, Chicago, Illinois 60610-0084

### Abstract

The properties of an x-ray Fourier-transform holographic instrument suitable for imaging hydrated biological samples are described.

### I. Introduction

Recent advances in coherent x-ray source technology are making diffraction-limited holograms of microscopic structures, with corresponding high spatial resolution, a reality. A high priority application of snapshot x-ray holography is the study of microscopic biological structures in the hydrated living state.[1] X-rays offer both high resolution and high contrast for important structures within living organisms, thereby rendering unnecessary the staining of specimens, essential for optical and electron microscopy, if the wavelength is properly chosen. Furthermore, the snapshot feature, arising from picosecond or subpicosecond exposure times, eliminates blurring occurring from either thermal heating[1] or normal biological activity of the sample. Finally, with sufficiently high photon fluxes, such as those available from x-ray lasers, the x-ray snapshot can be accomplished with a single pulse, thereby yielding complete three-dimensional information on a sample having normal biological integrity at the moment of exposure.

Fourier transform holography requires a reference source which emits spherical or convexly curved waves which interfere at the recording surface with the waves scattered from the specimen. In the envisioned configuration, the specimen is illuminated by a plane wave source.[2] This approach is called Fourier-transform-holography because, to a first approximation, spatial separations map uniquely to spatial frequencies at the recording surface. A configuration of this nature is particularly suited to the microholographic application, since it is essentially the only practical geometry permitting the use of a low resolution medium for the detector, such as a CCD array.[3] This

advantage arises naturally, since control over the fringe frequency can be readily obtained by simple adjustment of the geometrical parameters, such as the distances of the detector from the reference and/or the object. Additionally, because of the possibility of close relative placement of reference and object, the Fourier configuration is congenially suited to a source having a small beam size and a low divergence,[4] natural properties of a laser. The geometry of a system of this type is depicted in Fig. 1.

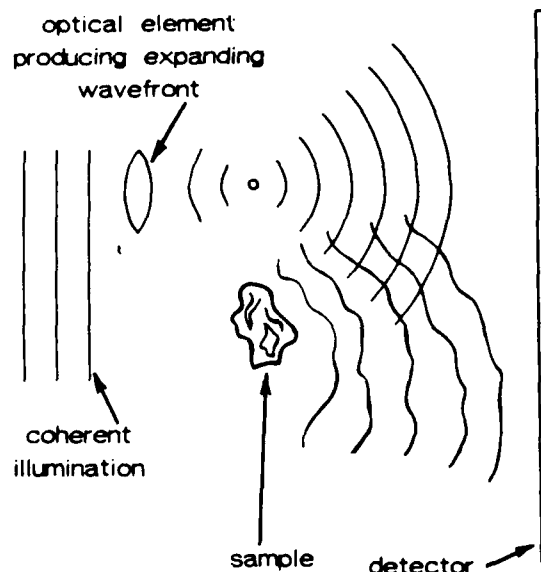


Figure 1. Geometry for Fourier-transform holography.

The ideal source, because of its very high peak brightness, would be an x-ray laser. Simple scaling shows that such systems will be capable of delivering enough energy in one pulse to make a holographic exposure ( $\geq 1000$  photons/pixel of the CCD array). However, it should be

mentioned that lower peak power x-ray sources, such as synchrotrons, may be employed using time exposures if the sample is sufficiently immobile and immune to radiation damage. For example, a specimen could be cooled to retard motion caused by normal biological activity. For hydrated materials, the desired wavelength is in the range spanning 25 – 45 Å, the well known[1] "water window".

Current developmental trends in digital processing and electronic imaging greatly favor digital (i.e. numerical) reconstruction of the 3-D image directly from the hologram. Together, the Fourier transform geometry, the CCD array detector, and the computer system for digital reconstruction, represent a basic triad for a future microholographic instrument. The overall anatomy of such a system is shown in Fig. 2. The AT presents itself as a practical, compact, and cost effective choice for the host computer. The holographic data are made available to the computer by a video digitizer, and a fast floating-point array processor is used to perform rapidly the necessary calculations. A high volume, fast-access data storage capability is also required. A schematic representation of the entire microscope is presented in Fig. 3.

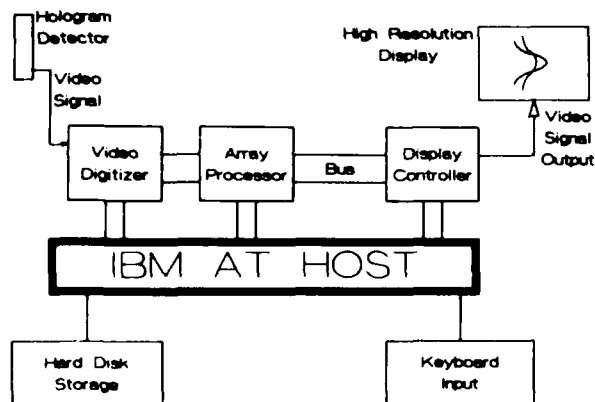


Figure 2. Image reconstruction system.

## II. The Target System

The target consists of the sample to be imaged, a reference scatterer, and a device suitable for mounting and positioning these components with respect to each other and the detector.

A critical element of this design is the reference scatterer which acts as the source of the reference wave. The spatial orientation of the reference scatterer cannot be controlled so it must be a sphere. Unlike the parabolic reference scatterer, usually discussed in connection with spherical Fourier-transform[5] holography, the spherical reference scatterer does not produce true spherical waves; they emanate from a line rather than a point and are spherical only at large distances. Furthermore, an ideal sphere would produce isotropic reference illumination, but, in the soft x-ray regime, reflectivity is a strong function of

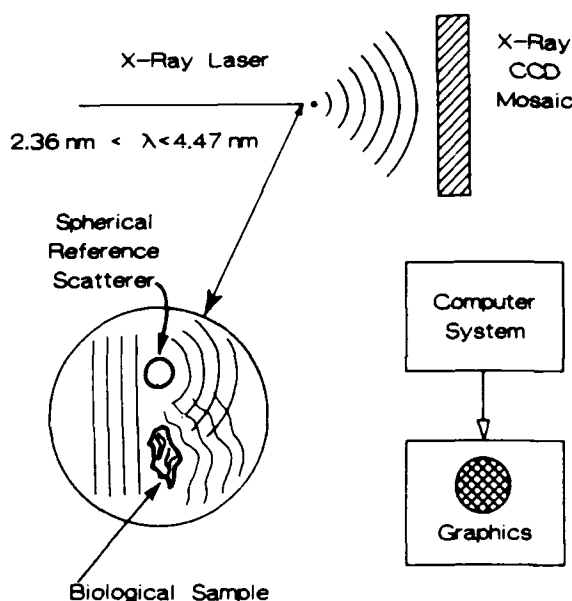


Figure 3. Schematic showing the primary components of the holographic microscope.

grazing angle. A survey of the periodic table[6] shows that nickel ( $Z = 28$ ) is clearly the best reflector for  $\lambda = 44.7 \text{ Å}$  (near the carbon K-edge), at grazing angles up to about  $14^\circ$ , and is surpassed only by rhenium ( $Z = 75$ ) and osmium ( $Z = 76$ ) at greater angles. The reference illumination scattered from nickel is judged to be adequate for good fringe visibility up to a grazing angle of about  $15^\circ$ , a point where it is  $\sim 3\%$  of the incident intensity. X-rays scattered from the specimen will also generally be less intense at larger angles, so the mismatch between the reference and signal waves is not expected to be great at these larger angles. A grazing angle of  $15^\circ$  corresponds to a total scattering angle of  $30^\circ$ , thus about  $\pi/9$  steradians will receive adequate reference illumination. For  $\lambda = 31.6 \text{ Å}$ , the wavelength of maximum contrast between water and protein, osmium is superior to nickel at  $10^\circ$ , a point where its reflectivity is about 6%. In this case, the maximum usable scattering angle is about  $22^\circ$ , a value corresponding to about  $\pi/17$  steradians.

The resolutions achievable in the transverse and longitudinal directions depend differently on the scattering angle  $\theta$ . Transverse resolution is limited to  $\sim \lambda/2\theta$ , while longitudinal resolution[3] has a limit given by  $\sim \lambda/4\theta^2$ . The usable scattering angles for both the  $44.7 \text{ Å}$  and  $31.6 \text{ Å}$  cases are sufficient to give a spatial resolution on the order of  $\lambda$  in both the longitudinal and transverse directions.

A technique exists for the fabrication of smooth, round, nickel spheres with diameters in the  $2 - 10 \mu\text{m}$  range. Smoothness of the reference scatterer, of course, is particularly important to avoid speckle.

For hydrated biological specimens, given the

opacity of water in the soft x-ray region, a useful and practical biological sample thickness would be approximately 1  $\mu\text{m}$ .

An imaging system of this type can, in principle, be used to investigate a wide range of specimens. One possibility involves the base-pair sequencing of the human genome. This could be accomplished by chemically marking the four bases with specifically associated linker-arms and tags involving groups of four corresponding heavy atoms. It appears that this chemical step can be readily performed with the appropriate polymerase. Exposures made with four properly selected wavelengths would then furnish the information necessary to reconstruct the base-pair sequence. Preliminary estimates indicate that this method of direct imaging of DNA for sequencing is competitive with other currently used approaches.

Clearly, samples other than biological entities can also be studied. For example, the physical characteristics of small-scale semiconductor components could be visualized.

A proper target system must exhibit several properties. It is, for example, desirable to have a statically mounted scattering system incorporating both the reference scatterer and the sample. In one possible embodiment, they are placed on a thin foil which is chosen to have a low scattering power so that the transmission of the soft x-rays is not appreciably influenced. Moreover, it is important that the structure not degrade the spatial coherence of the illumination, a criterion requiring that the foil be of sufficiently uniform thickness over the region exposed. Suitable materials for the foil are thin sections of low-Z material such as beryllium and carbon. Grids providing support of the films include structures made of beryllium, carbon composite, and nylon mesh coated with carbon, copper, or gold. Such grids, which are routinely used in electron microscopy, are available in a range of meshes, as well as in a honeycomb configuration, with round or slit hole designs. Carbon and beryllium films having a thickness of  $\sim 200 \text{ \AA}$  or less can be fabricated and should be satisfactory for this application.

Figure 4 shows a schematic representation of the spherical reference scatterer and the biological specimen under investigation mounted on a film which is supported by a grid structure. Since these films generally exhibit a low affinity for biological materials, the use of a thin layer of poly-L-lysine, which has a high charge affinity for many biological specimens, can be used to anchor the samples. Since the poly-L-lysine is optically thin and has an amorphous character, its presence does not confuse the scattered wave from the sample.

### III. Data Acquisition and Analysis

Since the Fourier-transform holographic configuration does not require a high-resolution recording medium, the detector can be a mosaic of charge-coupled devices (CCD), which are efficient,

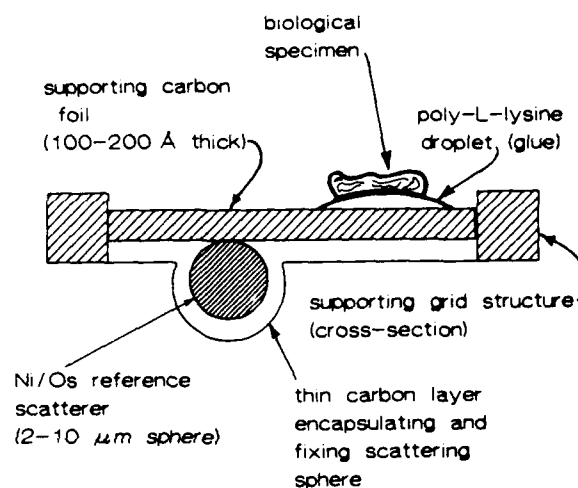


Figure 4. Sketch of one possible configuration of the holographic target (i.e. scattering system).

linear, and can be linked directly to a computer. Charge-coupled devices[7] capable of quantum efficiencies as high as 80% in the soft x-ray regime can be prepared by removing most of the backing layer of a conventional CCD. Such components are available in arrays with  $2000 \times 2000$  pixels. The spatial resolution of the detector is important in Fourier transform holography only as a constraint on the overall size of the instrument. However, the number of pixels will ultimately determine the volume of the field of view. Currently, a pixel size in the 10 to 15  $\mu\text{m}$  range is available.

The theoretical approach to the process of reconstruction is founded on a set of basis functions which map to individual points in the reconstruction space. A more detailed description of the procedure involved is described elsewhere.[8] With this approach, the object is described as a collection of point sources of scattered radiation. In the limit of large distances from the object and reference scatterers, the reconstruction reduces to a Fourier transform. However, in this paraxial limit, the analysis is restricted to a two-dimensional object occupying the plane parallel to the detector plane and to a small aperture for the detector.[9] In order to have high resolution in both the longitudinal and transverse directions, a large detector aperture is necessary and, consequently, the simple Fourier transform is no longer suitable as the reconstruction algorithm. A solution is found by the use of a different set of basis functions, not necessarily trigonometric, similar to the application of a Fourier transform. These functions can be thought of as the set of all holograms of the individual points which comprise the object. The projection or inner product of the holographic function, measured by the detector array and the basis functions, yields the amplitude of the points in the reconstructed object. In principle, it is desirable that the basis functions be orthogonal. In fact, however, absolute orthogonality is not present due to the detector specifications and the geometry of the

system. This feature, which will always be present in any finite system, is the main source of distortion in the reconstruction process.

It is possible to use digital processing to improve the image quality and performance of the system. Specifically, the "confusing wave" can be removed by applying a high pass frequency filter to the holographic function before performing the reconstruction. The "confusing wave" arises from the interference among waves emanating from the various scattering bodies within the object under investigation. The hologram produced from this interference naturally has low spatial frequencies, since these bodies are close together. What is of interest, of course, is the signal produced from the interference pattern of the scattering from bodies within the object with the scattered reference wave. If the reference scatterer is sufficiently far from the object, this important information can be concentrated in the signal at high spatial frequencies. Therefore, a high pass filter applied to the detected data can markedly simplify the reconstruction process. Furthermore, fast Fourier transforms can be adapted for use in this procedure, thereby enabling rapid and efficient computation.

An algorithm has been developed and tested in two dimensions for reconstruction of the physical characteristics of samples from measured spatial frequencies. Geometrical optics and plane-wave irradiation are assumed. It is also assumed that the reference scatterer is perfectly spherical.

#### IV. Computer Experiments

Theoretical simulations of the reconstruction algorithm have been performed as well as simple experiments on actual optically generated holographic data. To do this efficiently, the problem has been reduced to one transverse dimension. The reduction to single transverse dimensions can be done with no loss of generality, since the two transverse dimensions are exactly equivalent. The specimen was the "happy face" shown in Fig. 5a. Its horizontal dimension in the longitudinal direction and its vertical dimension in the transverse direction. This two-dimensional specimen was then numerically mapped into a one-dimensional hologram. The reconstruction algorithm was then applied. The demonstration is quite satisfying considering that it was performed with the rather limited computational capacity of an IBM PC/AT.

The loss of holographic signal in the region of large angle, due to the angular variation in the reflectivity of the Ni/Os scattering, is expected to affect both the resolution and contrast of the reconstruction. Therefore, the consequences of this situation have been computationally unmined. Consider the test object illustrated in Fig. 5a. Imagine the formation of a simulated hologram made with the use of basis functions properly corrected for the use of a spherical scatterer of nonvanishing radius and incorporating the

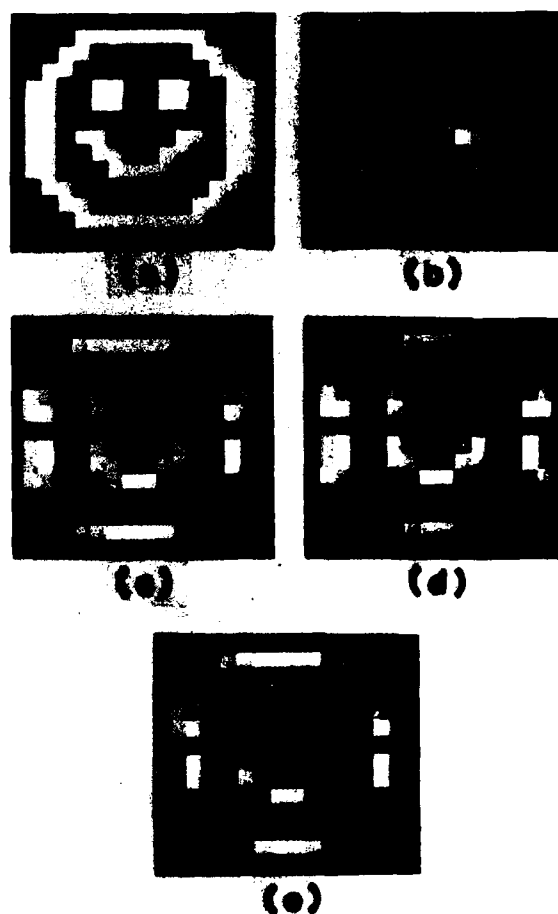


Figure 5. Computer simulations: (a) original test object; (b) image formed from hologram synthesized with fully corrected basis set but reconstructed with a primitive uncorrected basis set; (c) image produced by reconstruction with a fully corrected basis set; (d) image formed when angular variation in reflectivity is not accounted for in basis set for reconstruction; (e) reconstruction arising from the use of the fully corrected basis set with an appropriate preprocessing step on the holographic data.

angular variation of intensity in reflection. This model properly simulates the real physical situation in which an actual holographic exposure would be performed. Now consider the reconstruction of that hologram with a primitive basis set that incorporates neither of the corrections noted above. Obviously, the reconstruction accomplished in this manner does not take into account two important physical features of the true exposure. The result of this operation is the reconstructed image shown in Fig. 5b. The form of the object is essentially lost and no recognizable image is formed. Conversely, reconstruction of the hologram with the fully corrected basis set leads to the image illustrated in Fig. 5c. A clear and recognizable image appears.



The influence of the angular variation in scattering strength can be isolated by comparison with a reconstruction arising from the use of basis functions corrected for the radius of the spherical reference scatterer, but lacking the angular correction. The image thus formed is shown in Fig. 5d. The comparison of the images appearing in Fig. 5c and Fig. 5d reveals that the angular variation in scattering power leads to some distortion of the image, with respect to both spatial resolution and contrast, but that the degradation in image quality is not great.

Further study has indicated, however, that it may be possible to process the holographic information prior to reconstruction in such a way that the degradation of the image caused by the diminished reflection at large angles is significantly reduced. Fig. 5e illustrates the result of a selective preprocessing of the holographic data with the outcome that an improved image is obtained. Basically, the preprocessing step used enables the information in the fringes at the edges of the hologram to be effectively used in the reconstruction, while simultaneously preventing the introduction of distortions from other regions. We expect that procedures of this type can be further developed which, although not entirely eliminating the image distortion, will be effective in substantially ameliorating the loss of image quality due to the angular variation in reference sphere reflectivity.

Other causes of uncontrolled variations in the amplitude of the hologram can also degrade the quality of the image. These can occur from modulations in the sensitivity of the recording CCD array. In an extreme case, inoperative pixels, or rows of pixels, both common manufacturing defects, can cause a complete loss of information over certain portions of the holographic exposure.

The overall sensitivity of the reconstructed image to variations in the amplitude of the hologram has been examined and found to be remarkably low. Indeed, high quality images can be reconstructed from holograms grossly altered by the loss of amplitude information over substantial regions of the exposure. This finding is consistent with the known fact that holographic data are quite resistant to this type of damage.

The original test object, the reconstruction of the unflawed hologram, and the reconstruction of the hologram having a 200 pixel gap cut from the center, are shown in Fig. 6a, 6b, and 6c, respectively. For further comparison, Fig. 6d shows the reconstruction of the same hologram with a 400 pixel gap imposed at the center. This gap represents a very substantial amount of the holographic information, since the hologram is only 2048 pixels long.

Random flaws superimposed on the hologram, even with a modulation depth of one hundred percent, are not effective in destroying the image. An image rather close to that produced with the unflawed hologram is obtained, as shown in Fig. 6e.

These studies have demonstrated that an

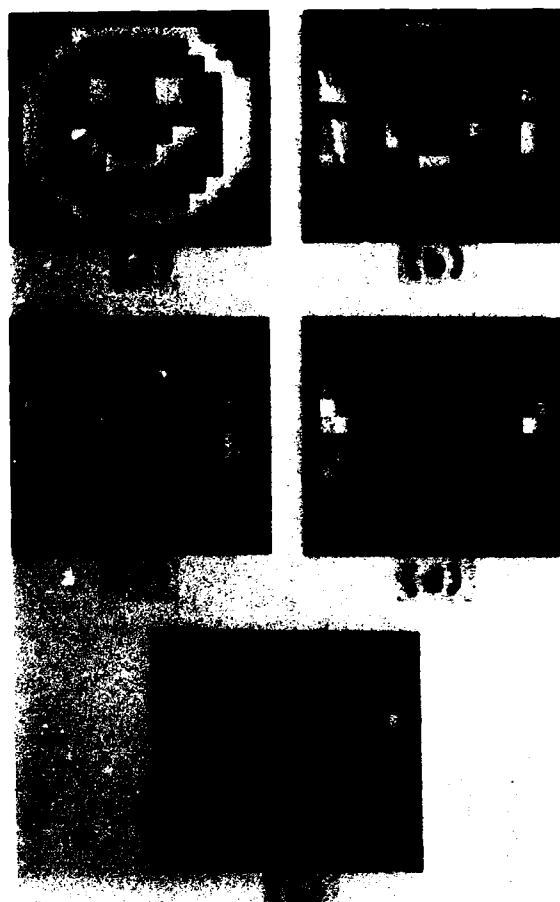


Figure 6. Computer simulations: (a) original test object; (b) reconstructed image of hologram of original test object with no amplitude variations imposed; (c) reconstruction of hologram having a 200 pixel gap imposed at the center; (d) reconstruction of hologram with a 400 pixel gap at the center; (e) reconstruction obtained with random flaws superimposed on the hologram with a modulation depth 100%.

astonishingly large fraction of the holographic data can be lost without destruction of the overall features of the reconstructed image.

## V. Conclusions

A complete system suitable for x-ray microholography has been designed. This includes target fabrication, reference wave production, the methods used for recording the hologram, and the reconstruction of the image from the holographic data. Furthermore, the approach has been verified by computer simulation and the performance of simple experiments.[10]

The development of a new x-ray microholographic technology applicable for structural assays of living biological materials has been advanced sufficiently so that a prototype instrument can be constructed. It is significant that recent

advances in computer technology particularly favor a design involving direct electronic recording.

## VI. Acknowledgements

The authors acknowledge valuable conversations with Jonathan L. Costa. This work has been supported by the Department of Energy, Office of Basic Energy Sciences, Division of Advanced Energy Projects, under Grant No. DE-FG02-86ER13610. This support does not constitute an endorsement of the views expressed herein by DoE.

† permanent address: Theoretical Division, MS-B210, Los Alamos National Laboratory, Los Alamos, NM 87545

## VII. References

1. J. C. Solem and G. C. Baldwin, "Microholography of Living Organisms," *Science* **218**, 229 (1982).
2. J. Winthrop and C. Worthington, "X-Ray Microscopy by Successive Fourier Transformation," *Phys. Lett.* **15**, 124 (1965); G. Stroke and R. Restrick, "Holography with Spatially Noncoherent Light," *Appl. Phys. Lett.* **7**, 229 (1966).
3. A. Kondratenko and A. Skrinsky, Optical Information Processing, Volume 2 (Plenum, New York, 1978) p. 1.
4. "Holography at X-Ray Wavelengths," by J. C. Solem, G. C. Baldwin, and G. F. Chapline, *Proc. Int'l. Conf. on Lasers*, pp. 293 - 305 (1981).
5. J. C. Solem and G. F. Chapline, "X-Ray Biomicroholography," *Opt. Eng.* **23**, 3 (1984).
6. A. H. Compton and S. K. Allison, X-Rays in Theory and Experiment, Van Nostrand (1935). Also see U. Fano and J. Cooper, "Spectral Distribution of Atomic Oscillator Strengths," *Rev. Mod. Phys.* **40**, 441 (1968).
7. J. Janesick et. al., "Potential of CCD's for UV and X-ray Plasma Diagnostics," *Rev. Sci. Instrum.* **56**, 796 (1985); K. Marsh et. al., "Nondispersive Spectroscopy and Imaging of Plasmas using a Charge-Coupled Device," *Rev. Sci. Instrum.* **56**, 837 (1985); D. Lumb, G. Hopkinson, and A. Wells, Advances in Electronics and Electron Physics (Academic, London, 1985) Vol. 64B, p. 467.
8. "A Description of the Theory and Apparatus for Digital Reconstruction of Fourier Transform Holograms," by W. S. Haddad, J. C. Solem, D. Cullen, K. Boyer, and C. K. Rhodes, summary presented on September 12, 1987 for Electronics Imaging '87, held on November 2 - 5, 1987 in Boston, MA.
9. R. Collier, C. Burckhardt, and L. Lin, Optical Holography (Academic Press, New York, 1971) pp. 58 - 68.
10. "Design for a Fourier-Transform Holographic Microscope," W. S. Haddad, D. Cullen, K. Boyer, C. K. Rhodes, J. C. Solem, and R. S. Weinstein, Proceedings of the International Symposium on X-Ray Microscopy, edited by D. Sayre, Brookhaven, NY, August 31 - September 4, 1987 (Springer-Verlag, Berlin, in press).

# First Images from the Stanford Tabletop Scanning Soft X-Ray Microscope

J. A. Trail and R. L. Byer

*Applied Physics Department, Edward L. Ginzton Laboratory  
Stanford University, Stanford, California 94305*

## Abstract

We have constructed a scanning soft x-ray microscope which uses a laser-produced plasma as the soft x-ray source and normal incidence multilayer coated mirrors in a Schwarzschild configuration as the focusing optics. The microscope operates at a wavelength of 140 Å, has a spatial resolution of 0.5 μm, and has a soft x-ray photon flux through the focus of  $10^4 \text{ s}^{-1}$  when operated with only 170 mW of average laser power. The microscope is compact; the complete system, including the laser, fits on a single optical table. In this paper we describe the microscope and present images of metallic microstructures.

## Introduction

Soft x-ray microscopes operating in the 'water window' between 2.3 nm and 4.4 nm are capable of imaging wet, live biological cells with a resolution many times that of a visible light microscope.[1] To date, the highest soft x-ray microscope resolution of 100 Å has been achieved with a contact microscope,[2] however much of the current effort is directed at developing scanning soft x-ray microscopes. Scanning microscopes expose the biological sample to the minimum dose of damaging radiation, and the data is immediately available on a computer where subsequent image processing can be performed. At present there exist three scanning soft x-ray microscopes operating in the 'water window', all using synchrotrons as the source of soft x-rays and Fresnel zone plates as the focusing optics.[3] Although their performances are comparable, the state-of-the-art is represented by the Stony Brook / Brookhaven microscope [4] with a resolution of 750 Å and a soft x-ray flux through the focus of  $2 \times 10^5 \text{ s}^{-1}$ .

The success of the synchrotron based microscopes is very encouraging, however few biologists have access

to such instruments. For soft x-ray microscopy to become more widely used it is necessary to have a compact microscope which can fit in the biologist's laboratory.

By combining a compact, high brightness, laser-produced plasma soft x-ray source with high throughput normal incidence multilayer mirror optics, we have built a scanning soft x-ray microscope similar in size and accessibility to an electron microscope. Our microscope is shown schematically in Fig. 1, and a photograph of the system is shown in Fig. 2. The length from source to detector is 1.4 meters. Although our ultimate goal is to construct a microscope which operates in the water window, the present microscope operates at a wavelength of 140 Å.

## The Microscope

The laser-produced plasma (LPP) is a compact, high brightness source of soft x-ray radiation.[5] In our present microscope the LPP is formed by focusing pulses of 1064 nm radiation from a Q-switched Quanta Ray DCR II Nd:YAG laser onto a rotating solid copper cylinder located inside a vacuum chamber. The laser operates at 10 Hz with a pulse length of 8 ns and pulse energies of up to 800 mJ. The present microscope operates with laser energies of only 20 mJ per pulse. With a focal spot diameter of 30 μm the resulting intensity on the copper target is  $\sim 4 \times 10^{11} \text{ W cm}^{-2}$ . The target is rotated on a 40 pitch threaded rod in order to produce a fresh area for each laser shot.

The diameter of the plasma source is dependent on pulse length and laser focal size. In our microscope the laser pulse length of 8 ns and focus of 30 μm result in a plasma diameter of  $\sim 100 \mu\text{m}$ , with the plasma radiating isotropically into  $2\pi$  steradians. As illustrated in Fig. 1 a small fraction of this radiation is collected by the Schwarzschild microscope objective and focused to form the microprobe. The objective has a focal length of 13

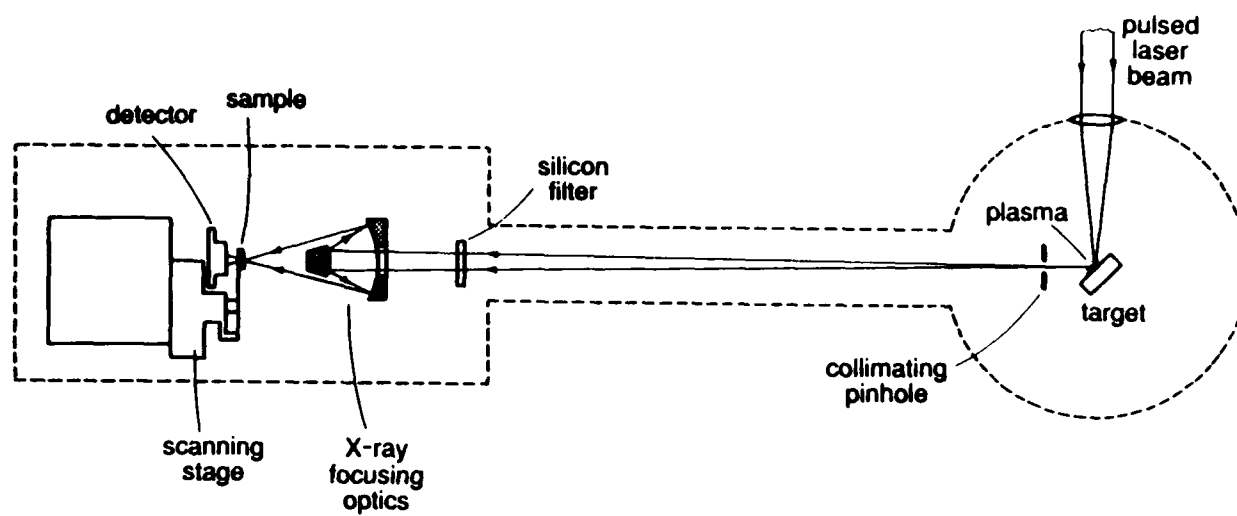


FIGURE 1. Schematic of the microscope showing the major components. The dotted line indicates the extent of the vacuum ( $< 10^{-5}$  torr). The distance from the plasma source to the MCP detector is  $\sim 1.4$  meters.



FIGURE 2. Photograph of the complete microscope. The laser is just visible at the top left of the optical table.

mm, so with the source - objective distance of 1.3 m the source is demagnified by a factor of 100. By using pinholes to aperture the plasma source we can ensure that the microprobe diameter is not limited by the demagnified source diameter.

The design of our Schwarzschild microscope objective has been presented previously.[6] The spherical zerodur mirror blanks were custom fabricated by Zygo Corporation, and the parameters are given in Table 1. Advantages of the Schwarzschild include high numerical aperture, zero spherical aberration, and relative ease of fabricating spherical mirrors.

Table 1 Schwarzschild Objective

	<u>Convex</u>	<u>Concave</u>
Radius of Curvature	13.4 mm	23.7 mm
Mirror Diameter	8.0 mm	22.2 mm
Surface Figure Error <sup>a</sup> (P-V)	160 Å	120 Å
Surface Figure Error <sup>a</sup> (rms)	12 Å	24 Å
Surface Roughness <sup>b</sup> (rms)	7 Å	7 Å

Numerical Aperture 0.3

a) Surface figure measured using a Zygo Mark III Interferometer.

b) Surface roughness measured using a Wyco Profilometer

The use of normal incidence focusing optics for soft x-rays is made possible by multilayer mirror coatings.[7,8] The mirrors of the objective were coated with a molybdenum / silicon multilayer designed to give a peak throughput of the objective at 140Å. These coatings were deposited by J.B. Kortright at the Center for X-ray Optics in the Lawrence Berkeley Laboratory. Figure 3 shows the measured [9] reflectance of the witness sample coated in the same run as the Schwarzschild mirror blanks. The measured peak reflectance is  $(55 \pm 5) \%$  with a bandwidth of 7Å (5%). The witness sample substrate is a polished silicon wafer with low effective surface roughness. The 7Å roughness of the Schwarzschild mirrors may reduce the peak reflectance by up to a third [10] to give a single mirror normal incidence reflectance of ~40%.

A consideration in constructing a two mirror objective with narrow bandpass mirrors is the overlap of reflectance of the two mirrors for the various rays passing through the objective. With the vertices of the two mirrors placed at the same distance from the sputtering source in the coating chamber the bandwidth overlap is virtually perfect across the full aperture of our objective. The expected throughput of the coated microscope objective is 8% across a 10 Å bandwidth centered at 140 Å.

The Mo/Si multilayer coating has high reflectance at visible wavelengths. This feature allows alignment of the mirrors with visible light, and also permits the microscope operator to look through the microscope at

the region of sample to be imaged via a TV camera and a flip mirror.

Proper alignment of the mirrors is critical to the achievement of high resolution. The mirror positions are adjusted by 5 optically encoded DC motors controlled by a personal computer. In the future this system will allow the final alignment to be performed using x-rays, however at present the mirror alignment is optimized using visible HeNe laser light.

The scanning stage used to scan the sample through the x-ray focus is a three axis (XYZ) Newport translation stage driven by encoded DC motors. This stage has a range of over 12 mm in all three axes and a resolution of 0.1 μm. For high resolution knife edge scans of the x-ray focus a low voltage (150V) piezoelectric transducer with a 15 μm range was incorporated into the X axis of the translation stage.

The x-ray photons transmitted by the sample are detected with a microchannel plate (MCP) detector. The MCP is better suited to the high peak flux of our pulsed system than a proportional counter, although it has the disadvantage of requiring a vacuum of  $10^{-5}$  torr.

In keeping with the spirit of the microscope the instrumentation is simple, compact, and easy to use. All control of the microscope is performed by an IBM AT personal computer with the software written in Pascal. A single rack of electronics interfaced to the computer is used to drive the motors for the scanning stage and mirror alignment. The signal from the MCP detector is processed in a boxcar integrator before being sent to the computer via an RS232 link.

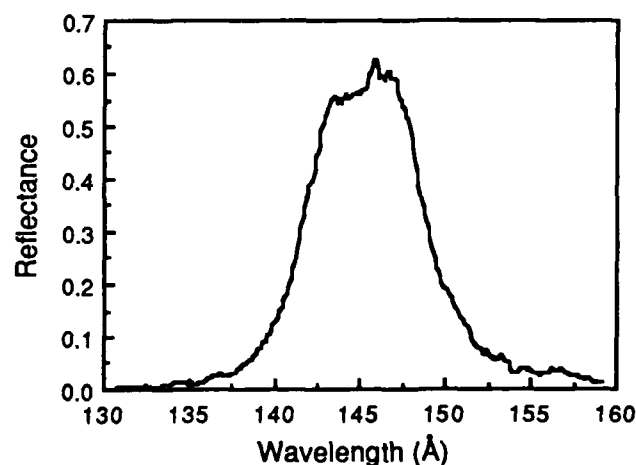


FIGURE 3. Measured reflectance of the witness sample for the Mo/Si multilayer coating deposited on the Schwarzschild mirrors.

## Results

The microscope resolution was determined by scanning a knife edge through the x-ray focus. Figure 4 shows

the result of one scan taken using the piezoelectric transducer and a step size of 600 Å. Using the criterion of 10 - 90% the resolution is  $0.8 \pm 0.1 \mu\text{m}$  while using the criterion of 25%-75% the resolution is  $0.5 \pm 0.1 \mu\text{m}$ . For this measurement a  $10 \mu\text{m}$  pinhole aperture was placed in front of the plasma to reduce the source image size to  $0.1 \mu\text{m}$ .

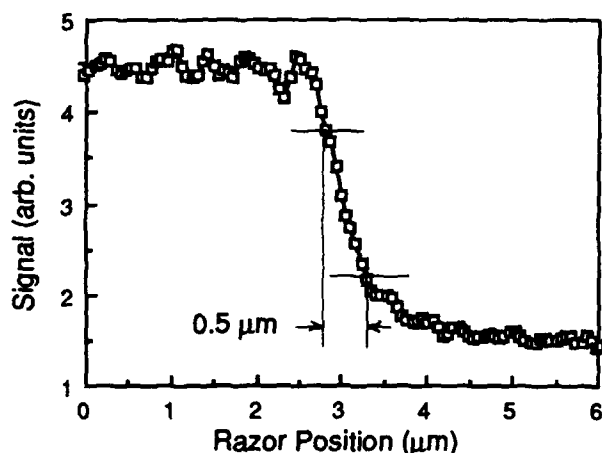


FIGURE 4. Razor edge scan through the x-ray focus demonstrating the  $0.5 \mu\text{m}$  resolution (25%-75%). The step size is 600 Å.

The factors influencing resolution and their estimated contributions are given below in Table 2. The present limiting factor in the resolution appears to be the mirror alignment. The mirrors are aligned to diffraction limited performance in the visible i.e., resolution  $\sim 0.9 \mu\text{m}$ , but it is quite possible that this is not sufficient to obtain the  $0.2 \mu\text{m}$  indicated in Table 2. The effect of mirror figure is an approximate estimate only and could be worse than  $0.15 \mu\text{m}$ , however it is unlikely to be as high as  $0.5 \mu\text{m}$ .

Table 2 Contributions to Focal Spot Diameter

Mirror Figure	$0.15 \mu\text{m}$
Diffraction ( $1.22 \lambda$ )	$0.03 \mu\text{m}$
Demagnified Source Size ( $10 \mu\text{m}$ pinhole)	$0.1 \mu\text{m}$
Sub-Total	$0.2 \mu\text{m}$
Mirror Alignment	$< 0.9 \mu$

With the  $10 \mu\text{m}$  pinhole aperture in front of the plasma, and using only 17 mJ per pulse incident on the copper target to produce the plasma, we obtain 1000 x-ray photons per pulse through the focus of the microscope. With the laser operating at 10 Hz this photon number corresponds to a flux of  $10^4 \text{ s}^{-1}$ .

Although the microscope operating wavelength of 140 Å is not appropriate for taking images of biological samples we have taken several images of artificial microstructures. One such sample is the resolution test pattern shown in the optical photograph of Fig. 5a. The pattern was produced by optical lithography and

consists of transparent areas in a free standing 1000 Å thick gold film. The lines and spaces of the pattern were intended to be  $5 \mu\text{m}$ ,  $2 \mu\text{m}$ , and  $1 \mu\text{m}$ , however over-etching during processing produced  $3 \mu\text{m}$  spaces and  $1 \mu\text{m}$  lines in place of the  $2 \mu\text{m}$  pattern and washed out the nominally  $1 \mu\text{m}$  pattern.



FIGURE 5a. Optical microscope image of the resolution test pattern. The pattern is etched in a 1000 Å free standing gold film and consists of lines and gaps of nominal widths  $5 \mu\text{m}$ ,  $2 \mu\text{m}$ , and  $1 \mu\text{m}$ . Over-etching has produced smaller lines and larger gaps.

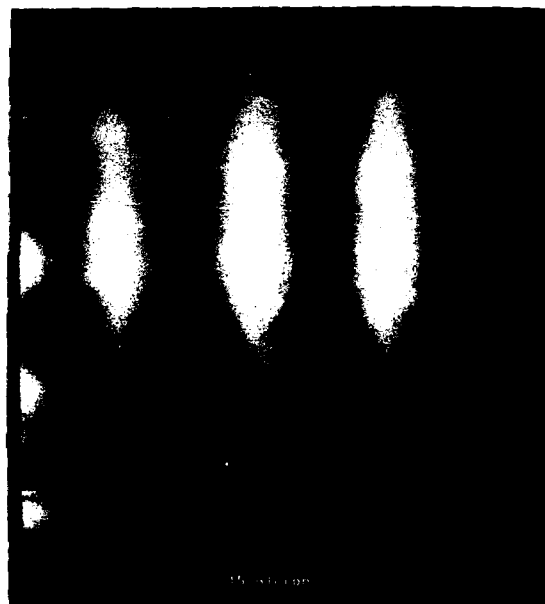


FIGURE 5b. Soft x-ray image of the  $3 \mu\text{m}$  space,  $1 \mu\text{m}$  line area of a test pattern sample nearly identical to the one shown in 5 a). The  $1 \mu\text{m}$  features are clearly visible.

Figure 5b is an x-ray image taken with our microscope of a nearly identical pattern fabricated on the same silicon chip. Note that this image was taken without

any aperture on the plasma source so the resolution is expected to be dominated by the source image diameter of 1  $\mu\text{m}$ . The x-ray image includes only the vertical bars of the 3  $\mu\text{m}$  space and 1  $\mu\text{m}$  line pattern. The visibility of the 1  $\mu\text{m}$  lines is consistent with the expected resolution of 1  $\mu\text{m}$ .

The x-ray image shown in Fig. 5b is a smoothed version of the original data. The original data consisted of a 60 x 30 pixel image with pixels 0.25  $\mu\text{m}$  across by 0.5  $\mu\text{m}$  high. Although there was sufficient x-ray flux to take a pixel with every laser shot the time to take a picture is currently limited by the motion of the scanning stage. This 60 x 30 image took 20 minutes to acquire.

### Summary

We have constructed a compact scanning soft X-ray microscope which fits entirely on a single optical table. Our approach is to use laboratory scale, high average power, pulsed lasers to produce a plasma soft X-ray source of high average brightness, and to combine this source with high throughput, multilayer coated normal incidence optics. The present microscope operates at a wavelength of 140  $\text{\AA}$ , has a resolution of  $0.5 \pm 0.1 \mu\text{m}$ , and an x-ray flux through the focus of  $10^4 \text{ s}^{-1}$  while using only 170 mW of laser power. We have demonstrated the imaging capability of the microscope by taking pictures of lithographically produced microstructures.

In the future the use of higher repetition rate ( $> 1 \text{ kHz}$ ) and shorter pulse (100 ps) lasers to drive the LPP source will reduce picture time and produce hotter, brighter plasmas with more emission at shorter wavelengths. Improvements in mirror alignment and surface figure should result in higher resolution, and extending operation to the more interesting region of the 'water window' should be possible with further progress in multilayer coatings and mirror surface quality. A compact microscope operating in the water window would provide an attractive complement to the more powerful but less accessible synchrotron based microscopes.

### Acknowledgements

The work at Stanford is supported by the National Science Foundation under grant ECS-8611875. We would like acknowledge Dr. J.B. Kortright at the Center for X-ray Optics, Lawrence Berkeley Laboratory, for supplying the multilayer coatings. The Center for X-ray Optics is supported by the Department of Energy under grant DE-AC03-76SF00098.

### References

- 1 J. Kirz and H. Rarback, *Rev. Sci. Instr.*, **56** 1, (1985).
- 2 R. Feder, V. Mayne-Banton, D. Sayre, J. Costa, B.K. Kim, M.G. Baldini, and P.C. Cheng, in *X-Ray Microscopy*, p279 (Springer, Berlin, 1984).
- 3 *X-Ray Microscopy II*, edited by D. Sayre et. al. (Springer, Berlin, Heidelberg, 1988).
- 4 H. Rarback, D. Shu, S.C. Feng, H. Ade, C. Jacobsen, J. Kirz, I. McNulty, Y. Vladimirovsky, D. Kern and P. Cheng, in *Ray Microscopy II*, edited by D. Sayre et. al. (Springer, Berlin, Heidelberg, 1988).
- 5 D.J. Nagel, C. M. Brown, M.C. Peckerar, M. L. Ginter, J. A. Robinson, T. J. McIlrath, and P. K. Carroll, *Appl. Opt.* **23**, 1428 (1984).
- 6 J.A. Trail and R.L. Byer, *Proc. SPIE*, **563**, 90, (1985).
- 7 T. W. Barbee, Jr., *AIP Conf. Proc.* **75**, 131 (1981).
- 8 E. Spiller, A. Segmuller, J. Rife, and R.P. Haelbich, *Appl. Phys. Lett.* **37**, 1048 (1980).
- 9 J.A. Trail, R.L. Byer, T.W. Barbee Jr., *Appl. Phys. Lett.* **52**, 269, (1988).
- 10 H. Hogrefe and C. Kunz, *Applied Optics*, **26**, 2851 (1987).

# Progress in Optical Reconstruction of Submicron X-Ray Holograms

D. Joyeux

*Institut d'Optique, CNRS, BP 43, 91406 Orsay Cedex, France*

F. Polack

*LURE, CNRS and Université de Paris XI, Centre Universitaire d'Orsay  
91405 Orsay Cedex, France*

## Abstract

We investigate the maximum resolution which can be obtained from x-ray holograms through optical reconstruction. This implies to reject paraxial approximations, i.e. to consider high numerical apertures, and to take into account the holographic aberrations. We determine first the limits to a perfectly corrected reconstruction, set by diffraction (in terms of numerical aperture and resolution). It is shown that the diffraction limit can be as good as  $\lambda_c/2.8$ , in a particular reconstruction configuration ( $\lambda_c$ : reconstruction wavelength). Discussion of practical implementation suggests that  $\lambda_c/2.2$  is reasonably feasible.

## 1. Introduction

Since Gabor's basic idea in 1948, the possibility of using holography for x-ray microscopy was considered by several authors [1-3]. Attempts at recording x-ray holograms were made as early as 1969 by Giles [4], under difficult experimental conditions, and then, since 1972 by other authors using synchrotron radiation sources [5,6]. In the very first experiments, the only reconstruction method, following Gabor's idea, was optics: visible or near visible wavelength was used, and a high magnification was sought. However, the reconstruction process was never investigated specifically in the scope of optimum reconstruction, although the existence of aberrations was always mentioned. The latter were analyzed in a classical 3rd order frame [3], and it was proved that

when the desired resolution becomes close to the reconstruction wavelength, the aberration level degrades significantly the image, and resolution is far from diffraction limited.

For this reason, and also because the quality of optical reconstruction is very sensitive to coherent noise, computer reconstruction became attractive in the recent years [7], with the parallel price decrease and power increase of microcomputers. However, this implies an intermediate digitization step, as long as the recording step involves photochemical recording (a real-time position-sensitive photon detector, with the required position resolution and accuracy would change this discussion). This digitization is a quite heavy process: in the case of a parallel reference beam, it requires a complex instrumentation with a very high dimensional accuracy in the hologram analysis.

On the other hand, we came to the idea that the conditions of a good optical reconstruction were not really investigated. To our knowledge, in particular, the question of the best possible, diffraction-limited (i.e. corrected for aberrations) optical reconstruction was never considered. It was assumed by everybody, including the present authors, that the ultimate limit was half the reconstruction wavelength, as in classical imaging. It is the main goal of this paper to investigate the theoretical conditions and performances of a corrected high aperture reconstruction. Then, the practical implementation problems will be discussed, and reasonable figures will be given.



## 2. The basic equations of Gabor holography

### 2.1 Notations and formulae

Throughout this paper, we shall consider only Gabor in-line holography, with a parallel reference beam. Reconstruction will always make use of a diverging wavefront (i.e. real source point), and of the first real converging order. Although general holographic equations imply algebraic parameters, these restrictions allow using arithmetic quantities, easier to manipulate.

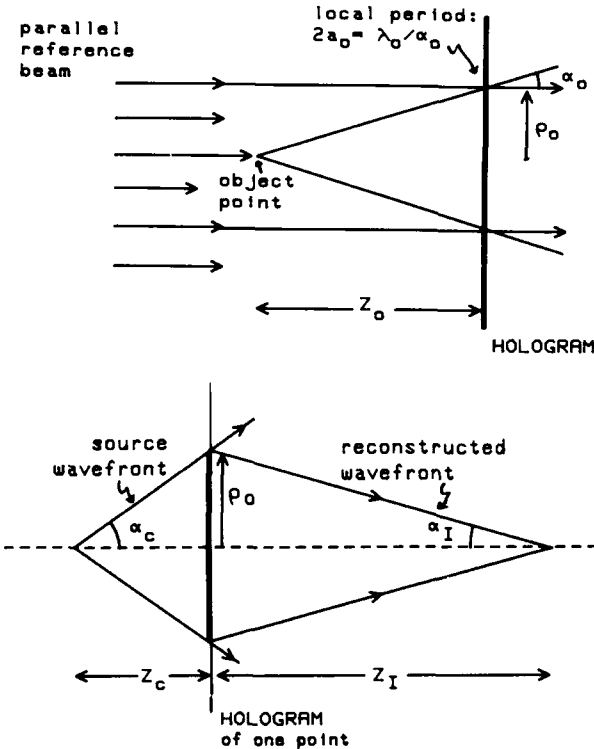


Figure 1. The holographic process: geometrical parameters. Top: recording step; bottom: reconstruction step

Following Meier's notations [8], Fig. 1 gives the useful geometrical parameters for both the recording and reconstruction steps. The object, reconstruction source, image distances to the hologram are  $z_o$ ,  $z_c$ ,  $z_I$ . Transverse coordinates are  $(x_o, y_o)$  or

$\rho_o = \sqrt{x_o^2 + y_o^2}$  in the hologram plane.  $\lambda_o$  and  $\lambda_c$  are respectively the recording and reconstruction wavelengths, with  $\lambda_c / \lambda_o = \mu$ . Because the reference beam is parallel, the recording step is shift invariant, i.e. the hologram of one object does not depend on its transverse position, except for a shift.

As well is known, the Gabor hologram of

one object point is a Fresnel zone pattern. A ray diffracted at angle  $\alpha_o$ , interferes on the hologram and produces a local spatial period  $2a_o$  such that  $a_o = \lambda_o / 2 \sin \alpha_o$ . The local period  $2a_o$  is recorded at the radial coordinate  $\rho_o = z_o \tan \alpha_o$ . The holographic magnification is:

$$M = 1 + z_I / z_c = (1 - z_o / \mu z_c)^{-1} \quad (1)$$

and the image and source positions are:

$$z_I = M z_o / \mu \text{ and } z_c = M z_o / (M - 1) \mu \quad (2)$$

### 2.2 Resolutions and numerical apertures

Analysing the performances of the holographic microscopy process requires considering three different (although related) resolutions. These are the "recorded resolution", the "image resolution", and finally "the holographic resolution" (the practical one), which is just the latter, divided by the holographic magnification.

The *recorded resolution* tells which object spatial frequencies contributed to the hologram formation. In other words, it describes the acceptance of the recording step, mainly limited by the coherence conditions and the recorder spatial cut-off frequency. It therefore also depicts the information content of the recorded hologram. By analogy with the formalism of resolution and numerical aperture in imaging (and according to Fig. 1), we call  $\sin \alpha_o^{\max}$  the recording numerical aperture (N.A.), and  $r_o = \text{MIN}(a_o)$

$= \lambda_o / 2 \sin \alpha_o^{\max}$  the recorded resolution [9].

In the case of a stigmatic (i.e. spherical) reconstructed wavefront, the *image resolution*, and the associated imaging N.A. are, as usual:  $r_I = \lambda_c / 2 \sin \alpha_I$ , and  $\sin \alpha_I$ , where  $\alpha_I$  is the marginal (edge) ray angle of the reconstructed wavefront. When the reconstructed wavefront is aberrated, i.e. non spherical, it is necessary to distinguish between paraxial and marginal N.A. (see Fig. 2). Whereas their difference is related to the aberration level, the paraxial N.A. gives the image resolution which could be obtained if a perfect correction was implemented.

Because this paper is focussed onto the reconstruction process, we assume in the next sections that the recorded N.A. is matched to the image aperture, i.e. that the edge recorded period diffracts the marginal incident ray into the marginal image rays. In other words, all the spatial frequencies contained in the hologram can be processed by the reconstruction step. Extension to non

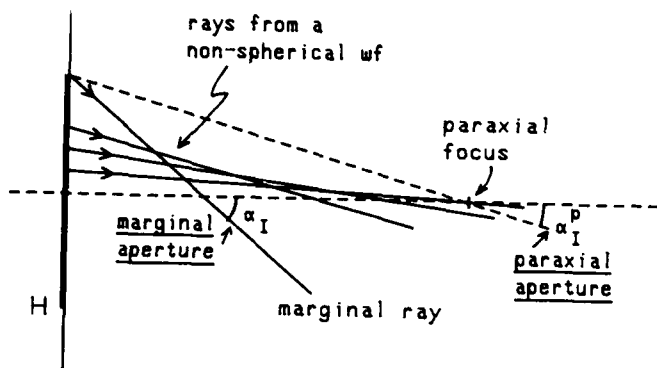


Figure 2. Marginal and paraxial NA's, in the case of a non spherical wavefront.

matched cases is straightforward.

Finally, the *holographic resolution*  $r_h$  is the image resolution "back to object", i.e.  $r_h = r_i/M$ . The aperture formalism suggests to introduce the "holographic N.A."  $HNA = M \sin \alpha_i$ , such that:  $r_h = \lambda_c / 2(HNA)$ .

It should be noted that we use no small angle approximations. Except when stating explicitly the paraxial approximation, we only assume that  $\lambda_c / \lambda_0 = \mu \gg 1$  and  $r_0 \gg \lambda_0$ , which are valid to an excellent accuracy in all the numerical cases we shall consider. The second approximation implies  $\alpha_0 \ll 1$  and  $\sin \alpha_0 \approx \alpha_0$ , and therefore:

$$\rho_0 \approx \lambda_0 z_0 / 2r_0 \quad (3)$$

### 3. The optimal setup in the paraxial case

Before proceeding with a rigorous, non paraxial analysis, we present shortly the paraxial case, in order to enlighten two deep differences between the reconstruction process at  $\lambda_c$ , and a simple imaging process using the same wavelength.

As we just recalled, the reconstruction consists in illuminating the hologram with a point source, located at  $z_c$  in front of the hologram. Choosing  $z_c$  determines the magnification  $M$ . It seems reasonable to design the setup for best resolution at minimum cost, and cost here means optics specifications, mainly numerical aperture. Therefore, considering the variations of the different N.A. with  $M$  should give all the useful information. By definition,  $\alpha_0 = \rho_0 / z_0 = \lambda_0 / 2r_0$  (Fig. 1), and (paraxial approximation),  $\alpha_i = \rho_0 / z_i$ ,  $\alpha_c = \rho_0 / z_c$ . From Eq. 2, we find:

$$\alpha_i = \lambda_c / 2Mr_0 = \mu \alpha_0 / M$$

$$\alpha_c = (M-1) \lambda_c / 2Mr_0 = (M-1) \mu \alpha_0 / M.$$

The holographic N.A.  $HNA = M \alpha_i$  is therefore  $HNA = \mu \alpha_0 = \lambda_c / 2r_0$ . These relationships are plotted on Fig. 3.

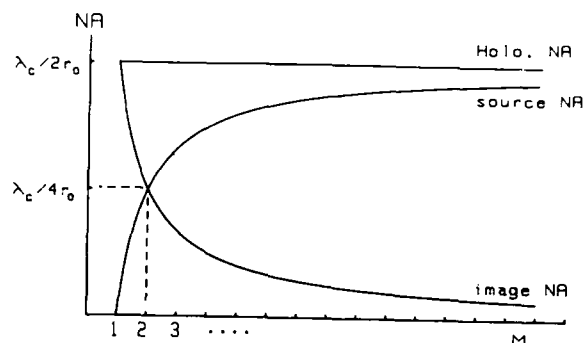


Figure 3. Recorded, image, and holographic NA's in the paraxial case ( $r_0 \ll \lambda_c$ ).

It is first found that the final resolution  $r_h = \lambda_c / 2HNA$  is always equal to the recorded resolution  $r_0$ .  $r_h$  does not depend on the magnification, which is very different of imaging an object through a lens. Therefore, the magnification cannot be chosen on a best resolution criterion. The second result, also specific to the holographic imaging process, is of primary practical importance in the microscopy process. The constant resolution  $r_h$  is obtained at a different cost, in term of the necessary optical apertures on the source and image sides. In particular,  $M=2$  allows working at  $NA \lambda_c / 4r_0$ , which is only half the value needed in ordinary imaging to obtain a final resolution of  $r_0$ . Obviously, the use of lower NA, with the same final resolution, is an advantage, especially if an exotic (UV) wavelength is to be used for resolution improvement.

However, improving the resolution as much as possible leads to a high reconstruction aperture, and therefore to a highly aberrated reconstructed image. It is intuitive that departure from the paraxial approximation can change the above results. Therefore, as long as we are looking for the best possible performances (highest resolution + lowest N.A.), we have to solve two different problems. The very basic one is to know, for each  $M$ , what are the best diffraction-limited resolution and the associated N.A., allowed by the laws of diffraction, i.e. when performing an aberration-corrected reconstruction. The solution of the second problem, namely the practical implementation of

corrected reconstruction, should take into account the results of the former.

#### 4. High aperture corrected reconstruction

We consider the holographic impulse response, i.e. the on-axis reconstruction of the hologram of one object point. In general, this yields a non spherical wavefront, when the incident one is spherical. As a matter of fact, the most natural correction scheme consists in compensating the incident wavefront, in order to obtain a spherical reconstructed wavefront. However, other schemes are possible, namely correcting the reconstructed wavefront, or partially correcting both sides.

We shall first treat the source correction case in detail (for  $1 < M < \infty$ ), because of its simplicity. Other cases, while more complex, proceed of the same approach. We shall discuss the split correction scheme for  $M=2$ , because of its practical interest.

##### 4.1 Correcting the source wavefront: diffraction limited performances

In order to make a rigorous analysis, we have to find out the real ray paths in the reconstruction process, without using small angle approximations (except  $\alpha_0 \ll 1$ ). The geometry of ray paths is depicted on Fig. 4.

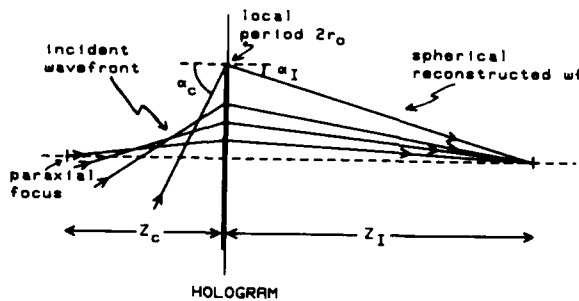


Figure 4. Ray paths for a stigmatic reconstructed wavefront.

Owing to the correction scheme chosen, all diffracted rays converge to the paraxial image position  $z_i$ . This is true in particular for the marginal rays, which are diffracted by the spatial period  $2r_0$ . Therefore, the incidence and emergence angles obey the grating equation:

$$\sin \alpha_c + \sin \alpha_i = \lambda_c / 2r_0 \quad (4)$$

From the expressions of  $\rho_0$  and  $z_i$  (Eqs 2,3), it follows:

$$\operatorname{tg} \alpha_i = \frac{\rho_0}{z_i} = \frac{\lambda_0 z_0 / 2r_0}{M z_0 / \mu} = \frac{\lambda_c}{2Mr_0} \quad (5)$$

which in turn produces:

$$\sin \alpha_c + \sin \alpha_i = M \operatorname{tg} \alpha_i \quad (6)$$

By the way, this equation is valid for each ray pair in the pupil, thus determining the correct incident wavefront shape.

When increasing the image aperture  $\alpha_i$ , the marginal ray incidence angle  $\alpha_c$  increases according to Eq. 6 (this is illustrated by Fig. 4, where the evolution of rays with increasing apertures is qualitatively correct). However, this process cannot work beyond the point where the incident ray is at grazing incidence. When this limit is reached,  $\sin \alpha_c = 1$ , and the image aperture and magnification are related through:

$$M \operatorname{tg} \alpha_i - \sin \alpha_i = 1 \quad (7)$$

Solving this equation for  $\sin \alpha_i$  vs  $M$  yields the maximum image aperture allowed by diffraction, when aberrations are perfectly corrected as indicated. In turn, the highest possible holographic N.A. ( $M \sin \alpha_i$ ), and therefore the best final resolution  $\lambda_c / 2(MNA)$  is straightforwardly deduced. The source paraxial aperture can be computed from  $\operatorname{tg} \alpha_c^p = \rho_0 / z_c$ , and  $M-1 = z_i / z_c$  (Eq. 1), yielding:

$$\operatorname{tg} \alpha_c^p = (M-1) \operatorname{tg} \alpha_i \quad (8)$$

However, it should be kept in mind that the source wavefront is not stigmatic: the marginal ray incidence is given by Eq. 6.

As in the paraxial case, the resulting NA's can be plotted vs  $M$  (Fig. 5). The main features are commented hereafter.

- 1) The highest possible holographic N.A. is not constant with magnification; therefore, an optimum reconstruction geometry exists, when looking for the highest resolution.
- 2) Except for  $M$  very close to 1, the highest possible holographic N.A. is always greater than 1, with a maximum of  $3\sqrt{3}/4 \approx 1.3$ , for  $M=3\sqrt{3}/2 \approx 2.6$ . In other words, the best resolution which can be obtained from the hologram, when correcting the incident wavefront, is  $\lambda_c / 2.6$ . It is obtained with an image aperture  $\sin \alpha_i = .50$ , and a paraxial source aperture  $\sin \alpha_c^p = .68$ , (but the margi-

nal source aperture is 1).

3) For high magnification, the maximum possible resolution is  $\approx \lambda_c/2$ . Eq. 5 yields  $\text{tg} \alpha_i \approx 1/M$ : the image aperture is very small.

The maximum paraxial source aperture  $\sin \alpha_c^p$  can be computed, using Eq. 8. One obtains  $\text{tg} \alpha_c^p \approx 1-1/M \approx 1$ , i.e.  $\sin \alpha_c^p \approx .71$ . This is (for large M) the maximum usable paraxial source aperture, corresponding to a marginal NA equal to 1.

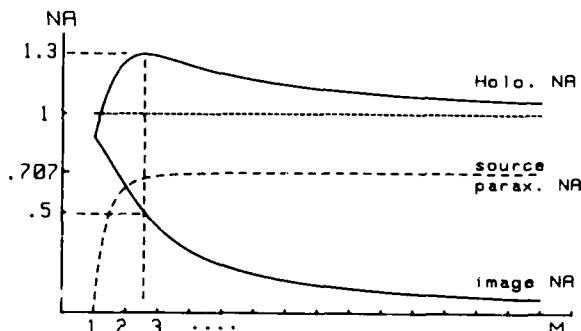


Figure 5. Extreme NA's allowed by diffraction, in the case of a perfectly corrected reconstructed wavefront.

4) The holographic resolution  $r_h$  can be compared to the recorded resolution  $r_0$  needed, i.e. corresponding to the marginal ray. From the definition of  $r_h$  and Eqs. 2-5, we have:

$$r_h = r_0 / \cos \alpha_i \quad (9)$$

In order to reconstruct with resolution  $r_h$ , a better resolution in the recording process is required. This overresolution of the recording step is the price to be paid for using an aberrating optical process (i.e. the holographic process), even if perfectly corrected.

#### 4.2 The symmetrical correction

**Principle.** Although reconstructing at  $M=2$  to 3 provides the best resolution, the low magnification value does not make the reconstructed image directly observable. The reconstruction process therefore requires two different optics, one specially corrected for hologram illumination, and the other being stigmatic, and providing a highly magnified image, both with reasonable apertures. Conversely, with a high magnification (a few tens at least), only the special optics on the source side is needed. The image can be observed directly (e.g. with a CCD or some other electronic camera), but the reso-

lution cannot be as good.

A good way to make the high-resolution, low magnification reconstruction much simpler would be to use identical optics for hologram illumination and image observation. This requires that the source and image wavefronts are strictly identical, including aberrations, which means that the correction process is split between the source wavefront and the image observation optics. In

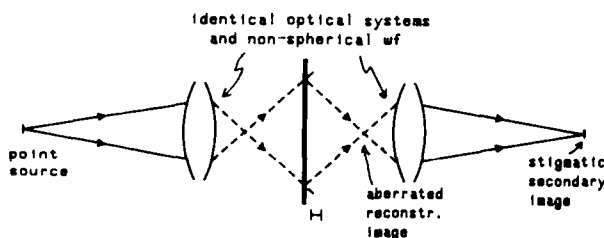


Figure 6. The symmetrical reconstruction scheme. The hologram is a symmetry plane for the whole system, including wavefronts.

such a system (Fig. 6), a point source produces a spherical wavefront, imaged by some special optics into the partially corrected wavefront. Because the reconstructed wavefront is identical to the incident one (except for propagation direction), an identical optics converts it into a stigmatic one, observable if the optics magnification is high enough.

Besides, reconstructing the hologram in reflection (relief hologram) would allow to use the same optics for illumination and observation, with two side advantages: higher diffraction efficiency than in transmission and no substrate absorption or thickness problem.

For better readability, Figs. 6-7 depict the transmission case. The required situation is realized (for on-axis reconstruction) when  $z_c = z_i$ , (i.e.  $M=2$ , for equal wavefront curvature), and when each pair incident-diffracted rays is symmetrical with respect to the hologram plane. This correction scheme, as the first one, cannot work for any image aperture: a maximum exists for corrected holographic N.A.

**The best diffraction-limited resolution.** As mentioned in Sect. 2.2, the corrected image resolution is given by the paraxial image aperture  $\alpha_i^p$  and the usual expression  $\lambda_c / 2 \sin \alpha_i^p$ .

Using the same equations as in Sect. 4.1 leads to different conclusions, due to the different correction scheme. The grating equation applied to the marginal ray pair be-

comes (using the symmetry condition) (Fig. 7):

$$2\sin\alpha_c = 2\sin\alpha_i = \lambda_c / 2r_0 \quad (10)$$

where  $\alpha_c$ ,  $\alpha_i$  are true incidence angles, different from paraxial aperture angles. Eq. 5 therefore does not hold any more.

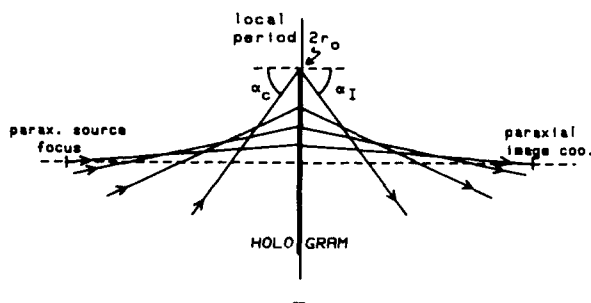


Figure 7. Ray paths for a symmetrical reconstruction scheme. The reconstructed wavefront is only partially corrected.

The highest paraxial aperture can be found out by noting that the extreme correction is reached when *both* incident and diffracted edge rays are at grazing angle, i.e.  $\alpha_c = \alpha_i = \pi/2$ . It follows (Eq. 10) that the smallest (usable for reconstruction) value of  $r_0$  is  $\lambda_c/4$  (incidentally,  $\lambda_c/2$  is the smallest spatial period  $2r_0$  which can be used in a diffraction process at wavelength  $\lambda_c$ ). From Eq. 3, the period  $\lambda_c/2$  is recorded at  $\rho_0 = \lambda_0 z_0 / 2r_0 = 2z_0/\mu$ . But for  $M=2$ ,  $z_c = z_i = 2z_0/\mu$  and we have  $\tan\alpha_i^p = \rho_0/z_i = 1$ .

Hence  $\sin\alpha_i^p = 1/\sqrt{2} = .707$ , the holographic N.A.  $M\sin\alpha_i^p$  is 1.41, and the best possible resolution is  $r_n = \lambda_c/2.8$ . Finally, because Eq. 2 is related to the paraxial coordinates, Eq. 7 is still valid with the paraxial image N.A. and  $r_n = r_0/\cos\alpha_i^p$ .

#### 4.3 Practical implementation of the on axis correction.

As usual, these maximum diffraction limited performances are difficult to produce practically, in particular because the optics design should compromise between high aperture and low stray light from optical surfaces. A detailed analysis of the holographic aberrations and of the perfect correction conditions is out of the scope of this paper, and will be published elsewhere. We

should only mention that optical design computations proved that a 4-component lens (with 2 refractive indices) gives a diffraction limited reconstruction (for one given  $z_c$ ), with a paraxial aperture in the range 0.50 to 0.55. Although the combination could in principle work down to  $\lambda_c = .18 \mu\text{m}$ , operation at  $\lambda_c \approx 2500 \text{ \AA}$  is certainly more practical. Table 1 shows the aperture and resolution values derived from the same marginal N.A. 0.66, in different reconstruction configurations.

To obtain better resolutions, it is necessary to decrease significantly the wavelength. This implies to use mirror optics, on-axis for shaping and mounting accuracy (thus with central obturation). We know, from recent realizations of the Institut d'Optique's optical workshop [10], that such optics are feasible, including a small aspherization [11], and work at 0.12-0.10  $\mu\text{m}$  with NA 0.25. The maximum reasonable aperture, however, is not yet fixed: NA=.4, if possible, would give the excellent figure of 650  $\text{\AA}$  at  $\lambda_c = 0.10 \mu\text{m}$ . Of course, reconstruction with such a short wavelength would be done with the synchrotron radiation source (SR), and in the vacuum.

Table 1. Practical NA's and resolution (Pa: paraxial; Ma: Marginal)

case 1: source wavefront correction					
M	source NA Ma (Pa)	image NA Ma=Pa	resolution		
			@ $\lambda_c$	@ 0.25 $\mu\text{m}$	
1	0.66 0.55	1 (1/M)	$\lambda_c/1.3$	0.19 $\mu\text{m}$	
2.6	0.66 0.53	0.38	$\lambda_c/1.9$	0.13 $\mu\text{m}$	
case 2: symmetrically split correction					
2	0.66 0.55	Ma Pa 0.66 0.55	$\lambda_c/2.2$	0.11 $\mu\text{m}$	

#### 5. Discussion: field correction and optical noise

These results pertain to the theoretical and reasonable resolution which can be obtained from an *on-axis, perfectly corrected* reconstruction. However, holograms of extended objects should be considered, which are reconstructed in noisy conditions, due to coherent stray light. These constraints introduce additional problems, the solution of which varies with the reconstruction scheme used.

In the symmetrical correction case, the observation optics must provide the same correction over the whole field. Of course this is not impossible with a refractive lens design, but it would certainly produce much more complex optics, which therefore would generate more noise, and probably lower average performances. Besides, it is well known that the stray light problems are even more critical with a reflection system (which would be used if reconstructing in reflection with only one optics). On the other hand, the field correction is practically impossible with the mirror optics which must be used at the shortest wavelengths, not speaking of the noise generated by the central obturation.

This suggests to implement a *scanning reconstruction device*, in which optics works always on-axis, by mechanically scanning the hologram itself over the desired field. Here, the pixel-sized detector is placed at the secondary on-axis image position, which is the optical conjugate of the source pin-hole. The main feature of such a design is to be very similar to a "*confocal microscope*" [12]. In particular, it can be expected to have the same excellent properties of low coherent noise and out-of-focus rejection (twin image and zero order), solving at once the main problems of the optical reconstruction. The scanning operation, although less comfortable than real time observation for device adjustment, could be expected to be done in a few seconds per image, owing to the high flux of the available sources: UV lasers or SR in the UV domain. Such a frame rate should give reasonable constraints of mechanical drift, even at the highest resolution.

In the high magnification geometry (with source wavefront correction and direct image observation), It can be shown that there are no field aberrations over the reconstructed field, once the on-axis point is well corrected. It is therefore possible to observe directly an extended field, with a practical resolution of  $\approx \lambda_c / 1.3$ , by using a source optics similar to optics to be used in the symmetrical case. Real time observation of a corrected image is probably an interesting feature of this set-up, despite its lower resolution. But the noise reduction problem should be taken into account, in particular through high quality lens coating and dust free operation.

## 6. Conclusion

The design and realization of the "reconstruction microscope" is the work of the next few years. So far, optical reconstructions



Figure 8. Experimental results. Top view: SEM image of a typical diatom. Middle view: x-ray hologram of a similar one (see ref. 9) Bottom view: optical reconstruction.

were attempted under very non-optimal conditions: red light (He-Ne laser), off-the-shelf microscope objective (with a high level of stray light), and the high magnification configuration. We used holograms recorded at LURE, in march 1987 [9]: objects are

diatoms, and the recording wavelength  $\lambda_0$  is 100 Å. Aberrations were partially corrected by use of a mirror microscope optics, adjustable for a variable spherical aberration (for compensation of cover glass thickness). A reconstructed image is presented on Fig. 8, together with the original hologram (phase contrast microphotography of the resist hologram), and a SEM image of a very similar diatom. Despite a weak contrast, and a high noise level, the main structure of the diatom is clearly seen. Resolution can be estimated to 0.6-0.5  $\mu\text{m}$ .

The theoretical results presented in this paper, as well as the practical implementation proposed, prove that optics can definitely do much better.

#### Acknowledgements

Part of this work was done with the financial support of DRET. We are indebted to Raymond Mercier (Institut d'Optique), who made optical design calculations, proving that a simple, .55 NA, refractive reconstruction optics is a realistic goal.

#### References

1. A.V. Baez, "A study in diffraction microscopy with special reference to X-rays," *J. Opt. Soc. Am.*, **42**, 756-762 (1952).
2. A. V. Baez, and H.M.A. El-Sum, "Effect of finite source size, radiation bandwidth, and object transmission in microscopy by reconstructed wavefronts," in *X-ray microscopy and microradiography*, V.E. Cosslett, A. Engström, and H.H. Pattee Jr, eds. (Academic Press, New York, 1957).
3. E.N. Leith, J. Upatnieks, and K.A. Haines, "Microscopy by wavefront reconstruction," *J. Opt. Soc. Am.*, **55**, 981-986 (1965).
4. J.W. Giles Jr, "Image reconstruction from a Fraunhofer x-ray hologram with visible light," *J. Opt. Soc. Am.*, **59**, 1179-1188 (1969).
5. S. Aoki, Y. Ichihara, S. Kikuta, "X-ray hologram obtained using synchrotron radiation," *Japan J. Appl. Phys.*, **11**, 1857-? (1972).
6. M.R. Howells, "Possibilities for x-ray holography using synchrotron radiation," in *X-ray microscopy*, G. Schmahl and D. Rudolph, eds. (Springer Verlag, Berlin, 1984).
7. C. Jacobsen, J. Kirz, M. Howells, K. McQuaid, S. Rothman, R. Feder, and D. Sayre, "Progress in high resolution x-ray holographic microscopy," in *X-ray microscopy II*, D. Sayre, M. Howells, J. Kirz, and H. Rarback, eds. (Springer Verlag, Berlin, 1988).
8. R.W. Meier, "Magnification and third-order aberrations in holography," *J. Opt. Soc. Am.*, **55**, 987-992 (1965).
9. D. Joyeux, S. Lowenthal, F. Polack, and A. Bernstein, "X-ray microscopy by holography at LURE," in *X-ray microscopy II*, D. Sayre, M. Howells, J. Kirz, and H. Rarback, eds. (Springer Verlag, Berlin, 1988).
10. J.P. Marioge, Institut d'Optique, Orsay, France; private communication (to be published).
11. J.P. Chauvineau, J.P. Marioge, F. Bridou, G. Tissot, L. Valièrgue, B. Bonino, "X-uv optics in near normal incidence realised at the Institut d'optique," in *Soft x-ray optics and technology*, E.E. Koch and G. Schmahl, eds. *Proc SPIE* 733, 301-305 (1987).
12. Numerous references can be found in *Scanned image microscopy*, E.A. Ash ed. (Academic Press, New York, 1980).

# X-Ray Holographic Microscopy: Improved Images of Zymogen Granules

Chris Jacobsen and Malcolm Howells

*Center for X-ray Optics, Accelerator and Fusion Research Division  
Lawrence Berkeley Laboratory, 1 Cyclotron Road, Berkeley, California 94720*

Janos Kirz

*Department of Physics, State University of New York, Stony Brook, New York 11794*

Kenneth McQuaid and Stephen Rothman

*Schools of Medicine and Dentistry, University of California, San Francisco, California 94143*

Soft x-ray holography has long been considered as a technique for x-ray microscopy [1]. It has been only recently, however, that sub-micron resolution has been obtained in x-ray holography [2-4]. This paper will concentrate on recent progress we have made in obtaining reconstructed images of improved quality.

The recording of our holograms has been described elsewhere [2,3]. Briefly, the holograms were recorded in November 1986 and February 1987 using  $\lambda_1 = 25 \text{ \AA}$  radiation from a  $N=10$  period soft x-ray undulator and a temporary beamline at the National Synchrotron Light Source 2.5 GeV storage ring [5]. (This system has since been considerably upgraded, and is now returning to normal operation with a brighter undulator and a permanent soft x-ray microscopy beamline [6]). We were able to obtain a coherent soft x-ray flux of about  $10^8$  photons per second through the use of a grating monochromator for temporal coherence and a spatial filtering pinhole for spatial coherence. Dry specimens supported on Formvar-film-coated electron microscope grids were illuminated by plane-wave soft x-rays, and were followed at multiples of  $400 \text{ \mu m}$  by PMMA and/or MMA-MAA photoresists used as holographic recording media in the Gabor geometry. The photoresists were then "developed" in the solvent MIBK to convert the incident x-ray irradiance distribution to a surface relief pattern; the contrast of the relief was enhanced by vacuum evaporation of Pd: Au at  $7^\circ$  grazing incidence. A transmission electron microscope was then used to enlarge the holograms  $\sim 2000\times$  and read out the information encoded in sub-micron fringes.

In principle, one could reduce the electron micrographs to a net hologram magnification  $m \approx 250$  and then obtain reconstructions at visible wavelengths, where the wavelength ratio

$$\mu \approx \left( \frac{6000 \text{ \AA}}{25 \text{ \AA}} \right)$$

would match  $m$ . If the distances between the illumination source and the hologram were similarly scaled between the recording and reconstruction steps, such a reconstruction would give a magnified image with no aberrations, in what was described by Gabor as "lensless microscopy" [7]. However, our holograms contain a highly non-linear mapping of the incident x-ray intensity, which would lead to a poor signal-to-noise ratio in the reconstructed image if no corrections were made. For that reason, we have chosen to adopt a numerical approach to hologram reconstruction. By digitizing the electron micrographs with a scanning microdensitometer, we are able to obtain a numerical map of electron film density. Through the use of a simple model for the photoresist exposure, development, and read-out process, an approximate mapping of film density back to incident x-ray irradiance can be made, at least for low spatial frequencies [8]. The linearized hologram is a diffracting structure which will focus an incident plane wave down to an image of the specimen (plus the "twin image" present in Gabor holography, and weak intermodulation terms). In fact, the optical reconstruction process with the original reference beam can be mimicked by computing the magnitude squared of the Fresnel transform of the hologram transmittance [9,10]. Ultimately,



the power of the numerical approach lies in the fact that it allows non-linear processing algorithms such as that of Liu and Scott [11] to be used to suppress the unwanted signals.

The holograms are of rat zymogen granules, which hold precursors of digestive enzymes in the pancreas. Following isolation by the standard technique [12], the granules were fixed in 1.5% glutaraldehyde in 150 mM sucrose, but were *not* stained with heavy metals in the manner which would be followed for transmission electron microscopy. The granule suspension was subsequently diluted further in sucrose, after which a micropipette was used to place a drop of the suspension on a standard 300 mesh TEM locator grid coated with  $\sim 100$  Å of carbon-reinforced Formvar. The excess liquid was wicked away, and the grid was then air-dried, leaving occasional isolated granules and, more commonly, granule clumps on the grid.

These objects have been examined by using various conventional microscopic techniques and by x-ray holography. Figure 1 demonstrates that these unsectioned preparations are sufficiently thick to appear as opaque objects when viewed in a 100 KeV transmission electron microscope. Furthermore, their small size means that, once again, only the outlines of granules in a clump can be resolved

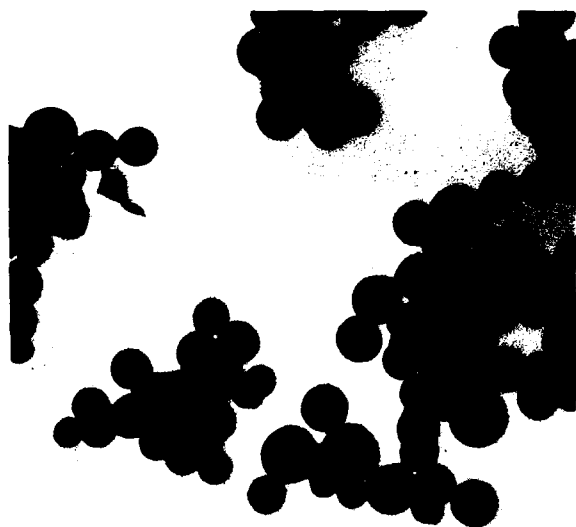


**Figure 1.** Transmission electron micrograph of fixed, air-dried, but unstained zymogen granules as prepared for x-ray holography. The unsectioned granules are spherical with a diameter of about  $0.6 \mu\text{m}$ , and thus appear opaque to a 100 KeV electron beam. Micrograph courtesy of T. Ermak.

with an optical microscope, as can be seen in Figure 2. The scanning electron micrograph of Figure 3 shows that the granule membrane remains in a spherical shape even when air-dried. Figures 1, 2, and 3 are all of different areas of the same specimen grid.

Figure 4 shows a section of a hologram and reconstructed image of the same granule clump as is shown in Figure 2. The holographic image is clearly consistent with the optical micrograph of Figure 2, except that much higher resolution information is contained in the holographic image. Fringes which would correspond to a resolution of about  $500$  Å are visible by inspection of the electron-microscope-enlarged hologram, and power spectra of hologram linescans suggest that information is recorded at or below the  $200$  Å level [3]. The reconstructed image in Figure 4 is the result of a  $512^2$  pixel sampling of the hologram, while Figure 5A shows a reconstructed image made from a  $1024^2$  pixel sam-



**Figure 2.** Optical micrograph of a different area of the same specimen grid as is shown in Figures 1 and 3. A  $400\times$  objective was used with a numerical aperture of 0.95; the diffraction-limited resolution of the micrograph is therefore about  $0.4 \mu\text{m}$ . Therefore, only the general outline of the  $\sim 0.6 \mu\text{m}$ -sized individual granules is visible. Because of waviness in the supporting Formvar film, the two smaller granule clumps at the bottom of the micrograph are in focus, while the larger clump at top is not. One granule clump is indicated for comparison with Figures 4, 5, and 6.



**Figure 3.** Scanning electron micrograph of a different granule clump from the same specimen grid as is shown in Figures 1 and 2. The fixed, air-dried, but unstained granules (with about 50 Å of Pt sputtered onto their surface) appear as perfectly smooth spheres for the first few seconds of SEM examination; the slight "rippling" that can be seen on the granule surfaces in the Figure is the result of radiation damage from the scanned electron beam. The radiation dose required to form the SEM image is three to four orders of magnitude higher than that required to record the x-ray hologram. Micrograph courtesy of D. Pardoe and J. Bastacky.

pling of the same hologram in which the diffraction-limited resolution would be 470 Å. (Because of sampling considerations, the images of Figure 5 are displayed with pixel sizes of 290 Å). Figures 5B, 5C, and 5D show the results of highpass filtering the reconstructed image to block out all information at spatial frequencies below  $(2 \times 3760)^{-1}$ ,  $(2 \times 2090)^{-1}$ , and  $(2 \times 990)^{-1} \text{ Å}^{-1}$ , respectively. Such a filtering process means that only information at a size scale smaller than

$$\Delta_{\text{cutoff}} = \frac{1}{2f_{\text{cutoff}}}$$

is preserved, so that Figure 5B shows only sub-3760 Å detail, Figure 5C shows sub-2090 Å detail, and Figure 5D shows only sub-990 Å detail. The Figures demonstrate that the reconstructed image contains almost exclusively sub-optical resolution information. Furthermore, granule edges clearly stand out in Figure 5D, indicating that the signal-to-noise ratio is still significant for strong sub-1000 Å detail.

Interpretation of the high-resolution information in the granule micrograph is a topic of ongoing study. As can be seen in Figure 6, a focal series of the granule shows a few "features" changing as

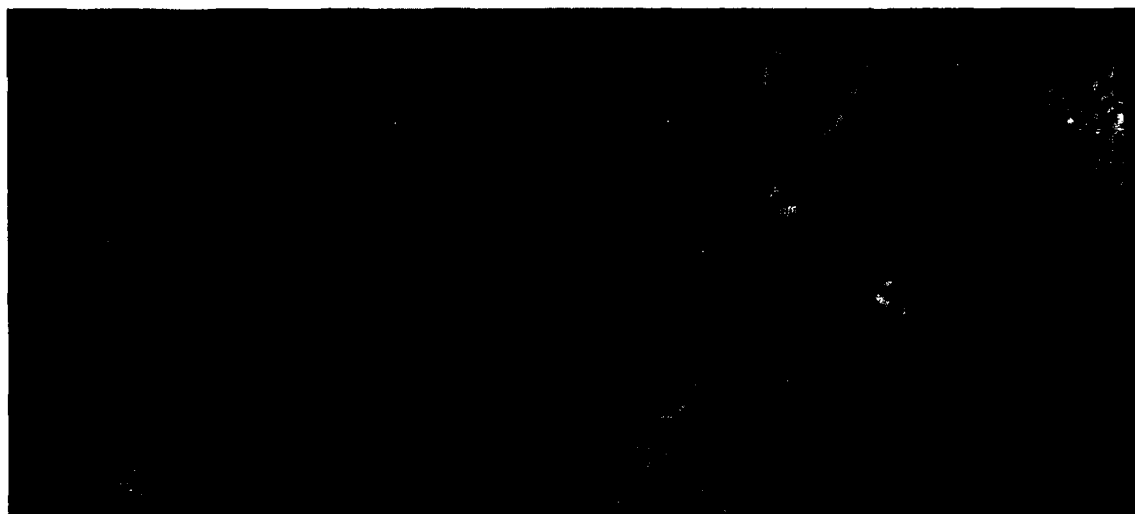


**Figure 4.** Portion of an x-ray hologram (left) and its reconstructed image (right) of the same granule clump as is indicated in Figure 2. Individual granules are clearly resolved in the reconstructed image, which emerges rather dramatically from the hologram.

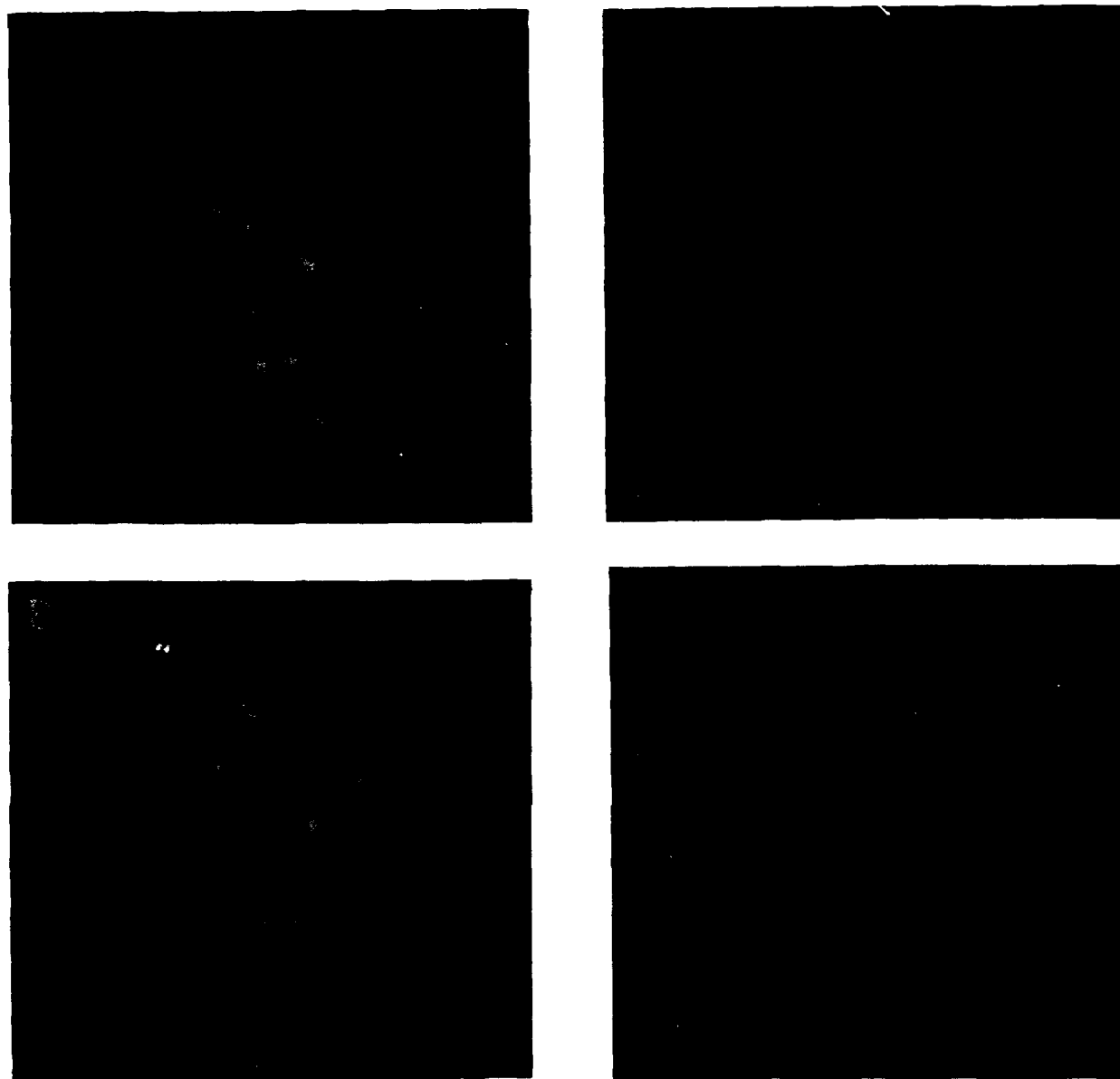


**Figure 5.** Enlarged,  $3.0\ \mu\text{m} \times 3.0\ \mu\text{m}$  views of the reconstructed image shown in Figure 4. **A:** the reconstructed image, with  $290\ \text{\AA}$  pixel size. **B:** the same image highpass filtered so that only sub- $3760\ \text{\AA}$  detail is shown. **C:** the same image highpass filtered so that only sub- $2090\ \text{\AA}$  detail is shown. **D:** the same image highpass filtered so that only sub- $990\ \text{\AA}$  detail is shown. As can be seen, most of the detail in the image is beyond the resolution limit of the optical microscope, and significant information appears to be contained at and below the  $1000\ \text{\AA}$  level.



**Figure 6.** A focal series of the granule clump shown in Figures 2-4. The numbers to the right of each sub-image indicate the assumed specimen-to-hologram separation distance  $f$  in  $\mu\text{m}$ . The focus chosen for Figures 4 and 5 was with  $f = 406 \mu\text{m}$ . As can be seen, some "features" in the image change as  $f$  is varied, presumably because they are in fact phase contrast fringes produced when an coherent imaging system is improperly focussed. Note that the diffraction-limited longitudinal resolution would be  $3.4 \mu\text{m}$  for this reconstruction.

the assumed specimen to hologram separation distance  $f$  is varied in  $2 \mu\text{m}$  increments (the diffraction-limited longitudinal resolution would be  $3.4 \mu\text{m}$  for this reconstruction). The changing "features" are presumably the result of focussing error aberrations, which produce contrast reversals as a coherent imaging system is brought into and then out of focus [13]. However, most high-spatial-frequency information remains unchanged in the focal series; further study will be required in order to determine whether these features are actual structures within the granules, artifacts resulting from the coherent imaging of granules stacked on top of each other, or an artifact of air-drying. Finally, it should be noted that the thickness of the granule clump is almost certainly less than the longitudinal resolution length, so that our current reconstructed images only contain two-dimensional information.

The attractions of holography as a soft x-ray imaging technique have been discussed elsewhere [14,15]. They include the ability to make use of single-shot x-ray sources if they become available at the required brightness, the fact that the focussing of the image is accomplished in the reconstruction stage (*without* additional exposure to x-rays), the natural way in which phase contrast can be utilized

in holographic imaging, and the possibility of extension to diffraction tomography for achieving high-resolution, three-dimensional images. Obtaining images which show detail not visible in optical or electron microscopes gives us confidence that soft x-ray holographic microscopy is a technique with considerable potential for high resolution imaging.

### Acknowledgements

We acknowledge valuable help and advice from P. Batson, J. Bastacky, J. Boland, M. Caldarolo, K. Conkling, C. Dittmore, T. Ermak, R. Feder, J. Grendell, D. Joel, T. Kondakjian, D. Pardoe, H. Rarback, and D. Sayre, as well as the generous assistance of the staff at the NSLS. This work was supported in part by the National Science Foundation under grant BBS-8618066 (J.K.) and the Director, Office of Energy Research, Office of Basic Energy Sciences, Materials Sciences Division, of the U.S. Department of Energy under contract DE-AC03-76SF00098. This work was carried out in part at the National Synchrotron Light Source, which is supported by the Department of Energy under contract DE-AC02-76CH00016.

### References

1. For summaries of preceding work, see: S. Aoki and S. Kikuta, "X-ray holographic microscopy", *Japan J. App. Phys.* **13**, 1385-1392 (1974); and M. R. Howells, M. A. Iarocci, and J. Kirz, "Experiments in x-ray holographic microscopy using synchrotron radiation", *J. Opt. Soc. Am. A* **3**, 2171-2178 (1986). A more recent review is contained in Section 4.1 of Reference 8.
2. M. Howells, C. Jacobsen, J. Kirz, R. Feder, K. McQuaid, and S. Rothman, "X-ray holography at improved resolution: a study of zymogen granules", *Science* **238**, 514-517 (1987).
3. C. Jacobsen, J. Kirz, M. Howells, K. McQuaid, S. Rothman, R. Feder, and D. Sayre, "Progress in high-resolution x-ray holographic microscopy", in D. Sayre, M. R. Howells, J. Kirz, and H. Rarback, eds., **X-ray Microscopy II** (Springer-Verlag, Berlin, 1988), pp. 253-262.
4. D. Joyeux, S. Lowenthal, F. Polack, and A. Bernstein, "X-ray microscopy by holography at LURE", in D. Sayre, M. Howells, J. Kirz, and H. Rarback, eds., **X-ray Microscopy II** (Springer-Verlag, Berlin, 1988), pp. 246-252; and D. Joyeux *et al.*, this volume.

5. H. Rarback, C. Jacobsen, J. Kirz, and I. McNulty, "The performance of the NSLS mini-undulator", *Nucl. Inst. Meth.* **A266**, 96-105 (1988).
6. C. J. Buckley *et al.*, Proceedings of the 1988 International Synchrotron Radiation Instrumentation conference, Tsukuba, Japan. (To be published in *Nucl. Inst. Meth.*)
7. D. Gabor, "Microscopy by reconstructed wavefronts", *Proc. Roy. Acad. Sci. London* **A197**, 454-487 (1949).
8. C. Jacobsen, "Soft x-ray holography microscopy of biological specimens using an undulator", Ph. D. dissertation, Department of Physics, State University of New York at Stony Brook, May 1988.
9. W. H. Carter and A. A. Dougal, "Field range and resolution in holography", *J. Opt. Soc. Am.* **56**, 1754-1759 (1966).
10. J. W. Goodman and R. W. Lawrence, "Digital image formation from electronically detected holograms", *Appl. Phys. Lett.* **11**, 77-79 (1967).
11. G. Liu and P. D. Scott, "Phase retrieval and twin-image elimination for in-line Fresnel holograms", *J. Opt. Soc. Am. A* **4**, 159-165 (1987).
12. T. H. Ermak and S. S. Rothman, "Internal organization of the zymogen granule: formation of reticular structures *in vitro*", *J. Ultrastructure Research* **64**, 98-113 (1978).
13. See e.g., Section 6-4 of J. W. Goodman, *Introduction to Fourier Optics* (McGraw-Hill Book Company, San Francisco, 1968).
14. M. R. Howells, C. Jacobsen, J. Kirz, K. McQuaid, and S. S. Rothman, "Progress and prospects in soft x-ray holographic microscopy", presented at the British Biophysical Society Conference on Modern Microscopies, London, United Kingdom, December 20-21, 1987 (to be published).
15. C. Jacobsen, J. Kirz, M. R. Howells, and S. Rothman, "Biological microscopy via x-ray holography", presented at International Conference on 3-D Image Processing in Microscopy, Gießen, Federal Republic of Germany, March 9-11, 1988. (To be published in *European J. Cell Biology.*)

## Amplitude- and Phase-Contrast X-Ray Microscopy

G. Schmahl, University of Göttingen  
Geiststraße 11, 3400 Göttingen  
Fed. Rep. of Germany

### Summary

X-ray photons in the wavelength range of about 0.5 - 5 nm are best suited for x-ray microscopy. In the wavelength range  $\lambda \geq 2.5$  nm the absorption cross sections are about one order of magnitude smaller than the cross sections for electrons in the energy range in which electron microscopy is performed. These absorption cross sections for soft x-rays are appropriate for high resolution investigation of biological specimens in their natural state having a thickness of up to about 10 micrometer. Especially interesting is the wavelength range between the K absorption edges of oxygen ( $\lambda = 2.34$  nm) and carbon ( $\lambda = 4.38$  nm) because in this wavelength range the radiation is weakly absorbed by water but strongly absorbed by organic matter resulting in a rather good amplitude contrast of wet specimens. For many elements and wavelengths phase shift is the dominating process and not photoelectric absorption. That means that phase-contrast x-ray microscopy can be performed with the following advantages compared to x-ray microscopy modes using amplitude contrast: For wavelengths larger than the carbon K-edge, the amplitude contrast of organic material surrounded by water is very low. To the contrary, for wavelengths slightly larger than  $CK_{\alpha}$  the phase contrast of such an object is high. Even in the wavelength range between the K-edges of carbon and oxygen (water window) wavelengths are found for which imaging in phase contrast is better concerning contrast and dosage compared to amplitude contrast imaging. In addition, imaging with phase contrast can be extended to wavelengths of about 0.5 nm with a dosage comparable to that necessary for imaging with amplitude contrast in the water window. The last point may be of practical importance in future work because with shorter wavelengths thicker specimens can be investigated than up to now. X-ray microscopy experiments performed in amplitude- and phase-contrast at the electron storage ring BESSY in Berlin will be discussed.

### References:

1. X-Ray Microscopy, eds. G. Schmahl and D. Rudolph, Springer Series in Optical Sciences Vol. 43, Springer Verlag (1984)
2. X-Ray Microscopy - Instrumentation and Biological Applications, eds. P.C. Cheng and G.J. Jan, Springer Verlag (1987)
3. X-Ray Microscopy II, eds. D. Sayre, M. Howells, J. Kirz and H. Rarback, Springer Series in Optical Sciences, Springer Verlag (1988), in press

## X-Ray Holography: X-Ray Interactions and Their Effects

Richard A. London, James E. Trebes, and Mordecai D. Rosen

*University of California, Lawrence Livermore National Laboratory  
Livermore, California 94550*

### Abstract

We summarize a theoretical study of the interactions of x rays with a biological sample during the creation of a hologram. The choice of an optimal wavelength for x-ray holography is discussed, based on a description of scattering by objects within an aqueous environment.

The problem of the motion resulting from the absorption of x rays during a short exposure is described. The possibility of using very short exposures in order to capture the image before motion can compromise the resolution is explored.

The impact of these calculation on the question of the feasibility of using an x-ray laser for holography of biological structures is discussed.

### Introduction

The imaging of biological samples using x-ray holography has long been recognized as a possibly powerful technique to gather information about structures on small scales [1]. Compared to optical light, x rays offer the possibility for finer resolution because of their shorter wavelength. Compared to electrons, x rays have the advantage of higher penetrability through water, thereby enabling the structure of living cells or organisms to be studied, avoiding unknown changes which may occur in the process of sample preparation for electron microscopy.

A group of physicists, biologists, and electrical engineers at the Lawrence

Livermore National Laboratory has been engaged in a study of the feasibility of producing useful, high-spatial resolution ( $\sim 300\text{\AA}$ ) 3-D images of biological structure within living cells using soft x rays. The group has explored candidate biological objects to image, studied the choice of wavelength based on the x-ray interactions with the sample, studied the design of a holography system, developed computer codes for simulation and reconstruction of holograms, and fielded analog holography experiments using visible light. There is also an ongoing effort to develop optically pumped x-ray lasers at Livermore.

In this paper we discuss one area of this work: the selection of a wavelength for holography based on the x-ray interactions with the sample. For a certain desired resolution, we apply three criteria: i) minimize the quantity of x rays with which the sample must be irradiated and thus minimize the required source energy, ii) minimize the absorption within the primary structures of interest, and iii) maximize the penetration of the x rays through the water surroundings. The first two criteria amount to maximizing the scattering efficiency of the sample, while at the same time minimizing the absorption. We also explore the influence of sample heating on the selection of an x-ray exposure length. The inherently short duration of x-ray laser pulses (10 psec - 10 nsec), potentially allows the imaging of dynamic processes, but unlike synchrotrons, precludes the use of conduction for removal of heat deposited in the sample by the x rays. The heat is expected to lead to hydrodynamic motions of parts of the sample. This may be

precludes the use of conduction for removal of heat deposited in the sample by the x rays. The heat is expected to lead to hydrodynamic motions of parts of the sample. This may be avoided by using very short pulses in order to capture the image before significant motion occurs [2-5].

The analysis of the wavelength selection criteria depends on a description of the interactions of x rays with the sample. We shall assume the sample to consist of protein and DNA structures within the aqueous environment of a cell. The primary interactions are elastic scattering and absorption. Scattering is essential to create a hologram. Absorption is an undesirable, but unavoidable consequence of illuminating a sample with x rays.

### X-Ray Interactions

In order to create a hologram, x-ray photons must be scattered by the sample. This requires a certain irradiating fluence, and an associated dose to the sample. Estimating the minimum number of scattered photons to obtain an image of a specified quality is a complex problem. In order to address this question in an approximate manner, we first specify the size of the smallest features which we wish to resolve ("object pixels"), and require that a certain number of photons be scattered from these features. Since larger features will scatter more photons, the smallest features place the limiting constraints on the x-ray irradiation and dose. In this paper we shall use  $10^3$  scattered photons per object pixel as the criterion.

Given the number of scattered photons,  $N_s$ , the fluence (energy per unit area) in the irradiating beam may be written:

$$F = N_s hc/(\lambda \sigma_s), \quad (1)$$

where  $\lambda$  is the x-ray wavelength and  $\sigma_s$  is the scattering cross section of the object pixel. For an optically thin sample, the absorbed dose (energy per unit mass) is given by:

$$D = F \kappa_a, \quad (2)$$

where  $\kappa_a$  is the absorption opacity (cross section per unit mass) of the material.

In order to make quantitative estimates of the required irradiating fluence and sample dose, we assume that each of the smallest features can be approximated by isolated spheres surrounded by a homogeneous medium. We use physical optics theory to calculate the x-ray scattering, following the book on light scattering by Van de Hulst [6]. The differential scattering cross section is a function of the

radius of the sphere ( $r$ ), the wavelength of the x rays, and refractive index of the object ( $m_1$ ) and that of the surrounding material ( $m_2$ ).

For the problems of interest, the refractive indices are near unity and the (complex) phase shift of the x-rays across the object is small. In this case, there exists a useful simplification to the scattering theory, namely the Rayleigh-Gans method, equivalent to the Born approximation in quantum scattering theory. The characteristic phase shift is defined as:  $\rho = 4\pi r |\Delta m|/\lambda$ , where  $\Delta m \equiv m_1 - m_2$ . The general conditions for the validity of the Rayleigh-Gans approximation may be stated as:  $|\Delta m| \ll 1$  and  $\rho \ll 1$ . The angular width of the scattered power is approximately  $\lambda/2\pi r$ . In the limit of interest ( $r \gg \lambda/2\pi$ ), the total cross section (integrated over angle) is:

$$\sigma_s = \frac{8\pi^3 r^4}{\lambda^2} |\Delta m|^2. \quad (3)$$

Writing the indices of refraction of the sphere and surroundings as:

$$m_{1,2} = 1 - \delta_{1,2} - i\beta_{1,2}, \quad (4)$$

where  $\delta$  and  $\beta$  are called the optical constants for a particular material, we can express the cross section as:

$$\sigma_s = \frac{8\pi^3 r^4}{\lambda^2} [(\delta_1 - \delta_2)^2 + (\beta_1 - \beta_2)^2]. \quad (5)$$

We follow Henke et al [7] in calculating the optical constants for a material from the atomic scattering factors. The use of atomic scattering factors for real materials is expected to introduce some errors in the optical constants, particularly near absorption edges, because of effects of atomic interactions. This is currently being investigated.

Using Eq. (5) and the data from ref. [7], we have calculated the wavelength dependence of the total scattering cross section for a 150 Å radius sphere of protein, both in vacuum and in water, shown in Figure 1.

For the more appropriate case of protein in water, the cross-section has a pronounced peak extending across the carbon K-edge at 43.7 Å, whereas for protein in vacuum, there is a minimum in this region. This difference results from the complicated behavior of the index components near the edge (the "anomalous dispersion"), and the large amount of cancellation which occurs between the index components of the protein and those of the water. For the case of protein in water, the main contribution to the scattering near the



carbon K-edge comes from the larger value of the real scattering factor for water as compared to that for protein (i.e.  $\delta_2 > \delta_1$ ). The fact that the cross-section is sensitive to the differences between the object and the surroundings emphasizes the importance of an accurate model for the composition of the materials under study, as well as the promise for achieving high sensitivity to spatial variations in elemental composition.

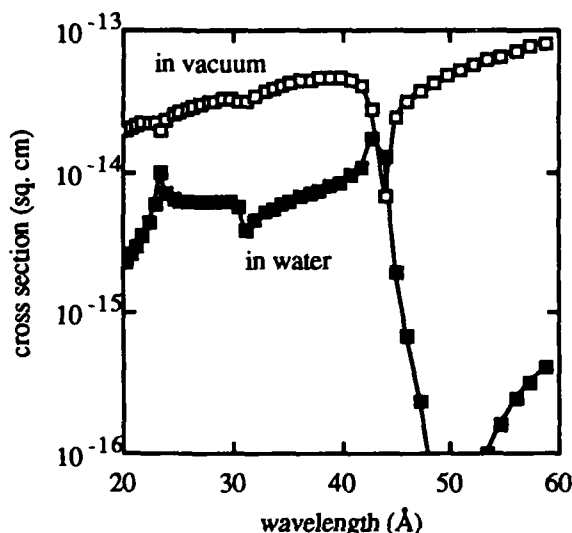


Figure 1. Scattering cross section for a 150Å protein sphere, both in vacuum and in water.

The small phase shift assumption behind the Rayleigh-Gans approximation breaks down for protein spheres larger than about  $2 \times 10^3$  Å. For larger spheres the anomalous diffraction approximation may be applied [6].

The penetration length for x rays is of interest in determining the overall size of a sample which could be imaged. The opacity is almost entirely absorptive and can be calculated from the imaginary scattering factors for each atom as described in ref. [7]. The e-folding penetration length in water ranges from 9  $\mu$ m at 23.2 Å (on the long wavelength side of the oxygen edge) to 2  $\mu$ m at 43.7 Å (the carbon edge). The penetration through protein is small ( $< 1/2$   $\mu$ m) at wavelengths shorter than the carbon edge, and jumps to about 2  $\mu$ m on the long wavelength side.

Several authors have discussed x-ray scattering cross-sections in connection with holography. Solem, Chapline, and Baldwin [2-5] have used a prescription based on quantum scattering theory for particles. In the weak scattering limit, their cross section is taken equal to the geometric cross section times the square of the extinction (mainly by absorption)

through the object. They include only the  $\beta_1$  term in Eq. (5), ignoring the real part of the index and the effect of the surrounding medium totally. In addition, it appears that they have a normalizing factor which is  $32/9 \approx 3.6$  times higher than in Eq. (5) in the weak scattering limit.

Recently, Howells [8] (see also ref. [9]) has discussed scattering by a self consistently defined resolution volume within the sample (generally an ellipsoid elongated in the direction of the incident wave). Within the resolution element, a coherent addition of scattering from the individual atoms is assumed, including both real and imaginary parts of the scattering amplitude. This prescription is in essential agreement with Eq. (5), for spheres the size of the resolution element, except that it does not account for the influence of the surrounding medium. In addition, we believe that the increased amount of scattering achieved by using an ellipsoid as compared to a sphere (of the same minor axis), may not be realized in practice, unless the feature under study is actually shaped like an ellipsoid with the appropriate aspect ratio and alignment.

As pointed out by Howells [8] and Jacobsen [9], the true resolution element for holography is approximately an ellipsoid. The depth resolution is about ten times worse than the transverse resolution, for typical sizes and wavelengths. This difficulty in achieving 3-D resolution is possibly overcome by taking several concurrent holograms at different viewing angles [10, 11].

## Fluence and Dose

Using Eqs. (1) and (5), we have calculated the wavelength dependence of the fluence for a 150Å radius sphere to scatter  $10^3$  photons. There is a dramatic dip near the carbon K-edge, with a minimum value of about  $3 \times 10^7$  erg  $\text{cm}^{-2}$ .

The doses to the protein and to the surrounding water, calculated from Eq. (2), are illustrated in Figure 2. It is apparent that for protein in water, the minimum dose is achieved just above the carbon K-edge, at a wavelength of about 44 Å. Both the fluence and absorbed dose scale as  $r^4$ . This means that images of slightly larger features of a sample might be possible with significantly less x-ray power and with less damage.

## Optimal wavelength

The analysis of the fluence, dose and attenuation length described above has several implications for the choice of an operating x-ray

wavelength. One of the advantages of soft x rays over electrons for imaging is their penetrability through water. To maximize this, one would like to work at short wavelengths, near the oxygen K-edge at 23.3 Å, where the penetration length is about 9 μm. However, to minimize the x-ray fluence, one would use wavelengths near the carbon edge. The dose jumps by a factor of about 10 in going from a wavelength of 43 Å, just below the edge to 44 Å, just above the edge, because of the sharp change in absorption opacity. Therefore, wavelengths right above the edge, say 44–45 Å, appear to be best for minimizing both the fluence and the dose to the sample. At 44 Å, the penetration length through water is about 2 μm, which may be sufficient for a sample placed in a small water filled container. In addition, since the penetration length in protein is maximized above the K-edge, holography of samples having a lot of protein in addition to the particular objects under study may be best done at 44 Å.

Another reason to prefer the longer wavelengths is the increasing difficulty of making shorter wavelength x-ray lasers.

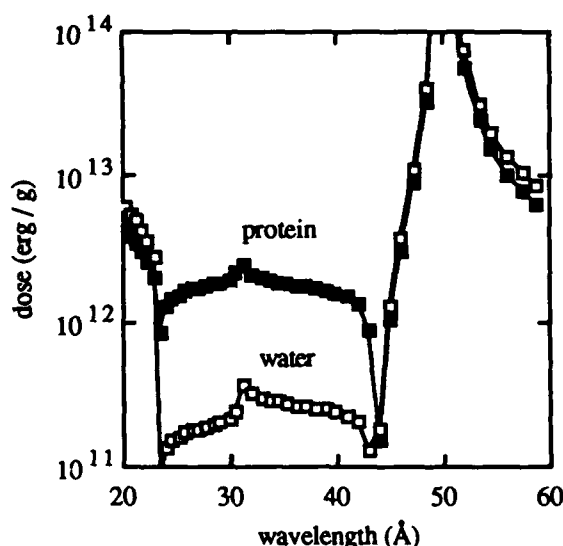


Figure 2. The dose absorbed by both the protein and the water in a sample. We have assumed that a 150 Å radius protein sphere scatters  $10^3$  photons.

Our findings are qualitatively different than the conclusions of previous workers who have suggested the "water window" - between 23.3 Å and 43.7 Å, as the best operating region [4]. We suggest working at slightly longer wavelength. The concept of the water window

originated in the field of x-ray microscopy. For this purpose, the important wavelength selection criterion is the contrast in absorption cross section between carbon and oxygen. The carrying over of the concept to holography was based on the idea that the scattering by a sample was dominated by the imaginary part of the index of refraction. As we have discussed, this is not generally true for the appropriate materials and wavelengths. Therefore the concept of the water window is apparently not valid for holography, although the optimal wavelength is only slightly outside of the window.

A similar analysis applied to phase contrast microscopy indicates that the water window is also not the best operating region for this technique [12, 13].

### Hydrodynamics and short pulse exposure

It is expected that x-ray absorption by the sample will lead to hydrodynamic motion, possibly compromising the spatial resolution of the hologram. In principle, this can be avoided by using a very short exposure in order to capture the image before significant motion occurs [2,4,5]. In this scheme, there exists a maximum allowable exposure time, obtainable either through a short duration x-ray pulse, or by fast shuttering of the recording device. To estimate the maximum exposure time, we shall use a hydrodynamics model presented by Solem [2,5] to make rough estimates of the amount of motion. The model is for a sphere embedded in an equal density surrounding material. It assumes a constant heating rate per unit mass in the sphere,  $H$ ; a ratio of heating of the sphere to that of the surrounding material,  $c$ ; and an adiabatic index equation of state for both materials, with index  $\gamma$ . The expansion of the sphere, for early times such that the radius has not yet doubled, is given approximately as:

$$r = r_0 + \left[ f(\gamma) \frac{c-1}{c} H \right]^{1/2} t^{3/2}, \quad (6)$$

where  $r_0$  is the initial radius,  $t$  is time and  $f(\gamma) = 2/3(\gamma - 1)/(\gamma + 1)^2$ . Solem suggests a value of  $\gamma$  of 1.1 for protein for temperatures less than  $10^3$  K. An ideal gas would have  $\gamma = 5/3$ . The contrast factor,  $c$ , is quite uncertain. The worst case is when the protein is heated, but the water is not ( $c = \infty$ ). Values as small as  $c = 1.1$  have been considered. We use Eq. (6) to find the maximum allowable pulse length by solving for the time at which  $r = 2r_0$ . Identifying the dose discussed above as  $D = (Ht)$ , and using a plausible range of  $\gamma$  and  $c$ , we estimate that maximum exposures between 15 and 50 psec would be required

to image a 150 Å radius protein sphere. Since the dose drops as  $r^{-4}$ , the limiting pulse length would increase as  $r^3$ . For example, an increase in the pulse length by a factor of three could be achieved by targeting 200 Å radius objects rather than 150 Å objects.

These estimates of the maximum exposure time must be regarded as very approximate, due to the simplicity of the models for x-ray scattering, equation of state, and hydrodynamics. We plan further work to refine these estimates.

## Conclusions

We have explored the choice of an optimal wavelength for x-ray holography of biological samples in an aqueous environment. The influential factors are the x-ray scattering and absorption by the sample. We have applied physical optics theory to calculate the scattering cross section of an idealized model of a sample, namely a sphere within a homogeneous medium. The optical constants of the materials have been calculated from atomic scattering factors.

We find that wavelengths slightly longer than the carbon K-edge at 43.7 Å minimize both the required irradiating fluence and the dose to the sample. The penetrability within the water is maximized near the oxygen K-edge at 23.3 Å, but is still reasonable above the carbon edge. It appears that the water window is not necessarily the best wavelength region for x-ray holography. We suggest a wavelength of 44 Å as a good trade-off between several factors.

The short exposure scheme to achieve an image before hydrodynamic motion compromises resolution has been explored. Estimates of the maximum exposure time for a 300 Å transverse resolution (i.e. diameter of sphere) are in the range 15 to 50 psec. Because of the rapid scaling with size, 45 to 150 psec exposures are estimated for 500 Å resolution.

We have estimated that approximately 40 μJ of spatially coherent x-ray energy is needed for holography in the Fourier transform geometry. This estimate assumes a focal spot 10 μm in diameter, and accounts for losses in the sample holder and x-ray optics, detector efficiency, and a total of three views to obtain adequate depth resolution. X-ray lasers with pulse lengths of 200 psec and energy of 500 μJ have already been demonstrated. Further developments towards achieving high power at shorter wavelength, shorter pulse lengths, and higher spatial coherence are called for in order to pursue the application of x-ray laser holography.

## Acknowledgments

We are grateful to the members of the group working on x-ray laser holography at Livermore for contributions to this research: J. Brase, M. Campbell, J. Gray, D. Matthews, D. Peters, D. Pinkel, and T. Yorkey. We thank R. More and A. Szoke for useful discussions. In addition, we thank C. Jacobsen for valuable discussions and for sending us an early copy of his Ph. D dissertation.

This work was performed under the auspices of the U. S. Department of Energy by the Lawrence Livermore National Laboratory under contract number W-7405-ENG-48.

## References

1. for a recent review see X-Ray Microscopy II, D. Sayre, M. Howells, J. Kirz, and H. Rarback, eds. (Springer-Verlag, New York, 1988).
2. J. C. Solem and G. C. Baldwin, "Microholography of Living Organisms," *Science*, **218**, 229 (1982).
3. J. C. Solem, "High-Intensity X-ray Holography: An Approach to High-Resolution Snapshot Imaging of Biological Specimens," Los Alamos National Lab. Rept. LA-9508-MS (1982).
4. J. C. Solem and G. F. Chapline, "X-Ray Biomicroholography," *Opt. Eng.* **23**, 193 (1984).
5. J. C. Solem, "Imaging Biological Specimens with High-Intensity Soft X Rays," *JOSA-B* **3**, 1551 (1986).
6. H. C. van de Hulst, Light Scattering by Small Particles, (Dover, New York, 1981).
7. B. L. Henke, P. Lee, T. J. Tanaka, R. L. Shimabukuro, and R. K. Fujikawa, "Low-Energy X-Ray Interaction Coefficients: Photoabsorption, Scattering, and Reflection," *Atom. Data and Nuc. Data Tables* **27**, 1 (1982).
8. M. Howells, "Fundamental Limits in X-Ray Holography," in X-Ray Microscopy II, D. Sayre, M. Howells, J. Kirz, and H. Rarback, eds. (Springer-Verlag, New York, 1988) p. 263.
9. C. Jacobsen, "X-Ray Holographic Microscopy of Biological Systems Using an Undulator", Ph.D. Dissertation, SUNY-Stony Brook, New York, (1988).
10. C. Jacobsen, this volume.
11. A. J. Devaney, private communication.
12. G. Schmahl, D. Rudolph, and P. Guttmann, "Phase Contrast X-Ray Microscopy - Experiments at the BESSY Storage Ring," in X-Ray Microscopy II, D. Sayre, M. Howells, J. Kirz, and H. Rarback, eds. (Springer-Verlag, New York, 1988) p. 228.
13. G. Schmahl, this volume.

#### DISCLAIMER

This document was prepared as an account of work sponsored by an agency of the United States Government. Neither the United States Government nor the University of California nor any of their employees, makes any warranty, express or implied, or assumes any legal liability or responsibility for the accuracy, completeness, or usefulness of any information, apparatus, product, or process disclosed, or represents that its use would not infringe privately owned rights. Reference herein to any specific commercial products, process, or service by trade name, trademark, manufacturer, or otherwise, does not necessarily constitute or imply its endorsement, recommendation, or favoring by the United States Government or the University of California. The views and opinions of authors expressed herein do not necessarily state or reflect those of the United States Government or the University of California, and shall not be used for advertising or product endorsement purposes.

---

**Part 4**  
**Optics and Detectors**

---

## Recent Advances and Prospects of Bragg-Fresnel Optics

V. V. Aristov

*Institute of Problems of Microelectronics Technology and High Purity Materials  
USSR Academy of Sciences, 142432 Chernogolovka, Moscow District, USSR*

Diffraction optics, i.e. Fresnel zone plates, holograms and diffraction gratings, has a limited application in the optical wavelength range. A decrease in wavelength to 100 nm and less changes conventional relationships between different types of optical elements owing to the change in the radiation-substance interaction since absorption starts to play a more important role as compared to refraction. Therefore at  $1 \text{ nm} \leq \lambda \leq 100 \text{ nm}$  focusing elements may be fabricated only from thin membranes distinguished by an abrupt change of either absorption (amplitude zone plates) or transmitted wave phase (phase zone plates). The possibility exists of fabricating kinoform plates in which the wave phase varies smoothly from 0 to  $2\pi$  because of a smooth increase in membrane thickness, the latter decreasing again to zero. A further decrease in the wavelength and the refractive index causes an increase in zone plate thickness up to  $10^{-2} \div 10^{-5}$  of radiation wavelengths which is required for attaining a  $\pi$  phase shift. In this case the membrane should be regarded as three-dimensional and, hence, a flat Fresnel lens becomes inefficient when fabricated without reference to three-dimensional scattering. In this wavelength range it is necessary that three-dimensional Bragg and Bragg-Fresnel elements should be used. Three-dimensional elements appear to be efficient for the whole short wavelength range  $10^{-2} \text{ nm} \leq \lambda \leq 100 \text{ nm}$ . In doing so, the use of Bragg diffraction enables fabrication of high resolution gratings, radiation modulators and prisms. Thus, two- and three-dimensional diffraction elements from the basis for production of multifunctional X-ray optics in a wide

wavelength range. It is essential that these elements can be reproduced in production quantities.

Below is a summary of the results obtained at the Institute of Problems of Microelectronics Technology and High Purity Materials (IPMT) of the USSR Academy of Sciences in 1984-88 [1-15]. Emphasis is placed on Bragg and Bragg-Fresnel elements that are fundamental for future X-ray optics.

### Elements of Two-Dimensional Diffraction Optics ( $0.5 \text{ nm} \leq \lambda \leq 100 \text{ nm}$ ): Advantages and Limitations

Fig. 1 shows a photograph of part of a Fresnel zone plate fabricated at IPMT. The minimum zone size is 350 nm, silicon layer thickness  $2.4 \mu\text{m}$ .

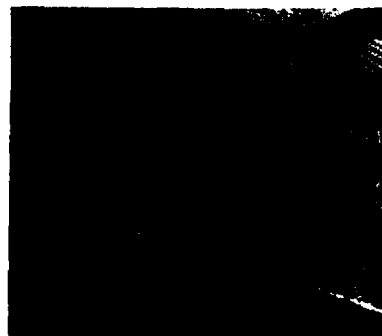


Figure 1. Part of a Fresnel zone plate.

This Fresnel zone plate is to be used for the 1 nm wavelength. The advantages

of Fresnel zone plates are simplicity of fabrication involving 2-3 precise operations, possibility of quantity production and simplicity of calculations.

The disadvantages of such elements are low thermal and radiation stability, limitations on the operating wavelength range ( $\lambda > 0.5 \div 1$  nm) and the maximum angular aperture owing to three-dimensional scattering ( $\varphi \leq (1-n)^{1/2}$ ), where  $n$  is the refractive index), a limitation on resolution to a value  $2\lambda(1-n)^{1/2}$ , impossibility of fabricating controlled and tunable elements, presence of chromatic aberrations.

### Elements of Three-Dimensional Diffraction Optics

- a) Bragg optical elements ( $0.01 \text{ nm} \leq \lambda \leq 0.5 \text{ nm}$ ).

X-ray radiation is effectively scattered by Bragg diffraction on a perfect crystal. By virtue of a regular arrangement of the lattice atoms, radiation scattering is enhanced in certain directions. Radiation scattered by a perfect crystal retains its coherent properties. The characteristic parameter of Bragg scattering is its extinction length  $\Lambda_e$  or the Bloch wavelength proportional to  $\lambda/(1-n)$  ( $n < 1$ ,  $\Lambda_e \approx 1-10 \mu\text{m}$ ). The Bloch wavelength rather than radiation wavelength determines spatial resolution and the spectral characteristics of Bragg elements. It is essential that the requirements on the precision of fabrication of x-ray optical Bragg elements are governed by the Bloch wavelength. Table 1 lists the elements of Bloch wave Bragg optics suggested by different authors. The technology of fabrication of various types of x-ray elements is being developed at IPMT. By way of illustration Fig. 2 shows a photograph of a silicon x-ray microinterferometer.



Figure 2. X-ray microinterferometer.

The disadvantage of Bragg optical elements is that the spatial resolution is limited by the Bloch wavelength. The theoretical description of the operation of such elements and, hence, their calculation are based on the dynamic theory of diffraction taking into account multiple radiation scattering inside the scattering volume.

The advantage of Bragg optics is that it can be most efficiently used to control hard x-ray radiation. It also allows application of microelectronic technology for reproduction of optical elements.

- b) Bragg-Fresnel optical elements ( $0.01 \text{ nm} \leq \lambda \leq 100 \text{ nm}$ ).

This type of optical elements was proposed and realized in some of our works [1-7, 11-14]. The studies of x-ray scattering on a perfect three-dimensional crystal are commonly reduced to the investigation of lattice distortions deforming the diffracting wave front. We have attempted to solve the reverse problem, namely, to use the potentialities of epitaxial growth of perfect films and microstructuring for fabrication of a "perfect" x-ray optical element with specified crystal defects which is capable of changing the wavefront of incident radiation in a preset way. For instance, a spherical wave may be focused into a small spot upon Bragg scattering on a film with a specific deformation gradient or amorphous layers [7].

Efficient Bragg elements may be fabricated for hard ( $\lambda < 1 \text{ \AA}$ ) and neutron radiation. A three-dimensional point hologram, being a system of ellipsoids and paraboloids, is an ideal Bragg-Fresnel lens. Such a lens is free from chromatic aberrations and focuses all wavelengths reflected by the lattice into one point. We obtained a three-dimensional system of Bragg-Fresnel zones for a perfect lattice composed of equidistant planes by superimposing ellipsoids on the lattice and separating the regions in which the positions of ellipsoid and lattice planes coincide or differ by no more than a quarter of the interplane distance. The focusing effect can be achieved by a zone-to-zone variation of the phase or coefficient of scattering.

We have fabricated various types of Bragg-Fresnel zone plates including phase zone plates on multilayer mirrors with Ni and C layers as well as on Si single crystals. The lenses were tested on SR facilities in Novosibirsk and Hamburg and by means of conventional point radiation sources. Focusing has been

Table 1.

X-Ray Optical Elements and Their Application

Optical elements	Authors	Application
1. x-ray interferometer	Bonse, Hart, 1965	a) measurement of refractive indices of materials b) measurement of defect stress fields with a sensitivity $\Delta d/d \sim 10^{-8}-10^{-9}$
2. x-ray micro-interferometer	Aristov, Snigirev, Nikulin, Yerokhin, Kuznetsov, 1987	a) local measurements of stress fields with a sensitivity $\Delta d/d \sim 10^{-8}$ and locality $\Delta r \approx 10$ nm b) formation of x-ray coherent beams c) spatial and time modulation of x-ray radiation, measurement of local displacements
3. x-ray prism	Aristov, Afanasyev, Kohn, Polovinkina, 1983	x-ray optical arrangements
4. zone plate for focusing of crystal Bloch waves	Indenbom, Suvorov E., 1979 Aristov, Basov, Suvorov A., Snigirev, 1988	precision x-ray topography
5. x-ray echelon	Aristov, Erko, Snigirev, Nikulin, Suvorov A., 1988	spectral measurements with a resolution $\Delta \lambda / \lambda \sim 10^6-10^8$



experimentally realized with a spatial resolution of  $1\text{ }\mu\text{m}$  and a diffraction efficiency 10-20%.

Therefore, one-dimensional Bragg-Fresnel elements are diffraction prisms, and two-dimensional ones are focusing lenses. In principle, it is possible to calculate the position of Bragg reflecting planes for a desired transformation of the wavefront. As in the case of Bragg optics of Bloch waves, plane shift can be controlled by the reflection coefficient. Bragg-Fresnel elements can be used in a wide wavelength range and exhibit greater mechanical, thermal and radiation stability when compared to Fresnel optics, the aperture and resolution being limited by the fabrication technology.

Bragg-Fresnel elements may be controlled by electrical and optical signals as well as by ultrasound.

The disadvantage of Bragg-Fresnel elements lies in the complexity of their calculation and fabrication. The calculation requires application of the dynamical scattering theory. The fabrication technology involves epitaxial growth of multilayer structure and precision microstructuring. With further development of technology and design methods, Bragg-Fresnel elements are most likely to become the basic elements of x-ray and neutron optics.

### Conclusion

The experiments performed point to the possibility of realizing various x-ray optical diffraction elements, namely, diffraction gratings, echelons, mirrors and monochromators, lenses, prisms, interferometers, modulators. The use of three-dimensional scattering on regularly arranged atoms of scattering material allows for devising a wide range of optical elements. Further improvement of x-ray optical elements calls for development of the epitaxial methods of perfect layer growth, the methods of microstructuring, ion implantation for creating a specific deformation gradient, improvement of other fabrication techniques and working out methods of calculation of three-dimensional x-ray optical elements and their systems.

### References

1. V.V.Aristov, A.A.Snigirev, Yu.A.Basov, and A.Yu.Nikulin, "X-Ray Bragg Optics", in Proceedings of the Conference on Short Wavelength Coherent Radiation: Generation and Applications (Monterey, USA, 1986).
2. V.V.Aristov, Yu.A.Basov, and A.A.Snigirev, *Pisma Zh. Tekh. Fiz.* **13**, 114-118 (1987).
3. V.V.Aristov, Yu.A.Basov, S.V.Redkin, A.A.Snigirev, and V.A.Yunkin, "Bragg zone plates for hard x-ray focusing", *Nucl. Instr. and Meth.* **A261**, 72-74 (1987).
4. V.V.Aristov, Yu.A.Basov, G.N.Kulipanov, V.F.Pindyurin, A.A.Snigirev, and A.S.Sokolov, *Pisma Zh. Tekh. Fiz.* **14**, 3-5 (1988).
5. V.V.Aristov, Yu.A.Basov, G.N.Kulipanov, V.F.Pindyurin, A.A.Snigirev, and A.S.Sokolov, "Image transmission by Bragg-Fresnel x-ray lens", *Opt. Commun.* **66**, 183-185 (1988).
6. V.V.Aristov, Yu.A.Basov, G.N.Kulipanov, V.F.Pindyurin, A.A.Snigirev, and A.S.Sokolov, "Focusing properties of a Bragg-Fresnel lens in the white spectrum of synchrotron radiation", *Nucl. Instr. and Meth.* (1988) to be published.
7. E.V.Shulakov, and V.V.Aristov, *Kristallografiya*. **33**, 13-21 (1988).
8. V.V.Aristov, A.A.Snigirev, A.M.Afanasyev, and V.G.Kohn, "Dynamical diffraction of x-ray spherical wave in two perfect crystals", *Acta Cryst.* **A42**, 426-435 (1986).
9. V.V.Aristov, V.G.Kohn, and A.A.Snigirev, *Kristallografiya*. **31**, 1059-1065 (1986).
10. A.V.Davydov, A.I.Erko, L.A.Panchenko, S.V.Redkin, G.D.Sazonova, and V.A.Yunkin, *Pisma Zh. Tekh. Fiz.* **13**, 1017-1020 (1987).
11. V.V.Aristov, A.I.Erko, and V.V.Martynov, "Principles of Bragg-Fresnel Multilayer Optics", *Rev. Phys. Appl.* **23**, 229-236 (1988).
12. V.V.Aristov, S.V.Gaponov, V.M.Genkin, Yu.A.Gorbatov, A.I.Erko, V.V.Martynov, L.A.Matveeva, N.N.Salashchenko, and A.A.Fraerman, *Pisma Zh. Eksp. Teor. Fiz.* **44**, 207-209 (1986).
13. V.V.Aristov, S.V.Gaponov, N.N.Salashchenko, and A.I.Erko, "Profiled multilayer mirrors for x-ray imaging and spectroscopy", *Optics News*. **12**, 128 (1986).
14. V.V.Aristov, G.V.Vereshchyagin, A.I.Erko, L.A.Matveeva, and D.V.Roshchupkin, "Observation of x-ray diffraction on a multilayer structure modulated by surface acoustic waves", *Pisma Zh. Tekh. Fiz.* **13**, 1288-1291 (1987).
15. V.V.Aristov, A.I.Erko, and V.V.Martynov, "X-ray Fourier optics" in Proceedings of the Conference on Short Wavelength Coherent Radiation: Generation and Applications (Monterey, USA, 1986).

# Reflectance of Aluminum Reflectors in the Extreme Ultraviolet

Marion L. Scott

*Materials Science and Technology Division, Los Alamos National Laboratory  
Los Alamos, New Mexico 87545*

## ABSTRACT

We have investigated a new concept in retro-reflectors for use in the extreme ultraviolet, namely, UHV aluminum coated, multi-facet, grazing-incidence mirrors. Our results indicate that this type of mirror, which utilizes total-external-reflectance, works very well in the wavelength range from 35 nm to 100 nm ( $89 \pm 3\%$  measured retroreflectance at 58.4 nm for a 9-facet mirror). However, the coated mirror surfaces must not be allowed to oxidize after deposition, which implies that the retro-reflector must be coated and used *in situ* or the oxide layer must be removed in a ultra-high vacuum (UHV) system.

## INTRODUCTION

The search for good reflector in the extreme ultraviolet (XUV) spectrum has gone on for many years. Some samples of silicon carbide and diamond have been shown to exceed 40% normal incidence reflectance at wavelengths greater than 60 nm. The silicon carbide results have not proven to be easily reproduced with thin film depositions. Diamond film technology has greatly improved in recent years, however, XUV reflectance measurements on these thin films have not yet come up to bulk values. Near-normal incidence reflectance measurements on multilayer coatings have reached 60% at 17 nm [1] but reproducibility has been a problem and multilayers at longer wavelengths have not been very successful. Also, multilayer reflectors will only reflect over a narrow spectral band.

Our present work on multi-facet reflectors was motivated by the resonator mirror requirements of an XUV free-electron-laser to be constructed at Los Alamos National Laboratory [2]. The resonator mirrors are required to equal or exceed 40% retro-reflectance over the wavelength range from 10 nm to 100 nm. It is possible to construct the XUV FEL in segments so that one resonator does not have to span the entire wavelength range, however, the wavelength tunability of the FEL necessitates that the resonator mirrors be as broad-band as possible. The total-external-reflectance of UHV aluminum at 58.4 nm measured in our previous work ( $98.66\% \pm 2\%$  for a single bounce at 80 degrees) indicated that a 9-facet reflector with this coating would yield a retro-reflectance between 74% and 100% at this wavelength [3].

## MULTI-FACET MIRROR

A 9-facet mirror structure was designed on the Los Alamos computer-assisted-design system and fabricated with the aid of a numerically-controlled mill (see Fig. 1). The nine silicon mirror substrates were fabricated by Laser Optics to a figure accuracy of  $1/20$  wave in the visible and 0.5 nm rms surface roughness. The assembled 9-facet mirror aligned with a visible HeNe laser is shown in Fig. 2. Note that the visible beam accurately strikes the center of each of the nine facets before exiting the array parallel to the input beam. This 9-facet structure is supported in our UHV deposition and analysis system by UHV alignment manipulators attached to each side of the three strut frame.



Figure 1. The 9-facet XUV mirror structure fabricated and measured at Los Alamos.

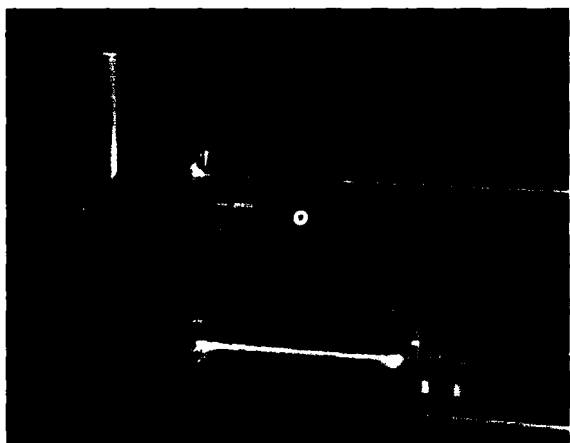


Figure 2. The 9-facet XUV mirror shown with a retroreflected HeNe alignment laser.

#### UHV DEPOSITION SYSTEM

Our UHV deposition system (illustrated in Fig. 3) has been previously described and only a cursory description will be given here. The UHV chamber has a base pressure of  $5 \times 10^{-10}$  Torr and is pumped with hydrocarbon free pumps to avoid carbon contamination of the coated reflector. A water-cooled e-gun source located in the lower part of the deposition chamber is shielded with a cylinder to avoid wide angle coating in the chamber. Some additional shielding inside the 9-facet array requires lateral movement of the array between the position for deposition and the position used in later reflectance measurements. The deposited coating thickness is monitored with a quartz crystal monitor connected to an IC 6000 rate controller.

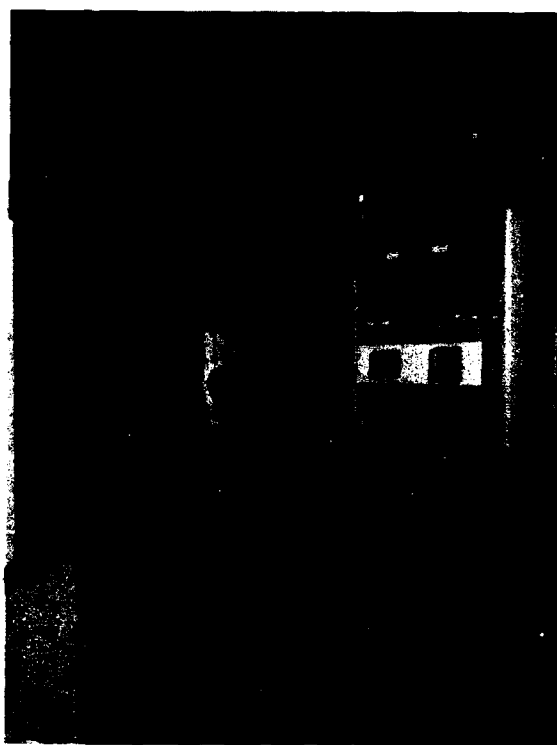


Figure 3. UHV deposition and analysis system utilized in demonstrating the 9-facet XUV reflector.

#### UHV ALUMINUM DEPOSITION

A thin film (70 nm) of high purity aluminum is deposited through appropriate

masking onto three of the nine silicon mirror substrates simultaneously, before rotating the structure to coat the remaining substrates in groups of three. We have achieved good results with a deposition rate of approximately 0.1 nm/sec although we have not performed measurements to determine whether this rate is optimum. After coating deposition on all nine mirror substrates, the mirror assembly is moved into position and aligned to make the XUV reflectance measurement at 58.4 nm.

#### IN SITU XUV REFLECTANCE MEASUREMENT

Many modifications were made to our UHV system to adapt the in situ XUV reflectometer (previously used to measure single-surface reflectance) to measure the reflectance of a 9-facet retroreflector. The XUV beam entrance to the UHV chamber had to be lowered and the sample holder had to be raised. The detector was mounted on a linear feedthrough in the top of the chamber and is capable of rotation about the axis of this magnetically coupled feedthrough. The high voltage and signal leads to the imaging microchannel plate detector are also in the top of the chamber for easy removal. The mirror array can be accurately aligned for reflectance measurement by use of the Huntington x,y,z rotatable feedthroughs on either side of the array.

The measurement of the reflectance of this 9-facet mirror at 58.4 nm was accomplished by first positioning the imaging detector in front of the XUV beam entrance to the UHV chamber and carefully noting the x,y position of the beam on the detector and recording the count rate of the source. Secondly, the detector is raised and rotated to intercept the XUV beam exiting the properly aligned, 9-facet mirror. The detector is positioned to place the beam image at the same spot on the detector as in the previous measurement and the count rate in this detector position is recorded.

A correction must be made to the raw count rates recorded in this manner because the detector responds to counts that are outside of the well defined beam image seen on the oscilloscope. These out-of-beam counts arise from scattering in the system, as well as dark counts from the detector. This correction is determined for each detector position by electronically gating out those counts which are outside the beam image to determine the ratio of beam to scattered counts.

The reflectance of the 9-facet array is then computed from the ratio of the corrected counts recorded from the beam exiting the array to those entering the array.

The result of averaging several such measurements on the 9-facet mirror array was  $89 \pm 3\%$ . This value is within the uncertainty of our previous single surface reflectance measurement on UHV aluminum at 80 degrees incidence angle raised to the ninth power (74% to 100%).

#### CONCLUSIONS

We conclude that an unoxidized, UHV aluminum, 9-facet reflector is an excellent XUV retroreflector at 58.4 nm. We also conclude that an XUV mirror constructed in this fashion will provide an adequate reflectance over a significant portion of the XUV spectrum (35-100 nm) to operate an XUV free-electron laser resonator.

#### ACKNOWLEDGEMENTS

The author would like to acknowledge the support of this work by the DOE Office of Basic Energy Sciences, Advanced Energy Projects Division.

#### REFERENCES

1. T. W. Barbee, Jr., S. Mrowka, and M. Hettrick, "Molybdenum Silicon Multilayer Mirrors for the Extreme Ultraviolet," *Appl. Opt.*, **24**, 883-886 (1985).
2. B. E. Newnam, "Multifacet, Metal Mirror Design for Extreme Ultraviolet and Soft X-Ray Free-Electron Laser Resonators," *Proceedings of Laser Induced Damage in Optical Materials: 1985*, *NBS Spec. Pub.* **746**, 261-269 (1988).
3. M. L. Scott, P. N. Arendt, B. J. Cameron, J. M. Saber, and B. E. Newnam, "Extreme Ultraviolet Reflectance Degradation of Aluminum and Silicon From Surface Oxidation," *Appl. Opt.*, **27**, 1503-1507 (1988).

## SOFT X-RAY LENSES WITH 400 Å OUTER ZONE WIDTH

Y. Vladimirovsky\*, D. Kern†, T.H.P. Chang†, W. Meyer-Ilse‡, P. Guttmann‡,  
B. Greinke‡, and D. Attwood\*

\*Center for X-ray Optics, Lawrence Berkeley Laboratory  
University of California, Berkeley, CA 94720, 415-486-4463

†IBM, T.J. Watson Research Center  
Yorktown Heights, NY 10598

‡Universität Göttingen, Forschungsgruppe Röntgenmikroskopie  
Geist Strasse 11, D-3400 Göttingen, FRG

### Summary

Fresnel zone plate lenses for focussing and imaging radiation in the 10-50 Å wavelength region have been fabricated with outer zone widths as small as 400 Å. The zone plates were fabricated by electron beam lithography using a high resolution vector scan system designed specifically for nanometer pattern writing. A special circular pattern generation technique, utilizing high speed polar/cartesian conversion was utilized. Field size was calibrated for squareness and orthogonality using electron beam lithography calibration marks and laser interferometry. Patterns were written in a 180-200 nm thick PMMA resist on a 30 nm gold electroplating base. The substrate was a 100 nm silicon nitride film. The pattern received a dose of 250  $\mu\text{C}/\text{cm}^2$  at 25 KeV. Special patterns requiring a thick central stop region, received a doubled dose, followed by a double development/double plating technique.

A method utilizing the phenomenon of form birefringence was used for monitoring the development of the fine features. In the optical microscope with polarized light and crossed analyzer, a distinct change of the reflected intensity is observed during the final stages of development.

Text patterns imaged at 45 Å wavelength demonstrate a spatial resolution approaching 500 Å. Measurements of zone plate efficiency are also described.

## Soft X-Ray Spectroscopy of Laser-Produced Plasma

Shi-sheng Chen, Zhi-zhan Xu\*, and Zheng-quan Zhang

Shanghai Institute of Optics and Fine Mechanics

Academia Sinica, P.O.Box 8211, Shanghai, China

Laser-produced plasmas emit intense X radiation primarily at sub-KeV Photon energies. Spectra in the sub-KeV region were measured with a pinhole transmission grating and grazing incidence spectrographs respectively. The transmission grating spectrometer with two pinholes of 25  $\mu\text{m}$  and 50  $\mu\text{m}$  in diameter is consisted of free-standing gold bars (1000 Lines/mm, bar thickness 0.45  $\mu\text{m}$ ). The wavelength resolution achieved in the spectrometer was 10 $\text{\AA}$ . The grazing incidence spectrograph is composed of a toroidal mirror and a concave grating. It is designed to cover the spectral range of 10 $\sim$ 450 $\text{\AA}$  in the first diffraction order. The angles of incidence on both mirror and grating are 87 $\cdot$  37.5 $^\circ$  in order to maintain good efficiency down to 20 $\text{\AA}$ . The spectrograph of 998.8 mm radius and 2400 grooves/mm, the grazing angle being 2 $^\circ$ .

The plasmas were produced by an aspherical lens with  $f=60\text{mm}$  focusing a high power Nd $^{3+}$  glass laser beam with pulseduration of  $\sim 200\text{ps}$  and energy of  $\sim 10\text{J}$  on flat targets with different atomic number Z.

The main results include identification and classification of spectra of XUV emission soft X-ray population inversion, and interpreting pinhole transmission grating spectra of low, intermediate, and high Z targets.

\* Also with China Center of Advanced Science and Technology (World Lab.), Beijing.

# Large Holographic Diffraction Gratings Made by a Multiple Exposure Technique

L. Wosinski and M. Breidne

*Institute of Optical Research, S-100 44 Stockholm, Sweden*

## Abstract

The maximum size of a holographic grating that can be manufactured in a specific set-up is, in principle, limited by the size of the collimating optics (mirrors) in this set-up. A technique, which permits to circumvent the limitation set by the mirrors and fabricate large holographic gratings, is described. The accuracy of phase agreement, when two gratings are bound together, is better than  $\lambda/20$ .

## Introduction

EUV and soft X-ray sources often requires grazing incidence optics in order to obtain high through-put. Therefore gratings (and mirrors) in monochromators and spectrometers have to have large dimensions. When fabricating holographic gratings, the area of exposing interference pattern is limited by the size of optics used in the recording system.

In this paper we describe a technique for fabrication of holographic, "combined" gratings by using a computer controlled system to keep the interference pattern stationary under multiple exposure process. The idea is very simple. On a large substrate gratings are exposed sequentially and in phase with help of a reference grating. To be able to do this, it is necessary to control the phase of the exposing interference pattern. The reference grating monitors both, frequency and phase errors. The active servosystem automatically counteracts any movements of the interference fringes and also permits multiple exposures with arbitrary adjusted phase [1]. In principle this technique can be used to make very large gratings.

## Phase control

In the described method, the fringe pattern, which serves to record the grating, is also projected on a reference grating of the same or almost the same spatial frequency and angular orientation. A moiré

pattern between the reference grating structure and the structure of the illuminating pattern is observed. When the frequency and orientation are completely matched, the interference pattern consists of an uniformly illuminated zero fringe. The relative intensity of the fringe indicates the phase difference between the grating structure and the illuminating pattern.

By providing the holographic set-up for making gratings with a reference grating, it is thus possible not only to observe and monitor the fringe movement, but also to adjust the exposing pattern relative to the grating with a very high degree of accuracy, which is necessary for multiple exposure technique.

Fig.1 shows the moiré pattern from the reference grating obtained, when the exposing pattern is of slightly different frequency and orientation. Such reference grating should be located on the same substrate as the grating to be made. This ensures that the position between the reference and the exposing pattern is constant over the surface, during the entire manufacturing process.

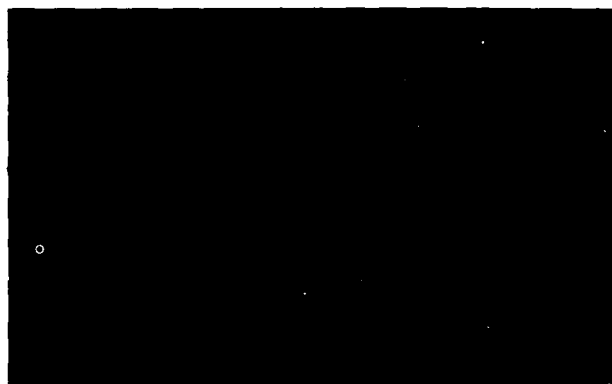


Figure 1. Photograph of the interferogram obtained at the reference grating, demonstrating imperfect adjustment of both, fringe density and angular orientation of the exposing pattern.

## Experimental details

The apparatus used in our laboratory for making multiple exposure gratings is presented in fig.2.

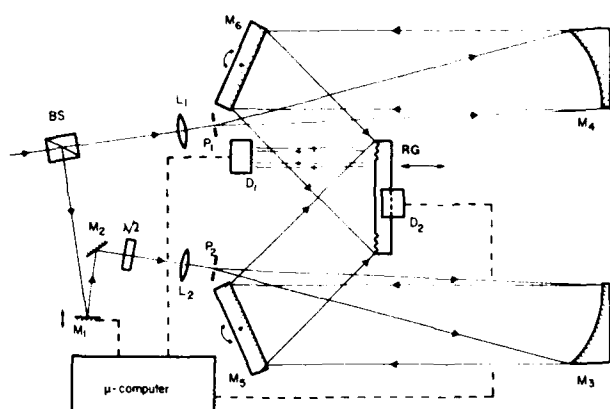


Figure 2. Arrangement for recording multiple exposure gratings. BS, beam-splitter; RG, reference grating; M, mirrors; L, lenses; P, pin-holes; D, detectors.

An Ar-laser beam is divided by the beam-splitter (BS), filtered and collimated by two off-axis parabolic mirrors  $M_1$  and  $M_2$  to obtain two plane wavefronts. The two beams reflect then from plane mirrors  $M_3$ ,  $M_4$  and form the interference pattern on the substrate surface with the reference grating situated on it. The light diffracted from the reference grating falls onto a photodetector  $D_1$  which continuously monitors the phase between the exposing pattern and the reference grating. The signal from the detector is fed to the computer. If the exposing pattern moves, the detector will see a change in irradiance. The computer checks the degree of movement and reacts by displacing mirror  $M_1$  an appropriate amount. The signal from detector  $D_1$  is normalized through division with a signal proportional to a total irradiance on the substrate. This signal is provided by a second detector  $D_2$ . In this way a change in laser power will not influence the location of the exposing pattern.

In the fabrication of multiple exposure gratings with phase alignment, two additional factors are important for a successful result, namely the frequency and angular orientation of all segment gratings must be precisely the same. To achieve this precision, when combining two or more segments, four additional detectors "observe" light diffracted from the reference grating and detect positions of moiré fringes. The plane mirrors  $M_3$  and  $M_4$  are mounted in such a way, that one of them can be precisely adjust through an axis parallel to the direction of fringes and the other one through an axis perpendicular to the fringes. After every change of the substrate position, the two plane mirrors are adjusted for "zero fringe" pattern from the reference grating and this moiré picture is hold during exposure by computer control system. Any changes in this picture, caused by instabilities in the system, are detected and the signals from the four detectors are

decoded and processed. Servo signals from the computer displace mirrors  $M_3$  and  $M_4$  in a manner which counteracts changes of frequency and orientation in the exposing pattern.

The system is designed to keep the patterns located with a deviation of less than one tenth of the grating period.

## Results and conclusion

Before starting the exposure, some data must be fed into the computer to provide correct control of the process. At a given wavelength, the efficiency of grating depends on grating geometry: grooves depth, profile and spacing [2]. After the calculation, required parameters are stored in the computer memory.

The phase control system allows to produce sequentially exposed gratings with high accuracy. Figure 3 shows an interferogram of such a grating composed of three subsequent elements.

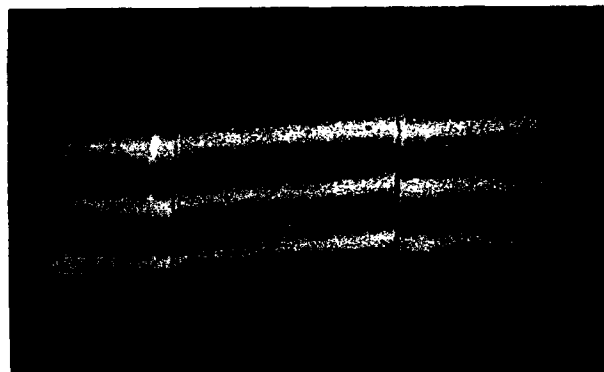


Figure 3. Interferogram of two boundaries between three subsequent gratings.

The accuracy of phase alignment is better than  $\lambda/20$ . In principle, this technique allows to make very large gratings consisting of many segments.

## References

1. M. Breidne, S. Johansson, L. E. Nilsson, and H. Åhlen, "Blazed holographic gratings," *Optica Acta* **26**, 1427-1441 (1979).
2. M. Breidne, A. Roger, "Optimization of the efficiency of plane gratings used in the soft X-ray region," *Opt. Commun.* **48**, 5, 301-305 (1984).



# Effectiveness of Metal-Coated Diffraction Gratings at Grazing and Near Normal Incidence as Harmonic Scrubbers

P. J. Wantuck and Q. D. Appert

*Los Alamos National Laboratory, Chemical and Laser Sciences Division  
Los Alamos, New Mexico 87545*

K. Tong and D. J. Pistoresi

*Boeing Aerospace Company, P.O. Box 3999, Seattle, Washington 98124*

## Abstract

High power free electron lasers (FEL) can produce significant amounts of harmonic radiation. These harmonic components represent a substantial damage threat to the optical elements comprising the laser resonator. In this paper we discuss the merits of using blind gratings in both the paraboloid and grazing incidence hyperboloid mirrors of a 1.06-micron FEL under construction by the Boeing Aerospace Company. Grating designs developed for use at grazing incidence are not very efficient for dispersing the harmonics. However, blind gratings positioned in the paraboloid exhibit better filtering capability.

## Introduction

A high power FEL will produce radiation at wavelengths that are harmonics of the fundamental. For a laser operating at 1.06 microns the harmonic wavelengths are defined as  $1.06/n$  microns where  $n = 1, 2, 3, \dots, m$ . For such an FEL, harmonic production will occur at both UV and VUV wavelengths. Experiments performed by Billardon et al.[1] have shown that UV harmonics can induce damage in FEL optical coatings. Higher order harmonics pose a threat to coatings through ionization processes. Multilayer dielectrics are particularly susceptible to such damage.

For long-term laser operation, the harmonic content of the FEL optical beam needs to be removed or at least substantially minimized. One possible filtering scheme would be to place a "blind" grating in the reflecting surface of an optical element of the

FEL resonator. Such a grating would be invisible to the fundamental wavelength but would diffract the harmonics out of the resonator plane. For an effective application, the gratings should exhibit high diffraction efficiency for the harmonic wavelengths.

The use of metal-coated diffraction gratings as harmonic filters is investigated for a 1.06-micron FEL tentatively planned for operation at Boeing in the early 1990 timeframe. This FEL features a grazing incidence ring resonator with two identical telescopes. Each telescope contains a grazing incidence hyperboloid mirror and a near normal incidence paraboloid mirror. The current resonator design sets the grazing angle to the hyperboloid at 87 degrees while the angle of incidence to the paraboloid is 6 degrees. A diffraction grating rhomb will be incorporated in the resonator for the purpose of sideband suppression and optical beam outcoupling.[2] A diagram of the proposed FEL resonator is shown in Fig. 1.

Because of its high reflectivity at 1.06 microns and anticipated resistance to laser-induced damage (high ionization potential), the various FEL optical elements will be coated with silver. Gold (which exhibits high reflectivity at 1.06 micron) represents another potential metal coating that could be employed with these resonator optics. However, the reflectance of gold degrades faster than silver in the UV and it is not as suitable a coating for gratings designed for harmonic dispersal. Thus, any gratings placed in the telescope mirrors would be silver coated. For the purpose of comparison, however, we have established grating designs using both metal coatings.

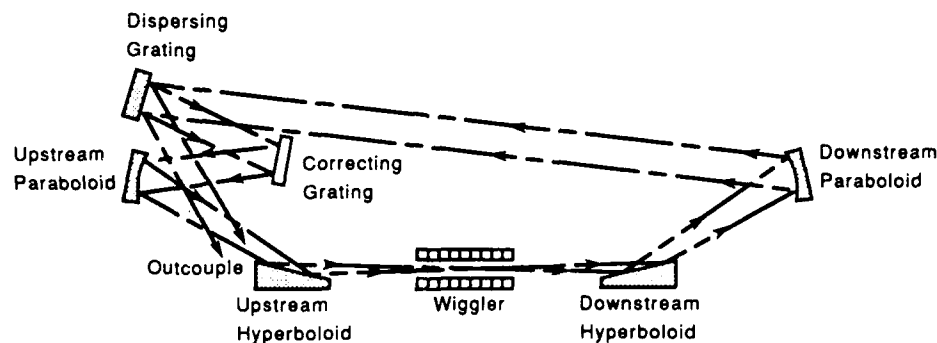


Figure 1. FEL ring resonator.

### Rhomb Grating Design for FEL Sideband Suppression

As mentioned above, a diffraction grating rhomb is to be used in the Boeing FEL for sideband suppression and outcoupling. Sidebands represent optical radiation at wavelengths other than the fundamental and are generated by unstable electron trajectories in the wiggler section of the laser.[3] These sidebands are detrimental to laser operation as they lower the extraction efficiency of the device. Because the travel time of light through a rhomb is a function of wavelength, the rhomb suppresses the sidebands by altering the temporal and spatial overlap of the sidebands and the electron beam pulse in the wiggler. As a result, the sidebands are not amplified. The rhomb grating designs for the Burst Mode FEL, a device operating at 0.6328 microns, were developed with the use of the OMEGA diffraction grating code. The OMEGA code provides a full vector simulation of bare metal gratings for any profile (blazed, sinusoidal, and lamellar) in the UV, visible, and infrared region by solving Maystre's integral method.[4] The code has been benchmarked in this optical regime and our results for the Burst Mode grating program provide yet another illustration of the code's predictive capabilities. Figure 2 shows OMEGA-predicted absolute diffraction efficiencies as a function of angle of incidence for a TE polarization (incident radiation electric field vector parallel to the grating grooves), silver-coated, sinusoidal grating. Figure 3 illustrates diffraction efficiency variation with angle of

incidence for a TE, silver-coated lamellar grating. We observe that with both profiles the agreement between predicted and measured efficiencies is quite good.

### Design Procedure for Diffraction Grating Harmonic Scrubbers

The surfaces of both the downstream (with respect to the clockwise propagating electron beam in the wiggler; see Fig. 1) paraboloid and the hyperboloid mirrors are candidates for a blind grating. The planned substrate material for these mirrors is single crystal silicon. Subsequent to polishing, a grating can be placed in the surface of these elements using current holographic grating fabrication technology. Grating fabrication techniques use interference-generated fringes to establish the required grating period in a photoresist covered material. After a (generally) one-step exposure, the photoresist is developed leaving a grating pattern in photoresist. This grating pattern is transferred into the substrate using an ion beam or reactive ion etch and then coated.

FEL physics codes predict that the third harmonic will exhibit the greatest intensity.[5] This corresponds to a 0.353-micron wavelength for a 1.06-micron device. The third harmonic is predicted to exhibit approximately a factor of 10 greater intensity than the second and a factor of 100 greater intensity than the fourth harmonic. Because of this predicted

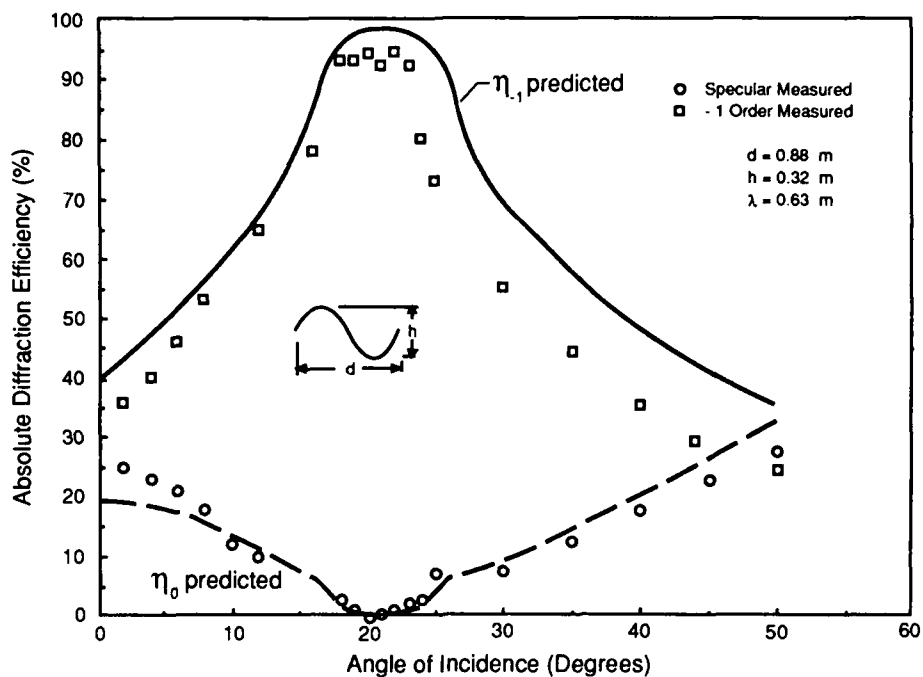


Figure 2. Predicted and measured diffraction efficiency vs. angle of incidence for a TE, silver-coated sinusoidal Burst Mode FEL grating.

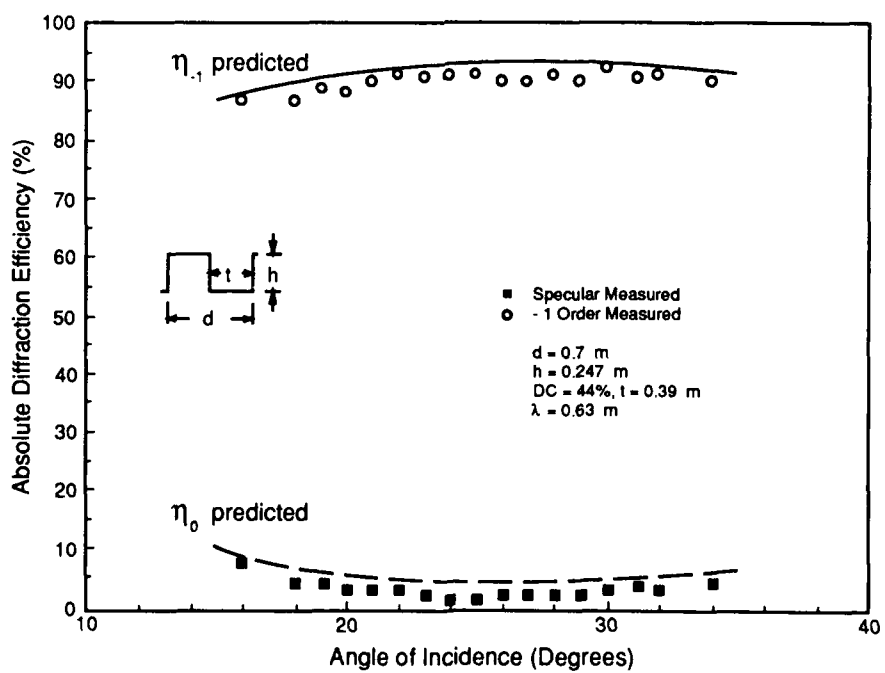


Figure 3. Predicted and measured diffraction efficiency vs. angle of incidence for a TE, silver-coated lamellar Burst Mode FEL grating.

harmonic intensity pattern, we attempted to optimize the blind gratings for maximum diffraction efficiency with the third harmonic.

The notion of a blind grating is easily understood by considering the grating equation, i.e.,  $\sin\theta_m = \sin\theta_i + m \lambda/d$ , where  $m$  represents the order number,  $\theta_m$  the diffraction angle for order  $m$ ,  $\theta_i$  the angle of incidence,  $\lambda$  the wavelength of the incident radiation, and  $d$  the grating period. For fixed wavelength and angle of incidence, the selection of groove spacing or period will determine what orders the grating will support. With only a specular order present, the grating acts like a reflective element to the incident radiation. The angle of incidence (AOI) for a grating placed into the surface of the hyperboloid mirror is 87 degrees, while for the paraboloid mirror the AOI is 6 degrees. One can readily establish that for 1.06-micron radiation incident at 6 degrees, the maximum groove period that can be utilized for a blind grating such that it will support no order other than the specular is 0.959 microns. With an angle of incidence of 87 degrees the groove spacing must remain smaller than 0.53 microns.

For a fixed groove period and grating material, diffraction order efficiencies are varied by adjusting parameters characteristic to the profile under consideration. For a sinusoidal profile grating, the groove depth is the important parameter, for a lamellar profile grating both the duty cycle and depth control the diffraction efficiency, while for a blazed grating the blaze and apex angles influence diffraction efficiency.

The efficiency characteristics of a grating also depend strongly upon the state of polarization of the incident radiation. High diffraction efficiency is generally obtained over a narrow range of  $\lambda/d$  ( $\lambda$  = wavelength,  $d$  = groove spacing) for TE gratings (electric field vector parallel to the grooves) whereas gratings operating in a TM mode (electric field vector perpendicular to the grooves) exhibit high diffraction efficiency over a wider range of  $\lambda/d$ . The rhomb gratings are designed to operate in a TE mode because the optical beam is polarized in the horizontal plane and the ring resonator configuration is positioned in a vertical plane. TM rhomb gratings installed in the resonator would exhibit diffraction out of the plane of the resonator and would require additional mounts, steering mirrors, and vacuum enclosures. Because the hyperboloid and paraboloid are set in orientations that support diffraction from TE gratings, only TE harmonic-filtering grating designs were evaluated in this study.

## Discussion and Results

We attempted to optimize the diffraction efficiency of bare metal, sinusoidal, and lamellar gratings for operation with the third harmonic at 0.353 microns. The Burst Mode grating rhomb program has demonstrated that gratings with such profiles can be fabricated to the size and tolerances required for the hyperboloid and paraboloid mirror harmonic gratings. Subsequent to this optimization, we then examined the diffraction efficiency of the gratings for the other harmonics (up to  $n=6$ ).

### 1. Grating at Grazing Incidence

Predicted absolute efficiency values for optimized grazing incidence, lamellar and sinusoidal gratings (silver- and gold-coated) are presented in Table 1. Gratings operating at grazing incidence are not very efficient at diffracting the harmonics. The silver-coated sinusoidal grating produced the highest total (absolute) diffraction efficiency for the third harmonic, namely, 10.9%. This efficiency represents the sum of the energy channeled into the -1 and -2 orders, both of which are supported with this design. As expected, gold-coated gratings exhibit even lower diffraction efficiency, due to the metal's decreased reflectivity (compared to silver) at 353 nm. For both the lamellar and sinusoidal gratings, the majority of the incident harmonic radiation is reflected into the specular or 0<sup>th</sup> order and channeled back into the resonator. Such low diffraction efficiency is presumably due to the extreme shading of the grooves by a beam impinging the grating with such a high angle of incidence.

### 2. Grating at Near Normal Incidence

Absolute diffraction efficiencies for a grating placed in the surface of the paraboloid are higher than those obtained for the hyperboloid. As noted previously, a grating blind to 1.06-micron radiation could have a groove period as large as 0.96 microns. Generally, gratings with large groove periods (0.9 microns), are easier to fabricate than those with smaller periods (0.5 microns). Therefore, we concentrated our optimization efforts for large period gratings. Predicted absolute efficiency values for a 50% duty cycle (well width/groove period: 0.45 microns/0.9 microns), lamellar profile grating as a function of groove depth are shown in Fig. 4. The best (and total) diffraction efficiency for the third harmonic is obtained for a groove depth,  $h$ , of 0.1 microns. For this particular groove depth, a total of 75.4% of the incident energy is predicted to

Table 1

Efficiency Results for Optimized Grazing Incidence Grating  
 $\lambda = 0.353 \mu\text{m}$ ,  $\theta_i = 87^\circ$ , TE Polarization,  $h$  = groove depth,  
 $t$  = well width,  $d$  = groove period,  $\eta$  = absolute efficiency

Lamellar

Coating	$h(\mu\text{m})$	$t(\mu\text{m})$	$d(\mu\text{m})$	$\eta_0(\%)$	$\eta_{-1} + \eta_{-2}(\%)$	$\eta_{\text{tot}}(\%)$
Ag	0.2	0.35	0.5	85.1	10.4	95.5
Au	0.2	0.35	0.5	80.0	5.8	85.8

Sinusoidal

Coating	$h(\mu\text{m})$	$d(\mu\text{m})$	$\eta_0(\%)$	$\eta_{-1} + \eta_{-2}(\%)$	$\eta_{\text{tot}}(\%)$
Ag	0.4	0.4	85.1	10.9	95.9
Au	0.45	0.5	81.1	5.6	86.7

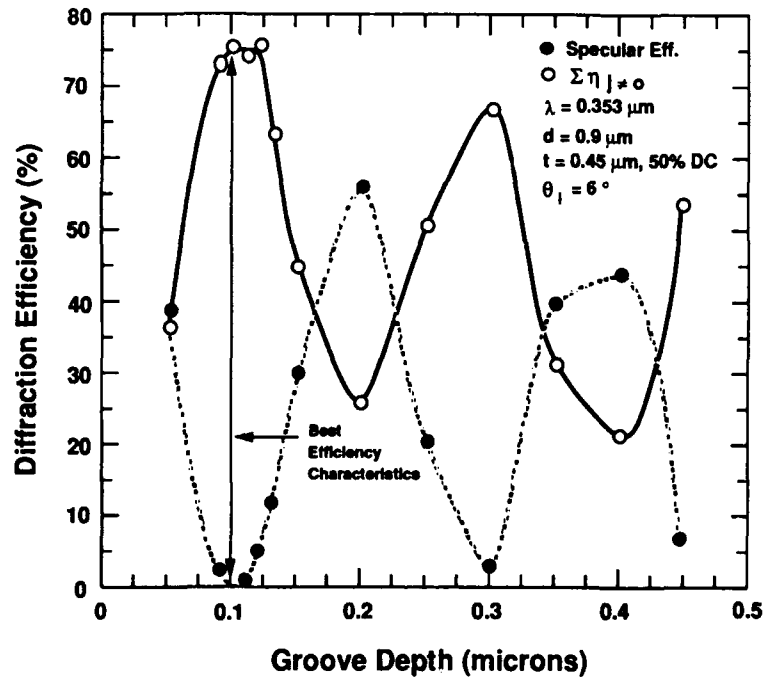


Figure 4. Predicted diffraction efficiency vs. groove depth for a 1111-line, nm, TE, silver-coated lamellar grating.

channel into the -1 and -2 orders with less than a 0.1% reflecting back into the resonator through the specular order. We define the total diffraction efficiency as the sum of the energy, in percent, that is distributed in the non-specular orders. The sum of the efficiency for all the supported orders is 75.5%, which agrees well with the 76.4% reflectance (calculated using optical constants provided in Palik[6]) predicted for silver at 353 nm at an angle of incidence of 6 degrees. Therefore, approximately one quarter of the incident radiation is absorbed by the silver coating. The duty cycle of this 1111-line/mm lamellar grating was varied between the extremes of 33 and 66% and the groove depth adjusted to maximize the total diffraction efficiency. For a well width,  $t$ , of 0.3 microns and a groove depth,  $h$ , of 0.1 microns, a maximum (best) total diffraction efficiency of 64% is obtained, while for a grating with a 0.6-micron step size (again  $h = 0.1$  microns) the maximum total diffraction efficiency increased to 71%. This efficiency variation is displayed in Fig. 5.

Similar performance is exhibited by the silver-coated sinusoidal grating with a groove period of 0.9 microns. A plot of predicted diffraction efficiency versus groove depth is shown in Fig. 6. A 1111-line/mm sinusoidal grating with a groove

depth of 0.14 microns diffracts 76.2% of the incident 0.353-micron radiation into the -1, -2, 1, and 2 orders while reflecting less than a 0.1% into the specular order. A 1250-line/mm grating ( $d = 0.8$  micron,  $h = 0.14$  microns) gave almost identical performance results to the 1111-line/mm grating. The predicted maximum total diffraction efficiency for the 1250-line/mm grating is equal to 75.9% while the specular order contained less than 0.1% of the incident third harmonic energy. Predicted efficiency curves for this sinusoidal grating are shown in Fig. 7.

The effect of reducing the groove period on the total diffraction efficiency is shown in Fig. 8 where we plot diffraction efficiency vs. groove depth for a 2000-line/mm sinusoidal grating. Note that the total diffraction efficiency for the third harmonic is less than that obtained for the 1111- and 1250-line/mm gratings.

Predicted efficiencies for gratings employing a gold coating are (approximately) a factor of two less than those calculated for their silver-coated counterparts. This behavior is not surprising. Gold exhibits high absorptivity with 353-nm radiation at an AOI of 6 degrees (36.3% reflectance, 63.7% absorption).

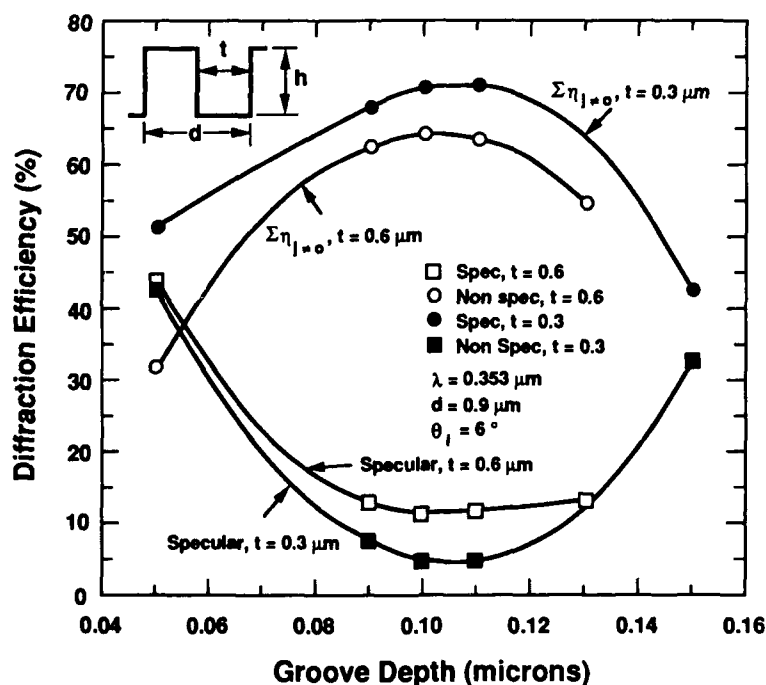


Figure 5. Predicted diffraction efficiency vs. groove depth for a 1111-line/mm, TE, lamellar grating for two duty cycles.

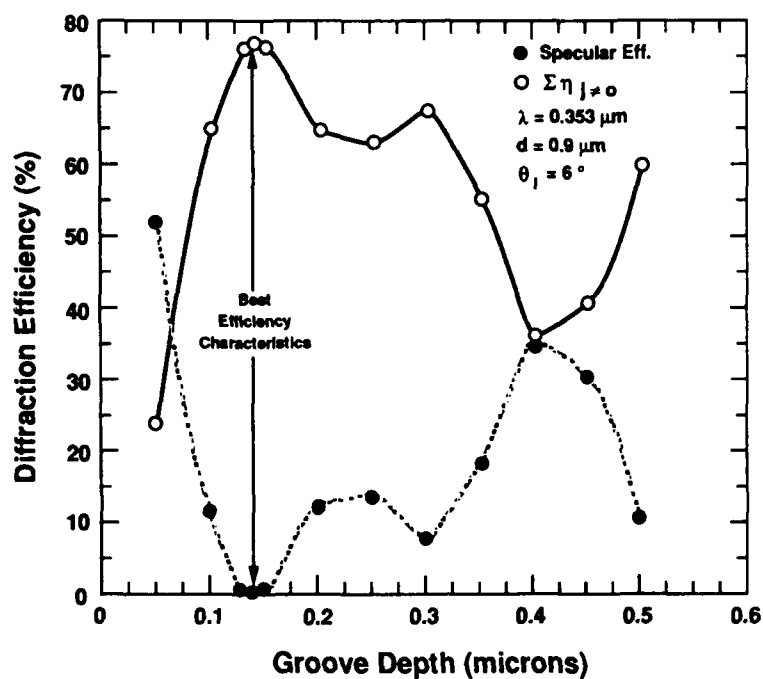


Figure 6. Predicted diffraction efficiency vs. groove depth for a 1111-line/mm, TE, silver-coated sinusoidal grating.

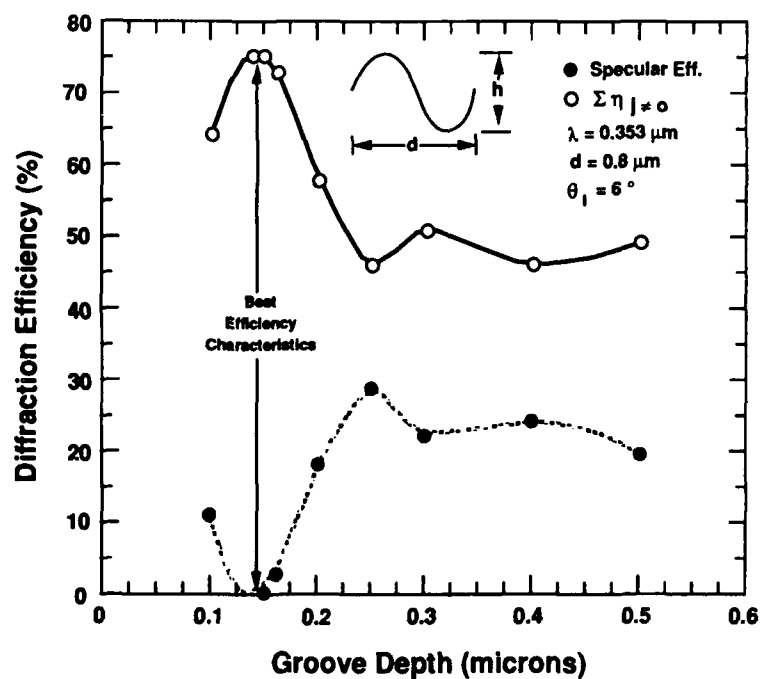


Figure 7. Predicted diffraction efficiency vs. groove depth for a 1250-line/mm, TE, silver-coated sinusoidal grating.

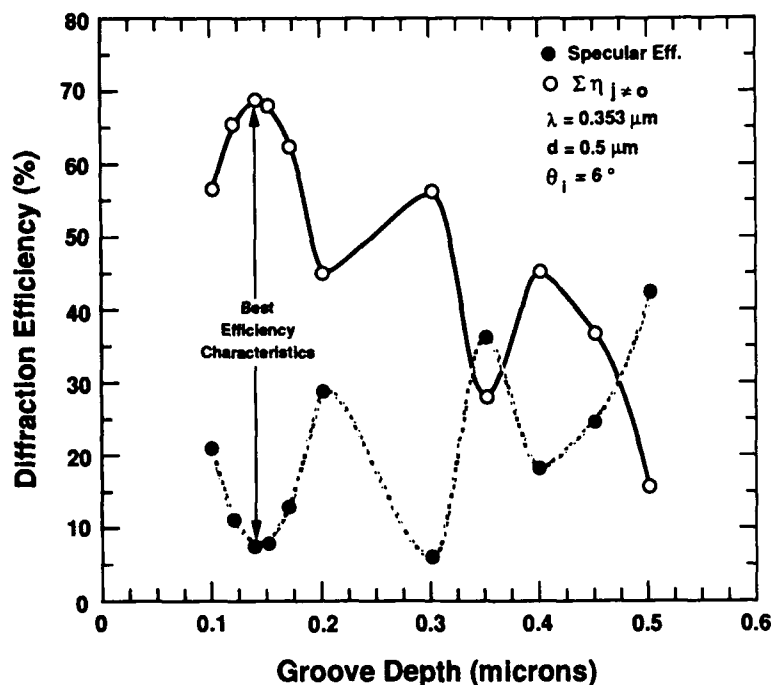


Figure 8. Predicted diffraction efficiency vs. groove depth for a 2000-line/mm, TE, silver-coated sinusoidal grating.

### 3. Harmonic Diffraction Efficiencies for Optimized 353-nm Gratings

Absolute predicted diffraction efficiencies for harmonics 1, 2, 4, 5, and 6 (1.06, 0.532, 0.266, 0.213, and 0.177 microns) for both the 1111-line/mm lamellar and sinusoidal gratings with silver coatings are displayed in Table 2. Note that both gratings are indeed "blind" to the 1.06-micron radiation with the incident light channeled into the specular order. Overall, the sinusoidal grating exhibits slightly better harmonic filtering characteristics. However, as wavelength decreases so does the total diffraction efficiency of the grating. As expected, this behavior is due to the decrease in reflectivity of the metal (and increase in absorption) as the wavelength decreases. The mean silver reflectance, defined as the average of both s and p polarization reflectance, for the various harmonics at an AOI of 6 degrees, is contained in Table 3. One can see that for the wavelengths examined, the sum of all the order efficiencies is approximately equal to the theoretical average reflectance of the metal. For any metal-coated grating the choice of coating limits the maximum obtainable diffraction efficiency, i.e., the total diffraction efficiency will not exceed the reflectance of the metal.

Although blind silver gratings are good filters of the high intensity third harmonic as well as the second (at near normal incidence), they are not very efficient at dispersing the shorter wavelength harmonics. We are currently examining coatings that could be applied over the grating surface to increase the harmonic filtering capabilities of the grating, yet not affect the fundamental. Gratings constructed of or coated with diamond may be effective in such an application.

### Summary

We have investigated the filtering capabilities of a bare metal, blind grating to FEL harmonics at both grazing and near normal incidence. Good filtering of the third and second harmonic of 1.06 microns can be obtained with silver-coated lamellar and sinusoidal gratings. However, metal reflectivity limits the effectiveness of the blind diffraction gratings at dispersing the lower wavelength harmonics.



Table 2

Efficiency Characteristics for Additional Harmonics with Optimized 0.353- $\mu\text{m}$   
Lamellar and Sinusoidal Grating for  $\theta_i = 6^\circ$

Lamellar: $h = 0.1 \mu\text{m}$ , $t(\text{well width}) = 0.45 \mu\text{m}$ , $d = 0.9 \mu\text{m}$ , $\eta_j$ = absolute efficiency (%) in order $j$											
$\lambda(\mu\text{m})$	$\eta_{-5}$	$\eta_{-4}$	$\eta_{-3}$	$\eta_{-2}$	$\eta_{-1}$	$\eta_0$	$\eta_{+1}$	$\eta_{+2}$	$\eta_{+3}$	$\eta_{+4}$	$\eta_{\text{tot}}$
1.06	-	-	-	-	-	97.9	-	-	-	-	97.9
0.53	-	-	-	-	36.3	32.1	26.9	-	-	-	95.3
0.265	-	-	2.6	1.5	6.3	6.5	6.5	1.9	0.7	-	26.0
0.212	-	1.6	0.7	0.9	0.5	17.9	1.0	1.3	2.1	-	26.0
0.177	0.9	0.8	-0	0.3	1.3	14.7	0.7	0.4	0.3	1.2	19.8
Sinusoidal: $h = 0.14 \mu\text{m}$ , $d = 0.9 \mu\text{m}$ , $\eta_j$ as above											
$\lambda(\mu\text{m})$	$\eta_{-5}$	$\eta_{-4}$	$\eta_{-3}$	$\eta_{-2}$	$\eta_{-1}$	$\eta_0$	$\eta_{+1}$	$\eta_{+2}$	$\eta_{+3}$	$\eta_{+4}$	$\eta_{\text{tot}}$
1.06	-	-	-	-	-	98.1	-	-	-	-	98.1
0.53	-	-	-	-	39.5	24.7	31.3	-	-	-	95.5
0.265	-	-	3.1	7.8	1.7	2.9	2.2	7.9	0.7	-	26.3
0.212	-	1.5	4.4	4.2	0.27	4.2	0.1	5.9	5.4	-	25.9
0.177	0.4	3.3	4.6	0.2	2.1	0.8	2.0	0.8	4.5	2.3	21.0

Table 3

Calculated Average Reflectance and  
Absorptance of Silver for the Harmonic  
Wavelengths at an Angle of Incidence of  $6^\circ$

$\lambda(\mu\text{m})$	Reflectance, R(%)	Absorption, A(%)
1.06	98.3	1.7
0.53	95.5	4.5
0.35	76.4	23.6
0.26	26.3	73.7
0.21	26.4	73.6
0.18	21.1	78.9

### Acknowledgment

This study was performed under the auspices of the  
Department of Energy and was supported by the  
United States Army Strategic Defense Command.

### References

1. M. Billardon, P. Elleuume, J. M. Ortega, C. Bazin, M. Bergher, M. Velghe, D. A. G. Deacon, and Y. Petroff, "Free Electron Laser Experiment at Orsay: A review," *IEEE Quant. Elec.* Vol. QE-21, pp. 805-823.
2. P. J. Wantuck, Q. D. Appert, E. J. Gratrix, and A. A. Hopkins, "A High Efficiency Diffraction Grating Design for a Rhomb Configuration," in print, *Proceedings of SPIE's 32nd International Technical Symposium*, August 14-19, 1988, San Diego, California.

3. D. C. Quimby, "Advances in Laser Sciences II," M. Lapp, W. C. Stwalley, and G. A. Kenney Wallace, eds., AIP Conference Proceedings No. 160, 142-6 (1987).
4. D. Maystre, "Integral Methods," in Electromagnetic Theory of Gratings. Topics in Current Physics, Petit, Ed., Vol. 9, Springer Verlag, New York, 1980, p. 63.
5. M. Soukup, Los Alamos National Laboratory, private communication.
6. D. W. Lynch and W. R. Hunter, "Comments on the Optical Constants of Metals and an Introduction to the Data for Several Metals," in Handbook of Optical Constants of Solids, E. Palik, Ed., Academic Press, New York, 1985, p. 275.

## Saddle Toroid Arrays: Novel Grazing Incidence Optics for Synchrotron X-Ray Lithography

R. J. Rosser and P. M. J. H. Wormell

*Room 305, Blackett Laboratory, Imperial College  
London SW7 2BZ, England*

### Abstract

Replacing the scanning mirror in a synchrotron lithography beamline with a fixed saddle-toroid array mirror will give uniform illumination over wafer-size fields, without the problem of moving parts in the high vacuum section of the beamline, the constraints of oscillating the electron beam in the storage ring or the engineering difficulties of moving the entire wafer alignment system.

Ray tracing results for one and two saddle-toroid systems are presented, showing that a single saddle-toroid mirror provides a satisfactory alternative to the scanning cylindrical mirrors used in existing lithography beamlines, if the input beam is uniform. A two element system, comprising a saddle-toroid and a cylindrical mirror, can be used to give a nearly rectangular patch of illumination, closely matched to the needs of lithography. However the total usable flux through the such a device is lower, because of the extra reflection.

Both designs require a uniform input beam and are not suitable for the gaussian profiled synchrotron beam. By using the techniques developed to produce micro-lens arrays, saddle-toroid arrays can be made which spatially average the beam. These provide outputs that are uniform, even from a synchrotron beam.

Though designed with storage ring x-ray lithography in mind, saddle-toroid arrays may have applications in expanding undulator and free-electron laser output.

Patents are pending.

### Introduction

X-ray lithography using synchrotron sources is rapidly approaching commercial reality. IBM has ordered its own compact, superconducting synchrotron from Oxford Instruments, England for delivery to their Fishkill, NY production facility in 1989, and several Japanese companies are reported to be building synchrotrons for production purposes [1]. Recently IBM announced the world's first semiconductor device produced entirely by x-ray lithography, manufactured at the U6 research beamline at the National Synchrotron Light Source [2]. All this activity indicates that within the next five years, x-ray lithography will become a production tool for producing integrated circuits.

Although synchrotron radiation has the necessary brightness for cost effective lithography, it has one major shortcoming - very low divergence in the vertical direction. The divergence is machine and wavelength dependant, but is typically 1mR at 1.0nm. The radiation at the end of a beam pipe is therefore an horizontal line, as wide as the apertures allows, but only about 10mm high at 10m distance. Lithography requires the illumination of rectangular masks measuring about 40mm by 50mm.

Three methods have been used to match the synchrotron output to the needs of lithography.

The simplest is to scan the wafer past the beam. In production, this would mean scanning the entire wafer alignment

system, weighing of the order of a ton., past the beam. Whilst not impossible, it is clearly not the ideal solution.

A second method is to oscillate the electron beam in the storage ring. On compact rings, with tight machine lattices, this can mean that only a small number of beamlines have satisfactory illumination.

The third is to have a scanning cylindrical mirror in the beamline. This is the method used with great success at the IBM U6 lithography research beamline, which produced the first chips made entirely by x-ray lithography. However there are potential problems in a production environment. The mirror is in a high vacuum region (typically  $10 \times 10^{-9}$  torr), necessary to avoid contamination and to allow the long electron beam lifetimes that make synchrotron radiation commercially viable. This high vacuum is maintained in a beamline for a length of at least 5m to allow sufficient acoustic delay that, in the event of an accident, a fast valve can close before the storage ring vacuum is compromised. If the scanning mechanism fails, as it is likely to do when used 24hrs a day, 365 days a year, it would be necessary to break and then remake the high vacuum in order to effect the repair. This means a shutdown of the order of DAYS because of the bakeout required to obtain high vacuums. Such delays are a nuisance in research; they would be intolerable in production.

This paper discusses a forth option; an array of micro saddle-toroidal mirrors that allows a fixed mirror to uniformly illuminate an area matched to the needs of a particular beamline.

#### **Saddle-toroids: definition and means of manufacture**

To understand saddle-toroid arrays (STA), it is first necessary to look at a single saddle-toroid. This is a toroid with a concave minor radius and a convex major radius, as shown in Fig. 1.

Such shapes do not appear to have been used very much in optical design, possibly because they would be difficult to make by conventional grinding. Bending sections of glass tubing has been shown to be a satisfactory and inexpensive way of making toroidal mirrors [4], and provides an easy means of making saddle toroids.

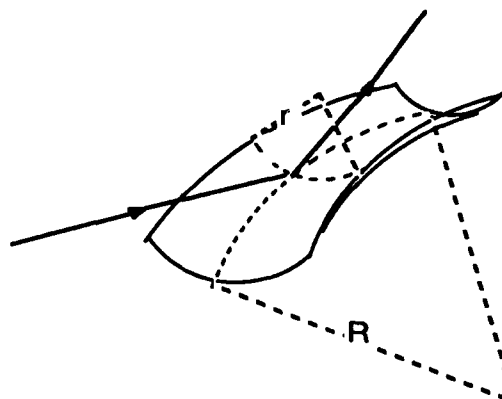


Figure 1. A saddle-toroid mirror.

#### **Saddle-toroid arrays: definition and means of manufacture**

A saddle-toroid array (STA) mirror is shown in figure 2 and consists of a large number (up to 1000) micro saddle-toroids all on the same substrate. Such devices can be made by standard techniques used in the microelectronics industry, as demonstrated by the production of arrays of micro lenses [5] or by micro machining of polymers using uv photoablation by excimer laser [6]. The simple method achieves high quality figure and surface

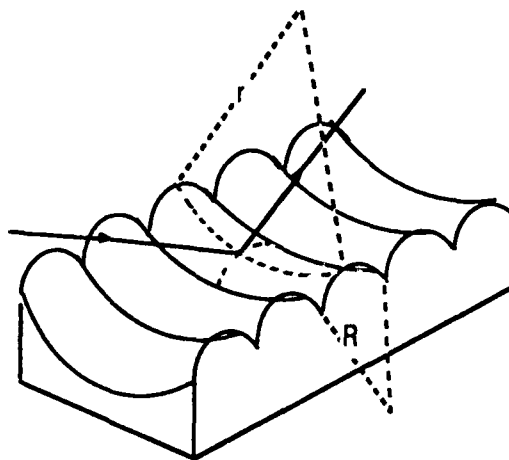


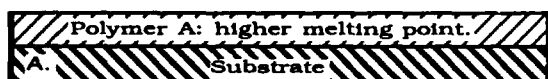
Figure 2. A saddle-toroid array. For clarity, only a small number of the elements of the array are shown, and the relative size of the minor radius  $r$  has been exaggerated with respect to the major radius  $R$ .

finish by exploiting surface tension.

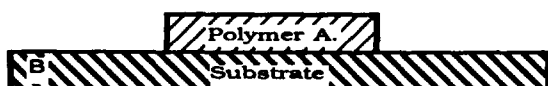
The stages of making a micro-lens are shown in Fig. 3. A circular pedestal of higher melting point polymer A is formed on the surface of the substrate. On top of the pedestal, a defined amount of lower melting point polymer B is deposited. The whole device is heated to a temperature at which B is liquid, but A is not, allowing it to flow to the perimeter set by the pedestal. Polymer B assumes a surface of minimum energy under surface tension, forming part of a sphere. If the pedestal is a line rather than a circle, the surface is part of a cylinder.

To produce an array of micro saddle toroids, the substrate is a cylindrical section of the appropriate radius. Strip shaped pedestals are constructed at right angles to the axis of the cylinder. On these, the right quantity of the lower temperature polymer is placed. When heated, surface tension molds the molten polymer into micro-saddle toroids. A thin layer of a suitable material, such as gold, is then evaporated on top to provide a surface suitable for reflecting x-rays.

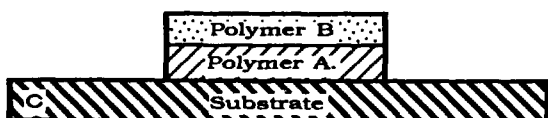
The technique should also work for other non-polymer materials. Should



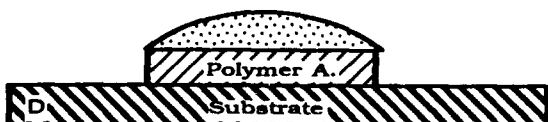
Step A. A coating of higher melting point polymer A is spun onto the substrate.



Step B. A pedestal of polymer A is produced by lithography.



Step C. A defined amount of lower melting point polymer B is applied.



Step D. The device is heated so that polymer B flows and assumes a minimum energy surface under surface tension, while polymer A remains solid.

Figure 3. Producing an array of micro lenses. Although only one lens is shown,

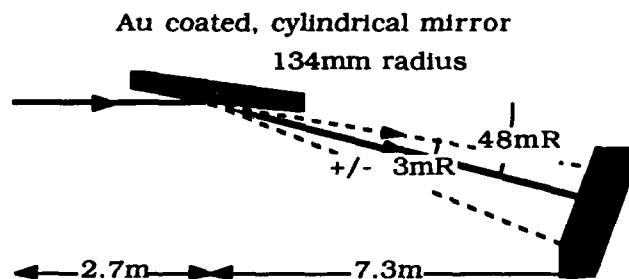
the technique allows an array of identical lenses to be formed on the same substrate.

having polymers in the design prove problematic, suitable metals could be substituted. One possibility would be to etch the pedestal directly into a glass substrate, on which a correct thickness layer of the appropriate metal had already been deposited.

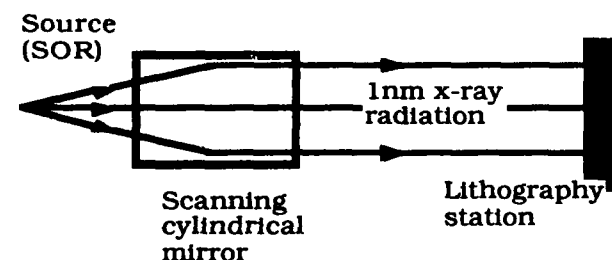
The reason for using saddle-toroid arrays is that a single saddle toroid will expand a beam, but the expanded beam will have the same non-uniformities as the incoming beam. In the case of a synchrotron, the beam has a gaussian profile in the vertical direction. In a scanning system, this is averaged out over the time of the scan. By using an STA mirror, each micro toroid sees a small sector of incoming beam and averages that over the entire output. In this way, the incoming beam is smoothed out, but using spatial rather than temporal averaging.

#### One element systems for lithography: cylindrical scanning mirror

In order to have a point of reference with



a. Side elevation



b. Plan view

Figure 4. The optical components of the IBM U6 beamline at the NSLS, (after Warlumont (3)).

which we could compare the predicted performance of our designs, and to ensure that the parameters used were close to what will be required in practice, we have used the IBM U6 beamline at the NSLS as a model [3].

The optical layout of the IBM U6 beamline is shown in Fig. 4, (3). The scanning cylindrical mirror is 2.7m from the tangent point, or effective source, and the exposure station is a further 7m downstream of the mirror. The mirror is gold coated and has a radius of 134mm. It is scanned  $\pm 3\text{mR}$  about a central offset of 48mR. (50mR is roughly 3degrees).

Using the Imperial College Optical Design Analysis Program, we ray traced the IBM system to obtain a reference figure for comparison. The footprint that would be produced at the lithography station is shown in Fig. 5.

This is a composite of the mirror used in five different positions, to simulate the effect of scanning the mirror. As can be seen from the broad crescent shaped footprint, roughly 35% of the light reflected from the mirror is outside a usable rectangular patch. In practice the situation is considerably worse, because the mirror has to be overscanned to prevent dwelling at either the top or the bottom and producing non-uniform exposure. Warlumont [3] gives the throughput at the U6 beamline as being 25% of what strikes the mirror. Assuming a reflectivity for Au of 75% at the 1.0nm, 20mR conditions that prevail, this means that about 25% of the light incident on the mirror is being lost due to overscan or other obscurations in the system. (i.e. if there was no need to

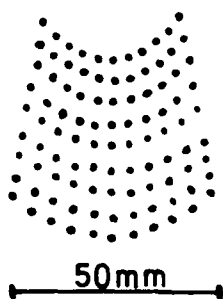


Figure 5. The patch of illumination produced at the lithography station by the scanning cylindrical mirror in the U6 beamline, ignoring beamline apertures.

overscan, and the only losses were the reflectivity and the light falling outside a usable rectangle, 48% of the light incident on the mirror would be usable for lithography. IBM reach similar conclusions claiming that a well designed scanning system could utilize 50% of the incident radiation).

#### One element systems for lithography: saddle-toroid mirror

The saddle toroid can be thought of as a cylindrical mirror which achieves dispersion in the vertical direction by being bent rather than scanned. The amount of bending in the major axis is relatively small for the designs required for synchrotron lithography, being of the order of 50m radius. This means that such optics could easily be formed by bending cylindrical mirrors.

Raytracing was done on a single saddle toroid designed to operate in the IBM U6 beamline. The minor radius was 134mm, the major radius 60 000mm. The spot diagram of the final output are shown in Fig. 6.

The output beam has a more pronounced crescent shape than the simple cylinder, and only 48% of the reflected light falls into a usable rectangle, as compared with 65% for a cylinder. However, because there is no need to scan the mirror, there are no other losses apart from the reflectivity. The total throughput would therefore exceed that experimentally obtained with cylindrical mirrors (almost 50% more) and would be

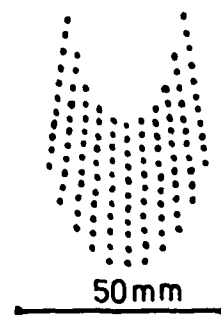


Figure 6. The patch of illumination produced at the lithography station by a single saddle toroid mirror.

within 26% of the most optimistic estimates for the maximum throughput for scanning cylinders.

The major disadvantage of using a simple saddle-toroid would be the non-uniformity of the illuminated area at the lithography mask, caused by the mirror merely expanding the gaussian profiled synchrotron light. This can be overcome by using a saddle-toroid array (STA) mirror, manufactured as described previously. This is a large number of micro saddle-toroids, all on the same cylindrical substrate, each of which disperses a small element of the input beam over the entire illuminated area. This averaging should ensure that the wafer is illuminated to the required  $\pm 10\%$  uniformity necessary for chip production.

There is a slight loss of throughput due to the micro saddle-toroids not covering 100% of the area of the substrate, as there must be a physical separation between individual elements. This would result in a throughput loss of between 1 to 4%, depending on the design details.

### Two mirror designs for lithography: theory

With two mirror systems it is possible to tailor the illuminated patch so that it matches the rectangular lithography masks. We investigated such systems to see if the benefit of a more rectangular beam outweighed the losses of a second reflective surface.

From the standard equations for grazing incidence mirrors:-

$$1/u + 1/v = 1/f \quad (1)$$

$$f = r/(2\sin\beta) \quad (2)$$

$$f = (R\sin\beta)/2 \quad (3)$$

where  $u$  is the object distance,  $v$  is the image distance,  $f$  is the focal length,  $\beta$  is the angle of grazing incidence,  $r$  is the minor radius of a toroid, and  $R$  is the major radius.

A two mirror system producing an output that is parallel in the horizontal plane needs to satisfy the following equations:-

$$1/u + 1/v = (2\sin\beta)/r \quad (4)$$

$$1/u' = (2\sin\beta')/r' \quad (5)$$

$$u' + v = d/(\sin\beta) \quad (6)$$

where the primed quantities refer to the second mirror, and  $d$  is the vertical separation of the mirrors as in Fig. 7.

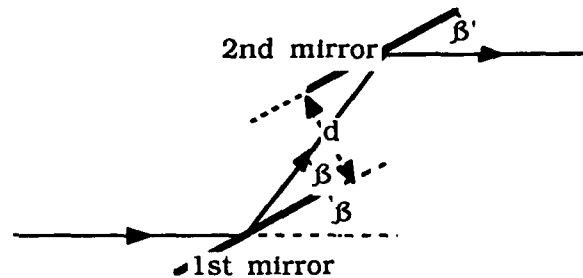


Figure 7. Notation used in discussing two mirror designs.

For simplicity,  $\beta = \beta'$ , giving an output beam that is parallel to the input beam. This would be of practical benefit as all points on the beamline would be at the same height,

$$\text{and} \quad r' = nr \quad (7)$$

where  $n$  simply a number defining the relationship between the two radii.

The problem is that given  $u$ ,  $\beta$ ,  $d$  and  $n$ , we need to find  $r$  and hence  $r'$ .

From Eqs. (4), (5) and (6) we can eliminate  $v$ ,  $u'$  and  $r'$  and end up with the following expression:-

$$r = (A \pm \sqrt{A^2 - B})/(2n) \quad (8)$$

$$\text{where} \quad A = (u(n+1)\sin\beta + d) \quad (9)$$

$$\text{and} \quad B = 4nuds\sin\beta \quad (10)$$

Using Eqns. (7) and (8), it was possible to raytrace a variety of combinations of minor radii, looking for combinations that would give the best shape of output beam. The optical set up was chosen so as to apply to the IBM U6 beamline, in order to be able to make comparisons with both the cylindrical and one toroid design.

Typical results are shown in Fig. 8, which shows the scale of each spot diagram and the shape of the beam at the plane of the lithographic mask.

The raytracing set up for the results shown was to have a source point, radiating

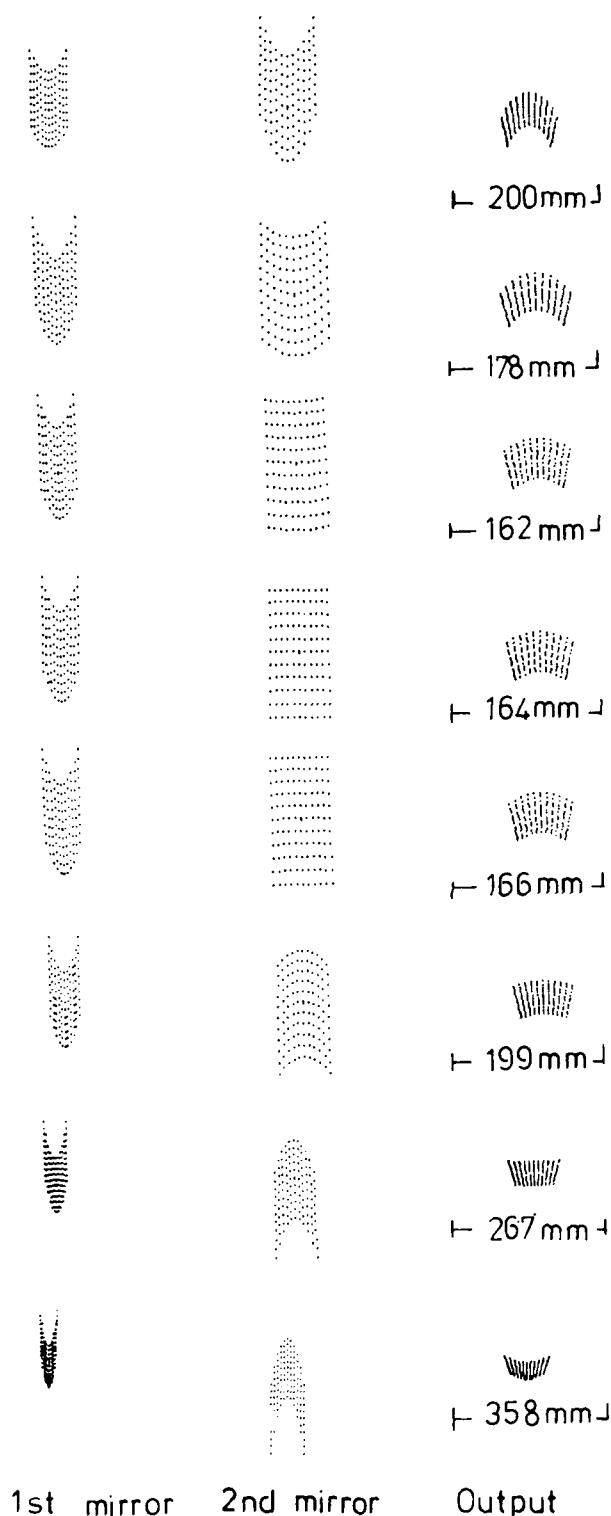


Figure 8. Spot diagrams for the cylinder-saddle-toroid systems listed in table 1, as produced by the Imperial College Optical Design Analysis Program.

uniformly in all directions. One meter away was an aperture measuring  $\pm 7.4\text{mm}$  in the horizontal direction and  $\pm 0.5\text{mm}$  in the vertical direction. This slit was then uniformly filled, creating a first approximation to synchrotron radiation. (The same slit aperture was used in the single cylinder and single toroid raytraces referred to previously). The centre of the 1st toroid was placed a further 1.7m downstream of the slit. The position of the second toroid was determined by the vertical separation  $d$ . This was chosen as 30mm, so that the separation between the line of the incoming beam and the exiting beam was 60mm. This allows the positioning of the statutory lead or uranium safety beamstop. The grazing angle of incidence was 20mR (1.5degrees). This means that the second mirror center was 1145.6mm from the first. The lithography station was placed a further 7m downstream.

The parameters for the spot diagrams shown in Fig. 7 are listed in table 1.

In these trials the first element was a cylindrical mirror and the second was bent into a saddle-toroid, with a major radius of 80 000mm.

The shape of the lithography mask illumination patch varied from a crescent to a near rectangle. At the optimum values the shape was such that 86% of it fell within a usable rectangle.

Table 1. Cylinder-toroid parameters

number	n	r (mm)	r' (mm)
1(top)	-0.4	413	165
2	-0.6	251	150
3	-0.66	222	146
4	-0.68	213	145
5	-0.70	205	144
6	-0.80	172	138
7	-1.00	127	127
8(bottom)	-1.20	98	118

This solution was a diluting one, in that the first mirror expands the beam and the second causes it to re converge. This means that the final intensity of the beam in the horizontal was slightly less than if the same fan of synchrotron radiation had been reflected by a single mirror. Compared with letting the beam



### Flux at the lithography station

Optical system	G	S	R	A	O	Total
No mirror, wafer scanned	1.0	1.0	1.0	1.0	0.5 (1.0)	0.5 (1.0)
Flat scanning mirror	1.0	1.0	0.75	1.0	0.5 (1.0)	0.375 (0.75)
Cylindrical scanning mirror	3.7	0.65	0.75	1.0	0.5 (1.0)	0.90 (1.80)
Stationary saddle-toroid	3.7	0.48	0.75	1.0	1.0	1.33
Stationary STA mirror	3.7	0.48	0.75	0.96	1.0	1.27
Stationary cylindrical + saddle-toroid	2.2	0.86	0.56	1.0	1.0	1.06
Stationary cylindrical + STA mirror	2.2	0.86	0.56	0.96	1.0	1.02

**G** Geometric compression; increased intensity due to horizontal focussing.

**S** Shape; mismatch between final beam and the rectangular mask.

**R** Reflectivity; Au coated, 1.0nm wavelength, 20mR grazing incidence.

**O** Over scan factor; based on the experimental results from U6 beamline.

**A** Aperture factor; accounts for STA mirrors having gaps between elements.

**T** Total: A relative figure of merit.

**Table 2. Comparison of photon intensity/ unit area at the lithographic station for different ways of matching synchrotron output to lithographic mask.shape**

expand naturally to a final point 10m from the tangent point, a single toroid or cylinder condenses the illumination by a factor of 3.7, while this two mirror system only condenses it by a factor of 2.2. That combined with the greater reflection losses of this system, 56% total reflectivity compared to 75% for a single surface, mean that the total usable fraction of light was down by about 21% from that of a single saddle-toroid system.

It seemed likely that there would be another set of solutions for a condensing system, in which the first mirror converges the beam and the second diverges it. We found that this was not possible.

The second mirror, the toroid, could be replaced by a STA mirror to give uniformity of illumination, but the throughput would be slightly less, due to the elements of the STA not completely covering the substrate. This would give an added loss of between 1 to 4%, depending on the details of the STA design.

### Conclusions

The single STA mirror should give 48% more usable flux than the scanning cylindrical mirror as set up at IBM's U6 beamline at the NSLS, and would be

within 26% of the most optimistic predictions for the throughput of a single scanning mirror.

The two element system with an STA mirror would be less efficient giving a predicted 41% improvement over the experimentally measured U6 results, and would be 29% less efficient than the most optimistic one mirror scanning system.

The STA mirrors would be in a high vacuum, but would have no moving parts. If constructed with two polymers they should last as long as gold coated replica gratings. If made of gold directly on quartz, they would be bakable and even longer lasting. They would require periodic, insitu cleaning with an oxygen ion plasma, but this could be carried out at predetermined times, and would not disrupt the schedule.

The optimum practical way of coupling the synchrotron beam to the lithography station would appear to be a single STA mirror.

### References

1. G.P. Williams, "Commercial synchrotron storage rings", Synch. Rad. News, vol 1, no 2, 21 (1988).
2. M. Belford, "X-ray lithography yields

- first computer chips at NSLS", BNL Bulletin, vol 42, no 29, 1 (1988)
3. J. Warlaumont, "X-ray lithography and storage rings", Nuc. Inst. and Methods. in Phy. Res. A246, 687-694 (1986)
  4. M. Faldon, R. Rosser, R.J. Speer, "Low cost adjustable toroidal mirrors", Applied Optics, vol 27, no 13 (1988)
  5. Z.D. Popovic, R. A. Sprague and G.A. Neville Connell, "Technique for monolithic fabrication of microlens arrays", Applied Optics, vol 27, no 7, 1281-1284 (1988)
  6. R. Rosser, UK patent application no. 8805776, (1988).

# Diffraction Contrast of a Bragg-Fresnel Lens in White and Monochromatic Radiation

V. V. Aristov, Yu. A. Basov, R. Frahm,\* W. Graeff,\* G. Materlik,\* and A. A. Snigirev

*Institute of Problems of Microelectronics Technology and High Purity Materials  
USSR Academy of Sciences, 142432 Chernogolovka, Moscow District, USSR*

*\*Hasylab DESY, D-2000 Hamburg 52, Federal Republic of Germany*

## Introduction

Recent advances in the studies of x-ray diffraction phenomena and the technology of structures with elements up to hundreds of angstroms in size open up possibilities for fabrication of effective x-ray focusing elements with three-dimensional Fresnel zone structures, namely, Bragg-Fresnel lenses (BFL) [1-4]. BFL differs favourably from the Fresnel zone plate by the absence of chromatic aberrations which is due to the high spectral selectivity of Bragg reflection,  $\Delta\lambda/\lambda \sim 10^{-4} \div 10^{-5}$ . This enables observation of focusing [5] and image transmission [6-7] in the white spectrum of synchrotron radiation (SR).

## Classical Diffraction

The zones of the BFL have a rectangular profile (Fig.1). The radiation scattering on such a relief has a fairly intricate pattern, i.e. Laue-Laue (L-L) and combined Bragg-Laue (B-L) and Laue-Bragg (L-B) diffraction is realized (lateral zone surface serves as an entrance slit for Laue diffraction) in addition to the Bragg-Bragg (B-B) case. Owing to the rectangular boundary conditions, the Bragg angle for the Laue case is shifted with respect to the  $\theta_B$ -Bragg angle for Bragg diffraction by

$\Delta\theta_{B-L} = \chi_0 / \sin 2\theta_B$  towards lower angles ( $\chi_0$  is the Fourier component of crystal polarizability). Therefore, the contribution of different types of diffraction to the formation of contrast by a crystal-lens in the observation plane can be varied by collimation and monochromatization of the SR beam and by varying the angle of its incidence on the crystal in the vicinity of  $\theta_B$  by  $\Delta\theta$ .

The experiment\* was performed in a double crystal scheme with preliminary monochromatization of incident radiation (wavelength  $\lambda = 1.83 \text{ \AA}$ , Si (111) reflecting planes) (Fig.2). The radiation source-BFL distance  $V_A = 40 \text{ m}$ , and

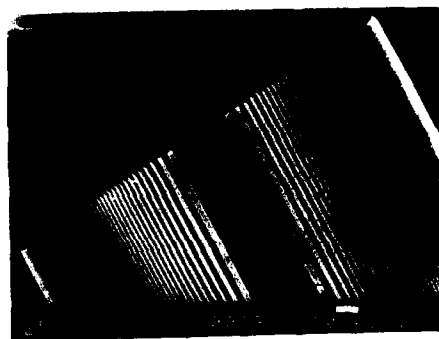


Figure 1. Bragg-Fresnel lens.

\* The experiments described here were carried out using DESY SR (Hamburg, FRG).

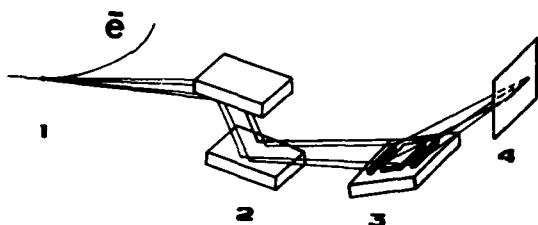


Figure 2. Double-crystal scheme with preliminary collimation and monochromatization of incident radiation.

the BFL - observation plane distance  $r_B = 0.047$  m. From the topographs shown in Fig.3 it is readily seen that at  $\Delta\theta \geq 0$  the observation plane exhibits an intricate interference pattern (Fig.3b,c). This results from the fact that the contribution of all the types of diffraction is approximately the same. At  $\Delta\theta = -\Delta\theta_{B-L}$  (the exact Bragg condition is fulfilled for the entrance for Laue diffraction) the contribution of B-B and B-L diffraction becomes negligible as compared to that of the two other cases. The diffraction pattern observed on the experimental topograph (Fig.3a) was produced by the coherent interaction of waves corresponding to L-L and L-B diffraction.

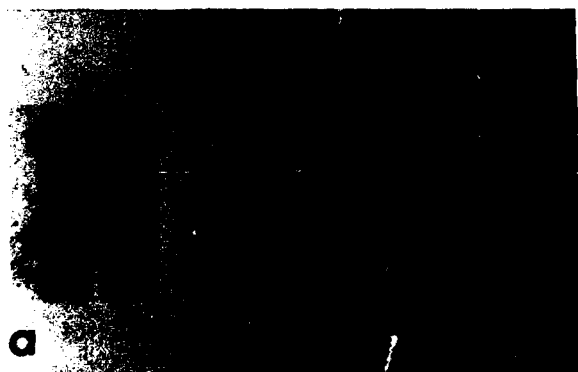


Figure 3. Experimental topographs:  
a -  $\Delta\theta = -\Delta\theta_{B-L}$   
b -  $\Delta\theta = 0$ ; c -  $\Delta\theta' > 0$

#### Conical Diffraction

A scheme of conical diffraction has been suggested [5] in which splitting into Fresnel zones is carried out in the direction perpendicular to the diffraction plane. The scheme involves only B-B

diffraction, and the lens is a phase one, i.e. the phase shift between the beams reflected from the upper and lower zone surfaces is defined by  $\Delta\varphi = 4\pi d \chi_0 h / \lambda^2$ , where  $h$  is the zone height.

In the present work conical focusing has been studied in the single-crystal (Fig.4) as well as double-crystal (Fig.5) schemes ( $r_A = 40$  m;  $r_B = 0.5$  m;  $\lambda = 2$  Å). In both experiments we used BFL (Si (111) reflecting planes) with a zone height  $h = 5.4$  μm which corresponds to a phase shift  $\Delta\varphi = 0.3\pi$  (the optimal phase shift  $\Delta\varphi = \pi$ ). The experimental topographs (Fig.6 and 7) show a focused image of the radiation source in the centre of the topographic image of the lens. Comparison of the topographs reveals that the contrast of the focused image of the radiation source is much more pronounced in the double-crystal scheme since radiation monochromatization in the direction perpendicular to the zone structure (along the crystal surface) causes the background level to decrease. Analysis of the topograph obtained (Fig.7) suggests that in the case in question the focusing efficiency was 10%, the size of the focused image 20 μm. Besides, with due regard for the reduction coefficient ( $K=80$ ) the scheme provides a source size  $\delta_s = 1.6$  mm which is coincident with the size of the radiating region.

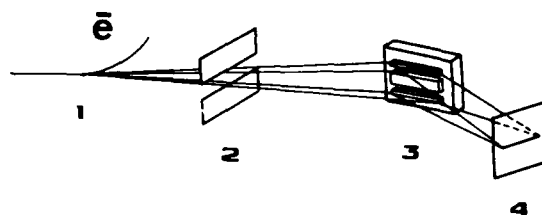


Figure 4. Scheme of conical focusing exclusive of monochromatization

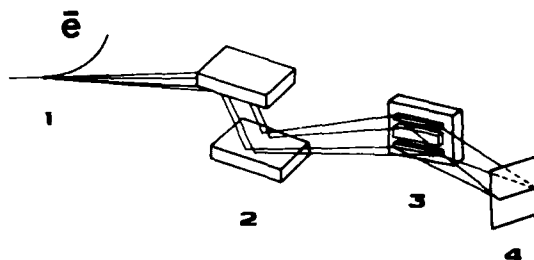


Figure 5. Scheme of conical focusing with monochromatization

200  $\mu\text{m}$



Figure 6. Experimental topograph obtained using the scheme shown in Fig.4.

200  $\mu\text{m}$



Figure 7. Experimental topograph obtained using the scheme shown in Fig.5.

## Conclusions

Thus, the experiments performed have led us to conclude that: 1. The scheme with preliminary collimation and monochromatization of incident radiation (Fig.2) offers variation of the contribution of each type of diffraction to formation of the pattern. The maximum image contrast is observed with deviation of the crystal with respect to  $\theta_B$  by  $\Delta\theta_B - \Delta$  towards lower angles.

2. The use of conical diffraction allows for obtaining a phase BFL. Moreover, monochromatization of incident radiation ensures a considerable increase of image contrast.

## References

1. Shulakov E.V., Aristov V.V. Kristallographiya, 33, 13-21 (1988).
2. Aristov V.V., Snigirev A.A., Basov Yu.A., Nikulin A.Yu., "X-ray Bragg Optics" In Proceedings of the Short Wavelength Coherent Radiation: Generation and Applications (Monterey, USA, 1986)
3. Aristov V.V., Basov Yu.A., Snigirev A.A. Pis'ma Zh.Tekh.Fiz., 13, 114-118 (1987)
4. Aristov V.V., Basov Yu.A., Red'kin S.V., Snigirev A.A., Yunkin V.A. "Bragg zone plates for hard X-ray focusing" Nucl. Instr. and Meth. A 261, 72-74 (1987).
5. Aristov V.V., Basov Yu.A., Kulipanov G.N., Pindyurin V.F., Snigirev A.A., Sokolov A.S., "Focusing properties of a Bragg-Fresnel lens in a white spectrum of synchrotron radiation" Nucl.Instr. and Meth. (1988) to be published.
6. Aristov V.V., Basov Yu.A., Kulipanov G.N., Pindyurin V.F., Snigirev A.A., Sokolov A.S. Pis'ma Zh.Tech.Fiz., 14, 3-6, (1988).
7. Aristov V.V., Basov Yu.A., Kulipanov G.N., Pindyurin V.F., Snigirev A.A., Sokolov A.S. "Image transmission by a Bragg-Fresnel X-ray lens" Opt. Commun. 66, 183-185 (1988).

# Proposed Method for the Measurement of the Spatial Coherence of Laboratory X-Ray Lasers

James Trebes, Troy Barbee, Howard Nathel, and Abraham Szoke

Lawrence Livermore National Laboratory, P.O. Box 808, Livermore, California 94550

## Abstract

A proposed method of measuring the spatial coherence length of laboratory x-ray lasers is described. The method is based on the coherence dependent interference pattern produced by double slit arrays. The neon-like Se laser at 208Å is used as an example.

The brightness and coherence of laboratory x-ray lasers needs to be improved in order to allow the use of these lasers in such applications as high resolution holography and nonlinear x-ray optics. It has been proposed to improve both the brightness and spatial coherence by the use of oscillator-amplifier x-ray laser configurations[1]. Experiments to verify this improvement will require the development of coherence diagnostics for x-ray lasers. This paper describes a spatial coherence diagnostic based on the coherence dependent interference patterns produced from arrays of double slits. This technique is an extension of the double pinhole method described in Born and Wolf[2].

The spatial coherence length of current x-ray lasers can be calculated assuming that they have a large number of transverse modes in the x-ray output. More formally this corresponds to the case when the coherence area at the x-ray laser output aperture is much smaller than the aperture itself. With this assumption and in the far-field the spatial coherence can be determined using the Van Citteret-Zernike theorem[2]. From this theorem the complex

degree of coherence ( $\mu$ ) between any two points in the x-ray laser output beam is given by:

$$\mu(\Delta x, \Delta y) = \frac{\int I(\xi, \eta) e^{i \frac{k}{z} (\Delta x \xi + \Delta y \eta)} d\xi d\eta}{\int I(\xi, \eta) d\xi d\eta}$$

where  $I(\xi, \eta)$  = intensity distribution in x-ray laser at output aperture.  $Z$  is the distance from the aperture to the position in the beam where the coherence is being evaluated. The geometry is shown in Fig. 1. A phase factor which is approximately 1 for all cases considered in this paper has been neglected.

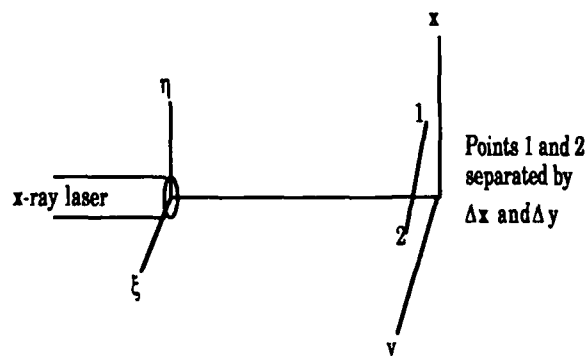


Fig. 1. Geometry for evaluating degree of coherence expression for determining spatial coherence between two points separated by  $\Delta x$  and  $\Delta y$ .

The spatial coherence length is defined as the distance between points 1 and 2 at which the complex degree of coherence decreases from  $\mu = 1$  to  $\mu = 0.88$  [ref. 2]. By assuming that  $I(\xi, \eta)$  is constant across the x-ray laser aperture, an analytic expression for  $\mu$  can be determined. The result is given by the following expression:

$$\mu(r) = \frac{r_2^2 \left[ \frac{2J_1(kr_2 \frac{r}{z})}{kr_2 \frac{r}{z}} \right] - r_1^2 \left[ \frac{2J_1(kr_1 \frac{r}{z})}{kr_1 \frac{r}{z}} \right]}{r_2^2 - r_1^2}$$

where  $J_1$  = the Bessel function of the first kind  
 $r_2$  = the outer radius of the x-ray laser aperture  
 $r_1$  = the inner radius of the x-ray laser aperture  
 $z$  = the axial distance to the position where the coherence is being determined  
 $r$  = the distance normal from the x-ray laser output axis to the position where the coherence is being determined.

This expression was evaluated for three laboratory x-ray lasers. An inner and outer radius were included since two of the lasers have annular emission regions. The results are listed in Table 1.

Table 1.  
Spatial Coherent Lengths for Select X-ray Laser Laboratory

X-ray Laser	Spatial Coherence Length
Se (208Å)	66 $\mu$ m (LLNL, circular)
C (182Å)	4 $\mu$ m (Princeton, annular)
C (182Å)	21 $\mu$ m (Rutherford, annular)

The complex degree of coherence can be measured directly from the coherence dependent interference pattern produced by multiple slits[2]. The intensity distribution

produced by an aperture illuminated with partially coherent x-rays is given by [ref. 3]:

$$I(x_1, y_1) = \frac{I_0}{(\lambda z)^2} \int P(\Delta x, \Delta y) \mu(\Delta x, \Delta y) e^{i \frac{k}{z} (x_1 \Delta x + y_1 \Delta y)} d\Delta x d\Delta y$$

where  $P$  is the autocorrelation aperture amplitude function,  $x_1$  and  $y_1$  are the spatial coordinates at the detector plane a distance  $z$  from the aperture, and  $\Delta x$  and  $\Delta y$  are the relative coordinates in the aperture. For multiple slits (width  $2a$ , height  $2b$ , and separation  $d$ ), this expression has been evaluated to give [ref. 4]:

$$I(x, 0) = I_0 \left( \frac{4ab}{\lambda z} \right)^2 \text{sinc}^2 \left( ka \frac{x}{z} \right) \left[ N + 2 \sum_{m=1}^{N-1} (N-m) \cos(kmd \frac{x}{z}) \right]$$

This expression is valid in the far-field and for  $y = 0$ .  $N$  = the number of slits. For 2 slits, the complex degree of coherence  $\mu$  is the fringe visibility in the interference pattern. Measuring the fringe visibility as a function of slit separation allows the spatial coherence length to be determined. The slit separation which produces a fringe visibility of 0.88 is the spatial coherence length in the x-ray laser beam.

A proposed diagnostic for measuring the fringe visibility as a function of slit separation is shown in Fig. 2. This diagnostic is designed to provide a time integrated measurement of the fringe visibility and therefore the spatial coherence of a 3 cm long, 100-kW neon-like selenium x-ray laser at 208Å. This diagnostic consists of a reflective array of slits placed 1.5 meters from the x-ray laser. At this position the slit separations required to adequately cover the calculated coherence length range from 500 to 50  $\mu$ m. The detector used is Kodak 101 x-ray film with a 1.5- $\mu$ m aluminum stray light filter. The detector is placed at  $z = 0.6$  meters from the slit array. At this distance the smallest fringe separation is 30  $\mu$ m, which can be easily resolved by the x-ray film. In order to make a time resolved measurement with a detector such as an x-ray streak camera, the slit array can be placed closer to the x-ray laser allowing smaller slit separations and larger fringe spacing to be used. This also increases the incident flux and therefore increases the intensity in the signal.

Use of reflective slits constructed from narrow bandpass multilayer x-ray mirrors rather than transmissive slits significantly improves the signal-to-noise ratio by eliminating broadband radiation. This broadband radiation is produced by the high temperature, highly ionized plasma constituting the x-ray laser. The reflective slits are fabricated by depositing multilayer x-ray mirrors in rectangular patterns on a superpolished substrate.

Calculated interference patterns for different slit separations are shown in Figs. 3 and 4. A measured source size of 50  $\mu\text{m}$  in radius was used in calculating the complex degree of coherence[5].

In principle the spatial coherence could be determined from the measurement of a single double slit measurement. This would, however, be dependent on a model for the complex degree of coherence. This function depends on the intensity distribution at the output of the x-ray laser. By making a series of measurements with different slit widths, the complex degree of coherence is mapped out and the coherence length determined is model independent. In addition, the intensity distribution can in principle be determined from the degree of coherence. By using slit separations smaller than the spatial coherence length, instrumental effects which may reduce the fringe visibility can be measured and deconvolved from the spatial coherence

length results. In the case of  $d \ll$  coherence length, the fringe visibility should be 1.

The spatial coherence diagnostic described above can provide time-integrated spatial coherence lengths for laboratory x-ray lasers. This diagnostic will be built and tested using the neon-like selenium x-ray laser. Future work will be directed toward developing time resolving versions of this system, the use of multiple rather than double slits, and the development of a suitable theoretical formalism for handling the case of highly coherent x-ray lasers when the coherence area is comparable to the x-ray laser output aperture. All of these concepts and diagnostics can be developed and tested on analog visible light laser systems[6]. This will also be explored.

## References

1. M. Rosen, et. al., Comm. Plasma Phys. Cont. Fusion, **10**, 245 (1987).
2. M. Born and E. Wolf, Principle of Optics, 6th ed., Pergamon Press, Oxford, England (1980).
3. J. Goodman, Statistical Optics, John Wiley and Sons, New York (1985).
4. T. Asakura and H. Fujii, Optik, **40**, 217 (1974)
5. D. Whelan, et. al., SPIE, **831**, 275 (1987).
6. H. Nathel, et. al., J. Opt. Soc. Am. B, **5**, 1528 (1988).

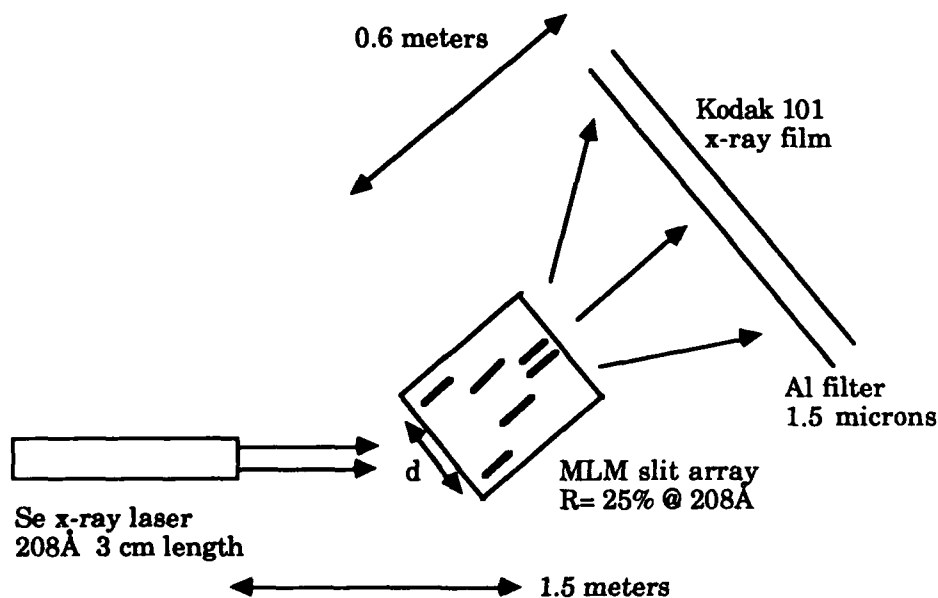


Fig. 2. Schematic arrangement of x-ray laser spatial coherence diagnostic utilizing multi-layer mirror array and x-ray film detector.



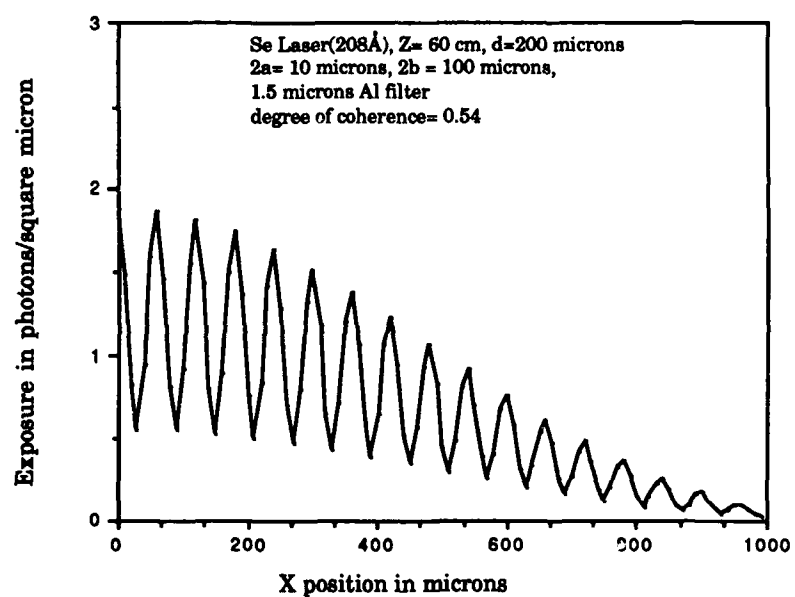
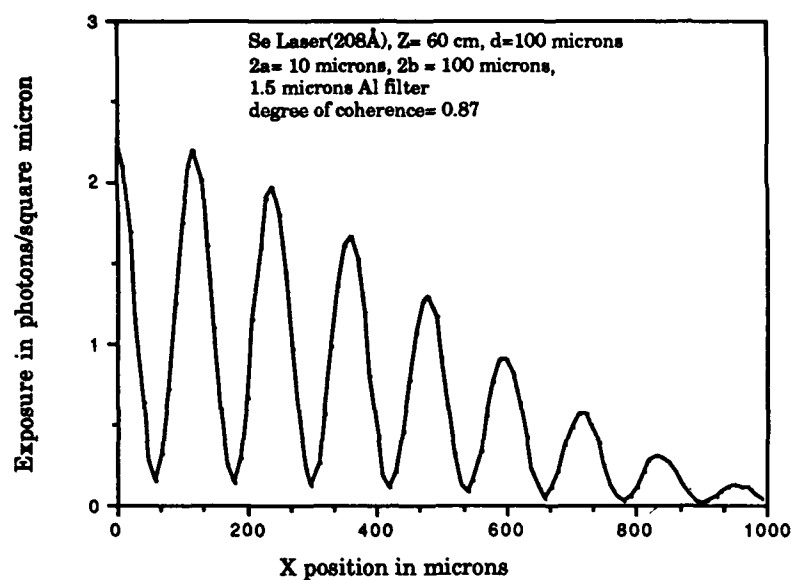


Fig. 3. The calculated interference patterns for a slit separation of 100 microns (top) and 200 microns (bottom). The fringe visibility of 0.87 at a separation of 100 microns indicates a coherence length of 100 microns.

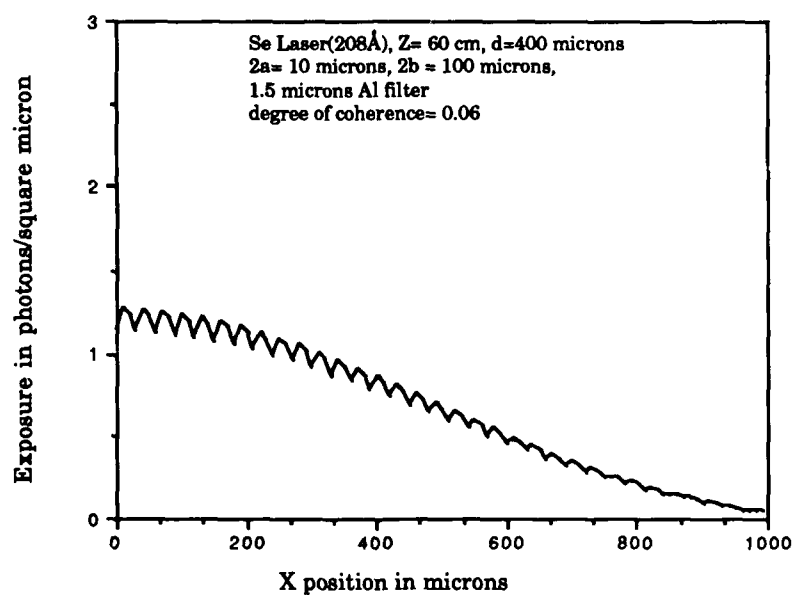
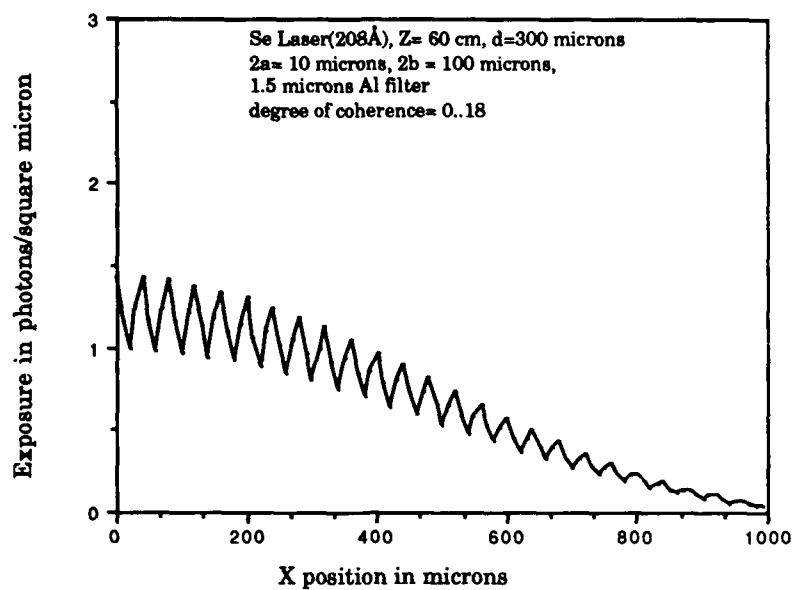


Fig. 4. The calculated interference patterns for slit separations of 300 (top) and 400 (bottom) microns.

#### Acknowledgements

This work was performed under the auspices of the U.S. Department of Energy by Lawrence Livermore National Laboratory under contract No. W-7405-Eng-48.

## **Coplanar vacuum photodiode for measurement of short-wavelength picosecond pulses**

**J. Bokor, A. M. Johnson, W. M. Simpson, and R. H. Storz**  
AT&T Bell Laboratories  
Holmdel, NJ 07733

A vacuum photodiode is the most elementary photoelectric detector. Such a device is sensitive to photon energies which exceed the photocathode work function in accord with the classical photoelectric effect. For vacuum ultraviolet and soft X-ray radiation, photoelectric quantum yields in excess of 50% can be reached.<sup>1</sup> With a carefully designed external circuit, the response time of such a detector is limited by the diode capacitance. The present state-of-the-art risetime in a commercial biplanar vacuum photodiode<sup>2</sup> is 60 psec.

Recent studies<sup>3</sup> have demonstrated the utility of the coplanar transmission line geometry with lateral dimensions of several micrometers for the generation and propagation of picosecond electrical pulses. We have realized an ultrafast vacuum photodiode detector by taking advantage of a microfabricated coplanar stripline geometry. Two parallel stripline electrodes themselves serve as the photocathode and collection anode. A representation of our initial devices is shown in Figure 1. In the application primarily envisioned for this device, namely the measurement of short soft X-ray pulses radiated by picosecond laser plasma sources, the photodiode is optimized to give high sensitivity for soft X-rays, while a small portion of the pump laser pulse used to create the plasma is also used to trigger a conventional photoconductive sampler in order to read out the photodiode pulse.

The device has been tested using 266 nm ultraviolet (UV) laser pulses of ~500 fsec duration derived from a compressed, mode-locked Nd:YAG laser. The results are shown in Figure 2. With 60 V applied bias, we obtained a 4 psec rise time and a 12 psec fall time. It was not possible to apply a higher bias voltage to this device due to avalanche breakdown of the silicon between the lines. By improving the device processing to eliminate the silicon between the striplines, higher bias voltage and hence higher speed

should be obtained.

## REFERENCES

1. J. A. R. Samson, *Techniques of Vacuum Ultraviolet Spectroscopy*, (Pied Publications, Lincoln, Nebraska, 1967).
2. e.g. Hamamatsu Corp., Middlesex, NJ. model R1328U.
3. M. B. Ketchen, et al., *Appl. Phys. Lett.* **48**, 751(1986).

Fig. 1: Coplanar vacuum photodiode and conventional sidegap photoconductive sampler.

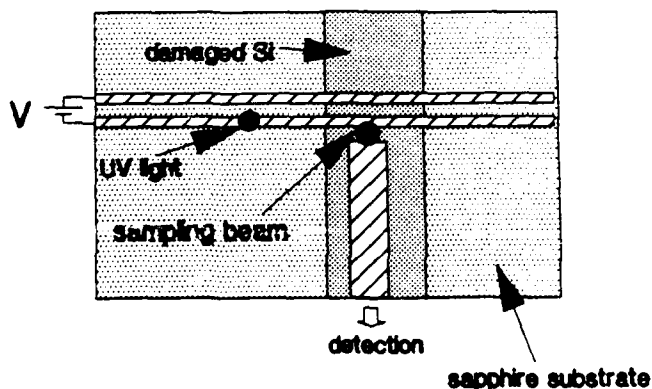
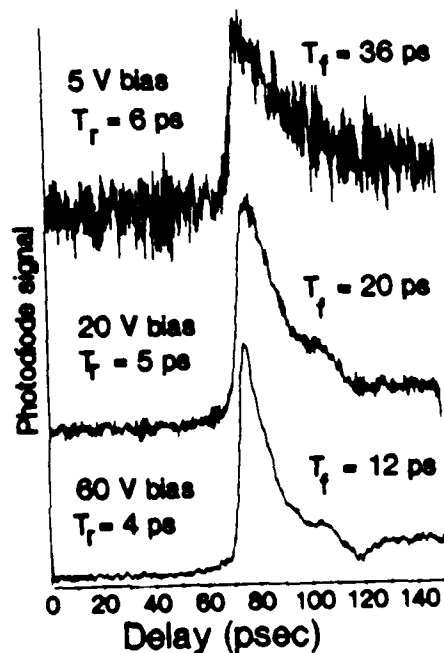


Fig. 2: Response of device to 500 fsec UV laser pulses at various applied bias voltages. The sidegap sampler was independently measured to have 2 psec response time.



## X-Ray Optics for X-Ray Laser Research Applications

N. M. Ceglio

*University of California, Lawrence Livermore National Laboratory  
P.O. Box 808, Livermore, California 94550*

### Abstract

State of the art capabilities in soft x-ray lenses, multilayer mirrors, beamsplitters, and synthetically generated holograms are reviewed. Application of these capabilities in recent x-ray laser cavity experiments, and to the development of a soft x-ray interferometer and a high intensity ( $\geq 10^{13}$  watt/cm<sup>2</sup>) soft x-ray laser are discussed.

### Introduction

The emerging field of x-ray optics has reached a new stage of maturation. There are currently available (albeit at lower efficiency) all the basic optical components typically taken for granted at visible wavelengths (lenses, normal incidence mirrors and beamsplitters, and holographic optical components), as well as high brightness, (partially) coherent sources (undulators, soft x-ray lasers, laser produced plasmas). Utilizing these capabilities we are taking the first tentative steps toward the development of sophisticated optical systems - interferometers, resonant laser cavities with focussed, high intensity output - at soft x-ray wavelengths. These advanced optical systems have the potential for thrusting us into a new era of modern x-ray optics in which high density, optically thick plasmas and materials may be probed, and nonlinear x-ray optical phenomena generated.

This manuscript is a brief review of recent accomplishments and current "work in progress" of the Advanced X-ray Optics Group at

Lawrence Livermore National Laboratory. As such it incorporates contributions by the group members (A. M. Hawryluk, D. G. Stearns, D. P. Gaines, ...) as well as outside collaborators: LLNL X-ray Laser Group (D. Matthews, C. Keane, B. MacGowan, J. Trebes, R. London, ...), LLNL Dept. of Chemistry and Materials Science (M. Sattler, ...), Dept. of Physics and Center for Solid State Science at Arizona State University (M. B. Stearns, A. K. Petford-Long, ...) and the PTB Institut, Berlin (M. Kuhne, P. Muller, B. Wende).

Specifically reviewed in the next section is progress in the design, fabrication, and performance of Fresnel zone plate lensing elements, multilayer mirrors, beamsplitters and holographic optical components. The final section is devoted to the near term application of these x-ray optics technologies. Recent results from double- and multi-pass x-ray laser cavity experiments are reported. In addition, "work in progress" toward the development of a soft x-ray interferometer and a high intensity soft x-ray laser is discussed, as well as their potential application in probing high density plasmas (interferometer) and generating non-linear x-ray optical phenomena (high intensity laser).

### X-ray Optical Components

Development of optical components for the manipulation of soft x-rays has enjoyed remarkably rapid progress in recent years [1-6]. This effort is motivated by a multidisciplinary interest in short wavelength radiation. Fresnel

zone plate lenses with ten-nanometer resolution are being developed for x-ray microscopy of live microbiological specimens, and for applications in solid state and surface physics, as well as integrated circuit mask inspection in x-ray lithography. Multilayer mirrors and beam-splitters are of broad interest for applications in spectroscopy, synchrotron beam manipulation, plasma physics, soft x-ray interferometry, and x-ray laser research.

Fresnel zone plates and phase plates provide the potential for diffraction limited x-ray imaging with a spatial resolution approaching the dimension of the minimum (i.e. outermost) zone width [7-10]. Fresnel zone plates with minimum zone widths of 500Å are currently operating as objective lenses in experimental x-ray microscopes covering the spectral range from 30Å - 45Å. These microscopes report image resolutions approaching 500Å in the imaging mode [11], and 750Å in the scanning mode [12]. More recently [3], Fresnel zone plates with 400Å minimum zone width have been used in an imaging microscope at 45Å for inspection of integrated circuit masks. A spatial resolution approaching 400Å - 500Å was reported.

Work is underway at a number of facilities to fabricate (using electron beam lithography) the next generation of Fresnel zone plate structures with minimum zone widths approaching 100Å. As linewidths become narrower the zone plate lens improves in both diffraction limited resolution ( $\delta \sim \Delta r$ ) and speed ( $f\# = \Delta r/\lambda$ ) [7]. (Where  $\delta$  is spatial resolution,  $\Delta r$  is minimum zone width,  $f\#$  is the f/number of the lens, and  $\lambda$  is the x-ray wavelength). Typically one does not expect zone plate lens efficiency to depend on linewidth, e.g., ideal first order diffraction efficiency is typically quoted as 10% for a zone plate and 40% for a phase plate independent of  $\Delta r$  [10]. However, as lens  $f\#$  is reduced below  $\Delta r/\lambda \sim 10$ , one is forced to view the zone plate lens as a three dimensional diffraction element. It is no longer accurate to treat it as a simple two dimensional diffraction mask. In particular one must take into account "waveguide" propagation effects for soft x-rays passing through the outer zones when  $\lambda \leq \Delta r$  and  $\lambda \ll t$  ( $t$  is the thickness of the zone plate structure). Such "waveguide" effects can have a significant influence on diffraction efficiency [13], and under some truly pathologic conditions even reduce zone plate resolution.

While significant progress in multilayer mirror fabrication has been recorded over a broad

front [1,2], the discussion here centers on Molybdenum/Silicon mirrors operating in a spectral band from 125Å to 220Å. This bandwidth is of particular interest because many of the laboratory x-ray lasers operate within this band (e.g., neon-like Selenium at 206.3Å and 209.6Å [14], hydrogen-like carbon at 181Å [15], neon-like Yttrium at 154.9Å [14], and neon-like Molybdenum at 131Å [16]). In addition silicon has L absorption edges at approximately 123Å, so that its absorption is low for  $\lambda \geq 125Å$ , providing a possibility of fairly efficient mirrors at these wavelengths. Equally important is the fact that the Mo/Si system exhibits good long term stability, and has layer interfaces which are reasonably sharp and well defined [17].

The Mo/Si multilayer mirrors are deposited using a multi-head magnetron sputter system in which all process parameters are actively feedback controlled (substrate temperature feedback control is also in the process of being implemented) and recorded into computer memory during layer deposition. In addition the mirror substrates undergo a compound rotation during sputter deposition to insure layer uniformity over the substrate area [5]. Test experiments indicate that the control systems provide layer-to-layer uniformity, and area-wide homogeneity (over a 3 inch diameter substrate) to better than  $\pm 1\%$ .

Multilayer mirror production and characterization follows a standard procedure: Once a wavelength and incidence angle have been chosen (e.g., 206.3Å at normal incidence for x-ray laser cavity), the appropriate multilayer mirror is designed (materials,  $d$  spacing,  $\gamma$  [ratio of high index material thickness to  $d$  spacing],  $N$  [number of layer pairs]) using a versatile computer code employing a matrix method to calculate the scattering at each interface and propagation through each layer [18]. Mirrors (along with control samples) are fabricated to the design specifications using the magnetron sputter system discussed above. The mirrors are then screened for correct " $d$ " and " $\gamma$ " values using small angle diffractometer measurements at the  $\text{CuK}\alpha$  line ( $\sim 8$  keV). The mirrors are next tested for x-ray reflectivity (and transmission in the case of beamsplitters) at the wavelengths and incidence angles of interest at the Bessy synchrotron [19]. Control samples are sectioned and thinned for TEM analysis in order to inspect interface sharpness, layer to layer uniformity, and layer smoothness [17,18].

Results from this detailed fabrication and characterization process are illustrated in Figs. 1 (a), (b), (c). Figure 1 (a) shows a TEM micrograph of a Mo/Si mirror with  $d = 115\text{\AA}$ ,  $\gamma = 0.51$ ,  $N = 25$  designed for use at normal incidence in a cavity experiment on the neon-like Selenium x-ray laser with laser lines at  $206.3\text{\AA}$  and  $209.6\text{\AA}$ . Figure 1 (b) shows the measured x-ray reflectivity of that same mirror at virtual normal incidence ( $\approx 0.5$  degrees off normal). The peak reflectivity of 28 % occurs at  $210\text{\AA}$  and the mirror bandpass (FWHM) is  $25\text{\AA}$ . Figure 1(c) shows the measured x-ray reflectivity for a mirror designed for use at normal incidence in a cavity experiment on the neon-like Molybdenum x-ray laser with lines at  $131\text{\AA}$  and  $132.7\text{\AA}$ . The mirror is a Mo/Si multilayer with the following characteristics:  $N = 30$ ;  $d \approx 71\text{\AA}$ ;  $\gamma \approx 0.4$ . The peak reflectivity of 61% occurs at  $\lambda = 130\text{\AA}$ , and the mirror bandpass (FWHM) is  $\approx 10\text{\AA}$ .

The current state of the art in Mo/Si multilayers over the spectral range  $125\text{\AA}$ -  $220\text{\AA}$  allows us to design, fabricate, and verify high efficiency, high optical quality mirrors with a high degree of confidence, as illustrated in Fig. 1.

The optical beamsplitter is a fundamental optical component the importance of which is often overlooked. It plays a vital role in holographic, interferometric, and schlieren systems. It is important as an output coupler for laser cavities, is useful for beam monitoring functions, and in general provides versatility in sophisticated optical applications. We have pioneered the development of multilayer beamsplitters for use at soft x-ray wavelengths [4,5,6,18,20,21]. Using silicon nitride membrane technology originally developed by the integrated circuit industry for x-ray lithographic applications [22], we have designed, fabricated, and tested Mo/Si multilayers supported by thin ( $\approx 300\text{\AA}$ ), x-ray transparent silicon nitride membranes. Details of beamsplitter fabrication are provided elsewhere [5,20]. Generally speaking, a polished silicon wafer is coated (via chemical vapor deposition) with a thin silicon nitride film onto which a Mo/Si multilayer is deposited (via magnetron sputtering). Using conventional patterning and anisotropic etch techniques [23], the underlying silicon is removed from an area typically  $10 - 20\text{ mm}^2$ , leaving a window of silicon nitride supported multilayer, which is partially reflecting and transmitting as schematically illustrated in Fig. 2.

Transmission electron micrograph of Mo/Si multi-layer  $d \approx 115\text{\AA}$   
 $N = 25$



Figure 1(a): TEM micrograph of a Mo/Si multilayer mirror designed for x-ray laser cavity at  $206.3\text{\AA}$  and  $209.6\text{\AA}$ .

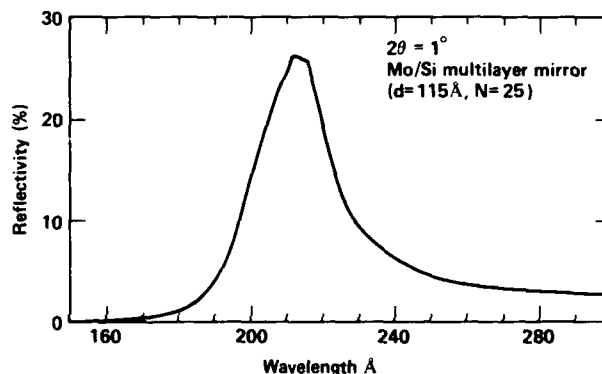


Figure 1(b): Measured x-ray reflectivity of multilayer mirror shown in Fig. 1(a).

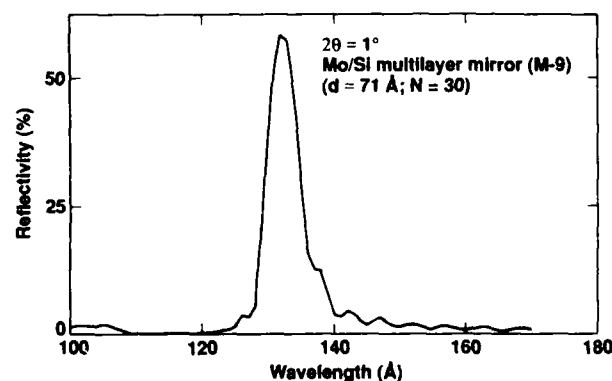


Figure 1(c): Measured x-ray reflectivity of Mo/Si multilayer mirror designed for x-ray laser cavity at  $131\text{\AA}$  and  $132.7\text{\AA}$ .

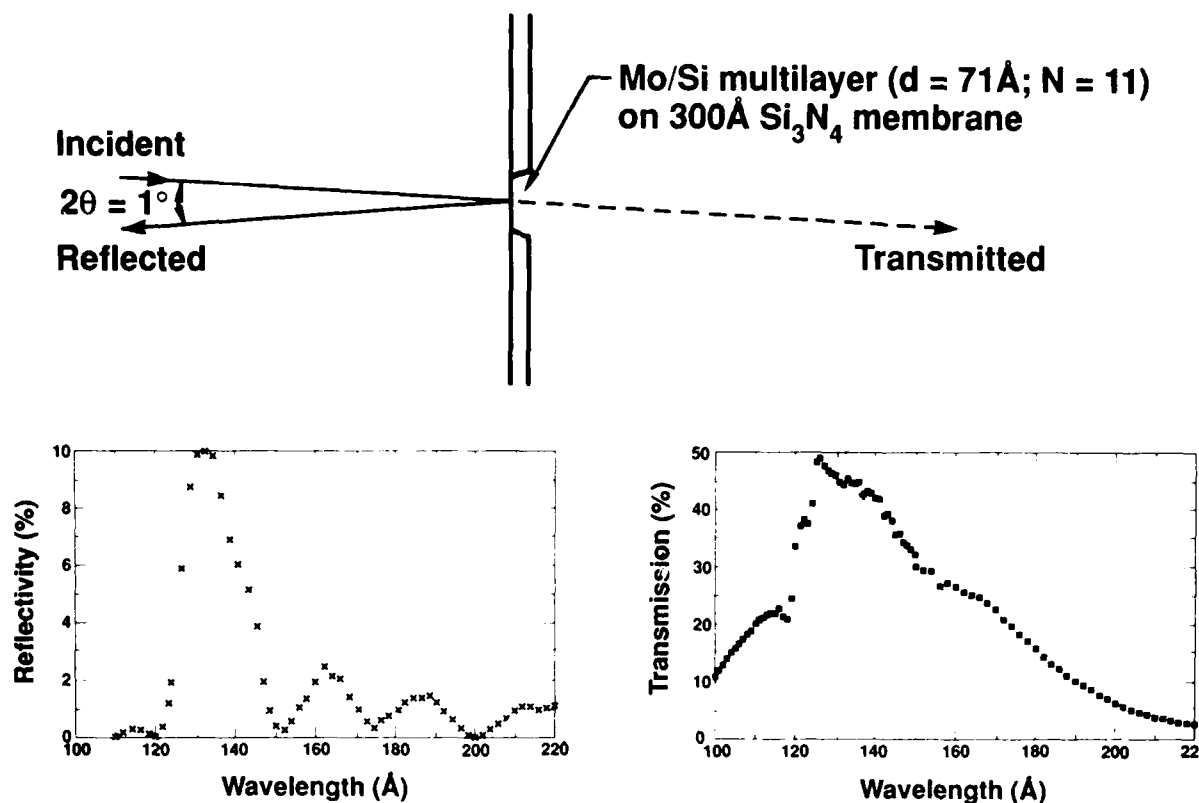


Figure 2: Schematic illustration of multilayer beamsplitter behavior along with measured x-ray reflectivity and transmission for a "top" side deposited beamsplitter designed for use at 131 $\text{\AA}$ .

The primary challenge in producing high optical quality soft x-ray beamsplitters lies in achieving a smooth interface between the silicon nitride (or other transparent support membrane) and the multilayer structure. It is not uncommon for the CVD silicon nitride film to have a surface roughness of order 10 $\text{\AA}$  - 15 $\text{\AA}$ . This roughness is replicated in the multilayer structure resulting in a reduced reflectivity [24] and possible wavefront distortion of the reflected beam. While efforts are underway to produce smoother silicon nitride films, improvements in beamsplitter performance have already been achieved by depositing the multilayer onto the back side of the silicon nitride membrane, after the silicon has first been anisotropically etched. In this procedure the silicon nitride film is deposited onto the highly polished silicon wafer. The interface between the silicon nitride and the silicon appears to be almost as smooth as the polished wafer. After the silicon has been etched away, the Mo/Si multilayer is then deposited onto the "smooth" surface of the silicon nitride that had been in

contact with the polished silicon. Figures 3 (a), (b) compare TEM micrographs of Mo/Si beamsplitters deposited on the "rough" top side of the silicon nitride (Fig. 3(a)), and deposited on the "smooth" bottom side of the silicon nitride (Fig. 3(b)). In Fig. 3(a) the beamsplitter specifications are: Mo/Si;  $d=115\text{\AA}$ ;  $\gamma \approx 0.51$ ;  $N=7$ ; silicon nitride=440 $\text{\AA}$ . In Fig. 3(b) the beamsplitter specifications are: Mo/Si;  $d = 65\text{\AA}$ ;  $\gamma \approx 0.4$ ;  $N = 13$ ; silicon nitride=3000 $\text{\AA}$ . Figure 3 shows the reduced roughness in the "bottom-side" deposited multilayers. Figure 4 illustrates the comparative performance of "top" and "bottom" side deposited multilayers versus multilayers deposited onto a polished silicon wafer. All samples were prepared in the same run of the magnetron sputter system. Nominally they are all Mo/Si multilayers with  $d = 65\text{\AA}$ ;  $\gamma \approx 0.3$ ;  $N = 13$ . As illustrated, peak reflectivities are 17%, 13.4%, and 9.7% for the multilayers deposited on the polished wafer, the "bottom" side of the silicon nitride, and the "top" side of the silicon nitride, respectively. These results



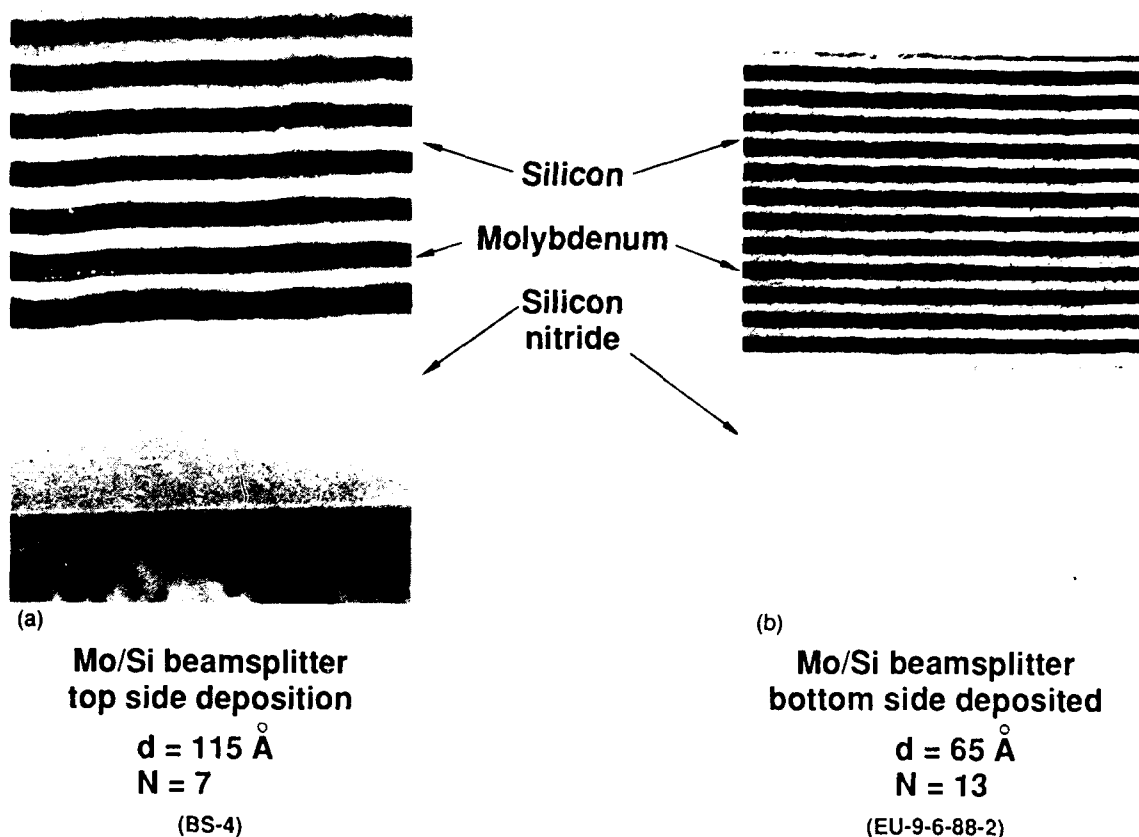


Figure 3: Comparative TEM micrographs showing multilayer beamsplitters which were (a) "top" side deposited and (b) "bottom" side deposited onto silicon nitride. The "bottom" side deposited layer has less interface roughness.

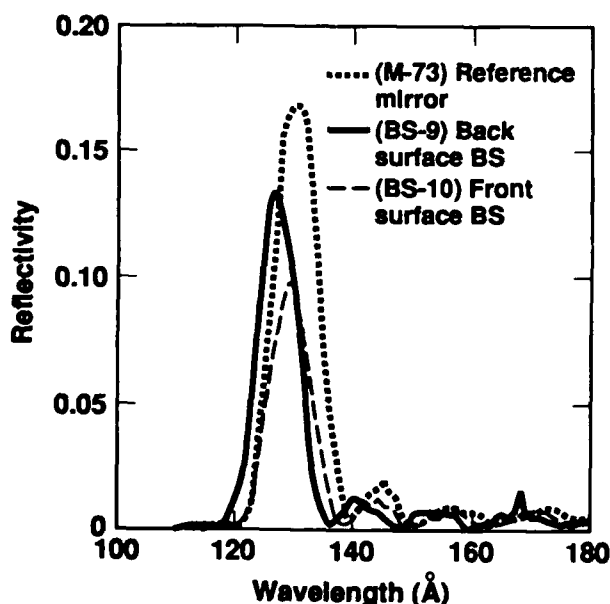


Figure 4: Measured x-ray reflectivities for multilayers deposited onto a polished silicon wafer (M-73); "bottom side" deposited onto silicon nitride (BS-9); and "top side" deposited onto silicon nitride (BS-10). All multilayers were fabricated on the same run.

indicate that the "bottom side" deposited beamsplitters, while better than the "top side" deposited optics, are not yet as good as has been achieved with multilayers deposited on highly polished substrates. (Note also the apparent shift in  $d$  spacing for the "bottom side" deposited multilayer presumably due to shadowing effects).

The value of synthetically generated holographic optical components is well established at infrared and visible wavelengths [25]. As generalized diffractive optical elements they represent the ultimate in the application of modern computer and microfabrication technologies to the control and manipulation of electromagnetic radiation. We have pioneered the development of synthetically generated holographic optical components for use at soft x-ray wavelengths [4,5,20,21]. We have combined nanometer lithographic techniques (UV holographic lithography, e-beam lithography, x-ray lithography) with multilayer thin film deposition capabilities to produce three dimensional diffractive structures, which are

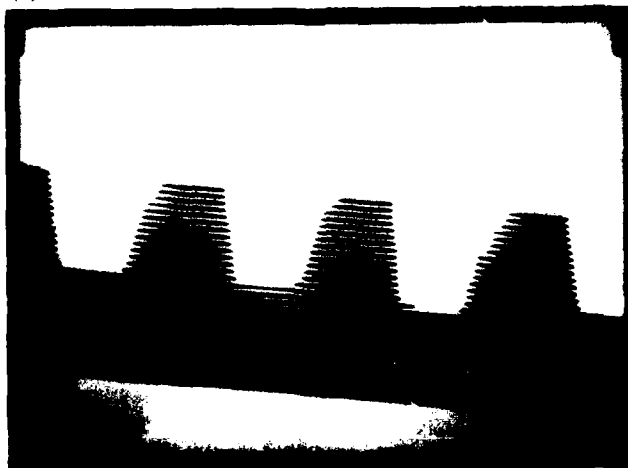
synthetically generated x-ray reflection holograms. Specifically, we have patterned 1000Å linewidth linear gratings into (and onto) multilayers to produce high efficiency, normal incidence reflection gratings (also called highly dispersive x-ray mirrors). We have also patterned micro-Fresnel zone plates onto multilayers to produce planar focussing mirrors. In principle, using e-beam lithographic capabilities, we could pattern multilayers in any generalized fashion allowing complete amplitude and phase control (if coherently illuminated) - and thereby focus control - over the reflected x-rays.

Details of the fabrication of holographic optical components (HOC) are provided elsewhere[5]. While a variety of techniques may be used in HOC fabrication, the patterned multilayer mirror shown in Fig. 5 was prepared as follows: the Mo/Si multilayer mirror was deposited onto a polished silicon wafer using magnetron sputtering; a 5000Å thick layer of photoresist was deposited atop the multilayer mirror and a 3000Å period linear grating pattern was recorded (i.e. exposed and developed) into the resist using UV holographic lithography. A thin layer (~500Å) of chromium was next evaporated (at oblique angle of incidence) atop the resist grating pattern. The Cr coated grating pattern was then used as a pattern mask for subsequent reactive ion etching into the multilayer. The etch gases used were a mixture of  $\text{CClF}_3$  and  $\text{O}_2$  (5% by mass flow rate) at 5 mTorr pressure. Figure 5 is a TEM micrograph of a sectioned and thinned piece of the grating-in-multilayer pattern. The grating period is

3000Å, the multilayer is Mo/Si, with  $d = 113\text{\AA}$ ,  $g \approx 0.4$ ; and  $N = 30$ . Special note should be taken of the remarkable control over structural detail, i.e. the layer to layer uniformity, the sharp interfaces between the Mo and Si layers, the precise etch control in providing edge definition of the grating pattern, the very few damaged layers, and no evidence of residue in the etched regions.

We have characterized the x-ray performance of such grating- in-multilayer holographic optical components at the Bessy synchrotron. The results from such a measurement are presented in Table 1. Shown are the measured diffraction efficiencies into the zeroth through fourth orders for a Mo/Si multilayer ( $d = 65\text{\AA}$ ;  $\gamma \approx 0.3$ ;  $N = 30$ ) patterned with a linear grating (period =  $1\text{ }\mu\text{m}$ ; reflecting line/space ratio  $\approx 1.1$ ) and illuminated at virtual normal incidence ( $\approx 0.8$  degree off normal) at  $\lambda = 130\text{\AA}$ . A control mirror (fabricated at the same time) was measured to have a normal incidence reflectivity of 43.5% at  $130\text{\AA}$ . From this value we can calculate the expected diffraction efficiency values from an ideal linear grating having the above characteristics. These calculated (theoretical) values are also listed in Table 1. The good agreement between the measured and calculated diffraction efficiency values at low orders is strong testimony to our ability to fabricate high quality holographic optical elements for soft x-ray wavelengths. The disagreement at higher orders is most likely due to sidewall taper in the real structures which is not accounted for in the ideal grating calculations.

(a)



(b)

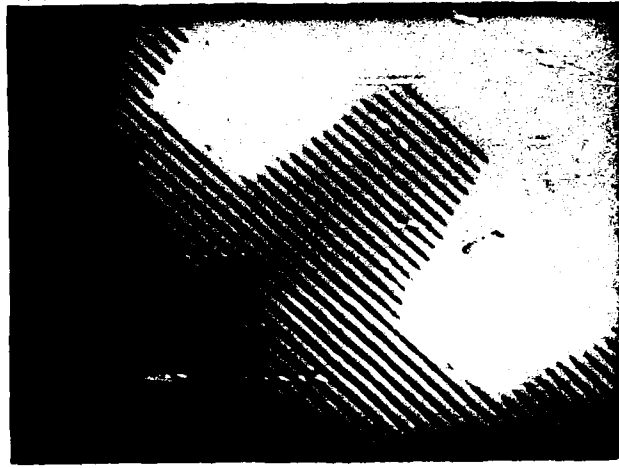


Figure 5: TEM micrographs of a 3000Å period grating etched into a Mo/Si multilayer mirror with  $d = 113\text{\AA}$ ;  $\gamma \approx 0.4$ ;  $N = 30$ .

TABLE I.

Measured and calculated diffraction efficiency values at  $\lambda = 130\text{\AA}$  for a linear grating etched into a Mo/Si multilayer. The disagreement for higher orders may be due to sidewall taper in the real structures which is not accounted for in the calculations.

<u>Diffracted Order</u>	<u>Measured Diffraction Efficiency</u>	<u>Calculated Diffraction Efficiency</u>
0th	11.3%	12.0%
1st	4.5%	4.4%
2nd	0.04%	0.03%
3rd	0.24%	0.46%
4th	0.05%	0.03%

### Applications

One of the early motivations for the development of normal incidence multilayer mirrors and beamsplitters was the need for resonant cavities for newly developed soft x-ray sources of amplified spontaneous emission [14,15,16,26]. Cavity development was and is viewed as a crucial step toward the ultimate transformation of these x-ray gain media into relatively efficient lasers with optimized divergence and coherence properties.

There are a number of obstacles to laser cavity development. Typical soft x-ray gain media are short duration, high temperature, high density plasmas produced by intense optical laser irradiation of foil, fiber, or solid targets. These gain media provide a hostile x-ray environment for cavity optics. In addition, the gain media may be subject to local inhomogeneities that could compromise coherent transport of amplified radiation, and the short gain lifetime (typically a few hundred picoseconds) leaves little opportunity for many amplification passes.

Significant progress has been made in addressing these challenges. Experiments demonstrating Mo/Si mirror survival (at least for the duration of the gain medium) in the hostile x-ray laser environment (of present generation laboratory x-ray lasers) have been completed, and are in agreement with calculations of anticipated mirror damage [27,28]. Double pass cavity experiments have been successfully

performed in neon-like Selenium at  $206.3\text{\AA}$  and  $209.6\text{\AA}$ , and in neon-like Molybdenum at  $131\text{\AA}$  and  $132.7\text{\AA}$  [29,30]. In these experiments the cavity output was time resolved permitting temporal separation and distinct identification of the single- and double-pass amplified beams. In addition to providing an unequivocal demonstration of double pass amplification, the 20 ps time resolution of these experiments provided two additional opportunities: it allowed direct calculation of the time varying "effective gain" of the medium [29]; and it provided a direct measurement of double pass: single pass amplification (on a single experiment) showing that beam intensity was increased by as much as 20X and beam brightness by as much as 600X (due to the 6X decrease in divergence).

The most advanced demonstration to date of soft x-ray laser cavity performance is illustrated in Fig. 6, in which the time resolved triple-pass amplified output (at  $206.3\text{\AA}$ ) from a multipass cavity is presented [31]. In this experiment the cavity consisted of a spherical mirror ( $R = 12\text{ cm}$ ) placed 3.5 cm from one end of the gain medium, and a flat beamsplitter placed 3.0 cm from the other end of the gain medium. The gain medium was a neon-like Selenium plasma, 2 cm long. The spherical mirror was a Mo/Si multilayer ( $d = 111\text{\AA}$ ;  $\gamma \approx 0.4$ ;  $N = 30$ ) deposited on a highly polished BK-7 substrate. Its measured reflectivity at  $206.3\text{\AA}$  was approximately 20%. The beamsplitter was a Mo/Si multilayer ( $d = 114\text{\AA}$ ;  $\gamma \approx 0.5$ ;  $N = 6$ ) supported by a  $400\text{\AA}$  thick silicon nitride membrane. Measured beamsplitter reflectivity and transmission at  $206.3\text{\AA}$  were 15% and 5% respectively.

The single-, double-, and triple- pass amplified signals are easily identified in Fig. 6. The double pass signal is 22X more intense than and the triple-pass signal approximately equal to, the single-pass ASE. The low intensity of the triple pass signal may be attributed to the short duration of the amplifier gain. These experiments provide strong encouragement for the viability of multipass cavity optics. If gain lifetime can be increased without compromising the survivability of the optics, the prospects for soft x-ray lasers with optimized efficiency, divergence, and coherence properties appears promising.

There is a great deal of discussion about the most appropriate near term applications for the x-ray laser and x-ray optics technologies illustrated herein [32]. A particularly promising

proposal, involving a marriage of the laser and optics technologies, is the development of a high intensity ( $>10^{13}$  watt/cm<sup>2</sup>) soft x-ray laser. Such a laser could deliver an unprecedented intensity of narrowband soft x-rays to a target and perhaps launch a new field of nonlinear x-ray optics by allowing the controlled laboratory study of laser-matter interactions at specific x-ray wavelengths at intensities never before achieved in the laboratory.

Conceptually, the high intensity laser would consist of a soft x-ray gain medium within a double or multipass cavity. The radiation emerging from the cavity would be imaged by a reduction lens (a Fresnel zone plate or a series of multilayer coated mirrors) to a small, high intensity spot. The potential for such a device is illustrated in the simple design study that follows:

For a gain medium we choose the well characterized neon-like Strontium laser [33], 5 cm long and approximately 200  $\mu$ m diameter. The dominant line emission is at 164Å. It exhibits a small signal gain of 4.5 cm<sup>-1</sup>, and has an anticipated (i.e. calculated) saturation intensity of  $2 \times 10^{10}$  watt/cm<sup>2</sup>, which should be achieved with a gain-length product of 15. In this design the ASE is double pass amplified using a normal incidence spherical multilayer mirror placed 2 cm from the end of the gain medium. The overall amplification length is therefore 10 cm, and the double pass cavity length is 14 cm. (The x-ray laser target will be redesigned to provide a gain duration greater

than the 470 ps required for the double pass traversal of the cavity). The mirror is assumed to have a reflectivity of 50 % at 164Å.

Under these conditions the radiation emerging from the double pass cavity would have an intensity

$$I_L = I_{\text{sat}} g(L - \ell) R \approx 3 \times 10^{11} \text{ watt/cm}^2$$

where

$$I_{\text{sat}} = \text{saturation intensity} = 2 \times 10^{10} \text{ watt/cm}^2$$

$$g = 4.5 \text{ cm}^{-1}$$

$$L = \text{amplification length} = 10 \text{ cm}$$

$$\ell = \text{saturation length (i.e. } g\ell = 15)$$

$$R = \text{mirror reflectivity} = 0.5$$

and a divergence

$$\Delta\theta = \frac{d_L}{L_0} = 1.4 \times 10^{-3} \text{ radian}$$

where

$$d_L = \text{diameter of laser gain medium} = 200 \mu\text{m}$$

$$L_0 = \text{cavity length} = 14 \text{ cm}$$

or equivalently a solid angle of

$$d\Omega \approx 2 \times 10^{-6} \text{ sr}$$

The laser output beam ( $3 \times 10^{11}$  watt/cm<sup>2</sup>, over a 200  $\mu$ m diameter, with  $2 \times 10^{-6}$  sr divergence solid angle) is imaged by an appropriate reduction camera of f/number,  $f^\#$ , to a spot size,  $d$ , where

$$d = d_L f^\# \Delta\theta.$$

For example, if  $f^\# = 7$

then,  $d \approx 2 \mu\text{m}$

and the focussed intensity is approximately

$$I_{\text{focus}} = 3 \times 10^{14} \text{ watt/cm}^2.$$

This value presumes a 10% first order diffraction efficiency for the reduction lens. It does not account for a possible fill factor loss (i.e. lens diameter smaller than beam diameter) or possible reduction lens damage. These matters are discussed in Appendix 1.

If one were to presume an  $f^\# = 2$  reduction lens, then the focussed spot diameter would be reduced to  $d \approx 0.6 \mu\text{m}$ , and the focused intensity would be

$$I_{\text{focus}} \approx 3 \times 10^{15} \text{ watt/cm}^2,$$

again accounting for lens efficiency but not for fill factor loss or possible lens damage (see Appendix 1).

The numbers presented here are intended only as a crude design study to illustrate the potential of the x-ray laser and optics technologies which are presently available. In the course of development, different design choices may be required, and an actual first generation system may miss the above design

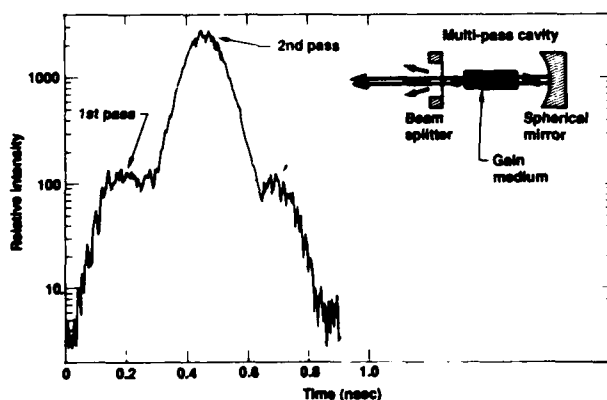


Figure 6: Time resolved multipass cavity output at 205.3Å. Total cavity length was 8.5 cm. The gain medium was a 2 cm long. The reduced amplification for the third and higher number of passes was due to the short gain lifetime.

goals by one or two orders of magnitude. Nevertheless, the message should be clear that the technology is at hand for the development of high intensity x-ray lasers which could parallel the development of high intensity optical lasers.

A reliable assessment of specific applications of the high intensity x-ray laser is difficult. However, one need only recognize how high intensity optical lasers have altered the scientific and technological landscape to appreciate the potential of such a capability at soft x-ray wavelengths. An area of application of particular interest to those of us working in x-ray optics is the generation and study of nonlinear x-ray optical phenomena driven by the large, high frequency electric fields that the high intensity laser could bring to bear on plasma or solid targets. For example, crude estimates of third harmonic generation in an appropriately engineered plasma indicate that at  $10^{14}$  watt/cm<sup>2</sup> perhaps a 1% conversion efficiency into the third harmonic (e.g., 164Å to 54.7Å) could be achieved [34]. While such estimates may at this early stage appear somewhat optimistic, the long term potential of this technology should be clear to anyone with more than a passing interest.

Another technological outgrowth from the recent advances in x-ray optical components (esp. mirrors and beamsplitters) and high brightness x-ray sources (esp. lasers, synchrotron undulators, and laser produced plasmas) will undoubtedly be the emergence of x-ray interferometry as a viable diagnostic tool. Interferometry has been used at visible and ultraviolet wavelengths for the study of aerodynamics and fluid flow, plasma dynamics and atomic phenomena [35]. At hard x-ray wavelengths it has been used to study crystal structure and surface topography [36]. However, to date there has been no significant interferometry at soft x-ray wavelengths owing to the lack of appropriate optics and sources. But, as described in this manuscript, the technological landscape has been changed, and the opportunity for the development of soft x-ray interferometry is upon us.

Short wavelength interferometry will allow the direct measurement of electron density profiles at well above the critical density for large scale laser produced plasmas. Such measurements have in the past been impossible. It is easy to show (see Appendix 2) that in a high density plasma with strong radial density gradients, the quantity

$$\int_0^{L_P} n ds \equiv (nL_P)_{\max} \propto 1/\lambda^2$$

Where  $L_P$  is the size of the plasma,  $n$  is the plasma electron density, and  $\lambda$  is the wavelength of the interferometric probe. This indicates that the maximum plasma "density-length product" which can be measured by the probe beam, increases quadratically as probe wavelength is decreased. The shortest wavelength at which plasma interferometry has been successfully applied is 2660 Å [37]. A decrease in probe wavelength to 131Å (where there exist high efficiency Mo/Si multilayer optics and the neon-like Molybdenum laser) would increase  $(nL_P)_{\max}$  by a factor of more than 400X.

Another intriguing short wavelength diagnostic possibility is Hook Interferometry [38] (i.e. interferometric spectroscopy) to address questions of atomic kinetics in high density plasmas by direct, time resolved measurement of population densities of excited states. The Hook method employs an interferometer (typically a Mach Zehnder, see Fig. 7) illuminated with collimated, broadband radiation. The resulting (blurred) fringe pattern is spectrally dispersed using an imaging spectrometer. The output (which can be displayed across the slit of a soft x-ray streak camera for time resolution) is then simply a linear fringe pattern displayed versus wavelength (see Appendix 3). However, in regions of anomalous absorption (i.e. at wavelengths near transitions) the fringes are not simply linear, in fact they form sharp hook patterns. The separation between the hooks depends on the population difference of the transition and the oscillator strength:

$$\Delta_H \propto \left\{ \int_0^{L_P} N_{ij} f_{ij} ds \right\}^{1/2}$$

where

$L_P$  = length of the plasma probed

$N_{ij} = N_i - N_j$  = population difference (cm<sup>-3</sup>)

$f_{ij}$  = oscillator strength for the transition at  $\lambda_{ij}$ .

Details of the Hook method are presented in Appendix 3. For our purposes here it is worth noting that with this technique the measureable quantity is a simple distance,  $\Delta_H$ , on the detector. As a result, the technique does not require careful photometry or detector linearity (as does absorption spectroscopy). It is best

suited for strong transitions (to give larger  $\Delta H$ ), has large dynamic range (since  $\Delta H \propto (N_{ij})^{1/2}$ ), and (since it measures phase shift away from line center) it is not sensitive to lineshape and can be used on optically thick transitions.

The Hook method is a sophisticated interferometric technique, powerful in its ability to provide detailed spectroscopic information about plasmas, which are otherwise difficult to access. Hook interferometry has never been successfully applied at soft x-ray wavelengths. Nevertheless, with the emergence of high brightness, broadband sources of x-rays (e.g., laser produced plasmas), high quality mirror, beamsplitter and imaging optics, and the strong interest in the atomic kinetics of large scale length plasmas (e.g., x-ray laser gain media), the time is right for a serious reevaluation of its role in modern x-ray optics.

### Summary

This manuscript is an attempt to provide a review of the current state of the art in optics and applications technologies being developed for and in conjunction with the development of

laboratory soft x-ray lasers. Topics covered include zone plate imaging optics, multilayer mirrors, beamsplitters, and holographic optical components, x-ray laser cavities and interferometric techniques for measurement of electron density profiles and atomic kinetics in high density, large scale plasmas.

### Acknowledgements

This manuscript is a distillation of the dedicated professional efforts of the members of the advanced x-ray optics group: A.M. Hawryluk, D.G. Stearns, D.P. Gaines, G. Howe, S. Hill, E. Utterback, W. Cook, H. Petersen, R. Hicks. In addition I would like to acknowledge the encouragement and support of E.M. Campbell and the cooperation and collaboration of D.L. Matthews and his x-ray laser group, without which much of this work could not have been accomplished.

This work was performed under the auspices of the U.S. Department of Energy by the Lawrence Livermore National Laboratory under contract number W-7405-Eng-48.

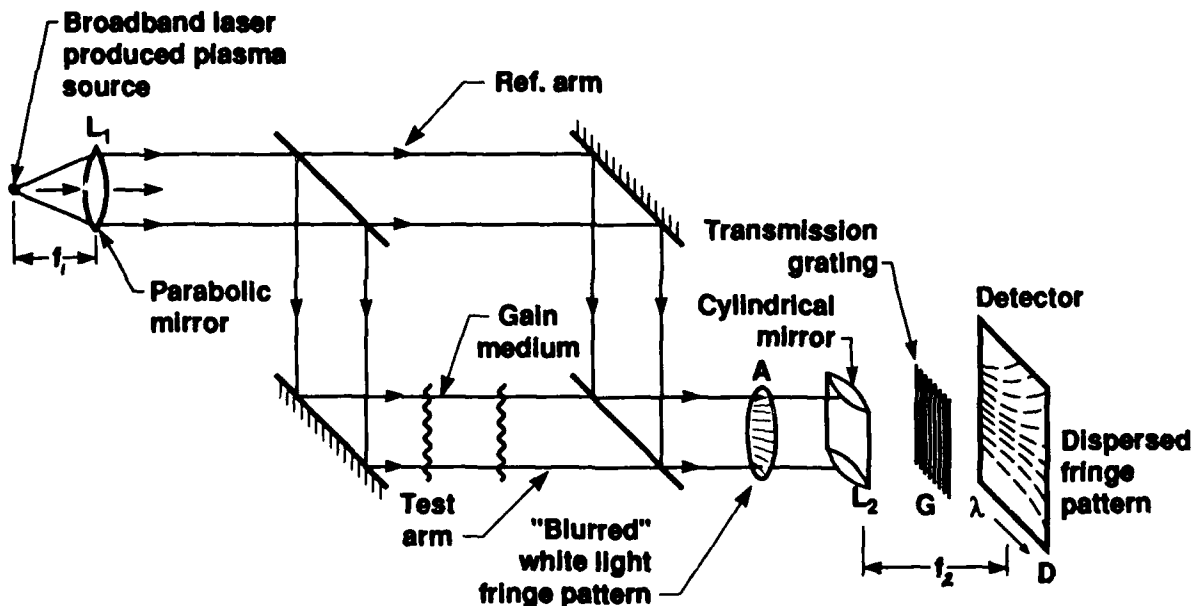


Figure 7: Schematic illustration of a Mach-Zehnder set-up for Hook Interferometry of an x-ray laser gain medium.

## References

1. Applications of Thin Film Multilayered Structures to Figured X-Ray Optics, G. Marshall, editor; Proceedings SPIE **563** (Bellingham, Washington, 1985).
2. Multilayer Structures and Laboratory X-Ray Laser Research, N.M. Ceglio, P. Dhez, editors; Proceedings SPIE **688** (Bellingham, Washington, 1986).
3. D.T. Atwood, et al., "X-Ray Microscopy for the Life and Physical Sciences", this conference proceedings.
4. N. M. Ceglio, "Advances in X-Ray Optics - '87, in X-Ray Microscopy II, D. Sayre, M. Howells, J. Kirz, and H. Rarback, editors (Springer Verlag, New York, 1987) p.130.
5. A. M. Hawryluk, N. M. Ceglio, and D. G. Stearns, "Applications of Microfabrication Technology to X-Ray Laser Cavities", to be published in Journal of Vacuum Science Technology, Nov.-Dec., 1988.
6. N. M. Ceglio, "Revolution in X-Ray Optics" to be published in Journal of X-ray Science and Technology, Jan., 1989.
7. N. M. Ceglio, "Impact of Microfabrication Technology on X-Ray Optics" in Low Energy X-ray Diagnostics, D.T. Atwood and B. L. Henke, editors (AIP, New York, 1981) p. 210.
8. J. Kirz, "Phase Zone Plates for X-rays and the Extreme UV", JOSA **64**, 301 (1974).
9. M. Young, "Zone Plates and Their Aberrations", JOSA **62**, 972 (1972).
10. N.M. Ceglio and H.I. Smith, "An Efficient Lensing Element for X-rays" in Proceedings VIII Int'l Conf. on X-ray Optics and Microanalysis, D.R. Beaman, R.E. Ogilvie, and D.B. Wittry, editors (Pendell Publishing, Midland, Michigan, 1980) p.255.
11. V. Bogli, P. Unger, and H. Beneking, et al., "Micro Zone Plate Fabrication by 100 KeV Electron Beam Lithography" in X-Ray Microscopy II, p.80.
12. H. Rarback, et al., "A Scanning X-ray Microscope with 75nm Resolution" Review of Sci. Instr. **59**, 52 (1988); also Y. Vladimirovsky, et al., "Zone Plate Lenses for X-ray Microscopy", Nucl. Instr. and Meth. **A266**, 324 (1988).
13. N.M. Ceglio, A.M. Hawryluk, D.G. Stearns, M. Kuhne, and P. Muller, "Demonstration of Guided-Wave Phenomena at Extreme Ultraviolet and Soft X-ray Wavelengths" Opt. Lett. **13**, 267 (1988).
14. D.L. Matthews, et al., "Demonstration of a Soft X-ray Amplifier", Phys. Rev. Lett. **54**, 110 (1985).
15. S. Suckewer, et al., "Amplification of Stimulated Soft X-Ray Emission in a Confined Plasma Column", Phys. Rev. Lett. **55**, 1753 (1985).
16. B.J. MacGowan, et al., "Observation of soft x-ray amplification in neonlike molybdenum", J. Appl. Phys. **61**, 5243 (1987).
17. A.K. Petford-Long, M.B. Stearns, C.H. Chang, et al., "High Resolution Electron Microscopy Study of X-ray Multilayer Structures", J. Appl. Phys. **61**, 1422 (1987).
18. D.G. Stearns, et al., "TEM and X-ray Analysis of Multilayer Mirrors and Beamsplitters" in Multilayer Structures and Laboratory X-Ray Laser Research, N.M. Ceglio and P. Dhez, editors, Proceedings SPIE **688**, 91 (Bellingham, Washington, 1986).
19. M. Kuhne, et al. "Characterization of Multilayer Structures for Soft X-ray Laser Research", Proceedings, SPIE **688**, 76 (1986).
20. A.M. Hawryluk, et al., "Soft X-ray Beamsplitters and Highly Dispersive Multilayer Mirrors for Use as Soft X-Ray Laser Cavity Components", Proceedings, SPIE **688**, 81 (1986).
21. N.M. Ceglio, et al., "Soft X-ray Laser Cavities", J. de Physique (Paris) **C6**, 277 (1986).
22. E.I. Bromley, J.N. Randell, D.C. Flanders, and R.W. Mountain, J. Vac. Sci. Tech. **B1**, 1346 (1983).
23. K. Bean, "Anisotropic Etching of Silicon", IEEE Trans. Elect. Devices, **ED-25**, 1185 (1978).
24. E. Spiller and A.E. Rosenbluth, "Determination of Thickness Errors and Boundary Roughness from the Measured Performance of a Multilayer Coating" Proceedings, SPIE **563**, 221 (1985).
25. B.R. Brown and A.W. Luhmann, Appl. Opt. **5**, 967 (1966).
26. B.J. MacGowan, et al., "Demonstration of Soft X-Ray Amplification in Nickel-Like Ions", Phys. Rev. A **59**, 2157 (1987).
27. N.M. Ceglio, et al., "X-ray Laser Cavity Experiments", SPIE Proceedings **688**, 44 (1986).
28. R.M. More, K.H. Warren, and Z. Zinamon, "Damage to Multilayer Mirrors in a Hostile Environment", SPIE Proceedings **688**, 134 (1986).
29. N.M. Ceglio, D.P. Gaines, R.A. London, J.E. Trebes, and D.G. Stearns, "Time Resolved Measurement of Double Pass Amplification of Soft X-Rays" to be published in Applied Optics, December, 1988.
30. N.M. Ceglio, D.P. Gaines, D.G. Stearns, and A.M. Hawryluk, "Double Pass Amplification of Laser Radiation at 131Å" to be published in Optics Communications 1988/89.

31. N.M. Ceglio, D.G. Stearns, D.P. Gaines, A.M. Hawryluk, and J.E. Trebes, "Multipass Amplification of Soft X-rays in a Laser Cavity", Opt. Lett. **13**, 108 (1988).
32. Proceedings of the First Symposium on the Applications of Laboratory X-Ray Lasers, N.M. Ceglio, editor, Lawrence Livermore National Laboratory Report #CONF-850293, (1985).
33. B.J. MacGowan, et al., "Progress Toward a 44Å Laser", this conference proceedings.
34. Private communication with D.G. Stearns, M. Perry, and O. Landen, Lawrence Livermore National Laboratory.
35. Physical Measurements in Gas Dynamics and Combustion, R.W. Landenburg, B. Lewis, R.N. Pease, and H.S. Taylor, editors (Princeton University Press, 1954).
36. D.P. Siddons, "Some Applications of X-Ray Interferometry" in Low Energy X-ray Diagnostics, p. 236.
37. D.T. Attwood, D.W. Sweeney, J.M. Auerbach, and P.H.Y. Lee, "Interferometric Confirmation of Radiation Pressure Effects in Laser Plasma Interactions", Phys. Rev. Lett. **40**, 184 (1978).
38. The use of the Hook Method for diagnosis of x-ray laser media was first proposed to me in a private communication by Dr. M. Kuhne, PTB Institute, Berlin.
39. W.C. Marlowe, "Hackenmethode", Appl. Opt. **6**, 1715, (1967).

## Appendix I

Details are provided for a zone plate reduction lens discussed with regard to the high intensity laser. In the calculations that follow all numbers are liberally rounded off and are therefore approximate.

Example 1: In this example an  $f \# = 7$  lens is presumed. Such a lens will have a minimum zone width of

$$\Delta r \approx 1150 \text{Å}$$

since

$$f \# = \frac{\Delta r}{\lambda}$$

for the zone plate lens. In this case it is acting as a simple reduction lens imaging the 200  $\mu\text{m}$  output aperture of the x-ray laser gain medium down to a 2  $\mu\text{m}$  diameter spot. The reduction factor is 100x so that

$$L \approx 100 f$$

where

$L$  = distance from x-ray laser to zone plate lens

$f$  = zone plate lens focal distance.

For the zone plate lens

$$f = f \# d_{zp}$$

where  $d_{zp}$  = diameter of the zone plate lens.  
 $d_{zp}$  is a design choice depending on the number of zones:  $d_{zp} = 4N \Delta r$  where  $N$  = number of zones.

We choose  $N = 5000$ , a difficult but not impossible fabrication challenge. The  $d_{zp} \approx 2.3 \text{ mm}$ ,  $f \approx 1.6 \text{ cm}$ ,  $L \approx 160 \text{ cm}$ . Now the x-ray laser beam size at 160 cm is

$$d_B = \frac{L_o + L}{L_o} d_L$$

where

$d_L$  = diameter of gain medium = 200  $\mu\text{m}$

$L_o$  = cavity length = 14 cm.

So,  $d_B \approx 2.5 \text{ mm}$ .

The fill factor for the zone plate lens is

$$F = \left( \frac{d_{\text{ap}}}{d_B} \right)^2 \approx .85$$

So that, for this example, the intensity at focus would be 85% of the  $3 \times 10^{14} \text{ W/cm}^2$  quoted in the text. Optical damage is always a consideration in dealing with high intensity laser light. The laser intensity at the plane of zone plate is

$$I_D = I_L \left( \frac{d_L}{d_B} \right)^2$$

where

$I_D$  = intensity at the zone plate which might possibly damage the optic

$I_L$  = output laser intensity =  $3 \times 10^{14} \text{ W/cm}^2$   
 In this case

$$I_D \approx 2 \times 10^9 \text{ W/cm}^2$$

Clearly such an x-ray intensity has the potential for damaging the zone plate lens.

If the damage (e.g., zone plate disassembly) occurs on a time scale long compared to that needed to modulate and thereby focus the x-rays, then it may be required to replace the lens after each laser shot (not a great inconvenience, since the laser target and cavity mirror will also be destroyed on each shot). However, if the damage process interferes with the focussing process, different design choices may be required. Such issues are best addressed experimentally.

Example 2:

The same calculations performed for an  $f \# = 2$ ,  $N = 5000$  lens are as follows:

$\Delta r \approx 325 \text{Å}$ ,  $d_{zp} \approx 650 \mu\text{m}$ ,  $f \approx 1.3 \text{ mm}$ .



The laser output is imaged down to a  $0.6 \mu\text{m}$  diameter spot. The reduction factor is  $333 \times$  so

$$L \cong 43.3 \text{ cm.}$$

Beam size at the lens is

$$d_B \cong 819 \mu\text{m.}$$

The fill factor is  $F \cong 0.63$ .

So that for this example the intensity at focus would be 63% of the  $3 \times 10^{15} \text{ W/cm}^2$  quoted in the text. The laser intensity at the plane of the zone plate is

$$I_D \cong 2 \times 10^{10} \text{ W/cm}^2.$$

## Appendix II

Interferometric Measurement of Radial Electron Density Profiles:

This technique has been applied by Attwood, et al. [37] for the diagnosis of laser produced plasmas with a probe beam of  $2660 \text{ \AA}$ . They used a double exposure holographic interferometry technique.

For convenience consider a cylindrically symmetric plasma of length,  $L_p$ , with radial electron density profile of scale length,  $l$ . The electron density profile may be written

$$n(r) = n_c \exp \left\{ -\frac{r-r_c}{l} \right\}$$

where

$n(r)$  = electron density

$n_c$  = critical electron density =

$$\frac{1.1 \times 10^{13}}{\lambda} (\text{cm}^{-3})$$

$r_c$  = radius of the critical electron density

$\lambda$  = probe wavelength.

Now the refractive index (real) of the plasma is

$$K = \left( 1 - \frac{n}{n_c} \right)^{1/2}$$

A ray passing through the plasma will be deflected by an angle  $\Delta\theta$  given by

$$\Delta\theta = \int_0^{L_p} \frac{\Delta_{\perp} K}{K} ds$$

which is evaluated as

$$\Delta\theta \cong \frac{1}{2} \frac{L_p}{l} \frac{n}{n_c}$$

the radiation passing through (and deflected by) the plasma is collected by an x-ray lens of

$f/\text{number}$ ,  $f\#$ . The largest deflection angle collected determines the maximum value of  $nL_p$ :

$$\Delta\theta_{\max} = \frac{1}{2f\#}$$

so

$$(nL_p)_{\max} = \frac{1.1 \times 10^{13} l}{f\#^2 \lambda^2} (\text{e/cm}^2)$$

A useful example:

For  $\lambda = 131 \text{ \AA}$

$l = 100 \mu\text{m}$  (typical x-ray laser gain medium)

$f\# \cong 3$  (i.e. zone plate lens with  $\Delta r \cong 400 \text{ \AA}$ )

$$(nL_p)_{\max} \cong 2 \times 10^{22} (\text{e/cm}^2)$$

so for  $L_p \cong 2 \text{ cm}$  (a very large scale plasma) one could access electron densities as great as  $10^{22} \text{ e/cm}^3$ .

## Appendix III

Hook Interferometry at Soft X-ray Wavelengths:

The details of the hook method of interferometry are well documented elsewhere [39]. The intention here is to provide a brief summary of the technique, paying specific attention to those details relevant to its implementation at soft x-ray wavelengths. A proposed Hook interferometer layout is presented in Fig. 7. Shown is a Mach Zehnder interferometer utilizing multilayer mirrors and beamsplitters (presumed  $25 \text{ \AA}$  bandwidth at a wavelength of choice). The system is illuminated with broadband emission from a small laser produced plasma. The emission is collimated by a grazing incidence reflection parabolic mirror ( $L_1$ ) with focal length,  $f_1$ . The interferometer has a reference arm and test arm (in which is placed the plasma to be probed, e.g., an x-ray laser gain medium) which are presumed slightly tilted to provide reference fringes at plane (A) prior to placing the plasma in the test arm. As shown, the "white-light" fringe pattern at plane (A) is blurred because the fringe spacing is wavelength dependent. The fringe pattern is focussed (in one dimension) onto a detector (D) using a grazing incidence reflection cylindrical mirror ( $L_2$ ) of focal length  $f_2$ .

Between  $L_2$  and (D) is placed a linear transmission grating (G) (with period  $p$ ) to disperse the fringe pattern. The dispersed fringe pattern, as illustrated, is linear and unblurred (with no plasma in the test arm). The fringe pattern may be analyzed as follows: On the optical axis of the interferometer the fringe number,  $P_0$ , is related to the optical path difference

$$P_0 \lambda = (n - n^*) L$$

where

$n$  = refractive index in test arm

$n^*$  = refractive index in reference arm

$L$  = geometrical path length

At a distance "Y" away from the optical axis the fringe number,  $p$ , is given by

$$Y = (p - P_0)W$$

where

$W = \lambda/\phi$ , is the fringe spacing

$\phi$  = tilt angle between the reference and test arm beams.

So

$$Y = \frac{P\lambda}{\phi} - (n - n^*) L/\phi \quad (A-1)$$

where

$$P = 0, \pm 1, \pm 2, \dots$$

yielding a fringe pattern in the  $(Y, \lambda)$  plane having slope  $(P/\phi)$  and intercept,  $-(n - n^*) L/\phi$ .

If we now introduce a plasma into the test arm, its refractive index is

$$\tilde{n} = n + i\beta$$

where the real part of the refractive index (near a transition  $\lambda_{ij}$  and neglecting electron density effects) may be written

$$n(\lambda) = 1 + \frac{r_0}{4\pi} \frac{(N_i - N_j) f_{ij} \lambda_{ij}^3}{(\lambda - \lambda_{ij})} \quad (A-2)$$

where

$r_0$  = classical electron radius =  
 $2.8 \times 10^{-13} \text{ cm}$

$f_{ij}$  = oscillation strength

$N_i$  = population density of state  $i$

$\lambda_{ij}$  = transition wavelength between states  
 $i$  and  $j$  ( $j > i$ )

If we next substitute equation (A-2) into equation (A-1), and set the derivative

$$\frac{dY}{d\lambda} = 0,$$

this defines the hook positions. Then the separation between the hooks in wavelength space is:

$$\Delta_H = \left\{ \frac{r_0 \lambda_{ij}^3}{\pi |p|} \int_0^L (N_i - N_j) f_{ij} ds \right\}^{1/2} \quad (A-3)$$

We can illustrate the application of equation (A-3) by a hypothetical example: Assume we are operating in a spectral band (135Å - 160Å) with

$$\lambda_{ij} \approx 150 \text{ Å}$$

$$\Delta N_{ij} \approx 10^{15} \text{ cm}^{-3}$$

$$f_{ij} \approx 0.4$$

$$L_p \approx 1 \text{ cm (x-ray laser gain medium)}$$

$$|p| \approx 10$$

$$f_1 \approx 30 \text{ cm}$$

$$f_2 \approx 100 \text{ cm}$$

$$p = 2000 \text{ Å}$$

We presume cylindrical mirror,  $L_2$ , has a 50  $\mu\text{m}$  focal spot matching the spatial resolution of the streak camera detector, D. (Since only hook separation is measured, one spatial dimension is adequate for the detector, providing a second dimension for time resolution.) The dispersion of the transmission grating spectrometer is

$$\frac{dx}{d\lambda} \approx \frac{f_2}{p} = 500 \mu\text{m}/\text{Å}$$

The hook separation in wavelength space is:

$$\Delta_H \approx \frac{2.8 \times 10^{-13} (1.5 \times 10^{-6})^3 10 (0.4)^2}{\pi 10}^{1/2}$$

$$\Delta_H \approx 0.35 \text{ Å}.$$

In the spatial plane of the detector

$$\Delta_H = 0.35 \left( \frac{dx}{d\lambda} \right) \approx 175 \mu\text{m}$$

a hook separation easily resolved by the 50  $\mu\text{m}$  resolution of the streak camera.

In such a hypothetical experiment one could in principle observe the time varying hook separations on a variety of lines (within the 25Å bandwidth of the optics) simultaneously. This would provide direct measurement of the temporal history of the populations of a number of states in the plasma, perhaps observing directly the creation of inverted populations on laser lines.

Throughout this analysis it is presumed that near transitions of interest the variation in refractive index due to anomalous dispersion is much greater than that produced by gradients in plasma density.

## Sub-Nanosecond, Photon Counting, Imaging, X-Ray Camera

D. A. Whelan,\* M. R. Carter, D. F. Price, and R. E. Stewart

*University of California, Lawrence Livermore National Laboratory  
P.O. Box 808, L-43, Livermore, California 94550*

### ABSTRACT

A high temporal bandwidth x-ray detector has been developed for time resolved one dimensional x-ray imaging experiments. The detector serves as a high gain, high quantum efficiency preamplifier for a streak camera, and consists of a reflective x-ray photocathode, an active microchannel plate, optional electrostatic optics, and a sub-nanosecond phosphor. The optional electrostatic optics allows the detector to be used for either two dimensional imaging with a 100 picosecond framing (without focusing optics), or as a high gain one dimensional imaging detector, with either a 100 picosecond gated Reticon camera, or a streak camera. Other versions of the one dimensional detector have been developed, in which the microchannel plate which employs a reflective photocathode on the front surface of the microchannel plate, is replaced with a transmission photocathode consisting of a photocathode deposited on a thin polypropylene foil. The detector exhibits a time resolution of 400 picoseconds FWHM, a spatial resolution of 350  $\mu\text{m}$  with an electron compression of ten to one (100 $\mu\text{m}$  resolution without compression). Quantum efficiency of 40% have been achieved, and effective quantum efficiency greater than 100% have been achieved with the one dimensional electrostatic optics. Data will be presented on the efficiency, time response and spatial resolution of the one dimensional detectors.

### INTRODUCTION

The development of ultra-fast, high resolution, sensitive x-ray detectors has become crucial to the development of advanced diagnostics for research in the fields of high density plasma physics, x-ray lasers and radiation transport. New instruments are being developed to allow spatially - temporally resolved, spectrally - temporally resolved, and spectrally - spatially - temporally resolved measurements of the x-ray emission from laser produced plasmas.

Time resolutions of 100 ps have been achieved using gated microchannel plate framing cameras<sup>1</sup>, these detectors are sensitive but require unique electronics to achieve good resolution and sensitivity. Streaked x-ray spectrometers have been developed, but have suffered from poor sensitivity.

We have developed a ungated microchannel plate x-ray detector with time resolution of about 400 ps. This allows high resolution spectral or spatial measurements to be made with good continuous time resolution. The detector spectral sensitivity is determined by the photocathode, and can be tailored to exhibit a desired response characteristics. We have used CsI and CuI photocathodes, for their high quantum efficiency, electrostatic focusing, and efficient fast phosphors such as Indium doped CdS or WL1201 to make the detector sensitive enough to detect single photons.

## X-RAY CAMERA DESIGN

The x-ray camera consists of a front surface reflective x-ray photocathode coated on the surface of a microchannel plate, focusing electrodes, and a metalized phosphor coated on a shaped fiber optic face plate, which serves as the anode. A schematic representation is shown in figure 1.

X-rays are incident onto the microchannel plate photocathode at an angle of  $35^\circ$  off normal, upon striking the photocathode a photoelectron is ejected. The detector is operated off normal because only photoelectrons ejected from within the channels are collected and amplified, the photoelectrons originating from the interchannel webbing have a vanishing small probability of traveling to the channels. Thus operating the detector off normal increases the effective detector area.

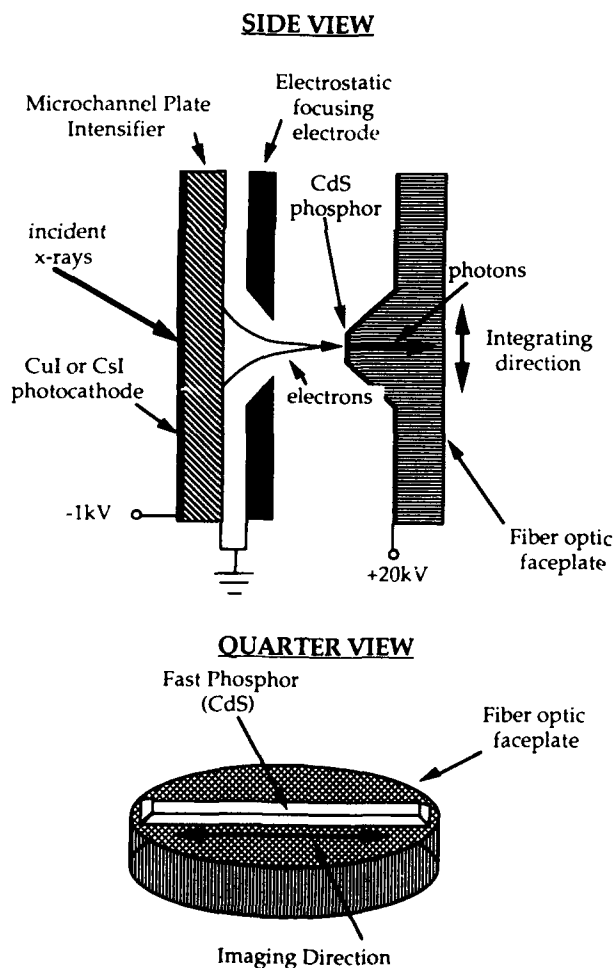


Figure 1. Schematic of a microchannel plate intensified x-ray camera.

The gain of the MCP, and thus the gain of the camera is determined by the bias voltage applied across the plate, gains of 100 to several 1000's are attainable. Electrons are emergent from a region  $5\text{ mm} \times 40\text{ mm}$  (integrating direction  $\times$  imaging direction, see figure #1), and are line focused onto the anode,  $0.5\text{ mm} \times 40\text{ mm}$ . This compression of the electrons in one dimension allows for enhanced signal sensitivity and an effective increase in the quantum efficiency. The focusing is stigmatic and preserves the spatial resolution in the imaging direction.

The anode consists of a shaped fiber optic coated with transparent metal film, a thin layer of fast phosphor, and finally over coated with a thin top layer of Aluminum. The Al also acts to block visible light from the fiber optic array, and to reflect phosphor emission back towards the fiber optic output. The fiber optic faceplate acts not only as the anode, but also allows for transmission of the light out of the vacuum system.

The emergent photons are then coupled to a coherent fiber optic bundle, whose other end is coupled to the front end of a Streak Camera. We have developed several other versions of this detector including a detector without the electron focusing electrodes for use as a two dimensional framing camera and one which uses a polypropylene supported transmission photocathode without microchannel plate.

## X-RAY PHOTOCATHODES

A reflective photocathode is constructed using an uncoated microchannel plate to which the active area is coated with  $2000\text{ }\mu\text{m}$  of gold. The gold layer provides a known photo electron yield for high energy x-rays which penetrate the top photocathode surface, and as an electrode to bias the MCP. The gold could also be replaced with poorer photo emitter to reduce detector sensitivity to high energy photons. The gold is deposited on the front surface at a grazing angle ( $15^\circ$ ) to prevent the gold from traveling down the microchannels. The CsI (CuI) photocathode is deposited on top of the gold at  $45^\circ$  using the technique developed by Whiteley et al. <sup>3</sup>

Several different x-ray photocathodes have been tried including Au, CuI, and CsI. Typical thicknesses for CuI and CsI are about  $.1\text{ }\mu\text{m}$ . The photocathode is deposited on the front of the MCP at a  $45^\circ$  angle. This is the nominal angle of incidence of the x-rays for most of our immediate applications. The expected front

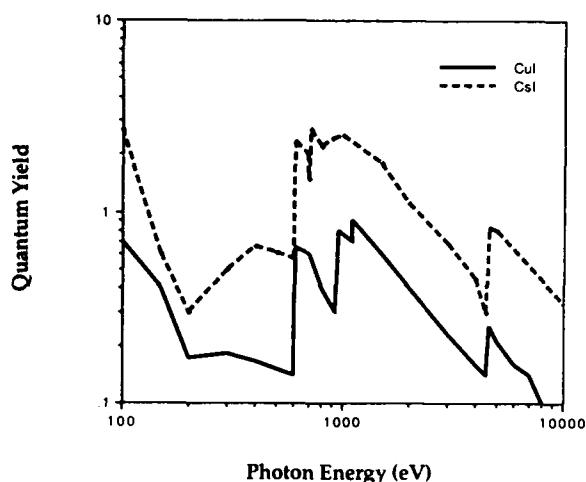


Figure 2. Expected front surface quantum yield for CuI and CsI photocathodes.<sup>2</sup>

surface quantum yields as measured by Henke<sup>2</sup> for CuI and CsI versus incident x-ray energy are shown in Fig. 2. CsI is expected to be about a factor of five more sensitive for x-rays from 600 eV to 1,000 eV.

A gold electrode is also deposited on the back surface of the MCP at an angle of  $45^\circ$ , this angle provides a small amount of gain spoiling at the end of the MCP reducing the angular spread of the electrons. Thus the electrons emitted from the photocathode surfaces within the channel walls are multiplied as they travel down the microchannels. Electron gains greater than 1000 can be expected from the MCP depending on the bias voltage.

The transmission photocathode design consisted of a thin polypropylene substrate (0.5  $\mu\text{m}$ ), onto which a 0.1  $\mu\text{m}$  Al electrode is deposited on the back (fiber optic) side. The CsI (CuI) photocathode is then deposited on top of the Al to a thickness of 1000 Å. The polypropylene and the Al are fairly transparent to x-rays above 400 eV (factor of 2 loss), thus the x-ray response is determined by the photocathode yield, which is well represented by the front surface yield shown in figure #2. The transmission photocathode design is simpler in construction and operation, but does not provide a variable gain detector.

### ELECTRON OPTICS

When resolution in only one dimension is desired one can further enhance the efficiency of the detector by compressing the electron current out of

the back of the MCP in one dimension. We have modeled the electron trajectories between the MCP and the phosphor for various electrode geometries.

Figure 3 shows a typical set of electron orbits between the MCP and the phosphor. In this case the back of the MCP and the focusing electrodes are grounded. The phosphor coated fiber faceplate is biased to +20 kV. The peak electric field between the focusing electrode and the faceplate is 6500 V/mm. We assume the electrons are emitted from the MCP normal to the surface with energy of 75 eV. We find, for this geometry, we can collect electrons from a 4.7 mm wide area of the MCP onto the 500  $\mu\text{m}$  wide area on the faceplate. This corresponds to a compression ratio of 9.4.

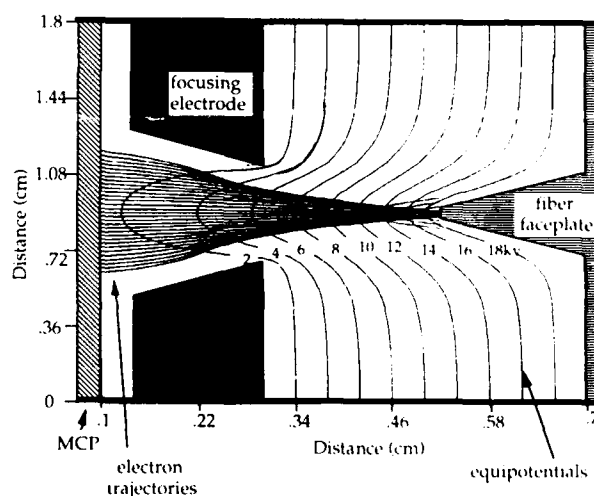


Figure 3. Electron trajectories between the MCP and the phosphor coated faceplate.

We have also studied the electron trajectories for more realistic initial conditions including, variations in initial energy and angle. We have found these effects to be relatively small over typical ranges expected for the output of the MCP.

We can also estimate the loss of spatial resolution in the direction perpendicular to the compression direction. We can calculate the transit time of the electrons from the MCP to the phosphor, assume an initial direction and velocity and calculate how far the electron travels in the resolution direction from the time it leaves the MCP until it impacts the phosphor. Typical initial angles are less than or equal to 10 degrees. Initial energies are typically less than 100 eV. This corresponds to a displacement of

about 100  $\mu\text{m}$ . The spatial resolution of the detector FWHM should be on the order of 200  $\mu\text{m}$ .

### PHOSPHORS

We examined two sub-nanosecond phosphors, which were developed by W. Lehman, for sensitivity, temporal emission characteristics, and spectral character. They were Indium doped Cadmium Sulfide (CdS) or WL1198 and Zinc oxide or WL1201. Indium doped CdS exhibited a fast emission at 520 nm (green), while WL1201 emits at 390 nm (blue) with a slightly longer time constant. The efficiency of WL1201 is approximately  $10^{-3}$  into  $4\pi$ , and that of WL1198 is about twice that.

Single crystal cadmium sulfide has been shown to emit in the red with a characteristic time of about 5  $\mu\text{sec}$ .<sup>4</sup> The red emission is suppressed for properly prepared indium doped CdS. By selecting only the smallest particles (diameter < 10  $\mu\text{m}$ ) in a batch of indium doped CdS, we are able to create a phosphor with both a fast green component (400 ps, 520 nm) and a slow red component (5  $\mu\text{sec}$ , 700 nm). Figure 4 shows the spectral output of small grain size indium doped CdS, showing a narrow emission centered at 520 nm and a much broader component centered near 700 nm. The spectrum in the red agrees well with that measured by Rotter.<sup>4</sup>

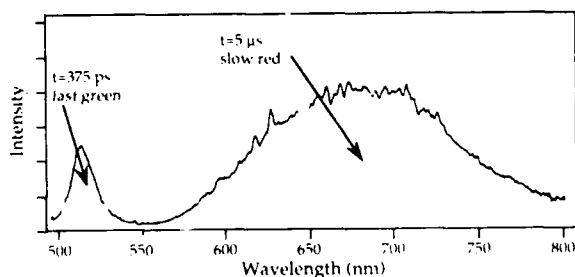


Figure 4. Spectral output of small grain size Indium doped Cadmium Sulfide.

By selecting only CdS particles larger than 10  $\mu\text{m}$ , we can eliminate the red emission. The resulting phosphor has a time response of about 400 ps. Our speculation is that the smaller particles are not properly doped with Indium resulting in significant red emission.

### EFFICIENCY

The efficiency,  $\epsilon$ , of the detector is defined as the ratio of the output fluence of the phosphor (into  $4\pi$ ) to the input x-ray fluence as shown below.

$$\epsilon = \frac{E_{\text{out}}}{E_{\text{in}}} = \frac{(\text{output fluence into } 4\pi \text{ in ergs/cm}^2)}{(\text{incident fluence in ergs/cm}^2)} \quad (1)$$

We have measured the detector efficiency and time resolution at the Janus laser facility at LLNL. The Janus laser is a frequency doubled YAG laser with output energies in the range of .01 J to 60 J at 532 nm. The 532 nm laser output was focused onto a Titanium target to approximately a 70  $\mu\text{m}$  diameter spot. The nominal laser energy was 0.1 J in 125 ps resulting in laser intensities of about  $2 \times 10^{13} \text{ W/cm}^2$ .

The resulting x-rays emitted from the target are viewed by the detector through a 100 eV wide bandpass filter consisting of a grazing incidence carbon mirror (1.9 degree incident angle) and a filter set containing Be, Fe, and Al filters. The transmitted x-rays with energies of  $750 \pm 50$  eV are incident on the detector. The incident x-ray fluence is measured just in front of the detector with a calibrated PIN diode. The PIN diode calibration is  $0.29 \text{ A/(W/cm}^2)$  for 700 eV x-rays.

Since the PIN diode does not have sufficient time response to follow the incident x-ray pulse, we must integrate the total current output from the PIN diode to determine the total x-ray fluence incident on the detector. We can then calculate the input x-ray flux in  $\text{W/cm}^2$  by dividing the total energy deposited by the time duration of the x-ray pulse as measured by a fast x-ray diode.

We measured the output of the detector with a microchannel plate intensified streak camera. The readout system is shown in Figure 5. The output light of the phosphor collected by a coherent fiber optic faceplate with a numerical aperture of .66. The light out of the faceplate is transferred to the streak camera through a 200  $\mu\text{m}$  core quartz fiber (NA .27).

We can calculate the output energy of the phosphor from the energy collected by the streak camera using the following expression:

$$E_{\text{sc}} (\text{ergs}) = \frac{E_{\text{out}}(4\pi) (\text{NA})^2 A_{\text{fiber}}}{2} = \frac{E_{\text{out}}(4\pi) \times 1.145 \times 10^{-5} \text{ cm}^2}{2} \quad (2)$$

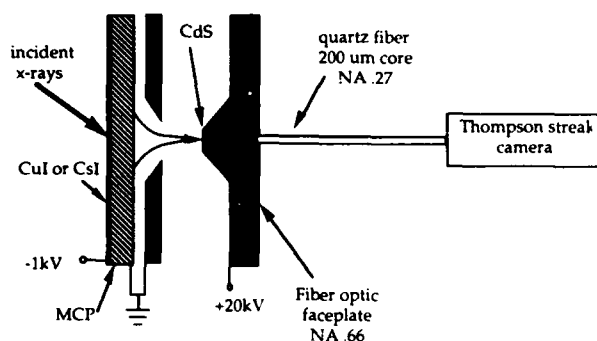


Figure 5. Detector-streak camera calibration setup

where  $E_{SC}$  is the energy (in ergs) recorded by the streak camera, NA is the numerical aperture of the quartz fiber (.27),  $A_{fiber}$  is the active area of the fiber ( $3.14 \times 10^{-4} \text{ cm}^2$ ). Equation 2 neglects any losses in the optical chain and assumes the output of the phosphor is isotropic.

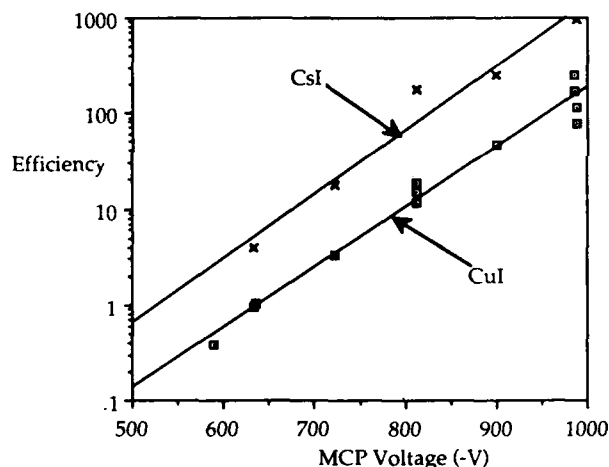


Figure 6. Detector efficiency for CsI and CuI photocathodes vs. MCP voltage

Figure 6 shows the measured detector efficiency, as defined in equations 1 and 2, for various microchannel plate voltages for both CuI and CsI photocathodes. For this data set the phosphor voltage was held constant at 17 kV. We find that the detector efficiency increases by about a factor of 2 for every 50 V increase in the MCP voltage. Peak efficiency of 1000 have been attained with CsI photocathode. We find that CsI is about a factor of 5 more efficient than CuI. This is in agreement with Henke's photocathode response data shown in figure 2.

We have also measured the efficiency of the detector versus phosphor voltage. Figure 7 shows the measured variation in efficiency vs. phosphor voltage for a fixed microchannel plate voltage (-985 V) and CuI photocathode. We find that the efficiency varies linearly with phosphor voltage with a threshold of about 9 kV. This threshold is due to electron energy deposition in the Al layer overcoating the phosphor.

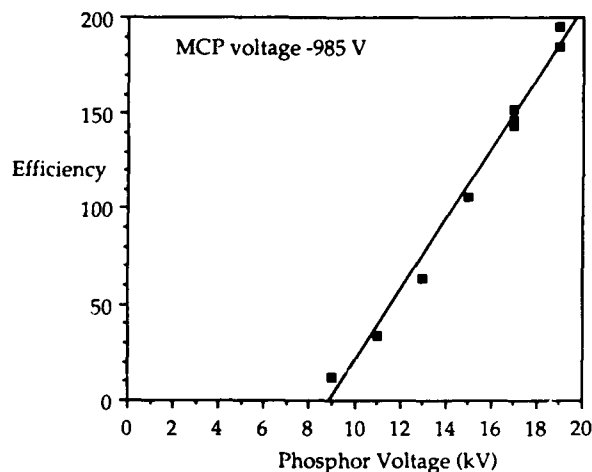


Figure 7. Measured detector efficiency for CuI photocathode vs. phosphor voltage (MCP voltage = -985 V)

### SPATIAL RESOLUTION

The spatial resolution of the detector is determined primarily by the electron focusing optics. The spatial resolution depends upon the velocity and angular distributions of the electrons emitted from the microchannel plate, and the flight time from the MCP to the phosphor coated faceplate. In order to integrate over a large area of the microchannel plate, we need a large electron compression between the output of the MCP and the phosphor. Large compression factors can be obtained by increasing the distance between the MCP and the phosphor. This results in longer electron flight times and thus decreasing spatial resolution. Our present application requires spatial resolution better than 500  $\mu\text{m}$ , and electron compression factors of about 10.

We have measured the spatial resolution of the detector by placing a 140  $\mu\text{m}$  wide slit just in front of the microchannel plate. A DC x-ray source illuminated the detector through the slit.

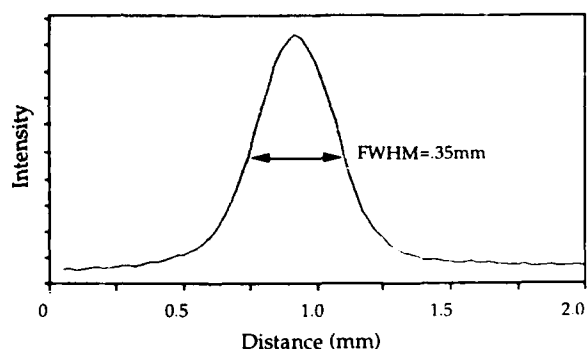


Figure 8. Output spatial profile of the detector illuminated by a 140  $\mu\text{m}$  wide slit.

The slit was oriented perpendicular to the imaging direction. The spatial profile of the light output was measured using a one dimensional, microchannel plate intensified, Reticon camera. Figure 8 shows the output of the detector in the imaging direction. We find that the full width half maximum of the output peak is about 350  $\mu\text{m}$ . We can estimate the resolution of the detector by subtracting the finite width of the slit in quadrature. We find that the spatial resolution is 320  $\mu\text{m}$ .

$$R = \sqrt{(350 \mu\text{m})^2 - (140 \mu\text{m})^2} = 320 \mu\text{m} \quad (3)$$

#### TIME RESPONSE

We have measured the detector time response at the Janus laser facility. The incident x-ray pulse has been measured at 215 ps full width half maximum. The output of the detector is sent to a Thomson streak camera through a 10 foot long quartz fiber array. The modal dispersion in the quartz fiber array has been measured at 250 ps. The streak camera has a time resolution of 8.7 ps. The detector output measured by the streak camera is shown in figure 9. The measured rise time (10% to 90%) is about 230 ps. The full width half maximum is 500 ps. We can calculate the detector time response by subtracting the modal dispersion in the fibers, and the finite incident pulse width.

$$T = \sqrt{(500 \text{ ps})^2 - (250 \text{ ps})^2 - (215 \text{ ps})^2}$$

$$T = 375 \text{ ps} \quad (4)$$

The measured time response is thought to be due largely to the phosphor decay time.

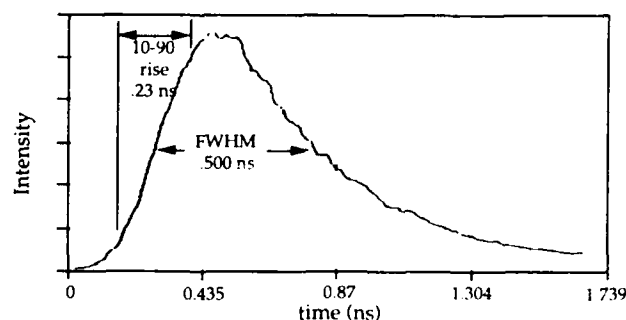


Figure 9. Streak camera measured detector time response.

#### CONCLUSIONS

We have developed an imaging x-ray detector with sub-nanosecond time response, high efficiency and good spatial resolution. The detector consists of an x-ray photocathode, a microchannel plate, one dimensional electron focusing electrodes and a fast phosphor. The measured time response is determined by properties of the phosphor. The measured time response is approximately 400 ps.

The efficiency of the detector, defined as the ratio of energy out of the phosphor into  $4\pi$  to the x-ray energy input, can be as high as 1000 for CsI photocathodes. Efficiencies for CuI are a factor of 5 less than CsI. The spatial resolution for the present detector assembly is about 320  $\mu\text{m}$ . This resolution can be improved by decreasing the electron transit time from the MCP to the phosphor at the expense of detector efficiency. Variations of the detector without the microchannel plate and the electron focusing have also been developed.

#### ACKNOWLEDGEMENTS

The authors wish to thank Mark Bowe, Carl Bruns, George Cameron, Mark Eckart, Richard Fortner, Mark Rotter, and Jim Swain for their help in this research. This work was performed under the auspices of the U. S. Department of Energy by the Lawrence Livermore National Laboratory under Contract N. W-7405-Eng-48.

\*Current address: Hughes Aircraft Corporation  
P.O. Box 92426,  
RS/R1/D417  
Los Angeles, California 90009



## REFERENCES

- 1.) B. K. F. Young, R. E. Stewart, and J. G. Woodworth, "Experimental demonstration of a 100-ps microchannel plate framing camera," *Rev. Sci. Instrum.* 57 (11), 2729-2732 (1986).
- 2.) B. L. Henke, J. P. Knauer, and K. Premaratne, "The characterization of x-ray photocathodes in the 0.1-10-keV photon energy region," *J. Appl. Phys.* 52 (3), 1509-1520 (1981).
- 3.) M. J. Whiteley, J. F. Pearson, G. W. Fraser, and M. A. Barstow, "The stability of CsI-coated microchannel plates x-ray detectors," *Nuclear Instruments and Methods in Physics Research*, 224, 287-297 (1984).
- 4.) M. R. Rotter, F. Roeske, P. M. Calavan, and S. S. Lutz, "Radiation-to-light converters for nuclear environments - deep red emitters", *SPIE*, 296, 183-190 (1981).

## Parabolic Mirror Electron Energy Analyzer for Multiphoton Photoemission Spectroscopy

L. D. Van Woerkom, D. J. Trevor, and R. R. Freeman

*AT&T Bell Laboratories, Murray Hill, New Jersey 07974*

### ABSTRACT

We report the use of a new, extremely efficient electron energy analyzer for recording high resolution electron spectra from multiphoton photoemission. The analyzer uses an electrostatic parabolic mirror and has a collection solid angle in excess of  $2\pi$  sr with an energy resolution of 35 meV at 1.8 eV. We have used this detector to record the above threshold ionization spectra emitted in xenon using a 275 fsec, 616 nm,  $2 \times 10^{14}$  W/cm<sup>2</sup> laser pulse.

We report the use of a new time-of-flight electron energy analyzer for recording high resolution electron spectra obtained in high intensity gas phase photoemission. This analyzer has a collection solid angle in excess of  $2\pi$  sr and an energy resolution of 35 meV at 1.8 eV while simultaneously preserving the angular information of the photoemission process. We have recorded the high resolution spectra of electrons emitted in high intensity, multiphoton photoemission in xenon with this analyzer. Because of the extremely high collection efficiency of this new detector, the recorded spectra are found to be free from effects of space charge.

Recent advances in high power, short pulse lasers have provided the means to probe new facets of the interaction of matter with high intensity radiation. Electron spectroscopy has long been the detection technique of choice in multiphoton ionization (MPI), in large measure

due to its ready interpretation in terms of the electronic structure of the target atom or molecule. However, at very high laser light intensities, several new, unexpected phenomena appear in the electron spectra of even the simplest atom. Chief among these is the appearance of multiple electron peaks separated by the photon energy, a result now generally referred to as "above threshold ionization" (ATI).[1] Recent experiments have shown that at ultra-short pulse excitation, the

individual ATI peaks break up into a large number of peaks which are separated from each other by energies on the order of their width, so that the well ordered, symmetric structure of long pulse ATI becomes a plethora of individual lines of varying strength and width.[2] The challenge, then, is to record these lines with sufficient signal-to-noise that they can be related to the structure of the atom in the high intensity radiation environment.

The problem that plagues virtually all multiphoton photoemission experiments is space charge. Because the lasers that produce the high energy pulses have low repetition rates, the detected electrons come from a relatively few number of laser shots. In order to record the energy of the emitted electrons with some accuracy, most analyzers collect only a small portion of the available  $4\pi$  solid angle: thus only a tiny fraction (typically  $\leq 10^{-3}$ ) of the electrons produced in each laser

pulse are recorded at the detector. Within each shot all of the electrons come from atoms which are ionized essentially simultaneously within the laser focus. If the number of ionized atoms is sufficiently large, the slower electrons will experience the field of the ions and have their energy reduced when measured at the detector. The signature of this effect is a preferential shift to lower energies of the low energy electrons, or a smearing of a broad distribution to lower energies. Indeed, in circumstances where the nascent energy distribution is not known, the presence of space charge can be extremely difficult to determine. The only way to deal with space charge is to reduce the number of ions made in each shot (by reducing the laser intensity or decreasing the gas pressure). In most experimental situations, where the signal-to-noise is limited by statistics, the price of this cure is severe in terms of experimental time.

The solution to this conundrum is to use a detector that collects all of the electrons from each laser shot, but possesses good energy resolution. Further, this ideal detector would preserve information about the angular distribution of the emission process as well. Currently the only detector that balances high collection efficiency with good energy

resolution is the magnetic bottle spectrometer of Kruit and Read.[3] Although this spectrometer collects 50% of the full solid angle, there are two potentially serious limitations: there exist large magnetic fields in the ionization region, and the angular information carried by the emitted electron can be difficult to extract due to the complex trajectories of the electrons through the magnetic field gradients.

We have built and tested a new large solid angle collection electron spectrometer that retains all of the original angular information of the electron and has good energy resolution over several electron volts of energy. The motion of electrons through spectrometer is analogous to trajectories of light in a parabolic mirror, and we have chosen to call it a "Parabolic Mirror Analyzer" (PMA). Fig. 1 shows a schematic of the spectrometer which consists of two parabolic grids separated by about 1 mm and a 75 mm diameter flight tube leading to large area microchannel plate (MCP) detectors. The parabolic grids have a focal length of 10 mm and the length from the focus to the detector is 980 mm. The laser passes through 5 mm holes cut in the grids with its focus set on the focus of the paraboloid. An electron emitted at the focus

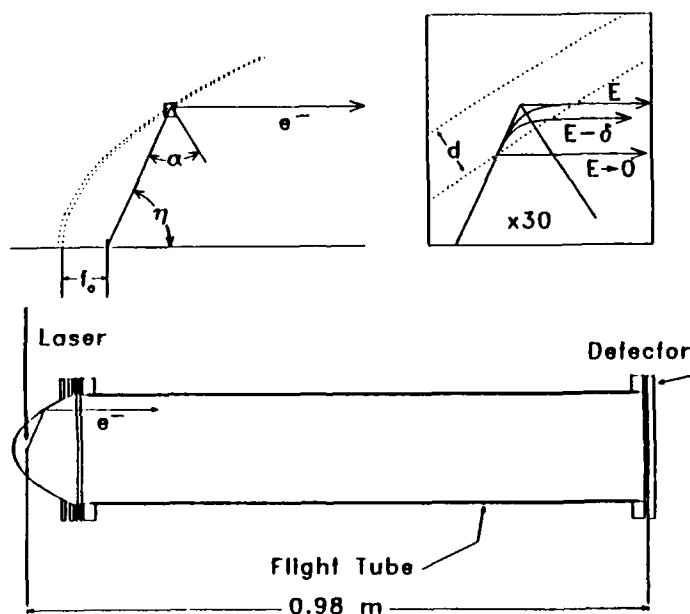


Fig. 1: A cross section of the time-of-flight spectrometer. The detail box shows electrons trajectories through the parabolic grids.

of the paraboloid travels in a straight line until it encounters the inner parabolic grid. It passes through the grid and experiences an electric field normal to the parabolic surface. The component of the electron's velocity normal to the surface is reversed and the electron passes back out through the inner grid and travels on a straight line path parallel to the flight tube to the MCP detector. This is illustrated in the top half of Fig. 1.

In the ideal case, the electron follows the optical analog trajectory and the entire process is just normal time of flight with an increased flight path (increased by twice the focal length of the parabola). In practice, however, the electron spends time between the parabolic grids while it is being reflected. This time, which depends upon the energy and angle of incidence of the electron, is a small fraction of the total flight time through the spectrometer. Thus the error in the calculated energy introduced by the neglect of this transit time is small. The upper right hand side of Fig. 1 shows three trajectories. This expanded region of the grids shows electron trajectories for energy  $E \rightarrow 0$  (the ideal optical analog),  $E$ , and  $E - \delta$  (the dashed line represents an equivalent optical path for energy  $E$ ). (The time to energy conversion and trajectory details are published elsewhere.[4])

For our considerations the ideal optical trajectory is sufficient. The main advantages of the PMA are twofold: First, in principle, a very large solid angle can be collected by the parabolic grids. For our present spectrometer the theoretical limit is about 60% of the full  $4\pi$ . In analogy to the optical parabolic mirror, all electrons with the same energy arrive at the detector at the same time, regardless of the angle of emission. Thus, good energy resolution is maintained. Second, the ionization region, which is at the focus of the paraboloid, is designed to be field-free since the reflection field is isolated between the two grids. (We have found this idealization to be only approximate for the grid structure we used here: for a reflection potential of 5 Volts we observed an uniform potential of something less than 20 meV in the ionization region.)

To test this instrument the MPI electron spectrum of xenon was measured using nanosecond pulses of 532 nm doubled Nd:YAG. A 30 mJ beam was focused with a 250 mm lens at the center of the parabolic

mirror through holes cut in the inner and outer grids. The electron spectra were digitized with a Tektronix 7912 digitizer, pulse discriminated by software and stored on an AT&T PC6300 computer for each shot. The pressure of xenon was kept less than  $10^{-6}$  Torr to avoid significant space charge broadening and shifting. Fig. 2 shows the photoelectron spectrum obtained after converting from time to kinetic energy using  $E = \frac{1}{2}mL^2/(t-t_0)^2 + E_0$  where  $t_0$  is the time offset and  $E_0$  is the contact potential offset. Bin widths constant in energy were generated from the time data, which is recorded with bin widths constant in time, by multiplying by the Jacobian of the time-energy transformation.

The two highest energy photoelectron peaks in Fig. 2 are due to the first above threshold ionization (ATI)[1] process, which corresponds to an overall seven photon absorption. The lowest energy peak shown is the  $^2P_{3/2}$  state of  $Xe^+$  produced by a six photon process with equivalent photon energy of 13.981 eV. The record length (512 channels) of the transient recorder excluded the  $^2P_{1/2}$  state from being

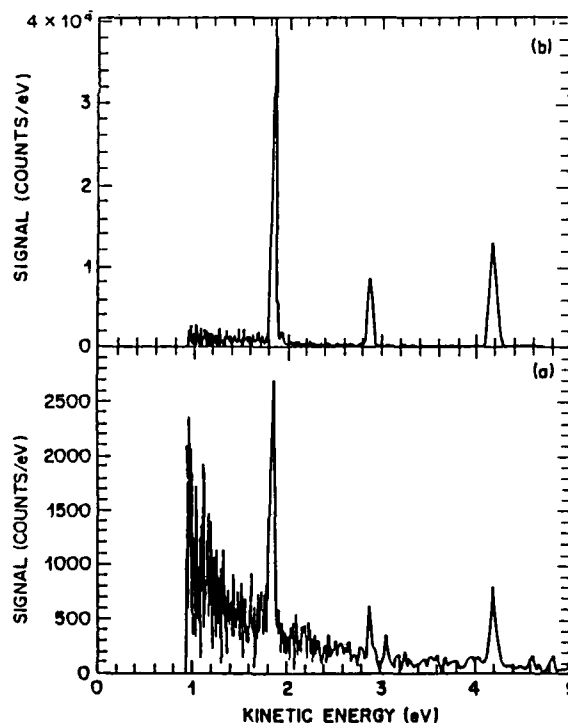


Fig. 2: TOF spectra of Xe taken with 30 mJ of 532 nm, 4 nsec laser pulses. In part (a) the grid is turned off and polarization is pointed down the tube. Part (b) shows the gain of 16 in signal obtained with -2.5 V on the outer grid and the laser polarization at  $80^\circ$ .

measured in these experiments. In the upper part of Fig. 2 the laser polarization vector was  $80^\circ$  with respect to the flight tube axis. All of the photoelectrons are collected by the grids, and the signal observed under these conditions is sixteen times larger than in the lower part where the polarization is aligned with the TOF axis and the mirror is turned off. The angular acceptance of the flight tube in the absence of the mirror is only 0.0046 str ( $4.4^\circ$ ) or 0.037% of the sphere. On the other hand the mirror subtends 8 str (64% of the sphere). Including the expected transmission reduction caused by passing through the inner grid twice of 0.64 ( $0.8^2$ ) the maximum gain in the use of this instrument is 1100. However, it is well known that this MPI source of electrons is highly peaked in the laser polarization direction[1]. Taking a conservative estimate for the opening angle of  $42^\circ$  which corresponds to a  $\cos^{10}\theta$  angular dependence, the straight TOF analyzer can collect at most 1.7% of the electrons. We thus estimate the maximum gain possible for this experimental configuration to be 37. Given the uncertainty in the angular distribution and the strong possibility that the grid's transmission for low energy electrons is less than their optical value, this is excellent agreement.

We have made use of the large solid angle collection efficiency to perform experiments on ATI in Xenon using femtosecond laser pulses. All of the data presented here was taken with 275 fsec pulses with approximately 200 microjoules per pulse. A colliding pulse mode-locked laser (CPM) produced 80 fsec nanosecond pulses at 616 nm and a repetition rate of 100 Mhz. Pulses were selected and amplified in a four stage dye amplifier pumped at 10 Hz by a Nd:YAG laser. The light was focussed with a 250mm focal length achromat lens into the paraboloid through small holes cut in the grids. The peak power density was  $2 \times 10^{14}$  W/cm<sup>2</sup>. The electron spectra were recorded and stored as in the testing experiments.

Fig. 3 shows the transformed time data into energy. Fig. 3a shows a large energy range with considerable structure. The periodic groups of peaks are due to the well known phenomena of ATI, with each group separated from its neighbor by the photon energy, 2.01 eV. The substructure within each group is due to the breakup of the ATI grouping introduced by the short pulse excitation, as discussed by Freeman *et al.*

The apparent loss in resolution for increasing energy is due to two factors: First, the resolution in energy is related to the time bins by

$$\frac{dE}{E} \propto \frac{dt}{t} \propto dt \sqrt{E} \quad (1)$$

where  $dt$  is a constant set by the transient digitizer sweep speed. For our data,  $dt$  is 4 nsec, and the resolution decays rapidly with increasing energy. Second, the ultrashort laser pulses have a bandwidth of nearly 8 meV, so that when 7-15 photons go into a given ATI peak, the apparent resolution is reduced.

Fig. 3b is an expanded view of the 1 to 2 eV region of the spectrum. The small narrow features between 1 and 1.4 eV are still further

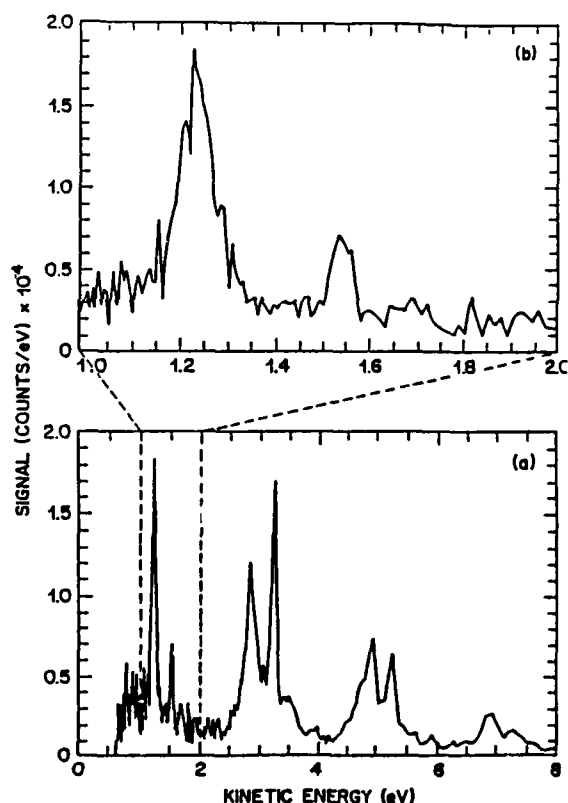


Fig. 3: a) Above Threshold Ionization data accumulated with the the PMA detector. The periodic groups of peaks are due to above threshold processes that occur at very high intensities. The structure repeats at an interval equal to the photon energy. b) High resolution plot of the region between 1 and 2 eV. The structure is due to atomic resonances made visible by the use of short pulses, as described in reference 2.

atomic resonances.[2] This figure illustrates that very good energy resolution is retained while collecting most of the electrons emitted.

Fig. 4 shows the effects of space charge on the time of flight spectrum for two gas pressures. The solid curve is taken with the PMA and less than  $2 \times 10^{10}$  Xe/cm<sup>3</sup>, well below the space charge limit. The dashed curve, taken without the PMA but with nearly  $2 \times 10^{12}$  Xe/cm<sup>3</sup> so as to record the same number of electrons, clearly shows a shift and long time tail on the longest time electrons (lowest energy). The large solid angle collection is evident by virtue of the high signal-to-noise present in the low density spectrum. The central point is that the PMA collects a large fraction of the electrons emitted, yielding high signal-to-noise while keeping the total number of ion charges well below the space charge limit.

In conclusion, we have demonstrated a new large solid angle electron spectrometer ideally suited for high power pulsed laser experiments. It features high collection efficiency with excellent energy resolution. The instrument is simple and elegant with no large fields in the ionization region. Several improvements and generalizations are currently being made. We are currently replacing the monolithic detector with a segmented detector in order to qualify the spectrometer's ability to record the angular distributions of the photoemitted electrons.[5]

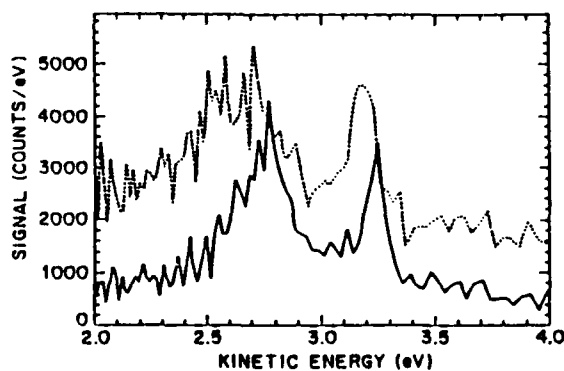


Fig. 4: The effect of space charge on the time of flight spectrum for two gas pressures. The PMA was used for the solid curve, with a gas density of  $2 \times 10^{10}$  Xe/cm<sup>3</sup>, while the dashed curve was obtained without the use of the PMA, but with  $2 \times 10^{12}$  Xe/cm<sup>3</sup> in order to obtain the same signal strength. The space charge in the latter case gives rise to shifts to lower energies and broadenings.

We have already demonstrated that the Parabolic Mirror Analyzer is easy to use and of great versatility in low data rate experiments such as short pulse multiphoton ionization.

## REFERENCES

1. P. Agostini, F. Fabre, G. Mainfray, G. Petite and N.K. Rahman, *Phys. Rev. Lett.*, **42**, 1127 (1979); R.R. Freeman, P. H. Bucksbaum and T. J. McIlrath, *IEEE JQE* **24**, 1461 (1988).
2. R.R. Freeman, P.H. Bucksbaum, H. Milchberg, S. Darack, D. Schumacher, and M.E. Geusic, *PRL* **59**, 1092 (1987).
3. P. Kruit and F.H. Read, *J. Phys. E: Sci Inst.* **16**, 313 (1983).
4. D.J. Trevor, L.D. Van Woerkom, and R.R. Freeman, to be published.
5. L.D. Van Woerkom, D. J. Trevor, and R.R. Freeman, submitted to *Optics Letters*.

---

**Part 5**  
**Spectroscopy and Other Applications**

---

# Vacuum Ultraviolet Laser Spectroscopy of Molecular Autoionizing States

D. Milburn, D. J. Hart<sup>a</sup>, and J. W. Hepburn<sup>b</sup>

*Centre for Molecular Beams and Laser Chemistry  
University of Waterloo, Waterloo, Ontario N2L 3G1, Canada*

## ABSTRACT

This paper describes a new apparatus which uses coherent vacuum ultraviolet light to photoionize molecules in a supersonic molecular beam, and energy analyzes the resulting photoelectrons by time of flight spectroscopy. The broadly tunable coherent VUV is generated by four wave sum mixing in Hg. Using this apparatus, we have studied the dynamics of autoionization for two different systems: spin-orbit autoionization in HI, and vibrational autoionization in NO. In both cases, our recent results have pointed out dramatic new features of the dynamics in these molecules.

## INTRODUCTION

Since the first third harmonic generation experiments in metal vapours were carried out in the early 1970's, producers of coherent vacuum ultraviolet (VUV) have proclaimed its virtues. Because synchrotron light sources were being developed at the same time, and had obvious virtues, these proclamations frequently took the form of somewhat specious comparisons between synchrotrons and coherent sources. The most frequently compared property was the spectral brightness, and the coherent sources won hands down, with orders of magnitude superiority. The reason for this is that the coherent sources are extremely high resolution compared to the incoherent synchrotrons, so the photon flux per unit bandwidth is far higher. For laser spectroscopists, used to striving for the highest possible resolution, this seemed to be a convincing argument in favour of the laser VUV

light sources. However, resolution is not always important, and sometimes the other features of a light source, such as tuning range, total photon flux, ease and reliability of operation, *etc.*, determine its usefulness. Thus, even in the 6 to 20 eV energy range, where good coherent sources have existed for more than decade, synchrotrons and lamps still rule supreme for experimental applications.

This does not mean that there are not frequent cases where coherent VUV sources are far superior, and in fact the point of this paper is to describe experiments that would not be possible without the use of a coherent VUV light source. What is meant by the *caveat* expressed above is that coherent VUV sources are useful for experiments which require the benefits of coherence, which include energy resolution (and therefore spectral brightness) and/or time resolution, and not necessarily useful for all experiments requiring VUV. Over the past few years, we have done a lot of work in photofragment spectroscopy, using coherent VUV for product detection. These experiments require spectroscopic detection of very low densities of photofragments formed under molecular beam conditions, and a great deal of information about the products is contained in the Doppler lineshape, so laser-based detection is an absolute necessity. To detect products like CO, H<sub>2</sub>, and a range of atoms, one must work in the VUV, and thus a coherent source of VUV is required. We have used four-wave sum mixing in Mg to generate broadly tunable and intense VUV, which has been used for laser-induced fluorescence (LIF) detection of CO and S products from photofragmentation of CS<sub>2</sub><sup>1</sup>, OCS<sup>2,3</sup>, Fe(CO)<sub>5</sub><sup>4,5</sup>, and glyoxal<sup>6</sup>. The success of these studies have clearly demonstrated the usefulness of coherent VUV for these types of experiments.

When coherent VUV generation by frequency mixing was first demonstrated, the potential application most commonly considered was

<sup>a</sup>present address: Laser Chemistry Group,  
National Research Council Ottawa, Ont., K1A 0R6

<sup>b</sup>Alfred P. Sloan Foundation Fellow, 1988-1990



spectroscopy. While the number of groups currently using coherent VUV for this purpose is limited, the papers of Stoicheff and coworkers on LIF of rare gas dimers in supersonic jets<sup>7</sup>, Lee and coworkers studies on photoionization spectroscopy<sup>8</sup> and our work on radiative lifetimes of perturbed  $^2\Delta$  states in NO<sup>9</sup>, illustrate the power of coherent VUV for spectroscopy. In this paper, we would like to discuss an application of coherent VUV that involves both spectroscopy and dynamics, the study of the dynamics of molecular autoionization. The process of autoionization in molecules is significantly more complicated than in atoms, and not nearly as well understood. In a molecule, there are many different ionization limits, corresponding to formation of the ion with varying degrees of internal excitation. Each of these ionization limits has Rydberg series converging on it, and as a result higher members of series converging on excited state ions can lie above lower ionization limits, as shown in figure 1. These Rydberg states can ionize by interacting with the various continua associated with the lower ionization limits, a process called autoionization. The excitation in the ionic core of a given Rydberg state (corresponding to the state of the ion in the limit for the series) can be an electronic or spin-orbit excited state in both atoms and molecules, the most common example being doubly excited states. This gives rise to electronic autoionization, a process that might be viewed as the same in atoms and molecules. However, the presence of rotational angular momentum can complicate even purely electronic autoionization, as it can couple to the electronic angular momenta and complicated the assignment of electronic states. Molecular Rydberg states can also be in excited vibrational and rotational states, giving rise to vibrational and rotational autoionization. Another complicating factor in molecules is that the lowest ionization limit is essentially always above the lowest dissociation threshold, and thus one may also have to take dissociative continua into account. In other words, predissociation of Rydberg states can often compete with autoionization, or even dramatically change the dynamics of the autoionization process. The two systems that will be discussed in this paper illustrate aspects of these complications that arise in molecular autoionization.

In the first study to be discussed, the high resolution and intensity of coherent VUV was exploited to study spin-orbit autoionization in HI, to understand the similarities and differences between HI and the isoelectronic atomic system, Xe. This search for similarities between spin-orbit autoionization in Xe, which is very well understood, and the less well understood HI was suggested by McGlynn<sup>10</sup>, but the highest resolution work done with incoherent sources, that of Eland and Berkowitz<sup>11</sup>, found only qualitative similarities between the photoionization spectra of Xe and HI in the energy range where there is spin-orbit autoionization. In the work reported here, the significantly better resolution of the coherent VUV source was used to look for sharp resonances in the photoionization spectrum of HI, while the higher

photon flux allowed the spectrum to be recorded for HI in a supersonic molecular beam. By using this combination, we showed that there are significant differences between the autoionization of 300K HI and 10K HI, and that the 10K HI actually does resemble Xe in its behaviour.

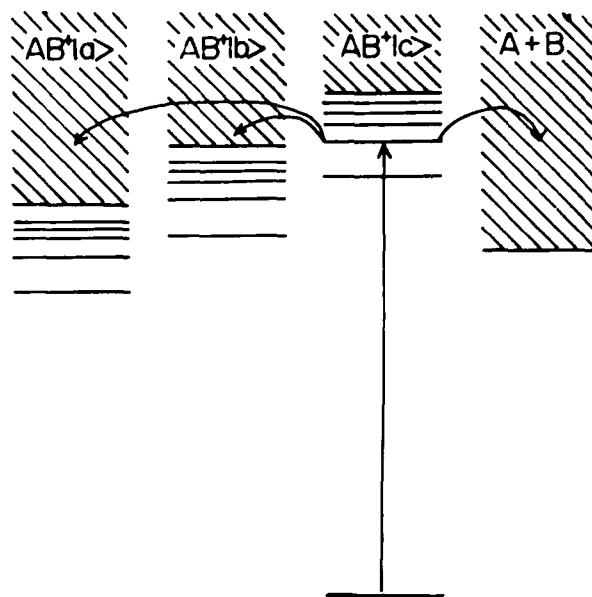


Figure 1

The second experiments to be discussed investigated vibrational autoionization in NO which, along with H<sub>2</sub>, has been a model system for this process. The unanswered question in NO relates to the quantum state distribution in the NO<sup>+</sup> products resulting from vibrational autoionization. With reference to fig. 1, when a Rydberg state that lies above several different ionization limits is populated, there are many possible product channels. Measurement of the branching into these channels, and how the nature of the Rydberg state affects that branching, provides important insight into the dynamics of the autoionization process. Making such a measurement requires selective excitation of a particular Rydberg resonance, followed by energy analysis of the resulting photoelectrons, which is impossible without the high spectral brightness of a coherent source. In the particular case of NO, previous work comparing the photoionization and absorption spectra showed the presence of autoionizing resonances which could only autoionize by a transfer of 2 or more quanta of vibrational energy from the core to the departing Rydberg electron<sup>12</sup>, in apparent violation of the  $\Delta v = -1$  propensity rule first derived by Berry<sup>13</sup>. Giusti-Suzor and Jungen<sup>14</sup> proposed an explanation for this behaviour, based on an interaction between the autoionizing Rydberg state and the dissociation continuum. In our study, we were able to probe, for the first time, the actual change in the core vibrational state by measuring the vibrational state distributions in the NO<sup>+</sup> ions resulting from autoionization of Rydberg states with varying degrees of vibrational excitation.

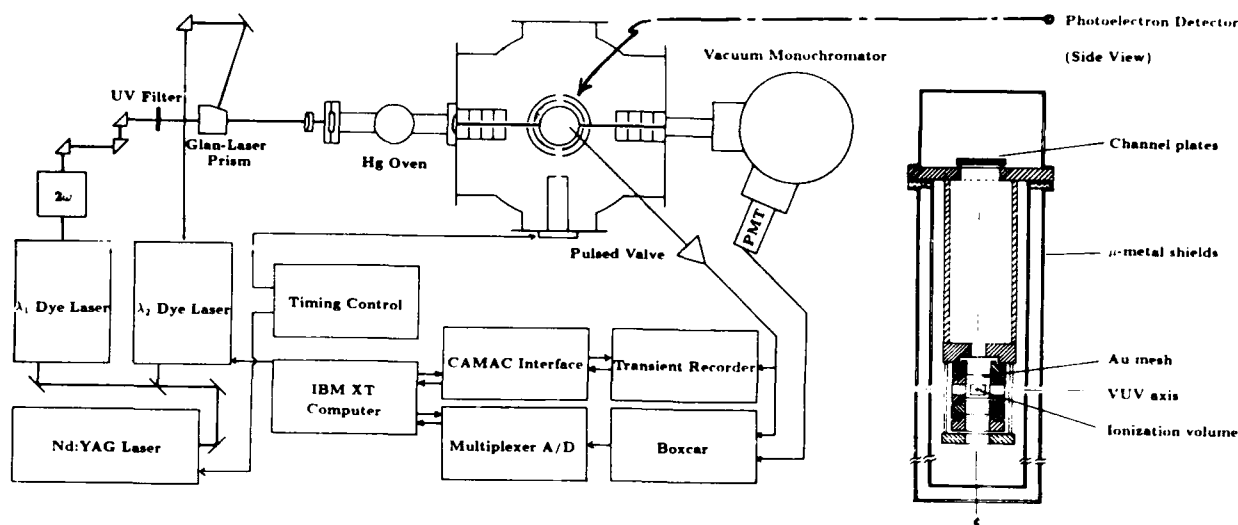


Figure 2

## EXPERIMENTAL

Both of the experiments described in this paper were carried out in the same apparatus, which is shown schematically in fig. 2. This machine used VUV continuously tunable below 130 nm to ionize molecules in a collimated supersonic beam, and employed a time of flight energy analyzer to detect the resulting photoelectrons.

The VUV was generated by four-wave sum mixing in Hg vapour<sup>15</sup>, using the  $6s7s(^1S_0) \leftarrow 6s^2(^1S_0)$  two photon resonance for resonant enhancement of the  $\nu_{VUV} = 2\nu_1 + \nu_2$  mixing process. Two Nd:YAG pumped dye lasers (Quanta-Ray DCR2A, Lambda Physik 2002E) were used as the driving lasers, with one fixed at the resonant wavelength of 312.8 nm, and the other tunable throughout the visible, from 396 nm to 770 nm, corresponding to VUV wavelengths from 112 nm to 130 nm. These two beams were overlapped in a Glan-laser prism and focussed into a Hg oven containing 10 torr of Hg and 60 torr of He. The resulting VUV was collimated by a LiF lens, and detected and monitored on the far side of the experimental chamber by a half meter Seya-Namioka vacuum monochromator with a solar blind phototube. The linewidth of the VUV was determined by recording the laser-induced fluorescence spectrum of CO in a supersonic beam, using the (0,0) band of the  $B^1\Sigma^+ \leftarrow X^1\Sigma^+$  system around 115 nm. Although the linewidth could be reduced below  $0.5 \text{ cm}^{-1}$ , this made it difficult to tune the VUV wavelength broadly, so a linewidth of  $0.75 \text{ cm}^{-1}$  was used for these experiments. Calibration of the dye lasers by optogalvanic spectroscopy on a U/Ne hollow cathode lamp made it possible to have an absolute VUV wavenumber calibration of  $\pm 0.2 \text{ cm}^{-1}$ . The average VUV intensity over the spectral range studied was estimated to be  $10^{10}$  to  $10^{11}$

photons/pulse, corresponding to a  $10^{-4}$ - $10^{-5}$  conversion efficiency, although significantly higher efficiencies were observed over the 119 to 129 nm range, in the region of Rydberg resonances in Hg<sup>15</sup>.

The molecular beam was generated from a pulsed supersonic source<sup>16</sup>, collimated by a skimmer and intersected with the VUV beam inside the photoelectron spectrometer. For the 300K HI experiments, an effusive source, consisting of a  $1/8''$  tube terminating in the experimental chamber, was used. The photoelectrons were detected in a time of flight spectrometer, shown in cross section in fig. 2, which was perpendicular to the plane formed by the VUV and molecular beams. The design was based on the threshold spectrometer of Tsai *et al*<sup>17</sup>, with a 31 cm flight tube separating the extraction optics from the channel plate detector. To measure the total photoionization cross section, an extraction field of 2 V/cm was applied across the ionization region, followed by a secondary acceleration, and detection of the total signal with a boxcar integrator (SRS 250). For recording the energy spectrum, no extraction field was used, a 0. to 0.5 V acceleration field was applied, and the signal was detected with a CAMAC based transient recorder (Transiac 2101S, 4100). To eliminate magnetic fields in the spectrometer, two nested magnetic shields were used, with 6 mm entry and exit holes for the laser and molecular beams. The VUV had to be carefully defined by optical baffles to prevent it from striking metal surfaces and generating background electrons. Experiments are being done to calibrate the collection efficiency of the spectrometer as a function of electron energy, and to provide an absolute energy calibration. Collection efficiency is estimated to be 0.1% to 0.01%, and the relative energy scale is accurate to 10 meV. The resolution, which is currently limited by the 10 nsec time resolution of the transient recorder, is 20 meV (FWHM), for electrons with energies less than 1 eV.

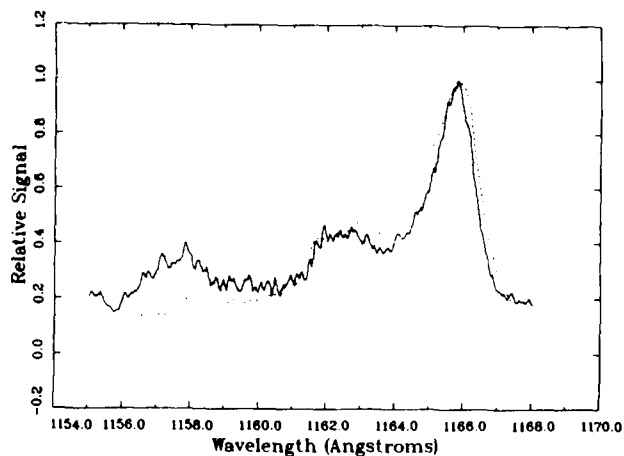


Figure 3

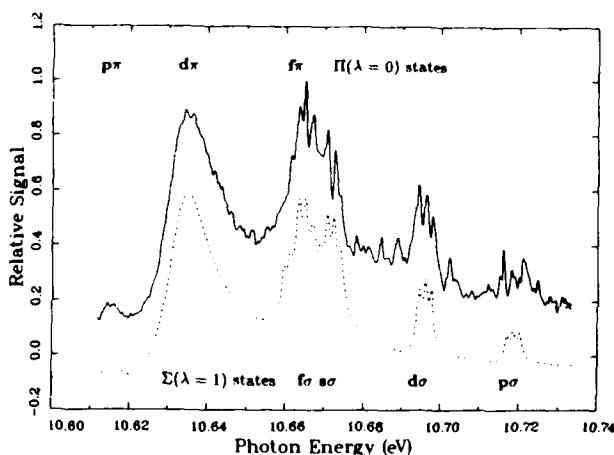


Figure 4

## RESULTS

### HI photoionization spectrum

These results will be published in detail elsewhere<sup>18</sup>, so only some of them will be summarized here. The major motivation for doing experiments on HI was a recent theoretical calculation by Lefebvre-Brion and coworkers<sup>19</sup>, which was restricted to the 115.5 nm to 116.8 nm spectral range, and predicted the presence of very strong, very narrow, autoionizing resonances, which had not been observed in previous work<sup>11</sup>. To compare with the previous photoionization spectrum, which had been recorded at 300K, an effusive source was used, and the spectrum was recorded between 112 nm and 120 nm. The spectrum recorded with coherent VUV was very similar to the previous, lower resolution spectrum, in spite of the roughly 10x improvement in resolution. In the region where the calculation had been done, there was no evidence for the predicted sharp, strong resonances, and the data was very much like

the previous spectrum. A portion of our 300K spectrum, between 115.5 nm and 116.8 nm, is shown in figure 3, along with the previous spectrum of Eland and Berkowitz<sup>11</sup>. However, the picture changed very dramatically when the spectrum of 10K HI was recorded, and these results are shown in figure 4. This spectrum is dominated by sharp resonances, with linewidths on the order of 10 cm<sup>-1</sup>. Also shown in fig. 4 is a simulated spectrum, which will be discussed briefly in the next section.

### NO photoelectron spectra

To date, we have obtained only preliminary results on NO, but these results are very exciting, and work on this problem is ongoing. Rydberg states above the NO<sup>+</sup>(v=1) limit have been probed, using VUV in the 128.4 nm to 129.4 nm spectral range. Several different Rydberg states in this range were looked at, first by recording the total photoionization cross section spectra for the different states, in the same way that this was done for HI. Once a particular band had been identified and characterized, the VUV was tuned so that particular lines in the band were excited, and the resulting photoelectrons were energy analyzed. The VUV was then tuned to the continuum just beside that line, and the photoelectron spectrum was collected for that excitation.

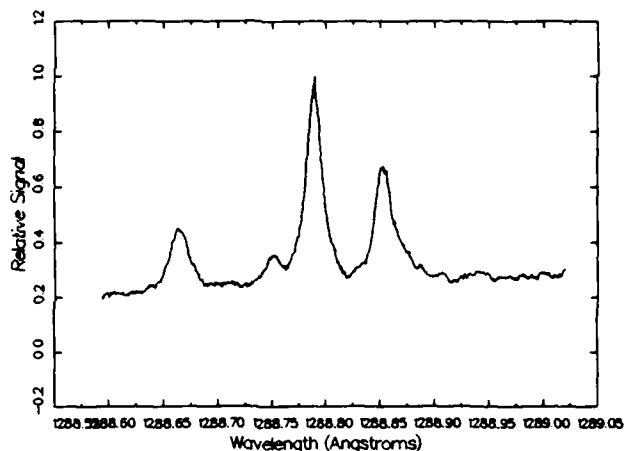


Figure 5

In figure 5, the photoionization spectrum for the 9sσ(v=2) ← X<sup>2</sup>Π<sub>1/2</sub>(v=0) band is shown. The individual rotational lines in this spectrum are resolved, and from the relative intensities of the R<sub>11</sub>(1/2) and R<sub>11</sub>(3/2) lines, a rotational temperature of 2 K was obtained for the NO in the supersonic beam. This degree of rotational cooling was necessary, because the spectrum of NO in this region is extremely congested, with bands every 50 cm<sup>-1</sup>. If the rotational temperature were significantly higher, spectral analysis and selective excitation would have been difficult. In figure 6, the photoelectron spectra taken for the 9sσ(v=2) state are shown. The top

spectrum is the result of exciting one of the rotational lines in the band in fig. 5, the middle one is the energy distribution resulting from excitation of the continuum in this region, and the bottom trace shows the difference between the two. In these spectra, the electrons have been accelerated by about 0.25 eV to enhance the transmission of the low energy electrons ( $\approx 60$  meV) corresponding to  $\text{NO}^+(v=1)$ . The peak at lowest energy corresponds to formation of  $\text{NO}^+$  in  $v=1$ , while the peak at higher energy is for  $\text{NO}^+$  in  $v=0$ . The reproducibility of the TOF spectra was checked by recording several spectra for continuum excitation in the region of a given band, and comparing the peak areas for the  $v=0$  and  $v=1$  peaks. In all cases, these areas showed only minor variations from spectrum to spectrum. The spectra shown in fig. 6 were recorded with only 2000 laser pulses of signal averaging, and the signal level was about 1 photoelectron per pulse.

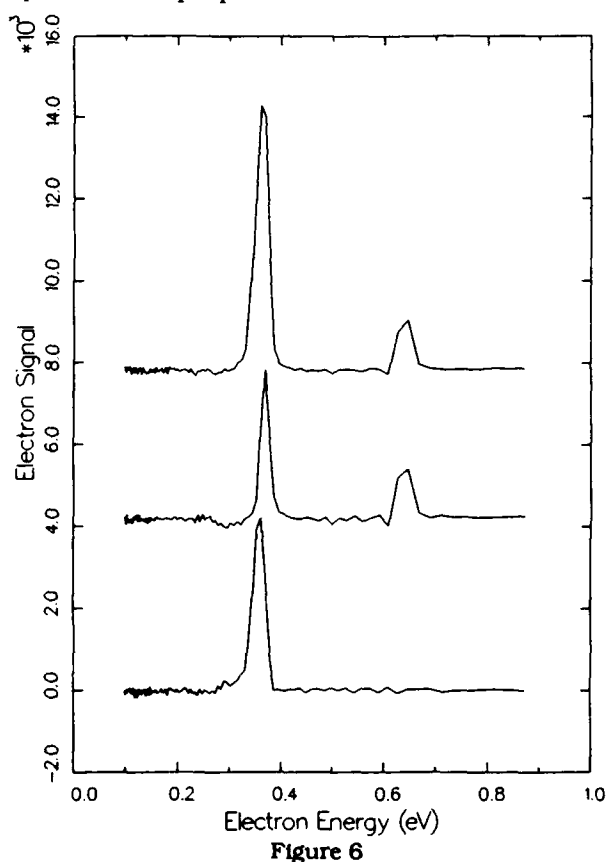


Figure 6

Data has been collected for several other bands, and as an example the spectrum of the  $5f(v=3) \leftarrow X^2\Pi_{1/2}(v=0)$  band is shown in figure 7, with the corresponding photoelectron spectra for one of the peaks, background continuum, and difference is given in figure 8. By comparing fig. 6 and 8, it can be seen that the products are very different for the two different Rydberg states. For the  $9s\sigma$  state, all of the additional ionization due to the autoionizing resonance generates  $\text{NO}^+(v=1)$  products, while for the particular peak of the  $5f$  state excited in fig. 8, all of

the additional  $\text{NO}^+$  is formed in  $v=0$ . Although a detailed assignment has not been made, it is obvious from the rotational structure in fig. 7 that there are two different Rydberg resonances in the spectrum, and this is reflected in the photoelectron spectra corresponding to different peaks. The three longest wavelength peaks result in a mixture of  $v=0$  and  $v=1$   $\text{NO}^+$  products, while the other peaks produce exclusively  $\text{NO}^+(v=0)$ , as shown in fig. 8. Other  $v=2$  Rydberg states investigated, the  $8f(v=2)$  and  $8p\sigma(v=2)$  produced only  $\text{NO}^+(v=1)$  products, while the  $6p\pi(v=3)$  state produced a mixture of  $\text{NO}^+(v=0)$  and  $\text{NO}^+(v=1)$ , and the  $5p\pi(v=4)$  state produced only  $\text{NO}^+(v=0)$ .

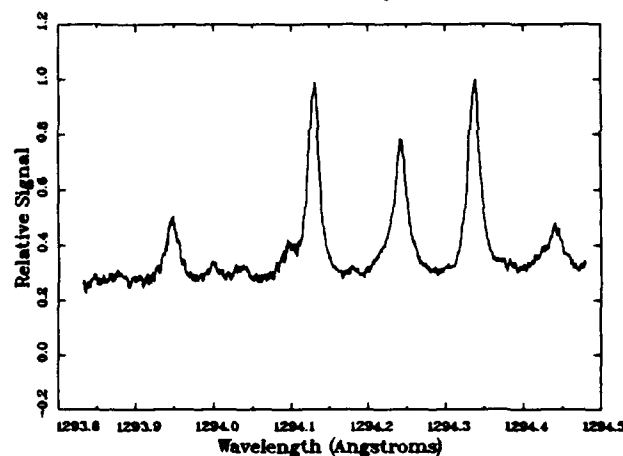


Figure 7

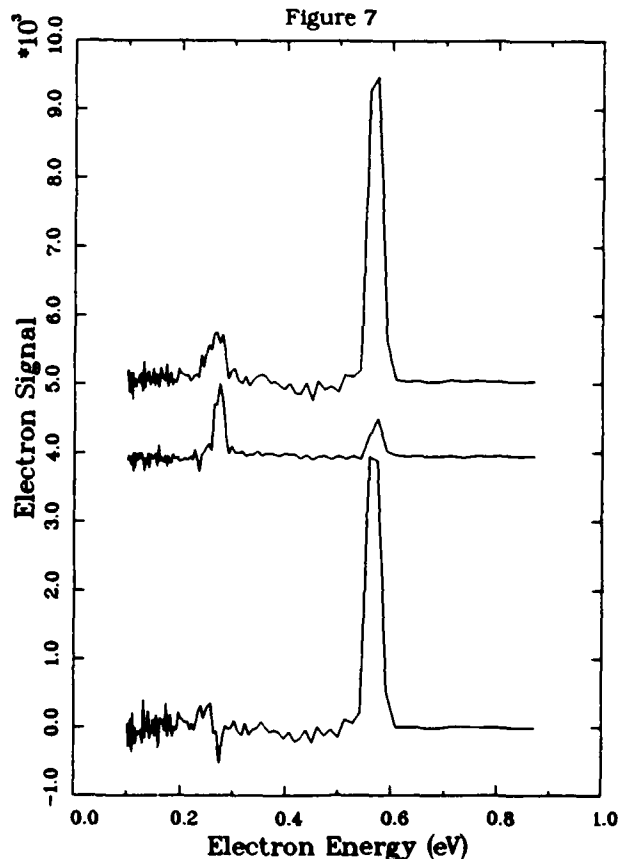


Figure 8

## DISCUSSION

### Spin-Orbit Autoionization of HI:

As mentioned in the previous section, the HI results will be discussed in detail in another paper<sup>18</sup>, so only a brief summary will be given here. The central concern of these experiments was to address the apparent discrepancy between the theoretical results and the previously measured photoionization spectra. The theory showed clear analogies between the autoionization of HI and Xe, while experiments showed little similarity in behaviour. In Xe, there are two Rydberg series, ns and nd, converging on the upper spin-orbit component of the ground electronic state of Xe<sup>+</sup>, the  $^2P_{1/2}$  state. The splitting between the  $^2P_{1/2}$  and  $^2P_{3/2}$  states is 1.3 eV, and ns and nd states above the lower  $^2P_{3/2}$  limit can autoionize, leading to a series of pronounced resonances in both the absorption and photoionization spectra of Xe. The nd series has very broad, assymmetric resonances, while the ns series consists of very sharp, strong resonances. HI is isoelectronic with Xe, and the HI<sup>+</sup> ground state also exhibits a large spin-orbit splitting into a  $^2\Pi_{3/2}$  ground state, and  $^2\Pi_{1/2}$  excited spin-orbit state. The configuration of HI, [core](5s $\sigma$ )<sup>2</sup>(5p $\sigma$ )<sup>2</sup>(5p $\pi$ )<sup>4</sup>, has atomic like 5p $\pi$  electrons, which can be promoted into Rydberg states, which converge on the ground state of HI<sup>+</sup>. Thus, in HI, one would also expect to see an s and d series converging on the upper  $^2\Pi_{1/2}$  state, with the reduced symmetry splitting the d states into d $\sigma$ , d $\pi$ , and d $\delta$ . Since the 5p $\pi$  electron is not purely "p", transitions to p and f Rydberg states are also expected. The theoretical calculation<sup>19</sup>, which was restricted to an energy interval corresponding to a change of 1 in principle quantum number, found a very broad, assymmetric d $\pi$ , d $\delta$  resonance, and a series of very sharp  $\sigma$  resonances (s $\sigma$ , p $\sigma$ , d $\sigma$ , f $\sigma$ ), the result that one would expect from taking a Xe atom and breaking its spherical symmetry.

This is not what has been observed, even at high resolution, for 300K HI, as can be seen from fig. 3. While rotational structure, ignored in the pseudo-atomic calculation, would break up the sharp resonances into several rotational lines, it happens that the rotational constant for the ground state of HI<sup>+</sup> (and therefore, of the Rydberg states corresponding to the ground state) is essentially the same as for HI, meaning that most of the sharp Rydberg states predicted should exhibit sharp Q-heads, with side R and P branches. In light of this, the appearance of the 10K spectrum, shown in fig. 4, is especially surprising in that it is dominated by a series of sharp resonances. The absence of these resonances in the 300 K spectrum results from more than additional rotational structure, as the Q-heads would persist with about the same intensity as the peaks seen in the 10 K spectrum.

To provide for a comparison with theory, and to assign the spectrum shown in fig. 4, we carried out a simulation, based on the expected spectroscopy of the autoionizing states. The simulated 10 K spectrum

shown in fig. 4 was calculated using a rotational temperature of 10K, which was in agreement with measurements made on CO under the same conditions. A rotational constant of 6.5 cm<sup>-1</sup> for the Rydberg states was used, a value consistent with the work of Tilford *et al*<sup>20</sup>. Fano line profiles were used for the resonances<sup>21</sup>, and their positions were determined by the standard quantum defect Rydberg formula. The linewidths, quantum defects, and relative cross sections for the various Rydberg states were used as parameters in the simulation, and the values used to calculate the spectrum shown in figure 4<sup>18</sup> were in reasonable agreement with those found by the *ab initio* multichannel quantum defect theory calculation<sup>19</sup>. The *ab initio* calculation ignored molecular effects such as vibration and rotation, so it really directly probed the "Xe-like" character of the HI spin-orbit autoionization. The 10 K data reflects the similarity in autoionization mechanism between Xe and HI. This similarity is shown even more dramatically by a direct comparison of our HI results with the same principal quantum number region in the Xe photoionization spectrum, shown in figure 9<sup>22</sup>. The Xe 8d resonance in fig. 9 shows the Beutler-Fano line profile, while the 10s resonance shown in fig. 9 has been instrument broadened, and the actual peak is even narrower. The close resemblance between the location, width, and lineshape of the 8d( $\pi, \delta$ ) and 10s $\sigma$  resonances in HI, and the corresponding 8d and 10s peaks in Xe reflects the equivalence of the autoionization mechanism in these two systems.

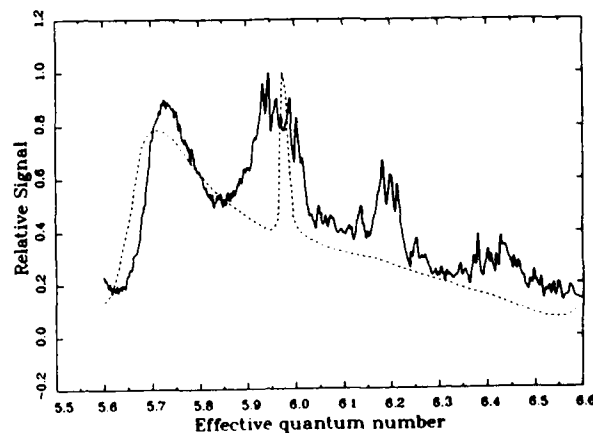


Figure 9

In light of this, the lack of sharp resonances in the 300 K HI spectrum is especially significant, as it may be indicating a difference in the dynamics of HI autoionization resulting from rotational excitation. At 10 K, HI is in J=0 and 1 only, while at 300 K, the most probable state is J=4, and only 10% of the total population in J=0 and 1. Because the Q branch lines should overlap in the HI spectrum, the linewidth of the higher J lines in the sharp resonances must be larger, resulting in a "washing out" of the sharp resonances in the spectrum as the rotational temperature is increased. One possible cause of this would be the L-S uncoupling caused by J, which was

discussed briefly by Lefebvre-Brion<sup>19</sup>. This uncoupling leads to a mixing of the various HI states that are labelled in fig. 4, as the quantum labelling shown is only approximate, and breaks down for a rotating molecule. These couplings are strongly  $J$  dependent, and could lead to a mixing between the longer lived Rydberg states corresponding to the sharp resonances, and the short lived ones, shortening the autoionization lifetime and broadening the linewidths as this coupling increases. The conclusion is that while HI shows Xe-like autoionization when it is not rotating, the atomic behaviour is washed out by rotational excitation, and the process of spin-orbit autoionization becomes more complicated than in atoms.

### Vibrational Autoionization of NO

Vibrational autoionization, a process peculiar to molecules, involves an exchange of energy between the vibrationally excited core of the Rydberg state and the Rydberg electron, resulting in a vibrational deactivation in the core, and ionization of the molecule. This process was first described by Berry<sup>14</sup> for  $H_2$ , and results from a kinetic energy coupling between the electronic and vibrational degrees of freedom, a breakdown of the Born-Oppenheimer approximation. The form of the term in the Hamiltonian responsible for this in Berry's original formulation resulted in a  $\Delta v = -1$  selection rule for the vibrational state of the core, if it behaved harmonically. Much smaller probabilities for  $\Delta v < -1$  resulted from anharmonicity in the core vibration. This behaviour, effectively minimizing the magnitude of  $\Delta v$  in the core, was called the vibrational propensity rule by Berry, and has been shown to work very well for  $H_2$ <sup>23</sup>.

In the case of NO, it would appear that it should also be an ideal model system for vibrational autoionization, and in the photoionization spectrum there are indeed several different autoionizing Rydberg series which converge on different vibrational states of the ground state of  $NO^+$ . However, in NO, where predissociation of the Rydberg states is known to occur<sup>24</sup>, the best photoionization spectrum recorded to date<sup>12</sup> shows strong resonances due to Rydberg states which can only ionize through  $|\Delta v| > 1$ , which should not happen in the presence of strong predissociation, if the propensity rule applies. Giusti-Suzor and Jungen<sup>14</sup> proposed an explanation for these observations, based on the well known Rydberg-valence state interactions which occur throughout the NO spectrum. By applying a form of quantum defect theory which included dissociation and ionization simultaneously, they were able to show that the autoionization process in NO is not purely vibrational, but is also actually promoted by predissociation. This runs counter to intuition, which has predissociation competing with, and thus inhibiting, autoionization. Their calculations were restricted to  $p\pi$  states below the  $NO^+(v=2)$  threshold, and they showed that for states above the  $v=1$  threshold that could not ionize by  $\Delta v = -1$  (i.e.

$5p\pi(v=4)$ ), there was comparable  $v=0$  and  $v=1$   $NO^+$  product, but always more  $v=1$  than  $v=0$ .

Our results support this theoretical work, but are much more dramatic in their departure from the propensity rule. For the  $9s\sigma(v=2)$  state, the expected behaviour for vibrational autoionization is observed. This state is above the  $NO^+(v=1)$  limit, so it can autoionize through a  $\Delta v = -1$  channel, and does so exclusively. This state is not strongly predissociated, as can be seen from the linewidths that we observed, which were laser limited. This means that for this state, one would not expect the predissociation induced autoionization to interfere strongly with the vibrational autoionization. Jungen's theoretical results for the  $9p\pi(v=2)$  and  $10p\pi(v=2)$  states also show the dominance of the  $\Delta v = -1$  channel for these predissociating states. Although we do not yet have data on these  $p\pi$  states, the other  $v=2$  Rydberg states that were looked at in our study showed strictly  $\Delta v = -1$  autoionization, and narrow linewidths.

For more highly vibrationally excited states in this energy range, the  $\Delta v = -1$  channel is closed. However, even for these states, the simple picture of vibrational autoionization would predict a minimum change in vibration of the core, resulting in  $NO^+(v=1)$  products. This is the opposite of what happens to the  $5f(v=3)$  state, which produces only  $v=0$   $NO^+$  products. This is not only in complete disagreement with the propensity rule, it is also a much more dramatic departure from propensity rule behaviour than was predicted for the  $p\pi$  states by Giusti-Suzor and Jungen. For these states, our data is not as good, but preliminary results would indicate that the  $6p\pi(v=3)$  states produces both  $v=0$  and  $v=1$   $NO^+$ , in agreement with theory, and the  $5p\pi(v=4)$  state seems to produce predominantly  $v=0$  product, where the theory predicts an equal mixture of 0 and 1. However, these resonances are weaker, and more data must be taken to confirm these preliminary results. In any event, the results on  $5f(v=3)$  are quite clear, and indicate that something is very strongly perturbing the vibrational autoionization process in this state. The lines observed are both symmetrical and narrow, which means that this state is neither strongly predissociated nor quickly ionized.

Much work remains to be done on this system. The resonances observed have to be assigned and characterized, and the lineshapes need to be analyzed. Better data needs to be collected for the  $p\pi$  resonances in this energy range, and the spectrometer has to be calibrated so that accurate  $NO^+$  branching ratios can be measured. We also hope to investigate autoionizing states at higher energy, above the  $NO^+ v=2$  and  $v=3$  thresholds, to provide more information on the dynamics of vibrational autoionization in NO when there are more available product channels. Finally, more theoretical work needs to be done, to explain the product branching ratios already observed.

## Summary

In this paper, we have discussed a new application for coherent VUV which, once again, demonstrates the usefulness of frequency mixing techniques for experiments in molecular physics. These experiments on autoionization dynamics have taken advantage of the resolution, intensity and collimation of the coherent source to carry out studies that would be impossible with other light sources such as synchrotrons. This data has revealed new features of the dynamics of molecular autoionization, and provide a challenge for the current theories. The results on spin-orbit autoionization found that molecular rotation has a very strong influence on this electronic autoionization process, and if the HI molecule can be cooled into a rotationless state, its behaviour resembles that of the isoelectronic Xe atom. The experiments on NO are similar to our other state resolved photofragmentation experiments, in that the quantum state distributions resulting from autoionization of specific Rydberg states have been determined. In this case, photoelectron spectroscopy following VUV laser photoionization of supersonically cooled NO has been used to find dramatic propensity rule violation in the vibrational autoionization of NO. Future experiments on these, and other similar systems are planned. Along with the capabilities already shown in this paper, the apparatus described can also easily be used to measure angular distributions of photoelectrons resulting from single photon ionization of molecules, and these angular distributions will be for specific product channels. Work in this area is planned for the near future.

## Acknowledgements

This work was supported by NSERC(Canada), and in part by the Petroleum Research Fund, administered by the American Chemical Society. We wish to thank Doug Cyr for his help with the NO experiments.

## References

- 1 I.M. Waller and J.W. Hepburn, *J. Chem. Phys.* **87**, 3261 (1987)
- 2 N. Sivakumar, I. Burak, W.-Y. Cheung, P.L. Houston, and J.W. Hepburn, *J. Phys. Chem.* **89**, 3609 (1985)
- 3 N. Sivakumar, G.E. Hall, P.L. Houston, J.W. Hepburn, and I. Burak, *J. Chem. Phys.* **88**, 3692 (1988)
- 4 I.M. Waller, H.F. Davis, and J.W. Hepburn, *J. Phys. Chem.* **91**, 506 (1987)
- 5 I.M. Waller and J.W. Hepburn, *J. Chem. Phys.* **88**, 6658 (1988)
- 6 I. Burak, J.W. Hepburn, N. Sivakumar, G.E. Hall, G. Chawla, and P.L. Houston, *J. Chem. Phys.* **86**, 1258 (1987)

- 7 A.A. Medej, P.R. Herman, and B.P. Stoicheff, *Phys. Rev. Lett.* **57**, 1574 (1986); P.R. Herman, P.E. LaRocque, and B.P. Stoicheff, *J. Chem. Phys.* **89**, 4535 (1988)
- 8 R.H. Page, R.J. Larkin, Y.R. Shen, and Y.T. Lee, *J. Chem. Phys.* **88**, 2249 (1988)
- 9 D.J. Hart and J.W. Hepburn, *J. Chem. Phys.* **86**, 1733 (1987)
- 10 H.T. Wang, W.S. Felps, G.L. Findley, A.R.P. Rau, and S.P. McGlynn, *J. Chem. Phys.* **67**, 3940 (1977)
- 11 J.H.D. Eland and J. Berkowitz, *J. Chem. Phys.* **67**, 5034 (1977)
- 12 Y. Ono, S.H. Linn, H.F. Prest, C.Y. Ng, and E. Miescher, *J. Chem. Phys.* **73**, 4855 (1980)
- 13 R.S. Berry, *J. Chem. Phys.* **45**, 1228 (1966)
- 14 A. Giusti-Suzor and Ch. Jungen, *J. Chem. Phys.* **80**, 986 (1984)
- 15 R. Hilbig and R. Wallenstein, *IEEE J. Quant. Electron.* **QE-19**, 1759 (1983)
- 16 T.E. Adams, B.H. Rockney, R.J.S. Morrison, and E.R. Grant, *Rev. Sci. Instrum.* **52**, 1469 (1981)
- 17 B. Tsai, T. Baer, and M.L. Horowitz, *Rev. Sci. Instrum.* **45**, 494 (1974)
- 18 D.J. Hart and J.W. Hepburn, *Chem. Phys.*, to be published
- 19 H. Lefebvre-Brion, A. Giusti-Suzor, and G. Raseev, *J. Chem. Phys.* **83**, 1557 (1985)
- 20 S.G. Tilford, M.L. Ginter, and A.M. Bass, *J. Mol. Spec.* **34**, 327 (1970); *ibid* **57**, 271 (1975)
- 21 U. Fano and J. Cooper, *Phys. Rev.* **137**, 1364 (1965)
- 22 The Xe spectrum shown is taken from ref. 11
- 23 *Photoabsorption, Photoionization, and Photoelectron Spectroscopy*, J. Berkowitz (Academic, New York, 1979)
- 24 E. Miescher, Y.T. Lee, and P. Gurtler, *J. Chem. Phys.* **68**, 2753 (1978)

## Time-resolved study of surface recombination at Si(111) surfaces

N. J. Halas and J. Bokor  
AT&T Bell Laboratories  
Holmdel, NJ 07733

At present, the technologically important phenomenon of nonradiative surface recombination at semiconductor surfaces and interfaces is very poorly understood. Since the phenomenon was initially described by Shockley, Bardeen, and others over 30 years ago, knowledge of the basic physics has progressed surprisingly little. We have endeavored to obtain a complete microscopic understanding of surface recombination at a semiconductor surface, including knowledge of the surface-state electronic structure and the detailed kinetics of the bulk-surface transfer of charge carriers. The Si(111) cleaved surface is an excellent model system for this study since the surface electronic structure is extremely well known experimentally and theoretically. There is a single intrinsic mid-gap state at 0.45 eV above the bulk valence band maximum (vbm) which is labelled  $\pi^*$ . Previously, infrared radiation was used<sup>[1]</sup> to selectively excite the  $\pi^*$  state without exciting the bulk and the details of its decay kinetics were measured. We have now directly observed the role played by this state in surface recombination of bulk electrons and holes.

Using 50 psec laser pulses at 532 nm, a bulk electron-hole plasma was excited. The time dependence of the bulk conduction electron density near the surface as well as the population arising in the  $\pi^*$  surface state due to surface recombination of the bulk carriers were monitored using time-resolved photoemission spectroscopy.<sup>[1]</sup> All of the relevant bulk-surface scattering rates have now been obtained.



It is clear from our measurements that transient surface charging occurs and significantly affects the bulk transport via the induced space charge field. From these and the previous measurements we have been able to construct a complete model for Si(111) 2x1 surface recombination which incorporates rate equations for the bulk-surface state dynamics as the boundary conditions on the transport equations for bulk electrons and holes, and includes the effects of the transient surface charge self-consistently. It appears that departures from the Shockley-Read-Hall steady state model of surface recombination should be quite common for photoexcited semiconductors in the subnanosecond regime.

#### *REFERENCES*

1. J. Bokor, R. Storz, R. R. Freeman, and P. H. Bucksbaum, *Phys. Rev. Lett.* **57**, 881(1986).

# Coherent Excitations of Nuclei in Crystals by Synchrotron Radiation Pulses

G. T. Trammell and J. P. Hannon

*Physics Department, Rice University  
Houston, Texas 77251*

## Abstract

Synchrotron pulses will excite low lying nuclear levels, and in crystals, will create nuclear exciton states which are spatially coherent superpositions of the various excited state hyperfine levels of all the nuclei in the crystal. The subsequent radiative decay is radically affected by coherence, exhibiting both a speed-up due to "coherent enhancement", and a quantum beat modulation of the decay rate which gives a periodic speed-up/slow-down of the rate for photon decay into the coherent channels. For a nuclear exciton in an antiferromagnet, the quantum beat modulation will result in an interesting "temporal pendulösung" effect.

## Introduction

Recently several groups have succeeded in producing well-defined nuclear excitonic states in crystals using synchrotron radiation pulses and studied experimentally some of the remarkable effects of coherence on the decay of these spatially coherent states: notably, the marked speedup of the decay rate and the quantum beats [1-8].

Synchrotron radiation from a source operating in the single-bunch mode consists of sharp pulses of about  $10^{-10}$ -sec duration and about  $10^{-6}$ -sec separation between pulses. Excited nuclear states of energy less  $\sim 100$  keV commonly have lifetimes in the range  $\Gamma^{-1} = 10^{-6} - 10^{-10}$  sec. If the pulse, monochromatized to perhaps 1-eV bandwidth at the nuclear transition, impinges on a small crystal containing the resonant nuclei, then the electronically scattered x rays, photoelectrons, etc., will emerge promptly during the  $10^{-10}$ -sec pulse, while those processes involving nuclear excitation will be delayed a mean time  $\Gamma^{-1}$ . Therefore, by using a timed detector which can recover from the prompt pulse in a time short compared to  $\Gamma^{-1}$ , the resonant and nonresonant events

can be separated temporally.

Because both the pulse duration and the transit time of the pulse across the crystal are short compared to the excited state lifetime  $\Gamma^{-1}$ , the pulse creates a collective nuclear excited state  $|\psi_e\rangle$  which is a spatially coherent superposition of the various excited state hyperfine levels of all the nuclei in the crystal [9,10]. The subsequent radiative decay is radically affected by coherence, exhibiting both a speed-up due to "coherent enhancement" [9,11-21], and a quantum beat modulation of the decay rate [9,20].

"Coherent enhancement" occurs when the waves emitted from the various nuclei in the crystal interfere constructively (this occurs, for example, when the exciton spatial phasing wave vector  $\mathbf{k}_0$  satisfies the condition for a Bragg reflection or for grazing incidence reflection). There is then an increase in the radiative width of the nuclear exciton, as compared to that of an isolated nucleus, arising from coherence. The partial widths for the incoherent decay processes (e.g., internal conversion) remain unchanged, leading to an increased probability for coherent radiative decay as compared to incoherent decay. Correspondingly, there is an increase in the radiative decay rate into the coherent channels, while the incoherent decay rates remain unchanged, and the decay of the nuclear exciton state  $|\psi_e\rangle$  is speeded up relative to the excited state decay of an isolated excited nucleus.

If, in addition, there are nuclear transitions of different frequencies at different sites (due to hyperfine splitting of each nucleus, or due to chemical shifts between different sites), then, in the coherent channels, there will also be periodic constructive/destructive interference between the waves of different frequencies emanating from the different sites, leading to a periodic speed-up/slow-down of the rate for photon decay into the coherent channels. These "quantum beats" in the coherent radiation occur at frequencies  $\Omega_B(n,m,\rho;n',m',\rho') =$

$\omega_{nm}(\rho) - \omega_{n'm'}(\rho')$ , corresponding to the difference frequencies of all allowed nuclear hyperfine transitions  $\omega_{nm}(\rho)$  from all the different nuclear sites  $\rho$ , from which the hyperfine splitting of both the excited and ground states may be found, as well as any energy shifts between nuclei located in different chemical or magnetic sites. There will also be quantum beats in the time spectrum for both the incoherently scattered  $\gamma$ -rays and the internal conversion electrons. For these spatially incoherent processes, there is only interference between transitions to the same ground state, so that here the beat frequencies reflect the splittings of the hyperfine levels of the excited state, with no information about the ground-state splittings or of the shifts between different sites.

For a nuclear exciton in an antiferromagnet, or any crystal in which the magnetic unit cell is larger than the chemical unit cell, the spatially coherent quantum beat modulation can result in an interesting "temporal pendulösung" effect. This will occur when the incident beam direction is chosen so that the resulting exciton spatial phasing wave vector  $\mathbf{k}_0$  satisfies the condition for a pure magnetic Bragg reflection (i.e.,  $\mathbf{k}_0$  satisfies a Bragg condition for the magnetic unit cell and simultaneously an "anti-Bragg" condition for the chemical unit cell). Under these conditions, the coherent emission will alternate back and forth in time between the forward transmission channel T, and the reflection channel R, with the switching rate determined by the quantum beat frequencies.

### Nuclear Exciton State

The important new element in the synchrotron pulse experiment is that the prompt, very well collimated incident pulse creates a spatially coherent excitation of the resonant nuclei in the crystal.

For a collection of  $N$  nuclei, located at sites  $\mathbf{R}_l$  ( $l = 1, \dots, N$ ), with the  $l^{\text{th}}$  nucleus initially in the  $m_l^{\text{th}}$  sublevel of its ground state,  $|g_l m_l\rangle$ , then the initial ground state of the system is

$$|\psi_0\rangle = \prod_{l=1}^N |g_l m_l\rangle |\chi_0\rangle,$$

where  $|\chi_0\rangle$  is the initial vibrational state of the crystal. The incident synchrotron pulse  $F(t)$  is highly collimated about the direction  $\mathbf{n}_0$ , and both the pulse duration and the transit time of the pulse across the crystal are generally short compared to the excited state lifetime  $\Gamma^{-1}$ . Neglecting multiple scattering, the resulting recoilless excitation just after the pulse transverses the system is [9]

$$|\psi_e\rangle = \sum_{l=1}^N e^{i\mathbf{k}_0 \cdot \mathbf{R}_l} \sum_{n_l} c_{n_l m_l} |e_l n_l\rangle |G_0(l)\rangle |\chi_0\rangle. \quad (1)$$

Here  $\mathbf{k}_0 = c^{-1}\omega_0 \mathbf{n}_0$ , where  $\omega_0$  is the mean transition frequency, and  $|G_0(l)\rangle$  indicates that all the other nuclei ( $l' \neq l$ ) are in their initial ground states  $|g_{l'} m_{l'}\rangle$ ,

$$|G_0(l)\rangle = \prod_{l' \neq l} |g_{l'} m_{l'}\rangle.$$

$c_{n_l m_l}$  gives the amplitude for exciting the nucleus at  $\mathbf{R}_l$  from  $|g_l m_l\rangle \rightarrow |e_l n_l\rangle$ , with no change in the vibrational state  $|\chi_0\rangle$ . For an electric or magnetic dipole transition,

$$c_{n_l m_l} = \frac{i}{\hbar} \sqrt{f} \langle e_l n_l | \mu | g_l m_l \rangle \cdot \mathbf{F}_{\omega_0},$$

where  $f$  is the Mössbauer probability for recoilless absorption,  $\mu$  is the dipole moment operator, and  $\mathbf{F}_{\omega_0}$  is the resonant Fourier component of the incident synchrotron pulse ( $\mathbf{F} = \mathbf{E}$  for E1 and  $\mathbf{F} = \mathbf{B}$  for M1 transitions),

$$\mathbf{F}_{\omega_0} = \int_{-\infty}^{\infty} \mathbf{F}(t) e^{i\omega_0 t} dt.$$

$|\psi_e\rangle$  is a collective nuclear excited state, i.e., a spatially coherent superposition of the various excited state hyperfine levels of all the nuclei in the crystal. In each contributing term, one nucleus is excited into one of its excited state hyperfine levels, and all the remaining nuclei remain in their initial ground states. The relative spatial phase is  $\exp(i\mathbf{k}_0 \cdot \mathbf{R}_l)$ . Hence  $|\psi_e\rangle$  is a *single exciton* collective state, with one excitation distributed coherently over the entire system, with a spatial phasing wave vector  $\mathbf{k}_0$ . It's important to note though that because of the hyperfine splitting,  $|\psi_e\rangle$  is not an energy eigenstate. As a consequence, there will be a quantum beat modulation of the subsequent decay.

$|\psi_e\rangle$  gives the recoilless single exciton contribution to the total state vector  $|\Psi\rangle$  which evolves from  $|\psi_0\rangle$  under the influence of the pulse perturbation. The normalization of  $|\psi_e\rangle$  is

$$\langle \psi_e | \psi_e \rangle = \sum_l \sum_{n_l} |c_{n_l m_l}|^2,$$

the probability that a single exciton is created by the pulse, with no change in vibrational state. There will also be contributions to  $|\Psi\rangle$  corresponding to single exciton states with recoil, and multiple exciton states with and without recoil. (For present synchrotron sources,  $\langle \psi_e | \psi_e \rangle \ll 1$ , so multi-exciton states need

not be considered.)

### Spatially Coherent and Incoherent Decay

The subsequent radiative decay,

$$|\psi_e\rangle \rightarrow |\psi_f\rangle + \gamma_k,$$

can be either spatially coherent, giving highly directional emission into the coherent channels, or spatially incoherent, giving essentially isotropic emission into  $4\pi$  sr.

Spatially coherent decay occurs when  $|\psi_e\rangle$  makes a radiative transition to the original ground state, i.e.,  $|\psi_f\rangle = |\psi_0\rangle$ . Viewed as a scattering process, the system resonantly scatters a photon  $|\mathbf{k}_0\rangle$  in the incident synchrotron pulse to a final state  $|\mathbf{k}\rangle$ , with the nuclear system undergoing the transition  $|\psi_0\rangle \rightarrow |\psi_e\rangle \rightarrow |\psi_0\rangle$ , i.e.,

$$\gamma_{\mathbf{k}_0} + |\psi_0\rangle \rightarrow |\psi_e\rangle \rightarrow |\psi_0\rangle + \gamma_{\mathbf{k}}.$$

This is coherent elastic resonant scattering, and corresponds to "multi-slit interference": it is impossible to tell at which nucleus the scattering took place, so the scattered wave amplitude is then the sum of the individual scattered wave amplitudes from all the nuclear sites, giving highly directional coherent scattering [as well as a weak diffuse contribution due to the "isotope effect"].

If  $|\psi_f\rangle \neq |\psi_0\rangle$ , the decay will be spatially incoherent. For single photon decay,  $|\psi_f\rangle$  can differ from  $|\psi_0\rangle$  only by the spin state of a single nucleus, e.g.,

$$|\psi_f\rangle = |g, m_l'\rangle |G_0(l)\rangle \quad (m_l' \neq m_l)$$

In this case the  $l^{\text{th}}$  site is "tagged" by "spin flip". Viewed as a scattering process, the scattering definitely occurred at the  $l^{\text{th}}$  nucleus. Thus the scattered wave amplitude only contains this single contribution, giving essentially isotropic (diffuse) scattering.

Similarly, if  $|\psi_e\rangle$  decays by internal conversion, then one of the atoms will be tagged, now by the difference in the initial and final electronic states. As a consequence, there can be no spatial coherence in internal conversion decay.

For simplicity, we have ignored here those processes in which the vibrational state of the crystal changes when the quantum is absorbed or emitted. These give rise to weak coherent inelastic effects, as discussed in Ref. [9].

### Coherent Enhancement and Speedup

For an isolated nucleus, the total width for the excited level is  $\Gamma = \Gamma_\gamma + \Gamma_\alpha$ , where  $\Gamma_\gamma$  is the partial

width for radiative decay, and  $\Gamma_\alpha$  is the partial width for internal conversion decay. For the synchrotron produced nuclear exciton state  $|\psi_e\rangle$ , the total decay width is increased by the effect of spatially coherent radiative decay,

$$\Gamma \rightarrow \Gamma' = \Gamma_c + \Gamma_\gamma' + \Gamma_\alpha,$$

where  $\Gamma_\gamma'$  is the partial width for spatially incoherent radiative decay, and  $\Gamma_c$  is the partial width for spatially coherent decay  $|\psi_e\rangle \rightarrow |\psi_0\rangle + \gamma_{\mathbf{k}}$ , given (in the Fermi rule approximation) by [11]

$$\Gamma_c(\mathbf{k}_0) = \Gamma_{\text{coh}} N^{-1} (4\pi)^{-1} \int d\Omega(\mathbf{n}) \left| \sum_{l=1}^N e^{-i(\mathbf{k} - \mathbf{k}_0) \cdot \mathbf{R}_l} \right|^2, \quad (3)$$

where  $\mathbf{k}_0 = k_0 \mathbf{n}_0$ ,  $\mathbf{k} = k_0 \mathbf{n}$ , and  $\Gamma_{\text{coh}} = [f C (2j_1 + 1) \Gamma_\gamma / (4j_0 + 2)]$ , where  $f$  is the Mössbauer factor,  $C$  is the abundance of the resonant nuclear isotope, and  $j_0$  and  $j_1$  are the spins of the nuclear ground and excited states. Here we have assumed that there is no hyperfine splitting of the nuclei. When the angular integration is carried out, for each open coherent channel  $(\mathbf{k}_0 + \boldsymbol{\tau})$  [the  $(\mathbf{k}_0 + \boldsymbol{\tau})$ -channel is open if  $|\mathbf{k}_0 + \boldsymbol{\tau}| = |\mathbf{k}_0|$  where  $\boldsymbol{\tau}$  is one of the reciprocal lattice vectors of the lattice], there will be a contribution [11,21]

$$\Gamma_{\text{coh}} 2\pi n \lambda^2 L_{\parallel}(\mathbf{k}_0 + \boldsymbol{\tau}),$$

where  $n$  is the number of nuclei per unit volume, and  $L_{\parallel}(\mathbf{k}_0 + \boldsymbol{\tau})$  is the thickness of the crystal in the direction of  $(\mathbf{k}_0 + \boldsymbol{\tau})$ .

Thus if the incidence direction  $\mathbf{n}_0$  is taken so that  $\mathbf{k}_0$  satisfies the condition for a symmetric Bragg reflection from a thin crystal of resonant nuclei  $M$ -layers thick, then there will be two coherent channels open, the reflection and transmission channels  $R$  and  $T$ , and the partial width for coherent decay will be [11,17,18]

$$\Gamma_c = \left[ \frac{4\pi n \lambda^2 d}{\sin(\phi_0)} \right] \cdot M \cdot \Gamma_{\text{coh}},$$

where  $\phi_0$  is the incidence angle with respect to the crystal planes, and  $d$  is the interplanar separation. For a sufficiently thick crystal, typically  $M \sim 10^3 - 10^4$  layers,  $\Gamma_c$  will exceed  $(\Gamma_\gamma' + \Gamma_\alpha)$ , and coherent decay will dominate incoherent decay. The nuclear exciton then de-excites at the speeded-up rate  $(\Gamma_c + \Gamma_\gamma' + \Gamma_\alpha)/\hbar$ , primarily via coherent radiative decay into either the  $R$ - or  $T$ -channel.

There will also be strong coherent enhancement when a crystal is excited at grazing incidence (which can be viewed as a zero angle Bragg excitation) [20], and even off-Bragg there is a contribution to Eq. (2) coming from coherent forward scattering. [However, there is an important distinction between the Bragg- and off-Bragg cases. The Bragg mode excitation is a true semi-stationary state radiative eigenmode with an enhanced width ( $\Gamma_c + \Gamma_\gamma' + \Gamma_a$ ), while the off-Bragg excitation is in fact a superposition of radiative eigenmodes of slightly differing frequencies].

### Spatially Coherent Quantum Beats

If there is hyperfine splitting of the nuclear levels, or if there are shifts between the levels of nuclei located in different chemical sites, there will be periodic constructive/destructive interference between waves of different frequency emitted from the different sites. This results in a striking "quantum beat" modulation of the spatially coherent decay rate,

$$\Gamma_c \rightarrow \Gamma_c(t),$$

varying periodically between "superradiant" and "subradiant" emission into the coherent channels, with beat frequencies determined by the frequency differences among the various transition resonances.

Letting  $R_l$  denote the lattice points of the crystal Bravais lattice, and denoting the equilibrium positions of the nuclei within the unit cell by basis vectors  $\rho$ , the photon potential for the spatially coherent emission,  $|\psi_e\rangle \rightarrow |\psi_0\rangle + \gamma_k$ , is given by [9,18]

$$A_\perp^{\text{coh}}(R, t) = -i \frac{1(t^*)}{R} S(k - k_0) \cdot \left[ \frac{k_0 C \sqrt{f}}{2j_0 + 1} \right] \sum_\rho \sum_{n,m} \times e^{-i\{[\omega_{nm}(\rho) - i\Gamma'/2]t^* + (k - k_0) \cdot \rho\}} \mu_{mn}^\perp(\rho) c_{nm}(\rho) \quad (3)$$

Here  $k = c^{-1}\omega_0 R/R$ ,  $t^* = (t - R/c)$  is the retarded time, and  $S(k - k_0)$  is the factor,

$$S(k - k_0) = \sum_l e^{-i(k - k_0) \cdot R_l},$$

which makes the coherent decay highly directional, into the open coherent channels. In the first Born approximation,  $\Gamma' = \Gamma = \Gamma_\gamma + \Gamma_a$ , while in the second Born approximation,

$$\Gamma'(t^*) = (1/t^*) \cdot \int_0^{t^*} [\Gamma_c(t) + \Gamma_\gamma'(t) + \Gamma_a] dt \quad (4)$$

The important new feature is that  $A^{\text{coh}}$  is a

superposition of damped waves,  $\exp\{-i[\omega_{nm}(\rho) - i\Gamma'/2]t^*\}$ , of all the various resonance frequencies  $\omega_{nm}(\rho)$  of all the nuclei within each unit cell. Furthermore, the amplitudes of the waves emitted at the site  $\rho$  within the unit cell are proportional to the spatial phase factor  $\exp[-i(k - k_0) \cdot \rho]$ . For the transmission channel T (i.e.,  $k = k_0$ ), this factor is +1, but for a reflection channel R, this factor will generally vary at different sites  $\rho$ , and will generally change with the order of the Bragg reflection. As a consequence, the pulsed coherent emission into the R- and T-channels can be out of phase, giving a "temporal pendulösung" effect.

The photon flux [ probability/cm<sup>2</sup>/sec of finding a photon at (R, t) ] for spatially coherent emission is given by

$$n_{\text{coh}}(R, t) = \left[ \frac{\omega_0}{2\pi\hbar c} \right] \cdot |A_\perp^{\text{coh}}(R, t)|^2 \quad (5)$$

and the partial width for coherent emission is then

$$\Gamma_c(t^*) = \frac{R^2 \int d\Omega_R n_{\text{coh}}(R, t)}{\langle \psi_e(t^*) | \psi_e(t^*) \rangle} \quad (6)$$

where  $\langle \psi_e(t^*) | \psi_e(t^*) \rangle = \exp(-\Gamma' t^*) \cdot \langle \psi_e | \psi_e \rangle$ . If there is no hyperfine splitting, then  $\Gamma_c(t) = \Gamma_c$ , the enhanced coherent decay rate given by Eq.(2). In the presence of splitting, there will be a "quantum beat" modulation of the coherent decay rate, with  $\Gamma_c(t)$  varying between a strongly enhanced peak decay rate and a strongly suppressed minimum decay rate. An example of this behavior is given below.

The "quantum beats" in the coherent radiation occur at the frequencies

$$\Omega_B(n, m, \rho; n', m', \rho') = \omega_{nm}(\rho) - \omega_{n'm'}(\rho')$$

corresponding to the difference frequencies of all allowed nuclear hyperfine transitions  $\omega_{nm}(\rho)$  from all the different nuclear sites  $\rho$ , thus furnishing a method for determining the hyperfine splitting of both the excited and ground states, as well as any energy shifts between nuclei located in different chemical or magnetic sites.

For the spin flip and internal conversion incoherent decay modes, there is no interference between waves from different sites, and at a particular site, the decay

is  $\sum_n c_{nm} |e_n\rangle \rightarrow |g m'\rangle$ , so the quantum beats only exhibit the splittings of the excited levels. There is no information about the ground state splittings or of energy shifts between different sites. Because there is no spatial coherence, there is no enhancement of the partial widths for incoherent decay,  $\Gamma_a + \Gamma_\gamma'$ . Furthermore,  $\Gamma_a$  and the spin flip contribution to  $\Gamma_\gamma'$  are time independent, in sharp contrast to  $\Gamma_c(t)$ . The spatially incoherent decay goes into all directions, and

in any particular direction, a quantum beat modulation will be observed. But since the contributing waves arise from different  $\Delta J_z$ -"oscillators", there will be no net interference when integrated over  $d\Omega_R$ . (There will, however, be a time dependence in the contribution to  $\Gamma_\gamma$  which arises from the diffuse elastic scattering associated with the "isotope effect", as we will discuss elsewhere.)

A striking example of the quantum beat modulation of the coherent rate has been observed in the experiments on yttrium-iron-garnet (YIG) [2,3]. In YIG there are two inequivalent sites, d1 and d2, with a shift  $\Omega_E \sim 6\Gamma$  between the resonance frequencies at the two sites. For the (002) Bragg reflection, the relative spatial phase factor  $\exp[-i(\mathbf{k} - \mathbf{k}_0) \cdot (\mathbf{p}_{d1} - \mathbf{p}_{d2})]$  is (-1) for the reflection channel R, and (+1) for the transmission channel T, giving coherently emitted fluxes [22]

$$|R_{(002)}(t)|^2 \propto e^{-\Gamma t} \sin^2(\Omega_E t/2), \\ |T_{(002)}(t)|^2 \propto e^{-\Gamma t} \cos^2(\Omega_E t/2),$$

with  $\Gamma$  given by Eq. (4). The partial width for coherent emission is, from Eq. (6),  $\Gamma_c(t) = \Gamma_c^{(R)}(t) + \Gamma_c^{(T)}(t)$ , where the partial widths for coherent emission into the R- and T-channels are, respectively,

$$\Gamma_c^{(R)}(t) = \Gamma_c \sin^2(\Omega_E t/2), \\ \Gamma_c^{(T)}(t) = \Gamma_c \cos^2(\Omega_E t/2),$$

where here

$$\Gamma_c = \left[ \frac{2\pi n \lambda^2 d}{\sin(\phi_0)} \right] \cdot M \cdot \Gamma_{\text{coh}},$$

gives the peak partial width for coherent emission into a single channel.

In the reflection channel  $R_{(002)}$ , there is thus an initial complete suppression of the coherent decay, followed by a delayed enhanced probability for photon emission at a time  $\sim \pi/\Omega_E \sim 50$  nsec. For the transmission channel, however, the relative spatial phase factor is (+1), giving initial constructive interference, and the coherent emission into  $T_{(002)}$  is  $180^\circ$  out of phase with the emission into  $R_{(002)}$ . Thus for the (002) Bragg reflection, the coherent decay should exhibit a striking "temporal pendulösung" effect, oscillating back and forth between the R- and T-channels at frequency  $\Omega_E$ . Because the coherent emission oscillates between the R- and T-channels,  $\Gamma_c(t)$  is time independent for the (002) reflection,  $\Gamma_c(t) = \Gamma_c$ .

This behavior can be changed by changing the order of the Bragg reflection. For example, for the (004)-Bragg reflection, the spatial phase factor is (+1) for both the R- and T-channels, so in this case the R- and

T-channels beat in phase with a  $\cos^2(\Omega_E t/2)$  dependence, with the partial width for coherent decay being

$$\Gamma_c(t) = \Gamma_c^{(R)}(t) + \Gamma_c^{(T)}(t) = 2\Gamma_c \cos^2(\Omega_E t/2).$$

Thus for the (004) reflection, in contrast to the (002) reflection,  $\Gamma_c(t)$  is time dependent, with the probability for photon decay (into either channel) being initially strongly enhanced, followed by complete suppression of coherent decay at a time  $\sim \pi/\Omega_E \sim 50$  nsec.

## Acknowledgements

Partial support for this work has been provided by the National Science Foundation under grant No. DMR-86-08248, by the SDIO/IST directed by NRL under grant N00014-86-C-2382, and by the Welch Foundation under grant C-1049.

## References and Notes

1. E. Gerdau, R. Rüffer, H. Winkler, W. Tolksdorf, C. P. Klages, and J. P. Hannon, Phys. Rev. Lett. **54**, 835 (1985).
2. E. Gerdau, R. Rüffer, R. Hollatz, and J. P. Hannon, Phys. Rev. Lett. **57**, 1141 (1986).
3. R. Rüffer, E. Gerdau, R. Hollatz, and J. P. Hannon, Phys. Rev. Lett. **58**, 2359 (1987).
4. G. Faigel, D. P. Siddons, J. B. Hastings, P. E. Haustein, J. R. Grover, J. P. Remeika and A. S. Cooper, Phys. Rev. Lett. **58**, 2699 (1987).
5. U. van Bürck, R. L. Mössbauer, E. Gerdau, R. Rüffer, R. Hollatz, G. V. Smirnov, and J. P. Hannon, Phys. Rev. Lett. **59**, 355 (1987).
6. G. Faigel, D. P. Siddons, J. B. Hastings, P. E. Haustein, J. R. Grover, and L. E. Berman, Phys. Rev. Lett. **61**, 2794 (1988).
7. S. L. Ruby, et al., to be published.
8. An observation of speedup using time-coincidence techniques has been made by G. V. Smirnov, Yu. V. Shvyd'ko, and E. Realo, Pis'ma Zh. Eksp. Teor. Fiz. **39**, 33 (1984) [JETP Lett. **39**, 41 (1984)].
9. G. T. Trammell and J. P. Hannon, Phys. Rev. B **18**, 165 (1978) and Phys. Rev. B **19**, 3835 (1979).
10. There are two equivalent approaches for treating the interaction of a synchrotron pulse with a system of nuclei. Because the temporal duration of the synchrotron pulse and its transit time across the system are short compared to the lifetime of the nuclear resonance, the formation of the intermediate excited state and its subsequent decay can be treated as two independent quantum-mechanical processes. Alternatively, the interaction can be treated purely as a resonance scattering problem. The first approach clarifies the idea of creating nuclear excitons with synchrotron radiation pulses. The second approach makes it easy to treat multiple scattering within the system,

and clarifies the distinction between spatially coherent and spatially incoherent decay of the nuclear exciton.

11. G. T. Trammell, in *Chemical Effects of Nuclear Transformations*, International Atomic Energy Agency, (IAEA, Vienna, 1961), Vol. I, p. 75. [Proceedings of the IAEA Symposium on the Chemical Effects of Nuclear Transformations, Prague, October, 1960 ].
12. G. T. Trammell, Phys. Rev. **126**, 1045 (1962).
13. M. I. Podgoretskii and I. I. Raizen, Zh. Eksp. Teor. Fiz. **39**, 1473 (1960) [JETP **12**, 1023 (1961)].
14. C. Muzikar, Zh. Eksp. Teor. Fiz. **41**, 1168 (1961) [JETP **14**, 833 (1962)].
15. D. F. Zaretskii and V. V. Lomonosov, Zh. Eksp. Teor. Fiz. **48**, 368 (1965) [JETP **21**, 243 (1965)].
16. A. M. Afanas'ev and Yu. M. Kagan, Zh. Eksp. Teor. Fiz. Pis. Red. **2**, 130 (1965) [JETP Lett. **2**, 81 (1965)].
17. J. P. Hannon and G. T. Trammell, Phys. Rev. **169**, 315 (1968); *ibid.*, Phys. Rev. **186**, 306 (1969).
18. J. P. Hannon, N. J. Carron, and G. T. Trammell, Phys. Rev. B **9**, 2791 (1974); *ibid.*, Phys. Rev. B **9**, 2810 (1974).
19. Yu. M. Kagan, A. M. Afanas'ev, and V. G. Kohn, Phys. Lett. **68A**, 339 (1978); *ibid.*, J. Phys. C **12**, 615 (1979).
20. J. P. Hannon, G. T. Trammell, M. Mueller, E. Gerdau, R. Rüffer, and H. Winkler, Phys. Rev. B **32**, 6363 (1985); *ibid.*, Phys. Rev. B **32**, 6374 (1985).
21. G. T. Trammell and J. P. Hannon, Phys. Rev. Lett. **61**, 653 (1988).
22. To simplify the discussion, we have assumed here that there are two unsplit resonances, located at sites d1 and d2 respectively, with a difference  $\Omega_E$  between the two resonance frequencies. In YIG, there is hyperfine splitting of the resonances at both the d1 and d2 sites, resulting in additional higher frequency quantum beat modulations, as discussed in Refs. [2] and [3].

## Nuclear Bragg Diffraction using Synchrotron Radiation

Rudolf Ruffer

II Institut für Experimentalphysik, Universität Hamburg  
D-2000 Hamburg 50, Luruper Chaussee 149, F. R. Germany

Nuclear Bragg diffraction in combination with synchrotron radiation will become a powerful new X-ray source in the Å-region. This new source exceeds already Mossbauer sources in brilliance giving Mossbauer scattering experiments further impetus. With the planned dedicated storage rings synchrotron radiation, filtered by measures of the Mossbauer effect, will not only allow new types of Mossbauer experiments but offers also a new X-ray source for  $\mu\text{eV}$  resolution and long coherence length X-ray optics.

The first experiments<sup>1</sup> had shown that there is a resonance in the diffraction spectra and even that the diffracted X-rays are highly monochromatic ( $\Delta E/E \approx 10^{-12}$ ). Although these experiments had shown the expected time behavior, an improved fast detector revealed the complete time spectra in all details<sup>2</sup>.

These experiments point out the basic phenomena connected with the nuclear Bragg diffraction of  $\gamma$ -quanta:

speedup (coherent enhancement), quantum beats, and  
polarization mixing (Faraday rotation, etc.).

The speedup in the time spectra - a dynamical effect of the diffraction, depends on the angle of incidence and is most pronounced at the beginning of the time spectra. This is clearly and very easily seen in the measurements of the antiferromagnetic  $^{57}\text{FeBO}_3$ .

In the quantum beats the hyperfine splitting of the nuclear levels and/or the resonance shifts between different nuclear sites in the crystal are expressed. The observation of quantum beats allows a sensitive and direct determination of the hyperfine interaction parameters.

Due to the fact that the nuclear Bragg diffraction is sensitive to the internal hyperfine fields, a strong polarization mixing of the scattering amplitudes may occur. Especially in the case of yttrium scattering iron garnet crystals, the spectra show a strong mixing depending on the directions between the  $\vec{B}$ -field and the  $\vec{k}$ -vector of the incident  $\gamma$ -ray.

### References

1. E. Gerdau, R. Ruffer, H. Winkler, W. Tolksdorf, C. P. Kleges, J. P. Hannon, Phys. Rev. Lett., 54, 835, 1985.
2. E. Gerdau, R. Ruffer, R. Hollatz, J. P. Hannon, Phys. Rev. Lett., 57, 1141, 1986.  
R. Ruffer, E. Gerdau, R. Hollatz, J. P. Hannon, Phys. Rev. Lett., 58, 2359, 1987.  
U. van Burck, R. L. Mobbauer, E. Gerdau, R. Ruffer, R. Hollatz, G. V. Smirnov, J. P. Hannon, Phys. Rev. Lett., 59, 355, 1987.

### Additional References:

1. J. P. Hannon, N. V. Hung, G. T. Trammell, E. Gerdau, M. Mueller, R. Rueffer, and H. Winkler, Phys. Rev. B32, 5068-5092 (1985).
2. J. P. Hannon, G. T. Trammell, M. Mueller, E. Gerdau, R. Rueffer, and H. Winkler, Phys. Rev. B32, 6363-6384 (1985).



**The production of long coherence-length hard x-rays using  
nuclear Bragg scattering of synchrotron radiation.**

*D. P. Siddons*  
*NSLS, Brookhaven National Laboratory*  
*Upton, NY 11973.*

**Summary**

Recently, several experimenters have successfully observed nuclear Bragg scattering from crystals containing  $^{57}\text{Fe}$ . By coherently exciting the 14.4keV resonance at the Bragg condition, almost pure beams of extremely monochromatic radiation can be generated. Although the intensities observed are so far quite low, the brightness produced by these techniques exceeds that available from radioactive sources. Instrumental improvements will soon make possible interesting new experiments. Several properties of the nuclear Bragg reflection process are interesting in themselves. These include the observation of beating in the time domain among hyperfine split resonance lines, and polarization mixing produced by scattering from oriented circularly polarized oscillators. Some speculations on the potential applications of this new source of long coherence-length radiation will be presented.

# Measurement of the Quenching of Spontaneous Emission Coefficients in Laser-Produced Plasmas

Y. Chung, H. Hirose,<sup>†</sup> and S. Suckewer<sup>‡</sup>

Princeton University, Plasma Physics Laboratory  
P.O. Box 451, Princeton, New Jersey 08543

## Abstract

The quenching of Einstein  $A$ -coefficients was observed by measuring the branching ratio of visible and VUV line intensities for CIV, CIII and NV ions.

## 1. Introduction

Since the formula for the Einstein  $A$ -coefficient was derived in the pioneering works of Weisskopf and Wigner(WW)[1] based on Dirac's theory of light, it has been widely accepted as valid in any practically important cases. In essence, the expression WW obtained was the same as that for a classical oscillating dipole except that the quantum mechanical dipole moment matrix element between the upper and the lower level of transition replaced the classical dipole moment. They also assumed an exponential decrease for the excitation probability of the upper state as *Ansatz* and proved it *a posteriori*.

However, the derivation of Einstein  $A$ -coefficient has often been the subject of rigorous theoretical investigation on the basis of other theories of light.[2,3] Even though essentially the same expressions as that of WW were obtained, it strongly suggests that the nature of light is not yet fully known. It was also noted by several authors[4-7] that the rate of spontaneous radiative decay can deviate significantly from Weisskopf-Wigner expression in certain environments where the atoms are located. Most notably, the spontaneous emission of radiation by an excited atom is completely suppressed in a cavity whose characteristic dimension is less than half the wavelength of the photon. It is believed that this effect is related to the decoupling of the vacuum

field and the radiating atom. In quantum electrodynamics(QED), the excited atom is driven to emit a photon and decay to a lower state by the fluctuation in the vacuum field if the atom is located in free space or a cavity whose dimension is much larger than the radiation wavelength. As the dimensions of the cavity become small compared to the radiation wavelength, the density of modes accessible to the atom decreases significantly. In this situation, the excited atom can no longer decay as freely as in the large cavity, and the radiative transition is effectively suppressed. A similar effect was also observed in the cyclotron radiation of an electron confined in a Penning trap[8] and has been predicted in solid state cavities.[9]

In a previous work,[10] the observation that the branching ratio of two radiative transitions originating from the same upper level decreased by about an order of magnitude at electron density of around  $10^{19}\text{cm}^{-3}$  compared to the ratio at  $10^{18}\text{cm}^{-3}$  led us to the conclusion that the coefficients of spontaneous emission were not constants. The term branching ratio in this paper denotes the ratio of the experimentally measured intensities of the visible and the VUV light unless specified otherwise. The spontaneous emission intensity  $I_{nm}$  (in photons) for transition  $n \rightarrow m$  is proportional to the upper level population density, the  $A$ -coefficient and a geometrical factor, that is,[11]

$$I_{nm} = k_n(r)N_n(n_e, T_e)A_{nm}. \quad (1)$$

Hence, the branching ratio for optically thin plasmas is the same as the ratio of the corresponding  $A$ -coefficients. Therefore, if the  $A$ -coefficients are constant independent of the electron density or other environmental factors, the branching ratio should re-

main constant even as we observe regions of different electron density in the plasma. It was our primary finding that this was not true.

The observed change of branching ratio could have been attributed to the following reasons:

- (1) self-absorption of the visible light
- (2) cut-off of the visible light in a region of high electron density where the plasma frequency  $\nu_p = \sqrt{\frac{n_e e^2}{m\pi}}$  is larger than the visible light frequency  $\nu_{VIS}$
- (3) refraction of the visible light out of the spectrometer line of sight
- (4) improper alignment of the spectrometers
- (5) stimulated emission of the VUV light at a level comparable to the spontaneous emission
- (6) non-linear detector sensitivity at low and high intensity
- (7) other experimental errors including misinterpretation of the data
- (8) deviation of the spontaneous emission coefficients from the vacuum (or low density) value.

An extremely careful examination, including supplementary experiments, of the other possibilities (1-7) confirmed the hypothesis that in higher-density plasmas the spontaneous-emission coefficients decreased. This may be a result of free electrons' interaction with atoms and ions. In previous work, we reported the first observation of a surprising decrease of the branching ratio of the visible to the VUV line intensities emitted by laser-produced plasmas with increasing plasma density using a novel VUV-visible duo-multichannel spectrometer.

In section 2, we will first describe measurements of the change of branching ratio of CIV (312 Å and 5801-5812 Å), CIII (574 Å and 5696 Å), NV (209 Å and 4603-4620 Å) transitions and recent results obtained from higher density plasmas produced by a ruby laser. These show an even larger decrease in branching ratio than could be obtained with a CO<sub>2</sub> laser as reported in Ref.10. In section 3 is shown our effort to explain this phenomenon, and in section 4, we will draw conclusions.

## 2. Experiment

In this section, we will describe: (1) experimental arrangements, (2) the branching ratio measurement experiment on CO<sub>2</sub>-laser-produced CIV and CIII ions, (3) measurement of the branching ratio

on ruby-laser-produced CIV ions, (4) measurement of the branching ratio on CO<sub>2</sub>-laser-produced NV ions, and (5) measurement of the light attenuation e.g., by self-absorption and refraction, due to the plasma.

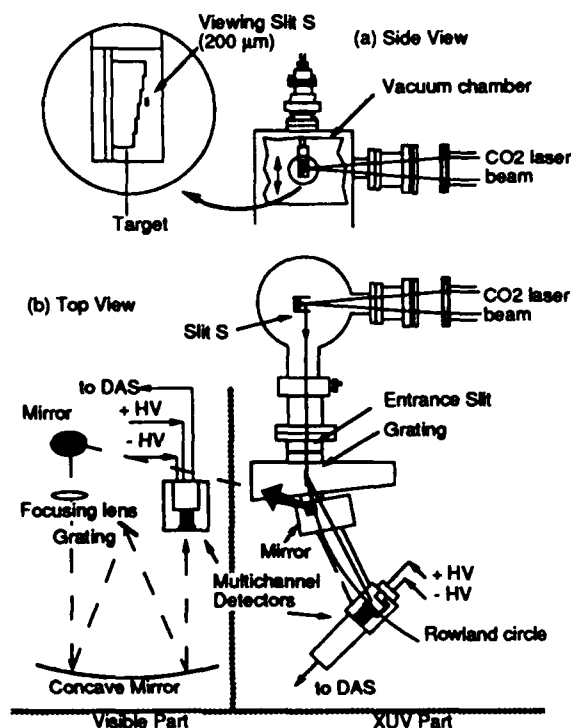


Figure 1. Experimental Setup

The experimental setup is shown in Fig. 1. The arrangement primarily consists of the lasers, the target chamber, the spectrometers and the supporting systems, such as vacuum pumps and the data acquisition system. The ruby laser is on top of the CO<sub>2</sub> laser and the two laser beams run parallel to each other. The CO<sub>2</sub> laser beam is focused onto the target by a NaCl lens of focal length  $f = 50\text{cm}$ , and the ruby laser beam is focused by a quartz lens of focal length  $f = 25\text{cm}$  after being redirected by a periscope into the CO<sub>2</sub> laser beam axis. The position of the focusing lens for the ruby laser beam can be adjusted up to  $\pm 3\text{cm}$  to provide optimal conditions for the generation of different ionization stages. The XeCl laser beam is positioned at approximately  $45^\circ$  to the CO<sub>2</sub> laser and the ruby laser. The characteristics of these lasers are summarized in Table 1.

Table 1

Laser	Energy(J)	Pulse(ns)	Beam Shape	Beam Size	Wavelength
CO <sub>2</sub>	10J	150ns	Annular	3.75" (OD), 1.75" (ID)	1060nm
Ruby	5J	20ns	Circular	1" diameter	694nm
XeCl	1J	40ns	Rectangular	3cm x 2cm	308nm

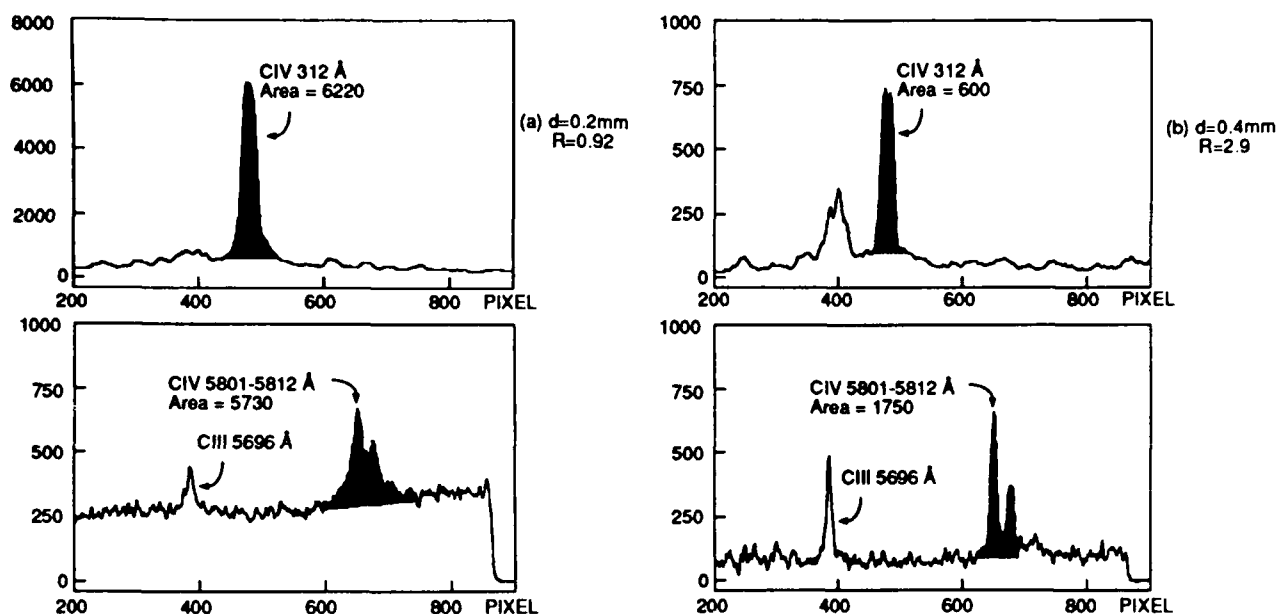


Figure 2. VUV and visible spectra of CIV taken simultaneously at a distance of (a)  $d = 0.2\text{mm}$  and (b)  $d = 0.4\text{mm}$  from the target surface. The upper ones are VUV spectra and the lower ones are visible spectra.

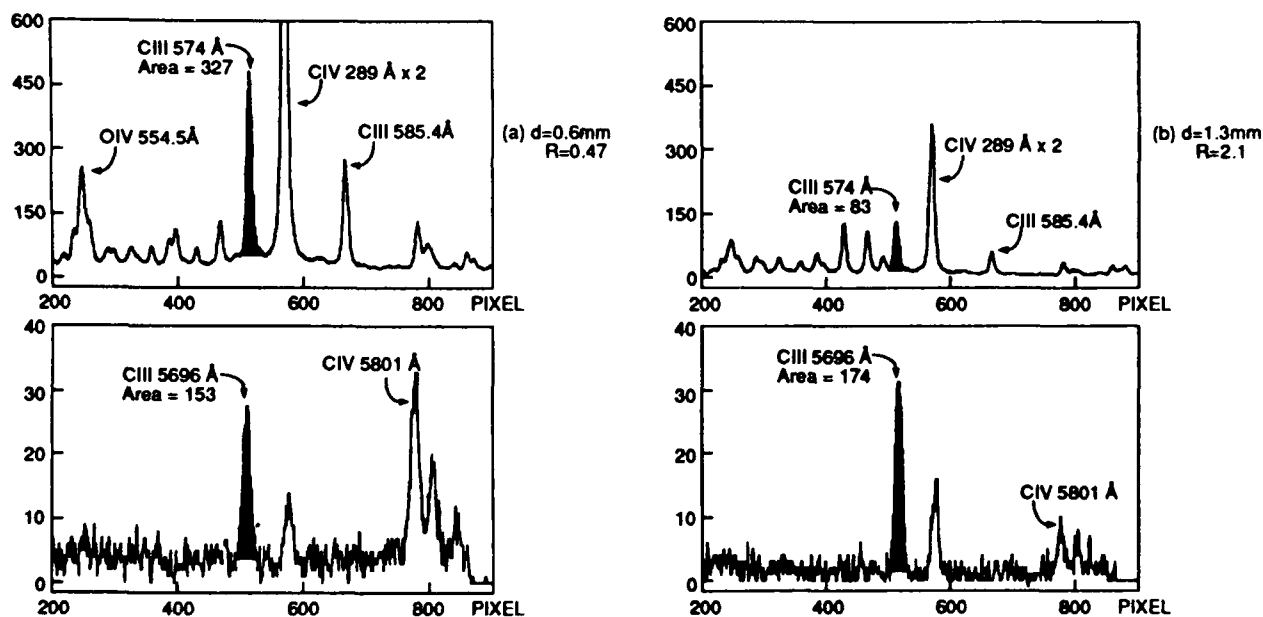


Figure 3. VUV and visible spectra of CIII taken simultaneously at a distance of (a)  $d = 0.6\text{mm}$  and (b)  $d = 1.3\text{mm}$  from the target surface. The upper ones are VUV spectra and the lower ones are visible spectra.

The plasma was created by interaction of the laser beam and a solid target in the vacuum chamber. The typical length of the target was 24mm and each step was 4mm long. Several targets of various widths ranging from  $200\mu\text{m}$  to 4mm were tested in this experiment. Even though narrower targets of width  $\approx 200\mu\text{m}$  gave results unaffected by VUV self-absorption, the signal to noise ratio was unac-

ceptably low. Moreover, these targets tended to be easily destroyed after a few shots of laser irradiation. Targets of width larger than 1mm didn't have this problem, but it was clear that there was VUV self-absorption close to the target. As a compromise, the targets were fabricated at  $300\mu\text{m} - 500\mu\text{m}$  for the measurement of the branching ratio. Targets of larger widths were used only to demonstrate the

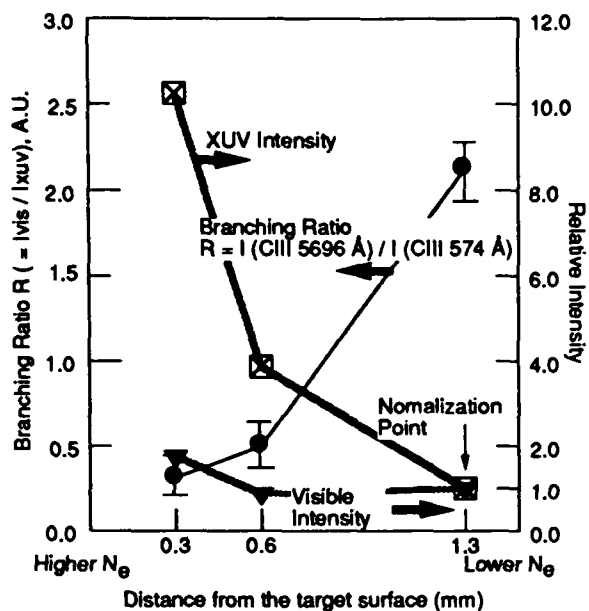


Figure 4. Branching ratio  $R = I_{\text{VIS}}/I_{\text{VUV}}$  for CIII 574 Å and 5696 Å lines as a function of distance from the target surface. Note that even though the VUV line intensity increases sharply near the target, the visible line intensity does not change very much.

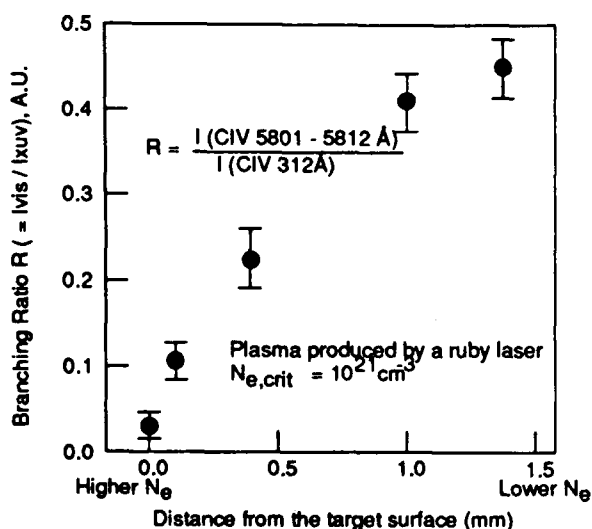


Figure 5. Branching ratio  $R = I_{\text{VIS}}/I_{\text{VUV}}$  for CIV 312 Å and 5801-5812 Å lines as a function of distance from the target surface. The plasma was produced by a ruby laser for higher density ( $10^{21}\text{cm}^{-3}$ ).

VUV self-absorption. The target had several steps (typically 6) as shown in Fig. 1, and plasmas at various distances from the target surface could be observed by moving the target up and down with a micrometer with vacuum feedthrough. The distance from observation region

to target surface increased by  $200\mu\text{m}$  with each step. The radiation emitted from the plasma first passed through a narrow slit S of  $200\mu\text{m}$  width,

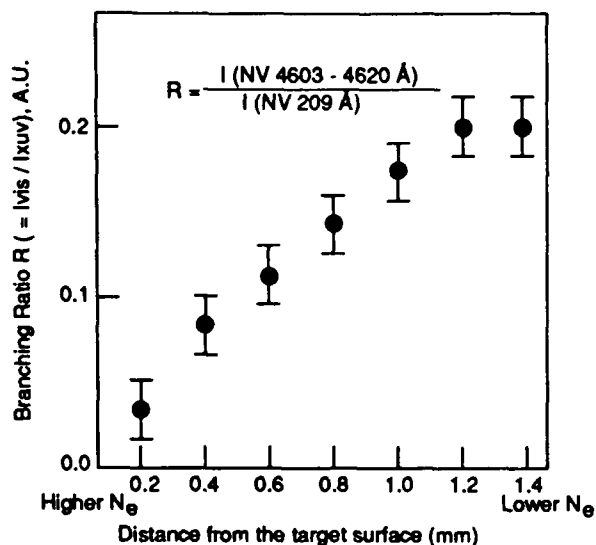


Figure 6. Branching ratio  $R = I_{\text{VIS}}/I_{\text{VUV}}$  for NV 207 Å and 4603-4620 Å lines as a function of distance from the target surface. The plasma was produced by a CO<sub>2</sub> laser.

which was fixed in the target chamber at a distance of 15mm from the target. The width of this slit S was also chosen as a trade-off between the signal to noise ratio and the spatial resolution of the measurement. Since the distance between the slit S and the target surface varied by  $200\mu\text{m}$ , we chose the slit width S to be  $200\mu\text{m}$  as well. A larger slit width would give better signal to noise ratio, but would also nullify the resolution provided by the target steps.

We used one or more of the lasers to produce the plasma. For the measurement of the branching ratio itself, we primarily used the CO<sub>2</sub> laser for producing relatively low density plasmas ( $n_e < 10^{19}\text{cm}^{-3}$ ) and the Ruby laser or the XeCl laser for high density plasmas ( $n_e < 10^{21}\text{cm}^{-3}$ ).

Fig. 2 shows the spectra obtained in the vicinity of CIV 312 Å and 5801-5812 Å (the shaded lines) at distances of (a) 0.2mm and (b) 0.4mm from the target, and Fig. 3 shows the spectra obtained in the vicinity of CIII 574 Å and 5696 Å (the shaded lines) at distances of (a) 0.6mm and (b) 1.3mm from the target. The branching ratio R was calculated from the ratio of the shaded areas of the visible and the VUV lines. It is shown clearly in Fig. 3 that while the VUV intensity drops by a factor of 4, the visible intensity even increases slightly as the distance d increases from 0.6mm to 1.3mm. The result of the measurement for CIII is presented in Fig. 4. We also measured the change of branching ratio for the CIV

312 Å and 5801-5812 Å lines with the ruby laser and NV 209 Å and 4603-4620 Å lines with the CO<sub>2</sub> laser. The results are shown in Figs. 5 and 6. The result for CIV 312 Å and 5801-5812 Å has already been reported in our earlier work.[Ref. 10, Fig. 3]

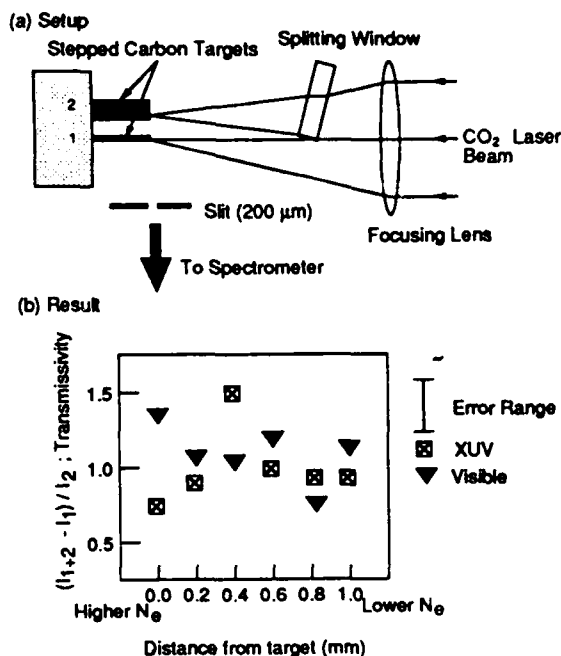


Figure 7. Absorption measurement experiment (a) experimental setup and (b) transmissivity of the plasma 1 created on the narrow target as a function of distance from the target.

To make sure that the branching ratio we measured was truly the ratio of the spontaneous emission intensities and was not affected by absorption, we measured the transmissivity of the plasma at various distances from the target. The experimental setup is shown in Fig. 7(a). The CO<sub>2</sub> laser beam was split into two identical beams by a NaCl window tilted at  $\approx 30^\circ$  with respect to the plane perpendicular to the beam axis. The resulting separation of the two plasmas created at the target 50cm away from the focusing lens was 2.5mm. The narrower target was 500 $\mu$ m wide and the other target was 2.7mm wide. The position of the beams were adjusted so that the plasmas were created at the center of the left target and at the edge of the right target. To measure the transmissivity of the plasma on the left target, we first obtained spectra from the left plasma and the right plasma separately by blocking one of the laser beams. Then we obtained the spectra with two plasmas. The measured intensities are denoted by  $I_1$  (left plasma),  $I_2$  (right plasma) and  $I_{1+2}$  (together), respectively in Fig. 7. The transmissivity  $T$

was taken to be

$$T = \frac{I_{1+2} - I_1}{I_2}$$

The result shows that within the experimental error there was insufficient absorption of visible light to account for the observed order of magnitude change in the branching ratio.

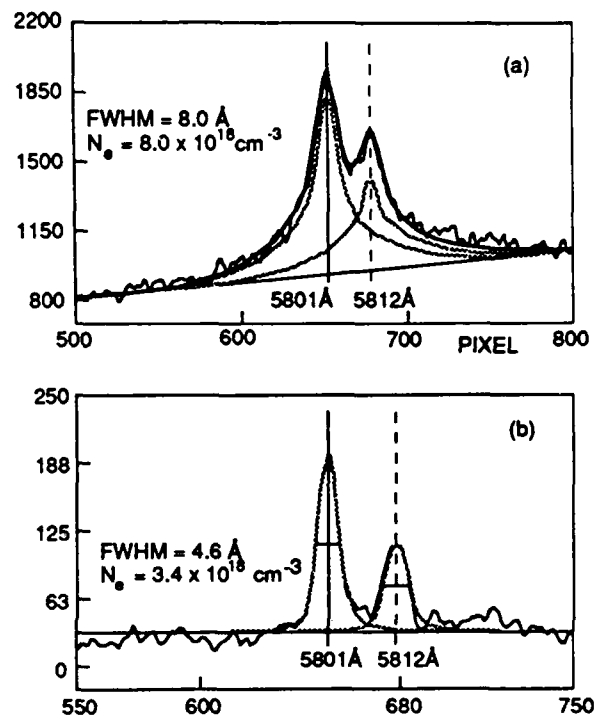


Figure 8. Fitting of the experimental data with the convolution of Lorentzian profiles of CIV 5801 Å and 5812 Å lines. (a)  $d = 0.2$ mm,  $R = 0.92$ , (b)  $d = 0.4$ mm,  $R = 2.9$ .

Another evidence that the spontaneous emission was not absorbed is manifest in the near perfect coincidence of the experimentally measured profile of CIV 5801 Å ( $J = 3/2$ ) and 5812 Å ( $J = 1/2$ ) and the convolution of their Lorentzian profiles with a 2:1 intensity ratio. Fig. 8 shows the fitting of the experimental data and the convolution of Lorentzian profiles of CIV visible lines is shown in Fig. 2. If there had been any absorption, the intensity ratio of the two lines would not be the theoretical ratio of 2:1 but closer to 1:1, since stronger line would be more absorbed. This analysis also strongly suggests that the plasma was optically thin.

Measurements of the branching ratio between two transitions that share the same upper level is independent of several factors concerning the population changes that could affect the line intensities. Here lies the simplicity of the principle involved in this experiment. Even though the measurement of

the temporal behaviour of the lines can be of assistance in understanding the change of the branching ratio, it was not deemed to be essential. Since the decay time of a transition is, except for the resonance transitions, equal to not the reciprocal of the corresponding  $A$ -coefficient but the radiative lifetime of an excited level which is given by the reciprocal of the sum of all the transition probabilities, i.e.,

$$\tau_i = \frac{1}{\sum_k A_{ik}}$$

Hence, all the transitions that branch from the same upper level should have the same temporal behaviour but with different amplitudes proportional to the  $A$ -coefficients. Therefore, assuming the plasma density was constant while the emission lasted so that the  $A$ -coefficients did not change, we would have

$$\frac{N_3(t_i)A_{32}\Delta t_i}{N_3(t_i)A_{31}\Delta t_i} = C(\text{constant}), \quad (3)$$

where  $N_3(t_i)$  is the upper level population at time  $t_i$  and  $\Delta t_i$  is the incremental time interval. If we take  $\Delta t_i \rightarrow 0$  and integrate over time, Eqs. (1) and (3) will give

$$\frac{I_{32}^T}{I_{31}^T} = \frac{\int I_{32}(t)dt}{\int I_{31}(t)dt} = \frac{k_{32}}{k_{31}} C,$$

which is also constant.  $I_{32}^T$  and  $I_{31}^T$  are the time-integrated intensities. This shows that change of the branching ratio  $R$  can be deduced from the change of the ratio of the time-integrated intensities alone.

As the final remark, we discuss uncertainties arising from the integration of the experimental profile used in the calculation of the branching ratio  $R$ . If the line is very broad, the boundary of the line profile to be integrated becomes less distinct, and this may introduce error in the integration. This can be quite a serious problem in the correct estimation of the total intensity when the background level is noisy or bumpy. Therefore, it is important to choose the end points of integration very carefully (and conservatively) in order not to underestimate the intensity of the visible transition at high plasma density. However, it is our belief the uncertainty in integration cannot account for the observed change in the branching ratio. Fig. 9 shows three cases of integration with different end points and the comparison of these values with the theoretical curve based on the assumption that the line profiles are Lorentzian. The end points we used for the actual calculation of the area are the same as the end points of the artificial background level line marked 1. This shows that as long as this artificial background level line does not deviate visibly from the adjacent background level, the error in the integration of the profile is

relatively small compared to the observed change in branching ratio.

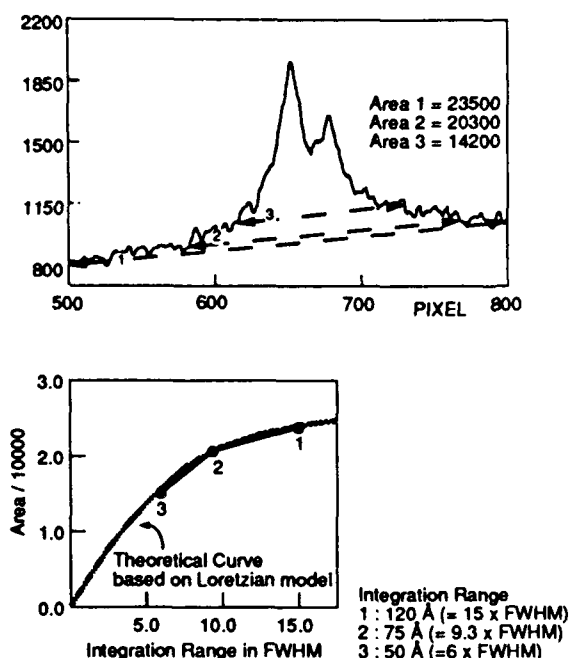


Figure 9. Estimation of error in integrating the line profile. The integration was done below the experimental profile and above the artificial background marked as dashed lines.

### 3. Theory

The theoretical effort has been on-going since we obtained the preliminary results from the experiments of measuring the branching ratio in CIV with a VUV multichannel detector and a visible monochromator two years ago. However, there does not yet exist a theoretical model that can clearly and unequivocally explain this phenomenon. In this section, we will describe our initial unsuccessful attempt, and then go on with a suggestion for possible future work.

We first speculated that the screening of the atomic potential by the surrounding plasma could modify the Coulomb field experienced by the electron and thus significantly change the transition probabilities. Several authors[12] have tried to obtain solutions of Schrödinger equation for a particle in a screened Coulomb potential. Russell and O'Connell calculated the spontaneous emission probabilities in the dipole approximation as a function of Debye-Hückel screening length  $r_D$  for hydrogen atom ( $Z = 1$ ) and showed that the spontaneous emission probabilities began to drop sharply at  $r_D = 50a_0$ , where  $a_0$  is the Bohr radius.

In our case, the Schrödinger equation was solved numerically for CIV ions in the electric potential of

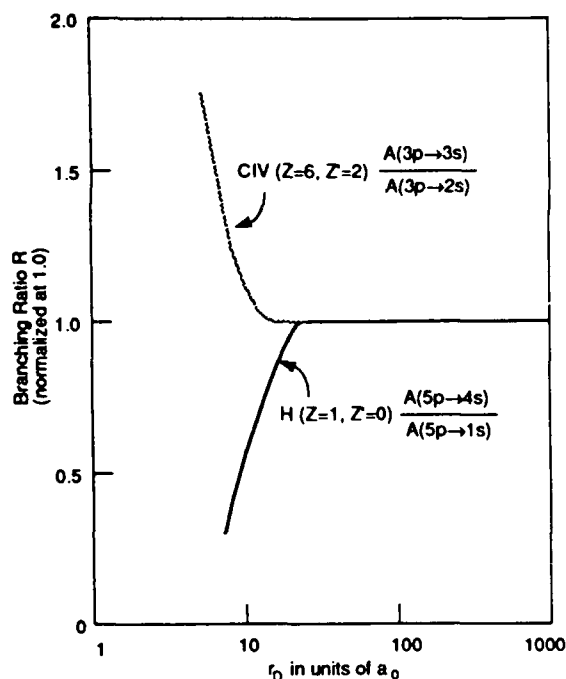


Figure 10. Theoretical branching ratio  $R$  obtained by solving Schrödinger equation with Debye-Hückel screened Coulomb potential for CIV ( $3p \rightarrow 3s$  and  $3p \rightarrow 2s$ ) and H ( $5p \rightarrow 4s$  and  $5p \rightarrow 1s$ ) as functions of the Debye radius  $r_D$ .

surrounding plasma. This potential was approximated by using Debye radius  $r_D \propto N_e^{-1/2}$ , assuming  $T_e$ , the electron temperature, to be constant. The transitions of the valence electron were assumed to occur in the internal potential of two bound electrons ( $1s^2$ ), approximated by a uniform charge cloud of radius  $R_0$  and influenced by the external field. Therefore, the potential  $V(r)$  was given by

$$V(r) = \begin{cases} \left[ \frac{Z'e^2}{2R_0} \left\{ 3 - \left( \frac{r}{R_0} \right)^2 \right\} - \frac{Ze^2}{r} \right] e^{-R_0/r_D} & \text{if } r \leq R_0 \\ - \left[ \frac{(Z - Z')e^2}{r} \right] e^{-r/r_D} & \text{otherwise,} \end{cases}$$

where  $e$  is the electron charge,  $r$  is the distance from the center of the charge cloud,  $Z = 6$  and  $Z' = 2$  for CIV and  $R_0$  was taken to be much smaller than  $r_D$ . Once the eigenfunctions were obtained by solving the Schrödinger equation, it was straightforward to obtain the branching ratio between the two transitions. In dipole approximation, the Einstein A-coefficients are given by

$$A(nl \rightarrow n'l') = \frac{4|\Delta E|^3}{3(2l+1)} S(nl, n'l'),$$

where

$$S(nl, n'l') = \sum_{m, m'} | \langle nlm | \mathbf{d} | n'l'm' \rangle |^2.$$

The theoretical branching ratio  $R$  between the two transitions,  $n_3l_3 \rightarrow n_2l_2$  and  $n_3l_3 \rightarrow n_1l_1$ , is then given by

$$R = \frac{A(n_3l_3 \rightarrow n_2l_2)}{A(n_3l_3 \rightarrow n_1l_1)}.$$

Fig. 10 shows the result obtained for the cases ( $5p \rightarrow 4s$ ,  $5p \rightarrow 1s$ ) of the hydrogen atom ( $Z = 1, Z' = 0$ ) and ( $3p \rightarrow 3s$ ,  $3p \rightarrow 2s$ ) of the CIV ion ( $Z = 6, Z' = 2$ ) as functions of the Debye radius  $r_D$ . For the transitions between lower lying states in the hydrogen atom, we obtained the same results as Russell and O'Connell. As  $r_D$  approaches  $10a_0$ , the branching ratio begins to increase very rapidly for the CIV ion in contrast to the hydrogen atom. For hydrogenic ions ( $Z > 1$ ), the higher the  $Z$  number, the less drastic was this effect. The main cause for the change in CIV was the changes in the transition strength  $S(nl \rightarrow n'l')$ , while in the case of hydrogen atom, it was the shift of energy levels. It must be noted here that this result is not consistent with the experimental results in that no line shift was observed with increasing electron density, i.e., with decreasing Debye radius. This inconsistency clearly indicates that (1) the Debye-Hückel screened potential is not valid in our case since the plasma parameter

$$g = nr_D^3$$

is not much larger than 1 and/or (2) the electron density is still too low for the screening effect to become important. Assuming  $T_e \approx 5\text{eV}$  and  $n_e \leq 10^{19}\text{cm}^{-3}$ , we have  $r_D > 100a_0$  and  $g \geq 1.5$ .  $r_D$  and  $g$  become larger as the electron density decreases if  $T_e$  is constant. This is far away from the region where the screening of the potential can alter the transition probability significantly, and we conclude that the quenching of Einstein A-coefficient as observed in the experiment is due to some cause other than the screening of the static Coulomb potential by the surrounding plasma.

A different approach to the development of a theoretical model has been the modification of the Weisskopf-Wigner (WW) approximation of exponential decay of excited atoms.[13-16] Ref. 14 is essentially an extension of the WW in the sense that the coupling between the first continuum of states to which the excited atom initially decays and the second continuum was taken into account. In this case, the decay rate of initial excited state can decrease if the first continuum of states is itself unstable and coupled to a still lower lying continuum of states. Even though the probability that the excited state stays there remains exponential, the decay rate may



be changed. If only the second continuum were considered in addition to the first continuum and if the coupling strengths  $V_{32}$  and  $V_{21}$  could be factored as  $V_{32} = F_0 G_0$  and  $V_{21} = F_1 G_1$ , the modified decay rate  $\gamma$  would be [16]

$$\gamma = \frac{\gamma_{GR}}{1 + H_1}, \quad (2)$$

where  $\gamma_{GR}$  is the Fermi Golden Rule rate, and  $H_1$  is an intrinsically positive quantity proportional to the square of the coupling strength  $V_{21}$ .

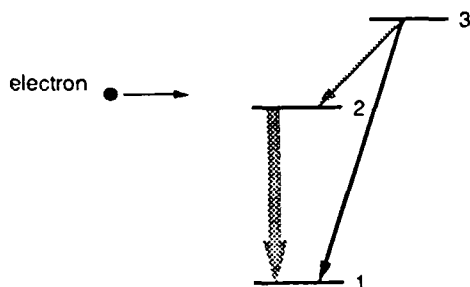


Figure 11. Hypothetical theory: radiative transition may be quenched when the coupling between the levels 2 and 1 becomes large through the collisional de-excitation by electrons.

We are presently following this line of approach and exploring the possibility of relating the rapid depletion of the lower level of transition by collisional de-excitation to the suppression of radiative decay from the initially excited level 3 (see Fig. 11). The transition between levels 2 and 1 is forbidden in the dipole approximation, and the level 2 would be metastable unless provided with other channels of decay. The coupling between the levels 2 and 1 is provided by collisional de-excitation whose rate will increase linearly with the electron density  $n_e$ .

#### 4. Conclusion

We have described the continuation of experiments to supplement the previous work in Ref. 10 on the change of branching ratio in high density plasmas and our theoretical efforts to explain it. Various possible explanations other than decrease of Einstein A-coefficients in high density regime were judged to be unfounded after very careful analysis of the data from the measurement of the branching ratio and other supporting experiments. At this time, we still lack a satisfactory theoretical explanation of why the branching ratio, hence the Einstein A-coefficient, changes in high density plasmas. However, we hope that future progress in the theoretical study will provide such an explanation and lead to better understanding of the atomic radiative processes in plasmas.

#### Acknowledgment

This work was supported by U.S. Department of Energy Advanced Energy Project of Basic Energy Sciences, Contract No. KC-05-01. This work was performed at the Princeton Plasma Physics Laboratory, which operates under U.S. Department of Energy Contract No. DE-ACO2-76CHO3073.

† Present address: Nagoya University, Nagoya, Japan

‡ Also at Dept. of Mechanical and Aerospace Engineering, Princeton University

#### References

1. V. Weisskopf and E. Wigner, "Berechnung der natürlichen Linienbreite auf Grund der Diracschen Lichttheorie," *Z. Phys.*, **63**, 54 (1930) [translated in *Atomic Spectra*, by W. R. Hindmarsh (Pergamon, London), p.304].
2. M. D. Crisp and E. T. Jaynes, "Radiative effects in semiclassical theory," *Phys. Rev.*, **179**, 1253 (1969)
3. A. O. Barut and J. F. van Huele, "Quantum electrodynamics based on self-energy: Lamb shift and spontaneous emission without field quantization," *Phys. Rev. A*, **32**, 3187 (1987)
4. E. M. Purcell, "Spontaneous emission probabilities in radio frequencies," *Phys. Rev.*, **69**, 681 (1946)
5. D. Kleppner, "Inhibited spontaneous emission," *Phys. Rev. Lett.*, **47**, 233 (1981)
6. R. G. Hulet, E. S. Hilfer, and D. Kleppner, "Inhibited spontaneous emission by a Rydberg atom," *Phys. Rev. Lett.*, **55**, 2137 (1985)
7. W. Jhe, et al., "Suppression of spontaneous decay at optical frequencies: Test of vacuum-field anisotropy in confined space," *Phys. Rev. Lett.*, **58**, 666 (1987)
8. G. Gabrielse and H. Dehmelt, "Observation of inhibited spontaneous emission," *Phys. Rev. Lett.*, **55**, 67 (1985)
9. E. Yablonovitch, "Inhibited spontaneous emission in solid-state physics and electronics" *Phys. Rev. Lett.*, **58**, 2059 (1987)
10. Y. Chung, P. Lemaire, and S. Suckewer, "Quenching of spontaneous emission coefficients in plasmas," *Phys. Rev. Lett.*, **60**, 1122 (1988)
11. H. Griem, *Plasma Spectroscopy* (McGraw-Hill, New York, 1964), p.229.
12. See K. M. Roussel and R. F. O'Connell, "Variational solution of Schrödinger's equation for the static screened Coulomb potential," *Phys. Rev. A*, **9**(1), 52 (1974) and the references therein.

13. S. D. Druger, "On the relation between random coupling and sequential intramolecular dynamics," *J. Chem. Phys.*, **73**, 2287 (1980)
14. E. J. Robinson, "Quenched exponential decay," *Phys. Rev. Lett.*, **57**, 1281 (1986)
15. Z. Deng and J. H. Eberly, "Effect of coherent continuum-continuum relaxation and saturation in multiphoton ionization," *Phys. Rev. Lett.*, **53**, 1810 (1984)
16. Z. Deng and J. H. Eberly, "Quenched decay into multiple continua," *Phys. Rev. Lett.*, **58**, 618 (1987)

# Ultra-High Resolution VUV-XUV Laser: Application to the Hyperfine Study of Krypton

A. H. Kung, T. Trickl,<sup>a</sup> E. Cromwell, M. J. J. Vrakking and Y. T. Lee

*Chemistry Department, University of California, Berkeley, California 94720*

*Material and Chemical Sciences Division, Lawrence Berkeley Laboratory  
Berkeley, California 94720*

## Abstract

A near-transform-limited VUV-XUV laser source with 210 MHz resolution has been constructed and used to study the hyperfine splitting, isotope shift, and lifetime of the three lowest ns ( $n=5,6,7$ ) Rydberg states of Krypton.

## Introduction

Transform-limited tunable lasers represent photon sources with the highest spectral purity and spectral brightness. The ability to deliver photons in the narrowest possible spectral width finds applications not only in high-resolution spectroscopy, but also in cases where efficient use of photons are desired. Examples of this are plenty in the field of chemical physics. Experiments involving selective excitation of molecules: stimulated-emission pumping studies, resonance-enhanced multiphoton excitation and ionization, laser-induced fluorescence, molecular beam excitation studies, and studies of molecules or impurities embedded in liquids, matrices, and crystals can all benefit from these lasers. Near transform-limited tunable pulsed lasers in the visible and near-uv have been available for several years.[1,2] Recently we have extended the tuning range of these types of lasers to the vuv and xuv region. In this article we shall describe the basic requirements and the approach we took for the laser development and a brief summary of the first application of this source: a hyperfine study of the ns Rydberg states of krypton. Details of the laser development and the krypton study have been submitted for publication elsewhere.[3,4]

## Design Goals

The goals follow from the desire that the source will be used for photoionization and LIF study of small to intermediate sized molecules in a pulsed molecular beam setting:

- \* broad tunability, at least from 70 nm to 160 nm;
- \* high spectral brightness, preferably transform-limited;
- \* high intensity,  $10^{15}$  to  $10^{16}$  photons per second at 10 Hz;
- \* uniform spatial profile;
- \* user friendly.

If these goals are met the laser source not only will be able to serve as a universal probe of many chemical processes but also as a powerful excitation source to initiate such processes.

## Approach

Since the first and foremost requirement for the source is broad tunability it is a simple choice to use the technique of four-wave mixing for the generation of vuv and xuv in the prescribed range. This well-established technique [5] has very broad wavelength coverage, potentially can be very efficient [6], and uses reliable commercial components. Successful exploitation of this technique, which involves high order nonlinear optical processes, requires careful control on the spectral, temporal, and spatial properties of the visible laser(s) used. For this reason the followings were chosen to constitute the major components of our system:

- \* a pulse-amplified CW single-longitudinal-mode dye laser for good frequency control;
- \* an injection-seeded Nd:YAG laser as pump laser for a smooth Gaussian temporal profile;
- \* side-pumped prism dye cells to preserve the spatial quality of the dye beam;
- \* a pulsed nozzle as the vuv generator for simplicity and flexibility in the choice of four-wave mixing medium;
- \* a 1-meter grating monochromator to disperse the vuv-xuv wavelengths from the incident visible and uv radiation.
- \* a Faraday optical rotator for isolation of the CW dye laser from the pulsed dye amplifiers;
- \* lens-pinhole-lens spatial filtering between successive stages of dye amplification to control amplified-spontaneous-emission growth.

Auto-tracked second-harmonic-generation crystals are used to convert the visible to the uv prior to the four-wave mixing stage. Table I is a summary of the performance of the laser. Entries to the table are self-explanatory. It is however necessary to point out that we measure a frequency shift of 0 to 20 MHz between the CW laser frequency and the amplified output frequency. This shift depends on the dye used in the amplifiers as well as the number of amplification stages used. At this point we are trying to understand the cause of this shift. But it is clear that for experiments where this shift is significant to the results it is necessary to determine the shift for each frequency measurement. Details of the characterization of the laser are provided in reference 4.

### Hyperfine study of Krypton

Utility of this source has been demonstrated in a high-resolution study of the  $4p-5s[3/2]$ ,  $-5s'[1/2]$ ,  $-6s[3/2]$ ,  $-6s'[1/2]$  and  $-7s[3/2]$   $J=1$  transitions of Kr spanning the spectral region from 123.6nm to 94.5nm. The ns states ( $n=5,6,7$ ) were studied using  $1 + 1$  resonant multiphoton ionization where the ns states form the resonant intermediate. Calibrations using known  $I_2$  frequencies yield an improved absolute calibration of the  $^{86}\text{Kr}$   $4p$ -ns transition frequencies by more than an order of magnitude. The hyperfine parameters for the  $5s[3/2]$  level are in very good agreement with those measured using interferometric techniques. This is the first time that determination of hyperfine parameters for the other levels listed above are possible. From these parameters we find that for  $n=5$  the  $jj$  quantum numbers are good to  $99.63 \pm 0.06\%$  while for  $n>5$  the  $jj$  quantum numbers are good to at least 99.99%.

Isotope shifts for the more abundant ( $>0.1\%$  natural abundance) isotopes were obtained. These shifts can be explained by the simple Bohr shift and the specific mass effect. To within our resolution we do not observe a volume effect on the shift. Lifetimes for the  $n=6$  and 7 states which are longer than the duration of our laser pulse can also be measured. Our lifetime results differ substantially from calculations reported in the literature. These results should form a basis for the atomic theorists to obtain an improved set of wavefunctions for Kr.

### Remarks

The laser system described above meets most of the goals outlined in the beginning of

Table I: Summary of Laser Performance

	<u>Visible</u>	<u>UV</u>	<u>VUV-XUV</u>
Energy	100 mJ	30 mJ	1 uJ
Bandwidth (FWHM)	91 MHz	140 MHz	210 MHz
Pulsewidth	7 nsec	<7 nsec	~4 nsec
Temporal Profile	near Gaussian	near Gaussian	near Gaussian
Tuning Range (tested)	562-620 nm	281-310 nm 222-240 nm	74-124 nm
Frequency Shift	Amplifier configuration and dye dependent		

this article. However, a major shortcoming is that the intensity falls short of the goal by 3 to 4 orders of magnitude. A second pulse-amplified single-mode dye laser system is under construction to provide a second frequency for resonance-enhanced four-wave mixing operation. This could improve the intensity by two orders of magnitude. Amplification in the vuv using inert-gas excimer systems or free-electron lasers is certainly possible. Other plans include use of tunable solid-state amplifiers (alexandrite, Ti-sapphire), use of high-repetition-rate pump lasers, and use of high power excimer lasers to facilitate efficient pumping of blue-green dyes.

This work is supported by the Director, Office of Energy Research, Office of Basic Energy Sciences, Chemical Sciences Division of the U.S. Department of Energy under contract no. DE-AC03-76SF00098.

[a] Present address: Max-Planck-Institut für Extraterrestrische Physik, 8046 Garching b. München, West Germany.

- [1] M.M. Salour, *Opt. Commun.*, **22**, 202 (1977).
- [2] P. Drell and S. Chu, *Opt. Commun.*, **28**, 343 (1979).
- [3] E. Cromwell, T. Trickl, Y.T. Lee and A.H. Kung, "Ultra-narrow bandwidth vuv-xuv laser system", submitted to the *Rev. Sci. Inst.*
- [4] T. Trickl, M.J.J. Vrakking, E. Cromwell, Y.T. Lee and A.H. Kung, "Ultra-high-resolution (1+1) photoionization spectroscopy of KrI", submitted to *Phys. Rev. A*.
- [5] G. Hilber, A. Lago and R. Wallenstein, preceding paper in this proceeding.
- [6] C.H. Muller III, D.D. Lowenthal, C.E. Hamilton and A.V. Smith, following paper in this proceeding.

# Non-Reciprocity of Autoionizing Interferences: Lasers Without Inversion

S. E. Harris

*Edward L. Ginzton Laboratory, Stanford University  
Stanford, California 94305*

## Abstract

Interferences of autoionizing lines may reduce or eliminate absorption of lower level atoms. Stimulated emission shows no such interferences, thereby allowing laser gain without population inversion.

## Introduction

During the last several years we have made significant progress toward the realization of a class of extreme ultraviolet and soft x-ray lasers where the upper laser level is embedded in the continuum of the valence electron [1]. The advantage of this type of laser, as compared to more typical ionic lasers, is that the upper laser level occurs at much lower energy, and therefore may be pumped by cooler x-rays or electrons; this allows the operation of such lasers at pumping energies and powers which are much lower than would otherwise be possible. Highlights of recent work include: the demonstration that levels in the continuum may be pumped by electrons and retain their metastability under practical operating conditions [2]; the development of the technique of depletion spectroscopy for the measurement of autoionizing lifetimes [3]; and most recently the demonstration of an extraordinary 12.8 eV laser in neutral Cs [4]. This laser achieves an equivalent small signal gain of  $\exp(83)$ , at a pumping energy of 3 joules in 20 psec.

An energy level diagram for the Cs laser is shown in Fig. 1. Though we have a good

understanding of the mechanism for pumping the upper level, we do not understand how inversion is obtained; that is, why do electrons not populate the lower laser level? Though earlier proposals [1] suggested the use of a ionizing laser to empty the lower level, no such laser was used in the Cs experiments.

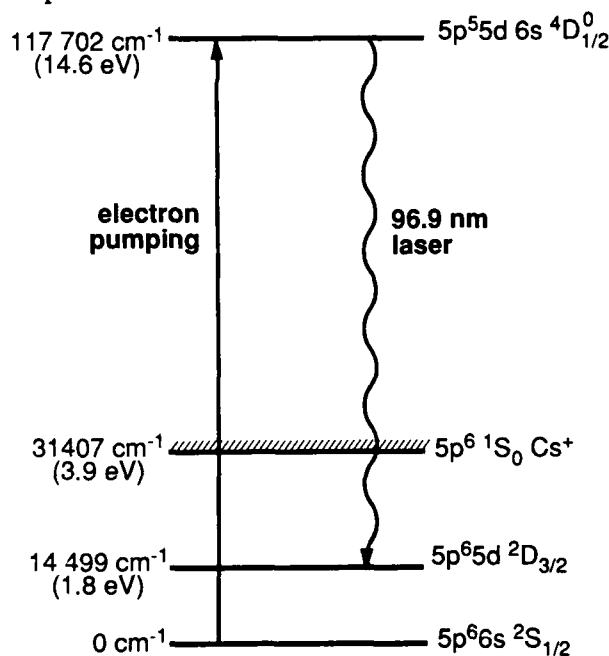


Figure 1—Partial energy level diagram for neutral Cs showing the laser transition.

In trying to understand this system the thought occurred to me that perhaps inversion is not necessary. Perhaps, interference between two autoionizing levels could result in a cancellation of

loss, while leaving the gain relatively unchanged. We soon found a precedent to this idea; i.e., the work of Arkhipkin and Heller [5] who show that a simple Fano interference between a discrete level and a continuum is non-reciprocal; that is, if the upper level is populated, the gain cross section will not exhibit interference.

Though of great conceptual interest, the effect of Arkhipkin and Heller is too small to be useful. The Fano interference occurs when the absorption of the discrete line has fallen to the level of the continuum. At the point of zero loss, the gain is that of the continuum itself. For alkali atoms this gain is often four orders of magnitude smaller than that of a peak discrete line gain.

In this work I consider the interference of two lines and a continuum. Here, the zero loss point occurs at approximately that frequency where there is a balance of virtual autoionizations, and the gain at this point may be very large. There is also a strikingly new effect: an upper populated level with zero oscillator strength to the lower laser level will acquire gain from a coupled nearby level, and will do so with zero absorption at line center.

It is particularly important that the interference of the two lines does not require the direct coupling of the electromagnetic field to the continuum. The essential ingredient of the non-reciprocity of gain and loss is lifetime broadening. Figure 2 shows several isomorphic systems to which the formulae given in section III apply. The systems share the common feature that virtual excitation of either of the two upper levels decays to an identical continuum. Because of its simplicity and potential application to artificially layered materials, the tunneling system is particularly interesting.

### Formulae Development

The development of the formulae will be given separately [6] and will only be sketched here. To start, the basis set for the development is that of the discrete bound levels and of the continuum. This allows a particle, at  $t = 0$ , to be put into the bound level. The effects described in this paper may well have gone undetected for so long as a result of the traditional use of the Fano basis set [7]. Though a superposition of Fano levels may be used to establish the initial condition, the mathematics of the subsequent evolution is difficult.

In this work, the continuum is eliminated by a method which is analogous to that of Cohen-Tannoudji, et al. [8]. One obtains three coupled

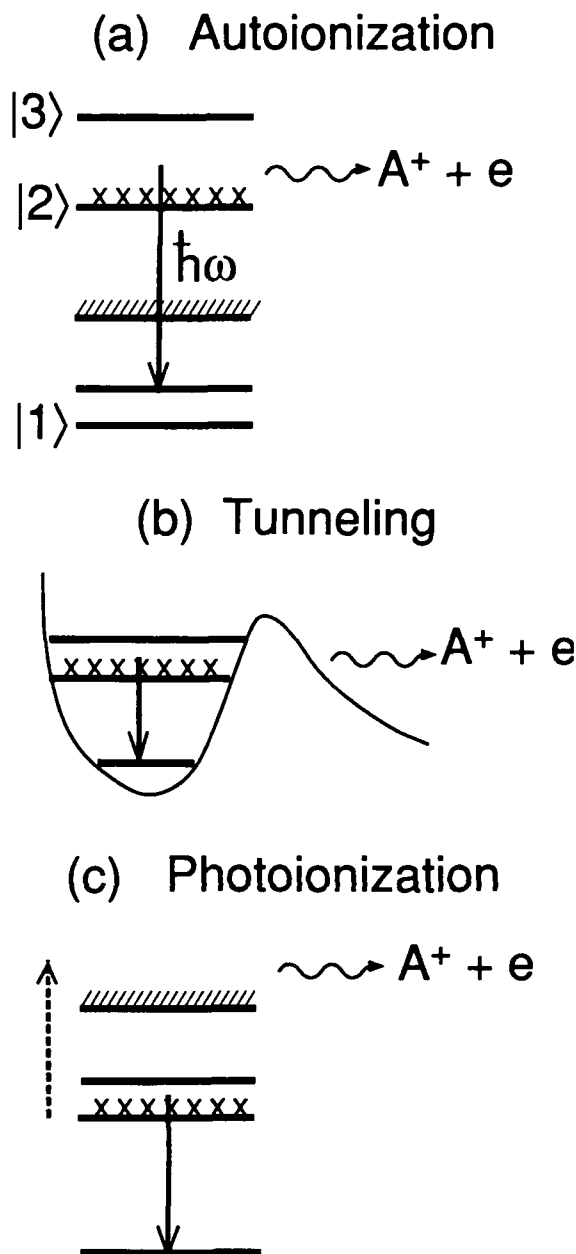


Figure 2—Energy level diagrams of three prototype systems that will exhibit nonreciprocal gain and loss profiles; in each case the upper two levels decay to the same continuum.

equations for the time varying amplitudes  $a_i(t)$  of levels  $|1\rangle$ ,  $|2\rangle$  and  $|3\rangle$ . These equations have as inputs the Rabi frequencies, autoionizing rates, and photoionization rates of the respective levels.

The formula for the absorption cross section is obtained by applying the  $t = 0$  boundary condition  $a_1 = 1$ ,  $a_2 = a_3 = 0$ , taking the E field to be very small, and solving for  $a_2(t)$  and  $a_3(t)$ . These quantities are then substituted into

the equation for  $a_1(t)$  to obtain the absorption transition probability and cross section.

The formula for stimulated emission is obtained by applying the  $t = 0$  boundary condition  $a_2 = 1$ ,  $a_1 = a_3 = 0$ , and solving (exactly) for  $a_2(t)$  and  $a_3(t)$ . This solution is then used, in the presence of a small  $E$  field, to find the  $t = \infty$  population of level  $|1\rangle$ . This quantity, divided by the coupled decay rate of the upper levels, gives the stimulated transition probability and gain cross section.

## Results

We give the results in terms of the Fano parameters  $\eta_i$  and  $q_i$ . The  $\eta_i$  are the detunings from the respective lines, each normalized to its autoionizing halfwidth. The  $q_i$  are the ratio of the Rabi frequency of each line to the square root of the product of its autoionizing time multiplied by its photoionization rate.

The absorption cross section normalized to the continuum cross section is then

$$\frac{\sigma_{ab}}{\sigma_c} = \frac{[\eta_3 q_2 + \eta_2 q_3 + \eta_2 \eta_3]^2}{[\eta_2^2 \eta_3^2 + (\eta_2 + \eta_3)^2]} \quad (1)$$

This result is implicit in Fano's original paper. Readily obtained special cases include a single line alone, a single line in a continuum, or two interfering lines without a continuum. (Note that to remove a line from this formula, one must set both its  $q = 0$ , and also its  $\eta = \infty$ ; thereby allowing both its oscillator strength and its autoionizing time to approach zero.) Two cases are of special interest; the zero which occurs at the balance of virtual autoionizations for strong lines and the zero which occurs at line center ( $\eta_2 = 0$ ) when  $q_2 = 0$ . This latter zero is the equivalent of the effect, which for a single line, is sometimes termed as a window resonance.

The cross section for stimulated emission, again normalized to the continuum cross section is

$$\frac{\sigma_e}{\sigma_c} = \left( \frac{\Gamma}{\Gamma_2} \right) \left[ \frac{q_2^2 \eta_3^2 + [(q_2 - q_3) - \eta_3]^2}{\eta_2^2 \eta_3^2 + (\eta_2 + \eta_3)^2} \right] \quad (2a)$$

where

$$\frac{\Gamma}{\Gamma_2} = \frac{(2 \Delta E)^2}{(\Gamma_2 + \Gamma_3)^2 + (2 \Delta E)^2} \quad (2b)$$

The factor  $\Gamma/\Gamma_2$  is the ratio of the autoionizing time of the coupled (level  $|2\rangle$  - level  $|3\rangle$ ) system to the autoionizing time of level  $|2\rangle$ , if alone. The quantity  $\Delta E$  is the spacing of levels  $|2\rangle$  and  $|3\rangle$ . As the spacing becomes large,  $\Gamma/\Gamma_2$  approaches one. For  $\Delta E$  small, the autoionization rate of level  $|2\rangle$  is suppressed. Equation (2b) has the condition that  $\Gamma_3 > \Gamma_2$ .

Perhaps the most interesting result of Eqs. (1) and (2) is obtained as  $q_2$  approaches or equals zero. One finds a nearly Lorentzian shaped gain profile centered on a line with zero oscillator strength. Figure 3 shows this result. Both gain and loss are plotted as a function of normalized detuning (in units of  $\eta_2$ ). The only parameter which varies between graphs is  $q_2$ . Note again, that it is level  $|2\rangle$  which is populated at  $t = 0$ , and whose oscillator strength is progressively reduced in this sequence of graphs. As noted, these graphs all assume  $q_3^2 = 1000$  and assume that this latter level is located two thousand linewidths of level  $|2\rangle$  from level  $|2\rangle$ .

## Detailed Balance

At first glance, one wonders whether results of this type violate detailed balance. The answer is that they do not and the reason is that detailed balance applies between the initial level and the final level. The initial level is level  $|1\rangle$  and the final level is an ion plus a free electron. To state this differently, if one attempted to make a recombination laser (starting with electrons and ions) by this method one could not do so. For a single line in a continuum, recombination exhibits a Fano profile [9]; and two lines in a continuum exhibit an interference of their (virtual) dielectronic recombinations.

It is important to note that we have included no other broadenings and thus direct population of level  $|2\rangle$  by a monochromatic photon from level  $|1\rangle$ , is not possible. All absorption leads (in a single step) to the production of a free electron. To the extent that other broadenings are on scale with the decay broadening, then level  $|2\rangle$  could be directly populated by photons from level  $|1\rangle$ , and the interference effects will be blurred.

## Angular Momentum

The above formulae have also assumed that all processes, i.e. the excitation of the continuum and of levels  $|2\rangle$  and  $|3\rangle$  all produce the same final continuum. For one dimensional tunneling this is the case. For certain special cases in atoms, this is



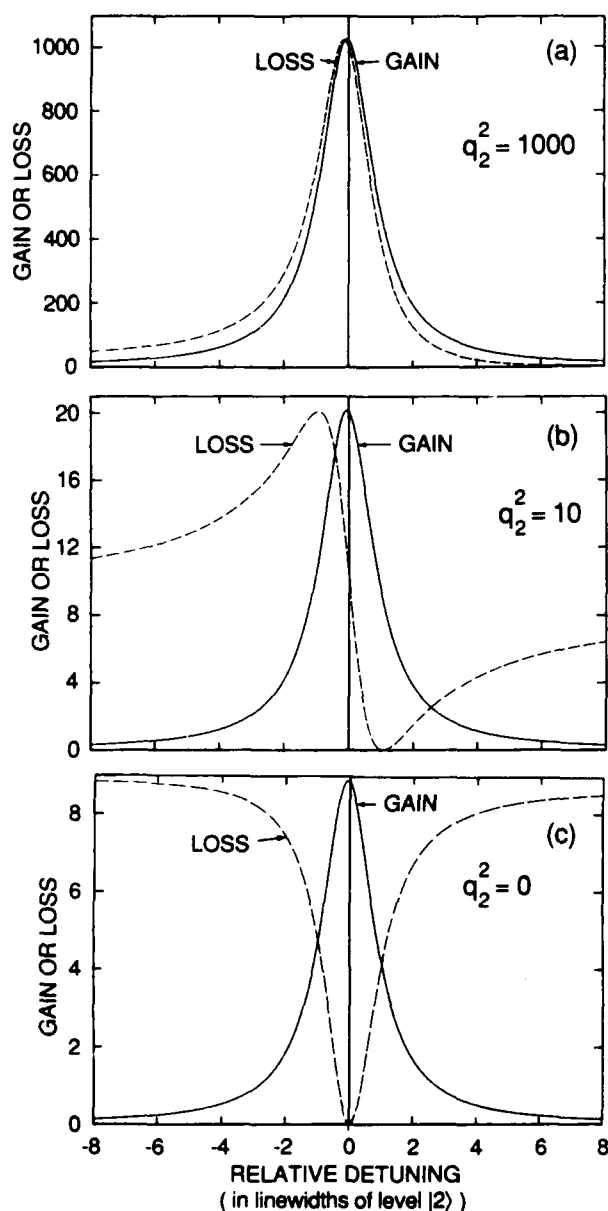


Figure 3—Gain and loss profiles of interfering levels. For the loss profiles,  $a_1 = 1$ ,  $a_2 = a_3 = 0$  at  $t = 0$ . For the gain profiles,  $a_2 = 1$ ,  $a_1 = a_3 = 0$  at  $t = 0$ . The only parameter which varies between Figures is  $q_2^2$ . The other parameters are  $q_3^2 = 1000$ ,  $\Gamma_2 = 1$ ,  $\Gamma_3 = 250$ . Levels  $|2\rangle$  and  $|3\rangle$  are separated by 2000 linewidths of level  $|2\rangle$ .

also the case and interferences are perfect. But in general different final electrons are produced and only identical electrons interfere. Levels  $|2\rangle$  and  $|3\rangle$  need not have the same  $J$  to interfere. Angular momentum is conserved between the photon and the initial and final levels, and not with regard to the virtual intermediate level.

## Summary

Though it is commonly believed that inversion is a requirement for stimulated emission, this does not appear to be the case. Interferences in absorption need not appear in emission. These effects may occur naturally in XUV and x-ray lasers or they may be synthesized using artificially layered materials. Interferences between discrete levels, even in the absence of photoionization are predicted. The tunneling system of Fig. 2 is the prototypical example.

The author gratefully acknowledges the support of the U.S. Air Force Office of Scientific Research, and the U.S. Army Research Office.

## References

1. S. E. Harris and J. F. Young, "Core-Excited Metastable Levels: Application to Spectroscopy, to the Generation of Picosecond Extreme-Ultraviolet Pulses, and to Lasers," *J. Opt. Soc. Am. B* **4**, 547-562 (April 1987).
2. J. C. Wang, R. G. Caro, and S. E. Harris, "Novel Short-Pulse Photoionization Electron Source:  $\text{Li}(1s2s2p)^4P^0$  Deexcitation Measurements in a Plasma," *Phys. Rev. Lett.* **51**, 767-770 (August 1983).
3. J. K. Spong, A. Imamoglu, R. Buffa, and S. E. Harris, "Laser Depletion Spectroscopy of Core-Excited Levels of Neutral Rubidium," *Phys. Rev. A* (to be published).
4. C. P. J. Barty, D. A. King, G. Y. Yin, K. H. Hahn, J. E. Field, J. F. Young, and S. E. Harris, "96.9 nm Saturated Laser in Neutral Cesium," *Conference on Short Wavelength Coherent Radiation: Generation and Applications*, North Falmouth, MA (September 1988).
5. V. G. Arkhipkin, and Yu. Heller, "Radiation Amplification without Population Inversion at Transitions to Autoionizing States," *Phys. Lett.* **98A**, 12-14 (October 1983).
6. S. E. Harris, "Lasers Without Inversion" (submitted for publication).
7. U. Fano, "Effects of Configuration Interaction on Intensities and Phase Shifts," *Phys. Rev.* **124**, 1866-1878 (December 1961).
8. C. Cohen-Tannoudji, B. Diu, and F. Laloe, *Quantum Mechanics*, Vol. II (Hermann, Paris, France, 1977), pp. 1343-1347.
9. B. W. Shore, "Parametrization of Absorption-Line Profiles," *Phys. Rev.* **171**, 43-54 (July 1968).

# Studies of Hot, Solid Materials Produced by an Ultrashort Pulse Laser

H. M. Milchberg

*Institute for Physical Science and Technology and Department of Electrical Engineering  
University of Maryland, College Park, Maryland 20742*

R. R. Freeman

*AT&T Bell Laboratories, 600 Mountain Avenue, Murray Hill, New Jersey 07974*

## Abstract

A series of ultrashort pulse laser-solid interaction experiments have been performed using copper and aluminum which illustrate charge transport properties of these strongly heated materials at near-solid density. In aluminum, as a Drude metal at the laser wavelength, the transport is seen to be strongly dominated by collisions with the appearance of a minimum mean free path. In copper, band absorption of the laser light is seen to be a strong process even at  $\sim 50$  eV temperatures.

In the context of using ultra-short pulse laser-produced plasmas as a source of ultra-short pulse soft X-rays, evidence is presented that heat loss mechanisms in these hot solids may not be sufficiently rapid to result in subpicosecond soft X-ray bursts.

## Reflectivity Results

Pulses of light of energy 0-5 mJ, ( $\lambda = 308$  nm), and 400 fs FWHM were specularly reflected (with beam mode preserved) from optically smooth metallic targets. The laser was operated at 10 Hz and the target was stepped at each pulse. The pulse leading edge ASE (amplified spontaneous emission) energy was kept below a fraction  $10^{-3}$  of the energy in the main ultrashort pulse. It was found that a fraction as small as  $10^{-2}$  was deleterious to the experiment because of absorption and scattering in a pre-expanded vapor or plasma.

Figure 1 is a plot of self-reflection (reflected energy/incident energy) vs. incident intensity for aluminum for S and P polarized light. With the assumption that aluminum's optical properties at 308 nm are described

by a Drude model index of refraction,

$$n^2 = 1 - \omega_p^2 / \omega(\omega + i\nu) \quad (1)$$

at all temperatures of this experiment, one can invert Fig. 1 to generate Fig. 2, a plot of resistivity,

$$\rho = m_e \nu / N_e e^2 \quad (2)$$

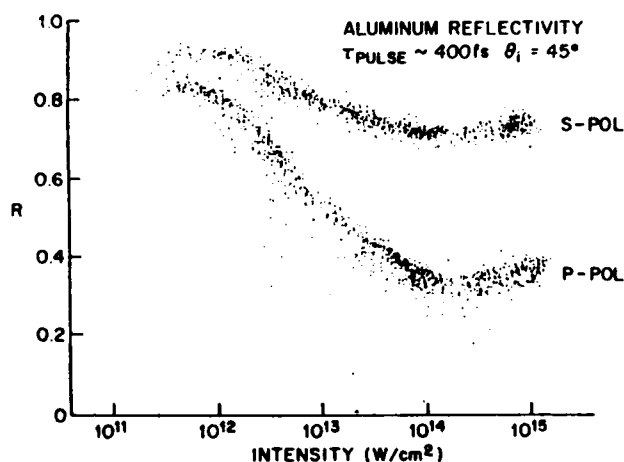


Figure 1. Self reflection as a function of intensity of S and P polarized light at 308 nm, for  $\sim 400$  fs FWHM pulses. Each point represents the reflection of a single pulse from an optically smooth Al surface.

Here  $\nu$  is the electron-ion collision frequency and  $N_e$  is the electron density.  $N_e$  is supplied by assuming local thermal equilibrium (LTE) [1], and in any case it is not strongly sensitive over our temperature range due to high 3-body recombination rates at these densities. The inversion procedure was performed by using the Fresnel equations

(for step-function interfaces) for the reflectivity, or by directly integrating the Helmholtz wave equations through a small ( $\ll \lambda$ ) gradient scale length [2]. At the levels of collisionality  $\nu$  in these experiments, both methods gave very similar results.

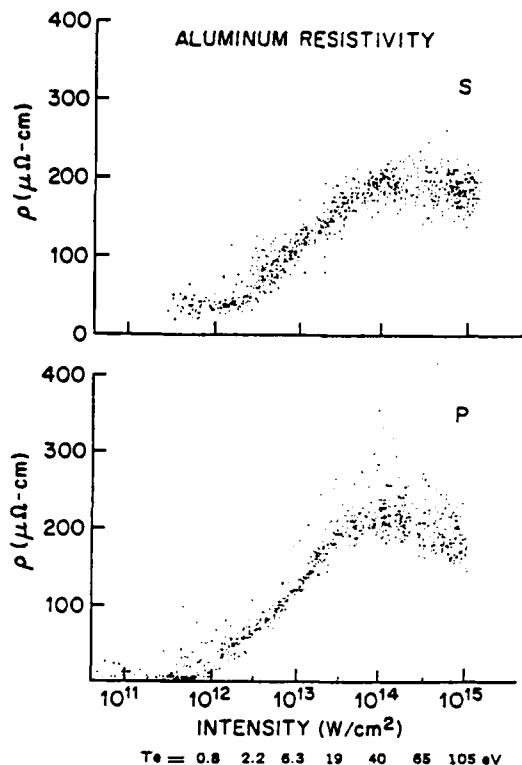


Figure 2. Resistivity vs. intensity and electron temperature for S and P polarization.

The similarity of the S and P results in Fig. 2 is a positive check on the data analysis, since the resistivity should be polarization independent. The temperatures indicated in Fig. 2 were obtained by monitoring the blue shift and broadening of the specularly reflected light with an optical multichannel analyzer [3]. This spectral modification was attributed to mass motion of the heated material given by

$$v_{\text{exp}} = \frac{2}{\gamma-1} (ZkT_e/m_i)^{1/2} \quad (3)$$

for unsteady flow into vacuum [4]. It was shown that self-phase modulation plays a negligible role in producing the shifts and broadenings. Fig. 2 illustrates three regions of electron transport, with a prominent saturation in the resistivity near 200  $\mu\Omega\text{-cm}$  for  $T_e \sim 40$  eV. For  $T_e < 5$ -10 eV,  $\rho$  increases approximately linearly with  $T_e$ , suggesting constant coupling between the

electrons and ions. In the region 10-40 eV,  $\rho$  is sublinear in  $T_e$ , indicating the presence of temperature dependent electron-ion coupling. The turnover in  $\rho$  at temperatures  $> 50$  eV is consistent with the behavior of a high temperature plasma: a decrease in  $\rho$  at high  $T_e$  due to the energy denominator in the electron-ion collision cross section. The maximum in  $\rho$  near 200  $\mu\Omega\text{-cm}$  and  $T_e \sim 40$  eV is identified as "resistivity saturation", and a calculation of the electron mean free path,  $\ell$ , using these measured values of  $\rho$  and  $T_e$  gives  $\ell \sim 3$  Å, which is approximately the interatomic separation in solid aluminum. This suggests that this is truly a limiting resistivity, independent of the specifics of material preparation.

A similar experiment was performed using copper. Figure 3 shows the results for S-polarized 400 fs FWHM pulses, with data from 20 ps pulses shown for comparison. The long pulse result of decreasing  $R$  with increasing intensity (temperature) is consistent with greater absorption in longer scale length copper plasma, and onset of non-specular reflection (resulting in light scattered outside the collection solid angle) due to refraction in the vapor/plasma and reflection from the presumably rippled critical density surface.

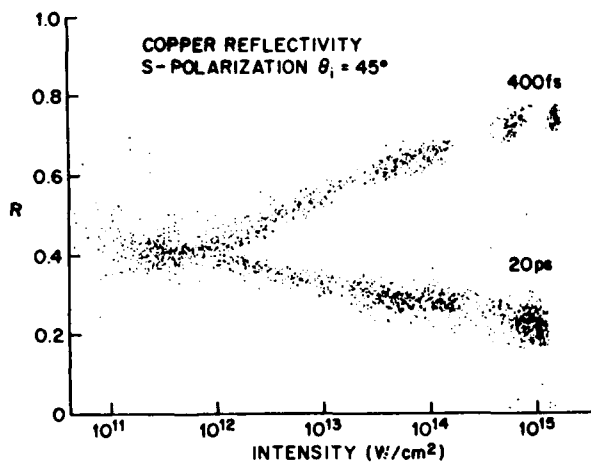


Figure 3. Self reflection vs. intensity for S polarized light from an optically smooth copper surface. Pulsewidths are 400 fs and 20 ps.

The rise in  $R$  with intensity for the 400 fs data illustrates the fundamentally different properties attributable to hot, near-solid density Cu in comparison to lower density copper plasma. The data of both pulse widths converge to the cold solid Cu reflectivity of  $\sim 40\%$  at low intensities. The absorption of the cold material is primarily 3d band absorption of 308 nm photons. Evidently, for short pulses (and near-solid

densities) the band continues to exist, and the rise in  $R$  with temperature might be related to the gradual promotion of electrons out of the band. We can roughly estimate the band "persistence" by comparing 3-body recombination rates (assumed into the band) at 30 eV and 100 eV, typical temperatures of this experiment. Using a rough formula based on a weakly coupled Maxwellian plasma,

$$v_{3b} \sim 10^{-27} N_e N_i (kT_e)^{-9/2} s^{-1} \quad (4)$$

for the 3 body recombination rate [5], gives  $\tau_{3b} = 14$  fs at 30 eV and  $\tau_{3b} = 3$  ps at 100 eV. This indicates that at 30 eV, the 3d band efficiently repopulates during the 400 fs laser pulse, with the excess energy being carried away by the third body, an electron in the conduction band. At 100 eV, however, the band is not repopulated during the pulse and so the amount of band absorption of UV photons decreases. The increase in reflectivity with intensity (and temperature) may thus indicate the depopulation of the 3d band.

#### Heat Loss from Hot Solid-Density Aluminum

If these ultrashort-pulse heated solid materials are to be a source of ultrashort pulse soft X-ray emission, and if the emission is thermal in character, it is important that the electron temperature decay on a time scale comparable to the laser pulse width. The dominant temperature drop mechanisms are expansion and thermal conduction. It may be shown (by assuming a black body emitter) that radiation contributes comparatively little to the drop in  $T_e$ . The temperatures measured from the Doppler shift and broadening due to the expanding interface [3] reflect cooling that has already occurred during the expansion, through conversion of electron thermal energy into directed ion kinetic energy. Losses due to thermal conduction can be assigned an upper bound as follows.

The measurement of  $\rho$  in hot solid aluminum as a function of temperature allows the determination of the thermal conductivity,  $\kappa$ , through the Weidemann-Franz relation,

$$\kappa = \frac{1}{\rho} \frac{\pi^2}{3} \left( \frac{k}{e} \right)^2 T_e \quad (5)$$

The maximum thermal flux  $q$  occurs for  $q = \kappa dT_e/dx = \kappa T_e/\delta = q(\max)$  where  $\delta$  is the absorption skin depth of the laser light in the material. The skin depth  $\delta$  is a minimum ( $\sim 100$  Å) at low  $T_e$  where  $v$  (and  $\rho$ ) is small and increases (to  $\sim 400$  Å) in the regime of high collisionality. Here, we take  $\delta = \delta_{\min} = 100$  Å and plot  $q(\max)/P(\text{abs})$  vs. incident power and temperature in Fig. 4, where  $P(\text{abs})$  is absorbed power obtained

from Fig. 1. This represents an upper bound on thermal conduction. The maximum thermal flux from the heated material is at most 25% of the absorbed power once  $T_e$  is greater than  $\sim 1$  eV.

The increase in the contribution of thermal conduction below  $\sim 1$  eV is due to the lower value of absorbed power in this range. At higher temperature, the approximate constancy of  $\kappa$  and linear scaling of  $T_e$  with  $P(\text{abs})$  results in a roughly constant fractional contribution of thermal conduction. At the higher temperatures at which soft X-ray sources might be considered, it is apparent from Fig. 4 that for solid aluminum, the temperature may not drop fast enough to produce a thermal soft X-ray emission pulse comparable in duration to the laser pulse. In fact, the observation that the target heats up substantially in the first place is testimony to the small contribution of competing loss mechanisms. Under these conditions, the temperature of hot solid aluminum depends on the absorbed energy rather than on peak power.

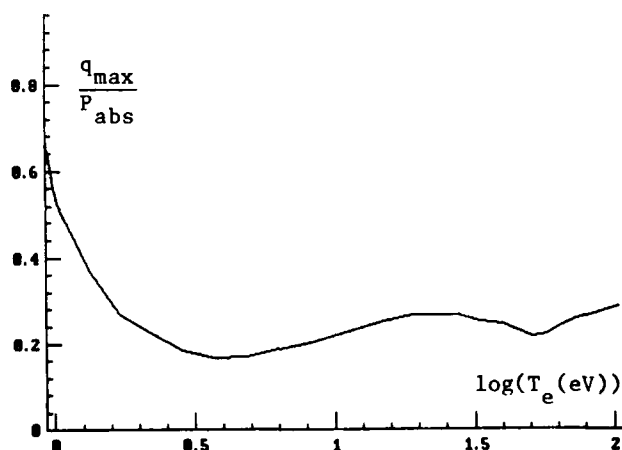


Figure 4. (Maximum rate of thermal conduction)/(absorbed laser power) vs. electron temperature. Thermal conductivity was determined from the measured resistivity (see text).

#### Conclusions

High energy, short pulse reflectivity measurements of solid materials indicate behavior quite different from lower density plasmas of comparable temperature. In a collision dominated material, aluminum, the onset and passage through a regime of "resistivity saturation" was observed, where the minimum electron mean free path was set by the interatomic spacing of the solid, independent of the extent of any further disorder in the material.

In copper, primarily a band absorber at

the incident laser wavelength, the persistence of band absorption at high temperature is explained by the high rate of band refilling at solid densities.

Determining hot solid aluminum thermal conductivity from measured resistivity allows an upper bound calculation of the effectiveness of thermal conduction cooling as a means to generate ultrashort soft X-ray bursts. The conclusion is that this loss mechanism is marginal.

#### References

1. H. R. Griem, Plasma Spectroscopy, (McGraw Hill, N.Y., 1964).
2. H. M. Milchberg and R. R. Freeman, submitted for publication.
3. H. M. Milchberg and R. R. Freeman, submitted for publication.
4. Ya. B. Zeldovich and Yn. P. Raizer, Physics of Shock Waves and High Temperature Hydrodynamic Phenomena, (Academic Press, N.Y., 1966).
5. R. C. Elton, in Methods of Experimental Physics, vol. 9 - Part A, Plasma Physics, ed. H. R. Griem and R. H. Lovberg, pp. 115-168 (Academic Press, N.Y., 1970).

# ALL SHORT PULSE MULTIPHOTON IONIZATION IS RESONANT IONIZATION

W. COOKE, UNIV. OF SOUTHERN CALIFORNIA  
R.R. FREEMAN, AT&T BELL LABORATORIES  
T.J. MCILRATH, UNIV. OF MARYLAND

## ABSTRACT

Energy resolved photoelectron spectra of multiphoton ionization taken with a 300 fs laser pulse at 616 nm shows that the ionization probability is highly structured as a function of laser intensity. The spectrum is consistent with all of the ionization occurring at intensity resonances.

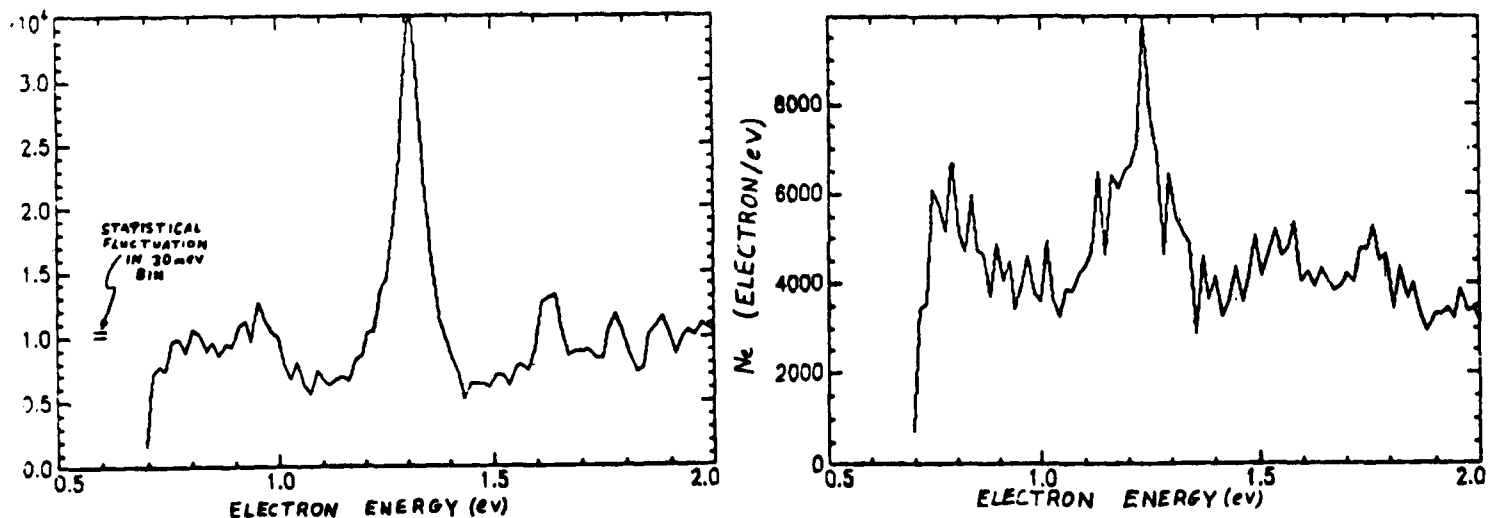
####

Photoelectron spectra have been obtained for photoelectrons resulting from multiphoton ionization using 300 fs pulses of 616nm radiation. The light pulses are sufficiently short that the electrons remained fixed during the duration of the light pulse. The result is that no energy is acquired or lost to the Ponderomotive potential during the duration of the pulse. The electrons therefore retain the directed velocity (velocity averaged over several optical cycles) which they possessed when produced. The electron energies were recorded with a time of flight spectrometer and the resulting spectrum is a record of the initial directed kinetic energy (total kinetic energy minus quiver energy) of the electrons.

The kinetic energy of the initial electrons is determined by the number of photons absorbed ( $Nh$ ) and the ionization energy of the atom ( $U$ ). If the number of photons absorbed is known, then the electron energy is known. The kinetic energy is partitioned between quiver energy (Ponderomotive energy) and directed kinetic energy. If the light pulse decays before there is significant movement of the electron, then the quiver energy follows the local intensity and

decays to zero with no transfer to directed kinetic energy. The deficit between the measured kinetic energy of the detected electron ( $1/2 mv^2$ ) and the initial energy of the electron ( $Nh\nu - U$ ) is a measure of the Ponderomotive energy at the time of ionization. Because the Ponderomotive energy is proportional to intensity, the kinetic energy spectrum of the electrons is a spectrum of the number of electrons produced as a function of laser intensity in the beam.

Figure 1 shows a typical spectrum. The ionization clearly has resonances with low ionization occurring at intensities above or below the resonance. We present angle resolved data as well as total electron yields and argue that the data shows that the ionization process is a resonant process in energy. This has several implications, including the prediction that ionization is spatially non-uniform with most ions formed in shells which surround largely unionized gas. It indicates that saturation phenomena are very difficult to achieve since increases in intensity simply increase the spatial extent of the shells, leaving the overall form of the structure unchanged. Finally it indicates that theories of Multiphoton ionization which do not include atomic structure can only be correct in a general, averaged sense. An interpretation of the resonances in terms of the Stark shifts of atomic levels has been developed but the interpretation of the data in terms of intensity resonances and non-uniform ionization is independent of these models.



---

## **Index of Authors**

---

42/100



## Index of Authors

- Ade, H. 274  
 Ando, Kozo 154  
 Aoyagi, Yoshinobu 154  
 Appert, Q. D. 329  
 Aristov, V. V. 318, 347  
 Atac, M. 202  
 Attwood, D. 274, 325  
 Bachor, H.-A. 125  
 Bado, B. 165  
 Baldwin, K. G. H. 125  
 Barbee, Troy 350  
 Barletta, W. 202  
 Barrow, V. 194  
 Barty, C. P. J. 13  
 Bashkansky, M. 236, 258  
 Basov, Yu. A. 347  
 Beethe, D. C. 99  
 Benerofe, S. J. 60  
 Bhowmik, A. 202  
 Bobbs, B. 202  
 Bokor, J. 355, 392  
 Bourgade, J. L. 2, 93  
 Boyer, K. 220, 225, 246, 284  
 Breidne, M. 327  
 Bucksbaum, P. H. 236, 258  
 Burnett, N. H. 84, 225  
 Byer, R. L. 290  
 Carillon, A. 21  
 Carter, M. R. 371  
 Casperson, Donald E. 242  
 Ceglio, N. M. 357  
 Chang, T. H. P. 274, 325  
 Chapple, P. B. 125  
 Chen, Shi-sheng 326  
 Cheng, Yongkang 129  
 Chung, Y. 402  
 Cline, D. B. 202  
 Combis, P. 2, 93  
 Cooke, W. 422  
 Corkum, P. B. 225  
 Cover, R. A. 202  
 Cowley, S. C. 251  
 Cromwell, E. 411  
 Cullen, D. 284  
 Daido, H. 47, 137, 141  
 Dalhed, S. 123  
 Denney, C. 157  
 Dhez, P. 21  
 DiCicco, D. S. 277  
 Dixon, F. P. 202  
 Dote, Toshihiko 154  
 Eberly, J. H. 266  
 Edwards, J. 194  
 Endoh, A. 167  
 Enright, G. D. 84  
 Falcone, R. W. 189  
 Feitisch, A. 163  
 Feldman, U. 106  
 Field, J. E. 13  
 Filbert, P. C. 133  
 Fill, Ernst E. 78  
 Frahm, R. 347  
 Freeman, Richard R. 214, 378, 418, 422  
 Fujimoto, T. 52  
 Gallardo, J. 202  
 Gauthe, F. Gadi 21  
 Gibson, G. 220, 246  
 Goldhar, J. 106  
 Graeff, W. 347  
 Greinke, B. 325  
 Gupta, A. P. 277  
 Guttman, P. 325  
 Haddad, W. S. 284  
 Hagelstein, P. L. 28, 123, 133  
 Hahn, K. H. 13  
 Halas, N. J. 392  
 Hamilton, C. E. 177  
 Hannon, J. P. 394  
 Hara, Tamio 154  
 Harris, S. E. 13, 209, 414  
 Hart, D. J. 384  
 Hepburn, J. W. 384  
 Herman, P. R. 47, 137, 184  
 Hilber, G. 175  
 Hirose, H. 402  
 Hirschberg, J. G. 277  
 Hodge, W. L. 133  
 Howard, W. M. 135  
 Howells, Malcolm 303  
 Iskander, N. 274  
 Jacobson, Chris 303  
 Jaegle, P. 21  
 Jamelon, G. 21  
 Jara, H. 220  
 Javanainen, J. 266  
 Jitsuno, T. 47  
 Johnson, A. M. 355  
 Joyeux, D. 295  
 Kaplan, A. E. 145  
 Kapteyn, H. C. 189  
 Kato, T. 52  
 Kato, Y. 47, 137, 141, 184  
 Katsuragawa, M. 67  
 Keane, C. J. 2, 93  
 Kern, D. 274, 325  
 Key, M. H. 47, 137  
 Kiehn, G. 194  
 Kim, D. 116, 277  
 King, D. A. 13  
 Kirz, Janos 303  
 Kitagawa, Y. 141  
 Klisnick, A. 21  
 Kmetec, J. D. 209  
 Kohler, D. A. 133  
 Kolonko, J. 202  
 Krishnan, M. 157  
 Krushelnick, K. 106  
 Kung, A. H. 411  
 Kuroda, H. 11, 65, 67  
 Kurosawa, Kou 184  
 Lago, A. 175  
 Lambropoulos, P. 256  
 Law, C. T. 145  
 Lee, Peter H. Y. 242  
 Lee, Yim T. 135, 411  
 LePell, P. D. 157  
 Leubner, C. 76  
 Levine, J. 157  
 London, R. A. 2, 93, 310  
 Louis-Jacquet, M. 2, 93, 123  
 Lowenthal, D. D. 177  
 Luk, T. S. 220, 233, 246  
 Ma, Zuguang 129

- MacGowawn, B. J. 2, 93, 123  
 Maine, P. 165  
 Marconi, M. C. 99  
 Masai, K. 52  
 Materlik, G. 347  
 Matthews, D. L. 2, 93  
 Maxon, S. 2, 123, 133  
 McIlrath, T. J. 422  
 McIntyre, I. A. 220, 246  
 McPherson, A. 220, 246  
 McQuaid, K. 274, 303  
 Meixler, L. D. 106  
 Meyer-Ilse, W. 274, 325  
 Milburn, D. 384  
 Milchberg, H. M. 418  
 Miura, E. 47, 137, 141  
 Mourou, G. 165  
 Muller, C. H., III 177  
 Muller, H. G. 265  
 Murnane, M. M. 189  
 Muroo, K. 11, 65, 67  
 Naccache, D. 2, 93  
 Naito, K. 11  
 Nakai, S. 47, 141  
 Nam, C. H. 106  
 Namba, Susumu 154  
 Nash, T. 157  
 Nathel, Howard 350  
 Navoda, C. L. 133  
 Newman, Brian E. 200  
 Nishihara, K. 141  
 Nishimura, H. 47, 137  
 Peek, J. M. 133  
 Pellegrini, C. 202  
 Peng, Huimin 69  
 Perez, J. D. 133  
 Peyrusse, O. 93  
 Pistoiresi, D. J. 329  
 Polack, F. 295  
 Price, D. F. 371  
 Puntajer, Anna K. 76  
 Rakowsky, G. 202  
 Rarback, H. 274  
 Rhodes, C. K. 220, 233, 246, 284  
 Robinson, J. 106  
 Rocca, J. J. 99  
 Rose, S. J. 47  
 Rosen, M. D. 2, 93, 123, 310  
 Rosman, R. 220, 246  
 Rosser, R. J. 277, 339  
 Rothman, S. 274, 303  
 Ruffer, Rudolf 400  
 Sarukura, N. 167  
 Sasaki, Wataru 184  
 Schappert, Gottfried 242  
 Schmahl, G. 309  
 Schumacher, D. W. 236, 258  
 Scofield, J. H. 133  
 Scott, Marion L. 322  
 Seely, J. 106  
 Shao, Yunfeng 69  
 Sheng, Jiatian 69  
 Sher, M. H. 60  
 Simpson, W. M. 355  
 Shiraga, H. 47, 137  
 Siddons, D. P. 401  
 Skinner, C. H. 116, 277  
 Smith, A. V. 177  
 Smith, R. 194  
 Snigirev, A. A. 347  
 Solem, J. C. 220, 233, 284  
 Stewart, R. E. 371  
 Storz, R. H. 355  
 Strickland, D. 165  
 Su, Q. 266  
 Suckewer, S. 36, 106, 116, 277, 402  
 Sun, Shangwen 129  
 Susskind, S. M. 251  
 Szoke, Abraham 350  
 Tachi, T. 47, 137  
 Takabe, H. 47, 137  
 Takagi, M. 47  
 Tallents, G. J. 47, 137  
 Tanaka, Y. 11, 65, 67  
 Tang, Chen 129  
 Thiell, G. 2, 93  
 Tighe, W. 106  
 Tong, K. 329  
 Trail, J. A. 290  
 Trammell, G. T. 394  
 Trebes, James E. 310, 350  
 Trevor, D. J. 378  
 Trickl, T. 411  
 Valeo, E. J. 116, 251  
 Van Woerkom, L. D. 378  
 Villagran Muinz, M. 99  
 Vladimirsky, Y. 274, 325  
 Voorhees, D. 116  
 Vrakking, M. J. J. 411  
 Wallenstein, R. 175  
 Wang, X. 202  
 Wantuck, P. J. 329  
 Watanabe, M. 167  
 Watanabe, S. 167  
 Wellegehausen, B. 163  
 Wendin, G. 246  
 Westenskow, G. 202  
 Whelan, D. A. 2, 371  
 Whitten, B. 93  
 Willi, O. 194  
 Wormell, P. M. J. H. 339  
 Wosinski, L. 327  
 Wouters, A. 116  
 Xu, Zhi-zhan 326  
 Yamanaka, C. 47, 141  
 Yamanaka, M. 47, 137  
 Yashiro, Hidehiko 154  
 Yin, G. Y. 13  
 Yoshida, Kunio 184  
 Young, J. F. 13  
 Yu, Junhua 129  
 Zhang, Guoping 69  
 Zhang, Zheng-quan 326